



Analyse structurale des complexes méiotiques formés par BRCA2-HSF2BP et leurs partenaires

Rania Ghouil

► To cite this version:

Rania Ghouil. Analyse structurale des complexes méiotiques formés par BRCA2-HSF2BP et leurs partenaires. Structural Biology [q-bio.BM]. Université Paris-Saclay, 2022. English. NNT : 2022UP-ASQ044 . tel-03976917

HAL Id: tel-03976917

<https://theses.hal.science/tel-03976917>

Submitted on 7 Feb 2023

HAL is a multi-disciplinary open access archive for the deposit and dissemination of scientific research documents, whether they are published or not. The documents may come from teaching and research institutions in France or abroad, or from public or private research centers.

L'archive ouverte pluridisciplinaire **HAL**, est destinée au dépôt et à la diffusion de documents scientifiques de niveau recherche, publiés ou non, émanant des établissements d'enseignement et de recherche français ou étrangers, des laboratoires publics ou privés.

Structural analysis of meiotic complexes formed by BRCA2-HSF2BP and their partners

*Analyse structurale des complexes méiotiques formés par BRCA2-HSF2BP
et leurs partenaires*

Thèse de doctorat de l'université Paris-Saclay

École doctorale n°569 : Innovation Thérapeutique : du fondamental à l'appliqué (ITFA)
Spécialité de doctorat : Biochimie et Biologie structurale
Graduate School : Santé et médicaments Référent : Faculté de pharmacie

Thèse préparée dans l'unité de recherche **Institute for Integrative Biology of the Cell (I2BC) (Université Paris-Saclay, CEA, CNRS)**, 91198, Gif-sur-Yvette, France,
sous la direction de **Sophie ZINN-JUSTIN**, directrice de recherche et sous le co-encadrement de **Marie-Hélène LEDU**, directrice de recherche

Thèse soutenue à Paris-Saclay, le 27 octobre 2022, par

Rania GHOUIL

Composition du Jury

Herman VAN TILBEURGH Pr., Université Paris Saclay	Président
Pierre-Damien COUREUX Pr., Université Lyon	Rapporteur & Examineur
Laurent MAVEYRAUD Pr., Université Toulouse III Paul Sabatier	Rapporteur & Examineur
Thomas ROBERT Dr., Centre de Biochimie Structurale Montpellier	Examineur
Sophie ZINN-JUSTIN Dr., CEA Saclay	Directrice de thèse

Titre : Analyse structurale des complexes méiotiques formés par BRCA2-HSF2BP et leurs partenaires

Mots clés : Cancer du sein, Stabilité du génome, Recombinaison Homologue en méiose, Biologie structurale, Cryo-EM

Résumé : BRCA2 est une protéine de réparation de l'ADN de grande taille (3418 acides aminés), mutée chez des patients atteints de cancers du sein, des ovaires et de la prostate. L'absence de BRCA2 entraîne également une infertilité. BRCA2 est essentielle pour la recombinaison homologue, un processus central à la réparation de l'ADN et la méiose. HSF2BP, un partenaire récemment identifié de BRCA2, est largement exprimé à la fois dans certaines cellules cancéreuses et dans les cellules méiotiques.

Au cours de ma thèse, j'ai caractérisé l'interaction entre BRCA2, HSF2BP et plusieurs autres protéines impliquées dans la recombinaison homologue méiotique. En utilisant divers outils biophysiques et biochimiques, j'ai pu décrire les interfaces entre ces protéines à une résolution atomique. Le complexe entre un fragment de BRCA2 et HSF2BP forme une structure 3D particulièrement inhabituelle en forme d'anneau. La fonction et le mode de régulation de ce complexe ne sont pas encore totalement compris.

Title: Structural analysis of meiotic complexes formed by BRCA2-HSF2BP and their partners

Keywords: Breast cancer, Genome Stability, Meiotic Homologous Recombination, Structural biology, Cryo-EM

Abstract: BRCA2 is a large DNA repair protein (3418 amino acids), which is mutated along its entire length in patients with breast, ovarian, and prostate cancers. BRCA2 deficiency also causes infertility. BRCA2 is essential for homologous recombination (HR), a process central to DNA repair and meiosis. HSF2BP, a recently identified BRCA2 partner, is widely expressed both in some cancer cells and in meiotic cells. Deletion of HSF2BP causes male infertility.

During my Ph.D. thesis, I characterized the interaction between BRCA2, HSF2BP, and several other proteins involved in meiotic HR. Using various biophysical and biochemical tools, I was able to describe the interfaces between these proteins at an atomic resolution. The complex between a BRCA2 fragment and HSF2BP forms a particularly unusual 3D structure with a ring shape. The function and mode of regulation of this complex are not completely understood yet.

Acknowledgement

This PhD project was carried out in the Structural Biology and Radiobiology Laboratory of the CEA Saclay. This manuscript is the result of many challenges and work that required the help and collaboration of several people. Each of my interactions has been very rewarding, and I have received tireless technical and moral support from all of them.

I sincerely thank all the members of my doctoral committee who took the time to evaluate this thesis: Pr. **Van Tilbeurgh**, Pr. **Coureux**, Pr. **Maveyraud**, Dr. **Robert** and Dr. **Zelensky**.

This work would not have been possible without the support of my thesis director and supervisor, **Dr. Sophie Zinn Justin** who gave me this opportunity and was my guide for these years. Thank you for your enthusiasm and motivation, for always showing devotion to your job. Thank you for teaching me how to work in science, for your availability, for your listening, for giving me suggestions on how to proceed, and for facing so many "everyday" problems. I thank you for your trust and for how you managed to give me more self-confidence.

Dr. **Marie-Hélène Le Du**, thank you for having co-directed my PhD project. Thank you for the X-ray crystallography training, for the interesting discussions, for the help and for all the support.

Many thanks to Dr. **Simona Miron**, with whom I shared this project. It was always interesting to discover and discuss good and bad results with you, thank you for the time, the help, and the good advice.

Before and during my PhD, I was fortunate to work with Dr. **François-Xavier Theillet**, who taught me almost everything I know about biochemistry and NMR spectroscopy. I thank you for your advice, for your availability, for your listening. You have guided me through these years in the lab with a lot of patience, for which I will be eternally grateful.

Thank you to Dr. **Pierre Legrand**, who provided advices and valuable inputs throughout my PhD project. Never reluctant to participate, and always a great help, you allowed us to overcome crucial difficulties during the project.

I also thank Dr. **Virginie Ropars** for her help in making important advances in the project possible, and for guiding me through many techniques in the laboratory.

Thank you to **Ana Arteni, Malika Ould Ali and Jean-Marie Winter** for their great help in the electron microscopy experiments and their valuable contribution to this project.

Finally, I would like to sincerely thank Dr. **Alex Zelensky** and his team at the Erasmus Center in Rotterdam. Without them, this study would not have had this multidisciplinary character. The collaboration was very dynamic, and I am very grateful for all the time spent in discussions that allowed me to develop these transdisciplinary skills. While the pandemic prevented us from working under normal conditions, you were able to find the time to conduct these experiments that were so important to the progress of the project. I thank you very much.

I would also like to thank all the current and former lab members who helped make this journey happier: **Murielle** “Mumu”, who was always kind and caring; **Manon**, **Agathe** for the good old times and their constant helpfulness. **Chafiaa**, **Amel** and **Fatima** for the laughs, the encouragement, and great times.

Paloma for her joy and support, **Sayma**, **YingYue**, **Hélène**, **Jessica**, **Liza**, **Anastasia**, and all the lab mates for their care and the work and non-work-related chats.

A special love note to my **Fouad**, I could never have done this without you and your unconditional support.

While this experience is coming to an end, I know that without the unwavering support of my family, I would never have been able to complete this stage. I thank my mother **Rebah**, my father **Jamel**, my brothers **Koussay** and **Elyes**, and my grandmother **Jedda** for always being with me no matter what, for their prayers, for their love, and for always being so proud of me.

Thank you to all my family, my friends, near and far. And finally, I would like to thank a person who is no longer with us, but who inspired and encouraged me for many years, **Naima**, to whom I dedicate this work.

Résumé français

BRCA2 est l'un des gènes de prédisposition au cancer les plus étudiés. La protéine codée par ce gène, BRCA2, a un haut poids moléculaire (3418 acides aminés), et est mutée indifféremment sur toute sa séquence chez des patients atteints de cancers du sein, des ovaires et de la prostate. L'absence de BRCA2 entraîne également une infertilité, chez la femme comme chez l'homme. BRCA2 est essentielle pour la recombinaison homologue (RH), un processus central à la réparation de l'ADN et la méiose. Au cours de la RH, BRCA2 agit comme chargeur de la recombinase RAD51 sur l'ADN simple brin. Les filaments RAD51-ADN simple brin contribuent ensuite à la recherche des brins d'ADN homologues, sur la chromatide sœur (en mitose) ou le chromosome homologue (en méiose), afin de promouvoir la réparation par RH. Nos collaborateurs Prof R. Kanaar et Dr A. Zelensky (Rotterdam, Pays-Bas) ont identifié un nouveau partenaire de BRCA2, HSF2BP, qui est largement exprimé à la fois dans certaines cellules cancéreuses et dans les cellules méiotiques. Des mutations dans HSF2BP causent des défauts de fertilité, la perte d'HSF2BP bloque la RH pendant la spermatogenèse.

D'un point de vue moléculaire, BRCA2 est principalement désordonnée, comme montré par RMN (Julien, Ghouil et al., *Biomolécules* 2021). Au cours de ma thèse, j'ai caractérisé l'interaction entre BRCA2, HSF2BP et plusieurs autres protéines impliquées dans la RH méiotique. En utilisant divers outils biophysiques et biochimiques, j'ai d'abord identifié un fragment de 51aa de BRCA2 responsable de la liaison à HSF2BP. J'ai résolu la structure 3D du complexe formé par les domaines d'interaction de BRCA2 et HSF2BP par cristallographie aux rayons X, en collaboration avec le Synchrotron SOLEIL (Ghouil et al., *Nat Commun* 2021). J'ai observé qu'un motif répété de 23 aa dans BRCA2 est capable de se lier à deux domaines armadillo de HSF2BP, et j'ai montré que deux peptides de BRCA2 se lient simultanément à quatre domaines armadillo de HSF2BP. Cette interaction est caractérisée par une affinité élevée ($K_d \sim 1$ nM) et conduit à la formation d'un tétramère de domaines armadillo. La délétion du premier motif de liaison dans BRCA2 entraîne une diminution de l'affinité entre BRCA2 et HSF2BP d'un facteur 1000 et empêche la tétramérisation du domaine armadillo de HSF2BP. Une analyse *in vitro* plus poussée de l'interaction entre le motif répété de BRCA2 et la protéine HSF2BP entière a révélé l'assemblage d'un grand oligomère de 900 kDa, dont la structure 3D a été caractérisée par cryo-EM (Ghouil et al., en cours de publication). Un fragment de BRME1, un partenaire de HSF2BP, inhibe la formation de cet oligomère.

La fonction de l'interaction entre BRCA2, HSF2BP et BRME1 a été étudiée à la fois dans des cellules cancéreuses et en méiose par nos collaborateurs. La surexpression de HSF2BP dans les cellules cancéreuses entraîne la dégradation de BRCA2 dans des conditions spécifiques de dommages à l'ADN, et ce processus n'est pas observé lorsque HSF2BP et BRME1 sont exprimés, ce qui suggère que la formation du grand complexe BRCA2-HSF2BP est obligatoire pour déclencher la dégradation de BRCA2 (Ghouil et al., en cours de publication). En méiose, l'assemblage de l'oligomère BRCA2-HSF2BP pourrait augmenter la concentration locale de

BRCA2 au niveau de la cassure double-brin. Cependant, cet oligomère n'est pas essentiel à la méiose, car les souris exprimant une protéine BRCA2 délétée d'un des motifs de liaison à HSF2BP restent fertiles (Ghouil et al., Nat Commun 2021).

Dans l'ensemble, ce travail fournit une description structurale de l'interaction entre une région intrinsèquement désordonnée de BRCA2 et de son partenaire HSF2BP, et révèle comment d'autres régions protéiques désordonnées, comme l'extrémité C-terminale de BRME1, sont capables de réguler la formation du complexe BRCA2-HSF2BP. La fonction de ce grand complexe, qui est hautement conservé et régulé, n'est pas encore bien comprise et sera le sujet d'études futures.

TABLE OF CONTENTS

INTRODUCTION	15
Chapter 1. DNA DAMAGE AND REPAIR PATHWAYS	16
I. Importance of the DNA Damage Response (DDR) in maintaining genome integrity	16
II. DNA Double-strand break (DSB) repair pathways	19
1. NHEJ	20
2. HR	20
3. The balance between NHEJ and HR	22
Chapter 2. MEIOSIS.....	24
I. Generality	24
1. The meiotic divisions and the importance of prophase I	25
a. The different stages of meiotic division	25
b. Role of HR in meiosis.....	28
2. Mitotic Vs Meiotic Homologous Recombination	28
a. Major differences in mitotic vs meiotic HR processes.....	29
b. HR mechanism in meiosis	29
i. DSBs formation	29
α. SPO11 and its partner TOPOVIBL	29
ii. Filament formation	30
α. RAD51 and DMC1.....	30
β. MEIOB-SPATA22	31
γ. BRCA2.....	32
δ. HSF2BP-BRME1	33
3. Resolution of the Holliday junctions	34
4. Impact of BRCA2 and its partners on fertility	34
Chapter 3. BRCA2 & MEIOSIS SPECIFIC PARTNERS: STRUCTURE AND FUNCTIONS.....	37
I. General properties of BRCA2	37
1. BRCA2 is a tumor suppressor	37
2. BRCA2 is mainly disordered.....	37
3. What is the oligomeric state of BRCA2?.....	39
4. How does BRCA2 interact with its partners?.....	42
a. DSS1	43
b. RAD51	44
c. DMC1.....	46
d. PALB2	48
e. PLK1	49
5. The recently discovered BRCA2 partner HSF2BP	51
a. BRCA2 and HSF2BP interact through an evolutionary-conserved interface	51
b. HSF2BP is mutated in fertility diseases.....	56
c. HSF2BP is a Cancer Testis Antigen	57
d. HSF2BP stability depends on its meiotic partner BRME1	60
e. HSF2BP also interacts with the complex formed by RPA, SPATA22, and MEIOB	64
Thesis project and purpose.....	68
MATERIAL & METHODS	70
I. Biochemistry	71
1. Commercial products	71
2. Protein expression vectors	71

3. Protein sequences.....	72
4. Competent bacteria production.....	74
5. Vectors transformation in <i>E. coli</i>	74
6. Protein expression	75
a. In rich medium.....	75
b. In minimal medium + ¹⁵ N, ¹³ C labeling.....	75
c. In minimal medium + selenomethionine labeling.....	76
7. Optimal protein expression conditions	76
8. Insect cell expression	77
a. Insect cell transfection	77
b. Protein expression.....	78
9. Protein purification	79
a. Purification of all BRCA2 constructs produced in bacteria	79
b. Purification of the BRCA2 fragment co-expressed with DSS1 in insect cells.....	80
c. Purification of HSF2BP	80
d. Purification of H2 and H3.....	81
e. Purification of SPATA22.....	81
9. Peptides.....	82
10. Figures	82
II. Methods	83
1. X-ray crystallography	83
a. Crystallization and data collection	84
b. Structure determination and data refinement.....	85
2. NMR spectroscopy.....	86
a. NMR for protein-protein interactions.....	86
b. Assignments of the NMR signals.....	87
3. Isothermal Titration Calorimetry ITC	88
4. SEC- Multi-Angle Light Scattering (MALS)	89
5. SEC-SAXS Small angle X-ray scattering (SAXS).....	90
6. Tycho NT6.....	92
7. AlphaFold 2.....	92
8. Electron Microscopy.....	93
a. Complexes formation.....	94
b. Negative-Staining Electron Microscopy.....	95
c. Cryo-EM.....	95
α. Grid preparation	96
β. Data acquisition	98
χ. Data processing	98
RESULTS	100
Chapter 1. BRCA2 interacts with a Testis Cancer Antigen.....	101
Preamble.....	101
1. Sample optimization	102
a. HSF2BP	102
b. H3 (or armadillo domain) and H2.....	103
c. BRCA2.....	104
2. Sample characterization.....	108
a. SEC- MALS.....	108
b. SEC- SAXS	108
3. Molecular characterization of the interaction BRCA2/HSF2BP.....	109
a. NMR analysis.....	109
b. Isothermal Titration Calorimetry	111
c. X-ray crystallography.....	111
4. Localization of the HSF2BP mutations found in patients with POI	114

<i>Article: BRCA2 binding through a cryptic repeated motif to HSF2BP oligomers does not impact meiotic recombination.....</i>	<i>116</i>
<i>Chapter 2. Ring complex formation</i>	<i>143</i>
Preamble	143
1. Attempt 1: crosslinker	145
2. Attempt 2: increase the complex concentration	146
3. Glacios DataSet	147
a. Cryo-EM grid preparation and data collection.....	147
b. Data processing	148
4. Krios DataSet 1	152
a. Cryo-EM grid preparation and data collection (Krios DataSet1).....	152
b. Data processing	152
5. Krios DataSet 2	154
a. Cryo-EM grid preparation and data collection (Krios dataSet2)	154
b. Data processing	154
<i>Article: BRCA2-HSF2BP Oligomeric Ring Disassembly by BRME1 Promotes Homologous Recombination.....</i>	<i>156</i>
<i>Chapter 3. Characterization of the interaction between BRCA2-HSF2PB and BRME1 ..</i>	<i>198</i>
I. Preamble	198
<i>Chapter 4. Characterization of the interaction between HSF2BP and SPATA22</i>	<i>202</i>
Preamble	202
1. Gel filtration chromatography	204
2. AlphaFold	205
3. Thermal stability of the armadillo domain in the presence of SPATA22	206
4. Isothermal Titration Calorimetry	207
a. First preliminary tests using H3 and SPATA22short	207
b. Interaction between HSF2BP and SPATA22N at 3 different temperatures.....	209
c. Interaction between H2 and SPATA22N	209
5. X-ray crystallography	210
<i>Chapter 5. BRCA2 CTD insect cells</i>	<i>212</i>
<i>DISCUSSION & PERSPECTIVES</i>	<i>215</i>
I. About BRCA2 and HSF2BP	216
II. The 3D structure of BRCA2 F15X bound to HSF2BP is original	217
1. The armadillo domain tetramerizes upon binding to BRCA2 F15X	217
2. How does the armadillo domain specifically recognize the BRCA2 motif and which other proteins contain this motif?	217
3. HSF2BP forms a ring-shaped complex upon binding to BRCA2.....	219
III. What is the function of the interaction between BRCA2 and HSF2BP?.....	220
IV. HSF2BP-BRCA2 ring assembly is regulated by BRME1 and SPATA22	222
V. Can these interactions be regulated by phosphorylation of intrinsically disordered regions in BRCA2, BRME1, and SPATA22?	223
<i>APPENDIX.....</i>	<i>225</i>
<i>REFERENCES</i>	<i>248</i>

LIST OF FIGURES

Figure 1. Estimated frequencies of DNA lesions and associated mutations.	16
Figure 2. Scheme of the major DNA lesions experienced by cellular genomic DNA.....	17
Figure 3. NHEJ and HR mechanisms of DSB repair.	19
Figure 4. <i>Schematic description of the HR mechanism.</i> (Dueva and Iliakis 2013).....	22
Figure 5. Meiotic and mitotic cell divisions.....	25
Figure 6. Stages of prophase I in meiosis.....	27
Figure 7. Role of HR in promoting the interaction between homologs and the formation of crossovers.	28
Figure 8. Core steps of mitotic and meiotic HR mechanisms.	33
Figure 9. The human MEIOB protein.	35
Figure 10. Disorder propensity as a function of BRCA2 residue number.	38
Figure 11. Conservation of BRCA2 residues calculated from an alignment of BRCA2 sequences from fish to human.	38
Figure 12. 3D reconstruction obtained from the analysis of negative-staining EM images ...	40
Figure 13. Impact of RAD51 binding on BRCA2 oligomeric state.	42
Figure 14. Crystal structures of BRCA2 DBD ,bound to either DSS1 (right) or DSS1 and a small ssDNA (left).	44
Figure 15. Crystal structure of a human complex between BRCA2 BRC repeat 4	46
Figure 16. Cryo-EM maps and models of DMC1-ssDNA.....	47
Figure 17. 3D structure of the BRCA2 peptide from K21 to A39 (in red) bound to PALB2 WD40 domain (in grey).	48
Figure 18. PLK1 interacts with BRCA2pT207.....	50
Figure 19. Identification of HSF2BP as a meiotic chromosomal protein in mice spermatocytes.	52
Figure 20. Identification of HSF2BP as a BRCA2-Interacting Protein.	54
Figure 21. Schematic representation of HSF2BP.....	55
Figure 22. Evolutionary conservation of the HSF2BP binding region of BRCA2 (F0: 2212- 2342).....	55
Figure 23. Expression levels of HSF2BP and Gapdh (a loading control) in different tissues.....	56
Figure 24. Expression of the meiosis-specific factor BRME1.....	61
Figure 25. Chromosome spreads of WT spermatocytes were stained for BRME1,SYCP3, and SYCP1.....	62
Figure 26. Characterization of the BRCA2-HSF2BP-BRME1 ternary complex.....	64
Figure 27. Models for the interactions between MEIOB, SPATA22 and RPA.....	65
Figure 28. Principle of protein X-ray crystallography.	84
Figure 29. P(r) functions for geometric bodies	91
Figure 30. Schematic operation principles of a transmission-and a scanning electron microscope (TEM).	96
Figure 31. Representative micrographs corresponding to outcomes from the sample vitrification step.....	97
Figure 32. General workflow of the single particle image processing.....	98
Figure 33. Last step of HSF2BP purification.	103
Figure 34. Last step of H3 purification.	104
Figure 35. The BRCA2 constructs used for my PhD project.	105

Figure 36. Example of optimization of the overexpression of a BRCA2 fragment in <i>E. coli</i> BL21 (DE3) Star	105
Figure 37. Last step of the purification of the BRCA2 fragment F0.....	106
Figure 38. Last step of the purification of the BRCA2 fragment F15X.....	107
Figure 39. SEC-SAXS curve.....	108
Figure 40. NMR identification of the H3 interacting region of BRCA2.	110
Figure 41. Complex formation and diffracted crystals.....	113
Figure 42. Localization of the POI-associated mutations in HSF2BP.	115
Figure 43. Negative Staining Electron Microscopy images of the HSF2BP-BRCA2 F15X complex.	144
Figure 44. Cross-linking of the complex HSF2BP - BRCA2 F15X with glutaraldehyde. ...	145
Figure 45. Last step of purification of the HSF2BP-F15X complex.....	147
Figure 46. A cryo-EM reconstruction calculated from the first Glacios dataset.....	149
Figure 47. 3D reconstructions of the rings.	151
Figure 48. Data collection and processing.	153
Figure 49. Data collection and processing.	155
Figure 50. Purification of HSF2BP+BRME1-M.....	199
Figure 51. SEC-SAXS experiment performed on the HSF2BP-BRME1-M complex.....	200
Figure 52. SEC-MALS of the HSF2BP-BRME1-M complex.	201
Figure 53. <i>In vitro</i> preliminary data on the interaction between HSF2BP and SPATA22. .	203
Figure 54. Analysis of the interaction between SPATA22 and HSF2BP/H3 by SEC.....	204
Figure 55. AlphaFold model of the complex between SPATA22 and H3.....	205
Figure 56. Thermal stability assays performed on the HSF2BP armadillo domain in the presence of SPATA22N.	207
Figure 57. ITC measurement of the interaction between H3 and SPATA22short.....	208
Figure 58. ITC measurement of the interaction between H3 and SPATA22long.....	208
Figure 59. Calorimetry measurements of the interaction between HSF2BP and SPATA22N peptide.	209
Figure 60. Calorimetry measurements of the interaction between (H2) and SPATA22N peptide.	210
Figure 61. Last step purification of BRCA22150-3197.....	212

LIST OF TABLES

Table 1. Selected cancer-testis antigens/genes.	58
Table 2. Plasmids for expression of BRCA2 constructs.	71
Table 3. Plasmids for expression of HSF2BP constructs	72
Table 4. Plasmids for expression of SPATA22 constructs.....	72
Table 5. Composition of M9 media.....	75
Table 6. Optimal protein expression conditions in bacteria.	76
Table 7. BRCA2 construct used for insect cell expression.	77
Table 8. Molecular weights and molecular extinction coefficients after cleavage (TEV or Thrombin) of proteins produced in this study.....	79
Table 9. Summary of all peptides used during this thesis	82

ABBREVIATIONS

AE	axial elements
AP	apurinic/apyrimidinic sites
BER	base excision repair
BIC	cancer information core
Bme	Beta mercaptoethanol
BRCA2	Breast Cancer susceptibility protein/gene 2
CE	central Elements
CEA	Commissariat à l’Energie Atomique
CTD	C-Terminal Domain
DBD	DNA Binding Domain
DSB	Double strand DNA break
dsDNA	Double-strand DNA
EDTA	Ethylenediaminetetraacetic acid
FL	Full Length
HEPES	4-(2-hydroxyethyl)-&-piperazineethansulfonic acid
COs	crossovers
CTA	Cancer Testis Antigen
CtIP	C-terminal-binding protein-interacting protein
DDR	Damage Response
Dpp	day post-partum
EM	Electron microscopy
EP	electroporation
GFP	Green folded protein
HBD	HSF2BP-binding domain
HDR	Homology-directed repair
HJs	Holliday junctions
HMQC	Heteronuclear Multiple-Quantum Correlation
HSQC	Heteronuclear Single-Quantum Correlation
I2BC	Institut de Biologie Intégrative de la Cellule
IPTG	Isopropyl b-D-A-thiogalactopyranoside
ITC	Isothermal Titration Calorimetry
LB	Luria Broth medium
M9	Minimum medium
MS	Mass Spectrometry
ON	Overnight
PBS	Phosphate Buffer Saline
PDB	Protein Data Bank
PMSF	Phenylmethylsulfonyl fluoride
PTM	Post-Translational Modification
RT	Room temperature
SDS-PAGE	Sodium Dodecyl Sulfate-Polyacrylamide Gel Electrophoresis SEC Size

SPOT-dis	Sequence-based Prediction Online Tools for disorder
TEV	Tobacco Etch Virus endopeptidase
HR	homologous recombination
HSF2	Heat shock factor2
IDRs	Intrinsically Disordered
MAMERR	MAle MEiosis Recombination Regulator
MEILB2	MEIotic Localizer of Brca2.
mESCs	mouse embryonic stem cells
MMC	mitomycin C
MMEJ	microhomology-mediated end-joining
MMR	mismatch repair
NHEJ	non-homologous end-joining
NOA	nonobstructive azoospermia
OB fold	oligosaccharide binding folds
PALB2	partner and localizer of BRCA2
PBD	Polo-box domain
PLK1	Polo-like kinases
POI	Primary Ovarian Insufficiency
RNS	Reactive Nitrogen Species
ROS	Reactive Oxygen Species
SC	synaptonemal complex
SFM	scanning force microscopy
SSA	single-strand annealing
SSB	Single Strand Break
ssDNA	single-strand DNA breaks
SYCP	synaptonemal complex protein
UV	ultraviolet
Wt	Wild Type

INTRODUCTION

Chapter 1. DNA DAMAGE AND REPAIR PATHWAYS

I. Importance of the DNA Damage Response (DDR) in maintaining genome integrity

Genome instability is defined as a higher than normal rate of mutation. It is a source of genetic diversity and natural selection. However, it can also have catastrophic consequences, causing age-related diseases such as cancers. Thus, the maintenance of genomic integrity is important for the survival of organisms. The DNA molecule is the template for the essential processes of replication and transcription. Even before the discovery of the double helix in 1953, it was known that DNA is highly vulnerable to chemical modification, which can cause numerous lesions ([Anthony Tubbs and André Nussenzweig, 2017](#)).

It has been estimated that each human cell is subjected to approximately 70,000 lesions per day ([Lindahl and Barnes, 2000](#)) (**Figure 1**). The majority of these lesions (75%) are single-strand DNA (ssDNA) breaks, which are caused by the cellular metabolism. When unrepaired, ssDNA breaks can be converted to DNA double-strand breaks (DSBs), which although much less frequent, are more dangerous.

Damage	Cytosine deamination	Depurination/depyrimidination	8-oxoG	SSB	DSB
Estimated frequency (per cell per day)	192	12,000/600	2,800	55,000	25
Predominant mutation	C>T	Substitutions	G>T	Substitutions, DBSs	Chromosome rearrangements

Figure 1. Estimated frequencies of DNA lesions and associated mutations.
([Anthony Tubbs and André Nussenzweig, 2017](#)).

DNA lesions can come from both endogenous and exogenous sources of DNA damage. Endogenous sources include spontaneous errors during DNA replication such as base hydrolysis, which leads to the formation of an abasic site and finally provokes base pair substitutions (Lindahl et al., 1993). Similarly, Reactive Oxygen Species (ROS) and Reactive Nitrogen Species (RNS) are generally produced as byproducts of multiple physiological activities in various subcellular sites (Cadet et al., 2013). These chemical compounds are responsible for a variety of DNA lesions derived from oxidative stress, including the generation of apurinic/apyrimidinic sites (AP), single- or double-stranded breaks, and base substitutions (Van Houten et al., 2017). Both ROS and RNS are considered as endogenous sources of DNA-damaging agents.

Exogenous sources, such as ultraviolet (UV) light or ionizing radiations (IR, X-rays), can also cause lesions in the DNA. The main consequence of UV rays on the DNA structure is the formation of covalent links between adjacent pyrimidine bases (photodimers), whereas IR induces base modifications, SSBs, and DNA double-strand breaks (DSBs) by direct ionization or indirect ROS production. Other exogenous sources of DNA damage are chemical agents used in cancer chemotherapy (alkylating agents, crosslinking agents such as mitomycin C (MMC) and cisplatin), or man-produced mutagenic chemicals (ex. polycyclic aromatic hydrocarbons or aldehydes in cigarette smoke) (Ciccia et al., 2010).

To preserve genomic integrity, cells have developed an arsenal of DNA healing strategies called the DNA damage response (DDR). These strategies target various types of damage and initiate the appropriate repair pathways or induce cell cycle arrest and/or apoptosis if not reparable (Figure 2).

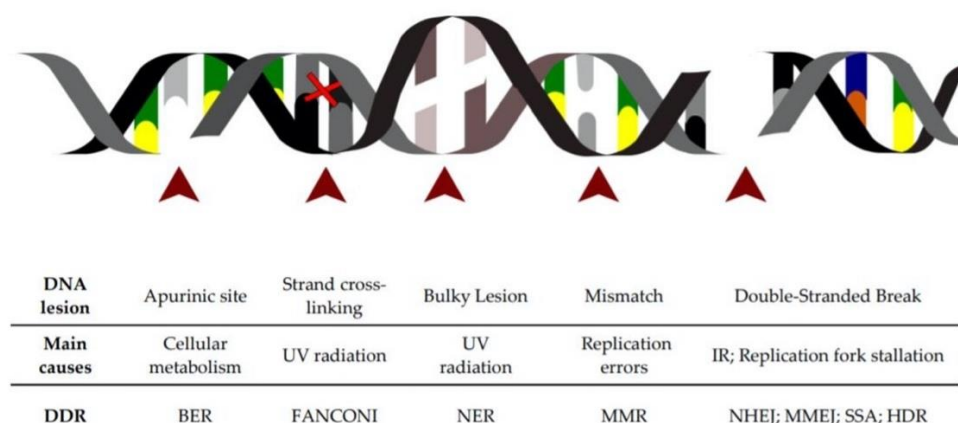


Figure 2. Scheme of the major DNA lesions experienced by cellular genomic DNA.

The table indicates the type of DNA lesion depicted in the figure above, its leading cause, and the DNA repair pathway engaged for its resolution (adapted from [Carusillo and Mussolino, 2020](#)).

Within the DNA repair pathways protecting cells from the various injuries to which they are exposed, we can cite: the pathway that repairs modified bases, base excision repair (BER) ([Lindahl et al., 2012](#)); the pathway that detects and removes misincorporated bases during DNA replication, mismatch repair (MMR) ([Modrich et al., 2006](#)); and the pathway for removing bulky adducts in DNA, nucleotide excision repair (NER). Each of these DNA repair pathways excises a damaged region and inserts new bases to fill the gap. Other pathways repair the highly toxic double-strand breaks: non-homologous end-joining (NHEJ), microhomology-mediated end-joining (MMEJ), single-strand annealing (SSA) and homology-directed repair (HDR or HR). The most studied of these pathways, NHEJ and HR, will be detailed in the next section.

If a DNA damage is not repaired, it may cause genomic instability and permanent mutations that are passed onto the next generations of cells. Genome instability is one of the cancer hallmarks ([Hoeijmakers et al., 2009](#); [Andor et al., 2017](#); [Hanahan and Weinberg, 2011](#)). Large scale sequencing and bioinformatics approaches have revealed a remarkable diversity of somatic mutations, as well as specific signatures of DNA damage and errors in DNA repair, in various cancers. The classic mutator hypothesis ([Loeb et al., 1974](#); [Nowell et al., 1976](#)) postulates that errors in DNA repair genes leads to genome instability, which in turn increases mutation rates at other genomic sites, leading to cellular transformation. More generally, mutations may occur if specific DNA repair and/or checkpoint pathways are inactivated, if DNA editing enzymes are deregulated, or if the damage load overwhelms DNA restorative capacity ([Tubbs & Nussenweig, 2017](#)). Whole-genome sequences of breast cancers have revealed deficiencies in both HR and MMR ([Morganella et al., 2016](#); [Nik-Zainal et al., 2016](#)). However, it remains puzzling why malfunction of DNA repair genes is associated with organ-specific cancers despite their ubiquitous expression and function in all cell and tissue types.

II. DNA Double-strand break (DSB) repair pathways

Among DNA lesions, DSBs are considered as extremely toxic and are the most complicated to repair (Chatterjee and Walker, 2017; Dexheimer et al., 2013). Efficient resolution of these lesions is a major challenge for the cell.

DSBs can be repaired by several pathways. Two of them are considered as the main DSB repair pathways: the homology-directed repair (HDR) also known as homologous recombination (HR) and the classical non-homologous end-joining (NHEJ) (Figure 3). Repair by HR depends on the recombinase RAD51, except in a specific type of HR called single-strand annealing (SSA), in which complementary strands of the homologous regions flanking the DSB anneal, producing an intermediate with two non-homologous 3'-ended tails that must be removed for new DNA synthesis and ligation to occur (Motycka et al., 2004; Symington et al., 2002). Classical NHEJ repairs DSBs by juxtaposing and ligating DNA ends, using very little (1-4 nt) or no complementary base pairing. More recently, alternative non-homologous end-joining pathways were identified, including the microhomology-mediated end-joining (MMEJ), which repair DSBs by annealing 2-20 bp stretches in case of overlapping bases flanking the DSB (Sfeir and Symington, 2015; Wang and Xu, 2017).

In the next section, I will give an overview of the two major pathways (Figure 3), focusing most of my attention on HR and its important mediator BRCA2.

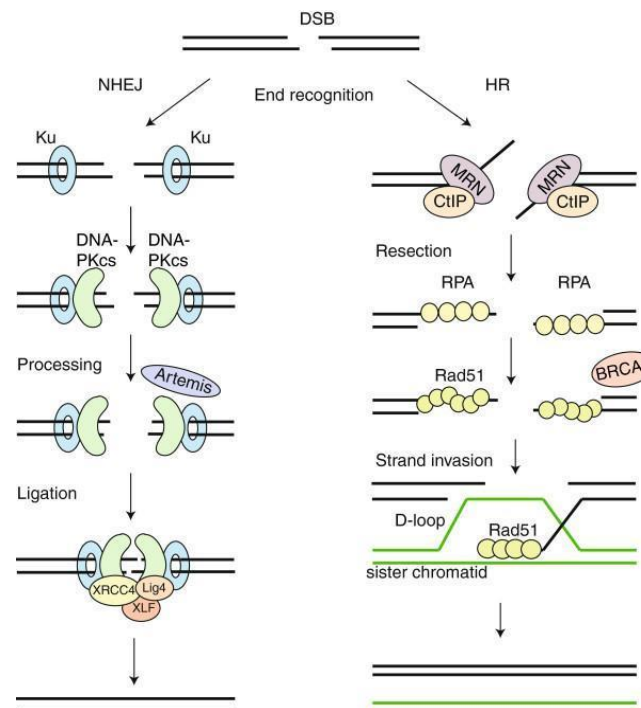


Figure 3. NHEJ and HR mechanisms of DSB repair.

NHEJ) It starts with the recognition of the DNA ends by the Ku70/80 heterodimer, which recruits DNA-PKcs. If the ends are incompatible, nucleases such as Artemis can resect them. The XRCC4-DNA Ligase IV-XLF ligation complex seals the break. **HR**) The MRN-CtIP-complex starts resection on the breaks to generate single-stranded DNA (ssDNA). After resection, the break can no longer be repaired by NHEJ. ssDNA is first coated by RPA, which is subsequently replaced by RAD51 with the help of BRCA2. The RAD51 nucleoprotein filaments mediate strand invasion on the homologous template. Extension of the D-loop and capture of the second end lead to repair (Adapted from [Brandsma et al., 2012](#)).

1. NHEJ

The NHEJ is responsible for most of the DSB repair events in higher eukaryotes ([Lieber et al., 2010](#)) and is considered to be a relatively simple pathway because it does not rely on any template and can remain active throughout the entire cell cycle. 60% of the breaks induced by genotoxic agents are repaired by NHEJ in vertebrates.

There are generally three phases in this DNA repair pathway: recognition of the break, maturation, and ligation.

Firstly, NHEJ starts with the recruitment of the Ku70/80 heterodimer to the DSBs DNA ends. Ku70/80 can slide inward to allow binding of other proteins to the DNA ends ([Walker et al., 2001](#)). For example, the DNA-PKcs (catalytic subunit of the DNA-dependent protein kinase) is recruited to the Ku70/80-DNA complex ([Hammel et al., 2010](#)). Indeed, the Ku70/80-DNA interaction induces a conformational change in the C-terminal extremities of Ku70 and Ku80 that promotes its binding to DNA-PKcs and the activation of this enzyme ([Lehman et al., 2008](#)). It has been proposed that DNA-PK forms a bridge between the break ends ([Chaplin et al., 2021](#)). Ku70/80 serves as a platform for the recruitment of not only DNA-PKcs but also other proteins involved in the NHEJ pathway, such as XRCC4, XLF (Xrcc4-like factor), WRN (Werner), PAXX (XRCC4 and XLF paralog) and ligase IV ([Ochi et al., 2015](#)). The ligation of the two DNA ends is further performed through the activity of polymerases that support the DNA ligase IV activity when ends are not compatible.

2. HR

While the NHEJ pathway is very efficient for complete break repair, it can be error-prone, whereas the HR pathway is error-free when using the correct homologous sequence,

allowing for more reliable DSB repair. The choice of the repair pathway depends on the cell cycle stage. HR is most active during the S and G2 phases of the cell cycle, when both sister chromatids are present, and one of these chromatids can be used as template to ensure high-fidelity transmission of the genetic information.

The mechanism of HR is based on the use of homologous sequences as templates to form synaptic intermediates through homologous pairing. During the S and G2 phases of the cell cycle, sister chromatids provide homologous sequences so that damage can be repaired reliably without genetic consequences. Homologous chromosomes can also be used as templates during the G1 phase of the somatic cell cycle, but this is mostly avoided because of loss of heterozygosity in this case. The core steps of the molecular machinery (presynaptic, synaptic, and postsynaptic) and the players in HR are conserved in all organisms, from bacteria to humans, as well as some bacteriophages and viruses ([Cromie et al., 2001](#)).

During HR, the first step called “initiation” (or presynaptic step) is the resection of the DNA break by DNA helicases and nucleases to create single-stranded DNA (ssDNA) ([Mimitou et al., 2009](#)). Proteins that take in charge the damaged DNA at this step are the MRN complex (MRE11-RAD50-NBS) and the C-terminal-binding protein-interacting protein (CtIP); these complexes work together to resect the broken ends of the damaged double-stranded DNA and generate 3' single-stranded DNA (ssDNA). Then, the ssDNA is protected by ssDNA-binding proteins (RPA). The breast and ovarian cancer susceptibility protein 1 (BRCA1) recruits PALB2 (Partner And Localizer of BRCA2) ([Zhang et al., 2018](#)), BRCA2, and RAD51, promoting the exchange of RPA by RAD51 ([Jensen et al., 2010](#); [Zhao et al., 2015](#)) (Figure 3). The RAD51 nucleoprotein filaments perform the "homology search, invasion, and strand exchange" (or synapsis) steps, including sequence complementarity search, synaptic complex formation, and mutual DNA strand exchange. During the "DNA strand synthesis and migration," the DNA molecule is elongated by strand synthesis and migration and can disrupt the paired DNA through the action of DNA motor proteins (synthesis-dependent strand annealing - SDSA), or by the capture of the second stabilized end. Finally, in a dissociation (or postsynaptic) step, the joined DNA molecules are separated by nucleolysis or by topological dissolution involving a type IA topoisomerase and a DNA helicase (**Figure 4**).

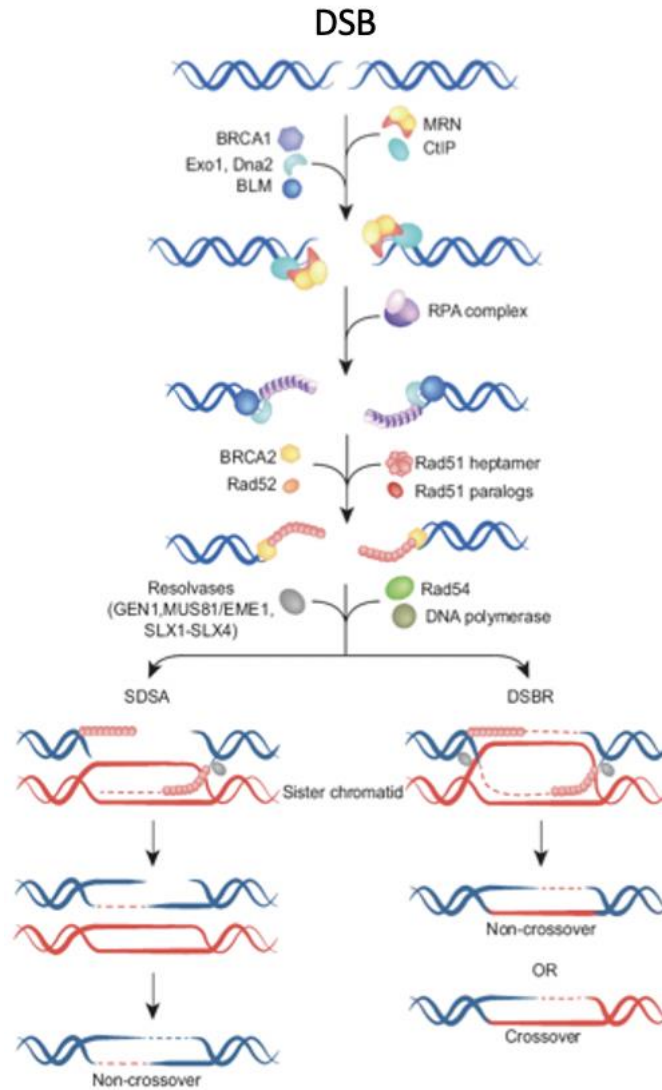


Figure 4. Schematic description of the HR mechanism. (Dueva and Iliakis 2013).

3. The balance between NHEJ and HR

How the cell determines whether to repair of a break by NHEJ or HR remains an active area of research. Choosing between HR and NHEJ involves regulatory factors (Lieber et al., 2010).

One of the main factors is, as mentioned above, the cell cycle phase: if a homologous DNA is not present near the DSB during S/G2, then HR cannot proceed, whereas NHEJ can repair DSBs throughout the entire cell cycle (Her et al., 2018). The sister chromatid is physically very close during the S phase, thereby providing a homology donor for HR.

The second factor that has been well studied is the DSB end structure. For example, in S phase, due to the lack of a NHEJ partner for binding to the DSB ends, DSBs end are mainly repaired by HR. In contrast, in the G2 phase, if DSBs are induced by ionizing radiation, 70% of these DSBs are rapidly repaired by NHEJ ([Shibata et al., 2017](#); [Chapman et al., 2012](#)).

Interestingly, at the beginning of the meiotic prophase I, both mechanisms can proceed with DNA damage repair. In fact, it was first supposed that, at this step, NHEJ is inhibited, and DNA damage repair is performed by HR to ensure genetic exchange between homologous chromosomes. However, it has been recently proposed that in response to exogenously induced DNA damage during the late stages of meiotic prophase I, NHEJ can be activated ([Enguita-Marruedo et al., 2019](#)). This shows how the balance between these two pathways can be regulated by the type of DNA damage during meiotic prophase I.

Chapter 2. MEIOSIS

I. Generality

Meiosis is a central process of sexual reproduction, in which diploid cells are converted into haploid cells. It is remarkably conserved across eukaryotes ([Thomas, L .2016](#)), and consists DNA replication step followed by two consecutive cell divisions. These divisions differ from mitosis in several ways. Mitosis involves the formation of two daughter cells whose genetic content is identical to each other and to that of the mother cell, whereas meiosis involves the decrease from a diploid mother cell ($2n$ chromosomes) to a haploid cell (n chromosomes) (**Figure 5**). Two haploid cells will then fuse during karyogamy, giving rise to a diploid cell containing two copies of the genome.

During sexual reproduction, chromosomal mixing takes place during the first meiotic division through the random distribution of paternal and maternal homologous chromosomes between the daughter cells. Intrachromosomal mixing occurs at the beginning of the first meiotic division as a result of exchanges of genetic information between chromosomes of paternal and maternal origins ([Zickler et al., 2016](#)).

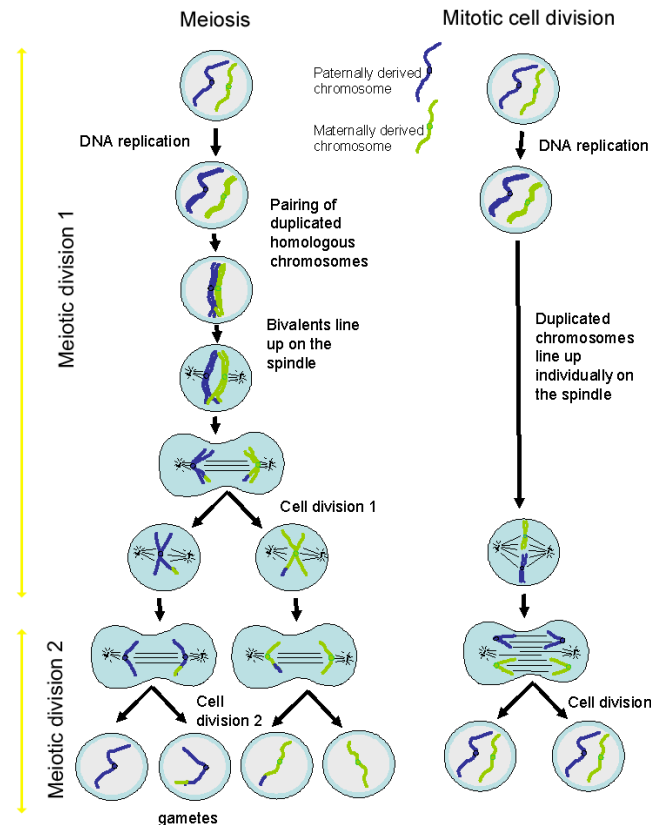


Figure 5. Meiotic and mitotic cell divisions.

(From [Histology Guide](#) © Faculty of Biological Sciences, University of Leeds).

1. The meiotic divisions and the importance of prophase I

a. The different stages of meiotic division

During meiosis, diploid cells undergo an S phase and then enter a long prophase to achieve proper alignment and segregation in the first division or meiosis I ([Hunter et al., 2015](#)). Prophase I is particularly important for the process of meiotic division because at this stage, the complete pairing of homologous chromosomes takes place through the formation of the synaptonemal complex and homologous recombination. These two processes are coupled together and set up the necessary elements for the segregation of homologous chromosomes. During meiotic prophase I, chromosome organization includes 4 different stages – leptotene, zygotene, pachytene, and diplotene, defined as follows.

At the preleptotene stage, the first meiosis-specific proteins of the axial element are loaded on chromosomes. **Leptotene** starts with the recruitment by the elongating axial elements (AE; ex: SYCP3 for synaptonemal complex protein 3) of sister chromatids that begin to form an array of loops. These axial elements promote the formation of double-strand breaks (DSB) through indirect interactions with the endonuclease Spo11. The loop organization of chromosomes contributes to DSB activity regulation. During the **zygotene** stage, homologous chromosomes start to pair through the formation of the synaptonemal complex (SC): the AE are held together by transverse filaments and a number of central elements (CE; ex: SYCE3 for synaptonemal complex central element protein 3). During the **pachytene** stage, homologous chromosomes are fully synapsed and the chromatin is organized in a tight loop-axis array, while COs appear at the end of pachytene (**Figure 6**). Finally, during **diplotene**, the SC is disassembled while homologs remain connected by the chiasmata ([Hunter et al., 2015](#); [Grey and de Massy, 2021](#)). Chiasmata are essential for segregating homologous chromosomes during meiosis and help maintain cohesion between homologous chromosome pairs. The mitotic division is different in that the kinetochores on the sister chromatids are oriented in a mono-direction during the first meiotic division. This orientation of the kinetochores and the chiasmata helps to form the metaphase plate and the migration of sister chromatid pairs to the same pole of the cell. During the second meiotic division, the chromosomes are oriented so that they can move more easily. This is similar to how they are oriented during a mitotic division. This bi-orientation of kinetochores allows the separation of sister chromatids during the second meiotic division ([Grey and de Massy, 2021](#)).

Defects or lack of meiotic recombination can lead to missegregation, infertility, and aneuploid diseases such as Down syndrome in humans ([Wartosch et al., 2021](#); [Grey et al., 2018](#)).

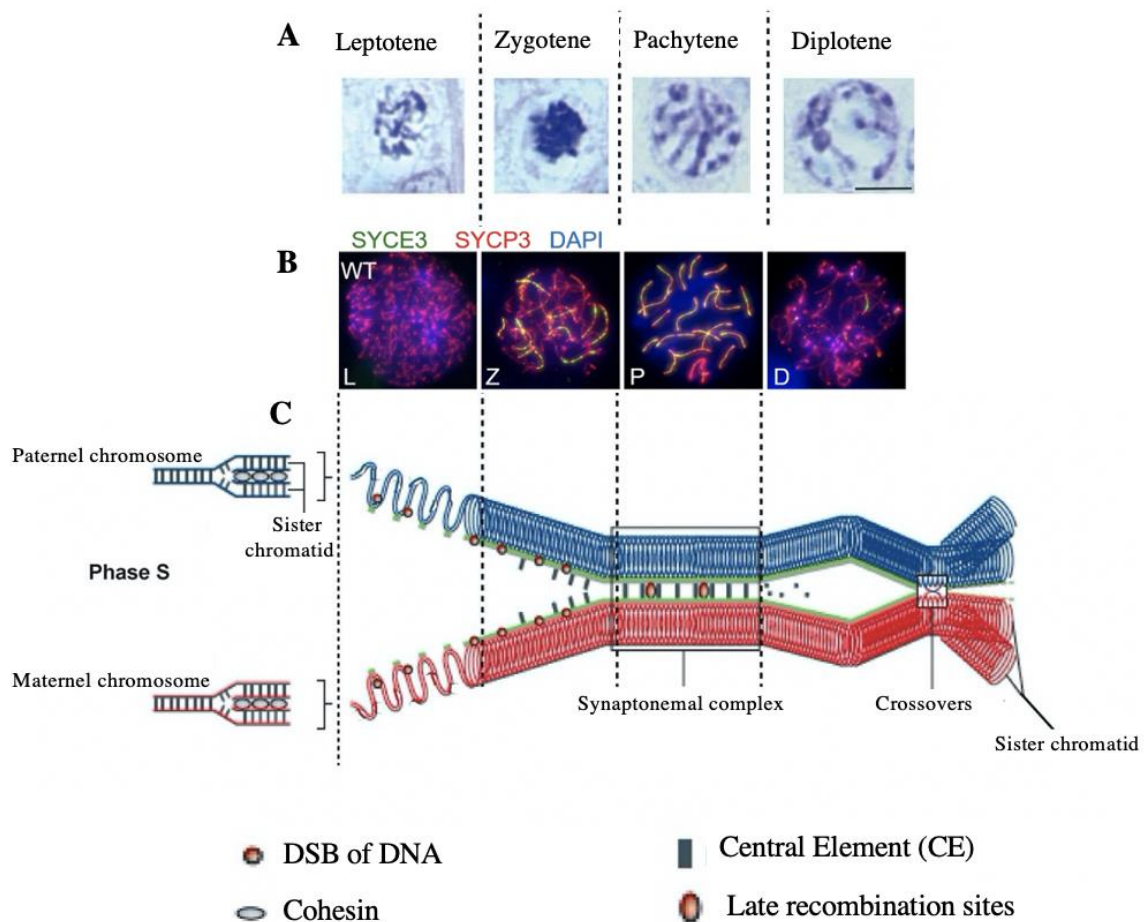


Figure 6. Stages of prophase I in meiosis.

(A) Hematoxylin/eosin-stained images of murine male germ cells acquired by light microscopy (adapted from [Souquet et al., 2013](#)) (B) Spermatocytes stained for Axial Elements (AEs) (SYCP3, red), Central Elements (CEs) (SYCE3, green, but appears yellow because of signal overlap), and DAPI. Leptotene (L), zygotene (Z), pachytene (P), and diplotene (D) (adapted from [Zhang et al., 2020](#)). (C) Diagram summarizing the key molecular events that take place during meiosis prophase I. After DNA replication, DNA DSBs are programmatically formed on the meiotic chromosomes, which also begin their condensation. The homologous chromosomes then synapse and the DSBs are repaired by homologous recombination. Some recombination intermediates are converted to crossovers (COs) (adapted from [Burgoyne et al., 2009](#)).

b. Role of HR in meiosis

The homologous recombination (HR) pathway is activated by the formation of DNA double-strand breaks (DSBs) during prophase I in most species, and their repair is completed at the end of pachytene (**Figure 6C**). DSBs are not randomly distributed throughout the genome, and the choice of the homologous chromosome is regulated. The pairing process helps each homolog to find and interact with its partner, and recombination (i.e., DSB formation and repair) helps to stabilize these interactions (**Figure 7**). This process is carried out in parallel for all chromosome pairs within the meiotic nucleus ([Zickler and Kleckner, 2015](#)). The two meiotic divisions result in the formation of haploid oocytes and spermatozoa.

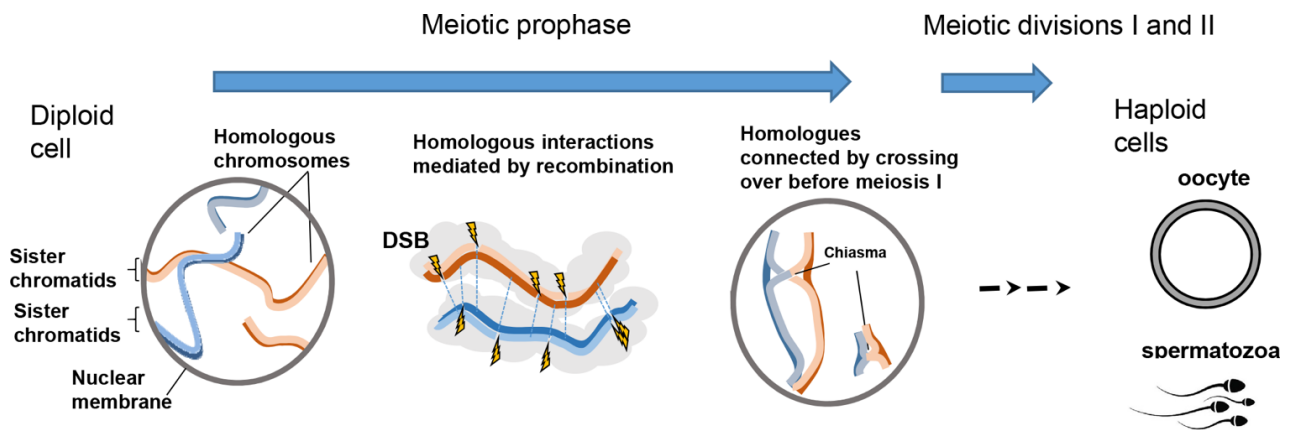


Figure 7. Role of HR in promoting the interaction between homologs and the formation of crossovers.

A small subset of DSB repair events, at least one per homolog pair, results in a crossover that is visualized as a chiasma that establishes a topological connection between homologs. These connections are essential for proper chromosome segregation during the first meiotic division (meiosis I) (adapted from [Grey et al., 2018](#)).

2. Mitotic Vs Meiotic Homologous Recombination

In germ cells, meiotic HR can be defined as a “specialization” of HR, as the main steps resemble the ones of mitotic HR, but with the use of a combination of ubiquitous and meiosis-specific factors to ensure its specific outcomes including CO formation and genetic diversity. The mechanisms underlying the specificity of meiotic HR remain unclear and necessitate further investigations. A better understanding of how meiosis-specific factors collaborate with

canonical factors of mitotic HR is needed to decipher the molecular bases of the functional regulation of recombination intermediates in meiotic HR.

a. Major differences in mitotic vs meiotic HR processes

Mitotic and meiotic HR share many common actors. For example, MRN, RPA, and RAD51 are involved in both processes. However, there are three major differences between these two processes. **First**, homologous chromosomes are used as a repair template in meiotic HR instead of sister chromatids in mitotic HR. **Second**, the ultimate goal of meiotic HR is to form COs that are essential for increasing genetic diversity and ensuring accurate chromosome segregation. On the other hand, the purpose of mitotic HR is to repair DNA damage, including DNA double-strand breaks (DSB), inter-strand crosslinks, and DNA gaps, for safeguarding genome integrity (Kim et al., 2010; Guillon et al., 2005). **Third**, DSBs are “intentional or programmed” in meiosis through the activation of the meiosis-specific endonuclease SPO11 (Keeney et al., 2006; Lange et al., 2016) and are distributed throughout the genome, while in mitosis DSBs are usually “accidental”, resulting from exposure to both endogenous and exogenous stresses (such as irradiations and anti-cancerous drugs) (de Massy et al., 2013; Lam et al., 2014) (Figure 8).

b. HR mechanism in meiosis

i. DSBs formation

Unlike mitotic HR which repairs accidental breaks, meiotic HR is initiated by the induction of programmed double-strand breaks (DSBs) (≈ 300 in mouse gametocytes).

α . SPO11 and its partner TOPOVIBL

Meiotic recombination is initiated by the recognition of hotspot DNA sequences by PRDM9, which introduces trimethylations of H3K4 and H3K36 on the adjacent nucleosomes. The doubly marked H3 is recognized by ZCWPW1. The pro-DSB factors MEI1, REC114, MEI4, IHO1, and ANKRD31 are recruited to the chromosome by an unknown mechanism and activate SPO11–TOPOVIBL (Figure 8). SPO11 is the evolutionary conserved enzyme catalyzing meiotic DSBs (de Massy, 2013). TOPOVIBL directly interacts with SPO11. It is

required for meiotic DSB formation and is essential for spermatocyte and oocyte development (Robert et al., 2016).

ii. Filament formation

Another specificity of meiotic HR is the selective invasion of the homologous chromosome by the presynaptic filament, instead of the homologous sister chromatid during mitotic HR.

α . RAD51 and DMC1

After the introduction of DNA double-strand breaks (DSBs), the MRN–CtIP complex and EXO1 resect the breaks to generate single-stranded DNA (ssDNA). The ssDNA is first coated by replication protein A (RPA), which is subsequently replaced by RAD51. The RAD51 recombinase was first discovered in yeast, it was recognized as an orthologue of the bacterial recombinase A (RecA) (Aboussekhra et al., 1992). RAD51 coats single-stranded DNA substrates to form the presynaptic helical nucleoprotein filament. A large number of organisms, including mammals, possess in addition to the recombinase RAD51, a meiosis-specific recombinase called DMC1 that forms the presynaptic filament together with RAD51 (Pittman et al., 1998; Shinohara et al., 2004; Dai et al., 2017).

RAD51 and DMC1 share ~50% amino acid identity and similar biochemical properties (Ogawa et al., 1993; Masson et al., 2001; Crickard et al., 2018). Data in yeast suggested that, in the meiotic presynaptic filament, RAD51 serves as a loading factor for DMC1, whereas the recombinase activity is ensured by DMC1, which tolerates synapsing between mismatched sequences (Cloud et al., 2012). Accumulated evidences further confirmed that the mismatch tolerances of strand exchange processes by RAD51 and DMC1 are quite different (Lee et al., 2015; Lee et al., 2017). Two exciting studies combining cryo-EM, molecular dynamics simulation, FRET assays and functional analyses recently provided molecular details explaining how, in RAD51 and DMC1, residues from loops 1 and 2 modulate the fidelities of these recombinases (Luo et al., 2021; Xu et al., 2021). In particular, V273 and D274 in human RAD51 loop 2, as well as P274 and G275 in human DMC1 loop2, are the key residues regulating mismatch tolerance during strand exchange in HR. These residues strongly contribute to the HR accuracy control mechanism in mitosis and meiosis.

RAD51 and DMC1 recombinases are ATP-modulated proteins. They form right-handed helical filaments on single-stranded DNA (ssDNA) (Yu et al., 2001) following a two steps mechanism:

nucleation on RPA-covered ssDNA, and elongation by cooperative polymerization along with DNA. RAD51 has a DNA-stimulated ATPase activity, and although ATP binding is necessary for presynaptic filament assembly, ATP hydrolysis leads to the turnover of RAD51 protomers from DNA (Chi et al., 2006). Single-molecule microscopy studies showed that nucleotide hydrolysis by RAD51 triggers a reversible structural transition leading to filaments with reduced helical pitch (Robertson et al., 2009). This transition is essential for further dissociation of RAD51 from ssDNA. Thus, attenuation of ATP hydrolysis in RAD51 leads to stabilization of the RAD51-ssDNA presynaptic filament and enhancement of DNA strand exchange. This is not true for DMC1, whose ATPase activity is not sufficient to stimulate DNA pairing and strand exchange (Chang et al., 2015).

After the assembly of the presynaptic filament and assisted by other proteins, RAD51 and DMC1 recombinases are able to perform homology search: they contact and probe duplex DNA throughout the genome and promote strand invasion leading to the formation of a 3-strands synaptic intermediate followed by a D-loop when the complementary DNA sequence has been found and aligned.

β. MEIOB-SPATA22

During mitotic HR, the ssDNA binding complex RPA precociously binds and protects ssDNA overhangs. In meiotic HR, two other actors are involved in protecting ssDNA: SPATA22 and MEIOB, which form a complex essential for meiotic progression (**Figure 8**) (Luo et al., 2013; Souquet et al., 2013). The protein MEIOB was discovered using two approaches in mice. On the one hand, the Gonad Development Laboratory (CEA Fontenay-aux-Roses) used a differential transcriptomic analysis based on the differential entry into germ cell meiosis between males and females (Souquet et al., 2013). On the other hand, Luo et al., (2013) used a screening approach for chromatin-associated proteins in meiotic cells. The SPATA22 protein was first identified in humans as a spermatogenesis associated gene in a differential transcriptomic analysis between fetal and adult testis (Sha et al., 2002). It was also identified in rats and mice following a random mutagenesis genetic screen (Ishishita et al., 2014).

MEIOB and SPATA22 are specifically expressed in germ cells (Hays et al., 2017; La Salle et al., 2012; Luo et al., 2013, Souquet et al., 2013). The role of MEIOB and SPATA22 in meiotic recombination has been studied by analyzing the phenotype of mice and/or rats invalidated for the genes encoding these proteins (Hays et al., 2017; Ishishita et al., 2014; La Salle et al., 2012;

Luo et al., 2013; Souquet et al. 2013). The absence of MEIOB or SPATA22 induces male and female sterility due to an arrest of meiotic progression of germ cells at a zygotene or pachytene-like stage (zygotene/pachytene-like) and is associated with germ cell apoptosis. MEIOB and SPATA22 are therefore essential for the progression of prophase I of meiosis. Furthermore, the interaction between the two proteins appears to provide interdependent stability in germ cells (Hays et al., 2017; Luo et al., 2013). The localization of MEIOB and SPATA22 to meiotic chromosomes and DSBs induced in somatic cells by genotoxic agents is also interdependent (Luo et al., 2013; Xu. et al., 2017).

The dynamics of MEIOB and SPATA22 follow those of other meiotic HR players such as RPA, RAD51, and DMC1 (Moens et al., 2002). MEIOB and SPATA22 co-localize with RPA and co-localize partially with RAD51 and DMC1 (Hays et al., 2017; La Salle et al., 2012; Luo et al., 2013; Souquet et al., 2013). The fact that MEIOB accumulates in the absence of DMC1 (Souquet et al., 2013) suggests that MEIOB is recruited to presynaptic filaments. A small proportion of MEIOB and SPATA22 colocalize with MSH4 or MLH1, subsequent players in recombination (Hays et al., 2017; Souquet et al., 2013). Altogether, these results suggest that MEIOB and SPATA22 participate in DSBs repair at early and later stages (as RPA).

χ . BRCA2

Recombination mediators are known as proteins that favor filament assembly and stabilization either by accelerating its nucleation on ssDNA or by decelerating its dissociation from ssDNA. *In vitro* assays showed that BRCA2 promotes filament installation by nucleating RAD51 onto ssDNA covered by RPA (**Figure 8**) (Jensen et al., 2010; Liu et al., 2010; Martinez et al., 2016). In mitotic HR, BRCA2 binds to the acidic protein DSS1, which competes with ssDNA for RPA binding, thus favoring RPA replacement by RAD51 on ssDNA (Zhao et al., 2015). It directly interacts with RAD51 through its 8 BRC repeats (Structure: 1N0W, Pellegrini et al., 2002). It also inhibits the ATPase activity of RAD51, thus stabilizing presynaptic filaments (Jensen et al., 2010; Petalcorin et al., 2017). In meiotic HR, BRCA2 also binds to DMC1, through both its BRC repeats (Martinez et al., 2016), and a small conserved region located between its BRC repeats and its folded DNA binding domain (Thorslund et al., 2007).

8. HSF2BP-BRME1

Very recently, HSF2BP (known also as MEILB2; see **Figure 8**) and BRME1 were identified as additional essential actors of meiotic HR. These proteins are expressed in embryonic stem cells, germinal cells, and some cancer cells. They assemble to form a complex in meiosis. Loss of either of these proteins leads to a reduction in RAD51 and DMC1 accumulation at meiotic DSBs, abolishment of crossover formation, and complete spermatogenesis failure (Zhang et al., 2019; Brandsma et al., 2019; Shang et al., 2020; Takemoto et al., 2020; Li et al., 2020; Zhang et al., 2020). Loss of BRME1 decreases the number of HSF2BP foci. As HSF2BP binds directly to both BRCA2 and BRME1, it was proposed that loss of HSF2BP or BRME1 causes compromised BRCA2 meiotic function.

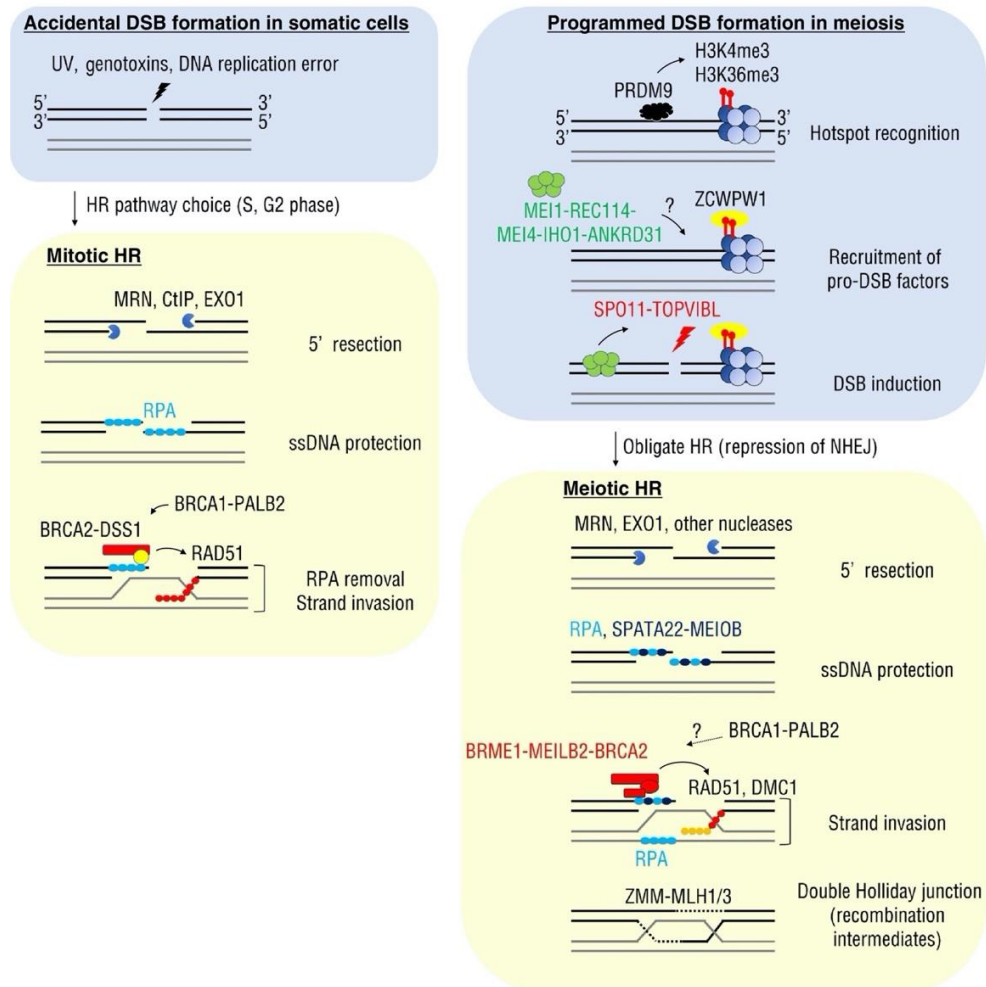


Figure 8. Core steps of mitotic and meiotic HR mechanisms.

(adapted from Zhang et al., 2021).

3. Resolution of the Holliday junctions

The capture of the second strand and ligation results in the formation of Holliday junctions (HJs). During meiosis, HJs are cleaved by endonucleases to generate DSBs that are essential for genetic mixing and proper chromosome segregation (Matos et al., 2011; Zakharyevich et al., 2012). These HJs are resolved to eventually produce crossing overs (COs) (Jasin and Rothstein, 2013; Blanco et al., 2014).

4. Impact of BRCA2 and its partners on fertility

Although BRCA2 has been mostly studied in the context of HR in somatic cells, it arguably has a more prominent role in meiotic HR, as across a broad range of species, fertility defects are the most common consequences of BRCA2 loss (Miao et al., 2019).

The key roles of the BRCA2 protein in mammalian gametogenesis and meiosis were demonstrated by generating *Brca2*-null mice carrying a human BAC containing the *BRCA2* gene (Sharan et al., 2004). This construct resolves embryonic lethality and the mice develop normally. However, transgene expression is low in the gonads and the mice are infertile, allowing examination of the function of BRCA2 in gametogenesis. BRCA2-deficient spermatocytes fail to progress beyond the early prophase I stage of meiosis. Observations on the localization of recombination and spermatogenesis-related proteins suggest that spermatocytes complete the early stages of recombination (formation of DNA double-strand breaks), but fail to complete recombination or initiate spermatogenic development. In contrast to the early arrest of spermatocyte meiotic prophase, some mutant oocytes can progress through meiotic prophase I, although with a high frequency of nuclear abnormalities, and can be fertilized and produce embryos. However, there is a marked loss of germ cells in adult females. Despite these findings, the detailed mechanism of BRCA2 in DSB repair and meiotic recombination remains poorly understood.

The *Spata22* gene was discovered during the characterization of a mutation causing infertility in mice, both males and females (La Salle et al., 2012). In these mice, the SPATA22 protein was not detected. Germ cells could not progress beyond early meiotic prophase, with subsequent germ cell loss in both males and females. Thus, the *Spata22* gene is essential for one or more key events of early meiotic prophase. Similarly, homologous deletion of the *Meiob*

gene in mice causes infertility in both sexes, due to a meiotic arrest at a zygotene/pachytene-like stage (Souquet et al., 2013).

In 2019, first cases of human infertility due to mutations in a meiosis-specific ssDNA-binding protein were reported. Primary Ovarian Insufficiency (POI, i.e. premature menopause), a major cause of infertility, affects about 1-3% of women under forty years of age. By studying the genomes of a family with several cases of POI, a homozygous variant of *Meiob* was identified, whose aberrant splicing leads to the production of a C-terminally truncated protein that cannot interact with SPATA22, abolishing their recruitment to DSBs (Caburet et al., 2019). The authors hypothesized that alterations of meiosis-specific ssDNA binding proteins could explain cases of ovarian insufficiency. Moreover, whole-exome sequencing of families with infertile patients revealed that a *Spata22* variant, coding for a protein unable to interact with MEIOB, as well as a *Meiob* variant, leading to loss of the MEIOB protein, could be responsible for the primary infertility of the patients (Wu et al., 2021). Another similar study performed on a family with POI as well as nonobstructive azoospermia (NOA) patients identified homozygous and heterozygous *Spata22* variants that could be the reason for the observed infertility syndromes (Yao et al., 2022). Finally, several studies identified *Meiob* variants in patients with POI or NOA (summarized in Wang et al., 2022). In some cases, the mutations are missense, which could give some mechanistical information about the function of MEIOB in meiosis (Figure 9).

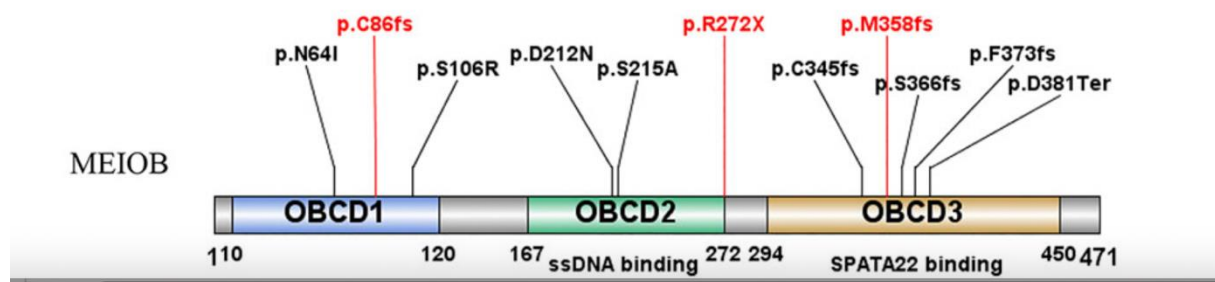


Figure 9. The human MEIOB protein.

consists of 471 amino acids, including three OB-fold domains. Three variants discovered in Wang et al. (2022) are shown in red font, whereas previously reported variants are displayed in black font. (Wang et al., 2022).

The *Hsf2bp* and *Brme1* genes are also essential for meiotic recombination. Inactivation of the mouse *Hsf2bp* gene results in male infertility due to a severe HR defect during spermatogenesis

(Brandsma et al., 2019; Zhang et al., 2019). The homozygous missense mutation HSF2BP-S167L was reported in women with POI ([Felipa-Medina et al., 2020](#)). Introduction of this variant in mice leads to subfertility and DNA repair defects during prophase I. Very recently, the homozygous mutations HSF2BP-C128R and L186P were similarly detected in patients with sporadic POI ([Li et al., 2022](#)).

Finally, in addition to the recombinase RAD51, vertebrates have five paralogs of RAD51, all members of the RAD51-dependent recombination pathway. Their functions in meiosis are not well-described. However, a truncating variant of one of these paralogs, RAD51B, was identified in women with POI ([Franca et al., 2022](#)). Mice expressing this variant exhibited meiotic DNA repair defects due to RAD51 and HSF2BP/BRME1 accumulation in the chromosome axes leading to a reduction of Cos.

Chapter 3. BRCA2 & MEIOSIS SPECIFIC PARTNERS: STRUCTURE AND FUNCTIONS

I. General properties of BRCA2

1. BRCA2 is a tumor suppressor

BRCA2 was first discovered in 1995 as a gene implicated in the predisposition to breast and ovarian cancer. Inherited mutations affecting a single copy of *BRCA2* can also increase the risk of cancers in the pancreas, male breast, prostate, and other cancers (Mersch et al., 2015). Furthermore, biallelic mutations in *BRCA2* are found in Fanconi Anemia patients resulting in a predisposition to various types of cancer at an early age (Wooster et al., 1995).

BRCA2 is a ubiquitous protein essential for embryonic development: *BRCA2* knockout mice show early embryonic lethality and hypersensitivity to irradiation (Sharan et al., 1997). Depletion of BRCA2 also causes a wide range of defects in DNA repair and recombination (Lee et al., 2007), regulation of telomere length (Min et al., 2012), mitosis (Takaoka et al., 2014), meiotic recombination, and fertility (Thorlsund et al., 2007, Choi et al., 2012, Mondal et al., 2012, Fradet-Turcotte et al., 2016, Malik et al., 2016).

In addition, BRCA2 has a protective function during replicative fork stalling that is mechanistically distinct from repair by HR (Schlachter et al., 2011). It stabilizes RAD51 filaments, which inhibit degradation of nascent strands at stalled forks.

2. BRCA2 is mainly disordered

BRCA2's involvement in such a large number of pathways might be explained by its huge size. Indeed, BRCA2 is 3,418-aa long (390 kDa) and is encoded by 27 exons of different lengths (Lo et al., 2003). Its amino acid sequence spans a spread of functional domains. We have calculated a disorder score for BRCA2 using the Webserver SPOT-Disorder2 (<http://sparks-lab.org/server/SPOTdisorder/index.php>) (Figure 10). This graph shows that BRCA2 exhibits a single folded domain of 700 residues, whose 3D structure in complex with

a single-stranded DNA and the small acidic protein DSS1 was determined using X-ray crystallography (Yang et al., 2002).

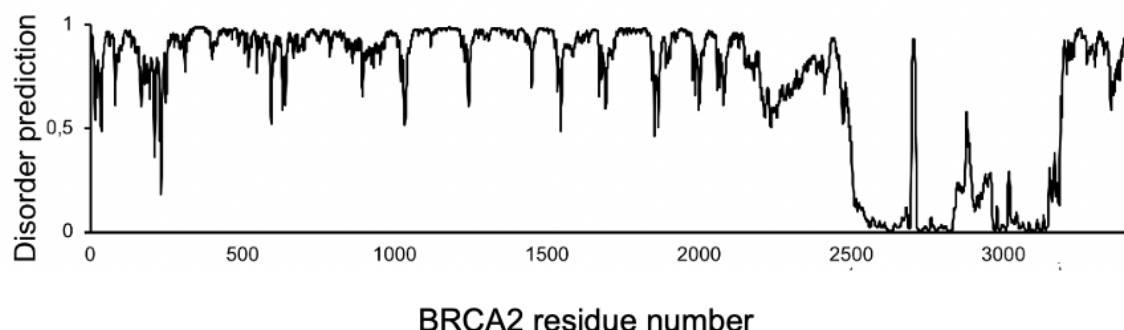


Figure 10. Disorder propensity as a function of BRCA2 residue number.

(Julien et al., 2021). Scores of 0 and 1 correspond to ordered and disordered residues, respectively. BRCA2 contains a single folded domain that binds to single-stranded DNA and the small acidic protein DSS1 (PDB: 1MJE, murine BRCA2).

The folded domain is the most conserved part of BRCA2 (**Figure 11**). The C-terminal region, including the folded domain and the disordered C-terminus, contains 27% of the tumor-derived missense mutations in the breast cancer information core (BIC) database, showing that it plays a crucial role in the tumor suppressive function of BRCA2 (Szabo et al., 2000). Moreover, almost all mutations yet classified as causing cancer in BRCA2 are located in this folded domain (Julien et al., 2021).

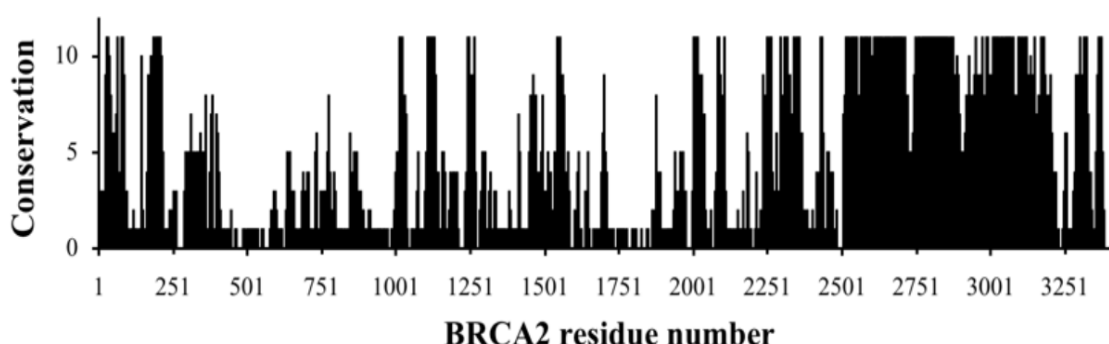


Figure 11. Conservation of BRCA2 residues calculated from an alignment of BRCA2 sequences from fish to human.

(Julien et al., 2021). The conservation score was calculated using JALVIEW. Scores of 0 and 11 correspond to non-conserved and strictly conserved residues, respectively.

All the rest of the BRCA2 sequence is predicted to be disordered (unable to adopt stable secondary and tertiary structures by itself) (**Figure 10**). Such protein regions are named Intrinsically Disordered Regions (IDRs) (Hernandez et al., 1986). The presence of “disorder” is the consequence of a lack of deep minimum in the conformational energy landscape of the protein, unlike that of a folded globular protein (Fisher et al., 2011; Dunker et al., 2011). IDRs (as well as Intrinsically Disordered Proteins, IDPs) have a high diversity of degrees of compactness and might fold upon binding to their partners (Dyson et al., 2002).

The best studied IDRs of BRCA2 are the 8 BRC repeats encoded by exon 11. These 8 similar motifs of about 35 aa in length are designated as BRC1 to BRC8. BRC1, BRC2, BRC4, BRC7, and BRC8 are especially well-conserved (Lo et al., 2003) and all repeats bind to the recombinase RAD51, with BRC1, BRC2, and BRC4 having the best affinity for RAD51, reducing the ATPase activity of RAD51 and enhancing DNA strand exchange by RAD51 (Carreira et al., 2011). Expression of BRC4 in cancer cells disrupts the BRCA2-RAD51 complex and results in radiation hypersensitivity and loss of G (2)/M checkpoint control (Chen et al., 1999). The BRC repeats also bind to the meiotic recombinase DMC1, and most tightly to the conserved BRC6, BRC7 and BRC8 (Martinez et al., 2016).

3. What is the oligomeric state of BRCA2?

The structural organization and putative dynamic rearrangement of BRCA2 are complicated by the presence of multiple predicted disordered regions in BRCA2. Understanding how BRCA2 operates means understanding how the regions of BRCA2, which interact with many partners, contribute to its function. Several groups recently purified full-length BRCA2 and used negative-staining electron microscopy (EM), scanning force microscopy, and fluorescence-based single-molecule analyses, to characterize the oligomeric state and the global shape of BRCA2 either free or bound to RAD51, DSS1, ssDNA. Super-resolution microscopy revealed that BRCA2 and RAD51 are separated at sites where they accumulate. This involves structural changes in BRCA2 in order to release RAD51 (Sanchez

et al., 2017; Whelan et al., 2018). Purified BRCA2 protein shows structural rearrangements upon RAD51 and ssDNA binding (Le et al., 2020; Sanchez et al., 2017; Sidhu et al., 2020). This apparent structural plasticity, which is thought to be characteristic of proteins with inherently disordered areas, could be important for BRCA2 activity in cells (Dunker et al., 2005; Gunasekaran et al., 2003; van der Lee et al., 2014).

The team of Xiaodong Zhang proposed, based on a negative-staining EM analysis of BRCA2, that BRCA2 exists as a dimer, when either free or bound to RAD51, and exhibits an oval kidney-bean shape. In the BRCA2-RAD51 complex, two sets of BRC repeats bind to a series of RAD51 molecules in the middle region (**Figure 12**) (Shahid et al., 2014). The altered shape observed in the BRCA2–RAD51 reconstruction, compared with that of BRCA2 alone, suggests that RAD51 binding induced structural rearrangements.

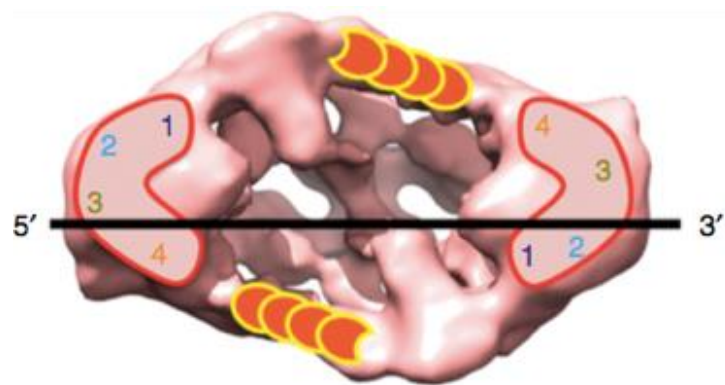


Figure 12. 3D reconstruction obtained from the analysis of negative-staining EM images of BRCA2 purified from HeLa cells (Shahid et al., 2014). This analysis proposed that, despite the wide range of particle sizes observed by EM, it can be concluded that BRCA2 exists as a dimer. Orange patterns represent RAD51 monomers attached to the BRC repeat motifs, numbers 1 to 4 correspond to the different structural motifs forming the folded DNA-binding domain of BRCA2.

The weak reducing conditions used in these EM experiments, whereas BRCA2 IDRs exhibit a high number of cysteines and the use of a cross-linking agent to stabilize the complex containing highly flexible regions, could have influenced this structural analysis of BRCA2, which needs to be confirmed by another team in the future.

More recently, Claire Wyman's team published a series of analyses aiming at describing the quaternary structure of BRCA2 and understanding which parts of BRCA2 are responsible for

its oligomerization, structural transitions and dynamic localization (Reuter et al., 2014; Sanchez et al., 2017; Sidhu et al., 2020; Paul et al., 2021). They followed the mobility of BRCA2 in live cells at the single-molecule level using both single-particle tracking and fluorescence correlation spectroscopy (Reuter et al., 2014). They found that nuclear BRCA2 exists in oligomeric clusters, and exhibits heterogeneous mobility. Despite its very different size, RAD51 showed a mobility similar to BRCA2, which suggested that these proteins belong to the same macromolecular complex both before and after induction of DNA damage. According to scanning force microscopy (SFM) imaging, purified BRCA2 was detected as a mixture of particles of different sizes (multimeric forms) and shapes (compact to expanded) (Sanchez et al., 2017). Incubation of BRCA2 with RAD51 resulted in a compact elongated conformation, which included multiple BRCA2 and RAD51 molecules per complex. In the absence of fixation, a lower number of BRCA2–RAD51 complexes was observed by SFM, indicating that interactions between BRCA2 and RAD51 are dynamic or transient in these conditions. Super-resolution imaging in cell nuclei also indicated that BRCA2 and RAD51 foci are close but distinct at the sites of DNA damage.

The same team of Claire Wyman further dissected the role of the different regions of BRCA2. The N-terminal and central region at 0°C showed a conformational flexibility close to that of the full-length protein, but already at 37°C, this flexibility is largely reduced when compared to the full-length protein (Sidhu et al. 2020). The central region plays a critical role in BRCA2 oligomerization: while both the N-terminal and central region, and the central and C-terminal region still form large oligomers, the N-terminal and C-terminal regions alone are significantly more monomeric (**Figure 13**). Consistently, after incubation with RAD51, full-length BRCA2 becomes largely monomeric (74%) and adopts a more regular compact structure (Sidhu et al., 2020; Paul et al., 2021). The large disordered N-terminal and central region of BRCA2 behaves as the full-length protein, being mainly oligomeric when free, and mainly monomeric when bound to RAD51 (Sidhu et al., 2020). More surprisingly, the central and C-terminal region is mainly oligomeric in both its free and bound states, suggesting that the N-terminal region is critical for RAD51 to disrupt BRCA2 oligomers. The authors concluded that there might be new RAD51 binding sites to be discovered in BRCA2, and in particular in its N-terminal region. They finally observed that full-length BRCA2 exhibits enhanced conformational flexibility when bound to ssDNA, and this is only true in the presence of its C-terminal region (Paul et al., 2021). This is consistent with the C-terminal folded domain being the main DNA binding site in BRCA2. All these analyses strongly suggested that the disordered regions of BRCA2

regulate its oligomeric state and its localization at the DSBs, that RAD51, through binding to different regions of BRCA2, disassembles BRCA2 oligomers, and that the CTD is essential for BRCA2 DNA binding and HR function.

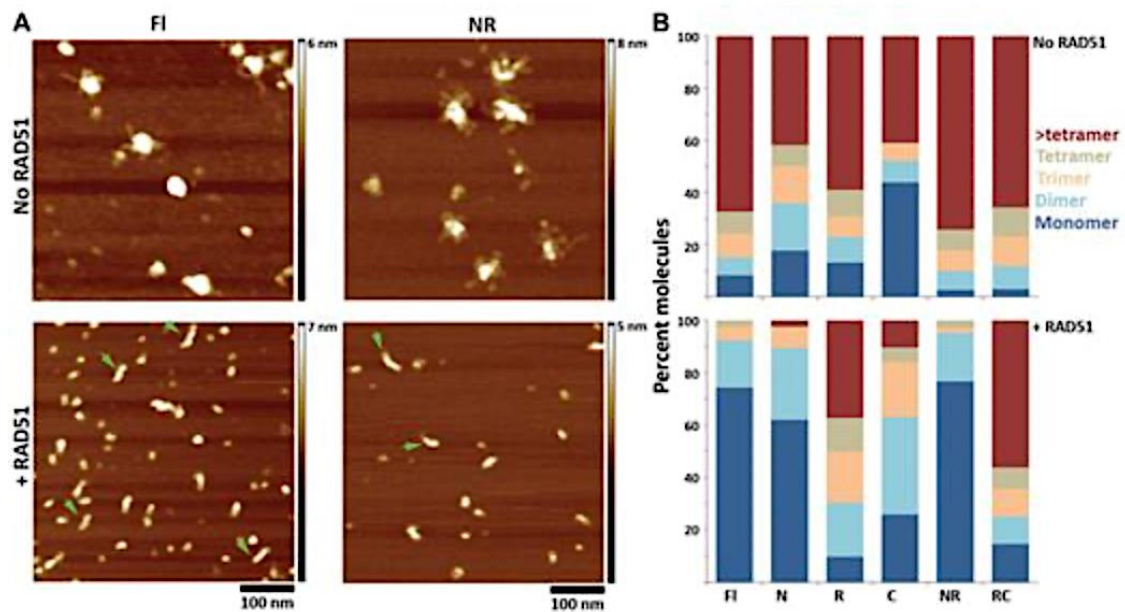


Figure 13. Impact of RAD51 binding on BRCA2 oligomeric state.

(Sidhu et al., 2020). (A) Representative scanning force microscopy (SFM) images of full-length BRCA2 and the N-terminal & central region (NR) of BRCA2 in the presence and absence of RAD51. (B) Histograms showing the oligomeric distribution of full-length BRCA2 and variants in the presence and absence of RAD51. N is the N-terminal disordered region (residues 1-939), R is the central disordered region containing the BRC repeats (residues 940-2130), and C corresponds to the small disordered region binding to HSF2BP, the folded DNA-binding domain and the small disordered C-terminal region of BRCA2 (residues 2131-3418).

4. How does BRCA2 interact with its partners?

Since its discovery, an increasing number of BRCA2 interaction partners have been identified; however, in most cases, the interaction is not clearly direct. Arguably, the search for new direct interactors of BRCA2 may be a good strategy to characterize its disordered regions whose functional roles are poorly understood. Indeed, the lack of significant sequence similarity with other human proteins as well as the low sequence conservation during evolution have impaired the identification of functional domains in BRCA2. I will provide a detailed

description of the interactions that have been structurally characterized, including those with ssDNA and RAD51, which I have already mentioned.

The folded region of BRCA2, also called DBD for DNA binding domain, contains 3 oligosaccharide binding folds, OB1, OB2, and OB3, as well as a helical domain. The crystal structures of the mouse and rat BRCA2 DBD revealed how BRCA2 binds to a short ssDNA and to the short acidic protein DSS1 (for Deleted in Split hand/Split foot protein 1).

a. DSS1

The 70-aa protein DSS1 is disordered in its free state, as revealed by NMR ([Paraskevopoulos et al., 2014](#)). It was independently isolated as a protein that binds to BRCA2 in a yeast double hybrid screen and in HeLa cells, but the molecular function of DSS1 and the significance of its interaction with BRCA2 are still unclear. Since DSS1 is a highly acidic protein, it was originally thought to mimic binding of ssDNA to the DNA binding domain of BRCA2 ([Yang et al., 2002](#)). The crystal structure of BRCA2 DBD bound to ssDNA and DSS1 revealed that these two ligands bind to two different regions of the BRCA2 DBD (**Figure 14**). DSS1 interacts through two motifs with the DBD: the N-terminal portion of DSS1 tunnels through the helical domain and crosses the interface between the OB1 and helical domains, whereas the C-terminal portion wraps around OB1 and ends up at the interface between OB1 and OB2 (**Figure 14**). DSS1 is still partially disordered when bound to BRCA2, as revealed by the lack of density observed for residues 1-5, 24-36, and 64-70 in the X-ray crystallography map of rat BRCA2 DBD bound to human DSS1 (PDB code 1IYJ). Several studies have confirmed that DSS1 maintains its inherent flexibility in other complexes as well ([Kragelund et al., 2016](#)).

Even though the importance of DSS1 in stabilizing BRCA2 was well established, its mechanistic role in HR regulation is not completely clear. It was shown that DSS1 directly interacts with RPA ([Zhao et al., 2015](#)). It acts as a ssDNA mimic that attenuates the affinity of RPA for ssDNA. A mutation in the solvent-exposed acidic domain of DSS1 compromises the efficacy of the RPA-RAD51 exchange.

RAD51 is a 43 kDa protein that has been intensely studied since its discovery. Multiple crystal structures, EM reconstructions along with recent high resolution cryoEM structures have given much insight into its function. RAD51 has a two-lobed architecture consisting of a mostly α -helical N-terminal domain of ~ 84 residues joined by a small helical linker to a larger C-terminal ATPase domain of ~ 240 residues ([Pellegrini et al., 2002](#); [Conway et al., 2004](#)). The crystal structure of the ATPase domain of human RAD51, the first to be reported for a RAD51 protein, was obtained in complex with the BRC4 motif of BRCA2 (**Figure 15**) ([Pellegrini et al., 2002](#)). In addition, it was reported that (1) the human RAD51 sequence 85-91, located between the N-terminal and the ATPase domains, closely resembles the BRC consensus sequence in BRCA2; (2) replacement of Phe 86 or Ala 89 with glutamic acid creates RAD51 mutants that are no longer capable of self-association or nuclear focus formation when expressed in mammalian cells. Thus, BRCA2 interacts with RAD51 by mimicking a structural motif that enables RAD51 to oligomerize, preventing its incorporation into nucleoprotein filaments.

The crystal structure of the filament formed by a gain-of-function mutant of yeast RAD51 that has an enhanced affinity for DNA was reported later ([Conway et al., 2004](#)). Single-molecule fluorescence analyses and crystallography studies identified some flexibility in the RAD51 nucleoprotein filaments, which adopt both compact and open forms. This variation depends on the presence of DNA along with the state of the bound nucleotide. The BRCA2 disordered C-terminus interacts directly with RAD51 filaments, but not monomers, by binding to an interface created by two adjacent RAD51 protomers. This interaction was not characterized by X-ray crystallography. However, it was reported that it stabilizes the filaments ([Esashi et al., 2007](#)). Consistently, in patients with an early-onset familial ovarian cancer associated with high genetic instability, expression of a BRCA2 protein truncated in its C-terminal part was reported, which leads to a defect in the regulation of the RAD51 filament ([Hakansson et al., 1997](#)).

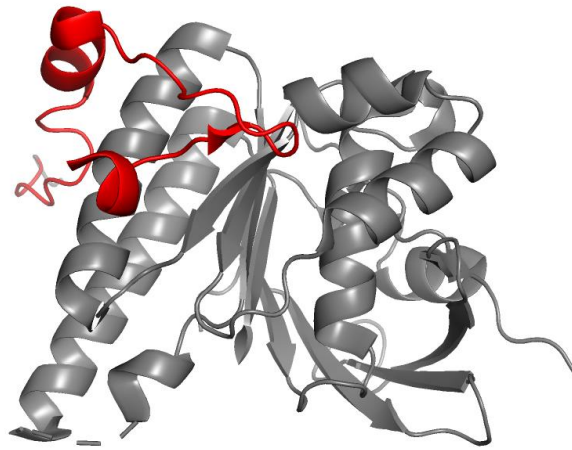


Figure 15. Crystal structure of a human complex between BRCA2 BRC repeat 4 (P1519-Q1551; BRC4) and the ATPase domain of RAD51 (PDB 1N0W; Pellegrini et al., 2002). RAD51 is in grey and the BRC repeat is in red. The BRCA2 BRC motif folds upon interaction with the RAD51 ATPase domain. It blocks ATP hydrolysis by RAD51 and favors nucleation of the ATP-bound form of RAD51 onto ssDNA.

Finally, cryo-EM studies of RAD51 filaments provided information on how DNA strands in the homologous dsDNA become separated in the synaptic phase of the DNA strand exchange reaction. Structures of presynaptic and postsynaptic complexes of human RAD51, as well as an intermediate state in the strand-exchange process, were reported, thus allowing visualization of strand separation of the incoming duplex partner within the synaptic complex (Xu et al., 2017).

c. DMC1

Human DMC1 is a recombinase that is 54% identical in sequence to human RAD51. The first direct interaction between BRCA2 and DMC1 was observed in the plant *Arabidopsis thaliana* (Siaud, et al., 2004) and was mapped to the BRC repeats (Dray et al., 2006). Later, in humans, the region comprised between BRC repeats and the DBD (between aa 2382 and aa 2411) was initially identified as responsible for binding to DMC1 (Thorslund et al., 2007). The TR2 region was also reported to bind DMC1 but with an affinity that is much weaker than for RAD51. Recently, the BRCA2 BRC repeats were shown to bind DMC1 (Martinez et al., 2016). The authors found that BRC6-8 bind to DMC1 with a greater affinity than RAD51.

The 3D structure of DMC1 was solved by X-ray crystallography ([Kinebuchi et al., 2004](#)). In this structure, monomeric DMC1 is very similar to monomeric RAD51; however, DMC1 forms an octameric ring as previously suggested ([Passy et al., 1999](#)). Residues involved in ssDNA and dsDNA binding were identified. Later, DMC1 filaments with ssDNA (presynaptic) and dsDNA (postsynaptic) were structurally characterized by electron microscopy ([Luo et al., 2021](#)) (**Figure 16**). Analysis of these structures suggested that the lineage-specific loop 1 Q244 (M243 in RAD51) helps stabilizing the DNA backbone, whereas loop 2 P274 and G275 (V273/D274 in RAD51) provide an open “triplet gate” for mismatch tolerance.

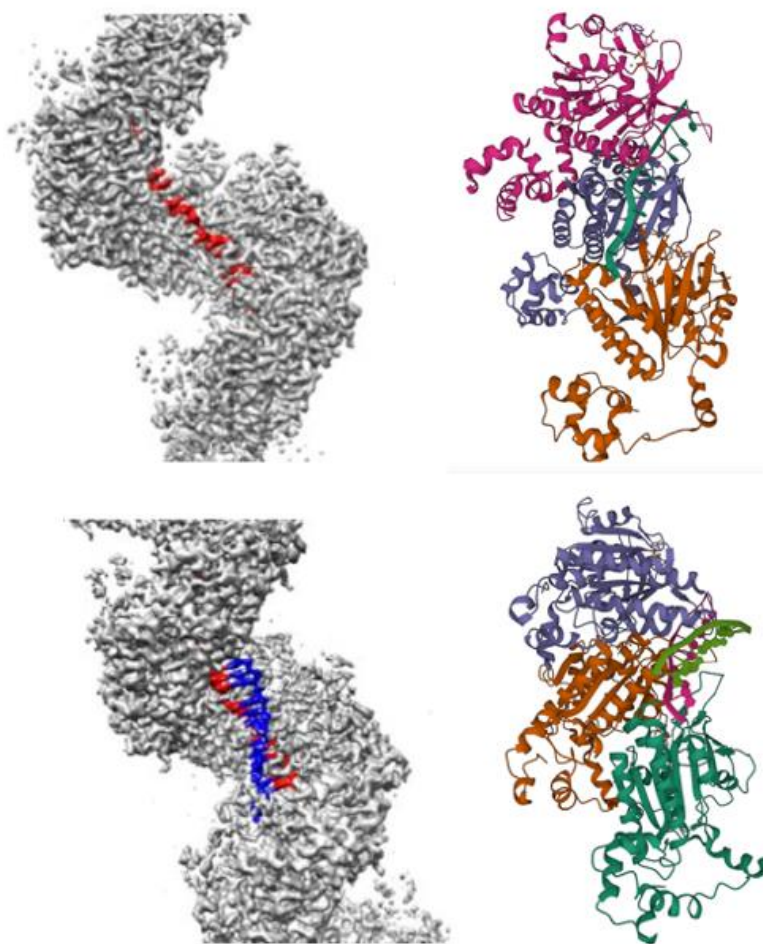


Figure 16. Cryo-EM maps and models of DMC1-ssDNA.

(Presynaptic filament, upper panel) and DMC1-dsDNA (postsynaptic filament, lower panel). The invading ssDNA strand (upper panel) and the complementary strand from the homologous dsDNA (lower panel) are in red and blue (left), and green and magenta (right), respectively. Each DMC1 protomer is colored differently on the right figure (adapted from [Luo et al., 2021](#)).

d. PALB2

PALB2 (partner and localizer of BRCA2) is a major breast cancer susceptibility gene. Several studies established substantial associations between germline *PALB2* pathogenic variants and ovarian, pancreatic, and male breast cancers (Antoniou et al., 2014). *PALB2* encodes for a 130-kDa protein with no clear functional domains other than a predicted amino-terminal coiled-coil structure and a carboxy-terminal WD40-repeat motif. BRCA2 function depends to a large extent on PALB2 for recruitment to nuclear foci and for much of its recombinational activity (Xia et al, 2006). PALB2 recognizes the extreme N-terminus of BRCA2, specifically a conserved region consisting of residues 10–40, in which cancer-associated missense mutations have been observed. In particular G25R, W31C and W31R result in loss of BRCA2 binding to PALB2 (Xia et al, 2006). W31S is nowadays being classified as pathogenic in the French variant database based on co-segregation analysis (S. Caputo, personal communication). The crystal structure of the C-terminal WD40 domain of PALB2 in complex with an N-terminal BRCA2 peptide was solved: a hydrophobic pocket at the surface of PALB2 recruits the BRCA2 region between K21 and A39 that forms a short α -helix upon binding (Figure 17) (Oliver et al., 2009).



Figure 17. 3D structure of the BRCA2 peptide from K21 to A39 (in red) bound to PALB2 WD40 domain (in grey).

(PDB 3EU7; Oliver et al., 2009). The BRCA2 peptide binds in a pocket formed by the tips of the fourth and fifth blades, on the face opposite to the common axial site of the domain.

e. PLK1

PLK1 is a member of the Polo-like kinases (Plks) family, a serine/threonine kinase family initially identified in *Drosophila melanogaster* (Sunkel & Glover, 1988). Plks were shown to be essential to cell life since their discovery: depletion of Plk in *Drosophila melanogaster* leads to chromosomal aberrations, including abnormal circular chromosomes, multipolar and connected poles during chromosome segregation, defects in chromosome segregation and polyploid cells (Sunkel and Glover, 1988). Plks are involved in several steps of the cellular division including mitotic entry and exit, spindle formation, cytokinesis and meiosis. PLK1 is also known to control many nonmitotic events, such as DNA replication and the DNA-damage response. Clinical evidence suggests that PLK1 has a pivotal role in human cancer development and could be a target for anticancer drug discovery (Strebhardt & Ullrich, 2006). PLK1 is highly expressed in a broad spectrum of malignant human tumors. High expression levels of PLK1 are often linked to high tumor grade and are correlated with a poorer patient prognosis, which strongly suggests an important role during tumor initiation and progression.

PLK1 is composed of a Polo-box domain (PBD) and a catalytic domain (**Figure 18A**). It is recruited to specific targets via its PBD domain (Elia et al., 2003). PBD interacts with phosphosites characterized by the consensus motif S-[pS/pT]-P/X (Elia et al., 2003). These phosphosites are provided by a priming phosphorylation event, usually mediated by CDK1 or other proline-directed kinases (Barr et al., 2004); however, PLK1 itself might create docking sites (Neef et al., 2003; Kang et al., Mol Cell 2006). It was reported that human PLK1 phosphorylates the N-terminal region of BRCA2, from aa 1 to aa 283, in mitosis (Lin et al., 2003; Lee et al., 2004). In our team, we showed that this N-terminal region of BRCA2 is disordered (Julien et al., 2020). We developed real-time NMR protocols for monitoring at the residue level phosphorylation with time in a large range of temperatures and pHs (Julien et al., 2020; Alik et al., 2020). Thus, we identified that PLK1 phosphorylates BRCA2 at 2 conserved positions: S193 and T207. We then revealed that BRCA2pT207 creates a docking site for the regulatory PBD domain of PLK1, and we solved the crystal structure of the complex between BRCA2pT207 and PBD (Ehlen et al., 2020) (**Figure 18B**). In collaboration with the group of Dr. Aura Carreira, we showed that this interaction contributes to the assembly of a quaternary complex involving BRCA2, PLK1, BubR1 (for Budding Uninhibited by Benzimidazole-

Related) and PP2A that regulates chromosome alignment in mitosis (Ehlen et al. 2020) (Figure 18C).

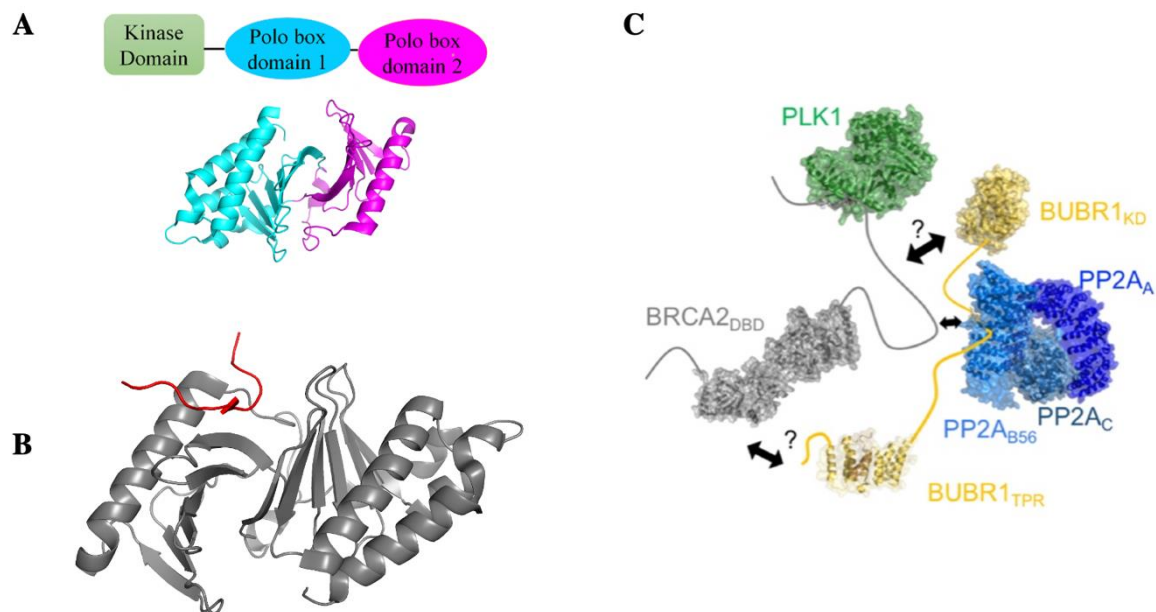


Figure 18. PLK1 interacts with BRCA2pT207.

(A) Structural organization of PLK1 (Sugunadevi Sakkiah et al., 2014). (B) 3D cartoon representation of the crystal structure of PLK1 PBD (in grey) bound to the BRCA2 peptide containing pT207 (in red) (PDB code: 6GY2; Ehlen et al., 2020). (C) Scheme of the BRCA2/PLK1/BUBR1/PP2A complex, assembled upon phosphorylation of Thr207 by PLK1 (adapted from Julien et al., Biomolecules 2021). Human BRCA2 (in grey) has a long N-terminal region, which interacts with PLK1 PBD upon phosphorylation of Thr207 by PLK1 (green). BRCA2 interacts with BUBR1 (yellow) through a controversial interface (arrows and question marks): Futamura et al. reported an interaction between BRCA2 from aa 2861 to aa 3176 and the kinase domain of BUBR1, whereas (Choi et al., 2012) reported an interaction between BRCA2 from aa 3189 to aa 3418 and the N-terminal region of BUBR1 including its TPR domain. BRCA2 and BUBR1 both interact with the same B56 subunit of the phosphatase PP2A (3D structure of the whole phosphatase formed by three subunits, in blue) (Xu et al., 2006).

More precisely, our model is that BRCA2 acts as a platform for bringing BUBR1 and PLK1 together and BUBR1 and BRCA2 compete for binding to the same B56 subunit of PP2A (Ehlen et al., 2020; Ambjørn et al., 2021). PLK1 phosphorylation of BUBR1 at tension-sensitive

regions contributes to the kinetochore-microtubule attachment control. PP2A further preserves the kinetochore-microtubule connection from excessive destabilization through these interactions. PLK1 binding is impaired in BRCA2 breast cancer variants S206C and T207A, resulting in unstable microtubule-to-kinetochore attachments, misaligned chromosomes, incorrect chromosome segregation, and aneuploidy (Ehlen et al., 2020).

5. The recently discovered BRCA2 partner HSF2BP

In the last decade, meiosis-specific factors that have no homologs in budding yeast, namely SPATA22, MEIOB, HSF2BP/MEILB2, and BRME1/C19orf57, were discovered and identified as Cancer Testis Antigens (La Salle et al., 2012) (Souquet et al., 2013) (Zhang et al., 2019) (Brandsma et al., 2019) (Felipe-Medina et al., 2020). They are expressed in embryonic stem cells, germinal cells, and some cancer cells. They assemble to form a complex in meiosis. This complex potentially interferes with somatic HR and contributes to genome instability (Brandsma et al., 2019; Jay et al., 2021; Sato et al 2020; Zhang. Al., 2019). It was shown by our collaborators Alex Zelensky & Roland Kanaar (Erasmus Medical Center, Rotterdam, The Netherlands) that one of the components of this complex, namely HSF2BP, directly interacts with BRCA2 (Brandsma et al., 2019).

a. BRCA2 and HSF2BP interact through an evolutionary-conserved interface

HSF2BP was discovered in 1998 as a testis-specific, heat shock factor 2 (HSF2)-binding protein in a yeast 2-hybrid screen (Yoshima et al., 1998). Heat shock factor 2 (HSF2) belongs to the vertebrate HSF family, which also includes HSF1, HSF3, and HSF4 (Rabindran et al., 1991; Sarge et al., 1991; Schuetz et al., 1991; Nakai and Morimoto, 1993; Nakai et al., 1997) and binds to heat shock elements (HSEs) located on the promoter regions of genes encoding heat shock proteins (HSPs). HSF1 and HSF3 respond to a heat shock stress and other environmental stresses and induce transcription of HSP genes (Baler et al., 1993; Sarge et al., 1993; Nakai, 1997). Unlike HSF1 and HSF3, HSF2 is not activated by such stresses but is thought to play an important role during differentiation and development.

The team of H. Shibuya then identified HSF2BP when searching for factors regulating meiotic DSB repair (Zhang et al., 2019). They examined the subcellular localizations of functionally uncharacterized proteins that are upregulated in murine germ line tissues using the *in vivo* electroporation technique (Morimoto et al., 2012; Shibuya, Morimoto, & Watanabe, 2014). This technique consists in efficiently electroporating DNA in living mice testis to trigger short-term transgene expression in spermatocytes (Figure 19A, B). It enables spermatocyte observations without the need for genetically engineered mice. It was initially used to dissect dynamic cellular events in live spermatocytes, including the movements of telomeres, chromosome axes, and centrosomes (Morimoto et al., 2012; Shibuya, Morimoto, & Watanabe, 2014). The same protocol was adapted to identify proteins located in meiotic recombination foci in spermatocytes (Zhang et al., 2019). One of the candidate genes of unknown function, 4932437G14Rik, known as *Hsf2bp*, showed a characteristic localization pattern specifically in early prophase I spermatocytes (zygote and early pachytene stages), in which punctate signals formed along the chromosomal axes, similar to the distribution of meiotic recombination nodules (Figure 19C).

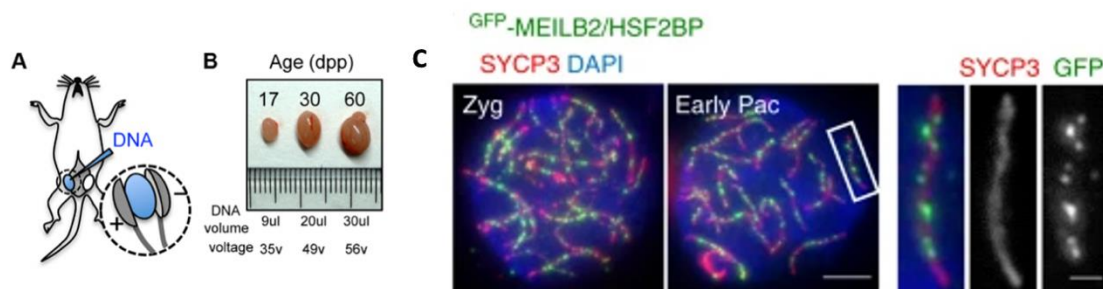


Figure 19. Identification of HSF2BP as a meiotic chromosomal protein in mice spermatocytes.

(A) Diagram of the *in vivo* electroporation (EP) procedure highlighting the injection of a DNA solution into the mice testis and the application of an electric pulse (Shibuya et al 2014). (B) Testes from mice of the indicated postnatal ages (dpp: day post-partum). The volume of the DNA solution and the voltage of the electric pulse is indicated (Zhang et al., 2019). (C) Wild-type (WT) spermatocytes expressing GFP-MEILB2/HSF2BP stained with the indicated antibodies and 4,6-diamidino-2-phenylindole (DAPI) (Zhang et al 2019).

The team of H. Shibuya then searched for partners of HSF2BP by yeast 2-hybrid using a mouse testis cDNA library. They identified a BRCA2 fragment, from aa 2117 to aa 2371, which bound to HSF2BP (Zhang et al., 2019). They further showed that HSF2BP is dispensable for the

introduction of meiotic DSBs, but essential for the recruitment of the recombinases RAD51 and DMC1. They observed that crossover formation is abolished in *Hsf2bp*^{-/-} spermatocytes. They also reported that, in these spermatocytes, the SPATA22 signal intensity is significantly higher and the SPATA22 foci abnormally accumulate toward the zygotene stages. HSF2BP and SPATA22 interact *in vivo* as observed by immunoprecipitation, which suggests that they may function together in meiosis.

The *in vivo* characterization of the HSF2BP-BRCA2 interaction was difficult because immunostaining of murine spermatocytes using BRCA2 antibodies only showed a cloudy signal that was hardly distinguishable from the background signal (Zhang et al., 2019). However, by overexpressing GFP-fusion constructs of BRCA2 by *in vivo* electroporation, the team of H. Shibuya was able to detect recombination nodule-like foci of BRCA2 fragments on the chromosome axes. Moreover, they showed that this localization of BRCA2 depends on its HSF2BP binding region, from aa 2117 to aa 2371, and that this region by itself is recruited to the recombination foci. They concluded that BRCA2 is localized at the DSB sites and that the HSF2BP binding region of BRCA2 is necessary and sufficient for this DSB localization. They also verified that, in *Hsf2bp*^{-/-} testes, the punctuate localization of BRCA2 fragments was abolished. They proposed that HSF2BP is able to recruit BRCA2 to the meiotic DSB sites, and renamed HSF2BP as MEILB2 for MEIiotic Localizer of Brca2.

The team of A. Zelensky and R. Kanaar also reported in 2019 the identification of an interaction between BRCA2 and HSF2BP (Brandsma et al., 2019). They had previously described efficient immunoprecipitation of BRCA2 partners from Brca2^{GFP/GFP} knock-in mouse embryonic stem cells (mESCs) (Reuter et al., 2014) and the phenomenon of BRCA2 degradation upon mild hypothermia (Krawczyk et al., 2011). Based on these results, they searched for BRCA2 partners whose abundance in the BRCA2-GFP immunoprecipitate co-varies with that of BRCA2 upon hypothermia treatment. They performed quantitative stable isotope labeling using amino acids in cell culture (SILAC)-based mass spectrometry experiments on the immunoprecipitates and identified HSF2BP as a protein whose abundance is correlated with that of BRCA2 (**Figure 20**). A reciprocal mass spectrometry experiment - GFP immunoprecipitation from *Hsf2bp*^{GFP/+} knock-in mESCs – validated the interaction between BRCA2 and HSF2BP.

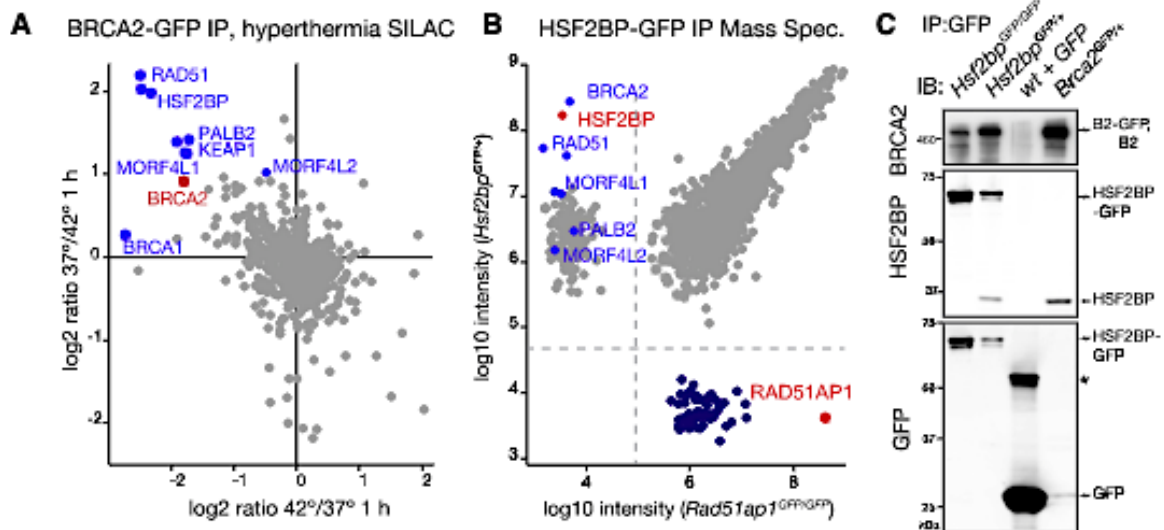


Figure 20. Identification of HSF2BP as a BRCA2-Interacting Protein.

(Brandsma et al., 2019) **(A)** SILAC ratios calculated from the mass spectrometric analysis of anti-GFP immunoprecipitates (IP) from *Brca2*^{GFP/GFP} mESCs (exposed to 42°C versus control). Known members of the BRCA2 complexes are indicated. **(B)** Mass spectrometry analysis of GFP IPs from *Hsf2bp*^{GFP/+} and *Rad51ap1*^{GFP/GFP} cells. Immunoprecipitation from *Rad51ap1*^{GFP/GFP} knock-in cells was used as a control to ensure that the identified interactions were not due to non-specific binding to nuclear GFP-tagged low-abundance DNA repair proteins. **(C)** GFP IPs from the indicated knock-in mESCs analyzed by immunoblotting with the indicated antibodies.

HSF2BP is a 334 aa protein widely conserved in vertebrate species. It is predicted as composed of an N-terminal α -helical domain, partly forming a coiled coil, and a C-terminal armadillo repeat domain (composed of four armadillo repeats) (**Figure 21**). The team of A. Zelensky and R. Kanaar searched for the binding domains in HSF2BP and BRCA2. Therefore, they engineered a series of FLAG-tagged BRCA2 fragment expression constructs and GFP-tagged HSF2BP expression constructs that they tested by co-immunoprecipitation in HeLa cells. The BRCA2-binding domain was mapped to the HSF2BP region from I93 to V334, including the armadillo domain. A point mutation in the armadillo domain, R200T, abolished the interaction. The HSF2BP-binding domain (HBD) in BRCA2 was mapped to a 68 aa region, from G2270 to T2337, located between the BRC repeats and the folded DNA binding domain. BRCA2 is not a particularly well-conserved protein. However, its HBD is well-conserved

within vertebrates (**Figure 22**). The team of A. Zelensky and R. Kanaar further showed using purified protein fragments that HSF2BP and the BRCA2 HBD fragment coeluted in a gel filtration experiment, showing that their interaction is direct. HSF2BP, either free or bound to HBD, was detected at elution volumes corresponding to large complexes, suggesting that the protein is elongated and/or oligomeric in its free and bound forms.

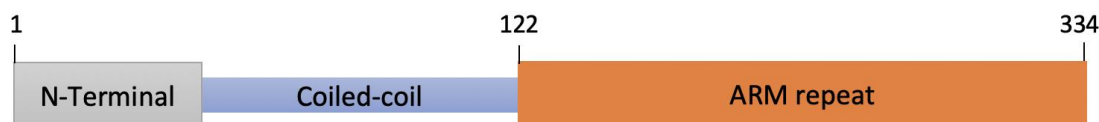


Figure 21. Schematic representation of HSF2BP.

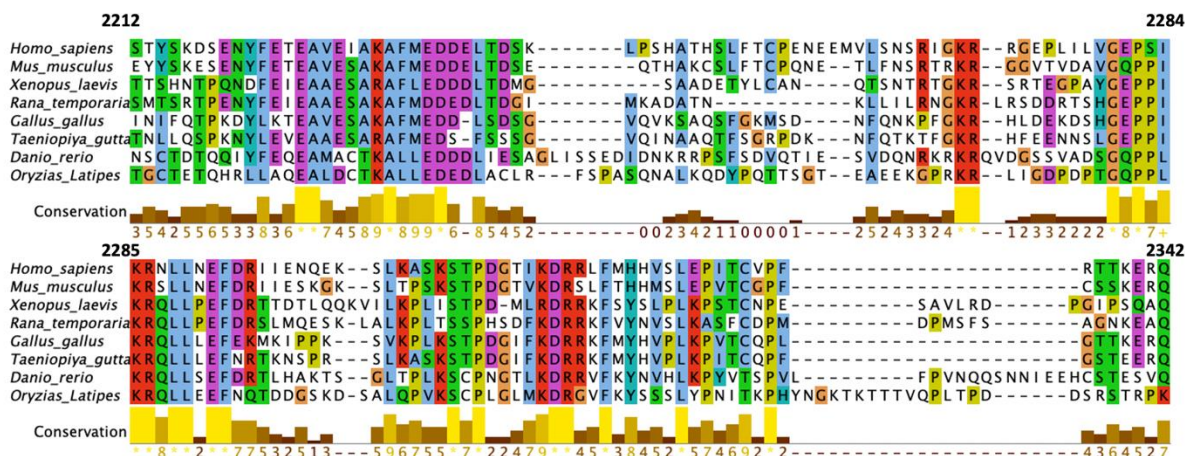


Figure 22. Evolutionary conservation of the HSF2BP binding region of BRCA2 (F0: 2212-2342).

Multiple alignments of human BRCA2 and a selected set of BRCA2 orthologs from various vertebrate species (mammals, frogs, birds, and fishes). The conservation, based on the chemical properties of the side chains, is scored by Jalview from 11(*) (strictly conserved) in yellow to 0 (no conservation) in black.

The team of A. Zelensky and R. Kanaar experimentally confirmed that the HSF2BP-BRCA2 interaction is evolutionarily conserved (Sato et al., 2020). Indeed, they first observed that (i) overexpression of HSF2BP in cancer cells disrupts HR in the context of DNA interstrand crosslink (ICL) repair, and (ii) this is due to the interaction between HSF2BP and BRCA2. Moreover, they revealed that, when human HSF2BP is expressed in *Xenopus* egg extracts, ICL

repair induces degradation of *Xenopus* BRCA2. These experiments further provided a mechanism for the function of overexpressed HSF2BP in tumors. Indeed, by triggering BRCA2 degradation, HSF2BP could induce a BRCAness phenotype leading to cancer-promoting genomic instability.

b. HSF2BP is mutated in fertility diseases

In normal tissues, the HSF2BP protein was so far only detected in embryonic stem cells and mouse testis (Brandsma et al., 2019) (Figure 23), and the main described phenotype of the *Hsf2bp* knock-out mice is meiotic HR failure resulting in defective spermatogenesis and infertility, which suggests that the physiological function of the protein is restricted to (male) germline (Zhang et al., 2019).

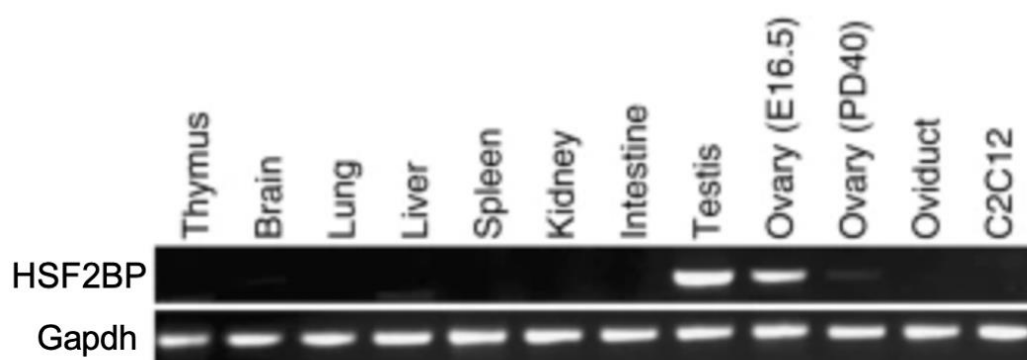


Figure 23. Expression levels of HSF2BP and Gapdh (a loading control) in different tissues. C2C12 is a mitotically rounding cancer cell line (Adapted from Zhang et al., 2019).

In addition, *Hsf2bp* knockout female mice exhibit subfertility due to a significant reduction in the numbers of RAD51 and DMC1 foci in oocytes (Zhang et al., 2019). Recently, homozygous missense variations in *Hsf2bp* were identified in families with POI (Felipe-Medina et al., 2020; Li et al., 2022). Different mutations were identified: homozygous S167L (no homozygous men were identified preventing the analysis of the impact of this variant on male fertility; Felipe-Medina et al., 2020); homozygous C128R and L186P (only women were screened; Li et al., 2022). S167L resulted in a reduced protein level of HSF2BP and subsequent insufficient BRME1, RAD51, and DMC1 proteins localizing at DSBs during meiotic recombination,

whereas C128R and L186P caused only a modest reduction in the HSF2BP protein level, but these variants were barely transferred into the nuclei. Their DNA repair capacities were also lower than those of the wild-type. More generally, recent studies with next-generation sequencing extremely expanded the spectrum of POI candidate genes and demonstrated that a large set of genes involved in meiotic processes, such as DSB end processing genes (EXO1, MND1 and MEIOB), HR genes (RAD51, MSH4, MSH5) and synaptonemal complex genes (SYCE1, C14ORF39, STAG3), were mutated in patients with POI ([França and Mendonca, 2020](#)).

c. HSF2BP is a Cancer Testis Antigen

As shortly mentioned above, HSF2BP is also overexpressed in some cancer cells. It is a Cancer Testis Antigen (CTA). What is a CTA?

CTAs were discovered during the search for surface antigens specifically expressed by tumor cells in order to use them as targets for immunotherapy ([Van Der Bruggen et al., 1991](#); [Van Pel et al., 1995](#)). MAGE-1 (Melanoma Antigen1) was the first discovered member of a large family of CTAs. MAGE genes, whose expression is restricted to the testis, are commonly expressed in tumors ([Simpson et al., 2005](#); [Van Der Bruggen et al., 1991](#)). Today, many genes are considered to be CTAs on the basis of their expression found in the testis/ovaries (or the placenta) and in cancer ([Gantchev et al., 2020](#)). This restricted expression coupled with the antigenic potentials of CTAs make them ideal targets for immunotherapy and targeted cancer therapies. The activation of CTAs in tumors seems to be strongly linked to epigenetic changes, mainly DNA methylation. Indeed, exposure to a demethylating agent is sufficient to induce the activation of the expression of certain CTAs (such as MAGE), which suggests a common mechanism between CTAs ([Coral et al., 2002](#); [De Smet et al., 1999](#); [Fratta et al., 2010, 2011](#); [Whitehurst, 2014](#)). In addition, bisulfite sequencing has shown that some CTAs have hypomethylated promoter regions in different tumors, which correlates with an activation of their expression ([Glazer et al., 2009](#); [Smith et al., 2009](#)). The use of pharmacological inhibitors of DNA methylation and/or histone acetylation increases the expression of CTA in different types of cancers ([Akers et al., 2010](#)).

A subset of CTAs with an emergent role in promoting cancer genome instability has been described as meiosis-specific CT proteins. These proteins regulate meiosis (Gantchev et al., 2020). Their gene expression patterns were analyzed across tumors and normal tissues using the Gene Expression Profiling Interactive Analysis (GEPIA; <http://gepia.cancerpku.cn>) database (Table 1). The functional significance of the expression of these germline proteins in normal somatic tissues is unknown. In cancer cells where these proteins are present and functional, the division may not be a strict mitosis, but rather a cancer “meiomitosis”. The clashing of both meiotic and mitotic pathways may result in increased genomic instability including chromosomal instability because the meiosis-specific CTAs can cause DSB formation, exchange events between chromosomes, spindle assembly defects and disruption of sister-chromatid cohesion (Gantchev et al., 2020).

Table 1. Selected cancer-testis antigens/genes.

Their established functions in meiotic chromosome metabolism and homologous recombination and their proposed roles in carcinogenesis (Jay et al., 2022).

■ Cohesins ■ DSB formation ■ Others
■ Recombination ■ SC components

Protein	Meiotic function	Proposed role in carcinogenesis
BJ-HCC-20A	Unknown	BRCA2 interaction, promotion of cell growth and inhibition of apoptosis [92, 94]
BRME1/ C19orf57	Required for DMC1 focus formation	Reduction in RAD51 focus formation [56, 59]
DMC1	Homologous recombination	Replication fork stability [68]; enable interhomolog biased recombination?
HELLS	Chromatin Remodeler	Interaction with E2F3 to promote tumor progression [83]
HOP2/PSMC3-IP-MND1	DMC1 accessory factor	Increase in chromosome mobility, telomere exchanges [70, 95]; cell cycle progression by upregulating E2F1 expression through interaction with KLF6 [75]
HORMAD1	Required for DSB formation and/or resection, SC formation	Promotes CtIP mediated resection [96] and RAD51 filament formation [97]; inhibition of HR [98]; prevents MCM8-MCM9 nuclear localization and limits MLH1 mismatch repair [99]
HSF2BP/ MEILB2	Required for DMC1 focus formation	Interference with BRCA2 function and HR [77]
MAGE-A4	Transcriptional repressor	Increase in translesion DNA synthesis [81]
MEIOB	ssDNA binding protein required for meiosis I progression	Homologous recombination deficiency and genome instability [39, 89]
PRDM9	Designates locations of DSBs	Whole-genome rearrangements [91]
RAD21L	Sister chromatid cohesion	Promotes homolog alignment [100]; aberrant chromosome segregation leading to genome instability [67, 101]
REC8	Sister chromatid cohesion	Tumor suppressor [84, 85]; increased cancer cell survival by facilitating ploidy reduction in endopolyploid cells [102]; promotes loss of mitotic kinetochores [90]
SMC1 β , STAG3	Sister chromatid cohesion	Increased expression in some cancers [67, 103]
SPO11	Catalytic component of complex that creates DSBs	Increased expression in certain cancers, induces DNA damage [69]; promotes loss of mitotic kinetochores [90]
SSX family	Transcriptional repressor	Genome instability [87]
SYCE1, SYCP1, SYCP2	Structural components of synaptonemal complex	Genome instability [105, 106]; expression in cancers [107, 108]
SYCP3	Lateral element of synaptonemal complex	Interferes with BRCA2, RAD51 function [109, 110]; interacts with AKT to promote tumor formation [76]; upregulates VEGF-C and VEGF-D to promote metastasis in lung cancers [82]
TEX12	Central element of synaptonemal complex	Centrosome amplification [111]

In the case of HSF2BP, because this protein directly interacts with BRCA2, a role in mediating BRCA2 function in cancer cells was studied. Overproducing HSF2BP caused cells to become sensitive to the ICL-inducing medicines cisplatin and mitomycin C, a phenotype that is similar to those of FA patient cells with dysfunctional FA proteins (Sato et al., 2020). The expression of HSF2BP R200T (an HSF2BP mutant with defective binding to BRCA2), or wild-type HSF2BP in cells with a BRCA2 isoform deleted from half of its HSF2BP binding region, did not sensitize cells to mitomycin C. Furthermore, overproduction of wild-type HSF2BP led to cellular sensitivity to the PARP inhibitor olaparib, which is also a characteristic of some FA patient cells (Sato et al., 2020). HSF2BP was demonstrated to decrease HR during ICL repair by reducing the recruitment of BRCA2 and RAD51 to ICLs (Sato et al., 2020). HSF2BP itself was recruited to the ICL in a BRCA2-dependent manner as its wild-type form co-immunoprecipitated with the ICL site, while the R200T mutant did not. Sato et al. (2020) monitored the levels of BRCA2 throughout ICL repair in *Xenopus* egg extracts, to get a mechanistic understanding of the impact of HSF2BP, and discovered that BRCA2 was progressively degraded during repair in the presence of wild-type HSF2BP, but not the R200T mutant; the degradation was ICL-dependent since it was not induced when a non-damaged control plasmid was replicated in the presence of hHSF2BP. These data suggested that HSF2BP-mediated removal of BRCA2 from the ICL caused a repair failure.

The p97 segregase is commonly involved in ubiquitin-mediated protein extraction from chromatin and proteasomal degradation (Franz et al., 2016). Sato et al. (2020) found possible ubiquitin chains on BRCA2 upon proteasome inhibition. Adding a proteasome inhibitor (MG-132) fully blocked BRCA2 degradation during ICL repair. Unexpectedly, adding this inhibitor in the absence of ICL did not cause BRCA2 degradation but still triggered BRCA2 depletion at ICL sites. Consistently, adding MG-132 did not rescue the HSF2BP-induced ICL repair defect. Moreover, adding a p97 inhibitor prevented HSF2BP-induced BRCA2 degradation.

d. HSF2BP stability depends on its meiotic partner BRME1

Recently, five groups independently reported that HSF2BP interacts with an uncharacterized protein encoded by the mouse gene *4930432K21Rik*, which corresponds to the human gene *C19ORF57*. This protein was named C19ORF57/BRME1 (Felipe-Medina et al., 2020), BRME1 for Break Repair MEiotic recombinase recruitment factor 1 (Takemoto et al.,

2020, Zhang et al., 2020), MEIOKE21 (Shang et al., 2020) and MAMERR (MAle MEiosis Recombination Regulator) (Li et al., 2020). It exhibits 600 aa with a high content in acidic residues, has no recognizable functional domains, and is intrinsically disordered (Felipe-Medina et al., 2020).

RT-PCR analyses specified the expression pattern of the *4930432K21Rik* gene in different mouse tissues. This gene was shown to be expressed specifically in adult testis and embryonic ovary, but not in other studied adult organs, indicating that the encoded protein is a germ-cell-specific factor. The human *4930432K21Rik* homolog was expressed not only in testis, but also in human cancers such as brain lower-grade glioma, ovarian serous cystadenocarcinoma, and thymoma, according to public RNA-seq data (Tang et al., 2017) (Figure 24).

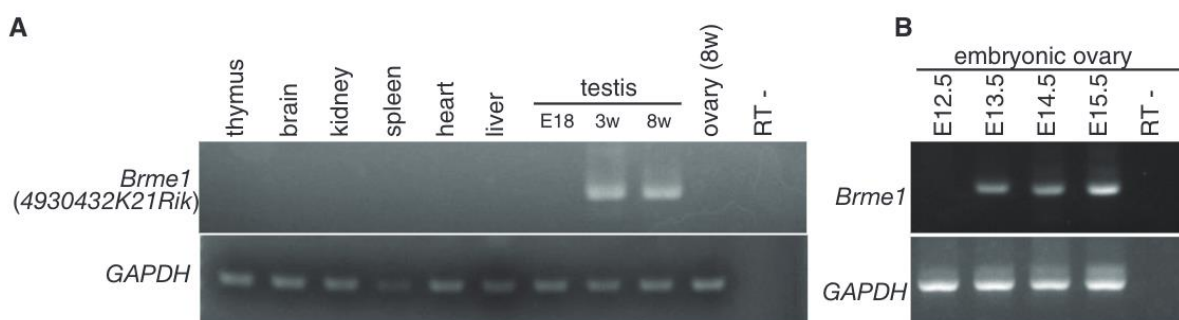


Figure 24. Expression of the meiosis-specific factor BRME1.

(A) Tissue-specific expression pattern of *4930432K21Rik/Brme1*. Testis RNA was obtained from embryonic day 18 (E18.5) testis and tissues from adult 8-week-old male mice. (B) Expression pattern of *4930432K21Rik/Brme1* in the embryonic ovary. Ovary RNA was obtained from E12.5–E15.5 female mice (adapted from Takemoto et al., 2020).

To investigate the intracellular distribution patterns of the BRME1 protein, spermatocyte spread chromosomes were immunostained with antibodies against BRME1, along with SYCP3 (a component of meiotic AE) and SYCP1 (a marker of homolog synapsis). This analysis revealed that the BRME1 protein is found in foci along the chromosomes (Figure 1C). The foci emerged at the leptotene stage. The number of such foci peaked at zygotene, with stronger signals, and then fell from pachytene onward, with residual foci persisting at diplotene. *Spo11* KO spermatocytes had no BRME1 foci, demonstrating that BRME1 nuclear localization is dependent on DSB formation (Lam and Keeney, 2014; Baudat et al., 2013). The BRME1

protein appeared as foci in embryonic oocytes in a similar manner as in spermatocytes. The localization pattern of the BRME1 protein was similar to that of components engaged in meiotic recombination, demonstrating that BRME1 is involved in DSB repair during meiotic recombination (**Figure 25**).

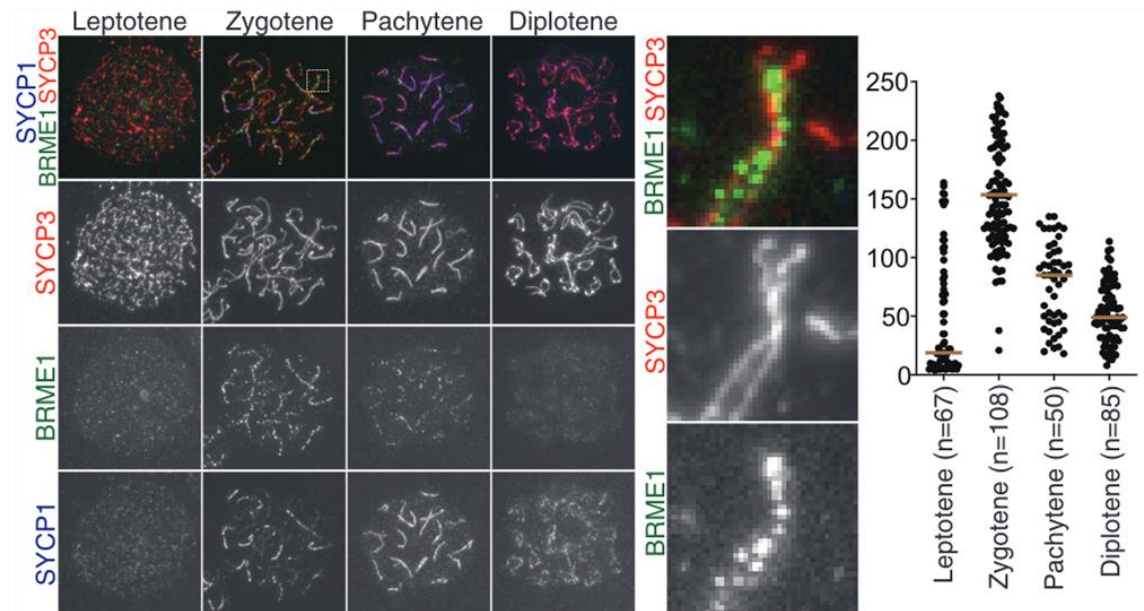


Figure 25. Chromosome spreads of WT spermatocytes were stained for BRME1, SYCP3, and SYCP1.

Enlarged images are shown to highlight axes that are going to be synapsed (middle). The numbers of BRME1 foci on SYCP3 axes are shown in the scatterplot with median (right). n indicates the number of cells examined. (Adapted from [Takemoto et al., 2020](#))

The interaction between HSF2BP and BRME1 was validated *in vivo* by co-immunoprecipitation (co-IP) of both proteins in mouse testis extracts ([Zhang et al., 2020](#); [Felipe Medina et al., 2020](#)). BRME1 perfectly co-localized with HSF2BP on the chromosome axes; this co-localization was verified by super-resolution microscopy ([Felipe Medina et al., 2020](#)). In accordance with the tight association of BRME1 with HSF2BP and their role in meiotic DSB repair, both HSF2BP and BRME1 colocalized with RPA and DMC1 foci ([Felipe Medina et al., 2020](#)). It was reported that, in testis extracts, BRME1, along with HSF2BP, form an enormous multimeric complex with BRCA2, PALB2, RAD51, and RPA ([Felipe Medina et al 2020](#)).

Transfection of HEK293T cells with a plasmid coding for BRME1 showed that this protein co-

immunoprecipitated with BRCA2 and HSF2BP once they were co-transfected, but not with BRCA2 alone (Felipe Medina et al., 2020). HSF2BP and BRME1 demonstrated a positive reciprocal co-IP with BRCA2. HSF2BP co-IP with RPA, PALB2, and RAD51, and BRME1 co-IP with RAD51 and RPA but not with PALB2. These interactions were further investigated using a cell-free TNT system and co-immunoprecipitation experiments, which revealed that none of them interacted directly, other than BRME1 and HSF2BP (Felipe Medina et al., 2020).

To understand whether HSF2BP localization depended on BRME1, HSF2BP was immunolabeled in *Brme1* ^{-/-} spermatocytes and oocytes (Li et al., 2020). Results showed a strong reduction of HSF2BP staining in *Brme1* ^{-/-} spermatocytes and a total absence in oocytes. Western blot analysis of HSF2BP in testis extracts from *Brme1* ^{-/-} mice showed a strong reduction compared with the WT control, suggesting that BRME1 is necessary for HSF2BP protein stabilization. Moreover, the localization of BRME1 at DSBs was dependent on HSF2BP, whereas the localization of HSF2BP at DSBs was not fully dependent on BRME1. Localization of BRME1 foci on chromosomes was also dependent on RPA and the MEIOB/SPATA22 complex. Li et al., (2020) conducted more studies to demonstrate the impact of BRME1 depletion on fertility. The male *Brme1* ^{-/-} mice were sterile, and DMC1/RAD51 recruitment in *Brme1* ^{-/-} spermatocytes was partially disrupted, resulting in unrepaired meiotic DSBs. More crucially, *Brme1* ^{-/-} spermatocytes had much lower levels of ubiquitination on the autosomes and XY body. They showed pachytene arrest and germ cell death. On the other hand, female *Brme1* ^{-/-} mice were fertile. They concluded that BRME1 regulates the ubiquitination of key meiotic proteins.

To delimit the protein domains involved in the interaction between HSF2BP and BRME1, three different fragments of BRME1 were expressed (N-terminal, central and C-terminal regions) (Zhang et al., 2020, Felipe Medina et al., 2020). The interacting domain is the C-terminal fragment of BRME1(P519–D605). HSF2BP interacts with BRME1 along with BRCA2, implying that they can form a ternary complex. Consistently, the BRME1-binding region of HSF2BP is its N-terminal helix α1, whereas the BRCA2-binding region of HSF2BP is its C-terminal armadillo-repeat domain that contains arginine 204, corresponding to R200 in human, the mutation of which abolishes HSF2BP-BRCA2 interaction (Brandsma et al., 2019; Zhang et al., 2020) (Figure 26).

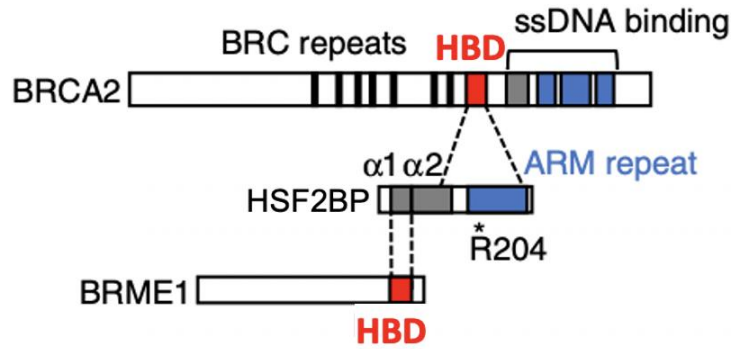


Figure 26. Characterization of the BRCA2-HSF2BP-BRME1 ternary complex.

Scheme of the interactions between BRCA2, HSF2BP, and BRME1. HBD: HSF2BP- binding domain; ARM repeat: armadillo-repeat domain (adapted from [Zhang et al., 2020](#)).

e. HSF2BP also interacts with the complex formed by RPA, SPATA22, and MEIOB

MEIOB and SPATA22 co-localize with RPA and partially co-localize with RAD51 and DMC1 ([Hays et al., 2017](#); [La Salle et al. 2012](#); [Luo et al., 2013](#); [Souquet et al., 2013](#)). They participate in DSBs repair at early and later stages (as RPA). Remote homology detection using HHpred detected evolutionary relationships between MEIOB and RPA1, and SPATA22 and RPA2 despite their low sequence identities (16 % and 13 % for MEIOB/RPA1 and SPATA22/RPA2, respectively). Consistently, MEIOB exhibits 3 OB domains ([Ribeiro et al., 2016](#)), and SPATA22 has an N-terminal disordered region with no apparent functional motif and a unique C-terminal OB domain ([Ribeiro et al., 2018](#)). The N-terminal fragment of the disordered region of SPATA22 is highly conserved. It could be involved in modulating the functions of SPATA22, as also proposed for RPA2. Structural models of MEIOB and SPATA22 individual subunits were generated using the RaptorX server and were assembled together, using the structure of the RPA-ssDNA complex as a homologous template ([Ribeiro et al., 2021](#)) (**Figure 27**).

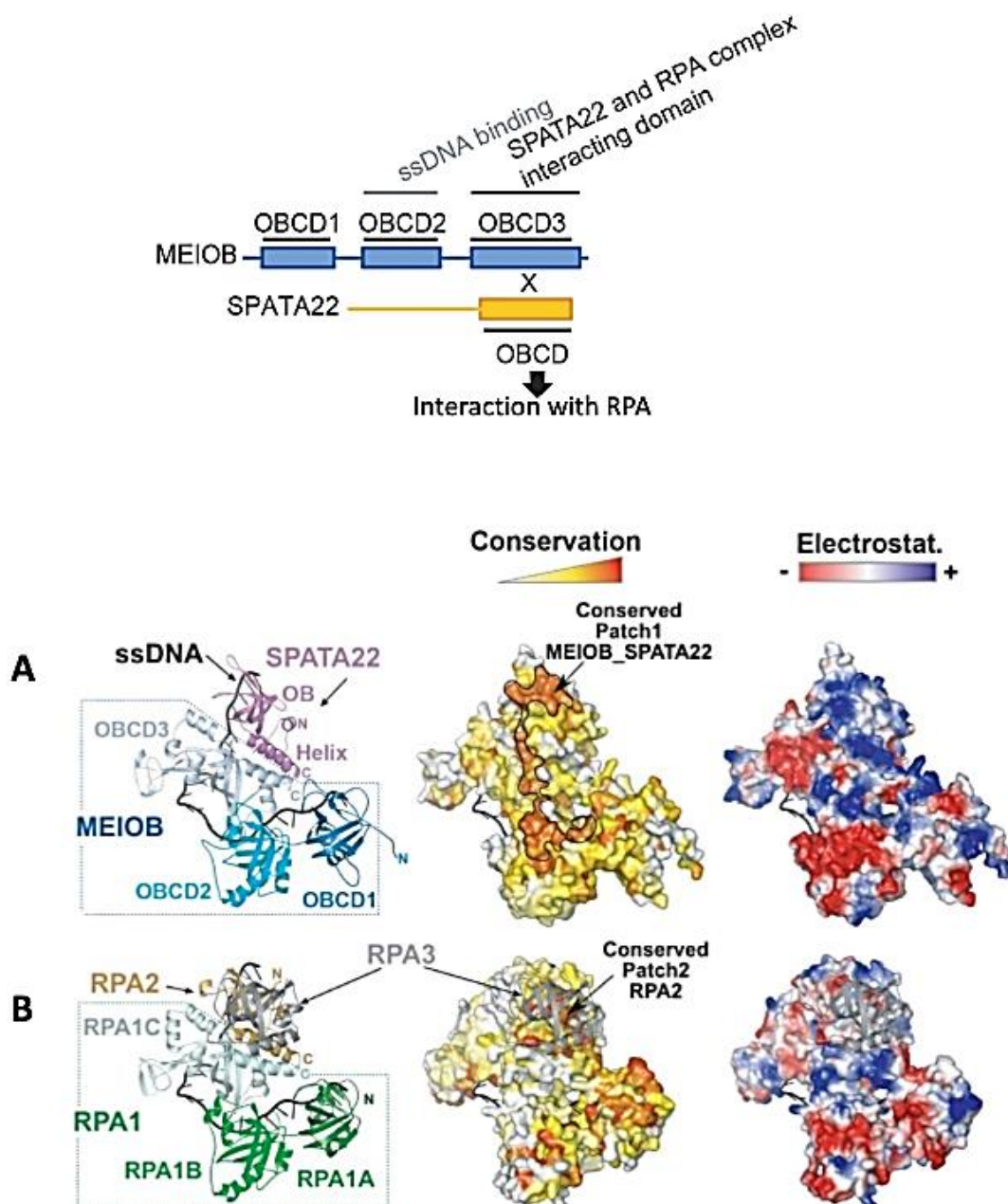


Figure 27. Models for the interactions between MEIOB, SPATA22 and RPA.

(Ribeiro et al., 2021) In the upper panel, a scheme summarizes the interactions identified between these 3 proteins. In the lower panel, in (A) a 3D model of the human MEIOB (blue) and SPATA22 (pink) complex bound to ssDNA (black) is represented as a cartoon. The three OB-fold containing domains of MEIOB (OBCD) are colored from dark to light blue from the N-terminus to the C-terminus. The disordered N-terminal region of SPATA22 is not shown. In (B), a 3D model of the human RPA1-RPA2-RPA3 complex is displayed as a cartoon, with RPA1 in green, RPA2 in yellow and RPA3 in grey. Both 3D models were generated using the template structure referenced as PDB 4GNX, corresponding to the RPA1-RPA2-RPA3

complex in *U. maydis*. Human RPA1, RPA2 and RPA3 subunits share 44 %, 38 % and 28 % of sequence identity with their *U. maydis* orthologs, respectively, allowing for the generation of a reliable comparative model. Human MEIOB and SPATA22 only share 16% and 13% of sequence identity with the *U. maydis* RPA1 and RPA2 proteins.

The interaction between MEIOB and SPATA22 is mediated by the C-terminal portions of MEIOB and SPATA22, which contain an OB domain in both proteins (Xu, Y. et al., 2017). These OB domains are necessary and sufficient for their interaction (Ribeiro et al., 2018). This is similar to what was observed for the RPA1 and RPA2 subunits of RPA. Also, if a conserved patch is observed at the surface of RPA2 that corresponds to the RPA3 binding site, such a patch is not conserved in SPATA22 (**Figure 26**). A different, elongated, conserved patch is observed at the surface of the MEIOB/SPATA22 complex, which could be a binding site for either the N-terminal region of SPATA22 or another yet unknown partner.

Given the homology of MEIOB with RPA1 and the positively charged groove observed on the surface of the 3D model of the complex MEIOB-SPATA22, it was proposed that MEIOB can also bind to ssDNA (**Figure 26**). Consistently, it was shown *in vitro* that MEIOB specifically binds to ssDNA via its central OB domain (equivalent to the DBD domain of RPA1) (Luo et al. 2013; Souquet et al. 2013). This ssDNA binding of MEIOB could participate in its recruitment directly to single-stranded intermediates during the recombination process.

In addition to the interaction of MEIOB, SPATA22, and ssDNA in murine germ cells, MEIOB is able to interact with RPA (Luo et al., 2013). These results correlate with the colocalization of MEIOB, SPATA22, and RPA at meiotic chromosomes and suggest that MEIOB and SPATA22 collaborate with RPA during meiotic HR (Hays et al., 2017; Luo et al., 2013; Souquet et al., 2013). To define how these three proteins interact, co-immunoprecipitation experiments were performed after overexpression of the mouse proteins in human cells. MEIOB and SPATA22 need to be co-expressed to co-immunoprecipitate endogenous RPA1 and RPA2 (Ribeiro et al., 2021). Moreover, MEIOB is directly associated with RPA1 (Xu et al., 2017). However, this interaction is weak compared to the interaction between MEIOB-SPATA22 and RPA, suggesting that MEIOB-SPATA22 interacts with the preformed RPA complex primarily through the MEIOB-SPATA22 dimerization core and that their interaction is further stabilized by secondary independent contacts between RPA1 and/or RPA2 and regions of MEIOB and SPATA22 located outside this dimerization core (Ribeiro et al., 2021).

The formation of a compacted mixed MEIOB/SPATA22/RPA/ssDNA complex was also observed, which might provide meiosis-specific early recombination intermediates preventing excessive RAD51 and DMC1 loading ([Ribeiro et al., 2021](#)).

In mice, HSF2BP, which is essential for the recruitment of RAD51 and DMC1 recombinases to recombination sites, interacts with SPATA22 and RAD51 ([Zhang et al., 2019](#)). And BRME1, the stabilizing partner of HSF2BP, interacts with MEIOB and SPATA22, and RAD51 ([Zhang et al., 2020](#)). Furthermore, HSF2BP and its partner BRME1 do not influence the localization of RPA, MEIOB, and SPATA22. It is possible that the interaction of HSF2BP/BRME1 with MEIOB and SPATA22 promotes correct recombinogenic filament formation and D-Loop formation. The described interaction between HSF2BP and SPATA22 indicates that SPATA22 may have its own interactions that would play a role in the functionality of the MEIOB-SPATA22 complex. While the C-terminal region of SPATA22 is involved in the interaction with its partner MEIOB ([Xu et al., 2017](#)), the function of the N-terminal region of SPATA22 is unknown to date. This region could serve as an interaction hub for the MEIOB-SPATA22 complex to direct the functionality of the complex during recombination.

Thesis project and purpose

BRCA2 is a major player in meiotic HR. Its absence causes a fertility defect in humans. The main purpose of my PhD project was to provide structural and biochemical knowledge on the interaction between a conserved BRCA2 region and HSF2BP. This last protein is essential for male fertility. Our initial hypothesis was that the interaction between BRCA2 and HSF2BP contributes to the essential meiotic functions of these proteins.

I had two main objectives:

- Structurally characterize the interaction between BRCA2 and HSF2BP and identify residues contributing to binding.
- Explore the relationship between binding & fertility.

During my PhD thesis, I studied the interactions between BRCA2, HSF2BP, and several other proteins involved in meiotic HR, in order to obtain molecular details about these interactions *in vitro*, and propose variants to test in cells, during HR and meiosis.

First, I characterized the three-dimensional structure of the BRCA2-HSF2BP complex by a combination of methods, including biochemistry, nuclear magnetic resonance, isothermal calorimetry titration, crystallography and cryo-electron microscopy. I also took advantage of the new AlphaFold bioinformatics tool recently released by DeepMind to identify new actors able to regulate the BRCA2-HSF2BP complex in meiosis.

I then focused on understanding the molecular events regulating the interaction between BRCA2 and HSF2BP. I structurally characterized these events, in order to pinpoint the associated regulation mechanisms.

My Ph.D. project is carried out in collaboration with the team of Prof. R. Kanaar and Dr. A. Zelensky (Erasmus University Medical Center, Rotterdam), who identified HSF2BP as a BRCA2 partner and characterized the function of this interaction in cells and in mice.

MATERIAL & METHODS

I. Biochemistry

1. Commercial products

EDTA 0.5 M was purchased from Sigma Aldrich (E7889-100ML), PBS 10X from Sigma Aldrich (D1408-500ML), TBS10X from Sigma Aldrich (ET220-1L), HEPES 1 M from Sigma Aldrich (H0887), PMSF 0.1 M from Sigma Aldrich (93482-250ML-F), benzonase from Sigma Aldrich (E1014-25KU), EDTA-free protease inhibitors (PI) from Roche (05056489001). Affinity and gel filtration columns were purchased from GE Healthcare: Histrap FF crude 5mL, HiLoadTM 16/600, SuperdexTM 75 PG, SuperdexTM 75 10/300 GL, SuperdexTM 200 PG, SuperdexTM 200 Increase 10/300 GL, Superose 6 increase. Centrifugal units were purchased from Amicon (UFC901024).

2. Protein expression vectors

All constructs encode human proteins. Most of the BRCA2 genes of interest were synthesized by Genscript after codon optimization for expression in *E. coli*. Constructs for expression of BRCA2 in insect cells were obtained by the CiGEX platform (Didier Busso CEA Fontenay aux Roses) using the human cDNAs.

Table 2. Plasmids for expression of BRCA2 constructs.

Plasmid name	Protein construct	Mutation	Vector	Antibiotic resistance	Description
BRCA2 F0(2212-2342) 130 aa	BRCA2-TEV site- GB1-Stop	C2332T	pET22-b	Amp	Conserved region between BRC repeats and DBD.
BRCA2 F _{NMR} (2252-2342) 90 aa	BRCA2-TEV site-GB1-Stop	C2332T	pET22-b	Amp	HSF2BP binding fragment deduced from NMR analysis.
BRCA2 F15x or BRCA2-HBD (2291-2342) 51 aa	BRCA2-TEV site-GB1-Stop	C2332T	pET22-b	Amp	HSF2BP binding region used for crystallogenesis.
BRCA2 exon 12 +CTD (2150-3197)	GST-TEV	WT	pFCGV	-	For insect cell production of a fragment including BRCA2F0 and DBD.
BRCA2 exon 12 +CTD (2150-3197) +DSS1	GST-TEV	WT	pFC-F	-	For co-expression in insect cells of BRCA2F0+DBD and DSS1.

All constructs coding for human HSF2BP fragments were provided by Alex Zelensky (Erasmus Medical Center, Rotterdam).

Table 3. Plasmids for expression of HSF2BP constructs

Plasmid name	Protein construct	Mutation	Vector	Antibiotic resistance	Description
HSF2BP (1-334)	6xHis-TEV	WT	pETM11	kanamycin	Full-length HSF2BP.
ARM or H3 (122-334)	6xHis-TEV	WT	pETM11	kanamycin	Armadillo domain.
H2 (107-334)	6xHis-TEV	WT	pETM11	kanamycin	C-ter region of helix α 2 +armadillo domain.
HSF2BP R200T	6xHis-TEV	R200T	pETM11	kanamycin	HSF2BP mutant defective for BRCA2 binding

Constructs for the expression of human SPATA22 in bacteria were obtained by the CiGEX platform (Didier Busso CEA Fontenay aux Roses) using the human cDNAs.

Table 4. Plasmids for expression of SPATA22 constructs

Plasmid name	Protein construct	Mutation	Vector	Antibiotic resistance	Description
SPATA22 long (1-238)	6His-Thrombin site	WT	pET15-b	Amp	Nter disordered region of SPATA22
SPATA22 short (1-131)	6His-Thrombin site	WT	pET15-b	Amp	Nter disordered and conserved region of SPATA22
OBFold SPATA22(224-363)	6His-Thrombin site	WT	pET15-b	Amp	C ter folded region of SPATA22

3. Protein sequences

In these constructs, the TEV site is colored in blue, 6-His-Tag is colored in yellow and the Thrombin recognition site is colored in green.

➤ **BRCA2 F0 (2213-2342)**

STYSKDSSENYFETEAVEIAKAFMEDDELTD SKLP SHATHSLFTYPENEEMVLSNSRIGKRRG
EPLILVGEP SIKRNLLNEFDRIIENQEKSLKASKSTPDGTIKDRRLFMHHVSLEPITTVPFR

TTKERQ**ENLYFQ**GSAGSAGMQYKLILNGKTLKGETTTEAVDAATAEKVFKQYANDNGVDGEW
TYDDATKTFTVTEGLE

➤ **BRCA2 F_{NMR} (2252-2342)**

LFTCPENEEMVLSNSRIGKRRGEPLILVGEPSIKRNLLNEFDRIIENQEKSLKASKSTPDGT
IKDRRLFMHHVSLEPITTVPFRTTKERQ**ENLYFQ**GSAGSAGMQYKLILNGKTLKGETTTEAV
DAATAEKVFKQYANDNGVDGEWTYDDATKTFTVTEGLE

➤ **BRCA2 F15X (2291-2342)**

NEFDRIIENQEKSLKASKSTPDGTIKDRRLFMHHVSLEPITTVPFRTTKERQ**ENLYFQ**GSAG
SAGMQYKLILNGKTLKGETTTEAVDAATAEKVFKQYANDNGVDGEWTYDDATKTFTVTEGLE

➤ **HSF2BP (1-334)**

MK**HHHHHH**PMSDYDIPTT**ENLYFQG**AMGEAGAAEEACRHMGTKEEFVKVR KKDLERLTTE
VMQIRDFLPRI LNGEVLESFQKLKIVEKNLERKEQELEQLKMDCEHF KARLETVQADNIR
EKKEKLALRQQ LNEAKQQLLQQA EYCTEMG AA ACTLLWGVSSSEEVVKAILGGDKALKFF
SITGQTMESFVKSLDGDVQELDSDESQFVFALAGIVTNVAAIACGREFLVNSSRVLLDTLQL
LGDLPKG QCTKLKVLMLMSLYNVSINLKGLKYISESPGFIPLLWWLLSDPDAEVCLH
VLRLVQSVVLEPEVFSKSASEFRSSLPLQ RILAMSKSRNPRLQTAAQELL EDLRTLEHNV

➤ **HSF2BP R200T**

MK**HHHHHH**PMSDYDIPTT**ENLYFQG**AMGEAGAAEEACRHMGTKEEFVKVR KKDLERLTTE
VMQIRDFLPRI LNGEVLESFQKLKIVEKNLERKEQELEQLKMDCEHF KARLETVQADNIREK
KEKLALRQQ LNEAKQQLLQQA EYCTEMGAA ACTLLWGVSSSEEVVKAILGGDKALKFF
SITGQTMESFVKSLDGDVQELDSDESQFVFALAGIVTNVAAIACG**R**EFLVNSSRVLLDTI
LQLLGDLPKGQCTKLKVLMLMSLYNVSINLKGLKYISESPGFIPLLWWLLSDPDAEVCLH
VLRLVQSVVLEPEVFSKSASEFRSSLPLQ RILAMSKSRNPRLQTAAQELLEDLRTLEHNV

➤ **H3 (122-334)**

MK**HHHHHH**PMSDYDIPTT**ENLYFQG**AEMGAACTLLWGVSSSEEVVKAILGGDKALKFFSIT
GQTMESFVKSLDGDVQELDSDESQFVFALAGIVTNVAAIACGREFLVNSSRVLLDTILQLLG
DLKPGQCTKLKVLMLMSLYNVSINLKGLKYISESPGFIPLLWWLLSDPDAEVCLHVLRLVQS
VVLEPEVFSKSASEFRSSLPLQ RILAMSKSRNPRLQTAAQELLEDLRTLEHNV

➤ **H2 (107-334)**

MK**HHHHHH**PMSDYDIPTT**ENLYFQG**GEAKQQLLQQA EYCTEMGAACTLLWGVSSSEEVVKA
ILGGDKALKFFSITGQTMESFVKSLDGDVQELDSDESQFVFALAGIVTNVAAIACGREFLVN
SSRVLLDTILQLLGDLPKGQCTKLKVLMLMSLYNVSINLKGLKYISESPGFIPLLWWLLSDP
DAEVCLHVLRLVQSVVLEPEVFSKSASEFRSSLPLQ RILAMSKSRNPRLQTAAQELLEDLRT
LEHNV

➤ **SPATA 22 (1-238)**

MGSSHHHHHHSSGLVPRGSQEFHMKRSLNENSARSTAGCLPVPLFNQKKRNRQPLTSNPLKD
DSGISTPSDNYDFPPLPTDWAVEAVNPELAPVMKTVDTGQIPHSVSRPLRSQDSVFNSIQSN
TGRSQGGWSYRDGNKNTSLKTWNKNDFKQPCKRTNLVANDGKNSCPMSSGAQQQKQLRTPEP
PNLSRNKETELLRQTHSSKISGCTMRGLDKNSALQTLKPNFQQNQYKKQMLDDIPEDNTLKE
TSLYQLQFKEKAS*

➤ **SPATA 22 (1-131)**

MGSSHHHHHHSSGLVPRGSQEFHMKRSLNENSARSTAGCLPVPLFNQKKRNRQPLTSNPLKD
DSGISTPSDNYDFPPLPTDWAVEAVNPELAPVMKTVDTGQIPHSVSRPLRSQDSVFNSIQSN
TGRSQGGWSYRDGNKNTSLKTWNKNDFKQP*

➤ **OB fold SPATA22 (224-363)**

MGSSHHHHHHSSGLVPRGSQMLDDIPEDNTLKETSLEYQLQFKEKASSLRIISAVIESMKYWREHA
QKTVLLFEVLAVLDSAVTPGPYYSKTFLMRDGKNTLPCVFYEIDRELPRILIRGVHRCVGNVDQKKN
FQCVSVRPASVSEQKTFQAFVKIADVEMQYYINVMNET*

4. Competent bacteria production

A 500 mL LB culture from competent bacteria BL21 (DE3) Star or Rosetta 2 is incubated for about two hours until OD_{600nm} reaches between 0.4 and 0.6. After that point, the bacteria's growth is stopped with incubation on ice. Then, the bacteria are centrifuged at 2800 g for 10 minutes at 4 °C and the supernatant is discarded. The pellet is resuspended in cold 30 mL of CaCl₂ 100 mM. After another 10 minutes of centrifugation at 4°C, the supernatant is discarded again and the pellet is resuspended in 8 mL of cold CaCl₂ 100 mM and 10% glycerol. Cells are divided into aliquots of 30 µL, flashed frozen in nitrogen, and conserved at -80°C.

5. Vectors transformation in *E. coli*

Vectors were purified using the New England BioLabs kit (reference #T1010L) from 6 mL of bacteria culture. Vectors were transformed in *E. coli* BL21(DE3) Star or Rosetta 2. The transformations were carried out by adding 100 ng of plasmid, onto about one billion of bacteria (50 µL). After 15 minutes of incubation on ice, the vector entry in the cells was triggered by a heat shock at 42°C during 45 s. Then, bacteria were resuspended in 800 µL of LB medium and incubated during 45 min at 37°C under agitation. Finally, the cells were spread on LB agar medium containing the appropriated antibiotic resistance, and incubated overnight at 37°C.

6. Protein expression

Three culture media were used in this study: Luria Broth (LB) or rich media, M9 minimum media (**Table 5**) and minimum media labeled with Selenomethionine. Antibiotics were used at concentrations of 100 ug/mL for ampicillin, 30 ug/mL for kanamycin, 30 ug/mL for chloramphenicol.

a. In rich medium

For all proteins, expression was performed in *E. coli* BL21 (DE3) Star except for HSF2BP, H2, and H3 which were expressed in BL21 (DE3) Rosetta2. The starter culture was done at 37°C overnight in LB medium containing antibiotics under agitation (180 rpm). Then, 20 mL of preculture were used to inoculate 800 mL of culture (LB or M9). When the OD_{600nm} reached 0.8 +/- 0.1, protein expression was triggered using IPTG (Isopropyl-β-D-thiogalactoside). Afterward, cultures were centrifuged at 3500 rpm during 20 minutes and each pellet was resuspended in 20 mL of lysis buffer (25mM Tris HCL pH8 , 250mM or 500mM of NaCl) before being frozen at -80°C and stored at -20°C during a maximum of 1-2 months.

b. In minimal medium + ¹⁵N, ¹³C labeling

This production protocol is used to label the protein with ¹⁵N or ¹³C for NMR experiments. The production protocol is the same as in rich medium, except that the LB medium is replaced by a minimal medium as described in table 5.

Table 5. Composition of M9 media.

Composition for 800mL of 1X M9 medium	
<ul style="list-style-type: none"> • 100mL M9 10X (60g Na₂HPO₄, 30g KH₂PO₄, 5g NaCl) • 2mL Trace Element 500X (EDTA 5 g /L, 13.4 mM FeCl₃-6H₂O, 0.83 g/L 3.1 mM, ZnCl₂ mg/L , 0.62 mM, CuCl₂-2H₂O 13 mg/L 76 μM, CoCl₂-2H₂O 10mg/L 42 μM, H₃BO₃ 10 mg/L 162 μM, MnCl₂-4H₂O 1.6 mg/L 8.1 μM) 	<ul style="list-style-type: none"> - 1mL MgSO₄ 1M - 0.3mL CaCl₂ 1M - 1 mM of Biotine - 1 mM of Thiamine - 2g Glucose ¹²C or ¹³C D-glucose - 0.5g ¹⁵NH₄CL or ¹⁴NH₄CL

c. In minimal medium + selenomethionine labeling

L-Selenomethionine is a naturally occurring amino acid containing selenium that is commonly used for the labeling of proteins to facilitate structural determination by X-ray crystallography using single-or multi-wavelength anomalous diffraction (SAD or MAD). The incorporation of heavy atoms such as selenium helps to solve the phase problem in X-ray crystallography (Larsson, A. M et al., 2009).

The media composition is the same as the minimum media mentioned above, except that 200 mg of each aa (except for methionine) and 125 mg of selenomethionine are added to 1 L of media.

7. Optimal protein expression conditions

For all proteins in this study, expression in bacteria was optimized. Therefore, 2*50 mL cultures of bacteria in LB medium supplemented with antibiotics were incubated at 37°C. After the cultures reached an OD_{600nm} of 0.6- 0.8, 1 mM IPTG was supplemented to the media. Cultures were then splitted in 3 flasks, which were incubated either at 20°C, 30°C or 37°C. Cultures at 37°C and 30°C were stopped after 3 hrs of induction, and culture at 20°C was stopped after an overnight (ON) induction. The cultures were then spun down 10 minutes at 3,000 g, resuspended in 1 mL of a water solution containing Tris-HCl at 50 mM, NaCl at 150 mM, 2 mM DTT, at pH 8.0, supplemented with lysozyme and benzonase. Samples were sonicated on ice for 2 minutes and spun down 5 minutes at 16,000 xg and 4°C. The total, supernatant and pellet fractions were analyzed using SDS-PAGE. Optimal protein expression conditions are summarized in table 6.

Table 6. Optimal protein expression conditions in bacteria.

Name	Bacterial strain for expression	Temperature and time	IPTG (mM)
BRCA2 F0(2212-2342) 130aa	<i>E. coli</i> BL21 DE3 Star	3h at 37 °C	1
BRCA2 F15x (2291-2343) 51aa	<i>E. coli</i> BL21 DE3 Star	3h at 37 °C	1
BRCA2 F _{NMR} (2252-2342) 90aa	<i>E. coli</i> BL21 DE3 Star	3h at 37 °C	1
HSF2PB (1-334)	<i>E. coli</i> BL21(DE3) Rosetta2	ON at 20 °C	0.2
H3 (122-334)	<i>E. coli</i> BL21(DE3) Rosetta2	ON at 20 °C	0.2
H2 (107-334)	<i>E. coli</i> BL21(DE3) Rosetta2	ON at 20 °C	0.2
SPATA22 long (1-363)	<i>E. coli</i> BL21 DE3 Star	ON at 20 °C	0.2
SPATA22 short (1-238)	<i>E. coli</i> BL21 DE3 Star	ON at 20 °C	0.2
SPATA22 OB Fold (224-363)	<i>E. coli</i> BL21 DE3 Star	ON at 20 °C	0.2

8. Insect cell expression

Insect cell expression was used only for the BRCA2 exon 12 CTD fragment (protocol by Virginie Ropars).

Table 7. BRCA2 construct used for insect cell expression.

BRCA2 exon 12 +CTD (2150-3197)	GST-Tev-BRCA2 (2441-3197)
BRCA2 exon 12 +CTD (2150-3197) +DSS1	GST-Tev-BRCA2 (2441-3197) + DSS1 Flag

```

GVSPYLSQFQQ DKQQLVLGTK VSLVENIHVL GKEQASPKNV KMEIGKTETF SDVPVKTNIE
VCSTYSKDSE NYFETEAVEI AKAFMEDDEL TDSKLPSHAT HSLFTCPENE EMVLSNSRIG
KRRGEPLILV GEPSIKRNLL NEFDRIENQ EKSLKASKST PDGTIKDRRL FMHHVSLEPI
TCVPFRITKE RQEIQNPFT APQGEFLSKS HLYEHLTLEK SSSNLAVSGH PFYQVSATRN
EKMRHLITG RPTKVFVPPF KTKSHFHRVE QCVRNINLEE NRQKQNIIDGH GSDDSKNKIN
DNEIHQFNKN NSNQAAAVTF TKCEEEPLDL ITSLQNARDI QDMRIKKKQR QRVFPQPGSL
YLAKTSTLPR ISLKAAGVGQ VPSACSHKQL YTYGVSKHCI KINSKNAESF QFHTEDYFGK
ESLWTGKGIQ LADGGWLIPS NDGKAGKEEF YRALCDTPGV DPKLISRIWV YNHYRWIIWK
LAAMECAFPK EFANRCLSPV RVLLQLKYRY DTEIDRSRRS AIKKIMERDD TAAKTLVLCV
SDIISLSANI SETSSNKTSS ADTQKVAIE LTDGWYAVKA QLDPPLLAVL KNGRLTVGQK
IILHGAEVLG SPDACTPLEA PESLMLKISA NSTRPARWYT KLGFFPDPRP FPLPLSSLFS
DGGNVGCVDV IIQRAYPIQW MEKTSSGLYI FRNEREEKE AAKYVEAQQK RLEALFTKIQ
EEFEEHEENT TKPYLPSRAL TRQQVRALQD GAELYEAVKN AADPAYLEGY FSEEQLRALN
NHRQMLNDKK QAQIQLEIRK AMESAEQKEQ GLSRDVTTVW KLRIVSYSKK EKDSVILSIW
RPSSDLYSL TEGKRYRIYH LATSLSKSKS ERANIQLAAT KKTQYQQLPV SDEILFQIYQ
PREPLHFSKF LDPDFQPSCS EVDLIGFVVS VVKKTGLAPF VYLSDECYNL LAIKFWIDLN
EDIKPHMLI AASNLQWRPE SKSGLLTIFA GDFSVFSASP KEGHFQETFN KMKNTVENID
ILCNEAENKL MHILHANDPK WSTPTKD

```

Flag DSS1

**SEKKQPVDLGLLEEDDEFEEFPAEDWAGLDEDEDAHVWEDNWDDDNVEDDFS NQLRAELEKHGYKMET
S***

a. Insect cell transfection

Plasmids were transformed in *E. coli* DH10EMBacY using a heat shock protocol. About 100 ng of plasmid was incubated with DH10EMBacY bacteria for 20 minutes at 4°C, then heat-shocked for 30 seconds at 42°C and incubated 3 minutes at 4°C. Finally, 950 µL of preheated LB medium was added to the bacteria. The sample was then incubated for 5h at 37°C with 900 rpm agitation. Transformed bacmid were selected on LB- agar plates containing 30 µg/mL kanamycin, 10 µg/mL tetracyclin, 10 µg/mL gentamycin, 1 mM IPTG, 80 µg/mL X-gal and incubated overnight at 37°C. During this incubation, the genes of interest were transferred to

the bacmid via transposition into the mini Tn7 attachment site. Successful integration results in disruption of the lacZ subunit-coding sequence. Hence, the bacterial colonies that contain bacmid carrying the inserted cDNA do not express the β -galactosidase, do not digest X-gal and therefore remain uncolored/ white, while the other colonies are blue.

Two white colonies were incubated in 2 mL LB supplemented with 30 ug/mL kanamycin, 10 ug/mL gentamycin for ON at 37°C. The Plasmid Miniprep kit from New England Biolabs Inc was used until protein precipitation. The supernatant was then supplemented with 44% isopropanol and spun down 10 minutes at 16,000 xg. EtOH 70% was then used to wash two times the pellet containing the baculovirus genome and then were dried at RT. Each pellet was then dissolved into 20 μ L sterile water, 200 μ L of Sf9 medium is added and the transfection mix was completed with 100 μ L of sf9 medium and 10 μ L of X-TremeGENE transfection reagent (Roche). The mix was then added to a 1.106 cell/mL culture of 1 mL. Plates were incubated at 27°C. About 60 hrs later, the supernatant containing the V0 generation of virus was collected and stored at 4°C.

For larger cultures, a V1 generation is produced from the V0 generation. To do so, 2.5 mL of V0 stock was added to infect 25mL of Sf21 cell culture at 0.5x10⁶ cell/mL and incubated at 27°C, 125 rpm (Infors) for two days in checking that the cell concentration does not exceed 2 x10⁶ cell/mL. Two days after the DPA (Day of proliferation arrest), the virions were recovered by centrifugation (supernatant) at room temperature, 600 rpm, 5 minutes and stored at 4°C with 5% of heat inactivated serum (Fetal Bovin Serum, Gibco) protected from light. The lifetime of V1 generation is about one year. From cell pellet of the V1 generation, a Western Blot is performed to control if our protein of interest is well expressed. The viral titer of V1 generation stock is determined by serial dilution in 96-well plate and using the Mac Grady method.

b. Protein expression

To produce the proteins of interest, 300 mL of insect cells (Sf21) at a cell concentration of 0.5x10⁶ cell/mL were infected at a MOI value (multiplicity of infection) of 5x10⁻³ with V1 stocks encoding CTD domain +/- DSS1. The MOI is defined as the number of virus particles used to infect each cell. Sf21 cells were cultured in serum- free SF900II medium (Gibco) at 27°C, 120 rpm in Infors system. Two days after infection (at DPA), the fluorescence of YFP protein was monitored by a benchtop flow cytometer (Guava easyCyte 6HT, Luminex Corp) to quantify the expression level of the protein of interest and cell population. When the

fluorescence reached a plateau (J+5 after infection or DPA+3), cells were collected by two successive centrifugations at room temperature. Cell pellets were flash-frozen in liquid-nitrogen and stored at -80°C.

9. Protein purification

Table 8 summarizes molecular weights (MW), molecular extinction coefficients at 280 nm ($\epsilon_{280\text{nm}}$) and isoelectric points of the proteins produced in this study. All these parameters were calculated using the ProtParam webserver (<https://web.expasy.org/protparam/>).

Table 8. Molecular weights and molecular extinction coefficients after cleavage (TEV or Thrombin) of proteins produced in this study.

Proteins	MW (kDa)	$\epsilon_{280\text{nm}}$ ($\text{cm}^{-1} \cdot \text{M}^{-1}$)	IP
BRCA2 F0	22.7	15930	4.99
BRCA2 F15X	13.9	1490	5.21
BRCA2 F _{NMR}	11.08	1490	8.90
HSF2PB	37.7	20970	5.43
H3	23.5	19480	5.46
H2	25	20970	4.96
SPATA22 long	26.7	27960	9.57
SPATA22 short	14.3	24980	9.46
SPATA22 OB Fold	17.8	17420	8.43
BRCA2 exon 12 +CTD (2150-3197)	119	118690	8.23
BRCA2 exon 12 +CTD (2150-3197) +DSS1	129	137170	5.9

a. Purification of all BRCA2 constructs produced in bacteria

The bacterial pellet was resuspended in 35 mL of a solution containing TBS1X at pH 8, 5 mM DTT, 1 mM PMSF, EDTA-free Protease Inhibitor Cocktail (Roche), 500 ug lysozyme, 0.5 µl benzonase supplemented with 1.5 mM MgCl₂. Cells were sonicated on ice for 2.5 minutes in total with 1s ON/1s OFF cycle of sonication (60% amplitude), and the lysate was clarified by centrifugation for 15 minutes at 15,000 xg at 4°C. The soluble fraction was loaded on a Ni-NTA poly-histidine-affinity column (5 mL HisTrap FF crude, GE Healthcare) at a 2 mL/min flow rate. The sample was then eluted with an imidazole gradient over 45 mL, the buffer containing TBS1X, 1 M imidazole, at pH 8. The sample was concentrated using Novagen

concentrators with 3 kDa cut-off membranes centrifuged at 5,000 xg. The tag was cleaved by the TEV protease (at a ratio of 2% w/ w) for 3 h and then loaded on a HisTrap column and the tag-free proteins were collected in the flow through. Finally, a size exclusion chromatography was performed on HiLoad Superdex 10/300 75 pg equilibrated in 25 mM Tris-HCl pH 7.5, 250 mM NaCl, and 5 mM β me. The quality of the purified protein was analyzed by SDS-PAGE 15% and the protein concentration was determined by spectrophotometry using the absorbance at 280 nm.

b. Purification of the BRCA2 fragment co-expressed with DSS1 in insect cells

The pellet was resuspended in 40 mL of a solution containing 20 mM Tris-HCl at pH 8.0, 50 mM NaCl, 1X protease inhibitors (EDTA-free Roche), 2 mM DTT, 1 mM EDTA, 1 mM PMSF, 5 mM MgSO₄, benzonase. After sonication at 10°C, the supernatant was incubated 20 minutes at room temperature with benzonase and centrifuged at 50 000 g for 15 minutes at 4°C. The soluble extract was then supplemented with 5 mM DTT and loaded onto glutathione beads. After 1 h of incubation at 4°C, glutathione beads were washed first with 1 M NaCl buffer and then with the purification buffer (50 mM Tris pH 8, 150 mM NaCl, 10 mM β -ME). The GST tag was cleaved with TEV protease for 2h, then the protein was recovered in the flow-through, another step of purification using a Heparin column was used to eliminate DNA, the protein was eluted with a solution containing 1 M of NaCl, the sample was concentrated using a membrane with a 3kDa cut-off and loaded on a SEC Superdex increase 200 10/300 GL column equilibrated in 25 mM Tris-HCl pH 7.5, 250 mM NaCl, 5 mM β me.

c. Purification of HSF2BP

The bacterial pellet was resuspended in 35 mL of a solution containing 25 mM Tris-HCl at pH 7.5, 500 mM NaCl, 5 mM β me, EDTA-free Protease Inhibitor Cocktail (Roche), 500 ug lysozyme, 0.5 μ l benzonase supplemented with 1.5 mM MgCl and 5% of glycerol. Cells were sonicated on ice 2.5 minutes in total with 1 s ON/1 s OFF cycle of sonication (60% amplitude), and the lysate was clarified by centrifugation during 15 minutes at 15,000 g at 4°C. The soluble fraction was loaded on a Ni-NTA poly-histidine-affinity column (5 mL HisTrap FF crude, GE Healthcare) at a 2 mL/min flow rate. The column was washed with a solution containing 25 mM Tris-HCl, 1 M NaCl. The sample was then eluted with an imidazole gradient over 45 mL, the buffer containing 25 mM Tris-HCl, 500 mM NaCl, 1 M imidazole, at pH 7.5. The sample was concentrated using Novagen concentrators with 10 kDa cut-off membranes centrifuged at

5,000 g . The tag was cleaved by the TEV protease (at a ratio of 2% w/ w) during an ON dialysis at 4 °C against 25 mM Tris-HCl pH 7.5, 250 mM NaCl, 5 mM β me, loaded on a HisTrap column and the tag-free proteins were collected in the flow through. Finally, a SEC purification was performed on a HiLoad Superdex 10/300 200 pg equilibrated in 25 mM Tris-HCl pH 7.5, 250 mM NaCl, 5 mM β me. The quality of the purified protein was analyzed by SDS-PAGE 15% and the protein concentration was determined by spectrophotometry using the absorbance at 280 nm.

d. Purification of H2 and H3

The bacterial pellet were resuspended in 35 mL of a solution containing TBS1X at pH 8, 150mM NaCl, 5 mM DTT, 1mM PMSF, EDTA-free Protease Inhibitor Cocktail (Roche), 500 ug lysozyme, 0.5 μ l benzonase supplemented with 1.5 mM MgCl . Cells are sonicated on ice 2.5 min in total with 1 s ON/1 s OFF cycle of sonication (60% amplitude), and the lysate was clarified by centrifugation during 15 minutes at 15,000 g at 4°C. The soluble fraction was loaded on a Ni-NTA poly-histidine-affinity column (5 mL HisTrap FF crude, GE Healthcare) at a 2 mL/min flow rate. The sample was then eluted with an imidazole gradient over 45 mL, the buffer containing TBS1X, 1 M imidazole, at pH 8. The sample was concentrated using Novagen concentrators with 3 kDa cut-off membranes centrifuged at 5,000 g. The tag was cleaved by the TEV protease (at a ratio of 2% w/ w) during 3 h and then loaded on a HisTrap column and the tag-free proteins were collected in the flow through. Finally, a SEC purification was performed on a HiLoad Superdex 10/300 75 pg equilibrated in 25 mM Tris-HCl pH 7.5, 250 mM NaCl, 5 mM β me. The quality of the purified protein was analyzed by SDS-PAGE 15% and the protein concentration was determined by spectrophotometry using the absorbance at 280 nm.

e. Purification of SPATA22

The bacterial pellet was resuspended in 35 mL of a solution containing 25mM Tris-HcL at pH 8, 150mM NaCl, 5 mM DTT, 1mM PMSF, EDTA-free Protease Inhibitor Cocktail (Roche), 500 ug lysozyme, 0.5 μ l benzonase supplemented with 1.5 mM MgCl. Cells were sonicated on ice 2.5 minutes in total with 1 s ON/1 s OFF cycle of sonication (60% amplitude), and the lysate was clarified by centrifugation for 15 minutes at 15,000 xg at 4°C. The soluble fraction was loaded on a Ni-NTA poly-histidine-affinity column (5 mL HisTrap FF crude, GE Healthcare) at a 2 mL/min flow rate. The sample was then eluted with an imidazole gradient over 45 mL,

the buffer containing 25mM Tris-Hcl, 150mM NaCl, and 1 M imidazole, at pH 8. The sample was concentrated using Novagen concentrators with 10 kDa cut-off membranes centrifuged at 5,000 g and then loaded onto a Heparin HP column to eliminate DNA by washing with a solution containing 1 M NaCl. The tag was cleaved with thrombin for 3h. Finally, a SEC purification was performed using a HiLoad Superdex 10/300 200 pg equilibrated in 25 mM Tris-HCl pH 7.5, 250 mM NaCl, 5 mM β ME. The quality of the purified protein was analyzed by SDS-PAGE 15% and the protein concentration was determined by spectrophotometry using the absorbance at 280 nm.

9. Peptides

Table 9. Summary of all peptides used during this thesis

Name	Peptide sequence
BRME1-C (649-668) 20 aa	PY PSKGPGNIPR GDPPWREL
BRME1-N (578-601) 24 aa	DPVAVAKAQPRTFVGIQASEASRM
BRME1 -M short (601-630) 30 aa	MEDATNVVRGLIVELSNLNRLIMGTHRDL
BRME1-M (602-641) 40 aa	EDATNVVRGLIVELSNLNRLIMGTHRDL EAFKRLNYRKTK
SPATA22N 23 aa	RSTAGCLPVPLFNQKKRNRQPLTSNPLKD
BRCA2 F 15X Δ 12 (2312 -2342) 31 aa	STPDGTIKDRRLFMHHVSLEPITCVPFRITTK
HSF2BP helix α 1 (19- 50) 32 aa	EFVKVRKKDLERLTTEVMQIRDFLPRI LNGEV

All peptides in this study were synthesized by Genecust, first solubilized in H₂O and then diluted into a buffer that depended on the experiment.

10. Figures

Figures were prepared using Microsoft Powerpoint version 16.42 or Affinity Designer 1.7.2. Molecular graphics images were produced using the PyMOL Molecular Graphics System, Version 1.2r3pre, Schrödinger, LLC or Chimera / ChimeraX package from the Resource for Biocomputing.

II. Methods

1. X-ray crystallography

X-ray crystallography is one of the most commonly used techniques, and certainly the oldest technique, giving access to the three-dimensional atomic structure of biological macromolecules (Le Du et al., [Introduction à la cristallographie biologique 2021](#)). The vast majority of detailed 3D information that is nowadays available has been discovered from single crystal X-ray diffraction studies. Over 166000 molecular structures have been determined by X-ray crystallography and deposited into the Protein Data Bank since its establishment in 1971. This corresponds to 86% of the structures available in the Protein Data Bank.

X-rays interact with electrons through a process called "diffraction," which results from the crystal's molecules regular arrangement (**Figure 28**). An X-ray sensitive detector is used to record the diffraction data. Since about 10 years, rapid readout detectors were installed on highly automated beamlines at synchrotrons. The duration of a single data collection is nowadays between 5 and 60 seconds (against 20 minutes to one hour 10 years ago). Intensities of diffraction maxima ("reflections" or "spots") are then indexed, integrated and scaled using a specialized software, usually XDS ([Kabsch, 2010](#)).

Each diffraction spot can be represented as a diffracted wave with an amplitude and a relative phase. The amplitude and phases (named "structure Factors"), altogether correspond to the Fourier transform of the electron density distribution within the unit cell of the crystal. If the phases were known, it would be straightforward to compute the electron density of the molecule. However, the reflected photons counted by the detector contain only information about the amplitude of the wave. This is the phase problem. It can be easily solved if we can make a good guess of the conformation of the molecule. Otherwise, the phases can be obtained by recording additional X-ray data on a protein sample enriched in selenomethionines, as you will see in my first X-ray study.

The interpretation of the diffraction data also depends on their maximum resolution. Assuming that a crystal consists of parallel planes of atoms and that reflections of X-rays from

successive planes interfere constructively to give rise to diffraction peaks, the resolution is the minimal separation of the crystal plans giving rise to an observable X-ray diffraction spot. Each diffraction spot in a diffraction pattern has a specific resolution. The higher the diffraction angle of a spot (i.e., the further from the center of the diffraction image where the incoming X-ray beam would hit), the higher is its resolution. It is directly related to the minimum distance separating the details of the electronic density. A resolution of 2 Å is sufficient to distinguish the position of the different amino acids of a protein or the bases of a nucleic acid, but not to identify the individual atoms. If some portions of a macromolecule are less ordered in the crystal than others, they will be described at a poorer resolution. The "resolution of an X-ray structure" derives from on the most ordered portions of the structure.

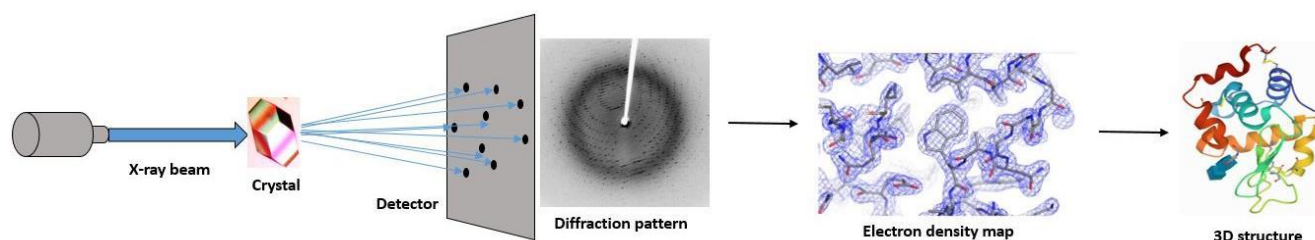


Figure 28. Principle of protein X-ray crystallography.

An X-ray beam hits a protein crystal. The regular arrangement of the molecules in the crystal leads to X-ray diffraction in some defined directions. Diffraction patterns are collected on a detector while rotating the crystal and then processed to generate an electron density map. The arrangement of atoms from the protein 3D model is refined through successive cycles of model building and refinement.

a. Crystallization and data collection

Initial crystallization conditions were evaluated using a high-throughput platform and commercial kits. The samples were sent to the High Throughput Crystallization and Fragment Screening Facility (HTX Lab, José Marquez team, EMBL, Grenoble) and tested using 6 commercial kits, each containing 96 conditions (576 different conditions).

The crystallization experiments were performed with a Mosquito-LCP robot (TTP Labtech) by vapor diffusion using sitting drops at 4°C and 20°C and droplets were formed by mixing 0.1

μL of the sample with 0.1 μL of reservoir solution. The crystallization trials were observed with a visualization robot Formulatrix RockImager that takes pictures of the drops at different times (day D+1, D+3, D+7, D+15, D+33, D+61, and D+ 87, respectively). The picture timeline allows following the evolution of the crystallization droplets and classifying them according to the state of the solution.

Prior to X-ray diffraction experiments, the complex between H3 and F15X was purified on a size exclusion chromatography column HiLoad Superdex 200 pg 16/600 (GE Healthcare) in a 25 mM Tris pH 7.5, 250 mM NaCl and 5 mM βME, in order to prevent the presence of aggregates. The complex was then concentrated up to 10 mg/mL.

The conditions that provided crystallization hits on the platform were reproduced and optimized in the laboratory by vapor diffusion using the hanging drops vapor diffusion method at 20°C with droplets formed by mixing 1 μL of the sample with 1 μL of the reservoir solution containing 100 mM MgCl₂, 100 mM MES pH 6 and 16% (w/v) PEG 3350. Needle crystals appeared within 3 days, and were grown for 1–2 weeks before being flash-cooled in liquid nitrogen with cryoprotection prepared using the reservoir solution supplemented with 20% glycerol.

X-ray diffraction data were collected on the beamlines PROXIMA-1 and PROXIMA-2 at synchrotron SOLEIL and reduced using the XDS package ([Kabcsch, 2010](#)).

b. Structure determination and data refinement

To solve the phase problem, we selected 3D structures of armadillo domains analogous to that of HSF2BP, as proposed by the HHPRED server ([Söding et al., NAR 2005](#)). We knew that the armadillo domain of HSF2BP dimerized from gel filtration analyses, but, as AlphaFold was not available at this time, we were not able to correctly select dimers of armadillo domains from the known 3D structures, to guess the assembly mode of the HSF2BP dimer. I tried to obtain the three-dimensional structure of the armadillo domain of HSF2BP by molecular replacement, using our selected monomeric armadillo models and the program MOLREP version 11.7.03 from CCP4. However, all my attempts failed. Pierre Legrand, from the Proxima 1 beamline, further calculated a set of HSF2BP armadillo models using the Robetta server ([Yang et al., 2020](#)). With one of these models, he obtained the first phases for a triclinic crystal form (table 2 in [Ghouil et al., 2021](#)). In the meanwhile, I produced a new protein sample in

which the armadillo domain was labeled with selenomethionines and I obtained new X-ray crystallography data on crystals obtained with this sample. The phases calculated by Pierre Legrand allowed finding the selenium substructure from this SeMet SAD dataset (wavelength of data collection: $\lambda = 0.97918 \text{ \AA}$; the crystal form was the same as that observed with the unlabeled sample). Later, a monoclinic crystal form (table 2 in [Ghouil et al., 2021](#)) was obtained from a complex with ARM and F15X containing 5 and 1 selenomethionine, respectively. The collected SeMet SAD dataset (wavelength of data collection: $\lambda = 0.97918 \text{ \AA}$) was used to directly calculate phases, without external model contributions and confirmed the initial model built in the triclinic crystal form. Selenomethionine sites were found using the SHELX C/D/E suite of programs. These sites were refined using PHASER version 2.8.2 in EP mode. The resulting Se SAD phases were improved by density modification using PARROT version 1.0.4 and a model automatically build using BUCCANEER version 1.6.10 confirming the sequence attribution for ARM and F15X. The model underwent iterative cycles of manual reconstruction in COOT and refinement in BUSTER version 2.10.3.

2. NMR spectroscopy

a. NMR for protein-protein interactions

NMR (Nuclear magnetic resonance) spectroscopy plays a major role in the determination of the structures and dynamics of proteins and other biological macromolecules. It has been used to solve the three-dimensional structures of more than 13,000 biomolecules or biomolecular complexes. NMR spectroscopy remains the only experimental technique that can access both structure and dynamics of IDPs at atomic resolution. It provides information about interactions displaying low (mM) to moderate (μM) affinities.

The most informative and widely applicable NMR experiments utilized for investigating binding events are the 2D Heteronuclear Multiple Quantum Correlation (HMQC) and 2D Heteronuclear Single Quantum Coherence (HSQC) acquired on a ^{15}N - and/or ^{13}C -labeled protein ([Williamson, 2013](#); [Furukawa et al., 2016](#)). In these experiments, the magnetic interactions between hydrogens (^1H resonance frequencies, also called chemical shifts, on the horizontal axis) and bounded nitrogens (^{15}N resonance frequencies, also called chemical shifts, on the vertical axis) are identified. One signal is observed for each backbone HN bond, i.e.,

each residue except proline. The frequency coordinates of this signal (i.e. its position in the spectrum) depend on the structural environment of the corresponding residue. Three different residues exhibit additional side-chain NH (arginine) or NH₂ (asparagine and glutamine) whose signals are also revealed.

In this study, we used NMR as a technique to study protein-protein interactions in solution, and specifically for locating binding sites on IDRs. We recorded 2D NMR spectra on our IDRs of interest, either free or bound to its partners. NMR is capable of detecting changes in the local environment of nuclei provoked by binding events. Thus, it is possible to identify the different residues of a protein involved in a binding interface. Analysis of the changes in chemical shift induced by protein-protein binding affords a wealth of information regarding not only the interaction site but also the binding affinity and kinetics.

Chemical shift titrations of IDPs with their binding partners often lead to either an absence of signals corresponding to the bound IDPs because of the large size of the complex or an excessive line broadening of the NMR resonances due to the fast exchange between the free and ligated forms occurring on the micro- to millisecond (μ s-ms) time scale. In order to overcome this problem, NMR exchange techniques were developed, which provide structural information on low-populated bound states of IDPs (detectable by the exchange experiments) obtained by adding small substoichiometric amounts of the binding partner ([Delaforge et al. 2018](#)). Thus, it is possible not only to identify IDP interacting residues, but also to characterize the structure of the bound complex ([Charlier et al., JACS 2017](#)).

NMR experiments were performed on 700 and 950 MHz Bruker Avance spectrometers, all equipped with a triple resonance cryogenic probe. Two-dimensional ¹H-¹⁵N correlation spectra were acquired using a HSQC pulse sequence at a temperature of 283 K, on a 3 or 5 - mm-diameter NMR sample tube, containing 80:20% H₂O/D₂O. All NMR data were processed using Topspin3.1 (Bruker) and analyzed with CCPNMR.

b. Assignments of the NMR signals

The ¹H-¹⁵N spectrum of the protein of interest has first to be assigned: each peak has to be associated with its corresponding residue in the protein sequence. This assignment requires the production of a ¹⁵N/¹³C-labeled NMR sample for recording of a series of 3D NMR spectra necessary for the NMR chemical shift assignment. It is the most time-consuming part of the

protocol. Due to their high flexibility, disordered proteins present a narrow ^1H - ^{15}N spectrum, with possible signal superimpositions. In order to prevent superimposition, deleterious for the precise spectral analysis, the size of the construct might be adapted, commonly it is limited to 100-200 amino acids. Working on large proteins (i.e., > 200 aa) also leads to low sensitivity in the case of folded proteins that tumble slowly. This is less a problem in the case of IDRs, which conserve their fast motion at any size. IDRs larger than 200 amino acids are thus still amenable to solution NMR, but their NMR assignment often necessitates the use of 4D and 5D NMR experiments to avoid peak superimposition.

We assigned the NMR signals of the BRCA2 F0 fragment using the following 3D ^1H - ^{15}N - ^{13}C correlation spectra: 3D HNCA, HNCACB, CBCA(CO)NH, HNCO, HN(CA)CO and HN(CO)(CA)NH experiments at 283 K, on 3 or 5- mm-diameter NMR sample tubes containing, 100 μM uniformly $^{15}\text{N}/^{13}\text{C}$ -labeled BRCA2 F15X, in 25mM Tris-HCl pH7, 250mM NaCl, 5mM βme and 80:20% $\text{H}_2\text{O}/\text{D}_2\text{O}$.

3. Isothermal Titration Calorimetry ITC

Isothermal titration calorimetry (ITC) is a powerful technique to study both protein-ligand and protein-protein interactions. It allows the direct determination of the thermodynamic parameters of the interaction: the enthalpy (ΔH), the association constant (K_a) and the stoichiometry of the interaction (N). The free energy (ΔG) of the interaction and its entropic ($-\Delta S$) component can be deduced from the association constant. The ITC instrument is composed of two identical cells surrounded by an adiabatic jacket. Temperature differences are detected between the reference cell (filled with water) and the sample cell containing the protein and increasing amounts of ligand. During the experiment, the ligand is progressively injected using a syringe into the sample cell. At each injection, heat is either produced or taken up (depending on the nature of the binding reaction). Measurements consist of the time-dependent input of power required to maintain equal temperatures between the reference and sample cells. Thus, the experimental raw data consists of a series of spikes of heat flow, with every spike corresponding to one ligand injection. These spikes are integrated, in order to obtain a sigmoidal curve corresponding to the heat as a function of the molar ratio of ligand / macromolecule.

All ITC titrations were performed on a VP-ITC instrument (Malvern) and data were analyzed using the Origin 7.0 software (OriginLab). The proteins/peptides were diluted in the appropriate buffer and dialyzed overnight. For concentration measurements, the optical densities were measured at 280 nm before each manipulation (for samples containing Tryptophan and Tyrosine).

The ITC titrations were performed using 500 μ l at 60-120 μ M of protein 1 in the syringe and 2.4 mL of protein 2 at 8-12 μ M in the cell, both proteins being in a solution containing 50 mM Tris HCl at pH 7.5, 250 mM NaCl, 5 mM β me. Measurements were performed at different temperatures (20°C and 10°C) with a first injection of 2 μ l during 4 s, followed by 29 injections of 10 μ l separated of 180 s intervals (see details in the results section).

4. SEC- Multi-Angle Light Scattering (MALS)

SEC-MALS is the combination of size exclusion chromatography with multi-angle light scattering measurements. Size-exclusion chromatography (SEC) separates molecules based on their hydrodynamic volume. Mass estimated from SEC depends on similarity in shape to a set of reference standards for accurate mass determination and fails for elongated or sticky proteins. In particular, from our experience, an IDP shows a mass that is approximately 3-times its theoretical mass. In a SEC-MALS experiment, the eluted fractions are analyzed by Multi-Angle Light Scattering (MALS). The intensity of the scattered light is measured, which is proportional to the molar mass in solution, independently of the shape of the molecule. Combining SEC, MALS and concentration detectors in an SEC-MALS experiment allows for more accurate mass measurements than SEC or MALS alone.

Experiments were performed by either Christophe Velours on the IB2C platform or Dr Gabriel David at Synchrotron SOLEIL. Two types of gel filtrations were used in this study (a Superdex 200 increase 10/300GL or a Bio-SEC 3 μ m, 300Å, 4.6 mm from Agilent), connected to a MALS mini-DAWN Treos (Wyatt) that measures light scattering at three angles (typically between 45°-135°). Before use, the column was equilibrated with 25 mM Tris pH7.5, 250 mM NaCl, 5 mM β me and calibrated with BSA concentrated at 10 mg/mL. Then, a volume of 20 μ L of freshly purified samples concentrated at 3.2 mg/mL for free HSF2BP, 7 mg/mL for HSF2BP helix α 1, 5 mg/mL for HSF2BP/BRME1 complex and 4.4 mg/mL for HSF2BP/F15X complex was injected onto the column at a flow rate of 0.2 mL/min.

5. SEC-SAXS Small angle X-ray scattering (SAXS)

SEC-SAXS is a powerful method for the structural characterization of proteins in solution. It provides information about the size and shape of proteins and complexes on a broad range of molecular weights (Kohn JE, 2004; Wilkins DK, 1999; Stumpe, 2007). It was used in this study to determine the average size and shape of the molecules, in particular those of free HSF2BP and H3/BRCA2 F15X complex. As the experiments are performed in solution, this technique provides information about 3D structures of proteins and protein complexes that either cannot be crystallized, or have known crystal structures and it is then important to verify that such structures are also present in solution.

The setup of a SAXS experiment is conceptually simple: a solution of particles usually placed in a quartz capillary is illuminated by a collimated monochromatic X-ray beam, and the intensity of the scattered X-rays is recorded by an X-ray detector. The scattering pattern of the pure solvent is collected as well and subtracted from that of the sample solution leaving only the signal from the particles of interest. The resulting scattering pattern is related to the overall shape and size of the particles under investigation (Jacques DA, 2010). Several characteristic parameters of the investigated sample can be obtained directly from the experimental scattering pattern including molecular weight, maximum dimension (D_{\max}), and the radius of gyration (R_g) that provides a measure of the overall size of the macromolecule.

From the slope of the linear fit of the logarithm of the scattered intensity $I(q)$ as a function of the square of the scattering vector q^2 , we can determine R_g , and the intercept between this fit and the y axis gives the forward scattering $I(0)$, which is proportional to the protein's molecular weight and concentration. The scattered intensity $I(q)$ is the Fourier transform of $p(r)$, the correlation function of the electronic density, which corresponds to the probability to find a scatterer at position r in the sample if another scatterer is located at position 0. This $p(r)$ can be viewed as the histogram of distances between all possible pairs of atoms within a particle (Figure 29). Three-dimensional models of the macromolecule can then be built for which the distance distribution function $p(r)$ fits with that deduced from the SAXS data.

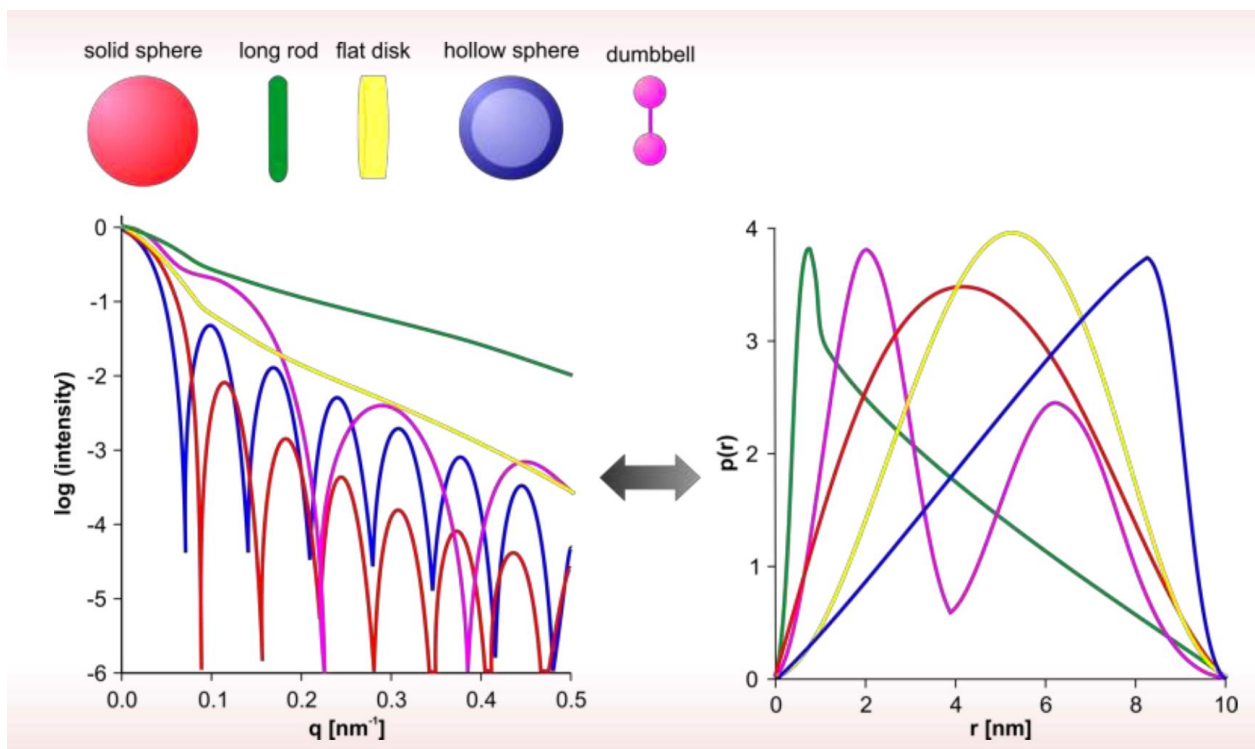


Figure 29. $P(r)$ functions for geometric bodies .

(Svergun et al., 2003).

The SAXS experiments were performed on the SWING beamline at Synchrotron SOLEIL. In these experiments, the scattering is detected within a narrow region around the incident beam. The X-ray scattering intensities were recorded on an Eiger X 4M detector under vacuum. As the SAXS experiment was coupled with SEC, 100 μ l of the sample at 10 mg/mL were loaded onto a Bio SEC-3 column (Agilent) equilibrated in 25mM Tris-HCl buffer, pH 7.5, 250mM NaCl, and 5mM β me, and the eluted sample was driven through a capillary to the SAXS cell. The scattered intensities as a function of the scattering angle were measured with a flow rate of 0.2 mL/ min. We thus obtained about 30-50 frames corresponding to the protein peak during the SEC elution. The data were analyzed using the FOXTROT software developed on the SWING beamline. I added the curves corresponding to either the buffer or the protein. I subtracted the buffer curve from the protein curve. This allowed to remove the buffer signal and to obtain the scattering due to the protein (or protein complex) only. Then, the final curve was analyzed by the ATSAS suite (Manalastas-Cantos et al., 2021) to calculate the particle radius of gyration (R_g), the largest interatomic distance (D_{max}), and the molecular weight (M_w).

6. Tycho NT6

This technique is used to measure the thermal stability of a protein or a protein complex. The instrument named "Tycho" by Nanotemper measures the fluorescence signal of tryptophan and tyrosine residues during the thermal denaturation of the sample. This signal depends on the environment of these residues; the progressive exposure of these residues to the solvent during protein unfolding is monitored, to calculate the inflection temperature of the process (or denaturation temperature). More precisely, the system measures the change in intrinsic fluorescence of the tryptophan and tyrosine residues, by detecting them at 350 nm and 330 nm, on a temperature range of 35-95 °C. The ratio between the fluorescence at these two wavelengths is plotted as a function of the temperature. The denaturation profile of the different protein complexes was compared to the denaturation profile of the protein alone. The observation of a significant difference between the denaturation temperatures measured before and after adding the ligand demonstrates that the protein interacts with its ligand. On the opposite, no difference does not mean that there is no interaction. Indeed, the detected aromatic residues might be located outside of the binding domain or binding might not cause stabilization of the complex. Destabilization of the complex compared to the free protein/ligand suggests that binding is associated with a conformational change.

Each sample was prepared with 10 µM of H2 to which was added 10-20 µM of the peptides BRCA2-HBD, and SPATA22N. Three different buffers, containing the same Tris-HCl pH 7.5 and 5 mM βME with the following salt concentrations: 250 mM NaCl, 250 mM NaCl + 5 mM MgCl₂, 25mM NaCl, were used. Fluorescence measurements were performed in different buffers to test the effect of sodium chloride and Mg²⁺ ion concentration on the interactions.

7. AlphaFold 2

Alpha Fold (AF) is a system developed by DeepMind and the European Bioinformatics Institute at EMBL to predict the 3D structure of a protein or protein complex from one or more amino acid sequences ([Jumper et al., 2021](#)). The input is either the primary amino acid sequence of the protein or a multiple sequence alignment (MSA). If no alignment is provided, AF will use a set of MSA tools to calculate its own alignment. From the analysis of this alignment, it will iteratively predict residue-residue proximities and a 3D fold. Further analysis of this fold is used to improve the sequence alignment and then the predicted 3D model. The final model

is analyzed to estimate its accuracy using two different parameters: pLDDT and PAE. The per-residue confidence metric called pLDDT (predicted local distance difference test, plotted as a function of the aa sequence) shows which region of the protein systematically adopts the same local 3D structure in all the calculated models. It is scored as modeled with high, medium and low confidence. Regions predicted with low confidence generally correspond to IDRs. When IDRs fold upon binding, the pLDDT score of the binding region increases to a high confidence score, reflecting the well-defined 3D structure of the bound IDR residues. The predicted aligned error (PAE, plotted as a heat map with the protein sequence in x and y) estimates the relative position error for each pair of residues. If a PAE is low, it indicates a confident relative predicted position between two residues (Mirdita et al., 2021; Tunyasuvunakool et al., 2021). This is useful for assessing inter-domain or inter-protein position accuracy. In the case of a folded domain binding to an IDR, the PAE between intermolecular pair of residues at the interface might be low, indicating that there is an interaction, while the pLDDT might suggest low confidence, if the bound structure of one of the partners is poorly-defined, as for example in a fuzzy complex. A low pLDDT score might also mean that there is no interaction between the two partners. If the 3D structure of the whole complex is well-defined, then both the pLDDT and the PAE will indicate a high-confidence model, which does not completely exclude that the interaction does not exist *in vitro* in the presence of the two partners. The prediction could also be true in the presence of additional molecules (ex: membrane) or simply be wrong.

AF2 was used to model the interactions between fragments of BRCA2, HSF2BP, BRME1, and SPATA22. Therefore, we ran a series of calculations through the Google Collab website: <https://colab.research.google.com/github/sokrypton/ColabFold/blob/main/AlphaFold2.ipynb>. More calculations were performed on a local version of ColabFold (Mirdita et al., 2022) running 12 iterations of Alphafold2 algorithm on the PROXIMA-1 beamline of the Synchrotron SOLEIL by Dr. Pierre Legrand. For each Alphafold2 runs, five models were generated that usually converged toward similar conformations. Quality of the obtained models were evaluated through their pLDDTs scores (good if above 70). These interactions were then tested *in vitro* by fluorescence and calorimetry.

8. Electron Microscopy

Cryo-electron microscopy is the newest technique giving access to the three-dimensional atomic structure of biological macromolecules. It uses a transmission electron

microscope to observe macromolecules in their native and hydrated states. Three scientists who particularly contributed to the development of this technique, Jacques Dubochet, Joachim Frank and Richard Henderson, received the Nobel prize of Chemistry in 2017. Nowadays, more than 11,000 structures solved by cryo-EM are available in the Protein Data Bank. Cryo-EM gives access to the three-dimensional structure of protein complexes in solution. It necessitates only small amounts of material (a few microliters at about 0.1-1 mg/ml) and can be applied to macromolecular complexes without any size constraint.

a. Complexes formation

A critical step for EM analysis is the preparation of a homogeneous sample. This can be complicated, in particular in the case of proteins with multiple conformations or weak affinity complexes. I have performed an EM analysis of the complex between BRCA2 F15X and HSF2BP FL. In this case, the affinity is nanomolar (see the Results section); however, the sample was not systematically forming homogeneous complexes.

To form the complex, I mixed BRCA2F15X and HSF2BP-FL with a ratio of 1:1.2 and loaded the sample onto a gel filtration. I used two different columns to purify the complex (Superdex200 increase 10/300 GL and Superose6 increase 10/300), equilibrated with either 25 mM HEPES pH 7.5, 250 mM NaCl, 5 mM β me, or 25 mM Tris -HCL pH 7.5, 250 mM NaCl, 5mM β me). Then, I selected the eluted fractions corresponding to the summit of the peak. The homogeneity of the complex was checked by 12% SDS-page gel stained with Coomassie Blue and negative staining EM.

With crosslinker agent: One of the several attempts to have a homogenous complex on the EM grid was performed using a crosslinking reagent (glutaraldehyde). I mixed BRCA2F15X and HSF2BP-FL with a ratio of 1:1.2 to achieve a final concentration of 3 mg/mL. The complex was then incubated for 15 minutes on ice. Glutaraldehyde was added to a final concentration of 0.05% and the mixture was incubated for 5 minutes at room temperature. The glutaraldehyde, $\text{CH}_2(\text{CH}_2\text{CHO})_2$, forms Schiff bases between the two carbonyl ends of glutaraldehyde and positively charged amino groups on the surface of the protein. It cross-links proteins that are in close contact (spacer arm of 5Å) (Migneault et al., 2004). The reaction was quenched by adding 0.1 v/v of 1M Tris-HCl pH 8.0. The mixture was injected onto a Superose 6 increase 10-300GL column, previously equilibrated with a buffer containing 25 mM Tris-HCl pH 7.5, 250 mM

NaCl, and 5mM β me. The homogeneity of the complexes was checked by 12% SDS-page gel stained with Coomassie Blue and negative staining EM.

b. Negative-Staining Electron Microscopy

Negative-staining electron microscopy (NS-EM) is a straightforward and powerful tool and is always recommended as a first step in an electron microscopy project. Compared to cryo-EM, sample preparation and image acquisition are faster and NS-EM can give ideas concerning sample quality, homogeneity, sample concentration, particle dispersion and coverage in the EM grid, thus saving numerous trials and error iterations in cryo-EM sample preparation (Booth et al., 2011). Images acquired in NS-EM can also be analyzed to generate low-resolution 3D reconstructions that can be used as a reference in cryo-EM data analysis (Carroni & Saibil, 2016).

The image formation is due to the sample's scattering of the electron beam. In NS-EM, the stain will appear dark as it contributes to the elastic scattering of electrons, while the mainly carbon-rich protein sample, due to scattering of electrons, will appear in varying intensities of white. Stain opaqueness is proportional to its atomic number; the higher the number, the higher the contrast that will be achieved. Most negative-staining compounds thus consist of heavy-atom salts (Booth et al., 2011), typically uranium, tungsten, osmium or molybdenum with the particular stain being chosen depending on the pH and coarseness of grain required. We used heavy metal stains like uranyl acetate, which strongly scatter electrons unlike low-mass atoms that constitute biological species. Uranyl acetate coats the macromolecule. However, NS-EM can cause artefacts in the final reconstruction, as for example sample flattening. Resolution limits for negative staining electron microscopy are between 18Å-20Å (Thompson et al., 2016).

For the BRCA2 F15X-HSF2BP FL complex, 5 μ L of diluted sample in 25 mM HEPES pH 7.5 250 mM NaCl and 5mM β me, were deposited on a glow-discharged EM grid coated with a continuous carbon film. Then, two droplets of 2% of uranyl acetate were applied successively. The excess of uranyl acetate was absorbed with Whatman filter paper, ashless grade. The grids were observed on a 120 kV Tecnai G-20.

c. Cryo-EM

We used the Single Particle Analysis (SPA) method to study our complex by cryo-EM. The purified macromolecule is applied onto a grid and flash frozen by plugging it into liquid ethane

in order to obtain a thin layer of vitreous ice. The transmission electron microscope (TEM) uses a particle beam of electrons to visualize specimens and generate a highly-magnified image. An electron gun at the top of the TEM emits electrons that travel through the microscope's vacuum tube. The TEM employs an electromagnetic lens which focuses the electrons into a very fine beam. This beam then passes through the specimen, which is very thin, and the electrons either scatter or hit a fluorescent screen at the bottom of the microscope. The macromolecule is present in multiple copies and different orientations on the grid. Its 2D projection images are collected and used for 3D reconstruction (**Figure 30**).

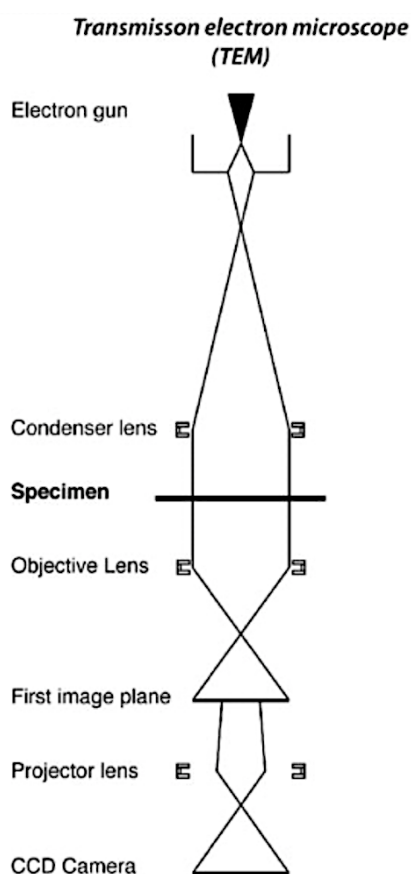


Figure 30. Schematic operation principles of a transmission-and a scanning electron microscope (TEM).

α . Grid preparation

First, a few microliters of the sample are deposited on the cryo-EM grid. Different types of grids differ by the nature of the metal that composes them (copper, gold or nickel), shape and size of holes (Lacey, C-flat and Quantifoil) and presence or not of a continuous layer of carbon. While gold supports are more expensive, they offer several advantages (no cytotoxicity,

reduced support wrinkling and movement due thermal contraction) compared to copper supports. In this study, many different grids were used to understand and optimize the vitrification of our complex.

The carbon layer presents on grids being hydrophobic, it is necessary to modify the surface of the grid to become more hydrophilic before applying the sample. This is a process called glow-discharging in which an electrical current is applied to the grid to ionize the support and increase the propensity of the support to adsorb protein molecules (Aebi & Pollard, 1987).

Then, the sample is blotted with filter paper to remove excess liquid and obtain a monolayer of the sample inside the holes. The grid is immediately and quickly plunge-frozen in liquid ethane (-182°C) and cooled down to the temperature of liquid nitrogen to obtain vitreous ice using a FEI Vitrobot Mark IV at 4°C (or 20°) with 100% humidity.

One of the main challenges during the plunge-freezing step is that it may induce sample aggregation (Figure 31). Blotting conditions are usually harsh for proteins and molecules being forced together into a thin layer of ice often translates into contact with the air-water interface, resulting in clustering of hydrophobic residues leading to denaturation and aggregation of the molecules.

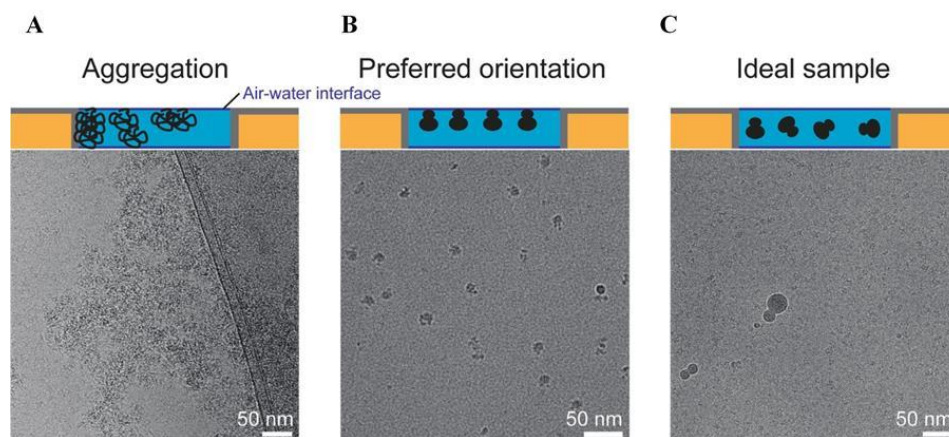


Figure 31. Representative micrographs corresponding to outcomes from the sample vitrification step.

(A) Particles can aggregate when having their hydrophobic pockets exposed to the air-water interface. (B) They can also be forced into one orientation during the plunge freezing. (C) The ideal micrograph should have the correct spread of particles in different orientations, so that image processing can succeed. Adapted from Brillault and Landsberg, 2020.

β. Data acquisition

CryoEM data were collected on Glacios (200 kV) in linear mode equipped with a Falcon 3 direct electron detector and on Titan Krios (300 kV) in counting mode equipped with a Gatan energy filter Bio-quantum/K3 camera at the NanoImaging platform, at Institut Pasteur with the help of Ana-Andrea Arteni, Malika Ouldali, Pierre Legrand and Jean-Marie Winter.

χ. Data processing

CryoSPARC software (Punjani et al., 2017) was used for image analysis, from motion correction to 3D classification (the data processing is detailed in the Results section). Image processing in SPA includes several steps and variables to consider before obtaining a scientifically accurate model of the biomolecule under study. A standard EM processing pipeline is shown in **Figure 32**.

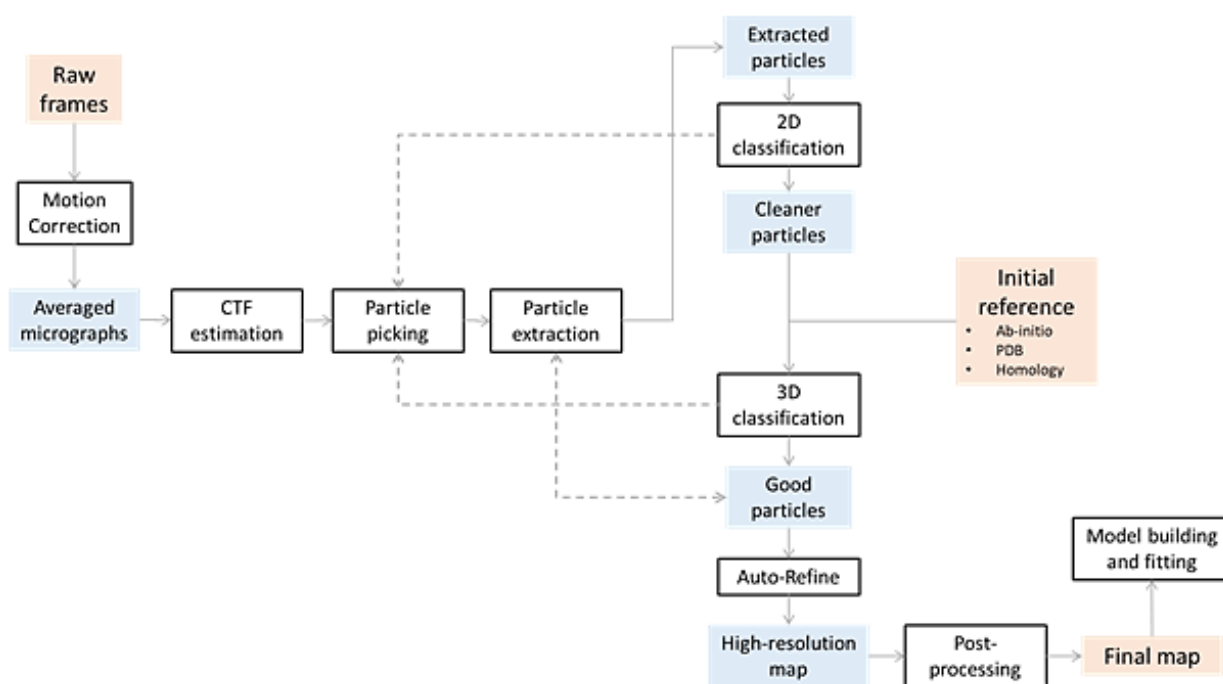


Figure 32. General workflow of the single particle image processing.

Arrows indicate the flow of the process needed to obtain a final map from initial raw frames collected in the microscope. Dashed arrows refer to optional steps that are usually taken, early per-particle CTF estimation in tilted data, and re-extraction of particles for high-quality reconstructions.

RESULTS

Chapter 1. BRCA2 interacts with a Testis Cancer Antigen

Preamble

BRCA2 has been mostly studied in the context of HR in somatic cells. However, it also has a prominent role in meiotic HR. Recently, several groups identified the meiotic HSF2BP as a new BRCA2-binding protein (Brandsma et al., 2019; Zhang et al., 2019). In a first study, the authors took advantage of the fact that BRCA2 can be degraded upon mild hyperthermia (42 °C) (Brandsma et al., 2019). Using mass spectrometry, they observed that several proteins, including HSF2BP, are simultaneously degraded in this condition. The interaction between BRCA2 and HSF2BP was further established by coimmunoprecipitation in mESCs. Interaction domains were mapped by coimmunoprecipitation using a series of tagged BRCA2 and HSF2BP expression constructs. This analysis showed that the HSF2BP-binding domain of BRCA2 is located between the BRC repeats and the DBD, whereas the BRCA2-binding domain of HSF2BP is located in the C-terminal region of this protein. Finally, recombinant protein fragments were produced in bacteria and used to demonstrate by SEC that the BRCA2 peptide from G2270 to A2351 directly binds to full-length HSF2BP. The elution volumes of HSF2BP, either free or bound to the BRCA2 peptide, suggested that this protein forms oligomers or highly elongated structures. In a second study, a search for partners of HSF2BP by yeast two-hybrid identified a BRCA2 fragment, from C2117 to S2371 (Zhang et al., 2019). This interaction was confirmed by coimmunoprecipitation in the mouse cell line B16-F1 and in testis extracts.

To study the interaction between BRCA2 and HSF2BP, my first objective was to produce and purify these two proteins, delimit the regions of interaction and design protein constructs allowing the production and purification of these regions. My goal was to obtain a three-dimensional structure of the complex and to further describe the interface between the disordered BRCA2 peptide and its meiotic partner HSF2BP.

Together with the team of Dr. A. Zelensky and Prof R. Kanaar (Erasmus Medical Center, Rotterdam, The Netherlands), we studied the structure and function of the interaction between BRCA2 and HSF2BP, working *in vitro*, in cells, and in a mouse model. In this part, I first describe in details my first (unpublished) attempts to characterize the 3D structure of the complex between BRCA2 and HSF2BP. Then, I introduce the published article that gathers our results and the work done by our collaborators.

1. Sample optimization

The production of recombinant proteins using bacterial/eukaryotic hosts is one of the main limiting steps when working on the 3D structure of biological macromolecules. Therefore, one of my first tasks was to develop a protocol to produce our proteins of interest that would give us pure samples (>95%) in large amounts (suitable for biophysical studies).

a. HSF2BP

The protocol describing the expression and purification of HSF2BP was provided by Dr. A. Zelensky (Master thesis of J. Veerman). Still, I optimized this protocol in order to get better yields and more stable proteins. In particular, most of the time, I performed only two steps of purification, including an affinity chromatography (Ni-NTA column) and a size-exclusion chromatography (Superdex 200pg). However, for some batches, the UV spectrum of the protein showed a high ratio $A_{260\text{nm}}/A_{280\text{nm}}$. I then performed an additional chromatography step using a heparin column. I obtained about 4 mg of pure protein per 800 mL of bacterial culture (**Figure 33**).

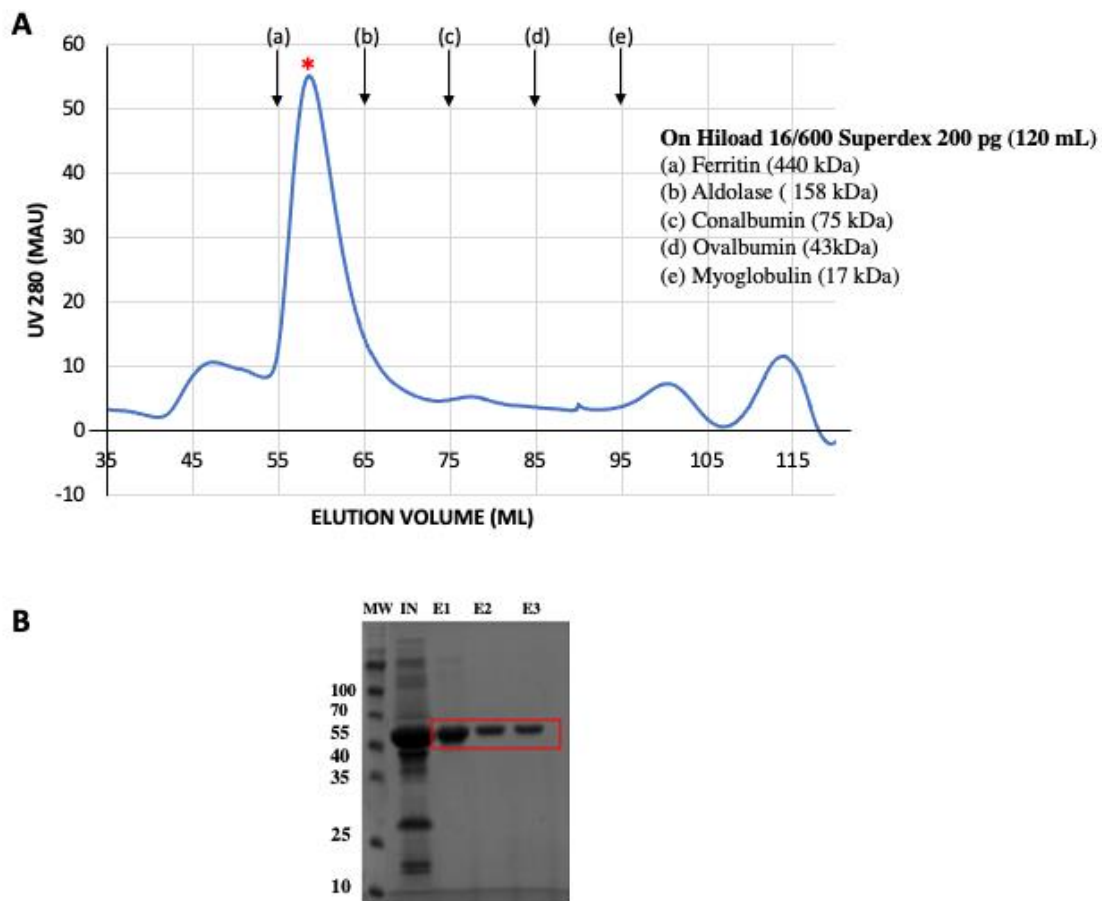


Figure 33. Last step of HSF2BP purification.

(A) Size-Exclusion Chromatography profile of HSF2BP showing the UV absorption at 280 nm. The column was a Hiload Superdex 200pg (GE Healthcare) and the buffer contained 25 mM Tris HCl at pH 7.5, 250 mM NaCl and 5 mM β me. Full-length HSF2BP was eluted at 60 mL (marked by a red star). **(B)** Coomassie-stained 15% SDS-PAGE of the SEC experiment. The lines correspond to: MW, molecular weights (kDa); IN, fraction loaded on the column; E1-3, fractions eluted around 60 mL.

b. H3 (or armadillo domain) and H2

H3 and H2 are two C-terminal fragments of HSF2BP, corresponding to the armadillo domain alone and the C-terminus of the predicted helix α 2 and the armadillo domain, respectively. These fragments were produced using the same protocol optimized in the lab (see the Material and Methods section). H3 was degraded after the first purifications. Therefore, its purification protocol including affinity chromatography, cleavage of the tag, and gel filtration chromatography was adapted to be performed in one day, which prevented protein degradation (**Figure 34**). H3 also does not tolerate freezing. Therefore, it was always purified just before

the experiments for which it was required. H2 was easier to work with. It could be frozen and unfrozen without precipitation or aggregation. Moreover, H2 was more stable: its denaturation temperature was 54.2°C, versus 42.1°C for H3 in our conditions, as measured by fluorescence.

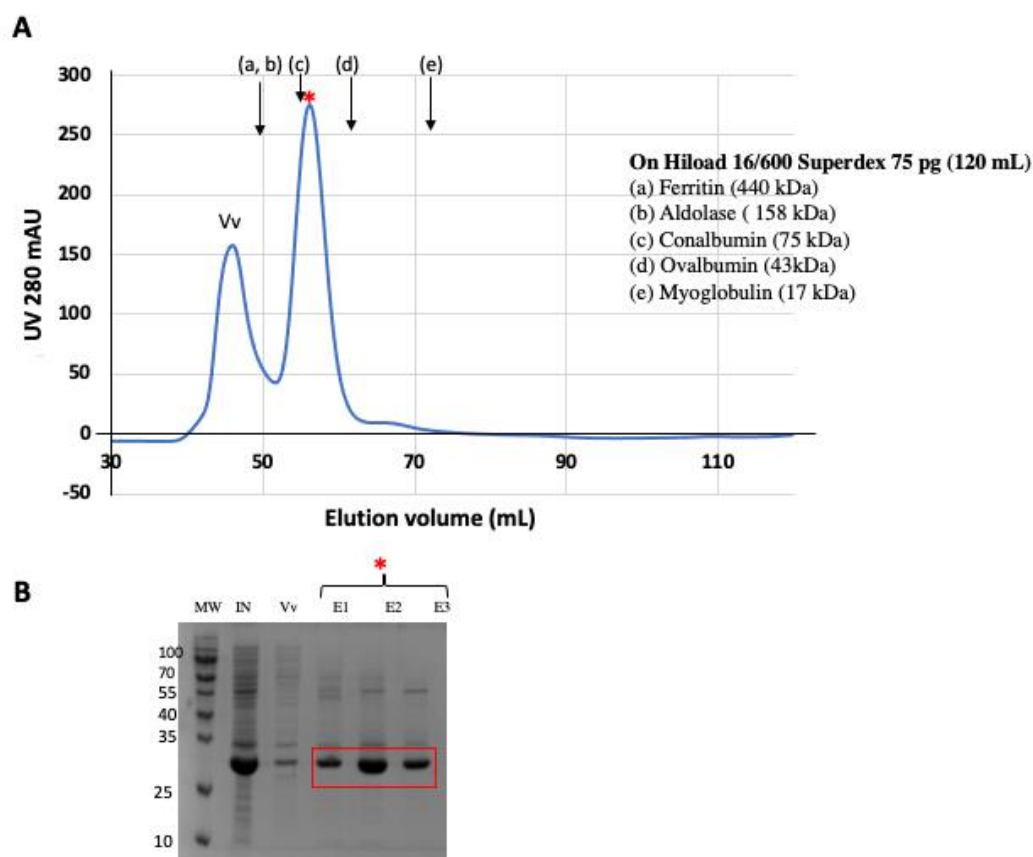


Figure 34. Last step of H3 purification.

(A) SEC profile of H3 showing the absorption at 280 nm on a Hiload Superdex 75pg (GE Healthcare), in 25 mM Tris HCl pH 7.5, 250 mM NaCl and 5 mM β me; H3 was eluted at 60 mL. **(B)** Coomassie-stained 15% SDS-PAGE of the SEC experiment. The lines correspond to: MW, molecular weights (kDa); IN, fraction loaded on the column; Vv: void volume of the column; E1-3, fractions eluted around 60 mL. I measured a yield of 4 mg of pure protein per 1.6 L of bacterial culture.

c. BRCA2

During my PhD, I produced different BRCA2 fragments, with different lengths, all located between the BRC repeats and the DBD (**Figure 35**). These fragments were overexpressed in large amounts as fusion proteins with a 6His-GB1 tag. I optimized their production and

purification, as reported (**Figure 36**; [Ghouil et al., 2020](#)). The tag was cleaved using the TEV protease, to obtain pure BRCA2 fragments. I produced these fragments in rich and minimum media (^{15}N , ^{13}C), in order to assign their NMR signals and further used NMR to delimit the HSF2BP interacting region. During the purification of these fragments, the main problem was proteolysis. Therefore, I had to purify these IDR quickly, in presence of large amounts of protease inhibitors. Also, all the BRCA2 fragments had no tryptophane and only F0 exhibited tyrosines; however, as they were expressed as fusion proteins with a TEV site between the BRCA2 fragment and GB1, after cleavage they all had a tyrosine coming from the TEV site. I followed their purification using their absorbance at 280 nm (**Figure 37**, **Figure 38**).

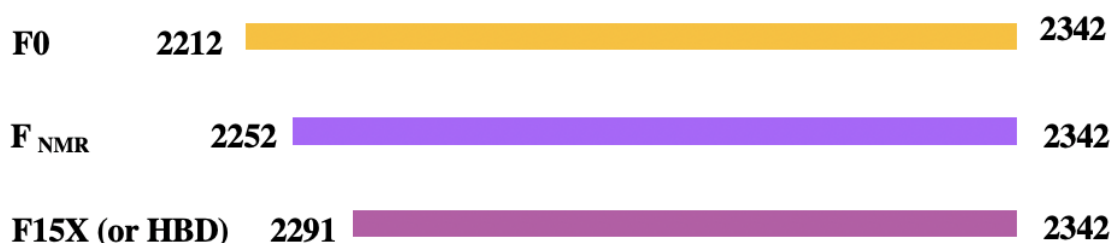


Figure 35. The BRCA2 constructs used for my PhD project.

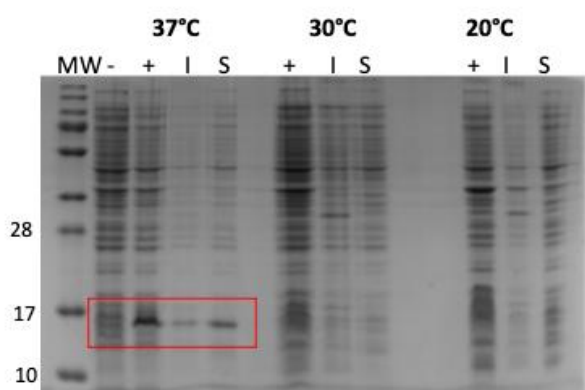


Figure 36. Example of optimization of the overexpression of a BRCA2 fragment in *E. coli* BL21 (DE3) Star

Coomassie-stained 15% SDS-PAGE of the bacterial extracts obtained after expression of BRCA2 F0, either without IPTG (-), with IPTG (+), and in this case, insoluble (I) and soluble fractions (S). The best overexpression conditions were at 37 °C during 3 hrs. In these

conditions, the fusion protein was mostly soluble. Such conditions were used for the expression of most of the disordered proteins in the lab.

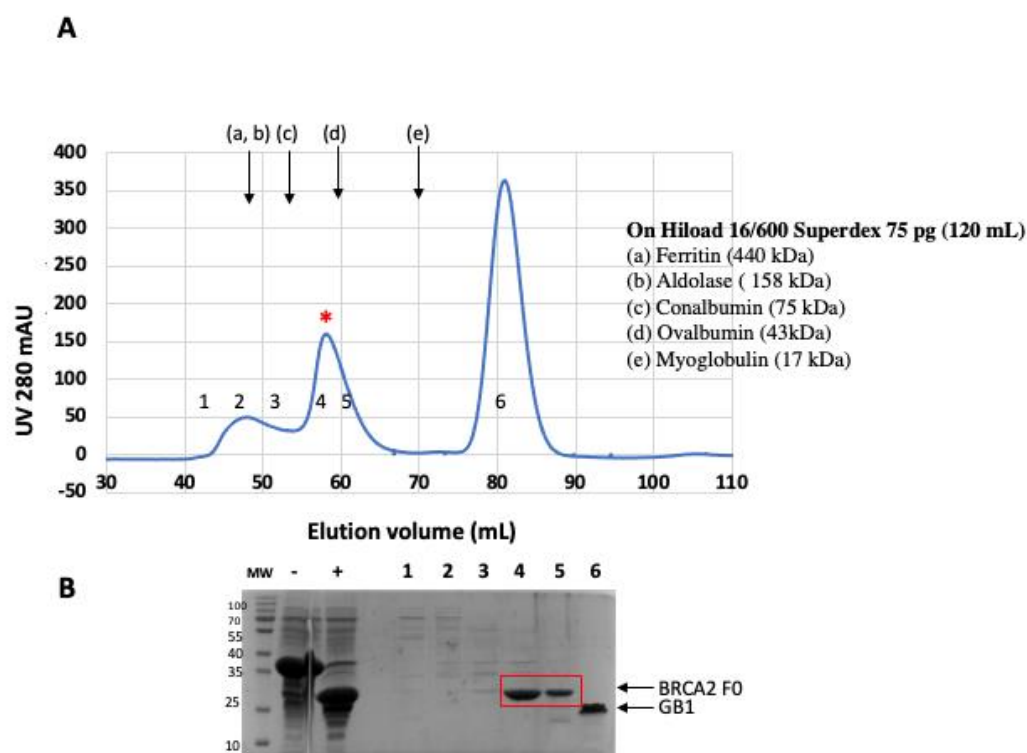


Figure 37. Last step of the purification of the BRCA2 fragment F0.

(A) SEC profile of BRCA2 F0, showing the absorption at 280 nm. The column was a Hiload Superdex 75pg (GE Healthcare), and the buffer was 50 mM Hepes pH 7, 50 mM NaCL, and 1 mM EDTA. **(B)** Coomassie-stained 15% SDS-PAGE of the SEC experiment. The lines correspond to: MW, molecular weights (kDa); (-) before TEV cleavage; (+) after TEV cleavage; (1-6) eluted fractions. The protein was eluted at 58 mL. I obtained a yield of 8 mg of pure protein per 800 mL of bacterial culture.

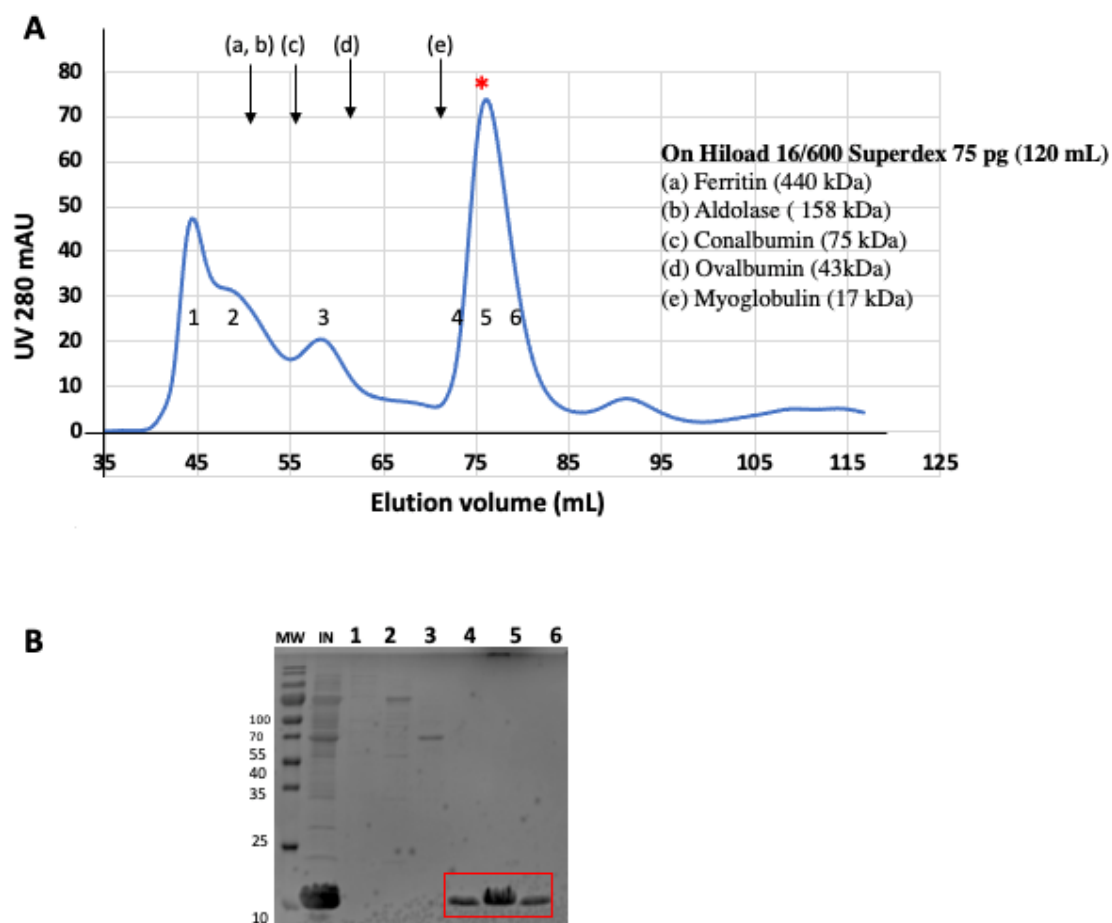


Figure 38. Last step of the purification of the BRCA2 fragment F15X

(A) SEC profile of BRCA2 F15X or HBD showing the absorption at 280 nm. The column was a Hiload Superdex 75pg (GE Healthcare), and the buffer was 25 mM Tris HCl pH 7.5, 250 mM NaCl and 5 mM β me. **(B)** Coomassie-stained 15% SDS-PAGE of the SEC experiment. The lines correspond to MW, molecular weights (kDa); IN: fraction loaded on the column; (1-6) eluted fractions. The protein was eluted at 77 mL. I obtained a yield of 10 mg of pure protein per 800 mL of bacterial culture.

2. Sample characterization

To characterize our proteins, I used different biophysical techniques.

a. SEC- MALS

To characterize the molecular mass of HSF2BP and its H3 armadillo domain, either free or bound to F15X (HSF2BP binding domain of BRCA2), I used SEC coupled to MALS (Multi-Angle Light Scattering). This analysis revealed that HSF2BP is eluted as a tetramer, free H3 is a dimer, and the complex H3 bound to F15X is a tetramer. These results are shown and discussed in the published results ([Ghouil et al., 2021](#); [Ghouil et al., submitted](#)).

b. SEC- SAXS

I used SEC-SAXS to characterize different proteins/complexes. In addition to the published experiments on HSF2BP and the complex between H3 and F15X, I characterized free H3, and my results confirmed that H3 is a dimer. The shape of the $P(r)$ is typical for an elongated globular protein (**Figure 39**). Consistently our crystal structure revealed an elongated dimeric H3 ([Ghouil et al., 2021](#)).

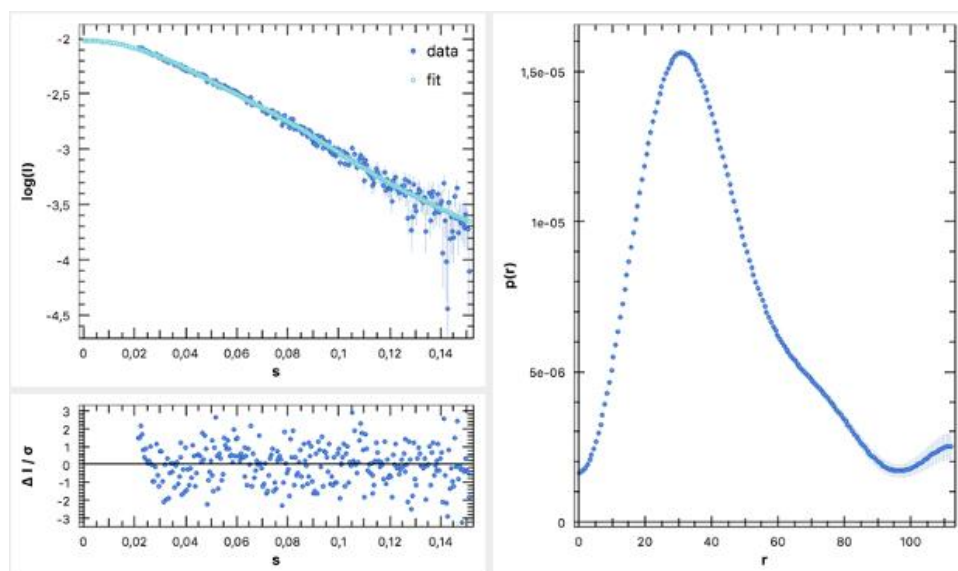


Figure 39. SEC-SAXS curve.

(left panel, SWING beamline at synchrotron SOLEIL) and associated distance distribution (right panel) obtained on free H3. The graph under the SAXS curve is the distance between the

experimental curve and the curve calculated from the $P(r)$, divided by the experimental error. The weak values observed in this graph demonstrate that the $P(r)$ distribution is consistent with the experimental SAXS curve. The profile of the $P(r)$ distribution indicates that the H3 dimer exhibits an elongated structure, with a D_{max} of 100 Å. Consistently, I later measured distances between 80 and 90 Å on the crystal structure of this dimer.

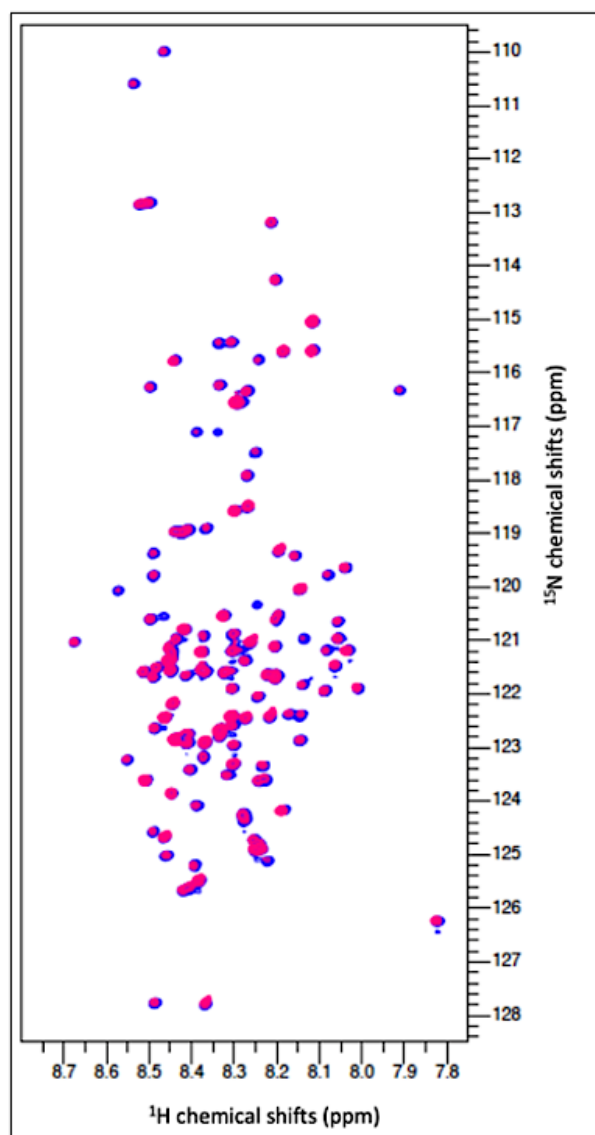
3. Molecular characterization of the interaction BRCA2/HSF2BP

a. NMR analysis

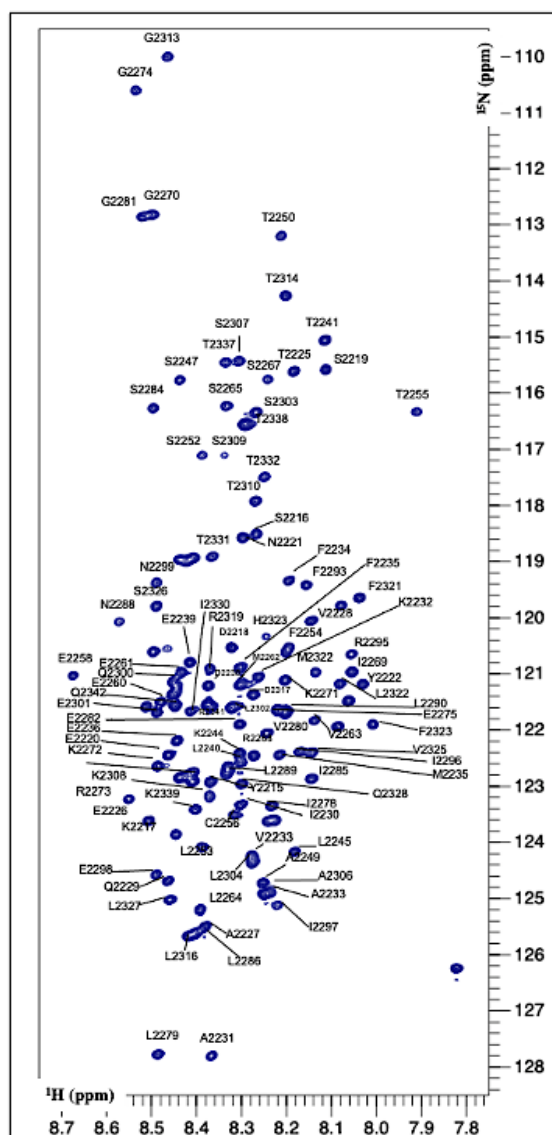
After obtaining pure samples of BRCA2 peptides and HSF2BP (full length and its armadillo domain), my second objective was to assign the NMR signals of BRCA2₂₂₁₂₋₂₃₄₂.

In this study, we experimentally confirmed that BRCA2₂₂₁₂₋₂₃₄₂ is a disordered peptide (**Figure 40**). Indeed, the amide ^1H chemical shifts of the peptide are all comprised between 8.0 and 8.6 ppm. Moreover, analysis of the $\text{C}\alpha$ and $\text{C}\beta$ chemical shifts showed that this peptide is disordered in solution: it only forms transient α -helices that are present at about 25% ([Ghouil et al., 2021](#)). We used the assignment of the ^1H - ^{15}N backbone signals of the protein to monitor the interaction with H3 using ^1H - ^{15}N 2D SOFAST-HMQC experiments. Addition of unlabeled H3 to a sample of ^{15}N labeled BRCA2₂₂₁₂₋₂₃₄₂ led to the vanishing of many HMQC resonances (**Figure 40**), confirming the capacity of this BRCA2 region to interact with H3 *in vitro*. A subset of resonances, corresponding to BRCA2₂₂₅₂₋₂₃₄₂, was strongly and homogeneously affected by H3 addition, suggesting that this subfragment of BRCA2 was responsible for H3 binding (**Figure 40**).

A



B



C

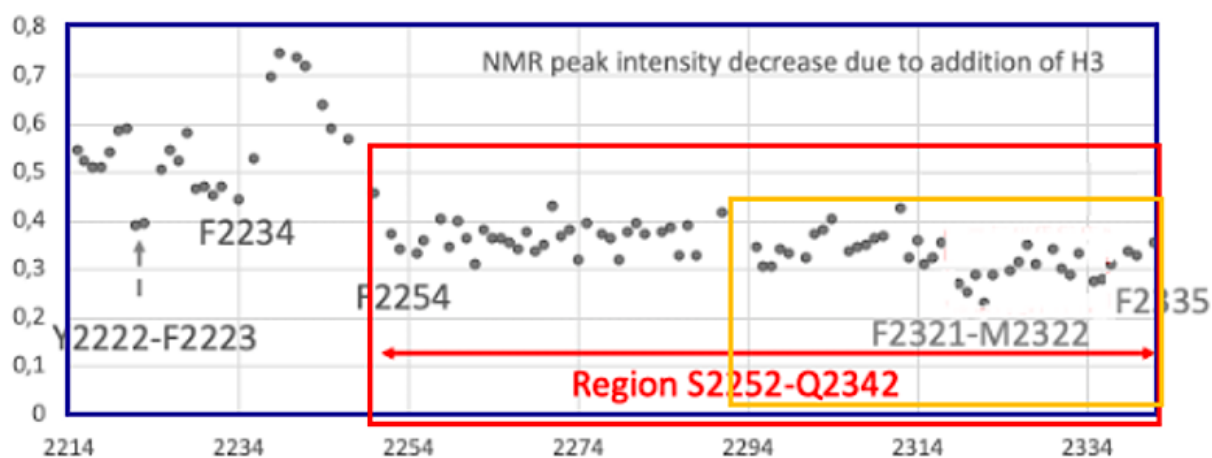


Figure 40. NMR identification of the H3 interacting region of BRCA2.

(A) Superimposition of the 2D NMR ^1H - ^{15}N HMQC-SO FAST spectra of BRCA2 F0 (blue) and BRCA2 F0 with H3 (red). (B) Assignment of the ^1H - ^{15}N HMQC-SO FAST spectrum of BRCA2 F0 in 50 mM Hepes pH 7, 50 mM NaCl, and 1 mM EDTA. These experiments were recorded at 950 MHz, 283 K, and pH 7.0. (C) ^1H - ^{15}N FAST-HMQC peak intensity ratios as a function of the residue number, calculated from the analysis of the NMR experiments displayed in (A). The regions corresponding to BRCA2 F0 (2212-2342), BRCA2 F_{NMR} (2252-2342), and BRCA2 F15X (2291-2342) are boxed in blue, red, and yellow respectively.

b. Isothermal Titration Calorimetry

Based on the NMR analysis, together with Dr. Miron, I measured the affinity between HSF2BP/H3 and BRCA2 F0, BRCA2 F_{NMR}, and BRCA2 F15X using Isothermal Titration Calorimetry (ITC). BRCA2 F0 binds HSF2BP with an affinity of 1 nM and binds H3 with a 24-fold weaker affinity (Table 1, [Ghouil et al., 2021](#)), suggesting that the coiled-coil domain contributes to the stabilization of the complex through its helices $\alpha 1$ and $\alpha 2$.

Comparing the affinity between H3 and the different peptides of BRCA2, we unexpectedly found that BRCA2 F15X binds 3-fold tighter to H3 than F0. Therefore, we decided to continue by focusing on the complex between H3 and BRCA2 F15X.

c. X-ray crystallography

I first tried to crystallize free HSF2BP, and then the complex between HSF2BP and BRCA2 F0. Crystallization experiments were carried out at the HTX lab (EMBL Grenoble), and monitored through the CRIMS website. In both cases, no crystals were obtained. I concluded that, as HSF2BP is predicted to have a coiled-coil domain, as well as a linker between the coiled-coil domain and the armadillo domain, it is very flexible and dynamic, and therefore it does not crystallize, either free or bound to BRCA2 peptides.

Therefore, I chose to use the armadillo domain of HSF2BP (H3), either free or bound to BRCA2 F0, but these samples also did not crystallize. I further tested H3 bound to F15X as it is the shortest interacting peptide deduced from the NMR experiments and shown by ITC to still have a high affinity for H3. A screen of crystallogenesis conditions for this complex at 12 mg/mL was performed at the HTX platform (EMBL Grenoble).

By analyzing the HTX results, two successful crystallization conditions were found: PEG3350, 0.2M MgCl₂, and PEG3350, 0.2M MgNO₃. I reproduced in the lab both conditions. Together with Dr. Virginie Ropars, I harvested the resulting crystals. They were tested on the PROXIMA-2 beamline (Synchrotron SOLEIL), and only one diffraction dataset was obtained at 2.7 Å. I worked on this dataset during the first lockdown, in order to solve the structure of the complex by molecular replacement. I found that the space group was P1 (triclinic). Then, I selected 3D structures of armadillo domains that were identified by HHPRED as reasonable templates for H3, and using different tools from CCP4 and PHENIX, I calculated density maps. However, as often for armadillo domains, my models were not sufficiently close to the true structure and my molecular replacement attempts were systematically unsuccessful. Later, Dr. Pierre Legrand tried molecular replacement using the same dataset. He used the Rosetta server ([Song et al., 2013](#)) to calculate several models of H3, and with one of these models, he was able to find a solution. In the meanwhile, I had reproduced these crystals but with proteins labeled with selenomethionine. First, I labeled only H3, and obtained crystals in the same conditions as before at HTX. Three of these crystals diffracted on MASSIF-1 at ESRF (Grenoble). But the resolution of the resulting datasets was between 4 and 8 Å with a very low Se-MAD anomalous signal (triclinic space group). Then, I labeled both proteins H3 and BRCA2 F15X, the complex was concentrated at 10 mg/mL, and I obtained 16 crystals always in the same conditions (15% of PEG3350, 0.2M MgCl₂, MES at pH6) (**Figure 41**). Crystals were frozen and Se-SAD data were collected on the PROXIMA-1 beamline (Synchrotron SOLEIL) at the selenium peak absorption wavelength. Seven crystals were used for the collection but only three of them diffracted with a maximum resolution of around 2.7 Å with space groups P2₁ (monoclinic) and C222₁ (orthorhombic). The diffraction data obtained on a monoclinic crystal showed a very good anomalous signal ($\lambda = 0.97918$ Å) that allowed to directly calculate phases, without external model contributions. Further details are provided in the Material and Methods section. Finally, with Dr. Ledu, I refined the structure using Buster version 2.10.3.

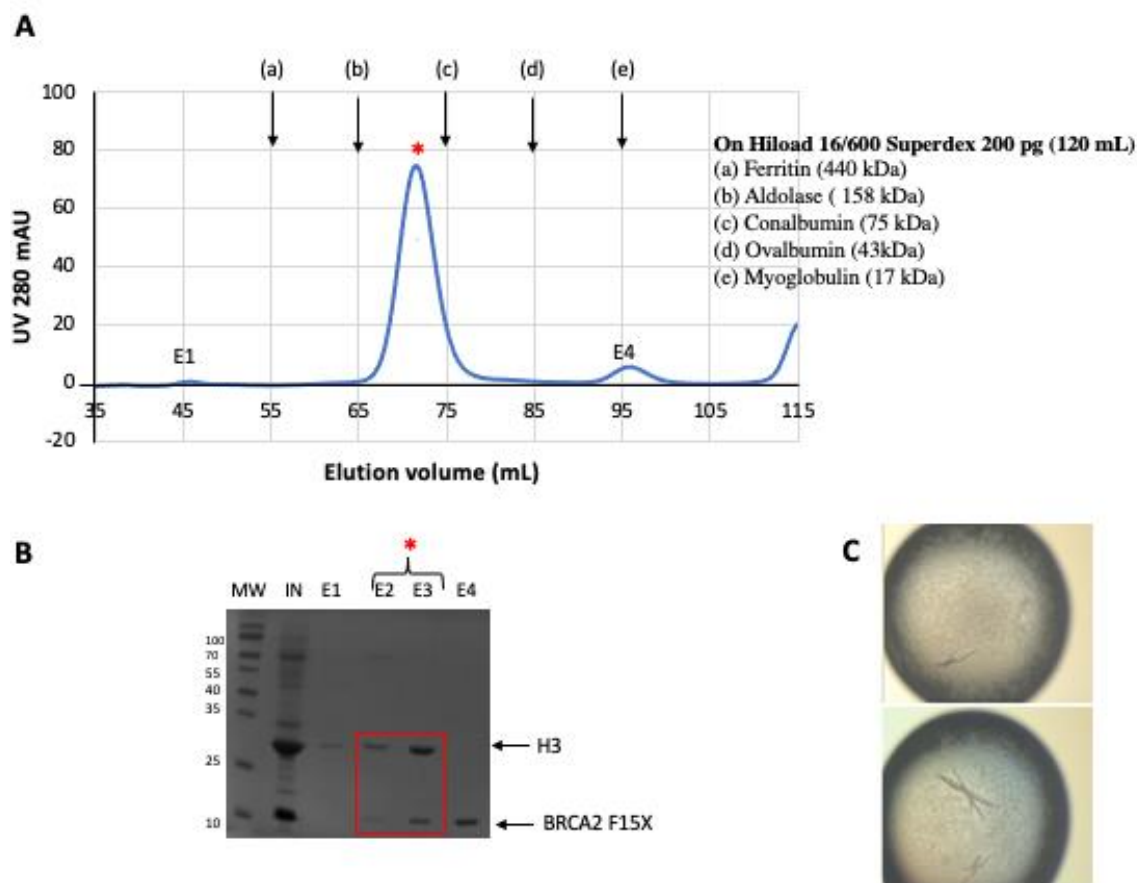


Figure 41. Complex formation and diffracted crystals.

(A) SEC profile of the co-elution of H3 bound to F15X showing absorption at 280 nm. The column is a Hiload Superdex 200pg (GE Healthcare), and the buffer is 25 mM Tris HCl pH 7.5, 250 mM NaCl, and 5 mM β me; H3-F15X was eluted at 70 mL. (B) Coomassie-stained 15% SDS-PAGE of the eluted fractions (IN input on the column, red box: the eluted complex). (C) Examples of crystals obtained with H3-F15X labeled with selenomethionine and concentrated at 10 mg/mL. These crystals were obtained in our lab in the conditions of 15% PEG3350, 0.2 M $MgCl_2$, MES pH 6.0, and 20% glycerol.

4. Localization of the HSF2BP mutations found in patients with POI

In recent studies, 3 homozygous missense variations in *HSF2BP* were identified in women affected by POI: S167L ([Felipe-Medina et al., 2020](#)), and C128R and L186P ([Li et al., 2021](#)). S167L resulted in a reduced protein level of HSF2BP and subsequent insufficient BRME1, RAD51, and DMC1 localizing at DSBs during meiotic recombination. C128R and L186P caused only a modest reduction in the HSF2BP protein level, but these variants were barely transferred into the nuclei. Their DNA repair capacities were also lower than those of the wild-type.

As I solved the 3D structure of H3, i.e. HSF2BP from E122 to V334, bound to BRCA2 F15X ([Ghouil et al., 2021](#)), I could localize these 3 mutations on the 3D crystal structure of H3.

Residues C128, L186, and S167 are very highly conserved in evolution and are located on the surface of the armadillo domain. C128 and L186 are located at the dimerization interface of H3, whereas S167 is accessible to the solvent in the monomer and also in the dimer structure (**Figure 42**). S167 is not located at the interface with BRCA2 F15X. It is probably involved in the interaction of HSF2BP with another partner, as HSF2 for example.

The impact of these mutations on the oligomerization state of H3 could be experimentally tested by SEC-MALS.

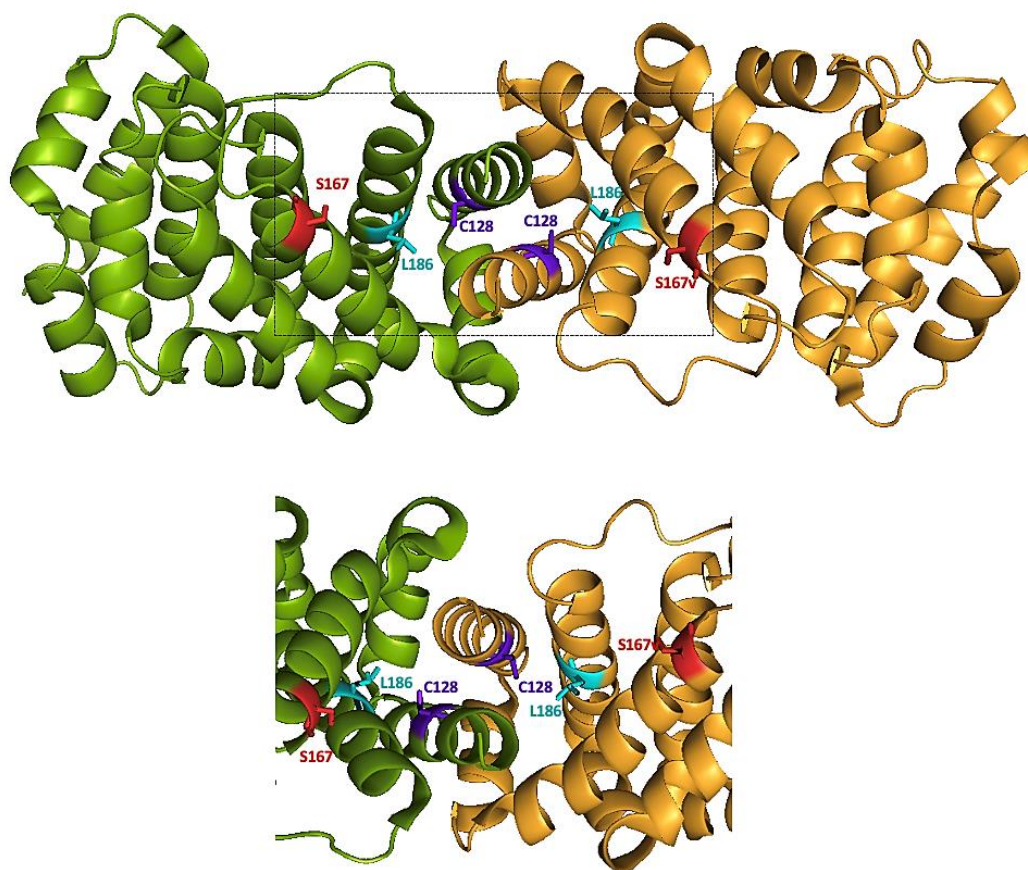


Figure 42. Localization of the POI-associated mutations in HSF2BP.

A cartoon representation of the crystal structure of the H3 dimer (monomers 1 and 2 in green and orange, respectively), displayed with the residues mutated in POI represented as sticks (red for S167 residues, cyan for L186 residues, and purple for C128 residues). The PDB reference of this structure is 7BDX.

Article: BRCA2 binding through a cryptic repeated motif to HSF2BP oligomers does not impact meiotic recombination

ARTICLE


<https://doi.org/10.1038/s41467-021-24871-6>

OPEN

BRCA2 binding through a cryptic repeated motif to HSF2BP oligomers does not impact meiotic recombination

Rania Ghoul^{1,10}, Simona Miron^{1,10}, Lieke Koornneef^{2,10}, Jasper Veerman³, Maarten W. Paul³, Marie-Hélène Le Du¹, Esther Sleddens-Linkels⁴, Sari E. van Rossum-Fikkert^{3,5}, Yvette van Loon³, Natalia Felipe-Medina⁶, Alberto M. Pendas⁶, Alex Maas⁷, Jeroen Essers^{3,5,8}, Pierre Legrand⁹, Willy M. Baarends⁴, Roland Kanaar^{3✉}, Sophie Zinn-Justin^{1✉} & Alex N. Zelensky^{3✉}

BRCA2 and its interactors are required for meiotic homologous recombination (HR) and fertility. Loss of HSF2BP, a BRCA2 interactor, disrupts HR during spermatogenesis. We test the model postulating that HSF2BP localizes BRCA2 to meiotic HR sites, by solving the crystal structure of the BRCA2 fragment in complex with dimeric armadillo domain (ARM) of HSF2BP and disrupting this interaction in a mouse model. This reveals a repeated 23 amino acid motif in BRCA2, each binding the same conserved surface of one ARM domain. In the complex, two BRCA2 fragments hold together two ARM dimers, through a large interface responsible for the nanomolar affinity — the strongest interaction involving BRCA2 measured so far. Deleting exon 12, encoding the first repeat, from *mBrca2* disrupts BRCA2 binding to HSF2BP, but does not phenocopy HSF2BP loss. Thus, results herein suggest that the high-affinity oligomerization-inducing BRCA2-HSF2BP interaction is not required for RAD51 and DMC1 recombinase localization in meiotic HR.

¹Institute for Integrative Biology of the Cell (I2BC), CEA, CNRS, Uni Paris-Sud, Uni Paris-Saclay, Gif-sur-Yvette, France. ²Department of Developmental Biology, Oncode Institute, Erasmus University Medical Center, 3000 CA Rotterdam, The Netherlands. ³Department of Molecular Genetics, Oncode Institute, Erasmus MC Cancer Institute, Erasmus University Medical Center, 3000 CA Rotterdam, The Netherlands. ⁴Department of Developmental Biology, Erasmus University Medical Center, 3000 CA Rotterdam, The Netherlands. ⁵Department of Radiation Oncology, Erasmus University Medical Center, 3000 CA Rotterdam, The Netherlands. ⁶Molecular Mechanisms Program, Centro de Investigación del Cáncer and Instituto de Biología Molecular y Celular del Cáncer (CSIC-Universidad de Salamanca), Salamanca, Spain. ⁷Department of Cell Biology, Erasmus University Medical Center, 3000 CA Rotterdam, The Netherlands. ⁸Department of Vascular Surgery, Erasmus University Medical Center, 3000 CA Rotterdam, The Netherlands. ⁹Synchrotron SOLEIL, L'Orme des Merisiers, Gif-sur-Yvette, France. ¹⁰These authors contributed equally: Rania Ghoul, Simona Miron, Lieke Koornneef. ✉email: r.kanaar@erasmusmc.nl; Sophie.ZINN@cea.fr; a.zelensky@erasmusmc.nl

Homologous recombination (HR) is involved in many aspects of eukaryotic DNA metabolism and is indispensable in two contexts: resolving replication problems and in meiosis. Homology search and strand exchange, the key events in HR, are performed by a nucleoprotein filament formed by the strand exchange protein RAD51 assembled onto the 3' single-stranded (ss) DNA overhang. In somatic animal cells, RAD51 loading onto ssDNA depends on BRCA2, which has multiple RAD51-binding sites and is required for focal accumulation of RAD51 at the sites of damage. Biochemical experiments suggest that BRCA2 acts as an HR mediator, displacing RPA, the protein that protects ssDNA by strongly binding to it, and forming functional RAD51 filament in its place¹. In vitro, BRCA2 can perform this function autonomously, but in cells, it depends on its “partner and localizer” PALB2².

Although BRCA2 has been mostly studied in the context of HR in somatic cells, it arguably has a more prominent role in meiotic HR, as across a broad range of species, fertility defects are the most common consequence of BRCA2 loss^{3–11}. In meiosis, HR functions to diversify as well as to preserve genetic information. This role is achieved by extending the core HR machinery (RAD51, BRCA2, and PALB2) with a set of meiosis-specific proteins, such as the DMC1 recombinase and the ssDNA-binding proteins MEIOB and SPATA22. BRCA2 binds DMC1 via the RAD51-binding BRC repeats encoded by BRCA2 exon 11^{12–14} and a DMC1-specific site encoded by exon 14¹³.

We identified HSF2BP as another BRCA2-binding protein, endogenously expressed in meiotic cells, and ectopically produced in cancer cells^{15–17}. HSF2BP is required for meiotic HR during spermatogenesis, but in somatic cells, it inhibits HR during DNA interstrand crosslink repair by triggering BRCA2 degradation. In addition to BRCA2, HSF2BP has been reported to interact with transcription factors HSF2¹⁸ and BNC1¹⁹, both required for normal fertility in mice^{20,21}. More recently, five groups independently reported that HSF2BP interacts with an uncharacterized protein named C19orf57, 4930432K21Rik, *BRME1*, *MEIOKE21*, or *MAMERR*. The two proteins co-localize in meiocytes, loss of *BRME1* closely phenocopies loss of HSF2BP, and the two proteins can affect each other's stability^{22–26}. The model put forward to explain the meiotic defects in knock out mice for either *Hsf2bp* or *Brme1* follows the PALB2 paradigm: HSF2BP and *BRME1* are proposed to act as “meiotic localizers” for BRCA2—and for each other^{25,27}. However, how HSF2BP, *BRME1*, and PALB2 contribute to BRCA2 localization in meiotic HR remains to be established. Also, in contrast to complete dependence of BRCA2 on PALB2 in somatic HR, the loss of the two meiotic localizers (HSF2BP and *BRME1*) causes a milder meiotic phenotype than *Brca2* deficiency in mice. *Hsf2bp* and even more so *Brme1*-knockout mouse models show pronounced sexual dimorphism: female meiotic defects are either weak^{22,27} or not detected^{16,23–26}, while *Brca2* deficiency affects both sexes⁴.

HSF2BP contains an N-terminal α -helical oligomerisation domain and a C-terminal domain predicted to adopt an Armadillo fold^{16,17,25}. We mapped the HSF2BP-BRCA2 interaction to the Armadillo domain of HSF2BP, and a 68 amino acid (aa) region of BRCA2 mostly encoded by exons 12 and 13, which is predicted to be disordered¹⁶. BRCA2 is a protein of 3418 aa that possesses a unique globular domain of 700 aa binding to ssDNA and the acidic protein DSS1²⁸. The high disorder propensity of BRCA2 is proposed to ensure its structural plasticity and its ability to orchestrate complex molecular transactions while balancing multiple interactions^{29,30}. However, interactions involving intrinsically disordered regions are difficult to predict and characterize structurally. Out of more than a dozen mapped protein interaction regions within the disordered part of BRCA2^{31,32}, only three were crystallized when bound to their folded partner,

either Rad51³³, PALB2³⁴ or PLK1³⁵. In all cases, the BRCA2 fragments became folded upon transient interactions characterized by affinities on the micromolar range.

In this study, we provide a detailed biophysical characterization of the HSF2BP-BRCA2 interaction and the changes in oligomeric state it induces. Its low-nanomolar affinity is orders of magnitude stronger than any other measured interaction involving BRCA2. We also describe the 3D structure of the complex between HSF2BP and BRCA2, which confirms the predicted ARM fold of HSF2BP and reveals the existence of a cryptic repeated motif encoded by exons 12–13 of BRCA2, responsible for binding to ARM oligomers. Finally, results from a mouse line engineered to disrupt the binding suggest that contrary to the prediction of the “meiotic localizer” model, this evolutionarily conserved high-affinity oligomerisation-inducing interaction of BRCA2 with HSF2BP is not required for meiotic HR.

Results

HSF2BP ARM binds disordered BRCA2 peptide with high affinity. Our previous analyses using coimmunoprecipitation identified the C-terminal part of HSF2BP I93-V334 and the BRCA2 fragment G2270-T2337 (F9) as interacting regions¹⁶. Extending this approach (Fig. 1a–c, Supplementary Fig. 1a, b), we narrowed down the minimal interaction region to E122-V334 in HSF2BP (fragment H3, hereafter referred as ARM, for “armadillo domain”) and to N2288-T2337 in BRCA2 (fragment F15). Further truncations resulted in loss or reduction in co-precipitation efficiency. We also extended our site-directed mutagenesis mapping: using a homology model of the HSF2BP ARM domain, we predicted solvent-exposed structural neighbors of R200, which we previously found to be required for BRCA2 binding, and made substitutions based on human polymorphism data (dbSNP). Whereas in our initial blind screen¹⁶ most substitutions preserved binding, GFP-HSF2BP mutated at residues N192, G199, Y238, N239 or N243 failed to co-precipitate Flag-F9 (Supplementary Fig. 1b, c). On the BRCA2 side, wild-type GFP-HSF2BP also did not interact with several Flag-F9 variants, mutated at residues S2309, R2318, or P2329 (Supplementary Fig. 1d). To characterize the direct interaction between HSF2BP and BRCA2 in vitro, we purified HSF2BP and its truncated variants, as well as the large BRCA2 fragment S2213-Q2342 (F0) showing high conservation during evolution (and including F15; Supplementary Fig. 2). We first performed an NMR analysis of F0, in order to identify the residues binding to ARM. Assignment and further analysis of the NMR ¹H, ¹³C, ¹⁵N, C β and Co chemical shifts of ¹⁵N-, ¹³C-labeled BRCA2-F0 showed that this peptide is disordered in solution: it only forms transient α -helices; in particular, region N2291-S2303 folds into an α -helix that is present at about 25% (Supplementary Fig. 3). Addition of unlabeled ARM causes a global decrease of the intensities of the 2D NMR ¹H-¹⁵N HSQC peaks of ¹⁵N-labeled F0, with region S2252-Q2342 (further called F_{NMR}), including the transient α -helix, showing the largest decrease (intensity ratio lower than 0.4; Fig. 1d). We concluded that the chemical environment of this region, larger than the previously identified F15 fragment N2288-T2337, is significantly modified in the presence of the ARM domain. Isothermal Titration Calorimetry (ITC) experiments revealed that F0 binds to both HSF2BP and ARM with a nanomolar affinity and a stoichiometry of 0.5, i.e., one BRCA2 peptide binds to two HSF2BP/ARM (Fig. 1e; Table 1). These affinity and stoichiometry are consistent with the more than twofold decrease in intensity observed by NMR when adding one ARM to one ¹⁵N-labeled F0; indeed, in these conditions, half of the F0 molecules were free and half bound to ARM. Also, HSF2BP binds about 25-fold tighter to F0 than does ARM. As a control, we verified that HSF2BP mutant

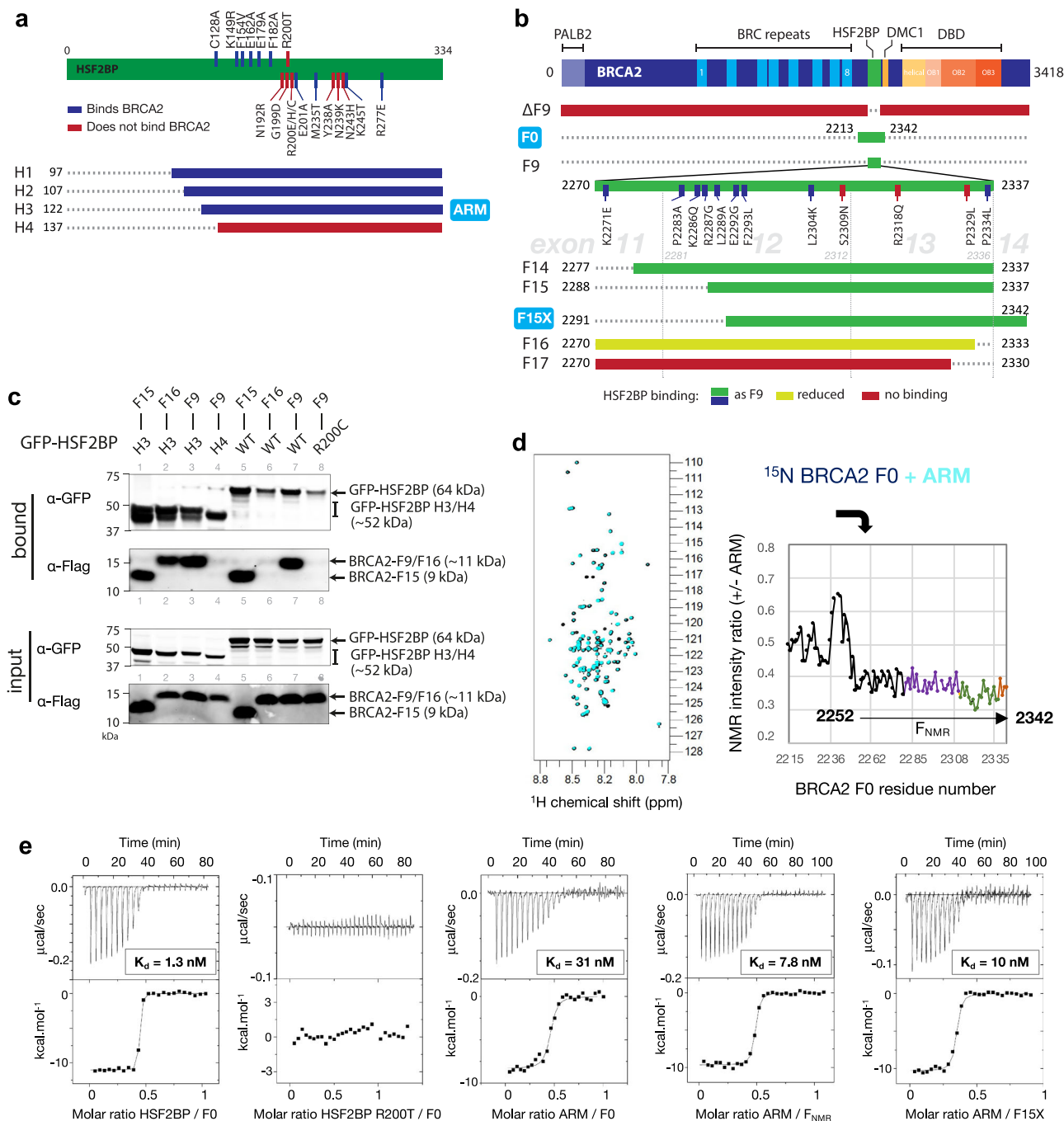


Fig. 1 The ARM domain of HSF2BP binds with a nanomolar affinity to a 52 aa BRCA2 peptide. **a** Schematic depiction of the truncation and substitution variants of HSF2BP used in this study. Substitutions tested previously are mapped above the bar, whereas those tested in this study are indicated below the bar. Truncation variants are colored based on their ability to bind BRCA2 peptides. **b** Schematic depiction of BRCA2 fragments and variants used in the study. Full-length BRCA2 is shown at the top with key domains indicated. Location of the fragment F9 identified previously and its truncations tested here are shown, with colors indicating the ability to bind HSF2BP. Fragments produced as recombinant proteins are indicated with blue labels. **c** Coimmunoprecipitation of GFP-HSF2BP (full-length wild-type (WT) or R200C variant, and fragments H3 (ARM) and H4) and indicated Flag-tagged BRCA2 variants. Proteins were transiently produced in HEK293T cells. **d** NMR characterization of BRCA2 residues involved in binding to the Armadillo domain of HSF2BP (ARM). 2D ^1H - ^{15}N HSQC spectra were recorded at 950 MHz and 283 K on the ^{15}N -labeled BRCA2 fragment F0 (S2213-Q2342), either free (100 μM ; dark blue) or in the presence of the unlabeled ARM domain (1:1 ratio; cyan). Ratios of peak intensities in the two conditions revealed that a set of peaks, corresponding to BRCA2 fragment F_{NMR} (S2252-Q2342), decreased by more than 60% after the addition of ARM. The points and curve fragments in purple, green, and brown correspond to residues encoded by exon 12, 13, and 14 of BRCA2, respectively. **e** ITC curves that reveal how either HSF2BP or its ARM domain (in the instrument cell) interacts with the BRCA2 fragment F0, F_{NMR} , and F15X (N2291-Q2342) (in the instrument syringe). The dissociation constants (K_d) are indicated. All experiments were duplicated, and the dissociation constants, stoichiometry, and thermodynamics parameters of each experiment are recapitulated in Table 1.

Table 1 Isothermal titration calorimetry data.

	Kd (±error) (M)	n	ΔH (±error) (kcal/mol)	ΔG (kcal/mol)	−TΔS (kcal/mol)
HSF2BP FL vs. F0—expt 1	1.3E−09 (0.3)	0.43	−11.0 (0.1)	−11.8	−0.8
HSF2BP FL vs. F0—expt 2	1.3E−09 (0.3)	0.47	−10.9 (0.1)	−11.9	−1.0
HSF2BP FL vs. F15XΔ12—expt 1	1.5E−06 (0.7)	0.89	−1.7 (0.3)	−7.8	−6.1
HSF2BP FL vs. F15XΔ12—expt 2	2.1E−06 (0.9)	0.90	−1.8 (0.2)	−7.6	−5.8
ARM vs. F0—expt 1	31E−09 (9.0)	0.45	−8.3 (0.2)	−10	−1.7
ARM vs. F0—expt 2	25E−09 (7.0)	0.49	−11.9 (0.2)	−10.1	1.8
ARM vs. F _{NMR} —expt 1	7.8E−09 (1.3)	0.47	−9.6 (0.1)	−10.8	−1.2
ARM vs. F _{NMR} —expt 2	13E−09 (4.0)	0.51	−9.4 (0.2)	−10.5	−1.1
ARM vs. F15X—expt 1	10E−09 (2.1)	0.33	−10.2 (0.1)	−10.6	−0.4
ARM vs. F15X—expt 2	9.4E−09 (2.3)	0.40	−9.2 (0.1)	−10.7	−1.5

R200T does not bind to F0, consistently with our previous report¹⁶. We further compared the affinity of ARM for F0, F_{NMR}, and F15X (the recombinant peptide N2291–Q2342, similar to F15 N2288–T2337 used in cellular assays). The affinities of ARM for F_{NMR} and F15X are not significantly different, being around 10 nM (Fig. 1e; Table 1). Unexpectedly, they are about threefold higher than the affinity measured between ARM and F0 (Fig. 1e; Table 1). Therefore, we decided to continue by focusing on the complex between ARM and F15X.

HSF2BP ARM domain tetramerizes upon binding to BRCA2.

First, we characterized the molecular mass of the ARM domain either free or bound to F15X. Biophysical analysis by SEC-multi angle light scattering (MALS) (Size exclusion chromatography—multiple angle light scattering) and SEC-SAXS (Small-angle X-ray scattering) revealed that, if free ARM is dimeric, the complex is tetrameric with an estimated molecular weight of 94 kDa (SEC-MALS; Fig. 2a) or 109 kDa (SEC-SAXS; Fig. 2b), for a theoretical mass of four ARM bound to two F15X of 108 kDa. In parallel, intensity curves measured by SAXS on the complex gave a distance distribution reflecting a nearly spherical shape, with a D_{max} of 104 Å and a R_g of 34 Å (Fig. 2b).

Crystals of the complex were obtained within a few days by hanging-drop vapor diffusion and diffracted up to 2.6 Å on PROXIMA-1 and PROXIMA-2 beamlines at the SOLEIL synchrotron. The structure of the complex was solved using a combination of Molecular Replacement and SAD approaches (see details in “Methods” section, Table 2 and Supplementary Fig. 4). The overall conformation of the structure is consistent with the SAXS data obtained in solution, as reflected by the low χ^2 value of 1.8 Å² obtained when fitting the SAXS curve deduced from the experimental structure to the experimental SAXS curve (Fig. 2b).

The crystal structure includes four ARM domains and two BRCA2 F15X peptides (Fig. 2c, d). The ARM domains A and D, as well as B and C, dimerize through a symmetric interface of about 950 Å², formed by their N-terminal regions from E122 to I156 (Fig. 2d; Supplementary Fig. 5a). This interface is mediated by hydrophobic residues from helices α 1, helices α 2, and the N-terminus of helices α 3. In contrast, the ARM domains A and C, as well as B and D, have a very small direct interface of less than 100 Å². They are juxtaposed, one chain being rotated around its main axis by about 90° relatively to the other and interact mainly through BRCA2 (Fig. 2c). The BRCA2 peptide in orange (chain E) runs along the V-shaped groove formed by chains A and C. Similarly, the other BRCA2 peptide (in red; chain F) runs along the groove formed by chains B and D. At the center of the tetramer, a symmetric interface of about 250 Å² is observed between the ARM domains A and B, which involves helices α 2 and helices α 5 (Supplementary Fig. 5b). This interface is poorly conserved. In summary, two ARM dimers interact through two

BRCA2 peptides to form a tetramer; within the tetramer, two types of conserved interfaces are observed, either between monomers from the same dimer (chains A and D, as well as B and C, see boxed view in Fig. 2d), or between the ARM domains and the BRCA2 peptides (see main panel in Fig. 2d).

Repeated motifs in BRCA2 hold together two HSF2BP ARM dimers.

The 3D structures of the complexes between, on the one hand, the ARM domains A and C and the peptide E, and on the other hand the ARM domains B and D and the peptide F, are remarkably similar (Fig. 3a). In these structures, two ARM monomers form a BRCA2-binding surface of 2740 Å², which is in the upper range of interaction surfaces, even for a complex between a folded domain and an intrinsically disordered peptide³⁶. The BRCA2 peptide engages 48 aa in this interaction. In chains E and F, the N-terminal sequence, from N2291 to E2328, interacts with ARM domains C and D, respectively, whereas the C-terminal sequence, from D2312 to T2338, interacts with ARM domains A and B, respectively. The 3D structures of the ARM domains interacting with the same region of the peptide are highly similar, whereas the 3D structures of two ARM domains interacting with different regions of the BRCA2 peptide show some local structural variations, as measured by the root-mean-square deviations between their Ca atoms (see Table in Fig. 3a and Supplementary Fig. 6). Another remarkable feature of this complex is that similar surfaces of the ARM domains recognize the N-terminal and the C-terminal regions of the BRCA2 peptide (Fig. 3b; Supplementary Fig. 7). Indeed, a surface of about 1540 Å² formed by helix α 1, helix α 4 and the N-terminal region of α 5, helix α 7 and the N-terminal region of α 8, helix α 10 and loop α 10 α 11, and finally loop α 12 α 13 on one ARM domain interacts with the N-terminal sequence of the BRCA2 peptide. A smaller surface of 1200 Å² formed by helix α 1, helix α 4 and the N-terminal region of α 5, helix α 7 and the N-terminal region of α 8, only the C-terminal region of α 10 and loop α 10 α 11 on the other ARM domain interacts with the C-terminal sequence of the peptide. The surface common to the two binding interfaces is conserved through evolution and mainly positively charged (Fig. 3c). The surface specific to the interface with the N-terminal region of the peptide, including the N-terminus of helices α 7 and α 10 and loop α 12 α 13, is less conserved.

Further analysis of the interface revealed that, even more strikingly, the N-terminal and C-terminal sequences of the BRCA2 peptide interacting with different ARM domains have similar structures (Fig. 3d). BRCA2 motif 1, from N2291 to G2313, and BRCA2 motif 2, from T2314 to R2336, can be nicely superimposed, and interact with the same surface of their respective ARM domains. Sequence alignment between the two motifs identified five identical residues: D2294/2317, R2295/2318, S2303/2326 (also a proline in some organisms), L2304/2327, and

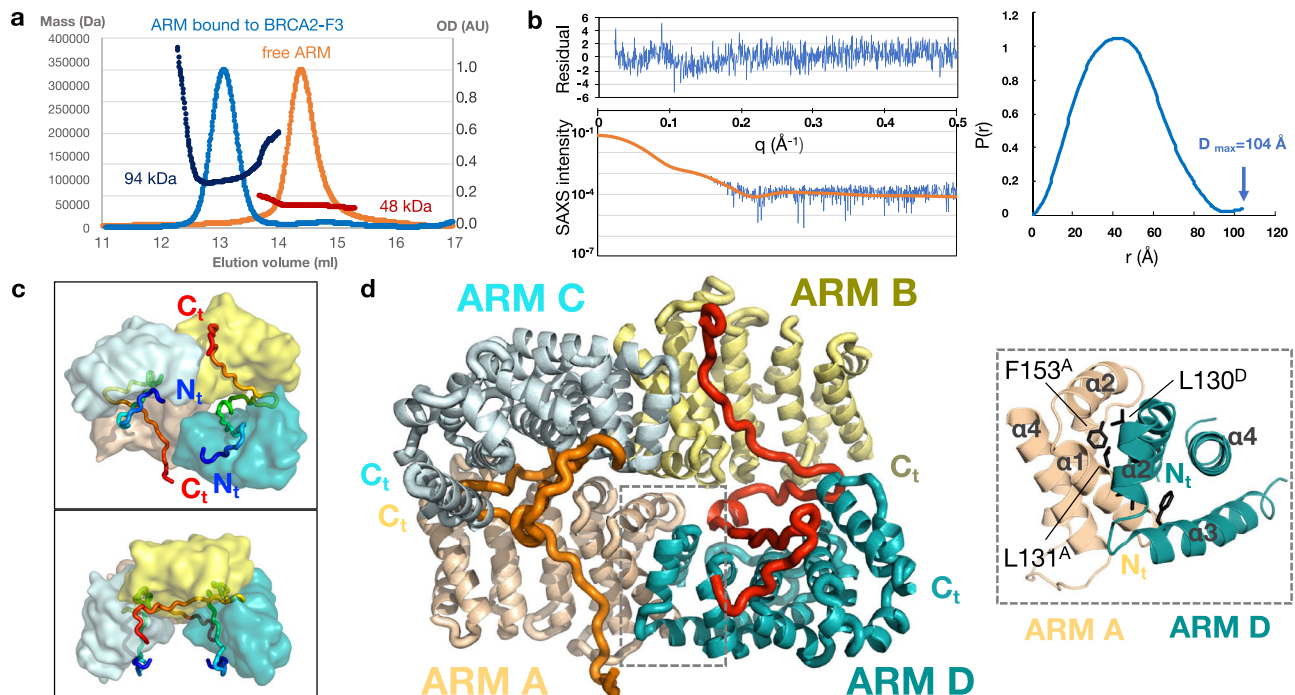


Fig. 2 The ARM domain tetramerizes upon BRCA2 binding. **a** SEC-MALS profiles from two independent experiments, performed either on free ARM (orange: OD normalized to 1; red: mass) or on ARM bound to F15X (light blue: OD normalized to 1; dark blue: mass) (column: Superdex 200 10/300 GL). **b** SEC-SAXS curve and resulting distance distribution obtained on ARM bound to F15X (blue). The experimental SAXS curve is compared to the theoretical SAXS curve calculated with CRYSOLOG from the X-ray structure of the complex (orange). Residual errors are plotted as a function of the scattering angle (resulting χ^2 value: 1.8 Å²). **c**, **d** Different views of the crystal structure of the complex, illustrating how the ARM dimers, formed by chains A (wheat) and D (teal) and chains B (yellow) and C (pale blue), are held together through their interactions with the BRCA2 peptides. **c** The ARM domains are represented as surfaces, whereas the BRCA2 F15X peptides are displayed as tubes colored from their N-terminus (blue) to their C-terminus (red). **d** The ARM chains are represented as cartoons, and the BRCA2 F15X peptides as orange (chain E) and red (chain F) tubes. A zoom view of the dimerization interface between ARM chains A and D is displayed in a dotted box: only helices $\alpha 1$ – $\alpha 4$ are displayed for clarity. The dimerization interface is mediated by hydrophobic residues from helices $\alpha 1$ (M123, A126, A127, L130, L131, and V134), helices $\alpha 2$ (V140, I144), and the N-terminus of helices $\alpha 3$ (L151, F153, and I156). About a quarter of this interface is due to the interaction between the highly conserved L131 and F153 from one monomer and the highly conserved L130 from the other monomer (side chains displayed as black sticks, L131 and F153 from chain A, as well as L130 from chain D are labeled).

P2311/2334, and two similar residues: A2306/P2329, S2309/C2332 (T2332 in our construct), which are all conserved through evolution (Fig. 3e; Supplementary Fig. 2). These residues interact with conserved residues from the ARM domains, as indicated in Fig. 3e. For example, D2294/2317 contacts R200 (helix $\alpha 5$) through a set of hydrogen bonds/salt bridges; R2295/2318 is hydrogen-bonded to S281 (helix $\alpha 10$); L2304/2327 contacts I242 (helix $\alpha 7$); S2309/C2332 and P2311/2334 interact W132 (helix $\alpha 1$); S2309/C2332 also contacts G188 and is hydrogen-bonded to N192 (helix $\alpha 4$). These conserved interactions between motif 1 and motif 2 of BRCA2 and two ARM monomers belonging to two different dimers trigger tetramerization of the ARM domain. In summary, analysis of the crystal structure of the BRCA2-HSF2BP complex identified a repeated motif in BRCA2 that is able to bind to the ARM domain of HSF2BP, thus causing tetramerization of the dimeric ARM domain.

Residues essential for HSF2BP binding to BRCA2. We compared the interface observed in our crystal structure with the point mutants we designed based on homology modeling of the solvent-exposed structural neighbors of R200 and analyzed by coimmunoprecipitation (Fig. 1a–c). Substitutions N192R, R200E/H/C, Y238A, N239K affected residues that are hydrogen-bonded to both motifs 1 and 2. Consistently, they totally abolished binding (Fig. 4a; Supplementary Fig. 1c, d). R277E modified a residue that is hydrogen-bonded only to motif 1; it strongly

decreased binding. G199D changed a residue that is completely buried in ARM, and abolished binding. N243H affected a residue that is totally buried at the interface with both motifs; it also totally abolished binding. M235T modified a residue that is half buried at the interface with both motifs. This variant still weakly bound to BRCA2. Only E201A and K245T, which changed two residues forming an intramolecular salt-bridge partially buried at the interface with both motifs, did not impact BRCA2 binding (Fig. 4a; Supplementary Fig. 1c, d). Altogether, coimmunoprecipitation assays validated the essential role played by the conserved ARM surface in binding to BRCA2 in human cells. Furthermore, these assays highlighted the critical role played by asparagine residues N192 and N239 from the ARM surface. Despite the lack of secondary structure elements in bound BRCA2, the presence of asparagine residues that interact through their side chains with the backbone amide proton and oxygen of BRCA2 residues mimics the formation of a β -sheet hydrogen bond network between the ARM domains and BRCA2 (Fig. 4b). These interactions are independent of the BRCA2 sequence, as they involve only the backbone atoms of BRCA2. On the BRCA2 side, consistently with our ITC results, the only mutations clearly decreasing or abolishing the interaction are in the region L2304–P2329 (Fig. 1b). Most mutations of residues defining motif 1 (L2304K, S2309N), and motif 2 (R2318Q, P2329L) either strongly decreased or abolished binding to HSF2BP (Fig. 4c, d; Supplementary Fig. 1e). In contrast, mutations of the highly conserved BRCA2 residues E2292, F2293, and P2334 did not result in any

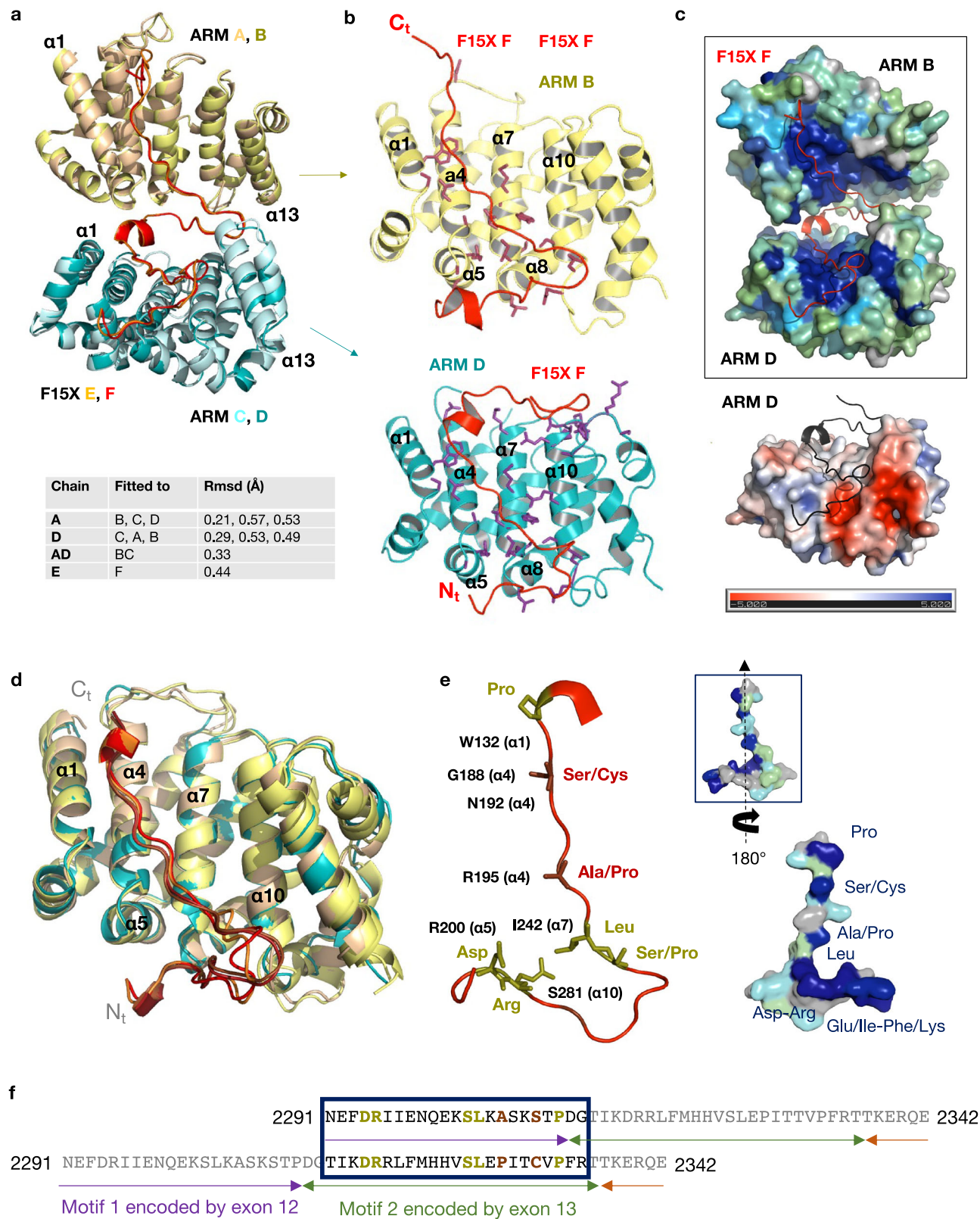
Table 2 Data collection and refinement statistics.		
	ARM-F15X-native	ARM-F15X-Se-Met
Data collection		
Space group	<i>P</i> 1	<i>P</i> 2 ₁
Cell dimensions		
<i>a</i> , <i>b</i> , <i>c</i> (Å)	52.45, 70.77, 75.87	52.89, 135.83, 75.79
α , β , γ (°)	96.47, 109.44, 103.99	90, 110.38, 90
Resolution (Å)	48.4–2.7 (2.77–2.7) ^a	49.6–2.6 (2.67–2.6) ^a
<i>R</i> _{pim}	0.053 (1.305)	0.062 (1.395)
<i>R</i> _{merge}	0.074 (1.837)	0.158 (3.589)
<i>I</i> / σ ⁱ	7.3 (0.6)	8.0 (0.5)
<i>I</i> / σ ^b	8.8 (1.3)	9.4 (0.9)
CC _{1/2}	0.997 (0.300)	0.998 (0.159)
CC _{1/2} ^b	0.997 (0.479)	0.998 (0.355)
Completeness (%)	96.7 (93.5)	100 (99.8)
Completeness (%) ^b	80.0 (38.1)	83.7 (28.4)
Redundancy	2.8 (2.8)	7.4 (7.5)
B Wilson		68.99
Refinement		
Resolution (Å)		49.6–2.6
No. reflections		25870
<i>R</i> _{work} / <i>R</i> _{free}		0.189/0.259
No. atoms		7383
Protein		7241
Ligand/ion		2
Water		140
Protein residues		945
B-factors		87.2
Protein		87.7
Ligand/ion		64
Water		62.5
R.m.s. deviations		
Bond lengths (Å)		0.013
Bond angles (°)		1.58
PDB entry code		7BDX
The anisotropic diffraction data for ARM-F15X-native were truncated using STARANISO to include all valid data (reflections with <i>I</i> / σ (<i>I</i>) of 1.2) to resolutions of: 2.68, 3.22 and 2.50 Å along the 0.705a* – 0.402b* – 0.584c*, 0.180a* + 0.970b* – 0.164c*, 0.196a* – 0.262b* + 0.945c* directions, respectively. Similarly, the anisotropic diffraction data for ARM-F15X-SeMet were truncated using STARANISO to include all valid data to resolutions of: 2.69, 2.91, and 2.47 Å along the 0.861a* – 0.508c*, b*, 0.052a* + 0.999c* directions, respectively.		
^a Values in parentheses are for highest-resolution shell.		
^b Values after truncation by STARANISO.		

loss of binding, despite F2293 and P2334 being buried at the interface with HSF2BP. These residues were mutated into leucine: their hydrophobic character was conserved, which might explain the lack of associated binding defect (Fig. 4d). In summary, the impact of human polymorphisms at the HSF2BP-BRCA2 interface was characterized, and a set of mutations of highly conserved residues was identified that severely decreased the interaction between these two proteins in cells.

Functional interaction with HSF2BP requires Brca2 exon 12. Previously, we showed that excising exon 12 from BRCA2 in human cells, mimicking a naturally occurring BRCA2 splice form, renders them completely resistant to the inhibitory effect HSF2BP has on HR in the context of DNA interstrand crosslink repair¹⁵. This suggested complete disruption of the functional interaction between HSF2BP and BRCA2Δ12. Analysis of our crystal structure revealed that exon 12 encodes motif 1, whereas exon 13 encodes motif 2 (Fig. 5a). Thus, deleting exon 12 should lead to the loss of more than half of the binding interface, and also to the absence of resulting tetramerization of the ARM domain. To test this hypothesis, we measured the affinity of HSF2BP for the F15X

peptide which has the sequence encoded by exon 12 deleted, named F15XΔ12 (D2312-E2342). This affinity is in the micromolar range, that is 1000-fold weaker than the affinity of HSF2BP for F0 (Fig. 5b). Moreover, the stoichiometry of the interaction is now 1, demonstrating that each HSF2BP molecule binds to its own BRCA2 peptide. Further analysis of the ARM-F15XΔ12 complex using SEC consistently showed that the ARM domain does not oligomerize upon binding to F15XΔ12 (Fig. 5c). To test the effect of exon 12 loss under physiological conditions, we created the *Brca2* exon 12 deletion in mouse embryonic stem (ES) cells, where HSF2BP is expressed natively¹⁶. To further validate the specificity of our system, we also engineered another *Brca2* in-frame exon excision, deleting exons 12–14 which encode all of BRCA2 residues involved in the interaction with HSF2BP (Fig. 5d). In addition to the different *Brca2* exon excisions we homozygously knocked-in GFP expression sequence at the 3' end of *Hsf2bp* or *Brca2* coding sequence^{16,37}. This allowed us to study HSF2BP-BRCA2 interactions under native expression levels, and at the same time take advantage of the highly efficient GFP nanobody precipitation, thus reducing the chance of missing any possible residual interaction between the proteins, while minimizing non-specific background associated with indirect immunoprecipitation. To avoid non-linear amplification in immunoblotting, we used fluorescently labeled secondary antibodies instead of enzymatic detection. Pull-downs from cells producing full-length, Δ12 or Δ12–14 BRCA2-GFP from engineered homozygous alleles revealed near-complete (by 95 ± 3%, *n* = 4) and complete abrogation of HSF2BP co-precipitation in Δ12 and Δ12–14, respectively (Fig. 5d). Pull down of HSF2BP-GFP from *Hsf2bp*^{GFP/GFP}*Brca2*^{wt/wt} OR Δ12/Δ12 OR Δ12-14/Δ12-14 ES cells revealed an essentially complete disruption (97–99%, *n* = 2) of co-precipitation in BRCA2-Δ12, and only background signal for BRCA2-Δ12–14 (Fig. 5e). Consistently, pull down of GFP-HSF2BP from HEK293T or HeLa cells showed no binding to several FLAG-F9 variants (Supplementary Fig. 1d). We also tested co-precipitation between human proteins in HeLa cells over-producing GFP-HSF2BP and producing full-length, Δ12 or Δ12–14 BRCA2 from engineered native alleles. Human BRCA2 and HSF2BP behaved similar to the mouse proteins (Fig. 5f) and consistent with the functional experiments we described before¹⁵. Thus, in agreement with our biophysical data, loss of *Brca2* exon 12 strongly decreased interaction with HSF2BP. To evaluate its effect on HSF2BP-BRCA2 in functional contexts in cells, we analyzed HSF2BP-GFP diffusion in living cells and its recruitment to ionizing radiation-induced nuclear foci, using the same engineered *Hsf2bp* and *Brca2* allele combinations in mES cells. Characteristic (BRCA2-like) constrained diffusion of HSF2BP-GFP we described before¹⁶ was dramatically affected by exons 12–14 deletions; in particular the slow-diffusing and immobile species were gone (Supplementary Movies 1–3). We further noted that in *Brca2* Δ12 and Δ12–14 cells, HSF2BP-GFP fluorescence intensity in the nucleus was reduced, and more fluorescence was observed in the cytoplasm, which made it altogether impossible to apply the quantitative single particle tracking analysis we used before. We observed a similar reduction in nuclear fluorescence and co-localization of HSF2BP-GFP with RAD51 in ionizing radiation-induced nuclear foci in immunofluorescence experiments (Fig. 5g, h). Taken together, this and the functional experiments in human *BRCA2*^{Δ12/Δ12} cells, indicate that exclusion of the BRCA2 domain encoded by exon 12 leads to a severe defect in the interaction with HSF2BP in cells.

High-affinity HSF2BP-BRCA2 binding dispensable for meiotic HR. Our biophysical data and functional experiments validated *Brca2*-Δ12 as a model to determine the functional importance of the



high-affinity interaction between BRCA2 and HSF2BP and of the resulting HSF2BP oligomerization. To study this in the context of meiotic HR, we created a *Brca2*^{Δ12/Δ12} mouse model (Fig. 6a–c). Consistent with the robust proliferation of the engineered BRCA2 Δ12 HeLa and mES cells, *Brca2*^{Δ12/Δ12} mice were viable, born at Mendelian ratios, and did not show any overt phenotypes. Contrary to our expectation, the Δ12 mutation did not phenocopy the *Hsf2bp*

knockout, as not only females, but also males were fertile, with normal sperm counts and a significant increase rather than a reduction in testis weight (Fig. 6d–g). Morphology of testis tubule sections was normal (Supplementary Fig. 8a). Molecular analysis of the meiotic prophase progression did not reveal any major defects: the small (6–18%) reductions in the number of recombinase foci were only significant for RAD51 in leptotene and zygotene

Fig. 3 The same conserved ARM surface interacts with both the N-terminal and C-terminal regions of the BRCA2 peptide, through a 23 aa motif.

a Superimposition of the complexes formed by two ARM domains and a BRCA2 peptide. The C α root-mean-square-deviation (Rmsd) values calculated between the different chains are recapitulated in the lower part of the panel. Additional views of the superimposed individual chains are displayed in Supplementary Fig. 7. **b** Zoom on the interfaces between ARM chain B and the C-terminal region of BRCA2 F15X chain F (upper view) and ARM chain D and the N-terminal region of BRCA2 F15X chain F (lower view). ARM residues that are either involved in hydrogen bonds or salt bridges with BRCA2, or buried (by more than 30 Å²) at the interface with BRCA2, are represented by colored sticks. They are labeled in Supplementary Fig. 7b, c. **c** Surfaces of ARM domains, colored as a function of sequence conservation (upper panel) or electrostatic potential (lower panel). In the upper panel, surfaces of ARM chains B and D are colored as a function of conservation scores calculated by ConSurf⁶⁵. High, medium, weak, and no conservation are indicated in dark blue, cyan, green, and gray, respectively. BRCA2 F15X F is represented as a red ribbon. In the lower panel, the surface of ARM chain D is colored from red (negatively charged) to blue (positively charged) and the N-terminal region of BRCA2 F15X F is displayed as a black ribbon. **d** Superimposition of the four ARM domains and their BRCA2-interacting peptides. The four ARM structures were aligned, and their BRCA2-interacting fragments are displayed. **e** Representation of the 3D structure of the BRCA2 motif binding to ARM domains. Residues strictly conserved between motif 1 and motif 2 are displayed as olive sticks. They correspond to D2294/2317, R2295/2318, S2303/2326, L2304/2327, and P2311/2334. Residues that are similar between the two motifs and conserved in BRCA2 are displayed as brown sticks. They correspond to A2306/P2329 and S2309/C2332 (mutated in T2332 in our construct to avoid oxidation of this residue). A set of conserved residues from ARM interacting with BRCA2, as defined in **b**, are indicated in black next to the BRCA2 residues when they directly interact with these residues. A boxed surface view of the peptide, in the same orientation as the cartoon view, is colored by conservation as in **c**. Turning this surface view by 180° reveals the conservation of the surface binding to ARM, including the conserved residues of motifs 1 and 2. **f** Sequence alignment of motif 1, interacting with ARM chains C and D, and motif 2, interacting with ARM chains A and B. Conserved residues are colored as in **e**. Motif 1 is encoded by exon 12, whereas motif 2 is encoded by exon 13.

(Fig. 6i–h). In addition, the frequency of MLH1 foci indicating meiotic crossover sites after successful HR was normal (Fig. 6k, Supplementary Fig. 8b). These results were not consistent with the proposed role of HSF2BP as a BRCA2 localizer in meiosis. We hypothesized that given the high-affinity interaction revealed by our ITC experiments, the dependence may be opposite: BRCA2 may bring HSF2BP to the double-strand breaks (DSBs). However, the number of HSF2BP foci was not significantly affected by *Brca2* exon 12 deletion, and for BRME1 foci only small (but statistically significant) reductions in leptotene and pachytene were measured (reduced by 23% and 6%, respectively Fig. 6l–n). Consistent with the robust accumulation of both HSF2BP and RAD51 to the meiotic DSB chromatin in *Brca2*^{Δ12/Δ12} testis, both proteins co-precipitated with BRCA2, and the effect of disrupting HSF2BP–BRCA2 interaction as revealed by our structure and variant mapping was smaller in the testis co-IPs (Fig. 6c). The difference can be caused by the potential contributions of other interactions, which are absent or substantially sub-stoichiometric in the experiments with purified or highly overproduced proteins (Fig. 5, Supplementary Fig. 1). Together with the weakened binding via motif 2 such compensatory interactions (e.g., mediated by other binding partners, chromatin, or post-translational modifications) may mask the meiotic defect resulting from *Brca2* exon 12 loss in the genetic background of the inbred laboratory mouse strain we used.

Discussion

In this paper, we analyzed the structural properties and functional consequences of the BRCA2–HSF2BP interaction and tested the emerging model of its involvement in meiosis. The essential roles of BRCA2 and HSF2BP in meiotic HR have been clearly demonstrated previously. BRCA2 interacts with both RAD51 and DMC1 recombinases, is required for their accumulation at meiotic DSB in mice and stimulates their activity in vitro. But how BRCA2 balances its activity with respect to RAD51 and DMC1 and integrates with the meiotic-specific HR machinery in a timely manner during meiosis remains unclear. Direct data on its behavior in meiocytes is scarce, and mechanistic models are mostly based on extrapolation. The proposed role of the recently identified HSF2BP, required for RAD51 and DMC1 accumulation at meiotic DSBs during spermatogenesis in mice¹⁶, is to bring BRCA2 to meiotic DSBs²⁷. We tested this hypothesis by disrupting the HSF2BP-binding region of BRCA2 in mice.

We first characterized the BRCA2–HSF2BP interaction in vitro. We had previously identified that the region of BRCA2 binding to

HSF2BP is located between its BRC repeats and its C-terminal DNA binding domain (Fig. 1b and ref. 16). Our structural analysis revealed that this BRCA2 region contains a duplicated motif, which was not previously recognized from its primary amino acid sequence. Each motif binds to the same residues of an Armadillo domain of HSF2BP (Fig. 3e). By itself, the Armadillo domain dimerizes through a conserved surface formed by helices α1 to α3 (Fig. 2d) and presents on each monomer a large conserved groove, which indicates a binding site for functionally important partners (Fig. 3c). Many Armadillo domains interact through their concave surface with largely disordered partners³⁸. The Armadillo domain of HSF2BP contains four Armadillo repeats (Supplementary Fig. 7a). Altogether, they form a positively charged groove delimited by helices α1, α4, α7, α10, and α13. This groove is able to recognize a 23 aa motif located in a conserved and disordered region of BRCA2. Because this motif is duplicated in BRCA2, and each motif binds to a different ARM dimer, the interaction triggers further oligomerization of the Armadillo domain into a tetramer. The affinity of BRCA2 for HSF2BP is 1 nM, which is significantly higher than the affinities yet measured between BRCA2 disordered regions and its partners PALB2, RAD51, and PLK1, all between 100 and 1000 nM^{33–35}. However, after deleting motif 1 encoded by exon 12, motif 2 alone binds to HSF2BP with a micromolar affinity and is unable by itself to trigger oligomerization of the ARM domain into a tetramer (Fig. 5b).

Consistent with our in vitro study, we observed in mouse ES cells that deletion of exon 12, coding for motif 1, causes a severe decrease in the BRCA2–HSF2BP interaction, and deletion of exons 12 to 14, coding for motifs 1 and 2, completely abolishes this interaction (Fig. 5d, e). We previously showed that HSF2BP mutation R200T abolishes localization of the GFP-tagged HSF2BP protein to mitomycin C-induced repair foci¹⁶. Consistently, we now demonstrated that the BRCA2 region encoded by exon 12 is responsible for HSF2BP localization at irradiation-induced DSBs (Fig. 5g). We further previously reported that, in human cells, excising exon 12 from BRCA2, mimicking a naturally occurring BRCA2 splice form, rendered them completely resistant to the inhibitory effect HSF2BP has on HR in the context of DNA interstrand crosslink repair¹⁵.

Based on these structural, biochemical, and functional experiments, we developed a *Brca2*^{Δ12} mouse line to test the emerging model, which posits that HSF2BP–BRME1 complex acts as a meiotic localizer of BRCA2^{25,27}, and thus predicts that

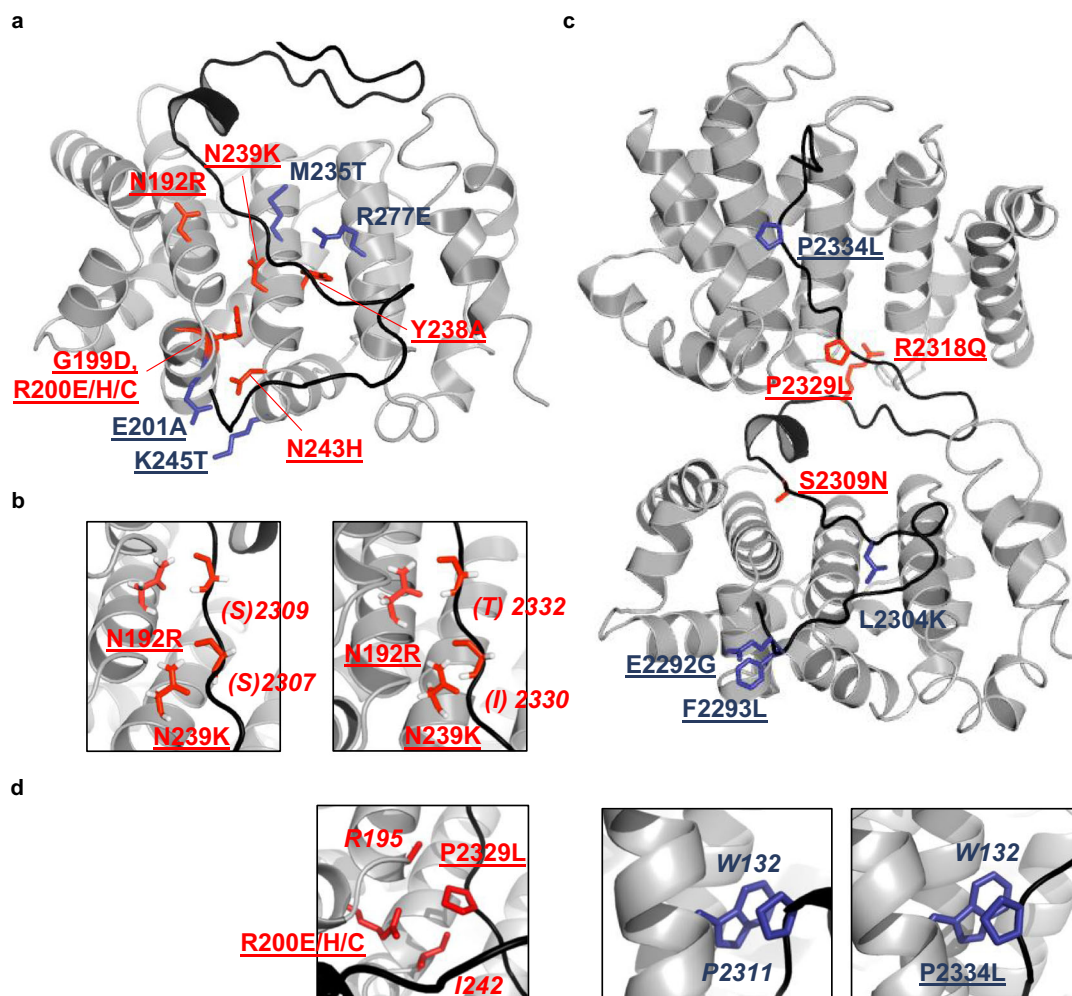


Fig. 4 Crystal structure explains the effect of human SNP variants on HSF2BP-BRCA2 interaction. **a** 3D view of the ARM chain D in complex with motif 1 of BRCA2 F15X chain F. The ARM and BRCA2 protein fragments are displayed as gray and black ribbons, respectively. The side chains substituted for coimmunoprecipitation studies are displayed in sticks, and colored as in Fig. 1a (red: no binding; blue: residual binding with the residue name underlined when wild-type binding was observed). **b** Zoom views on residues forming a hydrogen bond network between ARM and BRCA2 F15X. Asparagine side chains from ARM interact with backbone atoms from BRCA2 F15X. The side chains of BRCA2 are not displayed; consistently, the BRCA2 residue names are in brackets. Hydrogens were added to the crystal structure for clarity. **c** 3D view of the ARM chains B and D in complex with the BRCA2 F15X chain F. The ARM and BRCA2 protein fragments, as well as the mutated side chains, are displayed as in **a**, except that full labels are shown for BRCA2 residues. **d** Zoom views on BRCA2 F15X mutations P to L and their interacting residues in ARM chains B and D. Residues marked in italics have not been mutated in our study.

disengaging BRCA2 from HSF2BP will phenocopy *Hsf2bp* deficiency. However, we could not detect any major differences in meiosis in *Brca2*^{Δ12/Δ12} mice compared to *Brca2*^{+/+} (Fig. 6). **Not only females, but also males were fertile, had a normal sperm count and increased testis weights. While the latter is opposite to the greatly reduced testis sizes in *Hsf2bp* knockout and hard to explain, we noted a progressive increase in testis, epididymis, and body weights from +/+ to Δ/+ to Δ/Δ genotypes, although the differences in body and epididymis weights are not as notable or not even statistically significant, as was observed for testes weights. Regarding our detailed immunocytochemical analyses of the progression of homologous chromosome pairing and meiotic DSB repair during meiotic prophase, it is clear that these events occurred grossly normal, except for a significant although small reduction in the number of RAD51 foci in early stages. Still, the number of DMC1 foci, as well as MLH1 foci were normal indicating normal meiotic crossover formation after successful HR. Despite the clear reduction in BRCA2-HSF2BP interaction in *Brca2*^{Δ12/Δ12} testes, HSF2BP foci numbers were not significantly**

reduced. A small decrease in the number of BRME1 foci in *Brca2*^{Δ12/Δ12} leptotene spermatocytes may be indicative of some interdependence between BRCA2, HSF2BP, and BRME1, but hard to reconcile with the normal HSF2BP foci within the proposed models. Altogether, these analyses show that the high-affinity interaction between BRCA2 and HSF2BP, together with the oligomerization of HSF2BP triggered by this interaction, are not essential for HR in meiosis.

The BRCA2 localizer function of HSF2BP was suggested primarily based on the observation of the localization of recombinant GFP-tagged BRCA2 fragments produced by electroporation of expression constructs into wild-type and HSF2BP-deficient testis²⁷. In these experiments, a BRCA2 fragment including the HSF2BP-binding region and the C-terminal ssDNA binding domain co-localized with RPA2 at DSB sites in an HSF2BP-dependent manner²⁷. The presence of various ssDNA-binding proteins (SPATA22, MEIOB, and RPA) in HSF2BP and BRME1 immunoprecipitates further supported the model and led to the suggestion that HSF2BP and BRME1 act as adaptors, anchoring

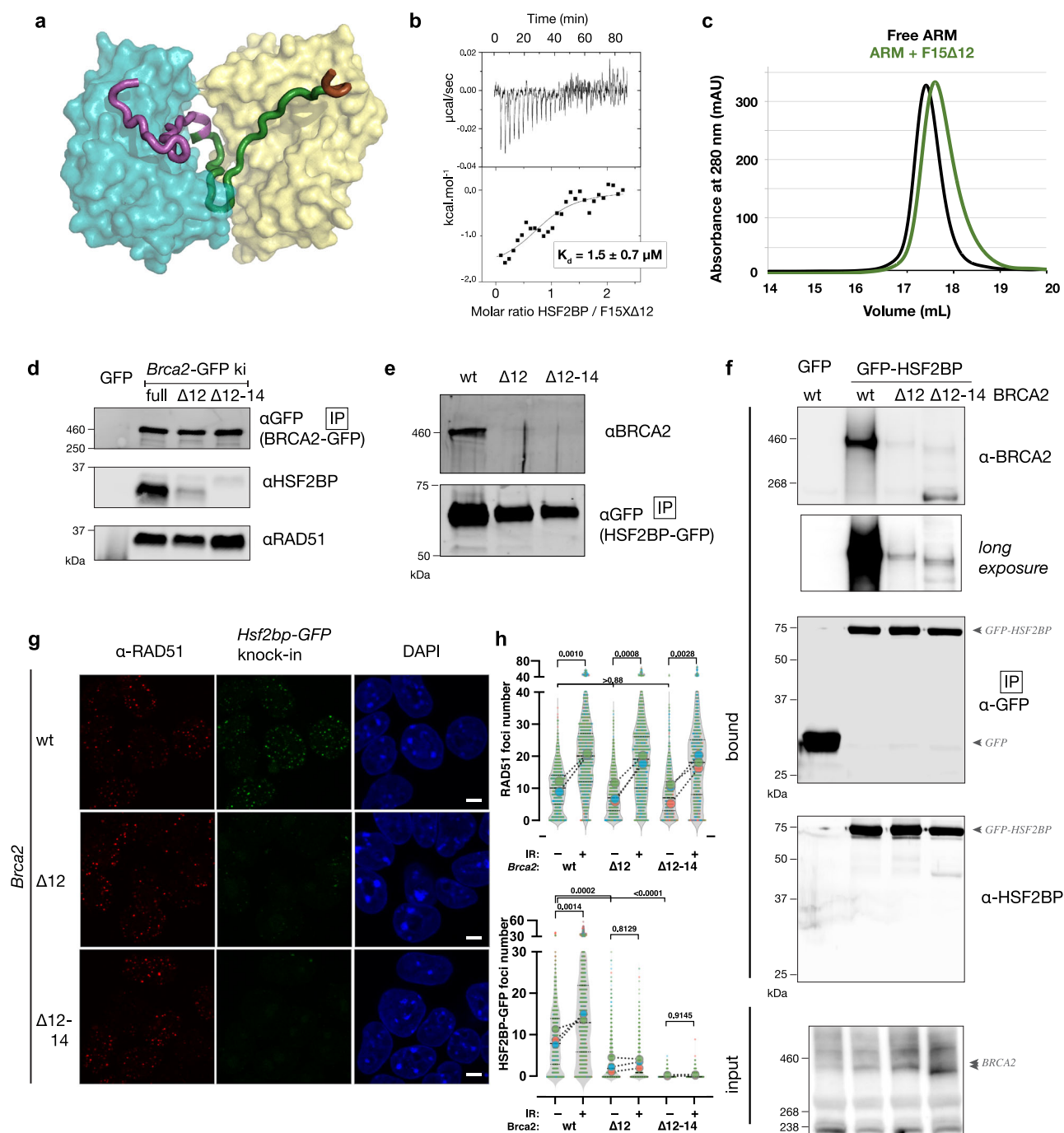
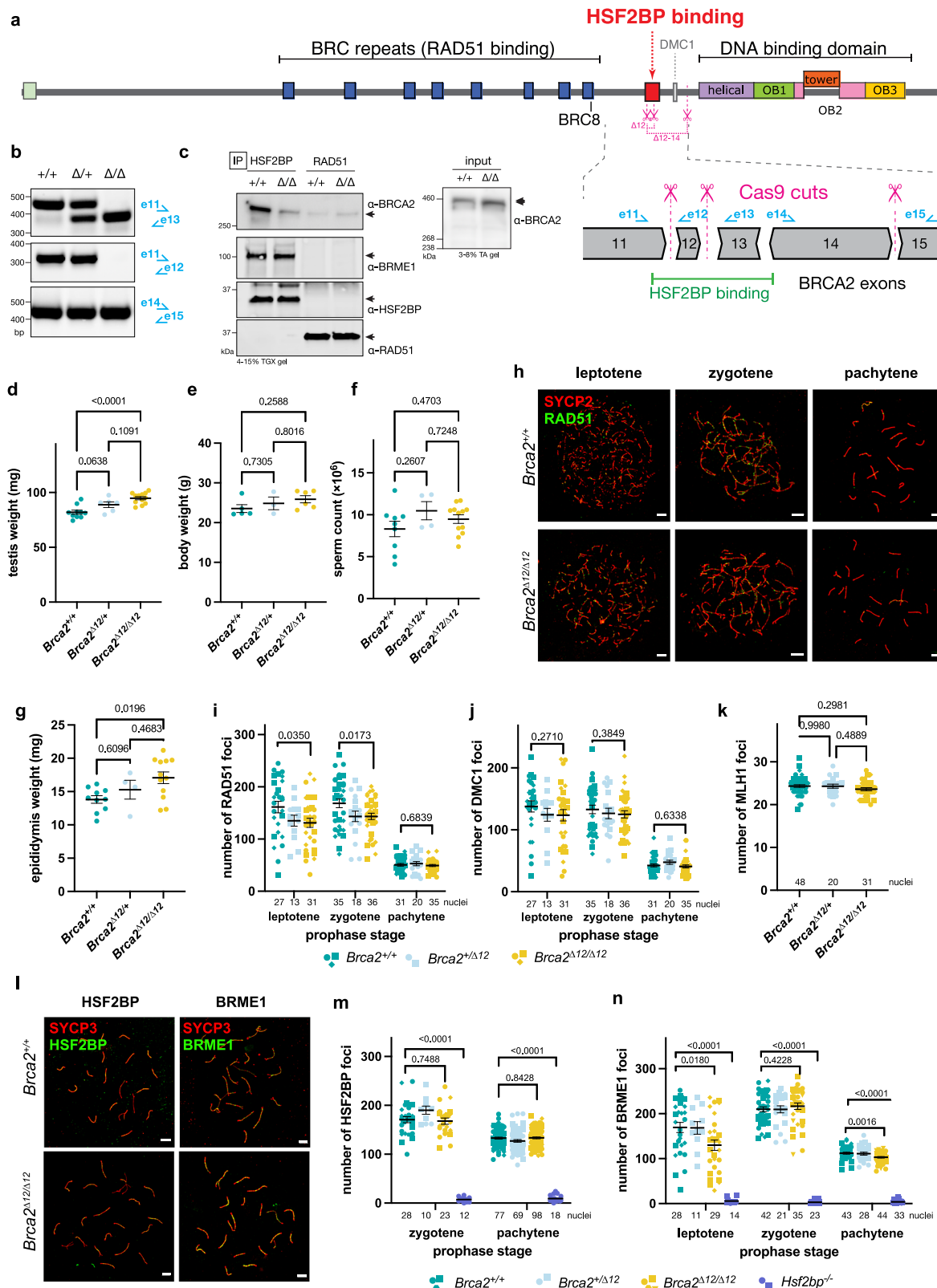


Fig. 5 Deletion of *Brca2* exon 12 disrupts HSF2BP-BRCA2 interaction in cells. **a** Structure of the HSF2BP dimer interacting with the BRCA2 peptide colored by encoding exon number. **b** ITC experiment with HSF2BP and a truncated variant of F15X peptide missing residues encoded by exon 12 (F15XΔ12). **c** ARM and the complex between ARM and F15XΔ12 analyzed by analytical gel filtration (column: Superose 6 Increase 10/300 GL). **d** Immunoblot analysis of proteins co-precipitated with anti-GFP nanobody beads from mES cells containing homozygous *Brca2*-GFP allele without (full) or with deletions of exon 12 or exons 12-14. The experiment was performed four times with similar results. **e** Immunoblot analysis of proteins co-precipitated with anti-GFP nanobody beads from double knock-in mES cells containing homozygous *Hsf2bp*-GFP and *Brca2* alleles without or with deletion of exons 12 or 12-14. The experiment was performed two times with similar results. **f** Immunoblot analysis of proteins co-precipitated with anti-GFP nanobody beads from HeLa cells stably overproducing GFP-HSF2BP or GFP control, and in which *BRCA2* allele was modified by excision of exons 12 or exons 12-14, or unmodified wild-type (wt) *BRCA2*. **g** *Hsf2bp*^{GFP/GFP}*Brca2*^{wt/wt}, *Hsf2bp*^{GFP/GFP}*Brca2*^{Δ12/Δ12}, and *Hsf2bp*^{GFP/GFP}*Brca2*^{Δ12-14/Δ12-14} mES cells were irradiated with 8 Gy, fixed after 2 h recovery, immunostained with anti-RAD51 antibody, mounted with DAPI, and imaged using laser confocal microscope. HSF2BP-GFP was detected by direct fluorescence. Maximum projection of three confocal slices (0.5 μm apart) is shown. Scale bar = 5 μm. **h** Quantification of HSF2BP-GFP and RAD51 foci from the experiments as the one shown in **g**. Data from three independent experiments are plotted following the SuperPlots approach⁶⁶: symbol colors indicate biological replicates ($n = 3$), small symbols show number of foci per nucleus, violin plot shows the combined frequency distribution, with lines indicating median and quartiles; large circles indicate means within replicates, dotted lines visualize changes after irradiation. Replica means were compared by one-way ANOVA with Tukey multiple comparison test, p -values are indicated.



BRCA2 to the protected ssDNA. Such adaptors have not been identified in somatic HR. Both BRCA2 and its equally important partner PALB2, also involved in meiotic HR³⁹, are well equipped for the recruitment to resected DSBs with a set of DNA-, RAD51- and chromatin-binding domains, and can stimulate RAD51 and/or DMC1 activity autonomously in vitro. As a localizer, HSF2BP neither mimics DNA as does the BRCA2-interacting protein

DSS1⁴⁰, nor interacts with ssDNA or dsDNA (Supplementary Fig. 9; see also ref. ²²). However, even with these reservations regarding the localizer model, we fully expected the HSF2BP-binding domain of BRCA2 to be essential for meiotic HR, because it is conserved, and no somatic function could be assigned to it by several previous studies in human cancer cells^{41,42}. The high evolutionary conservation of the BRCA2-HSF2BP interaction,

Fig. 6 Meiotic phenotype of *Brca2* exon 12 deletion mouse model. **a** Schematic depiction of the domain composition of the BRCA2 protein and the exons 11–15 encoding HSF2BP-binding and DMC1-binding domains. Introns are not drawn to scale; different exon phases are indicated by the shape of the boundary. Location of Cas9 cut sites for exon 12 and exons 12–14 excision is shown. **b** RT-PCR on cDNA from mouse testis with indicated genotypes confirming the loss of exon 12; primer locations are shown on the exon scheme in **a**. The PCR was performed twice with the same results. **c** Immunoblot analysis of proteins precipitated from *Brca2*^{+/+} and *Brca2*^{Δ12/Δ12} mouse testes using anti-HSF2BP antibody and, as control, with anti-RAD51 antibodies; and the input samples; performed as described in “Methods” section. The experiment was performed four times with similar results. **d** testis weight, **e** bodyweight, **f** sperm count, and **g** epididymis weight in *Brca2*^{Δ12/Δ12} and control mice. *n* = 5 animals for *Brca2*^{+/+}, *n* = 6 for *Brca2*^{Δ12/Δ12}, *n* = 3 (testis weight and bodyweight), and *n* = 2 (epididymis weight and sperm count) for *Brca2*^{Δ12/+}. Mean, s.e.m, and *p* values from one-way ANOVA with Tukey test are indicated. **h–n** Immunofluorescent analysis of meiotic protein localization on spermatocyte spreads from *Brca2*^{Δ12/Δ12} and control mice. Representative images (**h**, **i**; scale bars = 5 μm) and quantification of RAD51 (**i**), DMC1 (**j**), MLH1 (**k**), HSF2BP (**m**), and BRME1 (**n**) foci are shown with mean and s.e.m. indicated with error bars. Symbol shapes designate individual animals: *n* = 3 animals for *Brca2*^{+/+} and *Brca2*^{Δ12/Δ12}, *n* = 2 for *Brca2*^{Δ12/+}, *n* = 2 (BRME1), and *n* = 1 (HSF2BP) for *Hsf2bp*^{-/-}. Mean, s.e.m, and *p* values from two-tailed unpaired *t*-test for selected pairwise comparisons within prophase stages are indicated. The number of analyzed nuclei is indicated for each genotype and stage.

initially evident from sequence analysis and interchangeability of human and frog HSF2BP proteins in biochemical experiments¹⁵, is further emphasized by the structure we solved. The BRCA2-binding surface is a particularly highly conserved part of HSF2BP (Fig. 3c), and the cryptic BRCA2 repeats, to which it binds with a remarkable structural symmetry, are also highly conserved (Supplementary Fig. 2). This means that the oligomerization-inducing interaction between the two proteins is under strong selective pressure and thus functionally relevant. Further investigation of the role of HSF2BP and the HSF2BP-BRCA2 interaction in meiosis, and outside of it, is now required.

Our crystal structure also revealed the mechanism of BRCA2-induced HSF2BP oligomerization observed in the biochemical experiments (Fig. 2, refs. 16,25). The main contribution to the nanomolar affinity we measured comes from the large 2740 Å² interface between one BRCA2 peptide and two HSF2BP ARM domains from two different ARM dimers. A second contribution is made by additional contacts between two ARM dimers (Supplementary Fig. 5b). As the corresponding interface is small (350 Å² vs. twice 2740 Å² in one BRCA2-ARM complex), its contribution to the thermodynamic parameters we measured by ITC is not expected to be significant, and its role may be in establishing proper spatial orientation of the ARM domains. Thus, HSF2BP is able to oligomerize through several distinct mechanisms: it was previously reported that full-length HSF2BP contains an N-terminal domain forming coiled coils²⁵; we now show how its armadillo domains dimerize and further tetramerize upon binding to BRCA2. Each oligomerization mechanism can be under separate regulatory control, allowing HSF2BP to serve as a versatile and potent agent increasing the local concentration and/or modifying the oligomerization state of BRCA2. This can play a positive role in some contexts and be detrimental in others. For example, we previously found that HSF2BP, when produced ectopically in somatic cancer cells, interferes with the role of BRCA2 in DNA interstrand crosslink repair by causing its degradation¹⁵. The findings we report here suggest that this degradation, which is mediated by the p97 segregase and is proteasome-dependent, could result from HSF2BP-induced BRCA2 aggregation.

Altogether, we conclude that the evolutionarily conserved high-affinity oligomerization-inducing interaction mode between HSF2BP and BRCA2 we described in this paper is not required for the recruitment of RAD51 and DMC1 strand exchange proteins and for productive HR in meiosis. While this does not rule out that co-localization of HSF2BP and BRCA2 at meiotic DSBs via alternative compensatory interactions is essential, it raises the question as to why the peculiar repetitive structure evolved and remained conserved. It also opens the possibility that the meiotic function of HSF2BP associated with fertility may result from other interactions, mediated either by its N-terminal coiled-coil

domain, which binds BRME1, by the conserved surface of its ARM domain binding to other proteins with sequences similar to the cryptic repeat our structure revealed in BRCA2, or by other parts of the ARM domain.

Methods

Cells, DNA constructs, and transfection. HeLa (human cervical adenocarcinoma, female origin) and HEK293T (human embryonic kidney, female origin) cells were cultured in DMEM supplemented with 10% FCS, 200 U/ml penicillin, 200 μg/ml streptomycin. mES cell lines were derived from the IB10 cell line, which is a subclone of E14 129/Ola from male origin⁴³, specific pathogen free. Cells were cultured on gelatinized plastic dishes (0.1% gelatin in water) as described before⁴⁴ at atmospheric oxygen concentration in media comprising 1:1 mixture of DMEM (Lonza BioWhittaker Cat. BE12-604F/U1, with Ultraglutamine 1, 4.5 g/l glucose) and BRL-conditioned DMEM, supplemented with 1000 U/ml leukemia inhibitory factor, 10% FCS, 1x NEAA, 200 U/ml penicillin, 200 μg/ml streptomycin, and 89 μM β-mercaptoethanol.

Expression constructs for producing point mutation and truncation variants of HSF2BP and BRCA2 in human cells were engineered as described before¹⁶ in the PiggyBac vectors by Gibson assembly. For transient expression into HEK293T cells plasmid DNA was transfected using calcium precipitation method or PEI transfection. For stable integration into HeLa cells, PiggyBac expression vectors were co-lipofected together with PiggyBac transposase plasmid (hyPBBase⁴⁵) with Lipofectamine 3000 (Thermo Fisher).

GFP knock-in alleles in mES cells were engineered using the previously described CRISPR/Cas9-stimulated approach. All gRNAs were cloned into a derivative of pX459 vector. Excision of BRCA2 exon 12 from mES cells was performed with gRNAs targeting the same sequences in intron 11 and intron 12 as those used to produce *Brca2*Δ12 mouse alleles (see below). Excision of exons 12–14 was performed with gRNAs targeting the same sequence in intron 11, and the sequence in intron 14 CCAACCAGCCCGGTCAAGTT. IB10 or the previously described³⁷ *Brca2*^{GFP/GFP} were used as parental cell lines. Excision of exons 12–14 from HeLa cells was performed with the same gRNA target in intron 11 as used before and the following target in intron 14: AGGAGAGCATGTAAACTTCG. Cell lines and other biological materials generated for the study can be shared upon reasonable request, subject to institutional MTA. Cells were genotyped by PCR. Excision was further confirmed by RT-PCR analysis of the first-strand cDNA produced from total mRNA with oligo-dT primers with SuperScript II polymerase (Invitrogen).

Immunoprecipitation and immunoblotting. Cells were washed twice in ice-cold PBS and lysed in situ in NETT buffer (100 mM NaCl, 50 mM Tris pH 7.5, 5 mM EDTA pH 8.0, 0.5% Triton-X100) supplemented immediately before use with protease inhibitor cocktail (Roche) and 0.4 mg/ml Pefabloc (Roche) (NETT++); 450 μl NETT++ buffer was used per 145 mm dish ES cells, 1 ml for HeLa and HEK293T. After 5–10 min, cells were scraped off and collected in 1.5 ml micro-centrifuge tubes; lysis was continued for additional 20–30 min on ice, then mixtures were centrifuged (15 min, 4 °C, 14,000 × g) and the supernatant (input) was added to washed anti-GFP beads (Chromotek). Beads and lysates were incubated 2–4 h at 4 °C while rotating, washed three times in NETT++ buffer and bound proteins were eluted by boiling in 2x Sample buffer. Immunoblotting was performed following standard procedures with the following antibodies: anti-GFP mAb (Roche, #11814460001), anti-GFP pAb (Abcam #ab290 and Invitrogen #A11122), anti-RAD51⁴⁶, anti-BRCA2 mAb Ab1 OP-95 (Millipore #OP95), anti-BRCA2 (Abcam #27976), anti-Flag (M2 antibody, Sigma, F3165 and F1804). For quantitative immunoblotting fluorescently labeled secondary antibodies were used: anti-mouse CF680 (Sigma #SAB460199), anti-rabbit CF770 (Sigma #SAB460215); membranes were scanned using Odyssey CLx imaging system (LI-COR).

For testis immunoprecipitation, one whole testis was homogenized in 2 ml of NETT++ or RIPA++ (50 mM Tris HCl pH 7.5, 150 mM NaCl, 1% Triton-X100, 0.5% Na-deoxycholate, 0.1% SDS, 1 mM EDTA, 1 mM EGTA, supplemented immediately before use with cOmplete protease inhibitor cocktail (Roche, 11836145001) and 0.4 mg/ml Pefabloc (Roche)) buffer by 3–5 s pulse in Polytron homogenizer. The lysate was allowed to settle on ice for 20–40 min, transferred to mini-centrifuge tubes and cleared by 15 min centrifugation at maximum speed (~13,000 × g) at 4 °C. A 70 µl aliquot of the cleared supernatant was mixed with 70 µl of the 2× sample buffer and denatured for 5 min at 95 °C (input sample). The remainder of the supernatant was divided into two fractions, which were incubated with mixing at 4 °C for 4 h with homemade affinity-purified anti-HSF2BP (SY8127, 40 µg/IP), anti-RAD51 (2037, 2 µl/IP) or pre-immune sera (4 µl/IP) cross-linked using DMP to 50 µl magnetic protein A beads (BioRad SureBeads #161-4013). After incubation, beads were washed three times for 5 min at 4 °C with 1 ml lysis buffer, and then incubated for 5 min at 95 °C with 35 µl of 2× sample buffer to elute the bound proteins. All of the eluate was run in a single lane of a 4–15% TGX SDS-PAGE gel (BioRad #456-1084) and transferred to PVDF membrane, which was cut into three fragments: the top part was immunoblotted with sheep anti-BCRA2 antibody⁴⁷ followed by ECL detection with HRP-conjugated secondary antibody (ThermoFisher, A16041), the middle and bottom parts with anti-BRME1 and a mixture of anti-RAD51 and anti-HSF2BP followed by fluorescent detection. Input samples were analyzed separately on a low-percentage tris-acetate SDS-PAGE gel (3–8% NuPAGE, Thermo Fisher EA0375), suitable for detection of high-molecular weight proteins, such as BRCA2 in total cell lysates.

Protein expression and purification. Human full-length HSF2BP WT and R200T were expressed using a pETM11 (6xHis-TEV) expression vector in *E. coli* BL21 DE3 Rosetta2 cells, and purified as previously reported (Brandsma et al., *Cell Rep* 2019). The armadillo domain of HSF2BP, from aa 122 to aa 334, which we will further name ARM, was similarly expressed using a pETM11 (6xHis-TEV) expression vector in BL21 DE3 Rosetta2 cells and purified as full-length HSF2BP.

Human BRCA2 fragment F0 was expressed using a pET-22b expression vector as a fusion protein comprising BRCA2 from aa 2213 to aa 2342 (including mutation C2332T to avoid oxidation problems), a TEV site, a GBI and 6xHis tag, in *E. coli* BL21 DE3 Star cells. The BRCA2 gene was optimized for expression in bacteria and synthesized by Genscript. In addition, smaller BRCA2 fragments were produced using the same strategy: F_{NMR} and F15X corresponding to aa 2252 to aa 2342 and aa 2291 to aa 2343, respectively. The smallest fragment F15XΔ12, from aa 2312 to aa 2342, was synthesized by Genecust.

For NMR analysis, ¹⁵N- and ¹³C-labeled BRCA2 fragments were produced in *E. coli* BL21 DE3 Star cells grown in M9 medium containing either 0.5 g/l ¹⁵NH₄Cl or 0.5 g/l ¹⁵NH₄Cl and 2 g/l ¹³C-glucose, respectively. For crystallography, selenomethionine (SeMet)-labeled ARM and F15X were produced in transformed *E. coli* BL21(DE3) Rosetta2 (ARM) and Star (F15X) cells, respectively, grown in minimum medium (16 g of Na₂HPO₄, 4 g of KH₂PO₄, 1 g of NaCl, 0.5 g of EDTA, 0.4 g of FeCl₃, 0.04 g of ZnCl₂, 0.006 g of CuCl₂ 6 H₂O, 0.005 g of CoCl₂, 0.005 g of H₃BO₃, 4 g of glucose, 20 mg of thiamine, 20 mg of biotin, 1 g of (NH₄)₂SO₄, 0.5 g of MgSO₄, and 0.1 g of CaCl₂ in 1 l of MilliQ), supplemented with 200 mg of each amino acid and 125 mg of SeMet per 1 l of medium.

Protein expression was induced with 0.2 mM IPTG at an OD₆₀₀ of 0.6, and incubated further ON at 20 °C (HSF2BP), or induced with 1 mM IPTG and incubated for 3 h at 37 °C (BRCA2). Harvested cells were resuspended in 25 mM Tris-HCl pH 7.5, 500 mM NaCl (HSF2BP) or 150 mM NaCl (BRCA2), 5 mM β-mercaptoethanol, EDTA-free Protease Inhibitor Cocktail (Roche) and disrupted by sonication. Lysates were supplemented with 1.5 mM MgCl₂ and treated by Benzonase nuclease at 4 °C for 30 min, and then centrifuged at 48,384 × g at 4 °C for 30 min. After filtration (0.4 µm), the supernatant was loaded on a chromatography HisTrap HP 5 mL column (GE Healthcare) equilibrated with the buffer Tris-HCl 25 mM, pH 8, 500 mM NaCl (HSF2BP), or 150 mM NaCl (BRCA2) and 5 mM β-mercaptoethanol. The proteins were eluted with a linear gradient of imidazole. The tag was cleaved by the TEV protease (at a ratio of 2% w/w) during an ON dialysis at 4 °C against 25 mM Tris-HCl pH 7.5, 150 mM NaCl, 5 mM β-mercaptoethanol. The protein solution was loaded on a HisTrap column and the tag-free proteins were collected in the flow through. Finally, a size exclusion chromatography was performed on HiLoad Superdex 10/300 200 pg (HSF2BP) or 75 pg (BRCA2) equilibrated in 25 mM Tris-HCl pH 7.5, 250 mM NaCl (HSF2BP) or 150 mM NaCl (BRCA2), 5 mM β-mercaptoethanol. The quality of the purified protein was analyzed by SDS-PAGE and the protein concentration was determined by spectrophotometry using the absorbance at 280 nm. The protein thermal stability was evaluated using the simplified ThermoFluor assay available on the High Throughput Crystallization Laboratory (HTX Lab) of the EMBL Grenoble⁴⁸.

BRCA2 peptide structural analysis by NMR. The ¹⁵N/¹³C-labeled F0 fragment was analyzed by 3D heteronuclear NMR, in order to assign its H_N, N, C_α, C_β, and C_γ chemical shifts, and identify its binding site to HSF2BP. Therefore, 3D NMR HNCA, CBCACONH, HNCACB, HNCANNH, HNCOC, and HNCACO experiments were performed on a 700 MHz Bruker AVANCE NEO spectrometer equipped with a triple resonance cryogenic TCI probe at 283 K. The data were processed using Topspin 4.0 (Bruker) and analyzed using CCPNMR 2.4⁴⁹. Sodium

trimethyl-silyl-propane-sulfonate (DSS) was used as a chemical shift reference. Experiments were performed on a 5-mm-diameter Shigemi sample tube containing the 500 µM uniformly ¹⁵N/¹³C-labeled protein, in 50 mM Hepes pH 7.0, 50 mM NaCl, 1 mM EDTA, and 95:5% H₂O/D₂O. For binding studies, 2D NMR ¹H-¹⁵N HSQC experiments were recorded on a 3-mm-diameter sample tube containing the ¹⁵N-labeled F0 at 100 µM in the absence and presence of the ARM domain at 100 µM, on a 950 MHz Bruker Avance III spectrometer equipped with a triple resonance cryogenic TCI probe at 283 K.

Protein-protein interactions. ITC experiments were performed using a high-precision VP-ITC instrument (GE Healthcare) at 293 K. To characterize the interactions between HSF2BP and BRCA2 fragments (WT, variants), the proteins were dialyzed against 25 mM Tris pH 7.5, 250 mM NaCl, 5 mM β-mercaptoethanol. The HSF2BP (or ARM domain) was in the sample cell at 10–20 µM and was titrated by BRCA2 fragments at 40–100 µM, using 10 µL injections with 210 s intervals between each injection. The first 2 µL injection was ignored in the final data analysis. The integration of the peaks corresponding to each injection, the correction for the baseline and the fit were performed using the Origin 7.0 software provided by the manufacturer, to obtain the stoichiometry (N), dissociation constant (K_d), and enthalpy of complex formation (ΔH) for each interaction. These data are indicated in Table 1. Two replicates were performed for each experiment.

Size-exclusion chromatography (SEC) coupled to MALS was used in order to measure the molecular masses of the complexes in solution. Therefore, HSF2BP and ARM proteins were loaded in the presence and absence of the BRCA2 fragment F15X on a Superdex 200 10/300 GL (GE Healthcare) using a HPLC Shimadzu system coupled to MALS/QELS/UV/RI (Wyatt Technology). The chromatography buffer was 25 mM Tris-HCl buffer, pH 7.5, 250 mM NaCl, 5 mM β-mercaptoethanol. The proteins were injected at 0.8–1 mg/ml in 100 µL. Data were analyzed using the ASTRA software; a calibration was performed with BSA as a standard.

SEC coupled to SAXS is available on the SWING beamline at synchrotron SOLEIL, in order to obtain a distance distribution corresponding to each sample in solution. The free HSF2BP protein as well as the complex between ARM and F15X were analyzed using a Bio SEC-3 column (Agilent) equilibrated in 25 mM Tris-HCl buffer, pH 7.5, 250 mM NaCl, and 5 mM β-mercaptoethanol. The proteins were loaded at a concentration of 6 and 10 mg/ml, in order to observe an elution peak at an OD_{280nm} of 1 and 1.2 AU, respectively.

SEC was also used to characterize ARM and ARM bound to F15XΔ12. The ARM domain was loaded on a Superose 6 Increase 10/300 (GE Healthcare) alone (at 2 mg/ml) or bound to F15XΔ12 (at 5 mg/ml, ARM to peptide ratio 1:1.2) in 25 mM Tris-HCl buffer, pH 7.5, 250 mM NaCl, and 5 mM β-mercaptoethanol. The OD values from the elution of ARM alone were multiplied by 2.5 to be compared to the OD values from the elution of ARM bound to F15XΔ12.

Crystallization and structure determination. Prior to crystallization, the complex between ARM and F15X was loaded on a size exclusion chromatography column HiLoad Superdex 200 pg 16/600 (GE Healthcare) equilibrated in a 25 mM Tris pH 7.5, 250 mM NaCl and 5 mM β-mercaptoethanol, in order to prevent the presence of aggregates. The complex was then concentrated up to 10 mg/ml. Initial crystallization experiments were carried out at the High Throughput Crystallization⁵⁰. Crystals were prepared for X-ray diffraction experiments using the CrystalDirect⁵¹. Crystals were obtained using the hanging-drop vapor diffusion method at 291 K. One µl of protein and reservoir solution containing 100 mM MgCl₂, 100 mM MES pH 6 and 16% (w/v) PEG 3350 were mixed. Needle crystals appeared within 3 days, were grown for 1–2 weeks and were frozen in liquid nitrogen after cryoprotection using the reservoir solution supplemented with 20% glycerol.

X-ray diffraction data were collected on the beamlines PROXIMA-1 and PROXIMA-2 at the SOLEIL synchrotron (St Aubin, France) and reduced using the XDS package⁵². First phases for a triclinic crystal form (Table 2) were obtained by molecular replacement using the program MOLREP version 11.7.03 from CCP4⁵³ and different homologous models. One of the models obtained by the Robetta server⁵⁴ gave the best correlation in the final translation function. These phases allowed to find the selenium substructure from a SeMet SAD dataset from the same crystal form with only ARM protein-containing selenomethionines. Later a monoclinic crystal form (Table 2) was obtained from a complex with both ARM and F15X containing selenomethionines. The collected SeMet SAD dataset (wavelength of data collection: λ = 0.97918 Å) allowed to directly calculate phases, without external model contributions, and confirmed the initial model built in the triclinic crystal form. Se sites were found using the SHELX C/D/E suite of programs. These sites were refined using PHASER version 2.8.2 in EP mode. The resulting Se SAD phases were improved by density modification using PARROT version 1.0.4 and a model automatically build using BUCCANEER version 1.6.10 confirming the sequence attribution for ARM and F15X. The resulting model underwent iterative cycles of manual reconstruction in COOT⁵⁵ and refinement in BUSTER version 2.10.3⁵⁶ (Table 2). At the end of the refinement, 90% and 3.5% of the residues were in favored and outlier regions of the Ramachandran plot, respectively. Few residues were not visible in the electron density (L55 in chain B, V52 and Ala53 in chain C, loop 51–55, F169, and R208 in chain D, and H33 in chain F). These residues were included in the pdb file, but with

an occupancy of 0. The final pdb file and monoclinic dataset have been deposited in the Protein Data Bank (entry code 7BDX [<https://doi.org/10.2210/pdb7bdx/pdb>]).

Meiotic spread nuclei preparations and immunocytochemistry. Meiotic testicular cells were spread as previously described⁵⁷. For immunocytochemistry, the slides were washed in PBS (3 × 10 min), blocked in 0.5% w/v BSA and 0.5% w/v milk powder in PBS followed by staining with primary antibody which was diluted in 10% w/v BSA in PBS and incubated overnight at room temperature in a humid chamber. Subsequently, the slides were washed with PBS (3 × 10 min), blocked in 10% v/v normal goat serum (Sigma) in blocking buffer (supernatant of 5% w/v milk powder in PBS centrifuged at maximum speed for 10 min) followed by staining with secondary antibody which was diluted in 10% v/v normal goat serum (Sigma) in blocking buffer and incubated for 2 h at room temperature in a humid chamber. Finally, the slides were washed with PBS (3 × 10 min) and embedded in Prolong Gold with DAPI (Invitrogen). The following primary antibodies were used: mouse anti-DMC1 (1:1000, Abcam ab11054), mouse anti-SYCP3 (1:200, Abcam ab97672), mouse anti-MLH1 (1:25, BD Pharmingen 51-1327GR), and rabbit polyclonal anti-RAD51 (1:1000)⁴⁶, rabbit anti-HSF2BP (1:30, #1)²² and rabbit anti-BRME1 (1:100, #2)²², rabbit polyclonal anti-SYCP3 (1:5000)⁵⁸ and guinea pig anti-SYCP2 (1:100)⁵⁹ and guinea pig anti-HORMAD2 (1:100)⁶⁰. Secondary antibodies: goat anti-guinea pig Alexa 546 (Invitrogen, A-11074 1:500), goat anti-rabbit Alexa 488 (Invitrogen, A-11008 1:500), goat anti-rabbit Alexa 546 (Invitrogen, A-11010 1:500), goat anti-mouse Alexa 488 (Invitrogen, A-11001 1:500), goat anti-mouse Alexa 555 (Invitrogen, A-21422 1:500), and goat anti-mouse Alexa 633 (Invitrogen, A-21050 1:500).

Immunostained spreads were imaged using a Zeiss Confocal Laser Scanning Microscope 700 with 63x objective immersed in oil. All images within one analysis were taken with the same intensity. Images were analyzed using ImageJ (Fiji) software. BRME1, RAD51, and DMC1 foci quantification was performed using the ImageJ function “Analyze particles” in combination with a manual threshold and particles smaller than 0.0196 μm^2 and larger than 0.98 μm^2 were excluded. MLH1 foci were counted manually and blind by three individual researchers. HSF2BP foci quantification was performed using the ImageJ function “Analyze particles” in combination with a manual threshold. Since HSF2BP intensity is variable between slides and this influences the foci count because foci tend to merge as the intensity increases, size of particles was taken into account by adjusting the foci count in each nucleus in such a way that all large (equal to or larger than twice the average) HSF2BP-positive areas were divided by the average area size of 0.25 μm^2 to obtain more accurate foci number (this average focus size was calculated from particles analyzed of 15 wild-type and 16 *Brca2* ^{Δ 12/ Δ 12} nuclei with various HSF2BP intensities). Particles smaller than 0.0294 μm^2 were excluded. For both BRME1 and HSF2BP a mask of SYCP3 was used to reduce the background signal.

Statistical analysis. Statistical analysis was performed using GraphPad Prism software version 9. Statistical significance was determined using one-way ANOVA with Tukey test for comparisons involving more than two groups (genotypes, treatments) or using unpaired two-tailed *t*-test for comparison between *+/+* and Δ 12/ Δ 12 only in the experiments where the Δ 12/*+* group was not equally sampled (*n* = 2). Statistical details of the experiments can be found in the figure, figure legend or in the text of the results section, where *n* represents the number of animals. In addition, the number of measurements (nuclei) is reported on the panels in Fig. 6. Exact *p* values are reported on the panels.

Animals. All animals were kept in accordance with local regulations under the work protocols 17-867-11 and 15-247-20. Animal experiments were approved by the Dutch competent authority (Centrale Commissie Dierproeven) and all experiments conform to relevant regulatory standards. Female mice for CRISPR/Cas9 injection were C57BL/6 OlaHsd from Envigo, age 5 weeks. For spermatogenesis analysis male mice were sacrificed at the age of 6–15 weeks, except one wild-type (29 weeks) mouse used for RAD51, DMC1, and BRME1 foci quantification.

***Brca2* Δ 12 mouse generation.** *Brca2* Δ 12 mice were generated by two CRISPR/Cas9 cut excision, as described before¹⁶. Female donor mice (age 5 weeks, C57BL/6 OlaHsd from Envigo) were superovulated by injecting 5–7.5 IE folligonan (100–150 μl), IP (FSH hormone; time of injection \pm 13.30 h; day –3). Followed at day –1 by an injection of 5–7.5 IE chorulon (100–150 μl), IP (hCG hormone; time of injection 12.00 h). Immediately after the chorulon injection, the females were put with fertile males in a one to one ratio. Next day (0) females were euthanized by cervical dislocation. Oviducts were isolated, oocytes collected, and injected with ribonucleoprotein complexes of S.p.Cas9 3NLS (IDT cat. no. 1074181), crRNA, and tracrRNA (both Alt-r, synthesized by IDT). Target sequences for crRNA were TAATATTCCAACCCTCGTGT (upstream of *Brca2* exon 12) and TGA-GAAATGTACACCTCATT (downstream of exon 12). For ribonucleoprotein formation equal volumes (5 μl) of crRNA and tracrRNA (both 100 μM in IDT annealing buffer) were mixed, heated to 95 °C for 5 min and allowed to cool on the bench. The annealed RNAs (1.2 μl , 50 μM) were mixed with Cas9 (10 μl diluted to 200 ng/ μl in the DNA microinjection buffer (10 mM Tris-HCl, pH 7.4, 0.25 mM EDTA in water) at the final concentrations 0.12 μM Cas9, 0.6 μM of each of the two

crRNA:tracrRNA complexes in microinjection buffer. Foster mothers (minimum age 8 weeks) were set up with vasectomized males in a 2–1 ratio. Next day (0), pseudopregnant female (recognized by a copulation prop) were collected. For transplanting the injected oocytes, pseudopregnant female was anesthetized by an IP injection of a mix of Ketalar (12 mg/ml ketamine in PBS)-Rompun (0.61 xylazine mg/ml PBS) 100 μl per 10 g bodyweight). Post-surgery pain relief was given when the mouse was anaesthetized (S.C. Rimadyl Cattle, 5 mg/ml in PBS, dose 5 $\mu\text{g/g}$ mouse). Transplantation resulted in eight pups from a single litter, of which three (all female) contained the deletions in the targeted region, as determined by PCR genotyping. Different primer combinations were used for initial genotyping, but mB2i11-F1 AGCTGCCACATGATTCTGAG, mB2i12-R2 GGACTAAGAGGCAAGGCATCA, and mB2e12-R1 GCTTTTGAAGGTGT-TAAGGATTTT, were used routinely (Supplementary Table 1). Sequencing of the PCR products from the founder animals revealed mosaicism for the junctions between the two CRISPR/Cas9 cuts; deletion sizes were close to expected 713 bp, bigger (1179 bp) or smaller due to insertions of ectopic DNA. The experimental cohort was eventually formed through back-crossing and inter-crossing from one founder, with the deletion produced by direct ligation between the two Cas9 cuts. Routine PCR genotyping of was performed using MyTaq Red mix (Bioline) and using the mentioned primers in 1:0.5:1 combination, for simultaneous amplification of the wild-type and the Δ 12 alleles (PCR products 663 and 314 bp, respectively). RT-PCR verification was performed on first-strand cDNA produced from testis RNA with oligo-dT primers and SuperScript II polymerase; the following primers were used: e11 ACATTTTCTGATGTTCTCTGT; e12 GTGCCATCTGGA GTGCTTTT; e13 GTCGTGAGCCGTAAGATTG; e14 TCCCTGGAGACAT CAGCTT; and e15 GAGCTGCTTAGGAGAACATGC.

Adult wild-type and *Brca2* ^{Δ 12} males were sacrificed and weighed, and testes and epididymides were collected and also weighed. Epididymides were collected in PBS, dounce homogenized, and sperm cells were counted. For histological analysis, testes were fixed in 4% PFA in PBS (overnight) and further processed for histological analysis using standard methods. Other testes were placed in PBS and further processed for immunocytochemistry as described in the corresponding section. For fertility assessment, breedings were set up between *Brca2* ^{Δ 12/ Δ 12} and wild-type C57BL/6 animals.

Immunofluorescence and microscopy. Immunofluorescence staining was performed on ES cells grown overnight on a glass coverslip coated with laminin. Sterile 24 mm coverslip was placed in a 6-well plate, and a 100 μl drop of 0.05 mg/ml solution of laminin (Roche, 11243217001) was pipetted in the middle of it. The plate was left for ~30 min in the cell culture incubator, after which the laminin solution was aspirated, and cell suspension was placed in the well. DNA damage was induced by irradiation with 8 Gy X-ray followed by 2 h recovery. Cells were washed with PBS, pre-extracted in sucrose buffer (0.5% Triton X-100, 20 mM HEPES pH 7.9, 50 mM NaCl, 3 mM MgCl₂, 3 mM sucrose) for 1 min, fixed for 15 min in 2% paraformaldehyde in PBS at room temperature, immunostained with anti-RAD51 antibody and mounted with DAPI. Images were acquired using Leica SP8 confocal microscope in automatic tile scan mode. Maximum projections from a z-stack of three confocal planes through a 1 μm slice were produced for analysis. HSF2BP-GFP foci were quantified automatically using CellProfiler⁶¹. In short, nuclei were segmented using a global threshold (minimum cross-entropy) based on the DAPI signal. The masked images were used to identify HSF2BP foci using a global threshold (Robust background) method with two standard deviations above background. Subsequently the number of foci was counted per segmented nucleus.

For single particle tracking, cells were grown overnight in eight-well glass bottom dishes (Ibidi) coated with 0.05 mg/ml laminin. Prior to the experiment cell medium was replaced with imaging medium (Fluorobrite DMEM (Thermo Fisher), complemented with 10% FCS, 1x NEAA, 89 μM β -mercaptoethanol, 200 U/ml penicillin, 200 $\mu\text{g/ml}$ streptomycin, and 1000 U/ml leukemia inhibitory factor). Live-cell experiment was performed on a Zeiss Elyra PS complemented with a temperature-controlled stage and objective heating (TokaiHit). Samples were kept at 37 °C and 5% CO₂ while imaging. For excitation of GFP a 100 mW 488 nm laser was used. The samples were illuminated with HiLo illumination by using a 100 \times 1.57NA Korr α Plan Apochromat (Zeiss) TIRF objective. Andor iXon DU897 was used for detection of the fluorescence signal, from the chip a region of 256 by 256 pixels (with an effective pixel size of 100 \times 100 nm) was recorded at 19.2 Hz interval (50 ms integration time plus 2 ms image transfer time). EMCCD gain was set at 300. Per cell a total of 200 frames were recorded.

Reporting summary. Further information on research design is available in the Nature Research Reporting Summary linked to this article.

Data availability

The coordinates and structure factors file for the HSF2BP-BRCA2 complex described in the study were deposited in Protein Data Bank⁶², entry code 7BDX [<https://doi.org/10.2210/pdb7bdx/pdb>]. Source data are provided with this paper. The microscopy data generated in this study have been deposited in BioImage Archive⁶³ in BioStudies⁶⁴ database under accession code S-BIAD166 [<https://www.ebi.ac.uk/biostudies/BioImages/studies/S-BIAD166>]. Source data are provided with this paper.

Received: 22 January 2021; Accepted: 12 July 2021;

Published online: 29 July 2021

References

- Zelensky, A. N., Kanaar, R. & Wyman, C. Mediators of homologous DNA pairing. *Csh Perspect. Biol.* **6**, a016451 a016451 (2014).
- Xia, B. et al. Control of BRCA2 cellular and clinical functions by a nuclear partner, PALB2. *Mol. Cell* **22**, 719–729 (2006).
- Connor, F. et al. Tumorigenesis and a DNA repair defect in mice with a truncating Brca2 mutation. *Nat. Genet.* **17**, 423–430 (1997).
- Sharan, S. K. et al. BRCA2 deficiency in mice leads to meiotic impairment and infertility. *Development* **131**, 131–142 (2004).
- Siaud, N. et al. Brca2 is involved in meiosis in *Arabidopsis thaliana* as suggested by its interaction with Dmc1. *Embo J.* **23**, 1392–1401 (2004).
- Klovstad, M., Abdu, U. & Schüpbach, T. *Drosophila* brca2 is required for mitotic and meiotic DNA repair and efficient activation of the meiotic recombination checkpoint. *Plos Genet.* **4**, e31 (2008).
- Ko, E., Lee, J. & Lee, H. Essential role of brc-2 in chromosome integrity of germ cells in *C. elegans*. *Mol. Cells* **26**, 590–594 (2008).
- Shive, H. R. et al. brca2 in zebrafish ovarian development. *Spermatogenesis, tumorigenesis. Proc. Natl Acad. Sci.* **107**, 19350–19355 (2010).
- Martin, J. S., Winkelmann, N., Petalcorin, M. I. R., Mcilwraith, M. J. & Boulton, S. J. RAD-51-dependent and -independent roles of a *Caenorhabditis elegans* BRCA2-related protein during DNA double-strand break repair. *Mol. Cell Biol.* **25**, 3127–3139 (2005).
- Weinberg-Shukron, A. et al. Essential role of BRCA2 in ovarian development and function. *N. Engl. J. Med.* **379**, 1042–1049 (2018).
- Miao, Y. et al. BRCA2 deficiency is a potential driver for human primary ovarian insufficiency. *Cell Death Dis.* **10**, 474 (2019).
- Martinez, J. S. et al. BRCA2 regulates DMC1-mediated recombination through the BRC repeats. *Proc. Natl Acad. Sci.* **113**, 3515–3520 (2016).
- Thorslund, T., Esashi, F. & West, S. C. Interactions between human BRCA2 protein and the meiosis-specific recombinase DMC1. *Embo J.* **26**, 2915–2922 (2007).
- Dray, E., Siaud, N., Dubois, E. & Dautriaux, M.-P. Interaction between *Arabidopsis* Brca2 and its partners Rad51, Dmc1, and Dss1. *Plant Physiol.* **140**, 1059–1069 (2006).
- Sato, K. et al. HSF2BP negatively regulates homologous recombination in DNA interstrand crosslink repair. *Nucleic Acids Res.* <https://doi.org/10.1093/nar/gkz1219> (2020).
- Brandsma, I. et al. HSF2BP interacts with a conserved domain of BRCA2 and is required for mouse spermatogenesis. *Cell Rep.* **27**, 3790–3798.e7 (2019).
- Brandsma, I. et al. Overexpression of HSF2BP, a new BRCA2 interactor, results in a Fanconi anemia-like phenotype. In *Balancing Pathways in DNA Double Strand Break Repair* 98–140 (2016).
- Yoshima, T., Yura, T. & Yanagi, H. Novel testis-specific protein that interacts with heat shock factor 2. *Gene* **214**, 139–146 (1998).
- Wu, Y. et al. HSF2BP represses BNC1 transcriptional activity by sequestering BNC1 to the cytoplasm. *Febs Lett.* **587**, 2099–104 (2013).
- Zhang, X. et al. BNC1 is required for maintaining mouse spermatogenesis. *Genesis* **50**, 517–524 (2012).
- Kallio, M. et al. Brain abnormalities, defective meiotic chromosome synapsis and female subfertility in HSF2 null mice. *Embo J.* **21**, 2591–2601 (2002).
- Felipe-Medina, N. et al. A missense in HSF2BP causing primary ovarian insufficiency affects meiotic recombination by its novel interactor C19ORF57/BRME1. *Elife* **9**, e56996 (2020).
- Shang, Y. et al. MEIOK21: a new component of meiotic recombination bridges required for spermatogenesis. *Nucleic Acids Res.* <https://doi.org/10.1093/nar/gkaa406> (2020).
- Takemoto, K. et al. Meiosis-Specific C19orf57/4930432K21Rik/BRME1 Modulates Localization of RAD51 and DMC1 to DSBs in Mouse Meiotic Recombination. *Cell Rep.* **31**, 107686 (2020).
- Zhang, J. et al. The BRCA2-MEILB2-BRME1 complex governs meiotic recombination and impairs the mitotic BRCA2-RAD51 function in cancer cells. *Nat. Commun.* **11**, 2055 (2020).
- Li, M. et al. The Novel Male Meiosis Recombination Regulator (MAMERR) Coordinates the Progression of Meiosis Prophase I. *J Genet Genom.* <https://doi.org/10.1016/j.jgg.2020.08.001> (2020).
- Zhang, J., Fujiwara, Y., Yamamoto, S. & Shibuya, H. A meiosis-specific BRCA2 binding protein recruits recombinases to DNA double-strand breaks to ensure homologous recombination. *Nat. Commun.* **10**, 722 (2019).
- Yang, H. et al. BRCA2 function in DNA binding and recombination from a BRCA2-DSS1-ssDNA structure. *Science* **297**, 1837–1848 (2002).
- Sánchez, H. et al. Architectural plasticity of human BRCA2-RAD51 complexes in DNA break repair. *Nucleic Acids Res.* **45**, 4507–4518 (2017).
- Sidhu, A. et al. Conformational flexibility and oligomerization of BRCA2 regions induced by RAD51 interaction. *Nucleic Acids Res.* <https://doi.org/10.1093/nar/gkaa648> (2020).
- Prakash, R., Zhang, Y., Feng, W. & Jasin, M. Homologous recombination and human health: the roles of BRCA1, BRCA2, and associated proteins. *Cold Spring Harb. Perspect. Biol.* **7**, a016600 (2015).
- Martinez, J. S., Baldeyron, C. & Carreira, A. Molding BRCA2 function through its interacting partners. *Cell Cycle* **14**, 3389–3395 (2015).
- Pellegrini, L. et al. Insights into DNA recombination from the structure of a RAD51-BRCA2 complex. *Nature* **420**, 287–293 (2002).
- Oliver, A. W., Swift, S., Lord, C. J., Ashworth, A. & Pearl, L. H. Structural basis for recruitment of BRCA2 by PALB2. *Embo Rep.* **10**, 990–996 (2009).
- Ehlén, Å. et al. Proper chromosome alignment depends on BRCA2 phosphorylation by PLK1. *Nat. Commun.* **11**, 1819 (2020).
- Mészáros, B., Tompa, P., Simon, I. & Dosztányi, Z. Molecular principles of the interactions of disordered proteins. *J. Mol. Biol.* **372**, 549–561 (2007).
- Reuter, M. et al. BRCA2 diffuses as oligomeric clusters with RAD51 and changes mobility after DNA damage in live cells. *J. Cell Biol.* **207**, 599–613 (2014).
- Gul, I. S., Hulpiau, P., Saeys, Y. & Roy, F. van Metazoan evolution of the armadillo repeat superfamily. *Cell Mol. Life Sci.* **74**, 525–541 (2017).
- Hartford, S. A. et al. Interaction with PALB2 is essential for maintenance of genomic integrity by BRCA2. *PLoS Genet.* **12**, e1006236 (2016).
- Zhao, W. et al. Promotion of BRCA2-dependent homologous recombination by DSS1 via RPA targeting and DNA mimicry. *Mol. Cell* **59**, 176–187 (2015).
- Tavtigian, S. V., Byrnes, G. B., Goldgar, D. E. & Thomas, A. Classification of rare missense substitutions, using risk surfaces, with genetic- and molecular-epidemiology applications. *Hum. Mutat.* **29**, 1342–1354 (2008).
- Li, L. et al. Functional redundancy of exon 12 of BRCA2 revealed by a comprehensive analysis of the c.6853A>G (p.L2285V) variant. *Hum. Mutat.* **30**, 1543–1550 (2009).
- Hooper, M., Hardy, K., Handyside, A., Hunter, S. & Monk, M. HPRT-deficient (Lesch-Nyhan) mouse embryos derived from germline colonization by cultured cells. *Nature* **326**, 292–295 (1987).
- Zelensky, A. N., Schimmel, J., Kool, H., Kanaar, R. & Tijsterman, M. Inactivation of Pol θ and C-NHEJ eliminates off-target integration of exogenous DNA. *Nat. Commun.* **8**, 66 (2017).
- Yusa, K., Zhou, L., Li, M. A., Bradley, A. & Craig, N. L. A hyperactive piggyBac transposase for mammalian applications. *Proc. Natl Acad. Sci.* **108**, 1531–1536 (2011).
- Essers, J. et al. Analysis of mouse Rad54 expression and its implications for homologous recombination. *Dna Repair* **1**, 779–793 (2002).
- Min, J. et al. The breast cancer susceptibility gene BRCA2 is required for the maintenance of telomere homeostasis. *J. Biol. Chem.* **287**, 5091–5101 (2012).
- Dupez, F., Röwer, M., Seroul, G., Blot, D. & Márquez, J. A. A thermal stability assay can help to estimate the crystallization likelihood of biological samples. *Acta Crystallogr Sect. D. Biol. Crystallogr.* **67**, 915–919 (2011).
- Vranken, W. F. et al. The CCPN data model for NMR spectroscopy: development of a software pipeline. *Proteins Struct. Funct. Bioinform.* **59**, 687–696 (2005).
- Dimasi, N., Flot, D., Dupez, F. & Márquez, J. A. Expression, crystallization and X-ray data collection from microcrystals of the extracellular domain of the human inhibitory receptor expressed on myeloid cells IREM-1. *Acta Crystallogr Sect. F. Struct. Biol. Cryst. Commun.* **63**, 204–208 (2007).
- Zander, U. et al. Automated harvesting and processing of protein crystals through laser photoablation. *Acta Crystallogr Sect. D. Struct. Biol.* **72**, 454–466 (2016).
- Kabsch, W. XDS. *Acta Crystallogr Sect. D. Biol. Crystallogr.* **66**, 125–132 (2010).
- Winn, M. D. et al. Overview of the CCP4 suite and current developments. *Acta Crystallogr Sect. D. Biol. Crystallogr.* **67**, 235–242 (2011).
- Song, Y. et al. High-resolution comparative modeling with RosettaCM. *Structure* **21**, 1735–1742 (2013).
- Emsley, P., Lohkamp, B., Scott, W. G. & Cowtan, K. Features and development of Coot. *Acta Crystallogr Sect. D. Biol. Crystallogr.* **66**, 486–501 (2010).
- Bricogne, G. et al. *BUSTER version 2.10.3* (Global Phasing Ltd., 2020).
- Peters, A. H. F. M., Plug, A. W., Vugt, M. J. van & Boer, P. de SHORT COMMUNICATIONS A drying-down technique for the spreading of mammalian meiocytes from the male and female germline. *Chromosome Res.* **5**, 66–68 (1997).
- Lammers, J. H. et al. The gene encoding a major component of the lateral elements of synaptonemal complexes of the rat is related to X-linked lymphocyte-regulated genes. *Mol. Cell Biol.* **14**, 1137–1146 (1994).
- Winkel, K., Alsheimer, M., Öllinger, R. & Benavente, R. Protein SYCP2 provides a link between transverse filaments and lateral elements of mammalian synaptonemal complexes. *Chromosoma* **118**, 259–267 (2009).
- Wojtasz, L. et al. Mouse HORMAD1 and HORMAD2, two conserved meiotic chromosomal proteins, are depleted from synapsed chromosome axes with the help of TRIP13 AAA-ATPase. *Plos Genet.* **5**, e1000702 (2009).

61. Carpenter, A. E. et al. CellProfiler: image analysis software for identifying and quantifying cell phenotypes. *Genome Biol.* **7**, R100 (2006).
62. Berman, H. M. et al. The protein data bank. *Nucleic Acids Res.* **28**, 235–242 (2000).
63. Ellenberg, J. et al. A call for public archives for biological image data. *Nat. Methods* **15**, 849–854 (2018).
64. Sarkans, U. et al. The BioStudies database—one stop shop for all data supporting a life sciences study. *Nucleic Acids Res.* **46**, gkx965- (2017).
65. Ashkenazy, H. et al. ConSurf 2016: an improved methodology to estimate and visualize evolutionary conservation in macromolecules. *Nucleic Acids Res.* **44**, W344–W350 (2016).
66. Lord, S. J., Velle, K. B., Mullins, R. D. & Fritz-Laylin, L. K. SuperPlots: communicating reproducibility and variability in cell biology. *J. Cell Biol.* **219**, e202001064 (2020).

Acknowledgements

We thank Ambre Petitalot for the first purification of the BRCA2 F0 fragment, Christophe Velours on the I2BC protein–protein interaction facility for the SEC-MALS experiments, Guillaume Hoffmann and Jose A. Marquez for their advices during crystallogensis assays on the HTX platform, and Virginie Ropars for her great help during crystallogensis assays, crystal freezing, and X-ray crystallography data collection. We acknowledge SOLEIL for the provision of synchrotron radiation facilities and we would like to thank the respective staffs for assistance in using PROXIMA-1, PROXIMA-2, and SWING beamlines. We thank Nicole van Vliet for the assistance with the initial mouse experiments and Prof. Hyunsook Lee (Dept. of Biological Sciences, Seoul National University) for generously sharing the anti-BRCA2 antibody. We thank the Josephine Nefkens Cancer Program for infrastructure support. The research leading to these results has received funding from the European Community's Seventh Framework Program H2020 under iNEXT (grant agreement N°653706). It was also supported by the French Infrastructure for Integrated Structural Biology (<https://www.structuralbiology.eu/networks/frisbi>), ANR-10-INSB-05-01), by the CNRS IR-RMN-THC Fr3050 and by the CEA. This research was also funded by the Dutch Cancer Society and by the Gravitation program CancerGenomics.nl from the Netherlands Organization for Scientific Research (NWO) and is part of the Oncode Institute, which is partly financed by the Dutch Cancer Society.

Author contributions

R.K., S.Z.J. and A.N.Z. conceived the study. R.G., S.M., L.K., J.V., M.W.P., E.S.L., S.E.v.R.F. and A.N.Z. performed the experiments. M.H.L.D. and P.L. contributed to the determi-

nation of the crystal structure. Y.v.L. and A.M. created and maintained the mouse lines. N. F.M. and A.M.P. generated reagents. J.E., W.M.B., R.K., S.Z.J. and A.N.Z. supervised the work. J.E., W.M.B., R.K. and S.Z.J. secured the funding. S.J.D., A.N.Z. and R.K. wrote the paper with contributions from the other authors.

Competing interests

The authors declare no competing interests.

Additional information

Supplementary information The online version contains supplementary material available at <https://doi.org/10.1038/s41467-021-24871-6>.

Correspondence and requests for materials should be addressed to R.K., S.Z.-J. or A.N.Z.

Peer review information *Nature Communications* thanks Emmanuelle Martini and other, anonymous, reviewers for their contributions to the peer review of this work. Peer review reports are available.

Reprints and permission information is available at <http://www.nature.com/reprints>

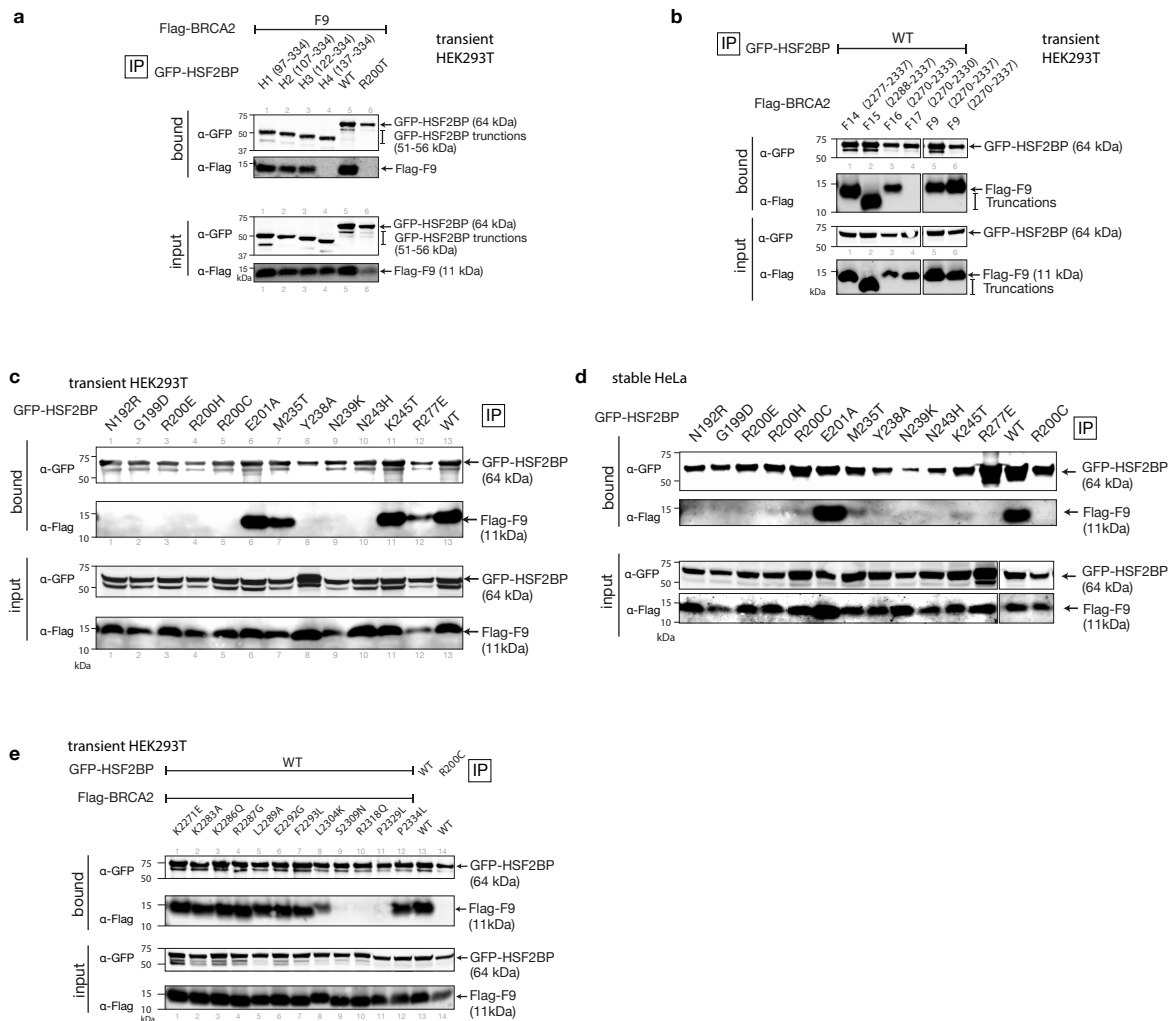
Publisher's note Springer Nature remains neutral with regard to jurisdictional claims in published maps and institutional affiliations.



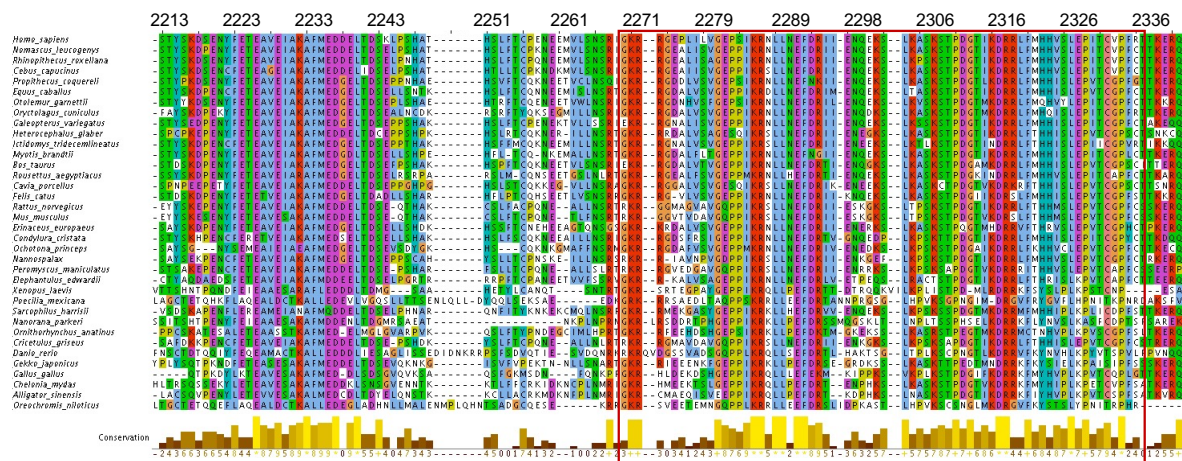
Open Access This article is licensed under a Creative Commons Attribution 4.0 International License, which permits use, sharing, adaptation, distribution and reproduction in any medium or format, as long as you give appropriate credit to the original author(s) and the source, provide a link to the Creative Commons license, and indicate if changes were made. The images or other third party material in this article are included in the article's Creative Commons license, unless indicated otherwise in a credit line to the material. If material is not included in the article's Creative Commons license and your intended use is not permitted by statutory regulation or exceeds the permitted use, you will need to obtain permission directly from the copyright holder. To view a copy of this license, visit <http://creativecommons.org/licenses/by/4.0/>.

© The Author(s) 2021

SUPPLEMENTARY INFORMATION



Supplementary Fig. 1 Co-immunoprecipitation of HSF2BP and BRCA2 variants **a** Full-length GFP-HSF2BP and its truncated versions (H1-H4) and Flag-tagged BRCA2 fragment F9 were transiently overproduced in HEK293T cells, co-immunoprecipitated using anti-GFP beads and analyzed by immunoblotting with anti-GFP and anti-Flag antibodies. **b** Full-length GFP-HSF2BP and Flag-tagged BRCA2 fragments were transiently overproduced in HEK293T cells, co-immunoprecipitated using anti-GFP beads and analyzed by immunoblotting with anti-GFP and anti-Flag antibodies. **c** Co-immunoprecipitation experiment from HEK293T cell lines transiently overproducing GFP-HSF2BP point mutants and a Flag-BRCA2 fragment corresponding to the previously identified minimal HSF2BP-binding domain (HBD, fragment F9, G2270-T2337)¹⁶. **d** As in panel (c), but fragments were produced by stable transformation of HeLa cells. **e** Co-immunoprecipitation experiment from HEK293T cell lines transiently overproducing GFP-HSF2BP and variants of the Flag-BRCA2-F9 fragment. Variant combinations shown in panels a-e were analyzed in at least two experiments with similar results.



Fragment identified in Brandsma et al. (2019)

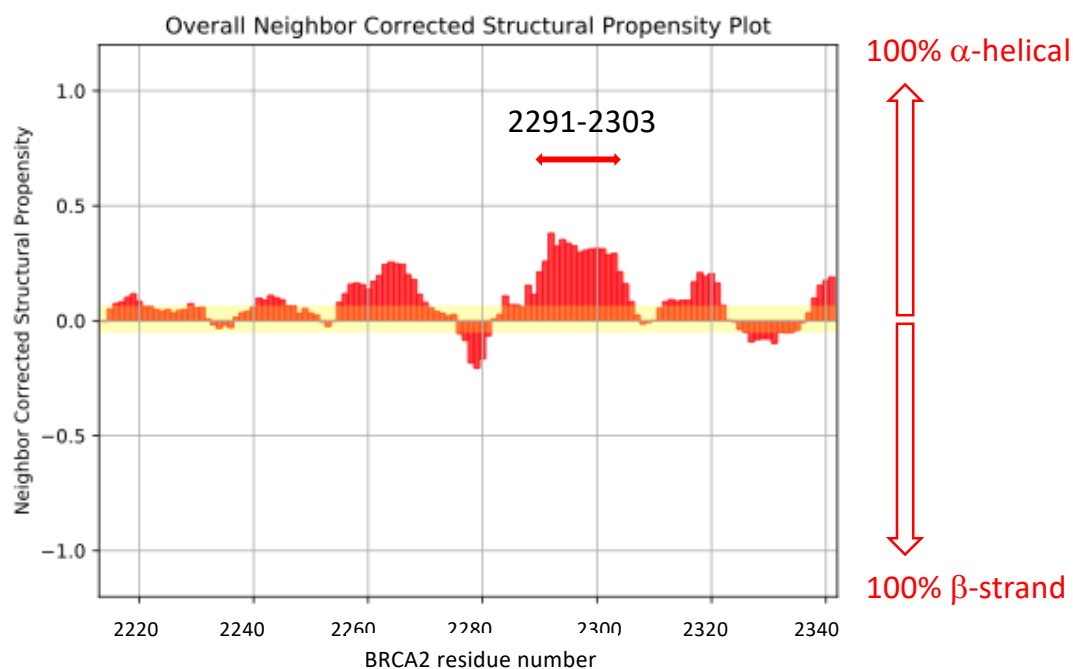
F0, for NMR

F_{NMR}

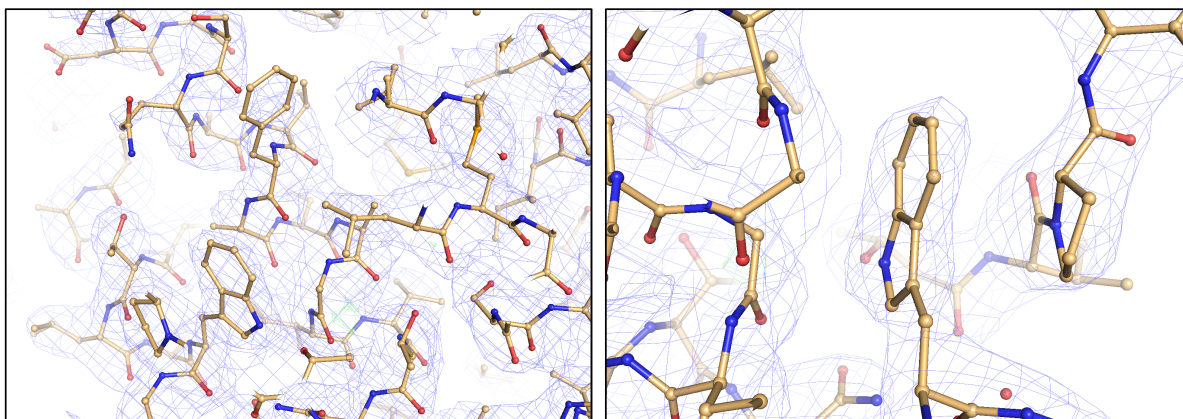
F15X, for X-ray crystallography

F15XΔ12

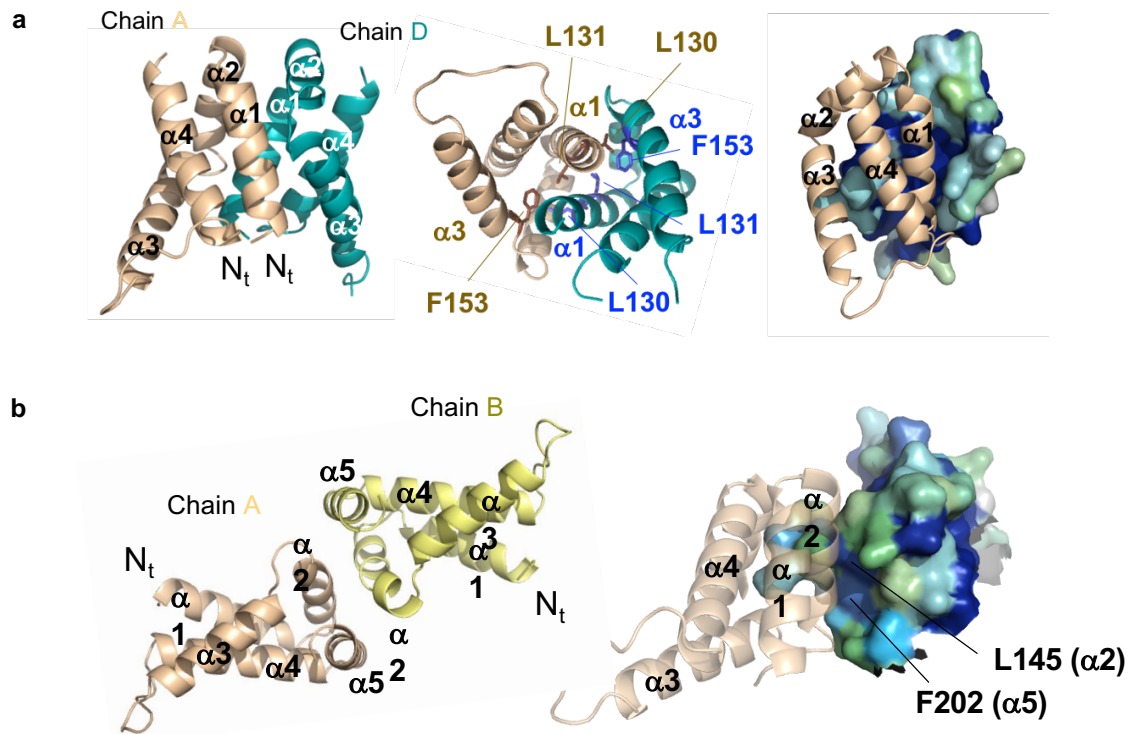
Supplementary Fig. 2 Sequence alignment of 36 BRCA2 homologs focused on region F0 (S2213-Q2342) of human BRCA2. Alignment and scoring were calculated using Jalview 2.10.1. The fragment previously identified as responsible for HSF2BP binding is boxed. The fragments produced for this study are indicated below.



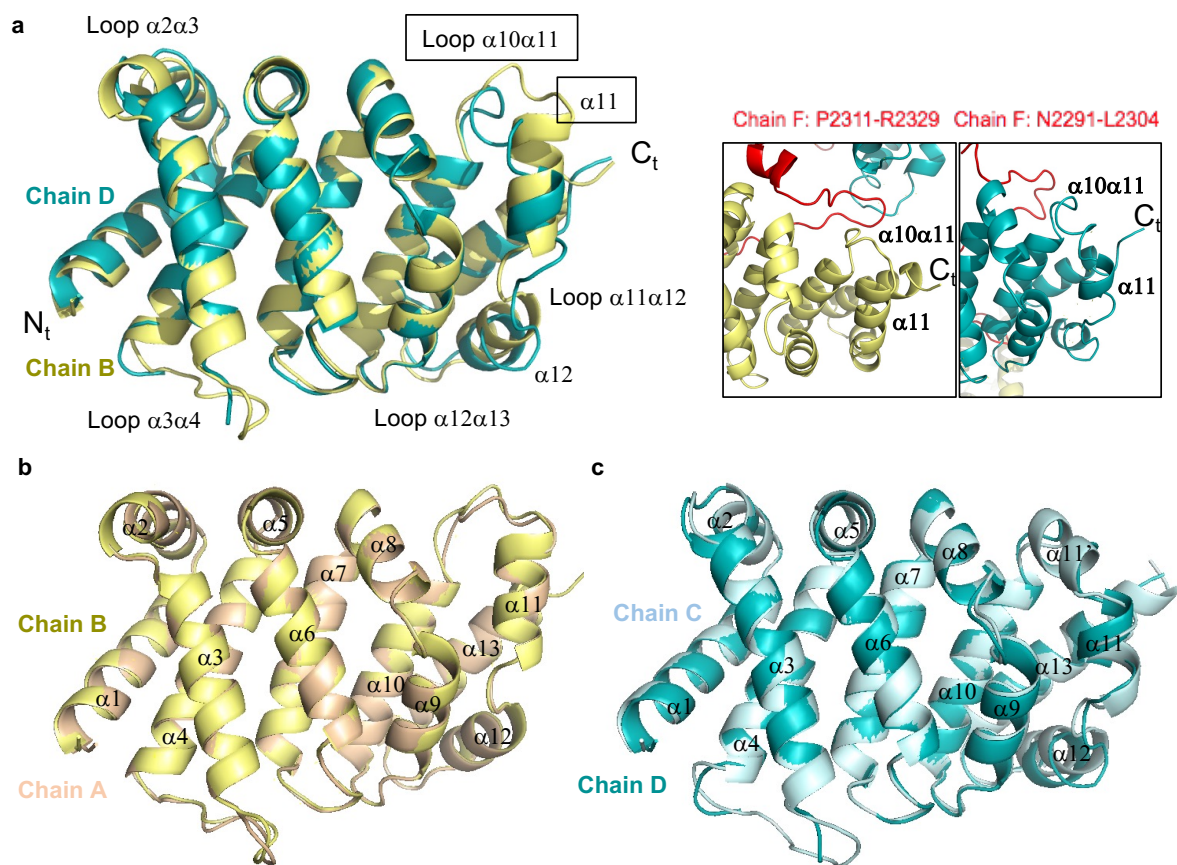
Supplementary Fig. 3 BRCA2 fragment F0 is disordered in solution. Analysis of the 3D heteronuclear NMR experiments recorded on the ^{15}N , ^{13}C labeled BRCA2 fragment F0 (S2213-Q2342) provided the chemical shifts for all Hn, N, Ca, Cb and Co nuclei. From these chemical shifts, the neighbor corrected structural propensity was calculated as a function of BRCA2 residue number, using the Webserver called “neighbor corrected structural propensity calculator” (<https://st-protein02.chem.au.dk/ncSPC/>; ⁶⁴). Positive and negative values correspond to populations with α -helical and β -strand conformations, respectively. In the case of BRCA2 F0, propensity values are all lower than 0.5, indicating that the protein is disordered in solution. Only region N2291-S2303 forms a transient α -helix present in more than 25% of the molecules.



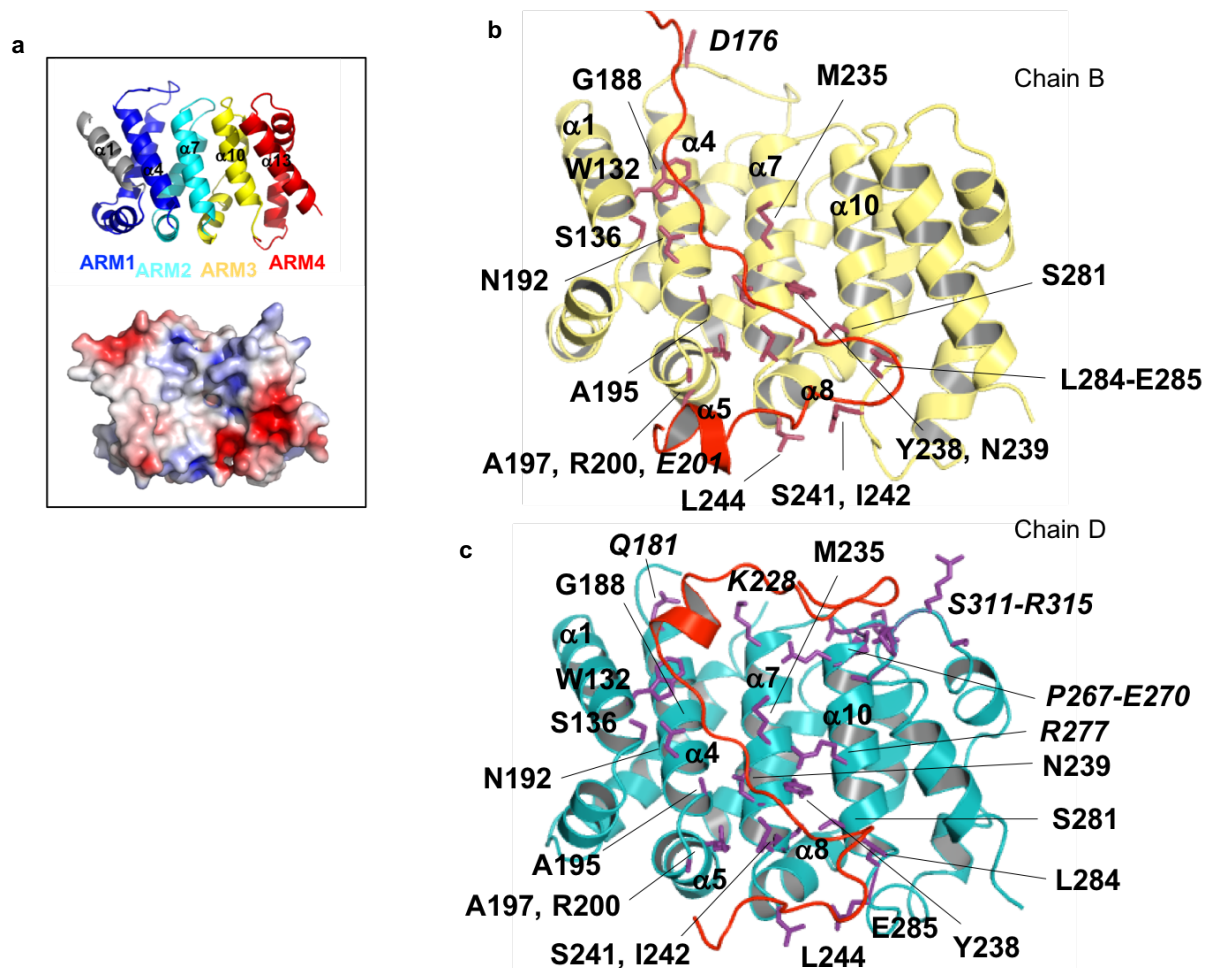
Supplementary Fig. 4 The crystal structure is nicely defined by the 2.6 Å resolution electron density. Example of the quality of the 2FoFc electron density map at 1.0 RMSD, showing a stacking between a tryptophane and a proline.



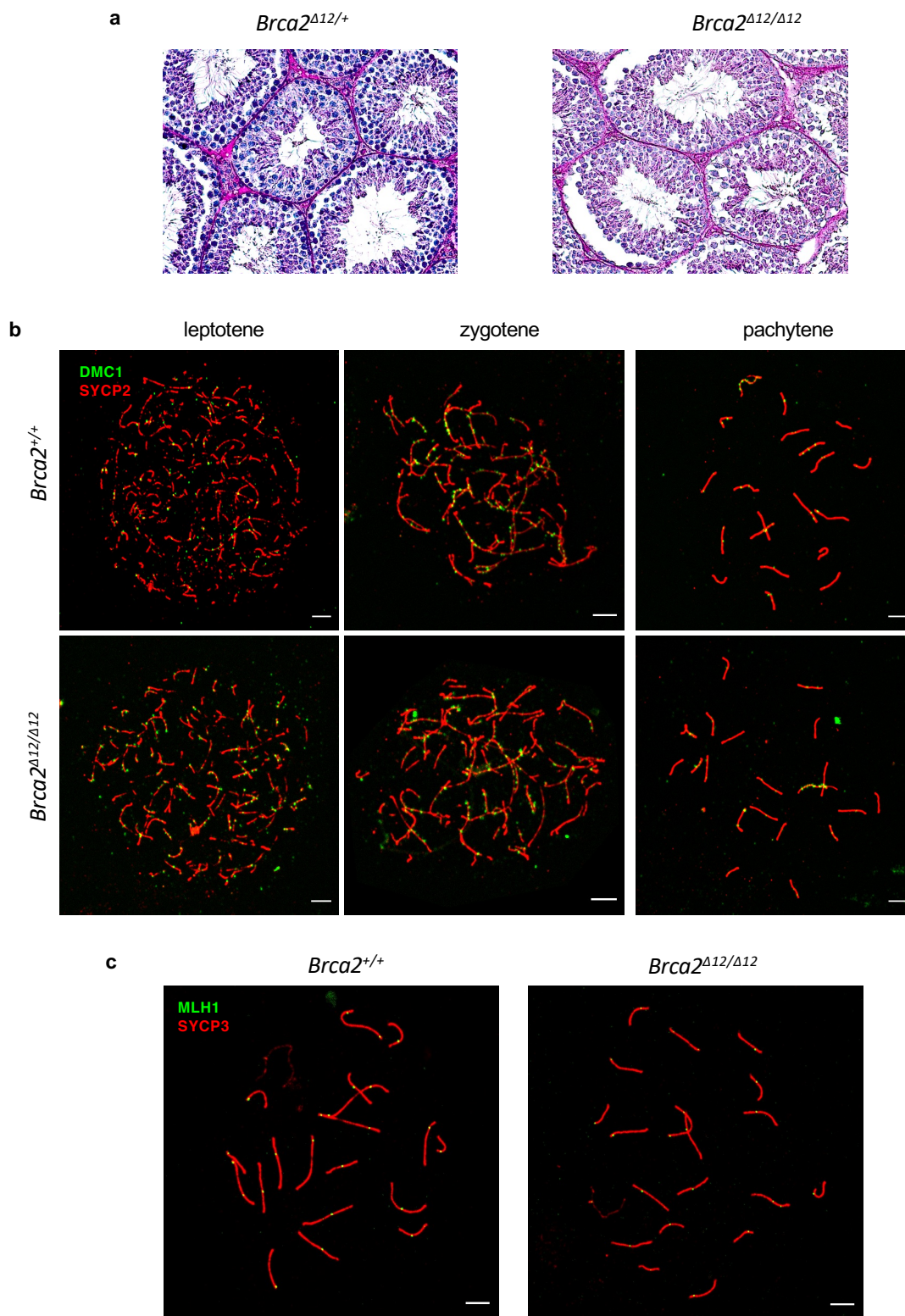
Supplementary Fig. 5 Oligomerization interfaces within the complex. **a** Dimerization interface observed between chains A and D. A similar interface is observed between chain B and C. In the left panel, the four N-terminal α -helices involved in the interface are displayed. In the middle panel, the three conserved residues of the interface are shown in sticks. In the right panel, the surface of chain D N-terminal helices is colored as a function of scores calculated by Consurf⁶². High, medium, weak and no conservation are indicated using dark blue, cyan, green and grey, respectively. **b** Central interface observed between chains A and B, resulting from the tetramerization of the ARM domains. Left panel: the symmetric interface of about 250 Å² involves helices $\alpha 2$ (K142, A143, K149 and A150) and helices $\alpha 5$ (N205, S206). Right panel: analysis of this interface using Consurf showed that it mostly comprises poorly conserved residues (see the surface representation of chain B). Only L145 in helix $\alpha 2$ and F202 in helix $\alpha 5$ are conserved; they interact with each other within each ARM chain, thus contributing to the interface between $\alpha 2$ and $\alpha 5$; however, they do not interact with conserved residues from the other chain.



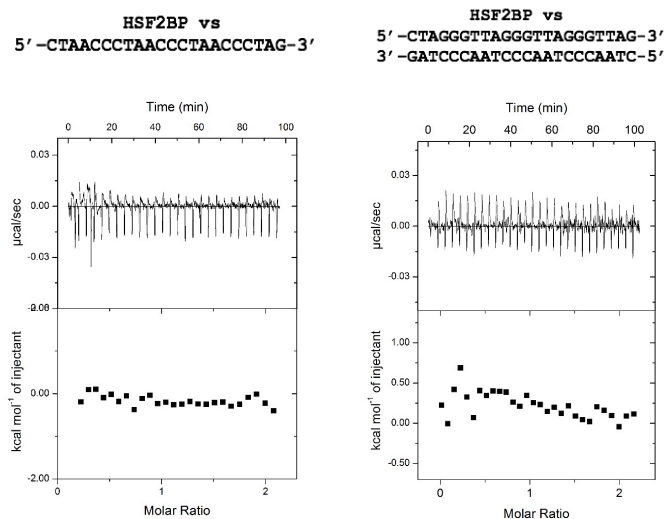
Supplementary Fig. 6 Structural variations are observed between ARM chains interacting with the N-terminal region of BRCA2 F15X and ARM chains interacting with the C-terminal region of BRCA2 F15X. a Superimposition of the structures of chains B and D, interacting with different parts of the BRCA2 peptide. Variations are observed, in particular in loop $\alpha 10\alpha 11$ and helix $\alpha 11$. These structural elements interact with either BRCA2 fragment P2311-R2319, or BRCA2 fragment N2291-L2304, as indicated in the boxed view. **b, c** Superimposition of the structures of (b) chains A and B, and (c) chains C and D, interacting with similar parts of the BRCA2 peptide. These structures are highly similar, as demonstrated by the low RMSD values measured between their backbone $C\alpha$ atoms, displayed in Fig. 3a.



Supplementary Fig. 7 A set of ARM residues interact with both the N-terminal and C-terminal regions of the BRCA2 peptide. **a** Cartoon view of the four Armadillo repeats of ARM, colored in blue, cyan, yellow and red. The electrostatic potential at the surface of the domain is displayed at the bottom of the panel, to highlight the positively charged character of the groove defined by helices $\alpha 1$, $\alpha 4$, $\alpha 7$, $\alpha 10$ and $\alpha 13$. **b,c** Zoom on the interfaces between (b) chain B and the C-terminal region of F and (c) chain D and the N-terminal region of F. ARM residues that are either involved in hydrogen bonds or salt bridges with BRCA2, or buried by more than 30 \AA^2 at the interface with BRCA2, are represented by colored sticks and labeled. Residues identified in only one of these two similar interfaces are labeled in italics.



Supplementary Fig. 8 **a** Representative histological images of testis cross-sections. Two animals per genotype were analyzed in a single experiment. **b** Representative images used for DMC1 foci quantification in Fig. 6i,j. **c** Representative images used for MLH1 foci quantification in Fig 6k. Scale bars = 5 μ m.



Supplementary Fig. 9 ITC analysis of the interactions between HSF2BP and DNA. HSF2BP (7-9 µM in the instrument cell) did not interact with ssDNA and dsDNA oligonucleotides (70-90 µM in the instrument syringe).

Supplementary Table 1. List of primers.

name	sequence 5'-3'
mB2i11-F1	AGCTGCCACATGGATTCTGAG
mB2i12-R2	GGACTAAGAGGCAAGGCATCA
mB2e12-R1	GCTTTTTGAAGGTGTTAAGGATTTT
e11	ACATTTTCTGATGTTCTGT
e12	GTGCCATCTGGAGTGCTTTT
e13	GTCGTGAGCCGGTAAGATTG
e14	TCCCTGGAGACACTCAGCTT
e15	GAGCTGCTTAGGAGAACATGC

Chapter 2. Ring complex formation

Preamble

To better understand the role of HSF2BP and its interaction with BRCA2, as we had previously solved the crystal structure of the armadillo domain of HSF2BP bound to BRCA2 F15X, we focused on the full-length HSF2BP protein in complex with BRCA2 F15X. HSF2BP exhibits two predicted N-terminal helices that were absent from our previous structural analyses. The structures and oligomerization properties of these helices were not characterized by us. They were characterized by the team of Dr H. Shibuya ([Zhang et al., 2020](#)). This team proposed that HSF2BP helices $\alpha 1$ and $\alpha 2$ mediated further oligomerization of HSF2BP.

Our SEC-MALS and SEC-SAXS experiments revealed that the HSF2BP protein forms a tetramer of 4 x 37 kDa with a Y shape in solution. By ITC, we showed that HSF2BP binds to our BRCA2 peptides with a nanomolar affinity. BRCA2 binding triggers HSF2BP oligomerization into a complex of 900 kDa, as seen by SEC-MALS. The denaturation temperature of the complex is pretty high, reaching about 60°C ([Ghouil et al., submitted](#)).

As crystallogenes of this 900 kDa complex did not give any positive results, we decided to study this complex using cryo-EM. First, Dr Simona Miron performed some negative-staining electron microscopy (NS-EM) on a sample of the complex just eluted from a SEC column. Together with Malika Ouldali and Dr Ana-Andrea Arteni, from the I2BC EM platform, she observed a ring-shaped complex with an outer diameter of about 200 Å (**Figure 43**). Classification of the ring images provided a more detailed view of these rings. Each ring contained 6 V-shape complexes, whose size was similar to that of our crystal structure of the HSF2BP armadillo domain bound to BRCA2 F15X.

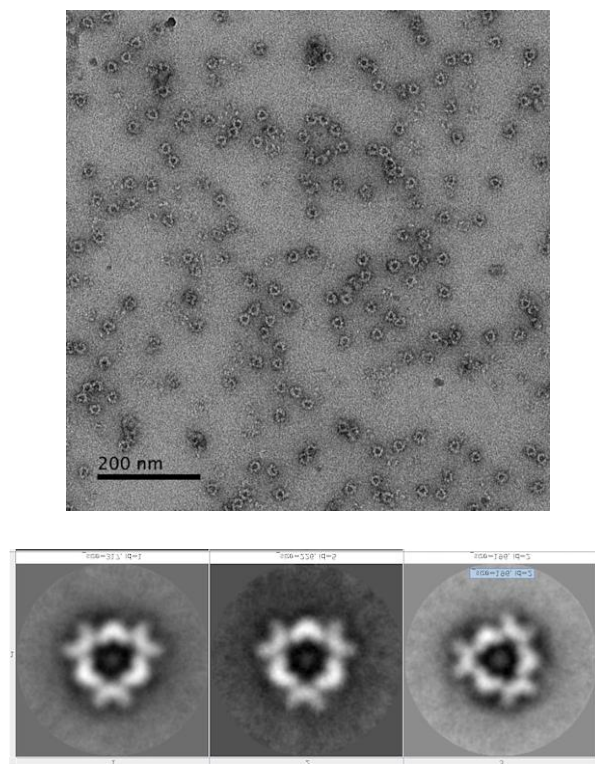


Figure 43. Negative Staining Electron Microscopy images of the HSF2BP-BRCA2 F15X complex.

The sample of the complex was diluted (1/10) in 25 mM HEPES pH 7.5, 250 mM NaCl and 5mM β me, to reach a concentration of about 0.05 mg/mL. 2% of uranyl acetate was added, and 3 μ l of the resulting solution was loaded on a grid. After the acquisition of the EM images, 2D classes were calculated, in order to obtain a more resolved view of the complex.

When trying to prepare our sample for cryo-EM, I eluted it from the SEC column at 0.1-0.5 mg/mL, and I tried to concentrate it. However, I never managed to concentrate it. Using a sample at 0.1-0.5 mg/mL, I further tried different grid preparation conditions. However, I could not observe the rings in the ice. I tried different approaches to modify the protocol used for the purification of the complex and avoid aggregation or protein denaturation during grid preparation.

1. Attempt 1: crosslinker

First, I tried to crosslink the complex on a column, so that it would not dissociate upon flash freezing. With the help of Dr V. Ropars, I tried to cross-link the complex using glutaraldehyde as a crosslinking agent.

Many different conditions were tested to produce optimal cryo-EM samples. I initially used off-column crosslinking with 0.05% (v/v) glutaraldehyde for 5–15 min at 4 °C. Then, I used on-column crosslinking, which consists of first, equilibrating the column with the cryo-EM buffer, and then injecting 500 µl of 0.2–0.5% (v/v) glutaraldehyde. After passing 6 mL of the cryo-EM buffer at a rate of 0.3 mL/min during which glutaraldehyde got diluted, the run was stopped. The injection loop was flushed with the cryo-EM buffer, and 500 µl of approximately 1 mg/mL BRCA2 F15X – HSF2BP was injected. The cryo-EM buffer was passed through the column at a flow rate of 0.25 mL/min, and fractions of interest were collected (**Figure 44**). Sample quality was assessed on 12% SDS–PAGE.

In both cases, this led to a much poorer quality of the sample, as seen by Negative Staining EM microscopy. The complexes showed broken ring shapes, and there was a lot of background noise on the grids.

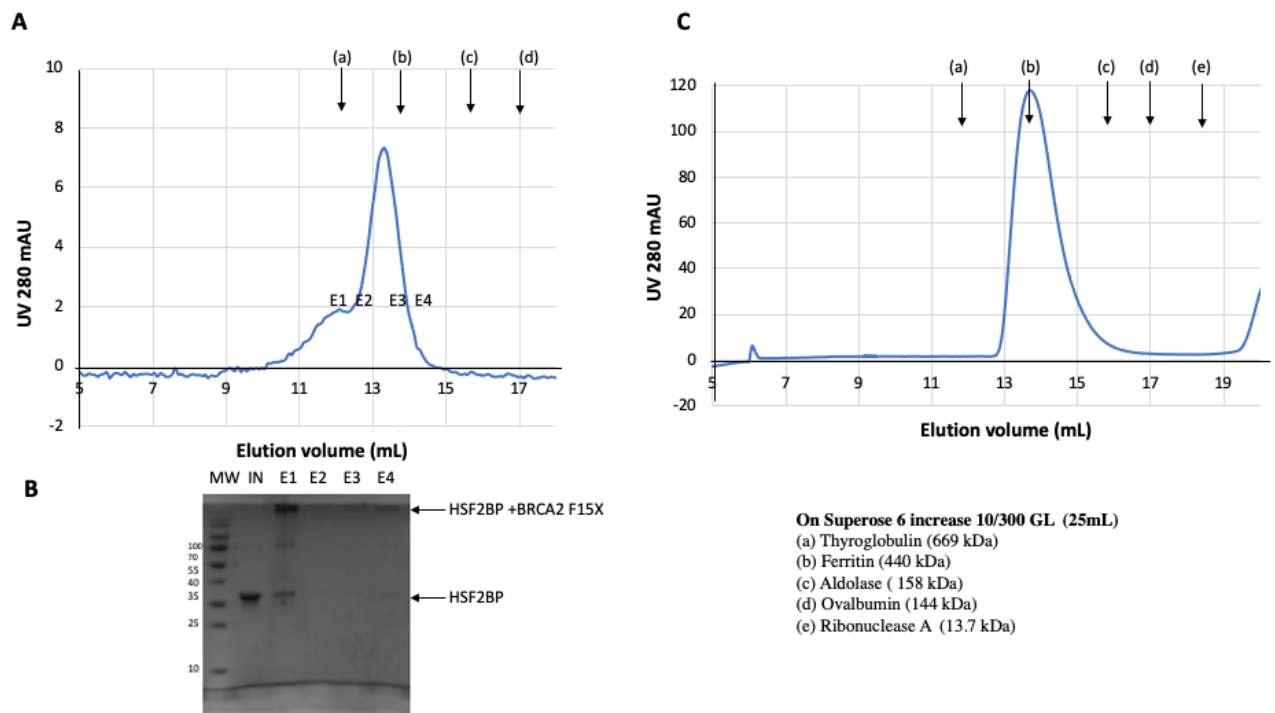


Figure 44. Cross-linking of the complex HSF2BP - BRCA2 F15X with glutaraldehyde.

(A) SEC profile of HSF2BP showing absorption at 280 nm. The column is a Superose 6 increase 10/300 GL, and the buffer is 25 mM Tris HCl pH 7.5, 250 mM NaCl, and 5 mM β me in the presence of a final concentration of 0.05% glutaraldehyde. (B) Coomassie-stained 15% SDS-PAGE of the eluted fractions showing 2 bands at around 40 kDa and more than 180 kDa corresponding to free and crosslinked proteins, respectively. (C) SEC profile of the complex using the on-column method. The column is a Superose 6 increase 10-300 GL, and the buffer is 25 mM Tris HCl pH 7.5, 250 mM NaCl, and 5 mM β me. The complex was eluted at 14 mL.

2. Attempt 2: increase the complex concentration

The first samples of HSF2BP bound to F15X prepared for EM were at **0.5 mg /mL**, allowing us to see ring-shaped complexes by NS-EM after dilution down to 0.05 mg/mL. However, we could not observe our complex by cryo-EM.

When attempting to concentrate the sample by centrifugation, I could not succeed in increasing the concentration of the complex. Also, when freezing and unfreezing the complex, the quality of the Negative Staining EM images decreased. However, by preparing the samples at a higher concentration prior to injection on SEC, I obtained a concentration at the top of the elution peak of **4 mg/ mL (Figure 45)**. I collected the top of this peak, which gave better results in negative staining and cryo-EM experiments.

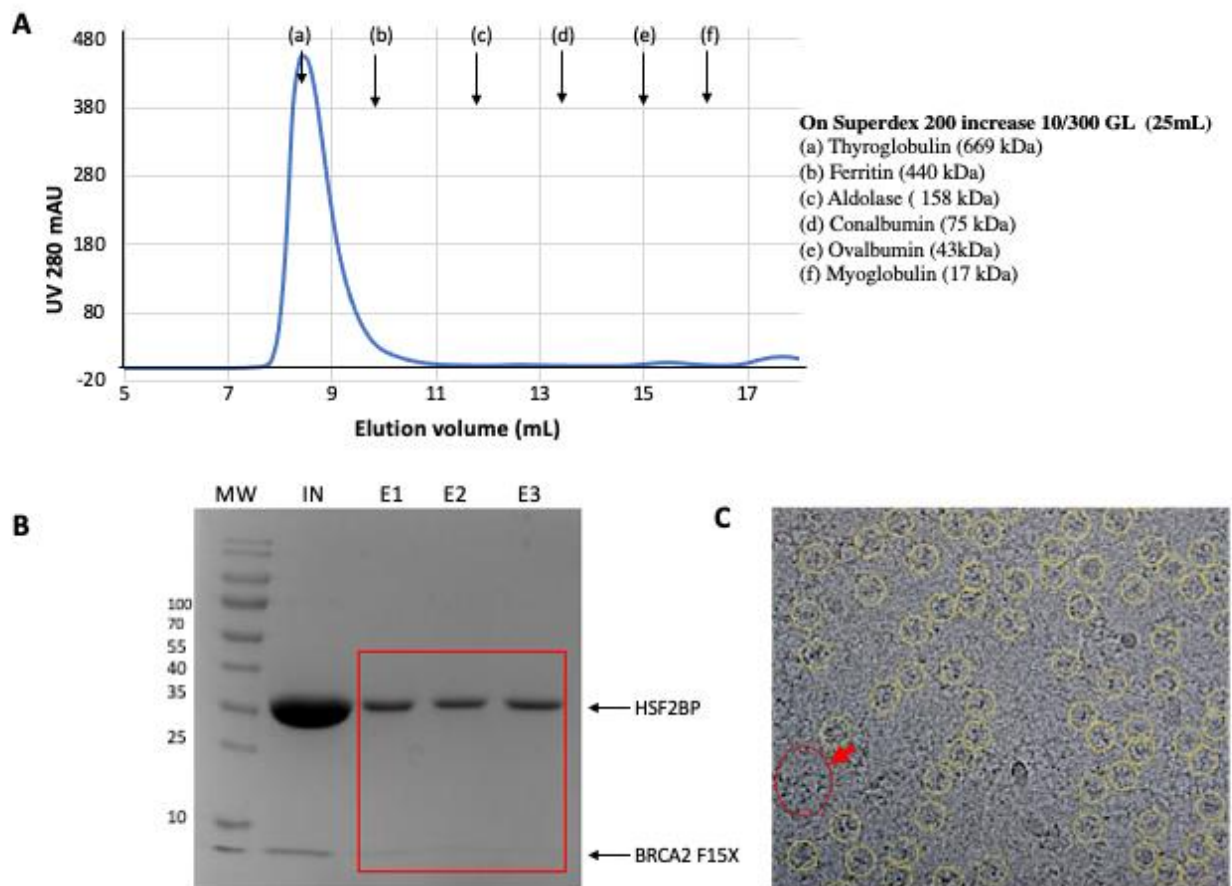


Figure 45. Last step of purification of the HSF2BP-F15X complex.

(A) SEC profile of HSF2BP bound to BRCA2F15X showing absorption at 280 nm. The column is a Superdex 200 increase 10-300 GL, and the buffer is 25 mM Hepes pH 7.5, 250 mM NaCl, and 5 mM β me. **(B)** Coomassie-stained 15% SDS-PAGE of the eluted fractions E1-3 (red box). The lines correspond to MW, molecular weights (kDa); IN: fraction loaded on the column; (E1-3) eluted fractions. The complex was eluted at 8.7 mL. **(C)** Example of a micrograph obtained at Institut Pasteur on one of the Glacios microscopes. Ring-shaped complexes are clearly visible on the whole image (yellow circles). Aggregated proteins are also observed (red circle).

3. Glacios DataSet

a. Cryo-EM grid preparation and data collection

For our first cryo-EM assays, we used copper 300 mesh Quantifoil R1.2/1.3 grids covered with a thin layer of continuous carbon. The grids were glow-discharged for 10 s at 25 mA in an EMS 100 Glow discharge unit. The 4 mg/mL purified complex was loaded on the grid at 4 °C and

100% humidity. The sample was vitrified by plunging it into liquid ethane at -182 °C, after blotting for 6.5 s using Force 2 with the Vitrobot Mark IV in Institut Pasteur.

High-resolution data were collected on one of the Glacios microscopes at Institut Pasteur, operating at 200 kV and equipped with a Falcon III (ThermoFisher) direct electron detector. 5834 films were collected for this dataset by Dr. P. Legrand.

b. Data processing

I performed data processing (motion correction and CTF estimation), particle picking and refinement with the cryoSPARC software. First, I did a blob picking on the 5834 micrographs, classified the particles into 50 2D classes, and I found 3 classes showing the ring shape complex. I further selected 4763 micrographs with a CTF fit lower than 8 Å, and did a template picking using these 3 classes on the selected micrographs. I repeated the picking and particle selection through 2D classification, in order to increase the number of particles that were classified into nice 2D classes (**Figure 46A**). At some point, I gathered about 280 000 particles and tried a first 3D *ab initio* reconstruction (3 models). I refined the best resulting volume, calculated from 90 000 particles, using a C3 symmetry, deduced from the analysis of the negative-staining EM images. To our surprise, I obtained an exciting 3D volume with a resolution that locally could reach 7 Å. This volume showed visible densities for the armadillo domain binding to BRCA2 F15X, as well as the coiled-coil regions of HSF2BP (**Figure 46B**).

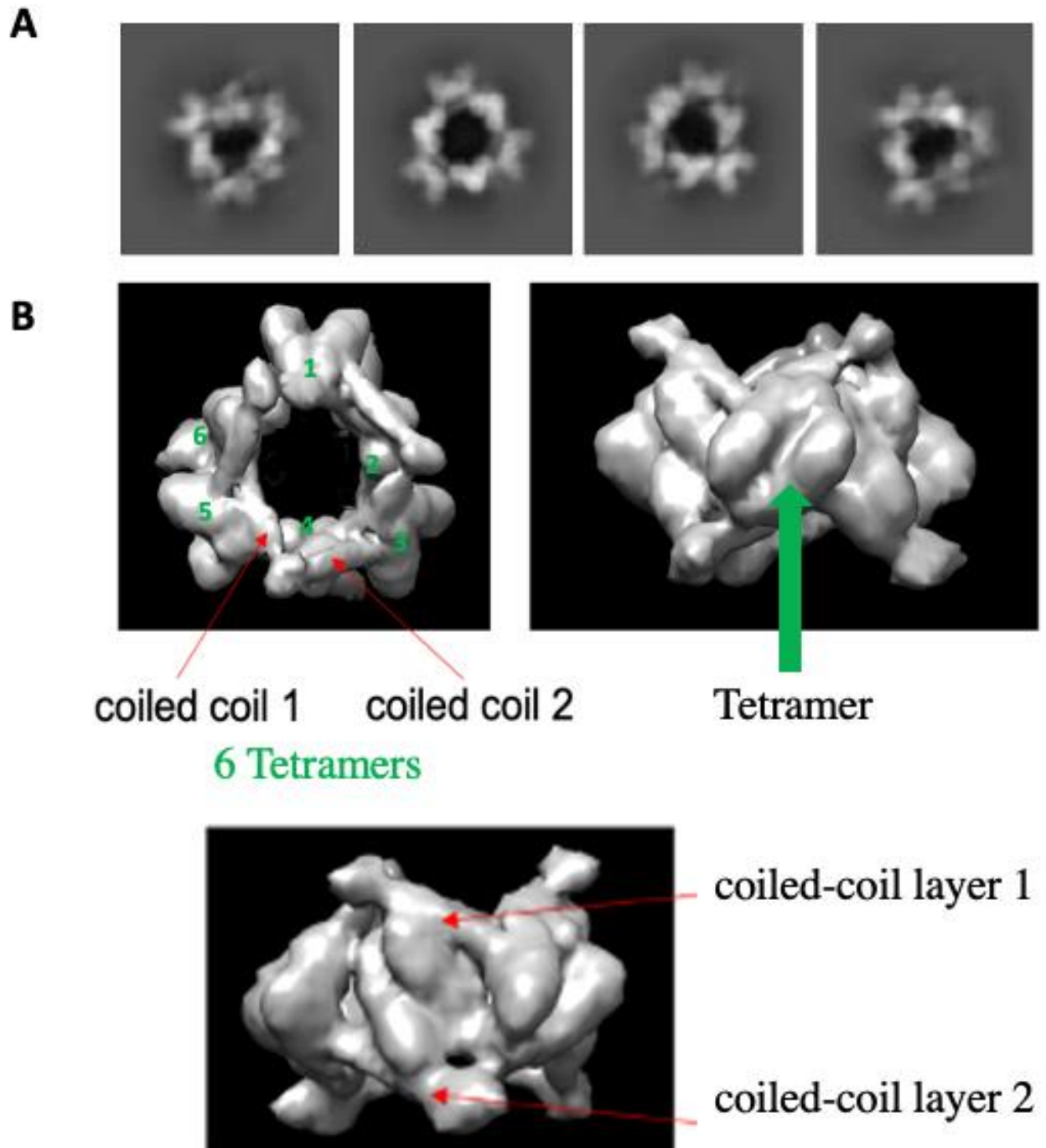


Figure 46. A cryo-EM reconstruction calculated from the first Glacios dataset.

(A) Typical 2D class averages. (B) Cryo-EM 3D reconstruction showing the first map volume obtained from the Glacios dataset. Red arrows indicate the tubes corresponding to the coiled-coil regions of HSF2BP, whereas green arrows indicate the 6 V-shaped volumes corresponding to our X-ray structure of H3 bound to F15X (map resolution is at best of 7 Å).

I tried to increase the resolution of my volume by increasing the number of particles and the range of orientations. I obtained up to 358 000 particles and a volume with a resolution of 6.7 Å, as given by CryoSPARC. By analyzing my volume, I noticed that I could use a D3 symmetry, which is a combination of 3-fold symmetry around the main axis of the ring and 2-fold symmetry around the 3 perpendicular axes going through the armadillo tetramers. Using this symmetry, I further refined my volume. However, I could never obtain a resolution better than locally between 6 and 7 Å (**Figure 47**).

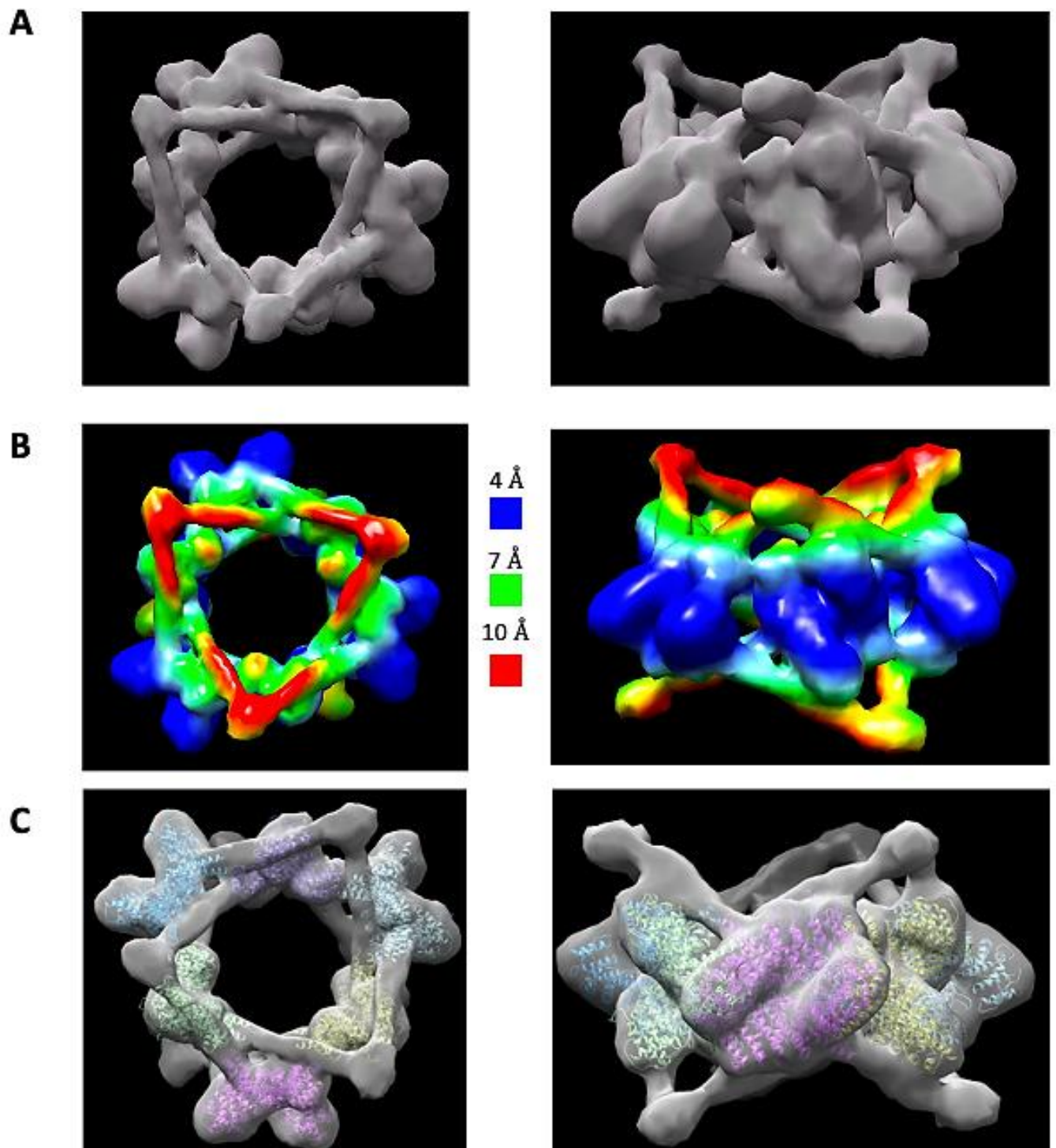


Figure 47. 3D reconstructions of the rings.

(A) Top and side views. (B) Same views as in (A) colored by local resolution. (C) Docking of the crystal structure of the tetramer of H3 bound to the BRCA2 F15X (PDB ID: 7BDX) into the EM reconstruction. The tetramer fits in the V shape blobs.

I noticed that there was a lot of aggregation on the grids, sometimes even covering whole micrographs. It was difficult to identify good particles close to or in the aggregates. I tried to improve particle picking using the cryoSPARC tool Topaz, introduced in version 2.12, which incorporates deep learning models to automatically select particles from a given set of particles. I trained Topaz on a set of particles of 180 000 particles that I selected, and used it to pick more particles; however, this approach did not improve the final resolution of the volume.

I concluded that I had to obtain new cryo-EM data, with less aggregates (and broken rings) and more orientations (most of my images were top views of the ring).

4. Krios DataSet 1

a. Cryo-EM grid preparation and data collection (Krios DataSet1)

Knowing that the problem of the first dataset is the aggregation of the sample on grids, extensive trials to optimize the grid conditions, to diminish aggregation and obtain good particle density and thinner ice were tested. Three types of grids (Lacey, Quantifoil R1.2/1.3 and Auflat 1.2/1.3 300 mesh gold/platinum), different blot times, and force blots were tested. All glow discharging experiments were done using an easiGlow® glow discharge machine (Pelco), and vitrification was performed at 4 °C under humidity of 100%, using the Vitrobot Mark IV (Thermo Fisher Scientific) at Institut Pasteur. I observed that grids with copper as support material resulted in more aggregation (Lacey, Quantifoil) and, in the case of Lacey grids, the particles were mainly distributed on the carbon. A gold/ platinum grid (Auflat) was tested and selected for the next cryo-EM experiments. After the deposition of 3 µl of sample on this type of grid, I found that the best grid was obtained when the blotting was performed during 3 s with a force -2.

4274 films were collected on the Titan Krios (300 kV) at Institut Pasteur (NanoImaging platform).

b. Data processing

CTF estimation was carried out on the 4274 aligned movies using the Patch CTF estimation routine from CryoSPARC. Then, I selected micrographs with astigmatism lower than 1000 Å, and a CTF between 3 and 7 Å. These micrographs were inspected to further eliminate clearly unsuitable data, such as drifted, aggregated, and contaminated images, using the slider-based

Curate exposures tool of CryoSPARC. I selected 100 really nice and well-resolved images to manually pick 3363 particles, and obtain the first 2D classes. From these classes, a template picking step was performed on all the selected 2982 micrographs. The data processing pipeline is published in Ghouil et al. (submitted). Using this pipeline, I obtained a 3D volume with a local resolution comprised between 4 and 10 Å.

The problem of not achieving a better resolution using this dataset could come from very different sources. First, we noticed that the microscope settings (CTF resolution, astigmatism, and average defocus) could be improved. For example, most of our micrographs had a CTF resolution higher than 5 Å (**Figure 48A**). Secondly, there is apparently a preferential orientation of the particles, even if we also picked a few side views (**Figure 48B**). Third, the low resolution could come from the high flexibility of the N-terminal part of HSF2BP (its coiled-coil domain), resulting in a fuzzy density for this region. We showed this using the 3D variability tool of CryoSPARC, which helps to visualize the structural heterogeneity due to flexibility in a dataset (Ghouil et al., submitted).

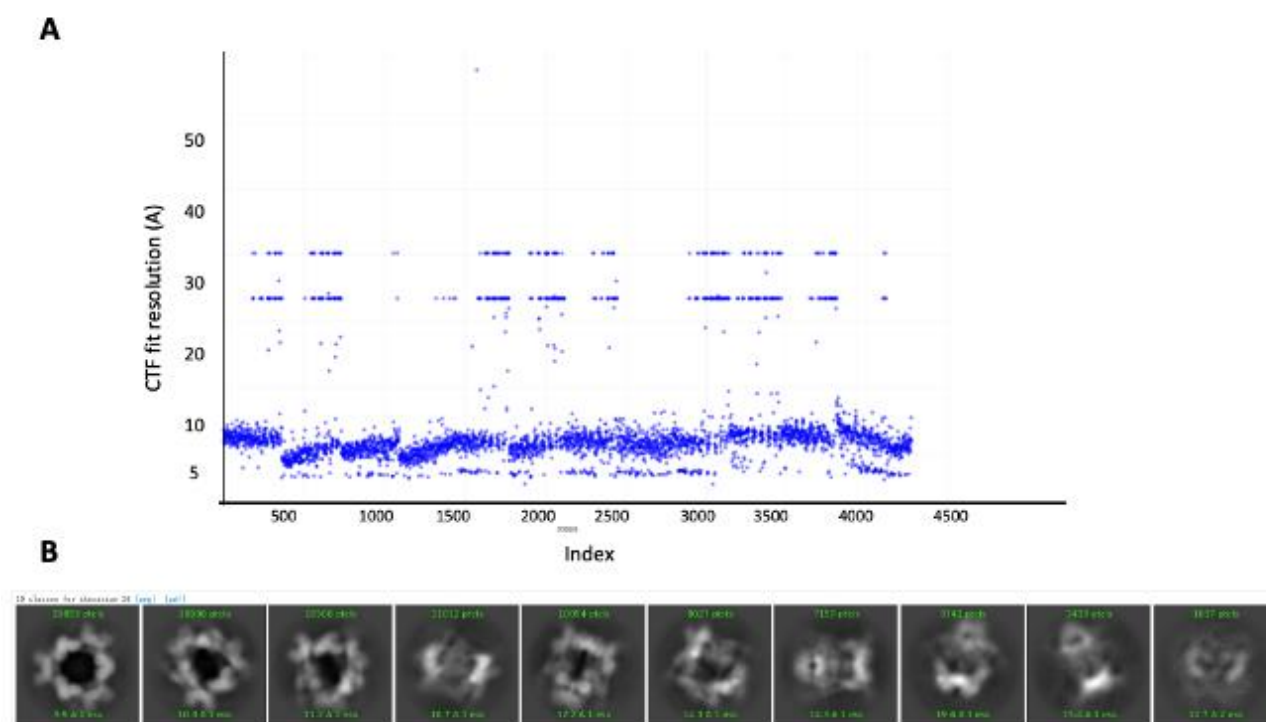


Figure 48. Data collection and processing.

(A) Plot of the CTF fit resolution of the 4274 movies. The minimal values are in the range 4-5 Å; (B) 2D classes used for the calculation of the 3D reconstructions.

5. Krios DataSet 2

a. Cryo-EM grid preparation and data collection (Krios dataSet2)

In order to obtain a better resolution map, I prepared a new sample and re-optimized the grid preparation conditions to reduce even more aggregation.

I tested the use of the Vitrobot at room temperature (22 °C), with the idea of favoring the correct assembly of the complex on the grids before freezing. Only one type of grid was used (UltraFoil R1.2/1.3, gold support with gold layer), glow discharge experiments were performed using an easiGlow® glow discharge machine (Pelco) for a short time of 15 s due to the fragility of these grids at 15 mA. Vitrification was performed at 4°C and 22 °C under 100% humidity. The grid selected to obtain the cryo-EM dataset was blotted for 5 s with a force of 2 at 22 °C. Micrographs were collected on a Titan Krios (300 kV) at Institut Pasteur (NanoImaging platform).

b. Data processing

We obtained a very good contrast with the Au grids. However, unexpectedly, we also observed a lot of aggregation, more than on the previous Titan dataset. CTF estimation was carried out using the Patch CTF estimation. 4259 micrographs with an estimated resolution better than 5 Å were analyzed (**Figure 49A**). After manual inspection to eliminate clearly unsuitable data, such as drifted and contaminated images that I manually detected, only 3009 micrographs were left for analysis. Particles were picked (**Figure 49B**), and then extracted with a box size of 400 Å, and subjected to several rounds of 2D classification in cryoSPARC to generate better templates. The best 220 000 particles were used for 3D reconstruction, but the map resolution was around 6.6 Å.

The problem of not having a better resolution map compared to the map obtained with the previous Krios dataset, despite the good microscope settings, could come from: firstly, a problem of a preferred orientation, as we can see in (**Figure 49C**), one main orientation was systematically found, whereas side views were detected in the previous dataset. Secondly, many broken rings were present in the picked particles, and it was difficult to discriminate between side views of full rings and top/side views of broken rings. Third, there was a lot of aggregates on the grids.

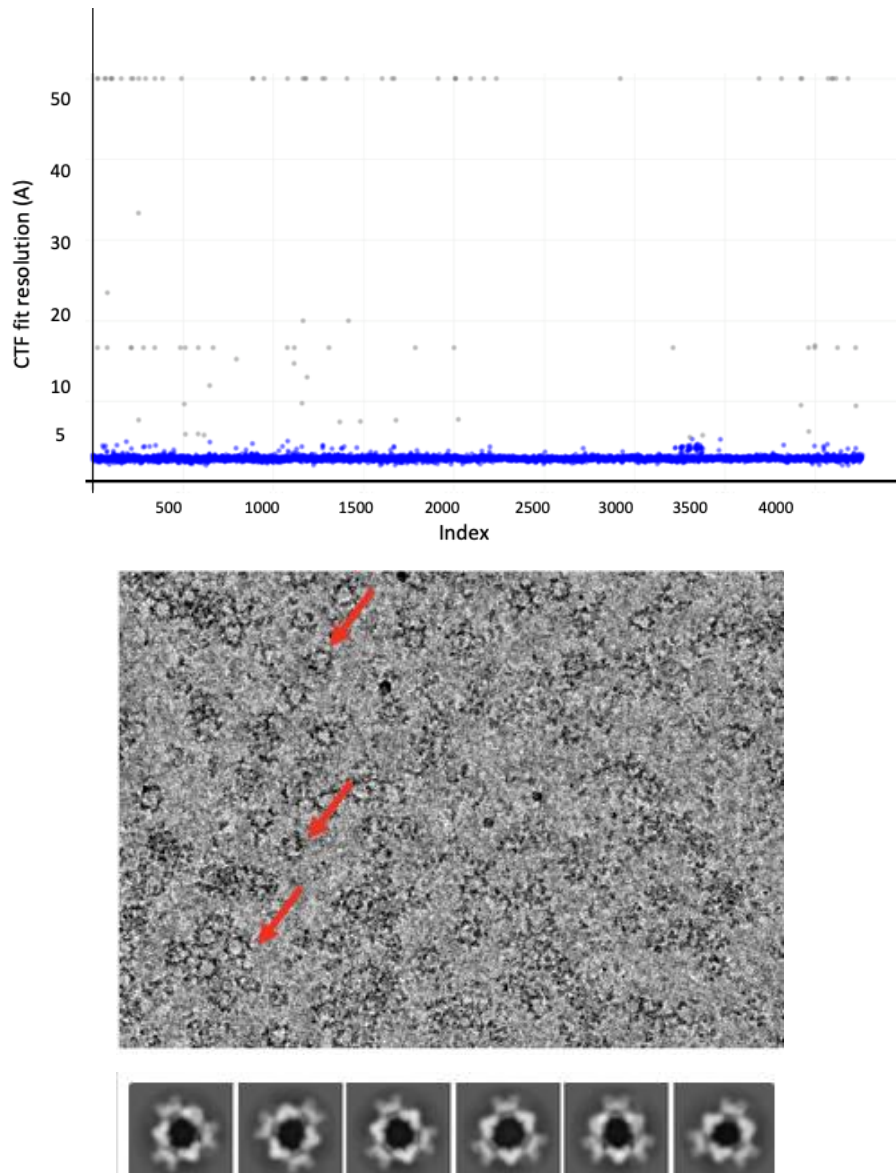


Figure 49. Data collection and processing.

(A) Plot of the CTF fit resolution of the 4259 movies, showing that the resolution was in general under 5 Å. **(B)** A typical cryo-EM image, showing several good-shaped ring complexes that were manually picked for further analysis (red arrows). **(C)** Typical 2D classes, showing mainly one preferred orientation of the ring complex.

Article: BRCA2-HSF2BP Oligomeric Ring Disassembly by BRME1 Promotes Homologous Recombination

BRCA2-HSF2BP Oligomeric Ring Disassembly by BRME1 Promotes Homologous Recombination

Rania Ghouil^{1#}, Simona Miron^{1#}, Koichi Sato², Dejan Ristic³, Sari E. van Rossum-Fikkert³, Malika Ouldali¹, Pierre Legrand⁴, Virginie Ropars¹, Gabriel David⁴, Ana-Andrea Arteni¹, Claire Wyman^{3,5}, Puck Knipscheer², Roland Kanaar^{3*}, Alex N. Zelensky^{3*}, Sophie Zinn-Justin^{1*}

¹ Institute for Integrative Biology of the Cell (I2BC), CEA, CNRS, Université Paris-Sud, Université Paris-Saclay, Gif-sur-Yvette Cedex, France.

² Oncode Institute, Hubrecht Institute–KNAW and University Medical Center Utrecht, Utrecht, The Netherlands.

³ Department of Molecular Genetics, Oncode Institute, Erasmus MC Cancer Institute, Erasmus University Medical Center, 3000 CA, Rotterdam, The Netherlands.

⁴ Synchrotron SOLEIL, HelioBio group, L'Orme des Merisiers, Gif sur-Yvette, France.

⁵ Department of Radiation Oncology, Erasmus MC Cancer Institute, Erasmus University Medical Center, 3000 CA, Rotterdam, The Netherlands.

These authors contributed equally.

* Correspondence: sophie.zinn@cea.fr, a.zelensky@erasmusmc.nl or r.kanaar@erasmusmc.nl.

ABSTRACT

In meiotic homologous recombination (HR), BRCA2 facilitates loading of the recombinases RAD51 and DMC1 at the sites of double-strand breaks. The HSF2BP-BRME1 complex interacts with BRCA2 to support its function in meiotic HR. In somatic cancer cells ectopically producing HSF2BP, DNA damage can trigger HSF2BP-dependent degradation of BRCA2, which prevents HR. Here we show that, upon binding to BRCA2, HSF2BP assembles into a large ring-shaped 24-mer consisting of three interlocked octameric rings. Addition of BRME1 leads to dissociation of this ring structure, and cancels the disruptive effect of HSF2BP on cancer cell resistance to DNA damage. It also prevents BRCA2 degradation during interstrand DNA crosslink repair in *Xenopus* egg extracts. We propose that the control of HSF2BP-BRCA2 oligomerization by BRME1 ensures timely assembly of the ring complex that concentrates BRCA2 and controls its turnover, thus promoting HR.

INTRODUCTION

In vertebrates, both somatic and meiotic homologous recombination (HR) require the BRCA2 protein^{1,2}. Its orthologues in fungi³, plants⁴ and invertebrates^{5–8} are also essential for meiotic HR, so this role is likely ancestral. Most mechanistic data on BRCA2, however, comes from studies in somatic cells, due to the strong association of BRCA2 with breast, ovarian, pancreatic and some other types of cancer⁹. These studies showed that BRCA2 interacts with and controls RAD51, a recombinase that performs the central HR reactions: homology recognition and strand exchange. Meiotic studies are hindered by the embryonic lethality of the *Brca2* knock-out in mice. A hypomorphic rescue transgene in a *Brca2* knock-out mouse strain confirmed the critical role of BRCA2 in mouse meiotic HR¹⁰. It was also demonstrated that BRCA2 interacts with the meiotic recombinase DMC1^{11–14}, a paralogue of RAD51. This suggested that BRCA2 may contribute to the correct balance in DMC1 and RAD51 loading that is essential in meiotic HR.

New tools to study the role of BRCA2 in meiosis were recently provided by the discovery that in mouse meiocytes and embryonic stem cells BRCA2 functions in complex with two previously uncharacterized germline proteins, HSF2BP (also called MEILB2) and BRME1^{15–18}. The reported phenotypes of three independent *Hsf2bp*^{17–19} and five independent *Brme1* knock-out mouse models^{16–22} are nearly identical. Loss of these proteins does not lead to embryonic lethality, but causes complete spermatogenesis failure due to severe reduction in RAD51 and DMC1 accumulation at meiotic DNA double strand breaks (DSBs), which prevents crossover formation^{17,18}. Loss of BRME1 decreases the number of HSF2BP foci. As HSF2BP directly binds to both BRCA2 and BRME1 (Figure 1A), it has been proposed that loss of HSF2BP or BRME1 compromises BRCA2 meiotic function, although the mechanism may be different²³ from the suggested “meiotic localizer of BRCA2” model¹⁸.

Paradoxically, when HSF2BP is produced ectopically in somatic cancer cells, it suppresses HR instead of supporting it as it does in meiocytes^{15,24}. We demonstrated genetically and biochemically that this is due to HSF2BP interaction with BRCA2: in these cells, formation of a complex between HSF2BP and BRCA2 impedes BRCA2 function during the repair of lesions induced by DNA interstrand crosslinking agents and PARP inhibitors (but not by ionizing radiation or the I-SceI nuclease)^{15,24}. Evolutionary conservation of the interaction between BRCA2 and HSF2BP allowed us to establish, using *Xenopus* egg extract interstrand crosslink repair assays, that the presence of HSF2BP leads to DNA crosslink-dependent proteasomal degradation of BRCA2 mediated by the p97 segregase²⁴, which disassembles ubiquitinated protein aggregates^{25,26}.

To study the molecular events triggered by the interaction between BRCA2 and HSF2BP, we previously solved the crystal structure of a 51-aa BRCA2 peptide (BRCA2-HBD) in complex with the C-terminal armadillo domain of HSF2BP (Figure 1A). This revealed a cryptic motif repeated twice in BRCA2-HBD and encoded by exons 12 and 13, respectively. Each motif binds to one armadillo domain^{23,27}. In the complex, two BRCA2-HBD peptides “staple together” two armadillo dimers, resulting in a high affinity interaction (Kd ~1 nM). In addition to the crystallized armadillo domain, HSF2BP contains N-terminal helices α 1 and α 2 (Figure 1A) that

assemble into oligomers in vitro. Helix $\alpha 1$ homotetramerizes when free in solution, and heterotetramerizes when bound to the C-terminal α -helical region of BRME1^{18,19,21}. Presence of these three HSF2BP oligomerization mechanisms — dimerization via armadillo and $\alpha 2$, tetramerization via $\alpha 1$ and hetero-oligomerization via BRCA2-HBD binding — led us to propose that HSF2BP is a polymerization agent for BRCA2, which could be behind its physiological function in meiotic HR and mediate its pathological effect in somatic HR²³. However, since the N-terminal helices of HSF2BP were missing from previous structural analyses, their effect on the HSF2BP-BRCA2 structure and function was uncharacterized²³. It was also not known how the interaction between HSF2BP helix $\alpha 1$ and BRME1 affects the oligomeric state of the BRCA2-HSF2BP complex and BRCA2 function in cells.

In this work, we obtained a cryo-EM derived model of the complex between full-length HSF2BP and BRCA2-HBD, determined how BRME1 affects the structure of this complex, and established a model explaining the opposite effects of HSF2BP on somatic and meiotic HR. Our work revealed that, upon binding to BRCA2, HSF2BP forms a large ($\varnothing \sim 200 \text{ \AA}$) ring-shaped 24-mer consisting of three interlocked octameric rings, with BRCA2 displayed on the outer surface of the ring. We also demonstrated that BRME1 disrupts this ring structure and acts as a protective disaggregation agent in specific cellular conditions.

RESULTS

HSF2BP is mainly a V-shape tetramer in solution

To understand how the N-terminal α -helical region of HSF2BP contributes to the assembly of the HSF2BP-BRCA2 complex, we first characterized full-length HSF2BP (37.6 kDa) and HSF2BP lacking helix $\alpha 1$ (G48-V334; 32.2 kDa) by size-exclusion chromatography coupled to multi-angle light scattering (SEC-MALS). At the concentration of the experiment ($\sim 10\text{-}30 \text{ \mu M}$), the apparent molar masses of the two samples are $136 \pm 7 \text{ kDa}$ ($n=2$) and $60 \pm 2 \text{ kDa}$ ($n=2$), respectively. This fits with tetrameric and dimeric states for HSF2BP with and without helix $\alpha 1$, respectively (Figure 1B; Suppl. Fig. 1A). Further characterization of HSF2BP by size-exclusion chromatography coupled to small-angle X-ray scattering (SEC-SAXS) showed that, in the conditions of this experiment (protein concentration $\sim 50\text{-}60 \text{ \mu M}$), the protein has a molar mass of $156 \pm 21 \text{ kDa}$ (Figure 1C). Thus, we confirmed that full-length HSF2BP is mainly tetrameric at concentrations above 10 \mu M . Moreover, the SAXS-derived atomic distance distribution curve of HSF2BP is bimodal, with a maximal distance at 250 \AA (Figure 1C). Consistently, *ab initio* molecular envelopes calculated from this curve using a 2-fold symmetry hypothesis have a V shape (Figure 1C; Suppl. Fig. 1B,C)²¹. Altogether, our data support a full-length HSF2BP model in which two dimeric fragments containing helices $\alpha 2$ and armadillo domains are connected through the tetrameric N-terminal helix $\alpha 1$.

HSF2BP and BRCA2 form a ring-shape complex that exposes BRCA2 on its outer surface

Having characterized the solution structure of free full-length HSF2BP, we measured the change in its oligomeric state induced by BRCA2. Tetrameric HSF2BP forms an $880 \pm 30 \text{ kDa}$

(n=2) complex when bound to BRCA2-HBD (N2291-Q2342), as measured by SEC-MALS (Figure 1D; Suppl. Fig. 1A). Its thermal stability also increases substantially, shifting from 45.9-46.7°C to 59-60.7°C (Figure 1E). Negative-staining electron microscopy (EM) revealed a ring-shaped complex with an outer diameter of about 200 Å (Figure 1F) and a 3-fold symmetry (Suppl. Fig. 2A). Further characterization by cryo-EM (Suppl. Fig. 2B) revealed a *D3* symmetry, defined as a 3-fold symmetry around the axis going through the center of the ring, as well as three 2-fold symmetries around perpendicular axes going through the center of the globular subvolumes (Figure 1G). Calculation of the local resolution of the cryo-EM map after refinement using this symmetry resulted in resolutions of 4-6 Å and 5-7 Å for the three inner and outer globular subvolumes, respectively. The tubular-shaped volumes extending out of the globular subvolumes (two tubes on both sides of each subvolume) are resolved at 6-8 Å. Analysis of the 3D variability of the complexes on the EM grids identified global breathing motions, which probably contribute to lowering the resolution of the cryo-EM map. The motion of largest amplitude is illustrated in Suppl. Fig. 2B. Despite the heterogeneous resolution of the cryo-EM map, both of the published crystal structures of the C-terminal armadillo domain of HSF2BP in complex with BRCA2-HBD^{23,27} could be readily fitted into each of the six globular subvolumes (Figure 1H). Remarkably, the BRCA2 peptides can also be traced through the cryo-EM map (Figure 1H, Suppl. Fig. 2C); they are located on the outer side of the map, their N- and C-termini being positioned around the ring complex (Figure 1I).

HSF2BP helices $\alpha1$ and $\alpha2$ connect BRCA2-bound HSF2BP armadillo tetramers in the HSF2BP-BRCA2 complex.

We further analyzed our cryo-EM map of the complex between HSF2BP and BRCA2-HBD, to describe the 3D structure of HSF2BP N-terminal α -helical region in this complex. First, we verified using SEC-MALS that HSF2BP lacking helix $\alpha1$ is not able to form a ring-shaped complex. We measured a molecular mass of 131 kDa for this HSF2BP mutant bound to BRCA2-HBD, confirming that the complex only contains 4 HSF2BP molecules bound to 2 BRCA2-HBD (theoretical mass of this complex: 142 kDa) (Suppl. Fig. 1A). Second, we modelled a dimer of full-length HSF2BP using AlphaFold²⁸. This prediction algorithm proposed five similar models for dimeric HSF2BP with high confidence (Suppl. Fig. 3A, B). In these models, each HSF2BP monomer is composed of strand $\beta1$ (F20-R24), helix $\alpha1$ (K25-I45) and helix $\alpha2$ (G48-S136) that overlaps with the armadillo domain (E122-V334). As a validation, we checked that the 3D model of the dimeric armadillo domain is superimposable with the 3D structure observed in the crystal (PDB code: 7BDX²³, Suppl. Fig. 3C). Third, we docked two dimeric HSF2BP models into the cryo-EM map of the complex between full-length HSF2BP and BRCA2-HBD (Figure 2A). Helices $\alpha2$ readily fitted into the electron density tubes extending out of the globular subvolumes corresponding to the armadillo domains bound to BRCA2-HBD. Helices $\alpha1$, on the other hand, fell into a poorly resolved zone connecting electron densities of two HSF2BP dimers (Figures 2A, B). In the resulting model of the complex, two HSF2BP dimers interact through their helices $\alpha1$ to form a V-shape tetramer. These tetramers interact two by two through the BRCA2-HBD peptides to form octamers. Three interlocked octamers (displayed in red, blue and green in the boxed frame of Figure 2A) form the final ring-shaped

24-mer protein assembly. The N-terminal region of HSF2BP contributes to the assembly of this large complex through interactions between helices $\alpha 1$ within each tetramer, and contacts between helices $\alpha 2$ and armadillo domains from different octamers. Indeed, in each octamer, two $\alpha 2$ coiled coils interact with a second octamer (specifically, with its helices $\alpha 2$ and armadillo domains), whereas the two other $\alpha 2$ coiled coils interact with the third octamer (also with its helices $\alpha 2$ and armadillo domains).

HSF2BP helix $\alpha 1$ forms a heterotetramer with an α -helical peptide from the C-terminal region of BRME1

Mouse HSF2BP binds directly to the meiotic protein BRME1¹⁶. The N-terminal helix $\alpha 1$ of HSF2BP interacts with the C-terminal region of BRME1^{16,20}. To further delineate the binding regions in the human proteins, we divided the C-terminal region of BRME1 (D578-L668) into three peptides: BRME1-M, corresponding to the central and well-conserved fragment, and BRME1-N and BRME1-C corresponding to the less conserved flanking regions (Figure 2C). Isothermal titration calorimetry (ITC) experiments revealed that only BRME1-M significantly bound to HSF2BP, and that its affinity was similar when measured against full-length HSF2BP (18 ± 3 nM) or HSF2BP helix $\alpha 1$ (25 ± 5 nM) (Figure 2D, Suppl. Fig. 4, Table 1). Thus, the C-terminal region BRME1-M (E602-K641) directly interacts with the HSF2BP N-terminal helix $\alpha 1$. This interaction is not expected to affect binding of BRCA2 to the HSF2BP C-terminal armadillo domain²³. Consistently, we found by ITC that BRME1-M is able to interact with HSF2BP bound to BRCA2-HBD (affinity: 34 ± 8 nM), and that BRCA2-HBD is able to interact with HSF2BP bound to BRME1-M (affinity: 13 ± 2 nM) (Figure 2E). Thus, HSF2BP simultaneously interacts with BRCA2-HBD and BRME1-M.

To elucidate how HSF2BP helix $\alpha 1$ interacts with BRME1-M, we crystallized HSF2BP helix $\alpha 1$ both alone and bound to BRME1-M. We solved the crystal structure of the human HSF2BP fragment from E19 to G48. Each monomer consists of a β -strand (residues F20-R24) and an α -helix (residues K25-L46), as predicted by AlphaFold (Suppl. Fig. 3). The asymmetric unit contains two molecules interacting through two antiparallel β -strands and parallel α -helices that assemble into a tetramer by application of a 2-fold crystallography symmetry (Figure 2F; Table 2). The tetramer exhibits parallel and anti-parallel α -helices. It is clamped at its extremities by the two anti-parallel β -sheets. We also solved the crystal structure of helix $\alpha 1$ bound to BRME1-M. Each BRME1-M monomer contains a large α -helix (residues T605-R638). The asymmetric unit contains a HSF2BP helix $\alpha 1$ and a BRME1-M peptide that forms a parallel heterodimer. Two of these dimers assemble into a parallel tetramer by application of a 2-fold crystallographic symmetry (Figure 2G; Table 2). The β -strands from the two HSF2BP peptides form an anti-parallel β -sheet. Comparison of the 3D structures of the two complexes revealed that BRME1-M disassembles HSF2BP helix $\alpha 1$ tetramers and suggested that it is further able to disassemble HSF2BP tetramers.

BRME1 binding to HSF2BP dissociates HSF2BP-BRCA2 ring complexes.

We then proceeded to determine the effect of BRME1 on the structure of the HSF2BP-BRCA2 complex. We observed using negative-staining EM that addition of BRME1-M to a 2:1 mix of

HSF2BP and BRCA2-HBD resulted in a near-complete disappearance of the large ring-shape complexes (Figure 3A). To replicate this dramatic effect under different experimental conditions and to quantify it, we performed single-molecule analysis using scanning force microscopy (SFM; Figure 3B,C). HSF2BP alone appeared on SFM scans as round objects with a volume distribution centered around 95 and 190 nm³. We surmised that under the low protein concentrations used for single-molecule SFM experiments, HSF2BP oligomer equilibrium may be shifted towards dimers and interpreted the two populations of objects as tetramers that, respectively, dissociated during deposition or remained intact (Figure 3B,C; Suppl. Fig. 5). Consistently, we observed that the armadillo domain alone appeared as smaller round objects with a volume distribution centered on 35 and 90 nm³, corresponding to monomers and dimers, respectively. By contrast, the volume distribution of the complexes formed by HSF2BP and BRCA2-HBD revealed significantly larger objects, with peaks at ~550 and ~2000 nm³ (Figure 3B,C; Suppl. Fig 5). Taking the 95 nm³ volume of HSF2BP dimers as the smallest unit and correcting for the increases in measured volume due to its ringed shape and scanning precision, we interpreted the minor sub-population of the largest objects (~2000 nm³) as the 24-mers. This was confirmed by analyzing the sample of HSF2BP-BRCA2-HBD that was purified by Size-Exclusion Chromatography (SEC) and used in the EM analyses. Addition of BRME1-M to the HSF2BP-BRCA2-HBD sample resulted in a significant reduction in apparent object size, which, when quantified, corresponded to a complete disappearance of the 24-mer population. Consistently, the number of tetramer- and dimer-sized objects increased. Thus, we demonstrated using different methods that BRME1 can act as a dissociation factor for HSF2BP-BRCA2 oligomers.

BRME1 protects cancer cells from BRCA2 inhibition by HSF2BP

In our previous work, we demonstrated that ectopic HSF2BP compromises BRCA2 function and causes BRCA2 proteasomal degradation. This degradation involved the p97 segregase²⁴, an hexameric protein that unfolds and disassembles ubiquitylated substrates, to pull proteins out of membranes, segregate proteins from partners for downstream activity or unfold proteins for proteasomal degradation²⁹. Given the dissociative effect of BRME1 on HSF2BP-BRCA2 multimers, we hypothesized that de-aggregation by BRME1 will cancel the effect of HSF2BP. To test this hypothesis, we stably produced in HeLa cells HSF2BP alone and together with BRME1 (Figure 4A,B) and measured their effect on resistance to DNA interstrand crosslinking agents and PARP inhibitors (Figure 4C-E). BRME1 on its own had no effect on the cell sensitivity to DNA damage, but it completely abolished the sensitization induced by HSF2BP, consistent with our hypothesis. The C-terminal HSF2BP-binding part of BRME1 had the same protective effect as the full-length protein, demonstrating that disrupting BRCA2-HSF2BP multimerization may be sufficient to protect BRCA2 function. We also found that the HSF2BP variant lacking the tetramerization-mediating helix α 1 does not sensitize cells. Taken together, these data suggested that HSF2BP-BRCA2 oligomerization compromises BRCA2 function and that BRME1 prevents this by dissociating the oligomers.

BRME1 prevents HSF2BP-induced BRCA2 degradation.

To establish the mechanism by which HSF2BP attenuates BRCA2 function, we previously studied the repair of a single chemically defined and site-specific cisplatin DNA interstrand crosslink in a plasmid replicating in *Xenopus* egg extract²⁴. These biochemical experiments showed that both *Xenopus* and human HSF2BP inhibits replication-dependent restoration of the genetic information at the crosslink as measured by the regeneration of a restriction enzyme site. We demonstrated using two-dimensional agarose gel electrophoresis that the HR step and not the preceding steps (recognition, signaling, crosslink unhooking by nucleases, or translesion synthesis) of the reaction was inhibited, and that the immediate reason for the inhibition was HSF2BP-induced BRCA2 degradation. To determine whether the protective effect of BRME1 we observed in cancer cells ectopically producing HSF2BP would also manifest biochemically, we performed the same *Xenopus* egg extract assays (Figure 4F-G) in the presence of either the BRME1-M peptide, which binds HSF2BP α 1, or the adjacent BRME1-C peptide, which does not bind HSF2BP (Figure 2C,D). Consistent with the cancer cell data, BRME1-M reverted the inhibitory effect of HSF2BP on the interstrand crosslink repair reaction (Figure 4F), and specifically suppressed the reduction in the formation of HR repair intermediates monitored by two-dimensional agarose DNA gel electrophoresis (Figure 4G); the non-binding BRME1-C peptide had no such effect. Moreover, HSF2BP-induced BRCA2 degradation was completely abolished by the BRME1-M but not the BRME1-C peptide (Figure 4H). Combined with the structural and cancer cell data, this suggests that BRME1 acts as a disaggregation factor for HSF2BP-BRCA2 complexes, preventing their recognition by the p97/VCP segregase and degradation by the proteasome.

DISCUSSION

The HR mediator BRCA2, as well as the newly described meiotic proteins HSF2BP and BRME1, participate to meiotic HR. They are essential for male fertility. Recent studies revealed that, in germline cells, BRCA2 functions in a tight, likely constitutive, complex with HSF2BP and BRME1. BRCA2 directly binds to HSF2BP via a unique repeat-mediated oligomerization-inducing mechanism. BRME1 also directly binds to HSF2BP and phenocopies it. In this paper, we extended our structural characterization of this germline BRCA2 complex²³, by studying the full-length HSF2BP, rather than only its armadillo domain, in complex with several BRCA2 and BRME1 peptides. Our findings support our previous proposal that HSF2BP can act as a polymerization factor for BRCA2, thanks to three oligomerization mechanisms: two intrinsic to HSF2BP (homo-oligomerization of α 1 and dimerization via α 2+armadillo) and one extrinsic, mediated by the repeats encoded by exons 12 and 13 of BRCA2 (Figure 5). In addition, our study reveals several properties that we did not anticipate from the previous analyses, most importantly: tetramerization of HSF2BP into a V-shaped structure revealed by SAXS, and formation of a large ring-shaped 880 kDa hetero-oligomer consisting of 24 HSF2BP and 12 BRCA2-HBD molecules organized into three interlocked diamond-shaped octameric (8×HSF2BP + 4×BRCA2-HBD) rings, revealed by cryo-EM and supported by SFM, SEC-MALS, AlphaFold modelling and X-ray crystallography (Figures 1-3). We also delineated a BRME1 α -helical peptide that can bind and displace helix α 1 of HSF2BP, thus disrupting the tetramer formed by helix α 1 in HSF2BP and the 24-mer complex formed by full-length HSF2BP upon binding to BRCA2-HBD (Figures 2-3). Altogether, our results provide a molecular mechanism for the aggregator-disaggregator model explaining the apparently opposite effects of HSF2BP on BRCA2-mediated HR in somatic vs germline cells.

The remarkable ring structure of the HSF2BP-BRCA2 complex revealed by our cryo-EM analysis comes from two new properties of HSF2BP we identified: (1) HSF2BP is a tetrameric protein with a V-shape, the angle at the bottom of the V being defined by the $\alpha 1$ -mediated tetramerization constraint; (2) in the ring-shaped HSF2BP-BRCA2 complex, the $\alpha 2$ coiled coils of the three octamers interact through interfaces that are evolutionary conserved. Indeed, a relatively constrained V-shape favors the formation of an HSF2BP octamer upon binding to the BRCA2 peptide. In this octamer, the $\alpha 2$ coiled coils lie in the same plane. They outline a diamond shape, the angle at the vertex formed by the armadillo domains ($\sim 104^\circ$) being defined by the BRCA2-dependent tetrameric structure described previously, and the supplementary angle at the $\alpha 1$ vertex ($\sim 76^\circ$) being favored by the HSF2BP tetramerization mode revealed in this study. The structural origin of this last angle value is not clear and it may have a degree of flexibility in solution, but we postulate that such angle value must be constrained to explain why HSF2BP bound to BRCA2-HBD organizes into closed diamond-shaped octamers rather than linear polymers. These octamers could not be structurally characterized independently, as three of them interlock to form the observed ring, which is the preferred conformation for the complex. Evolutionary conservation of the complex, which allowed us previously to use human and frog HSF2BPs interchangeably in biochemical experiments, suggested an explanation to this. Contacts between the interlocked octamers are mainly mediated by helices $\alpha 2$: in each octamer, two $\alpha 2$ coiled coils interact with a second octamer, whereas the two other $\alpha 2$ coiled coils interact with the third octamer. While the details of these interfaces are missing, they coincide with patches of conservation at the HSF2BP surface. The other patches correspond to the established functions of HSF2BP, namely the groove binding BRCA2-HBD and the $\alpha 1$ regions involved in tetramerization. We surmise that the conservation of octamer intersections reflects the functional importance of the ring.

The distinct structure of the HSF2BP-BRCA2 ring complex and the multiple conserved features of HSF2BP that determine it make it tempting to speculate that such spatial organization is functionally relevant. There are multiple precedents for the specific role of ring-shaped complexes in DNA metabolism and HR specifically, from sliding clamps and hexameric helicases to the octameric ring formed by DMC1. However, the ring we characterized is larger than the ring complexes that encompass DNA: it has an inner diameter of 100 Å compared to 25 Å for hexameric helicases or 35 Å for PCNA^{30,31}. Also, the inner surface of HSF2BP-BRCA2 is negatively charged (Suppl. Fig. 7), and HSF2BP has no detectable affinity for DNA²³, whereas the inner surfaces of the DNA-encompassing rings are positively charged. Given the proposed role of HSF2BP at resected meiotic DSBs coated by ssDNA-binding proteins RPA, SPATA22 and MEIOB and the reported interactions between HSF2BP and these proteins, it is notable that the opening of the ring is sufficiently large to accommodate protein-coated ssDNA (~ 40 -80 Å^{32,33}). It is also notable that BRCA2-HBD molecules are all exposed on the outer surface of the ring, so that BRCA2 would not interfere with potential content threaded through the opening.

The major issue for these hypotheses is the disruptive role of BRME1 on the ring structure, and the strong phenotypic and cytological similarity between BRME1 and HSF2BP mutants,

1 which suggests that the two proteins function as a complex in meiosis. In this context, we
2 propose that, in the presence of BRME1, an alternative HSF2BP tetrameric conformation is
3 formed, linked by two BRCA2 molecules and blocked by four BRME1 molecules from forming
4 higher-order assemblies. This is supported by the appearance of particles with close to
5 tetrameric volumes, as observed in our SFM experiments, in the presence of both BRCA2-HDB
6 and BRME1-M (Figure 3). The BRME1-flanked HSF2BP tetramer may carry out some or all of
7 the known HSF2BP functions in meiosis. This complex has a 2-fold symmetry and could bridge
8 two other entities as has been shown for monopolin, a V-shaped dimeric protein bridging
9 kinetochores during yeast meiosis ³⁴. However, it is possible that BRME1 serves as a
10 regulatory factor that ensures that the HSF2BP-BRCA2 ring is assembled at the right time and
11 place, preventing ectopic BRCA2 polymerization that can have detrimental effects, as
12 revealed by our study of cancer cells discussed below. The release of BRME1 from HSF2BP
13 could be controlled by post-translational modification or other mechanisms, such as
14 competition with partners. In this regard, it is remarkable that HSF2BP α 1 can both homo-
15 and heterotetramerize. Most helix α 1 surface is evolutionarily conserved (Suppl. Fig. 8),
16 suggesting that both homo- and hetero-tetramerization are important for HSF2BP function.
17 Taken together, we hypothesize that organizing BRCA2 into a ring-shaped oligomer that can
18 encompass objects the size of protein-coated ssDNA is an important feature of HSF2BP that
19 is under positive evolutionary selection.

20 While the relevance of the ring-shaped BRCA2-HSF2BP complex in meiosis remains to be
21 revealed, we suggest that it resolves the arguably most puzzling observation about HSF2BP,
22 namely its apparently opposite effects on somatic vs meiotic HR (Figures 4-5). We previously
23 found that ectopic HSF2BP in human cancer cells or *Xenopus* egg extracts suppresses HR
24 during interstrand crosslink repair by inducing BRCA2 degradation. This degradation is
25 dependent on the p97 segregase, which processes protein aggregates ²³. We hypothesized
26 that the polymerizing effect of HSF2BP on BRCA2 turns into aggregation in ectopic settings,
27 thus inducing p97-dependent BRCA2 degradation. It was however not clear what restricts this
28 polymerization both spatially, stopping the formation of endless HSF2BP-BRCA2 chains via
29 α 1- and BRCA2-linked armadillo connections, and temporally, restraining it to specific ectopic
30 contexts. Circularization into octamers and ring complexes explains why HSF2BP-BRCA2 can
31 diffuse through the cytoplasm without forming linear chain aggregates even in the absence
32 of BRME1. Aggregation followed by proteasomal degradation thus happens only at the stalled
33 replication fork. It may be triggered by high local concentration of the proteins, which
34 manifests cytologically as foci. Additional oligomerizing interaction between BRCA2 complex
35 proteins can exacerbate this. Alternatively, the aggregation-sensing machinery may be more
36 active at the crosslink-blocked fork, which is known to recruit ubiquitin ligases and the
37 VCP/p97 segregase itself. BRME1 acts as a disaggregation factor. It was not present in the
38 cancer cells that we used during our first analyses, explaining why we initially observed a
39 disruptive effect for HSF2BP. Differential expression of HSF2BP and BRME1, as well as
40 alternative splicing of *BRCA2* exon 12 ^{17,23,35-37}, provide cancer cell with an evolutionary
41 platform to drift between genomic instability and drug resistance.

1 In conclusion, HSF2BP can polymerize BRCA2 into a large ring-shaped structure, consisting of
2 three interlocked BRCA2-bound HSF2BP octamers. Formation of this complex is regulated by
3 BRME1. Under specific DNA damage conditions, ectopic expression of HSF2BP in cancer cells
4 can trigger BRCA2 aggregation and degradation, resulting in genomic instability. When
5 HSF2BP is expressed physiologically, along with BRME1, aberrant formation of this complex
6 is prevented. We propose that the ring-shaped complex timely concentrates and organizes
7 BRCA2 and other bound proteins and can accommodate ssDNA coated with ssDNA binding
8 proteins, in order to facilitate BRCA2-mediated DSB repair in meiocytes.

METHODS

Protein expression and purification

Human HSF2BP, either full-length or without helix α 1 (from G48 to V334), was expressed using a pETM11 (6 \times His-TEVsite) expression vector in *E. coli* Rosetta2 pLysS strain. A starter culture (LB + 50 μ g/ml kanamycin, 30 μ g/ml chloramphenicol) was grown overnight at 37 °C, used to inoculate 1 L of LB which was grown at 37 °C until the OD600 reached 0.6. Expression was induced by addition of IPTG to 0.2 mM, and continued at 20°C overnight. Harvested cells were resuspended in 25 mM Tris-HCl pH8, 500 mM NaCl (HSF2BP), 5 mM β -mercaptoethanol, EDTA-free Protease Inhibitor Cocktail (Roche) and disrupted by sonication. Lysates were supplemented with 1 mM MgCl₂ and treated by Benzonase nuclease at 4 °C for 30 min, and then centrifuged at 15.000 \times g at 4 °C for 30 min. After filtration (0.4 μ m), the supernatant was loaded on a chromatography HisTrap FF crude 5 mL column (GE Healthcare) equilibrated with Tris-HCl 25 mM pH 8, 500 mM NaCl and 5 mM β -mercaptoethanol. HSF2BP (either full-length or without helix α 1) was eluted with a linear gradient of imidazole. The tag was cleaved by the TEV protease (at a ratio of 2% w/ w) during an ON dialysis at 4 °C against 25 mM Tris-HCl pH 7.5, 250 mM NaCl, 5 mM β -mercaptoethanol. The protein solution was loaded on a HisTrap column and the tag-free HSF2BP (either full-length or without helix α 1) was collected in the flow through. Finally, a size exclusion chromatography was performed on HiLoad Superdex 10/300 200 pg equilibrated in 25 mM Tris pH 7.5, 250 mM NaCl, 5 mM β -mercaptoethanol. The quality of the purified protein was analyzed by SDS-PAGE and the protein concentration was determined by spectrophotometry from the absorbance at 280 nm.

The gene coding for BRCA2-HBD (BRCA2 residues 2291 to 2342, including mutation C2332T to avoid oxidation problems) was optimized for expression in bacteria and synthesized by Genscript. It was cloned in a pET-22b vector. This vector was used to express a fusion protein comprising BRCA2-HBD, a TEV site, GB1 and a 6xHis tag in BL21 DE3 Star cells. BRCA2-HBD was purified as previously reported²³.

Peptides coding for HSF2BP helix α 1 (residues 19 to 50) and BRME1 C-terminal region (BRME1-N: residues 578 to 601; BRME1-M: 602 to 641; BRME1-C: 649 to 668) were purchased from Genecust.

The complex between HSF2BP and BRCA2-HBD was prepared by mixing the two proteins at a molar ratio of 1:1.5. The mix was concentrated by centrifugation at 4500 \times g using 3 kDa cutoff membrane at 4°C, and then loaded on a size exclusion column Superdex 200 increase 10-300 GL (GE Healthcare) equilibrated with 25 mM Hepes pH 7.5, 250 mM NaCl, 5 mM β -mercaptoethanol. The peak fractions were collected and further analyzed by EM.

The thermal stability of HSF2BP either free or bound to BRCA2-HBD was evaluated using the simplified Thermofluor assay available on the High Throughput Crystallization Laboratory (HTX Lab) of the EMBL Grenoble³⁸.

SEC-MALS

Size-exclusion chromatography (SEC) coupled to multi-angle light scattering (MALS) was used in order to measure the molecular masses of the complexes in solution. Therefore, HSF2BP, either full-length or without helix $\alpha 1$, was loaded in the presence or absence of BRCA2-HBD, on a Superdex 200 10/300 GL (GE Healthcare) or a BIOSEC 3 column (Agilent), using a HPLC Agilent system coupled to MALS/QELS/UV/RI (Wyatt Technology). The chromatography buffer was 25 mM Tris-HCl buffer, pH 7.5, 250 mM NaCl, 5 mM β -mercaptoethanol. The proteins were injected at 1-7 mg/ml in 20-100 μ l. Data were analyzed using the ASTRA software; a calibration was performed with BSA as a standard.

SEC-SAXS

SEC coupled to small angle X-ray scattering (SAXS) is available on the SWING beamline at synchrotron SOLEIL, in order to obtain a distance distribution corresponding to each sample in solution. The free HSF2BP protein was analyzed using a BIOSEC 3 column (Agilent) equilibrated in 25 mM Tris-HCl buffer, pH 7.5, 250 mM NaCl, and 5 mM β -mercaptoethanol. The protein was loaded at a concentration of 6 mg/ml, in order to observe an elution peak at an OD_{280nm} of 1 AU.

Sample preparation for EM

The complex between HSF2BP and BRCA2-HBD was diluted to approximately 0.05 mg/ml and analyzed with the negative-staining EM technique, using 2 % uranyl acetate in aqueous solution. A non-diluted sample (2-4 mg/ml) was further analyzed by cryo-EM. An aliquot of 3 μ l was deposited onto freshly glow-discharged, 300-mesh Gold / Platine grids (Protochips). Grids were frozen in liquid ethane using a Vitrobot Mark IV (ThermoFischer) at 100 % humidity, 4 °C, using a blotting force of -2 and a blotting time of 3s.

Cryo-EM data acquisition and image processing

Movies were collected with EPU software on a Titan Krios electron microscope (Thermo Fisher Scientific) operating at 300 keV, using a Gatan K3 direct electron detector coupled with a Bioquantum energy filter with 20 eV slit (Suppl. Table 1). Defocus range was between -0.6–2.5 μ m, with a pixel size of 0.85 Å, and the total dose was 40 electrons/Å² distributed on 40 frames. Movie frames were aligned using MotionCor2³⁹, with applied dose compensation. Motion-corrected micrographs were imported into CryoSPARC⁴⁰. Contrast transfer function (CTF) parameters were estimated using CTFFIND4⁴¹.

Then, as described in Suppl. Fig. 2B, 3363 particles were manually picked from 2982 micrographs, extracted particles were processed for 2D classification, and the resulting 2D classes were used for template picking. Four initial models were generated by *ab initio* reconstruction, and further heterogeneous refinement of these models enabled the selection of 312 000 particles associated with the best model. After 2 rounds of heterogeneous refinement using the same volume four times to sort good and bad particles, 112 000 particles

1 were selected that were associated to the best model. These particles were used to obtain 10
2 2D classes that were used as templates for particle picking. Four models were again generated
3 by *ab initio* reconstruction, and further heterogeneous refinement of these models enabled
4 the selection of 153 000 particles. These particles were used for homogeneous and then non-
5 uniform refinement using a D3 symmetry, resulting in a final model at 4.3 Å.

6 ***Building and refinement of the cryo-EM model***

7 The density map of the complex was of sufficient quality (resolution: 4-8 Å) to fit the crystal
8 structure of the armadillo domain of HSF2BP in complex with BRCA2-HBD (PDB codes: 7BDX
9 and 7LDG) in ChimeraX. In the peripheral region of the complex, the N-terminal helices of
10 HSF2BP were found to be more flexible, such that the local resolution map was in the range
11 6–8 Å. In these regions, AlphaFold models guided model building. All figures were prepared
12 using UCSF Chimera and UCSF Chimera X.

13 ***Crystallization and structure determination***

14 The synthetic peptides corresponding to helix $\alpha 1$ of HSF2BP (E19-V50) and BRME1-M (E602-
15 K641) were dissolved in 25 mM Tris pH 7.5, 250 mM NaCl and 5 mM β -mercaptoethanol. The
16 concentration of the helix $\alpha 1$ peptide was 10 mg/mL. This peptide was mixed with the
17 BRME1-M peptide to reach a concentration of 5 mg/mL. Crystallization assays were carried
18 out at 277 K in the High Throughput Crystallization (HTX) laboratory (EMBL Grenoble). Several
19 crystallization conditions were identified within one day and the crystals were grown within
20 two weeks. The crystals were prepared for X-ray diffraction experiments using the
21 CrystalDirect harvesting and processing robot ⁴². The best crystals diffracted at 1.47 Å ($\alpha 1$)
22 and 1.98 Å ($\alpha 1$ /BRME1-M) of resolution. They were obtained by sitting drop vapor diffusion
23 against reservoir containing 0.2 M LiCl, 0.1 M sodium acetate trihydrate, pH 5, and 20%
24 PEG6000 for $\alpha 1$ and 0.1 M HEPES sodium salt, pH 7.5, 40% PEG200 for $\alpha 1$ /BRME1-M complex.
25 Diffraction data were collected on the *MASSIF*-1 beamline of the ESRF synchrotron (EMBL
26 Grenoble). Datasets were indexed and integrated using XDS⁴³. The three-dimensional
27 structures were solved by molecular replacement using the PHENIX Phaser software ^{44,45} and
28 an input coordinate file calculated by AlphaFold2 ²⁸, were iteratively improved by manual
29 reconstruction in COOT ⁴⁶, and were refined using the PHENIX Refine and BUSTER (Global
30 Phasing Limited) ⁴⁷ software. A summary of crystallographic statistics is shown in Table 2A,B.

31 ***Isothermal Titration Calorimetry (ITC) experiments***

32 Using a VP-ITC Calorimeter (GE Healthcare), we characterized the interactions in solution
33 between the HSF2BP protein (either full-length, or the peptide corresponding to helix $\alpha 1$) and
34 the BRME1 peptides (BRME1-N, BRME1-M, BRME1-C). The experiments were performed at
35 two temperatures, 293 K and 303 K, and duplicated. The buffer was 25 mM Tris buffer, pH
36 7.5, 250mM NaCl and 5 mM β -mercaptoethanol. 8-13 μ M of HSF2BP (either full-length or
37 helix $\alpha 1$) in the cell was titrated with 80-130 μ M of BRME1 peptide (either BRME1-N, BRME1-
38 M or BRME1-C) in the injection syringe. We also tested the interactions of HSF2BP bound to
39 BRCA2-HBD with BRME1-M, and HSF2BP bound to BRME1-M with BRCA2 fragments. The

experimental conditions were similar, with 10 μ M of the complex in the cell, and either 200 μ M of BRME1-M, or 55-60 μ M of BRCA2 fragments in the injection syringe. In all cases, 10 μ L of the syringe volume were injected every 210 s, except for the first injection which was of 2 μ L and which was ignored in the final data analysis. This analysis was performed using the Origin 7.0 software provided by the manufacturer, in order to obtain the stoichiometries, equilibrium constants and thermodynamic parameters of the binding reactions. A summary of the ITC data is shown in Table 1.

Scanning Force Microscopy (SFM).

Images were obtained on a NanoScope IV SFM (Digital Instruments; Santa Barbara, CA) operating in tapping mode in air with a type J scanner using silicon probes, ACT-W, with a tip radius <10 nm and a resonance frequency range of 200–400 kHz (AppNano, Santa Clara, CA). Images were processed using Nanoscope analysis (Bruker) for background flattening. The protein volumetric analyses were done using IMAGE SXM 1.89 (National Institutes of Health IMAGE version modified by Steve Barrett, Surface Science Research Centre, Univ. of Liverpool, Liverpool, U.K.). Kernel density analysis and plotting was done using the R software.

Sample preparation for SFM

All dilutions, reactions and depositions were done in a buffer containing 25 mM Tris-HCl (pH 7.5), 250 mM NaCl and 5 mM β -mercaptoethanol. HSF2BP was diluted 10000 times to final concentration of 12 nM and deposited onto a freshly cleaved mica (Muscovite mica, V5 quality, EMS). After 30 sec the mica was washed with H₂O and dried with a stream of filtered air. HSF2BP and BRCA-HBD₂₂₈₈₋₂₃₃₇ complex was prepared by mixing 80 μ M HSF2BP with 120 μ M BRCA-HBD₂₂₈₈₋₂₃₃₇, followed by incubation on ice for 15 min. One half of the reaction was diluted 10000 times, deposited onto a freshly cleaved mica, washed with H₂O and dried with a stream of filtered air. Another half of the reaction was further incubated with BRME1 peptide (molar ratio HSF2BP:BRME1-M=1:1) on ice for 10 min. Sample was diluted 10000 times, deposited on mica, washed with H₂O and dried with a stream of filtered air.

Cell culture, constructs and stable cell line generation.

HeLa (human cervical adenocarcinoma, female origin) cells were cultured in DMEM supplemented with 10% FCS, 200 U/ml penicillin, 200 μ g/ml streptomycin. Expression constructs for stable production of GFP-HSF2BP, Flag-BRME1 and their truncation variants were engineered as described before¹⁷ in the PiggyBac vectors by Gibson assembly and verified by sequencing. The constructs were co-transfected in combinations shown in Figure 3A and together with the PiggyBac transposase expression plasmid (hyPBase⁴⁸) using Lipofectamine 3000 (Thermo Fisher) in 6-well plates seeded with 400,000 HeLa cells the day before. Selection with 1.5 μ g/ml puromycin for GFP-HSF2BP constructs and 800 μ g/ml G418 for Flag-BRME1 constructs was started two days after transfection and maintained for 8 days. The resulting resistant mixed cell population was used for clonogenic survival assays.

Clonogenic survival assays

Clonogenic survival assays were performed in 6-well plates in technical duplicates. Untreated control wells were seeded with 100 cells per well in 2 mL media. Higher seeding densities of 400 and 1000 cells per well were used in the wells treated with higher drug concentrations. One day after seeding, the drugs were added: mitomycin C (MMC, Sigma, M4287-2MG), cisplatin, talazoparib (BMN-673, Axon medchem, #2502). After 2-hour (MMC) or overnight (cisplatin, talazoparib) incubation, drug-containing media was removed, wells were rinsed with PBS and refilled with 2 mL fresh media. Colonies were stained (0.25% Coomassie brilliant blue, 40% methanol, 10% acetic acid) on day 10 after seeding. Plates were photographed using a digital camera, images were analyzed using OpenCFU software to quantify the colonies.

Co-immunoprecipitation and immunoblotting

Cells were grown in 10 cm dish to near-confluence, washed twice with PBS and lysed in situ in 1 ml NETT buffer (100 mM NaCl, 50 mM Tris pH 7.5, 5 mM EDTA pH 8.0, 0.5% Triton-X100) supplemented immediately before use with protease inhibitor cocktail (Roche) and 0.4 mg/ml Pefabloc (Roche) (NETT++). After 5-10 min, cells were scraped off and collected in 1.5 ml microcentrifuge tubes; lysis was continued for additional 15-20 min on ice, then mixtures were centrifuged (15 min, 4 °C, 14000 rcf), 70 µl of the supernatant was collected as input sample, mixed with 2× Laemmli sample buffer and denatured for 5 minutes at 95 °C. The rest of the supernatant was mixed with 8 µl anti-GFP beads (Chromotek, gta-20). The mixture was incubated for 2 h at 4 °C while rotating, washed three times in NETT++ buffer and bound proteins were eluted with 70 µl 2× sample buffer, 5 min incubation at 95 °C. 15 µl bound and 7 µl input sample was separated on 4-15% TGX SDS-PAGE gel (BioRad #456-1086) and transferred to PVDF membrane (Immobilon-FL, Millipore, IPFL00010). Immunoblotting was performed following standard procedures with anti-GFP rabbit pAb (Invitrogen, A11122) and anti-Flag mouse mAb (M2 antibody, Sigma, F3165) antibodies, followed by detection with fluorescently labeled secondary antibodies were used: anti-mouse CF680 (Sigma #SAB460199), anti-rabbit CF770 (Sigma #SAB460215). Membranes were scanned using Odyssey CLx imaging system (LI-COR).

ICL repair assay

ICL repair assays were performed as described^{49,50}. *Xenopus* egg extracts (HSS and NPE) and a plasmid containing a site-specific cisplatin ICL (pICL) were prepared as described previously^{51,52}. pICL (9 ng/µl) and pQuant (0.45 ng/µl) were first incubated in a high-speed supernatant (HSS) of egg cytoplasm for 20 min at room temperature, which promotes the assembly of prereplication complexes on the DNA. Addition of two volumes nucleoplasmic egg extract (NPE) supplemented with ³²P-α-dCTP, triggers a single round of DNA replication. Where indicated, His-tagged human HSF2BP (0.45 µM), BRME1-M peptide (1.35 µM), or BRME1-C peptide (1.35 µM) was added to NPE prior to mixing with HSS. Aliquots of replication reaction (4 µl) were stopped at various times with 45 µl Stop solution II (50 mM Tris pH 7.5, 0.5% SDS, and 10 mM EDTA). Samples were incubated with RNase (0.13 µg/µl) for 30 min at 37 °C followed by proteinase K (0.5 µg/µl) overnight at room temperature. DNA was extracted using phenol/chloroform, ethanol-precipitated in the presence of glycogen (20 µg) and

resuspended in 4 µl TE (10 mM Tris pH 7.5 and 1 mM EDTA). ICL repair was analyzed by digesting 1 µl extracted DNA with HincII, or HincII and SapI, separation on a 0.8% agarose gel in 1x TBE buffer, and quantification using Typhoon TRIO+ (GE Healthcare) and ImageQuant TL software (GE Healthcare). Repair efficiency was calculated as described ⁵³.

Two-dimensional gel electrophoresis (2DGE)

2DGE was performed as described previously ⁵⁴. Replication intermediates of pICL at various times were extracted and digested with HincII. Fragments were then separated on a 0.4% agarose gel in 0.5x TBE buffer at 0.86 V/cm for 24 h at room temperature. The lanes of interest were cut out, casted across the top of the second-dimension gel consisting of 1% agarose with 0.3 µg/ml ethidium bromide, and run in 0.5x TBE containing 0.3 µg/ml ethidium bromide with buffer circulation at 3.5 V/cm for 14.5 h at room temperature. The gel was dried on Amersham Hybond-XL membrane and exposed to a phosphor screen. DNA was visualized using a Typhoon TRIO+.

DATA AVAILABILITY

The coordinates and structure factors file corresponding to the crystal structures of HSF2BP helix <1 and the complex between HSF2BP helix <1 and BRME1-M described in the study were deposited in the Protein Data Bank (PDB) under the entry codes XXX and YYY, respectively [<https://www.XXX>]. The EM data generated in this study was deposited in PDB database under accession code XXX [<https://www.XXX>].

REFERENCES

1. Holloman, W. K. Unraveling the mechanism of BRCA2 in homologous recombination. *Nat Struct Mol Biol* 18, 748 754 (2011).
2. Zelensky, A. N., Kanaar, R. & Wyman, C. Mediators of Homologous DNA Pairing. *Csh Perspect Biol* 6, a016451 a016451 (2014).
3. Kojic, M., Kostrub, C. F., Buchman, A. R. & Holloman, W. K. BRCA2 Homolog Required for Proficiency in DNA Repair, Recombination, and Genome Stability in *Ustilago maydis*. *Mol Cell* 10, 683–691 (2002).
4. Siaud, N. *et al.* Brca2 is involved in meiosis in *Arabidopsis thaliana* as suggested by its interaction with Dmc1. *Embo J* 23, 1392 1401 (2004).
5. Weinberg-Shukron, A. *et al.* Essential Role of BRCA2 in Ovarian Development and Function. *The New England journal of medicine* 379, 1042–1049 (2018).
6. Klovstad, M., Abdu, U. & Schüpbach, T. *Drosophila* brca2 Is Required for Mitotic and Meiotic DNA Repair and Efficient Activation of the Meiotic Recombination Checkpoint. *Plos Genet* 4, e31 (2008).
7. Ko, E., Lee, J. & Lee, H. Essential role of brc-2 in chromosome integrity of germ cells in *C. elegans*. *Mol Cells* 26, 590–4 (2008).
8. Martin, J. S., Winkelmann, N., Petalcorin, M. I. R., Mcilwraith, M. J. & Boulton, S. J. RAD-51-dependent and -independent roles of a *Caenorhabditis elegans* BRCA2-related protein during DNA double-strand break repair. *Mol Cell Biol* 25, 3127 3139 (2005).
9. Li, S. *et al.* Cancer Risks Associated With BRCA1 and BRCA2 Pathogenic Variants. *J Clin Oncol* JCO2102112 (2022) doi:10.1200/jco.21.02112.
10. Sharan, S. K. *et al.* BRCA2 deficiency in mice leads to meiotic impairment and infertility. *Development (Cambridge, England)* 131, 131 142 (2004).
11. Martinez, J. S. *et al.* BRCA2 regulates DMC1-mediated recombination through the BRC repeats. *Proc National Acad Sci* 113, 3515 3520 (2016).
12. Seeliger, K., Dukowic-Schulze, S., Wurz-Wildersinn, R., Pacher, M. & Puchta, H. BRCA2 is a mediator of RAD51- and DMC1-facilitated homologous recombination in *Arabidopsis thaliana*. *New Phytol* 193, 364 375 (2012).
13. Thorslund, T., Esashi, F. & West, S. C. Interactions between human BRCA2 protein and the meiosis-specific recombinase DMC1. *Embo J* 26, 2915 2922 (2007).

14. Dray, E., Siaud, N., Dubois, E. & Doutriaux, M.-P. Interaction between Arabidopsis Brca2 and its partners Rad51, Dmc1, and Dss1. *Plant Physiol* 140, 1059–1069 (2006).
15. Brandsma, I. *et al.* Overexpression of HSF2BP, a new BRCA2 interactor, results in a Fanconi anemia-like phenotype. in *Balancing Pathways in DNA Double Strand Break Repair* 98–140 (2016).
16. Zhang, J. *et al.* The BRCA2-MEILB2-BRME1 complex governs meiotic recombination and impairs the mitotic BRCA2-RAD51 function in cancer cells. *Nat Commun* 11, 2055 (2020).
17. Brandsma, I. *et al.* HSF2BP Interacts with a Conserved Domain of BRCA2 and Is Required for Mouse Spermatogenesis. *Cell Reports* 27, 3790–3798.e7 (2019).
18. Zhang, J., Fujiwara, Y., Yamamoto, S. & Shibuya, H. A meiosis-specific BRCA2 binding protein recruits recombinases to DNA double-strand breaks to ensure homologous recombination. *Nat Commun* 10, 722 (2019).
19. Felipe-Medina, N. *et al.* A missense in HSF2BP causing Primary Ovarian Insufficiency affects meiotic recombination by its novel interactor C19ORF57/BRME1. *Elife* 9, e56996 (2020).
20. Shang, Y. *et al.* MEIOK21: a new component of meiotic recombination bridges required for spermatogenesis. *Nucleic Acids Res* gkaa406- (2020) doi:10.1093/nar/gkaa406.
21. Takemoto, K. *et al.* Meiosis-Specific C19orf57/4930432K21Rik/BRME1 Modulates Localization of RAD51 and DMC1 to DSBs in Mouse Meiotic Recombination. *Cell Reports* 31, 107686 (2020).
22. Li, M. *et al.* The Novel Male Meiosis Recombination Regulator (MAMERR) Coordinates the Progression of Meiosis Prophase I. *J Genet Genomics* (2020) doi:10.1016/j.jgg.2020.08.001.
23. Ghouil, R. *et al.* BRCA2 binding through a cryptic repeated motif to HSF2BP oligomers does not impact meiotic recombination. *Nat Commun* 12, 4605 (2021).
24. Sato, K. *et al.* HSF2BP negatively regulates homologous recombination in DNA interstrand crosslink repair. *Nucleic Acids Res* (2020) doi:10.1093/nar/gkz1219.
25. Ramadan, K. p97/VCP- and Lys48-linked polyubiquitination form a new signaling pathway in DNA damage response. *Cell Cycle* 11, 1062–1069 (2012).
26. Ju, J.-S., Miller, S. E., Hanson, P. I. & Weihl, C. C. Impaired Protein Aggregate Handling and Clearance Underlie the Pathogenesis of p97/VCP-associated Disease*. *J Biol Chem* 283, 30289–30299 (2008).

27. Pendlebury, D. F., Zhang, J., Agrawal, R., Shibuya, H. & Nandakumar, J. Structure of a meiosis-specific complex central to BRCA2 localization at recombination sites. *Nat Struct Mol Biol* 28, 671–680 (2021).
28. Jumper, J. *et al.* Highly accurate protein structure prediction with AlphaFold. *Nature* 596, 583–589 (2021).
29. Franz, A., Ackermann, L. & Hoppe, T. Ring of Change: CDC48/p97 Drives Protein Dynamics at Chromatin. *Frontiers Genetics* 7, 73 (2016).
30. Krishna, T. S. R., Kong, X.-P., Gary, S., Burgers, P. M. & Kuriyan, J. Crystal structure of the eukaryotic DNA polymerase processivity factor PCNA. *Cell* 79, 1233–1243 (1994).
31. Dieckman, L. M., Freudenthal, B. D. & Washington, M. T. The Eukaryotic Replisome: a Guide to Protein Structure and Function. *Subcell Biochem* 62, 281–299 (2012).
32. Ribeiro, J. *et al.* The meiosis-specific MEIOB–SPATA22 complex cooperates with RPA to form a compacted mixed MEIOB/SPATA22/RPA/ssDNA complex. *Dna Repair* 102, 103097 (2021).
33. Yates, L. A. *et al.* A structural and dynamic model for the assembly of Replication Protein A on single-stranded DNA. *Nat Commun* 9, 5447 (2018).
34. Corbett, K. D. *et al.* The Monopolin Complex Crosslinks Kinetochore Components to Regulate Chromosome-Microtubule Attachments. *Cell* 142, 556–567 (2010).
35. Meulemans, L. *et al.* Skipping Nonsense to Maintain Function: The Paradigm of BRCA2 Exon 12. *Cancer Res* 80, 1374–1386 (2020).
36. Li, L. *et al.* Functional redundancy of exon 12 of BRCA2 revealed by a comprehensive analysis of the c.6853A>G (p.I2285V) variant. *Hum Mutat* 30, 1543–1550 (2009).
37. Bièche, I. & Lidereau, R. Increased level of exon 12 alternatively spliced BRCA2 transcripts in tumor breast tissue compared with normal tissue. *Cancer Res* 59, 2546–50 (1999).
38. Dupeux, F., Röwer, M., Seroul, G., Blot, D. & Márquez, J. A. A thermal stability assay can help to estimate the crystallization likelihood of biological samples. *Acta Crystallogr Sect D Biological Crystallogr* 67, 915–919 (2011).
39. Zheng, S. Q. *et al.* MotionCor2: anisotropic correction of beam-induced motion for improved cryo-electron microscopy. *Nat Methods* 14, 331–332 (2017).
40. Punjani, A., Rubinstein, J. L., Fleet, D. J. & Brubaker, M. A. cryoSPARC: algorithms for rapid unsupervised cryo-EM structure determination. *Nat Methods* 14, 290–296 (2017).

41. Rohou, A. & Grigorieff, N. CTFFIND4: Fast and accurate defocus estimation from electron micrographs. *J Struct Biol* 192, 216–221 (2015).
42. Zander, U. *et al.* Automated harvesting and processing of protein crystals through laser photoablation. *Acta Crystallogr Sect D Struct Biology* 72, 454–466 (2016).
43. Kabsch, W. XDS. *Acta Crystallogr Sect D Biological Crystallogr* 66, 125–132 (2010).
44. Afonine, P. V. *et al.* Towards automated crystallographic structure refinement with phenix.refine. *Acta Crystallogr Sect D Biological Crystallogr* 68, 352–367 (2012).
45. Liebschner, D. *et al.* Macromolecular structure determination using X - rays, neutrons and electrons: recent developments in Phenix. *Acta Crystallogr Sect D* 75, 861–877 (2019).
46. Emsley, P., Lohkamp, B., Scott, W. G. & Cowtan, K. Features and development of Coot. *Acta Crystallogr Sect D Biological Crystallogr* 66, 486–501 (2010).
47. Bricogne, G. *et al.* *BUSTER version 2.10.3*. (Global Phasing Ltd., 2020).
48. Yusa, K., Zhou, L., Li, M. A., Bradley, A. & Craig, N. L. A hyperactive piggyBac transposase for mammalian applications. *Proc National Acad Sci* 108, 1531–1536 (2011).
49. Räschle, M. *et al.* Mechanism of replication-coupled DNA interstrand crosslink repair. *Cell* 134, 969–980 (2008).
50. Knipscheer, P. *et al.* The Fanconi anemia pathway promotes replication-dependent DNA interstrand cross-link repair. *Science (New York, NY)* 326, 1698–1701 (2009).
51. Sparks, J. & Walter, J. C. Extracts for Analysis of DNA Replication in a Nucleus-Free System. *Cold Spring Harb Protoc* 2019, pdb.prot097154 (2019).
52. Enoiu, M., Ho, T. V., Long, D. T., Walter, J. C. & Schärer, O. D. Construction of plasmids containing site-specific DNA interstrand cross-links for biochemical and cell biological studies. *Methods Mol Biology Clifton N J* 920, 203–219 (2012).
53. Knipscheer, P., Räschle, M., Schärer, O. D. & Walter, J. C. Replication-coupled DNA interstrand cross-link repair in *Xenopus* egg extracts. *Methods Mol Biology Clifton N J* 920, 221–243 (2012).
54. Long, D. T., Räschle, M., Joukov, V. & Walter, J. C. Mechanism of RAD51-Dependent DNA Interstrand Cross-Link Repair. *Science* 333, 84–87 (2011).

ACKNOWLEDGEMENTS

We warmly thank Christophe Velours (I2BC) for the first series of SEC-MALS experiments; Aurélien Thureau (SAXS beamline, Synchrotron SOLEIL) for discussions about the SAXS data analysis; Florine Dupeux and all the HTX Lab staff for the crystallogenesis and crystallography experiments; Marie-Hélène Le Du for helpful advice in crystallogenesis; Jean-Marie Winter (Institut Pasteur) and Stéphane Bressanelli (I2BC) for their help during the cryo-EM analyses; the staff of the I2BC computing facility (I2BC/SICS) for facilitating data management and accessibility.

The research leading to these results has received funding from the European Community's Seventh Framework Program H2020 under the project iNEXT discovery (grant agreement N°871037). It has also benefited from the platform of cryo-EM of I2BC supported by the French Infrastructure for Integrated Structural Biology (FRISBI, ANR-10-INSB-05) and by the CEA.

AUTHOR CONTRIBUTIONS

Conceptualization, S.M., A.Z., S.Z.J.; methodology, R.G., S.M., K.S., M.O., P.L., V.R., A.A.A, A.Z.; formal analysis, R.G., S.M., K.S., P.L., C.W., P.K. A.Z., S.Z.J.; investigation, R.G., S.M., K.S., M.O., A.A.A., P.L., G.D., A.Z.; writing—original draft preparation, A.Z., S.Z.J.; writing—review and editing, R.G., S.M., A.Z., S.Z.J.; visualization, A.Z., S.Z.J.; supervision, S.M., C.W., P.K., R.K., A.Z., S.Z.J.; project administration, A.Z., S.Z.J.; funding acquisition, R.K., A.Z., S.Z.J. All authors have read and agreed to the published version of the manuscript.

COMPETING INTERESTS

The authors declare no competing interests.

FIGURES

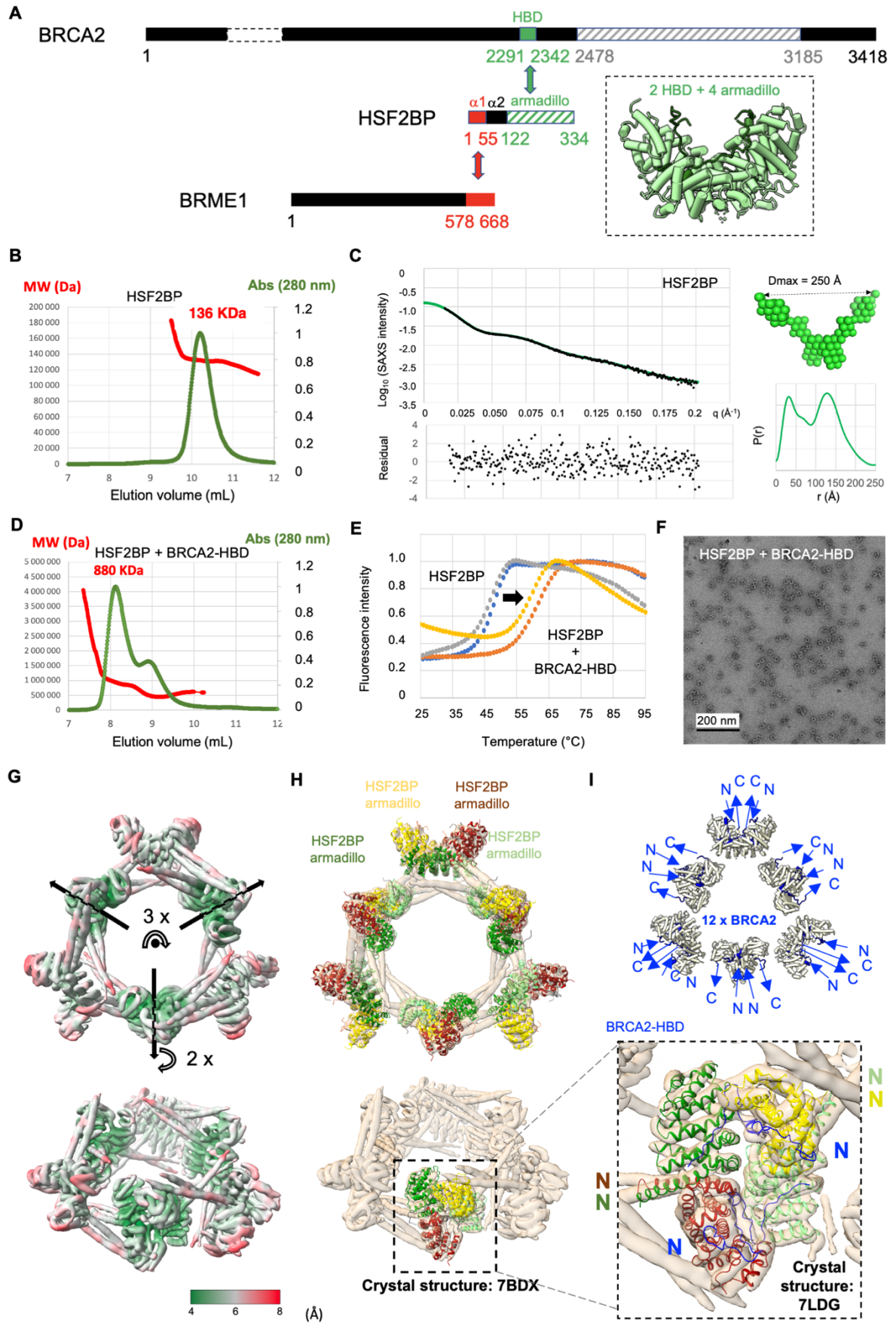


Figure 1. HSF2BP oligomerizes into a ring-shaped complex upon binding to BRCA2-HBD. (A) Representation of the sequences of BRCA2, HSF2BP and BRME1, and of their interacting regions. Folded domains of known 3D structure are marked with stripes. Regions of BRCA2 (HBD: residues 2291 to 2342) and HSF2BP (armadillo: residues 122 to 334) that were crystallized together are colored in green, and their 3D structure is represented as a green cartoon (PDB code: 7BDX; this 3D structure contains 2 HBD and 4 armadillo, as indicated). Regions of HSF2BP and BRME1 that interact are colored in red ¹⁶. **(B) SEC-MALS analysis of full-length HSF2BP, showing that the protein is eluted as a tetramer.** The normalized absorbance at 280 nm is overlaid with the molar mass (Da), and both parameters are plotted as a function of the elution volume. The experiment was performed on a Superdex 200 10/300 GL (GE Healthcare). As the mass of HSF2BP monomer is 37.6 kDa, this protein is mainly in a tetrameric state in the conditions of the experiment. A duplicate of this experiment, as well as a control experiment performed using HSF2BP lacking helix α 1, are shown in Suppl. Fig. 1A. **(C) SEC-SAXS curve and resulting distance distribution, obtained on full-length HSF2BP.** The experimental SAXS curve (in black dots) is plotted as a function of the scattering angle. The fitted curve (in green) is the Fourier Transform of the distance distribution $P(r)$ curve. The residual values (in black dots) were calculated as the experimental minus the fitted SAXS intensity values, divided by the experimental errors. The distance distribution $P(r)$ is plotted in arbitrary units as a function of the distance, the maximal distance being 250 Å. The deduced HSF2BP mass is 156 ± 21 kDa, consistent with a tetrameric state. Calculation of an *ab initio* model (average model in green spheres; more models in Suppl. Fig. 1B,C) from the SAXS data suggests that HSF2BP has a V shape. **(D) SEC-MALS analysis of HSF2BP bound to BRCA2-HBD, showing that the resulting complex has a mass of 880 kDa.** The normalized absorbance at 280 nm is overlaid with the molar mass (Da), and both parameters are plotted as a function of the elution volume. The experiment was performed on a Superdex 200 10/300 GL (GE Healthcare). **(E) Thermal stability of HSF2BP, either free (blue: 7 mg/ml; grey: 14 mg/ml) or bound to BRCA2-HBD (yellow: 1 mg/ml; orange: 12 mg/ml).** The denaturation temperature of HSF2BP shifted from 45.9-46.7°C to 59-60.7°C upon binding to BRCA2-HBD. **(F) Negative-staining EM image obtained on a sample of HSF2BP bound to BRCA2-HBD using 0.2% of uranyl acetate.** The protein concentration of the sample was about 0.05 mg/ml. **(G) Cryo-EM map of HSF2BP bound to BRCA2-HBD.** Top and side views are displayed with an electron density threshold of 0.07. The map shows a 3-fold symmetry around the axis going through the center of the ring, and three 2-fold symmetries around perpendicular axes going through the center of the globular subunits (D_3 symmetry). It is colored as a function of the local resolution: from green (4 Å) to red (8 Å). **(H) Docking of the crystal structure of the complex between HSF2BP armadillo domain and BRCA2-HBD (PDB: 7BDX or 7LDG) into the cryo-EM map.** In the top view, a crystal structure is positioned in each of the six globular subvolumes of the map, whereas in the side view, only one crystal structure is displayed, and a zoom view highlights the nice agreement between this structure and the cryo-EM map. Each crystal structure contains four armadillo domains (HSF2BP₁₂₂₋₃₃₀ in 7BDX and HSF2BP₁₀₅₋₃₂₉ in 7LDG; in light green, yellow, green and maroon) bound to two BRCA2-HBD peptides (not visible in the main views; visible in blue in the zoom view; see also Suppl. Fig 2C to zoom on the BRCA2-HBD peptide structure fitted into the cryo-EM map). The N-termini of the armadillo domains, as well as of the BRCA2 peptides, are indicated with a colored N in the zoom view. **(I) Orientations of the N- and C-termini of the 12 BRCA2 peptides in the complex.** All the BRCA2 extremities are located on the outer surface of the ring shape.

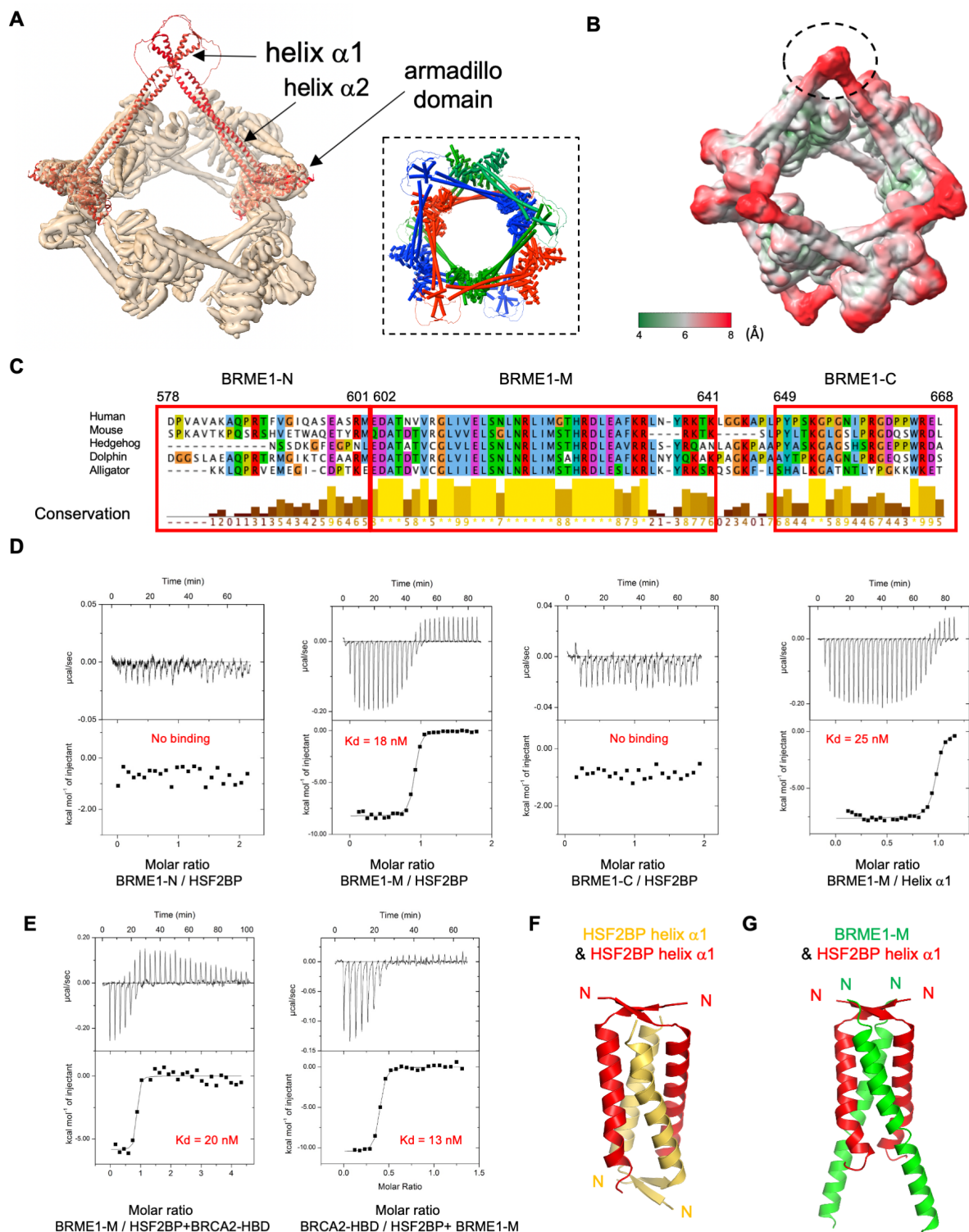


Figure 2. Helix $\alpha 1$ auto-assembles in HSF2BP-BRCA2 and binds to BRME1. (A) Docking of the N-terminal predicted coiled-coil regions of HSF2BP, composed of helices $\alpha 1$ and $\alpha 2$, in the map regions connecting the armadillo domains. The map is displayed with an electron density threshold of 0.07. The cartoon views of the two AlphaFold models are colored in red. Each model consists of a disordered region, a short helix $\alpha 1$, a large helix $\alpha 2$ and an armadillo domain, similar to that of 7BDX. In the boxed panel, 3 pairs of HSF2BP tetramers docked into the cryo-EM map are displayed in 3 different colors. These figures were obtained using ChimeraX. (B) Cryo-EM map displayed with a lower electron density threshold (0.03) and colored as a function of the local resolution. The colors are the same as in Figure 1G. A dashed oval identifies the map region corresponding

1 to the 4 helices $\alpha 1$. **(C) Sequence alignment of the C-terminal region of a set of five BRME1 proteins, showing**
2 **a representative sequence diversity.** Three human peptides, named BRME1-N, BRME1-M and BRME1-C,
3 corresponding to the boxed sequences, were further analyzed. **(D) ITC curves identifying the BRME1 sequence**
4 **binding to HSF2BP.** These experiments were all performed at 30°C. Additional experiments performed at 20°C
5 are detailed in Suppl. Fig. 4 and Table 1. **(E) ITC curve showing that BRME1-M and BRCA2-HBD do not compete**
6 **for binding to HSF2BP.** These experiments were performed at 20°C. **(F) Crystal structure of HSF2BP peptide**
7 **E19-V50 (helix $\alpha 1$).** The two monomers observed in the asymmetric unit are colored in red, whereas the two
8 other monomers positioned after application of a 2-fold crystallography symmetry are colored in yellow (Table
9 2). **(G) Crystal structure of the HSF2BP peptide E19-V50 (helix $\alpha 1$, in red) bound to the BRME1 peptide E602-**
10 **K641 (BRME1-M, in yellow).** Each asymmetric unit contained a HSF2BP-BRME1 dimer. The heterotetramer was
11 calculated by application of a 2-fold crystallography symmetry (Table 2).
12

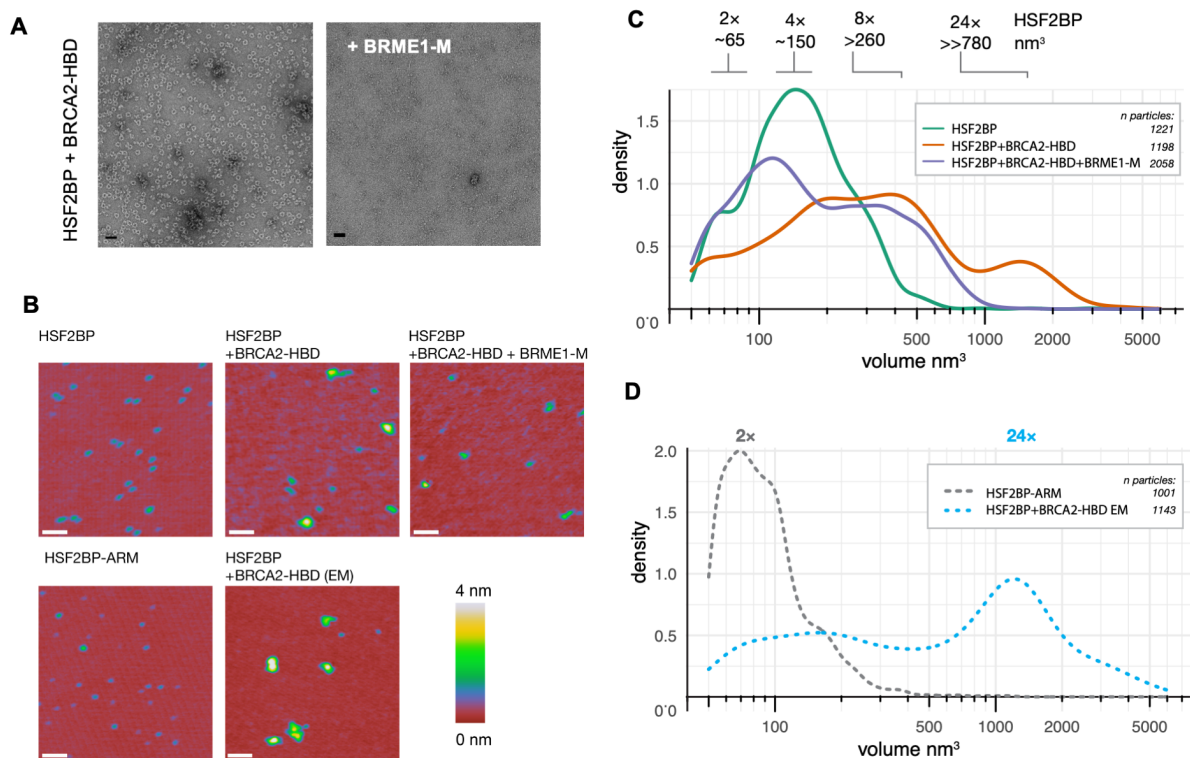


Figure 3. BRME1 disrupts the HSF2BP-BRCA2 oligomers. (A) Negative staining EM images recorded on the complex formed by HSF2BP and BRCA2-HBD in the absence (left) and presence (right) of the peptide BRME1-M. The conditions are the same as in Figure 1F. **(B)** Representative SFM images of HSF2BP, its armadillo domain (HSF2BP-ARM), HSF2BP+BRCA2-HBD and HSF2BP+BRCA2-HBD+BRME1-M. The complexes were assembled just before deposition on mica for SMF analysis. Only the sample prepared for EM was purified by gel filtration. Scale bar = 100 nm. **(C)** Kernel density plots of the particle volume distributions for HSF2BP and its complexes with BRCA2-HBD and BRCA2-HBD+BRME1-M. The number of particles is indicated in the legend, the replicate of the experiment is shown in Suppl. Fig. 5. **(D)** Kernel density plots of particle volume distributions of the HSF2BP-ARM fragments and HSF2BP+BRCA2-HBD complexes prepared following the protocol used for EM. These were used to determine the volumes of the dimers and the ring-shaped 24-mer, respectively. The experiment was done once, number of analyzed particles is indicated.

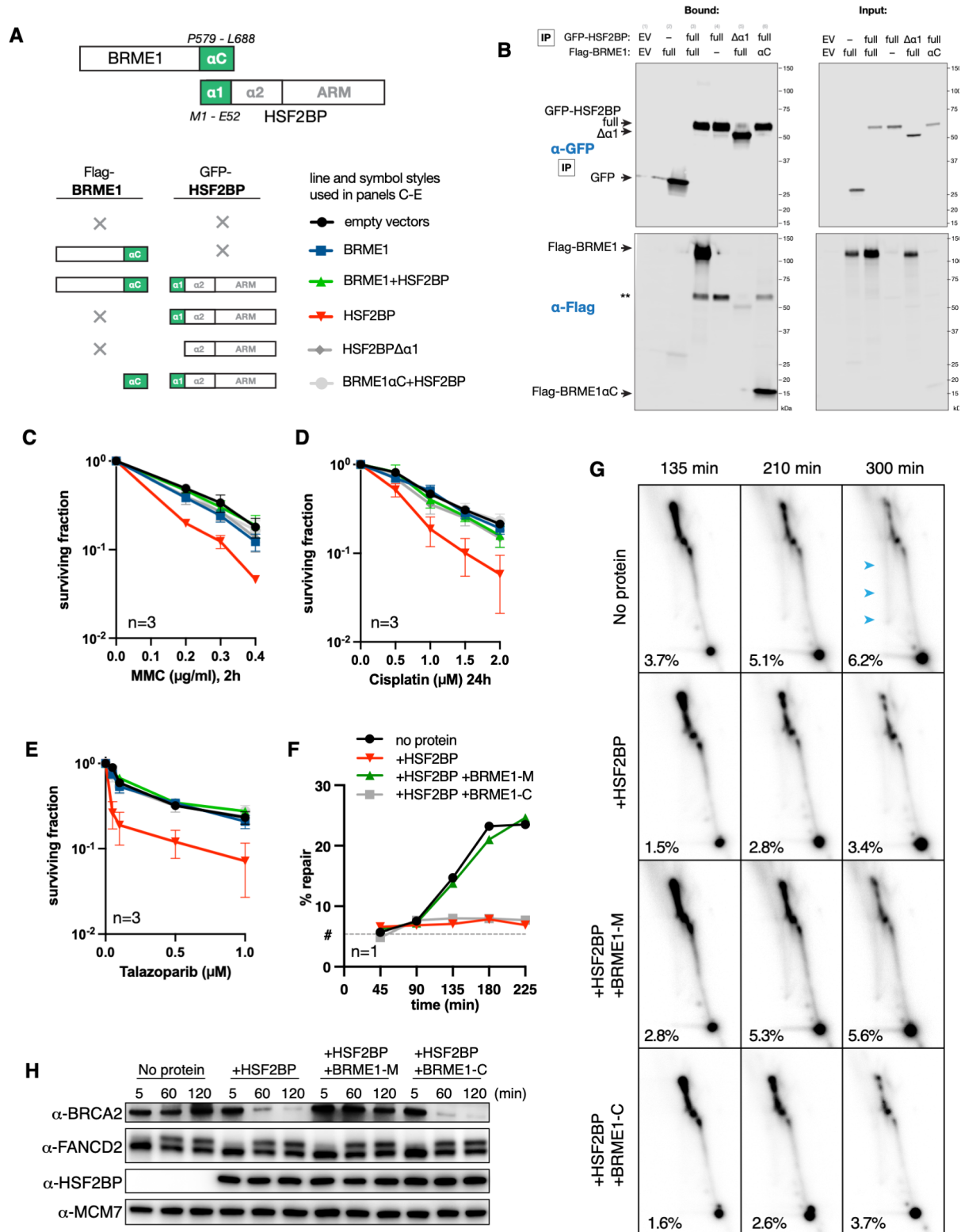


Figure 4. BRME1 protects cancer cells from HSF2BP and prevents BRCA2 degradation during interstrand crosslink repair. (A) Schematic depiction of the HSF2BP and BRME1 fragments used in the congenic survivals shown in panels (C-E). Interacting α -helices are shown as green blocks, the six combinations of HSF2BP and BRME1 variants used in the survivals are shown next to the corresponding line styles used in panels (C-E); \times indicates that the protein was not present. (B) Co-immunoprecipitation of HSF2BP and BRME1 variants used in clonogenic survivals. Proteins eluted from the anti-GFP beads were revealed by immunoblotting with anti-GFP rabbit pAb (Invitrogen, A11122) and anti-Flag mouse mAb (M2 antibody, Sigma, F3165) detected using

fluorescently labeled secondary antibodies. **(C-E) Clonogenic survival of HeLa cells stably producing HSF2BP and BRME1 variants, as indicated in panel (A).** Cells were treated with mitomycin C (MMC), cisplatin or talazoparib. The experiment was repeated three times, means and s.e.m. are plotted. **(F) Efficiency of synthetic cisplatin interstrand crosslink repair in *Xenopus* egg extract in the presence or absence of HSF2BP, the BRME1 peptides BRME1-M (binding HSF2BP) and BRME1-C (not binding HSF2BP)** (see Figure 2C,D). See Sato *et al.* 2020 for the detailed description of the assay ²⁴. Replicates of the experiment are shown in Suppl. Fig. 6A,B. **(G) HR intermediate formation during the repair of synthetic cisplatin DNA interstrand crosslink in *Xenopus* egg extract monitored by 2D agarose gel electrophoresis.** The reactions were carried out in the presence or absence of HSF2BP, the BRME1 peptides BRME1-M and BRME1-C (see Figure 2C). The X-arc that contains HR intermediates is indicated by blue arrows in the upper right panel, percentage of the signal localizing to it is indicated, as detailed previously ²⁴. A replicate of this experiment is shown in Suppl. Fig. 6C. **(H) Effect of HSF2BP and BRME1-M or BRME1-C peptides on the endogenous *Xenopus* BRCA2 protein during the time course (5-120 min) of the interstrand crosslink repair reaction.** Antibodies used for immunoblotting are indicated. See Sato *et al.* 2020 for the validation and analysis of the dependencies of BRCA2 protein degradation induced by HSF2BP ²⁴. A replicate of this experiment is shown in Suppl. Fig. 6D.

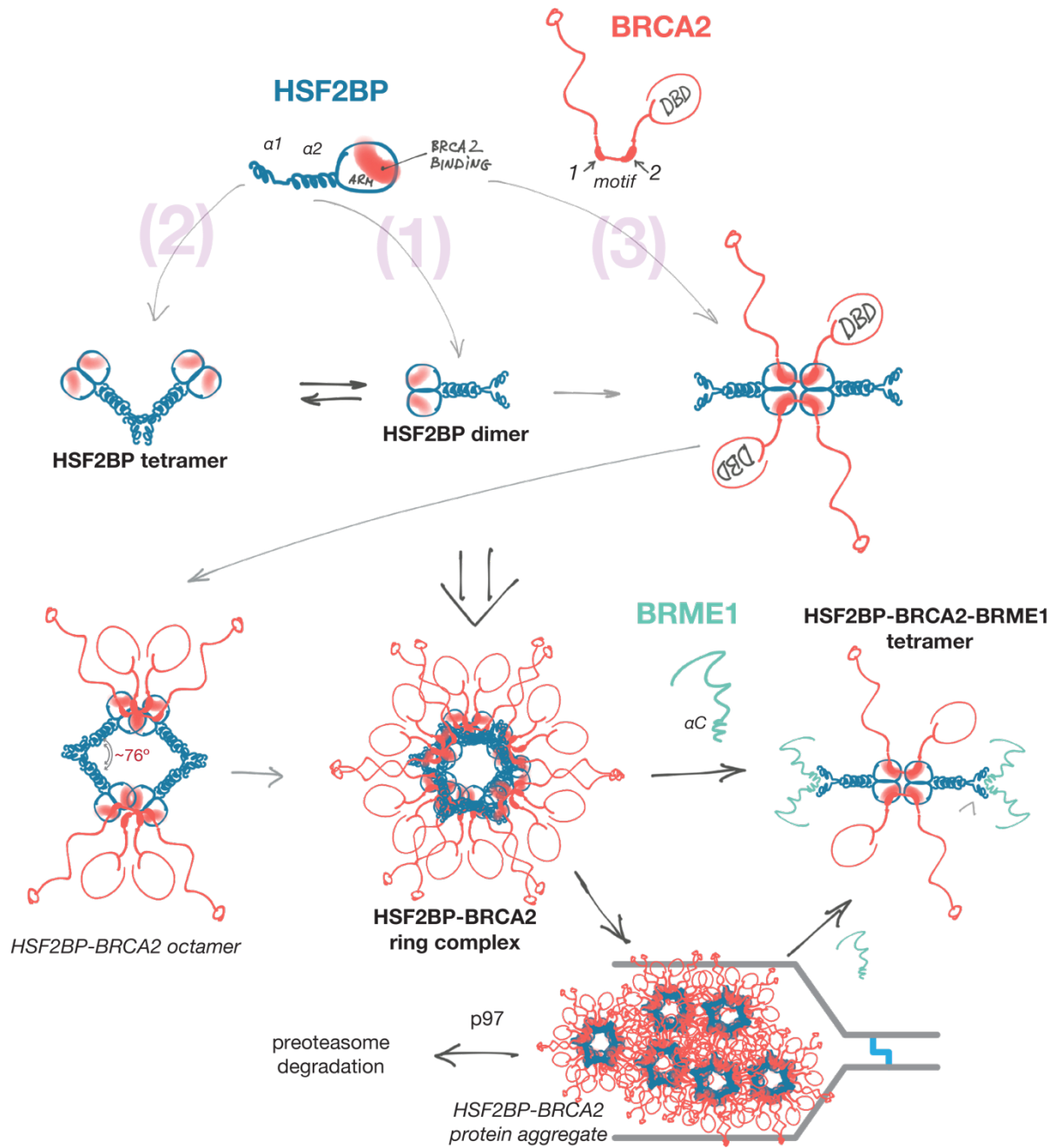


Figure 5. Oligomeric states of HSF2BP and the “aggregator-disaggregator” model proposed to explain the effects of HSF2BP and BRME1 on BRCA2 in somatic and germline cells. Oligomers observed experimentally are indicated in bold. Two intrinsic (1) (2) and one BRCA2-mediated (3) oligomerization mechanisms result in the formation of a constitutive homodimer, a V-shaped tetramer and a large ring complex. This concentrates and organizes BRCA2, but at replication fork stalled at crosslink, it results in aggregation and proteasomal degradation of BRCA2. BRME1 competes with one of the oligomerization mechanisms (2), resulting in the formation of a $4 \times \text{HSF2BP} : 2 \times \text{BRCA2} : 4 \times \text{BRME1}$ complex and thus preventing or reversing BRCA2 aggregation.

TABLES

Table 1. Binding parameters deduced from the ITC analyses.

	Kd (M) (\pm error)	n	ΔH (kcal/mol) (\pm error)	ΔG (kcal/mol)	$-T\Delta S$ (kcal/mol)	T (K)
HSF2BP vs BRME1-M	1.1E-08 (3.5)	0.77	-5.7 (0.07)	-10.6	-4.90	293
HSF2BP vs BRME1-M	1.8E-08 (2.7)	0.88	-8.2 (0.06)	-10.7	-2.50	303
HSF2BP vs BRME1-N	undetectable					293
HSF2BP vs BRME1-N	undetectable					303
HSF2BP vs BRME1-C	undetectable					293
HSF2BP vs BRME1-C	undetectable					303
HSF2BP $\alpha 1$ vs BRME1-M	2.5E-08 (4.5)	0.96	-7.6 (0.06)	-10.5	-2.90	303
HSF2BP $\alpha 1$ vs BRME1-M	2.1E-08 (4)	0.93	-1.2 (0.05)	-10.2	-9.00	293
HSF2BP+BRME1-M vs BRCA2-HBD	1.3E-08 (2)	0.37	-10.5 (0.13)	-10.4	-0.10	293
HSF2BP+BRME1-M vs BRCA2 ₂₂₁₃₋₂₃₄₂	7.8E-09 (1.8)	0.35	-10.9 (0.12)	-12.6	-1.70	293
HSF2BP+BRCA2-HBD vs BRME1-M	3.4E-08 (8)	0.87	-4.4 (0.06)	-10	-5.60	293
HSF2BP+BRCA2-HBD vs BRME1-M	2.0E-08 (19)	0.8	-5.8 (0.22)	-10.2	-4.40	293

Table 2. Data collection and refinement statistics related to the crystal structures of HSF2BP helix $\alpha 1$ and HSF2BP helix $\alpha 1$ bound to BRME1-M.

	HSF2BP- $\alpha 1$	HSF2BP- $\alpha 1$ / BRME1-M
Data collection		
Space group	$P 4_3 3 2$	$I 4_1 2 2$
Cell dimensions		
<i>a</i> , <i>b</i> , <i>c</i> (Å)	79.81, 79.81, 79.81	73.87, 73.87, 92.80
<i>a</i> , <i>b</i> , <i>c</i> (°)	90, 90, 90	90, 90, 90
<i>Z</i>	2	1:1
Wavelength (Å)	0.96546	0.96546
Resolution (Å)	60.0 - 1.48 (1.52 - 1.48)	36.9 - 1.9 (1.95 - 1.9)
Estimated resolution limit (Å)*	1.48, 1.48, 1.48	2.44, 2.44, 1.71
<i>R</i> _{pim}	0.021 (0.565)	0.019 (0.976)
<i>R</i> _{merge}	0.050 (1.393)	0.049 (2.384)
<i>I</i> / <i>σI</i>	15.0 (1.2)	12.8 (0.7)
<i>CC</i> _{1/2}	0.999 (0.559)	0.999 (0.429)
Completeness (%)	99.8 (99.9)	99.6 (99.6)
Redundancy	6.6 (6.8)	6.9 (6.9)
<i>R</i> _{merge} *	0.049 (1.049)	0.041 (0.691)
<i>I</i> / <i>σI</i> *	15.8 (1.6)	20.3 (3.4)
<i>CC</i> _{1/2} *	0.999 (0.610)	0.999 (0.820)
Completeness (%)*	94.9 (50.6)	61.5 (15.6)
Refinement		
Resolution (Å)	56.43 - 1.48 (1.52 - 1.48)	36.9 - 1.9 (2.04 - 1.9)
No. reflections	14159 (430)	6522 (384)
<i>R</i> _{work} / <i>R</i> _{free}	21.27/21.66	23.34/24.36
No. non-hydrogen atoms		
Protein	506	551
Ligand/ion	10	38
Water	56	28
<i>B</i> -factors		
Protein	35.8	52.0
Ligand/ion	21.2	86.0
Water	48.0	71.6
R.m.s. deviations		
Bond lengths (Å)	0.008	0.008
Bond angles (°)	0.94	0.88
PDBID	????	????

Values in parentheses are for highest-resolution shell.

Dataset from one single crystal used per structure.

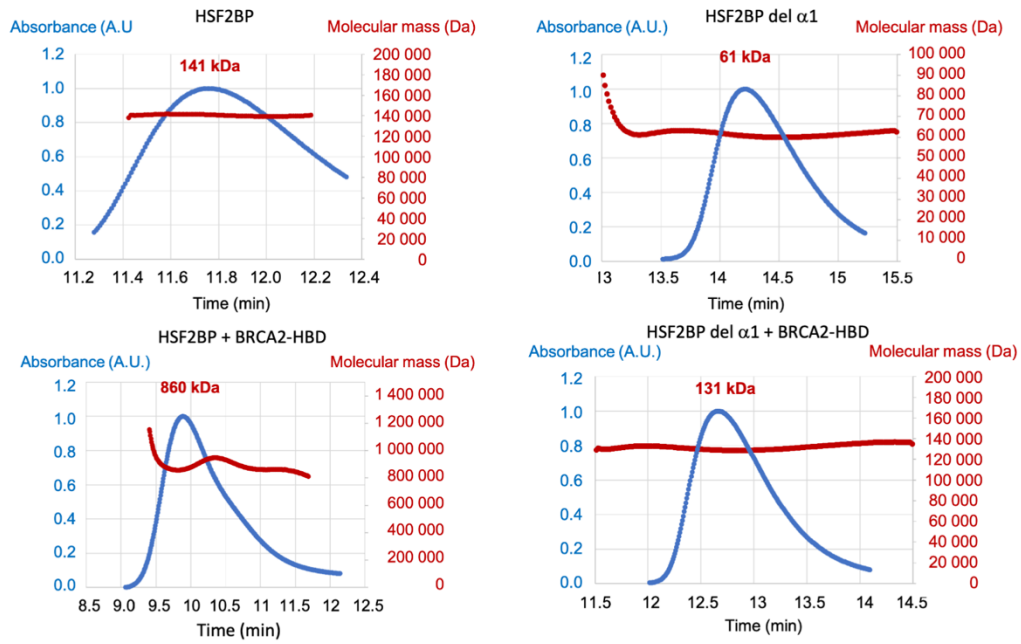
*Values calculated after truncation by STARANISO. Estimated resolution limits along the three crystallographic directions *a**, *b**, *c**.

Supplementary Figures and Tables

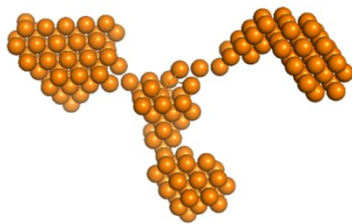
Supplementary table 1. Cryo-EM data collection, refinement and validation statistics

	#1 name (EMDB-xxxx)
Data collection and processing	
Voltage (kV)	300
Electron exposure (e-/Å ²)	40
Defocus range (μm)	-0.6-2.5
Pixel size (Å)	0.85
Symmetry imposed	D3
Initial particle images (no.)	312 000
Final particle images (no.)	118 000
Map resolution (Å)	4.3
FSC threshold	0.143
Map resolution range (Å)	4-11

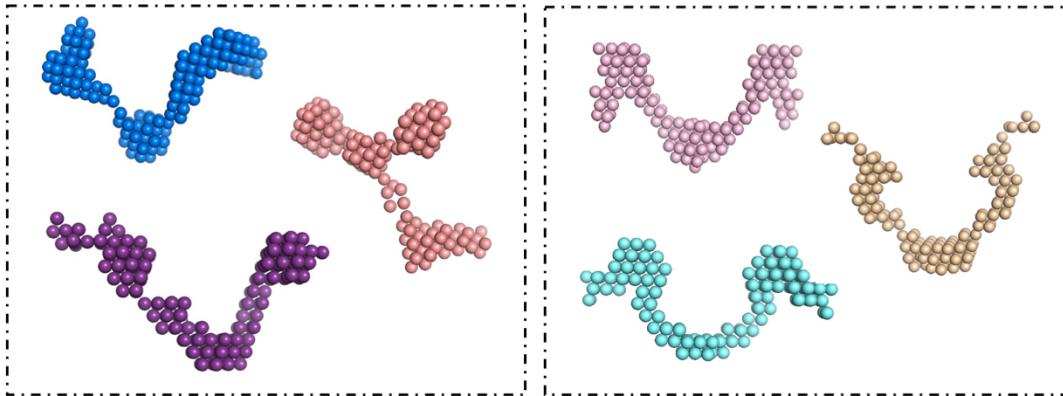
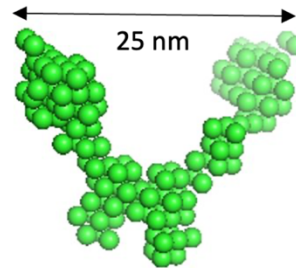
A



B

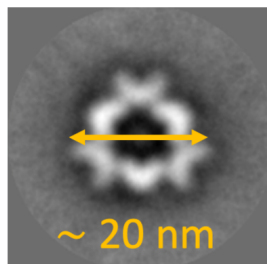


C



Suppl. Figure 1. Extended data for the SEC-MALS and SEC-SAXS analyses shown in Figure 1. (A) SEC-MALS analyses performed on a BioSec 3 with a flow rate of 200 μ l/min. HSF2BP either full-length or deleted from helix $\alpha 1$ (HSF2BP fragment from G48 to V334) was characterized either free or bound to BRCA2-HBD. The measured molecular masses revealed that the HSF2BP mutant is dimeric (theoretical mass of the dimer: 64 kDa) and assembles as a tetramer when bound to BRCA2-HBD (theoretical mass of the 4:2 complex: 142 kDa). (B,C) Models of full-length HSF2BP calculated using the program DAMMIF from SEC-SAXS data. (B) Models calculated without making any hypothesis on the symmetry of the complex. (C) Models calculated by hypothesizing that the complex has a 2-fold symmetry, as it is formed from two dimers. In both cases, 10 models were calculated. The upper panels show the average models. The lower panels display three representative models.

A



B

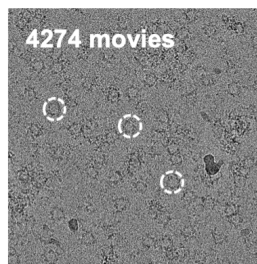


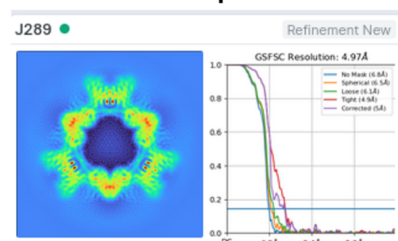
Image inspection:
2982 images with CTF fit res < 8 Å

Manual picking: 3363 particles

2D classes, template picking, 2D
classification, 4 *ab initio* volumes

Heterogeneous refinement
Best class:
312 000 particles

Homogeneous refinement
First map at 5 Å



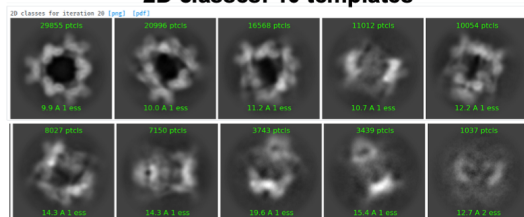
Template Picking
2105 micrographs
with CTF fit resolution < 6 Å

Ab initio calculation of 4 volumes
Heterogeneous refinement
Best class: 153 000 particles

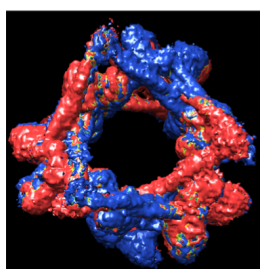
Homogeneous + local refinement:
4.3 Å



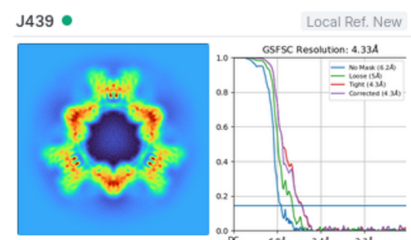
2D classes: 10 templates



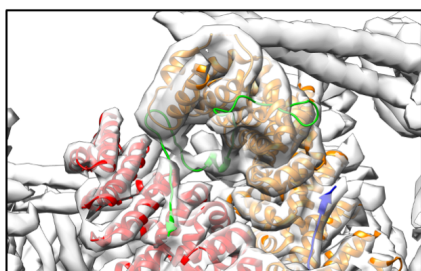
3D variability analysis



Homogeneous + local refinement: 4.3 Å



C

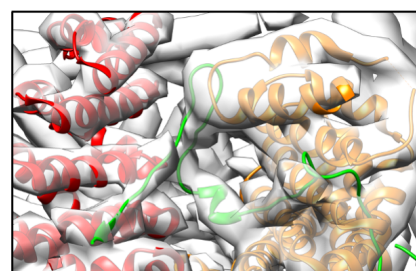


HSF2BP
armadillo dimer 1

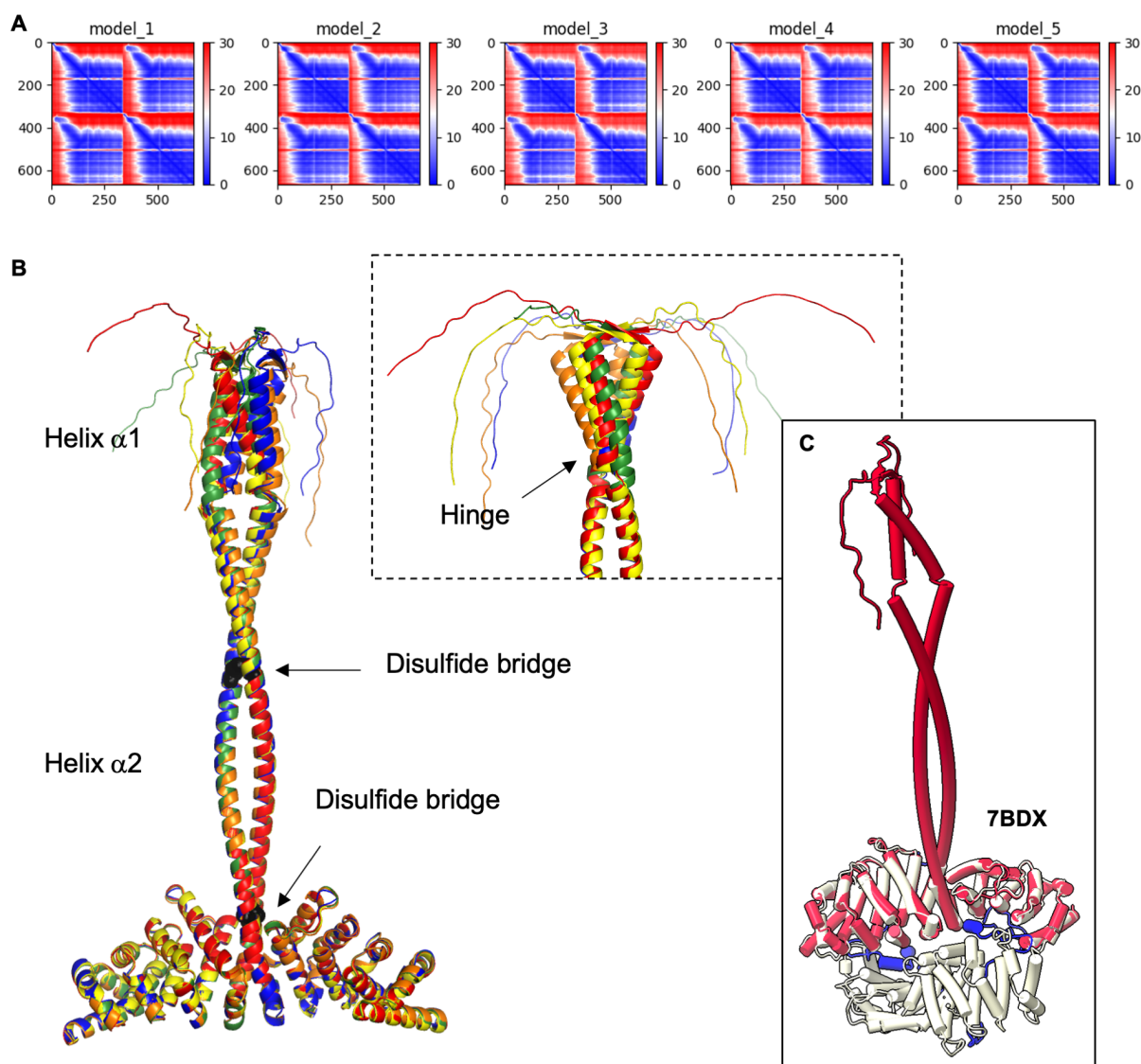
HSF2BP
armadillo dimer 2

BRCA2-HDB

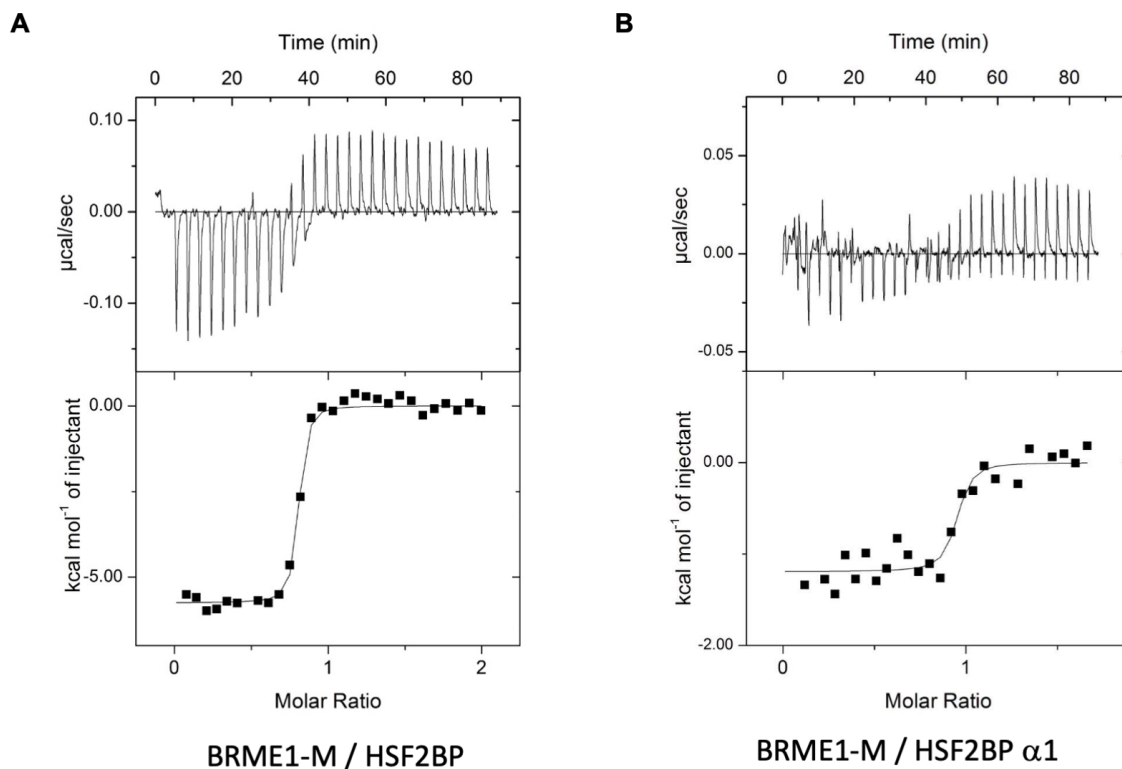
BRCA2-HDB



1 **Suppl. Figure 2. Extended data for the cryo-EM analysis shown in Figure 1. (A) A typical 2D class obtained from**
2 **the analysis of negative-staining images recorded on full-length HSF2BP bound to BRCA2-HBD. (B) Flow chart**
3 **of the processing of the cryo-EM data recorded on HSF2BP bound to BRCA2-HBD.** The whole analysis was
4 performed by CryoSpark. The 3D variability of the complex is illustrated by superimposing two maps (in red and
5 blue, respectively) corresponding to the extreme frames of a series of 20 frames describing the motion of largest
6 amplitude identified by CryoSpark. **(C) Docking of the crystal structure (PDB 7BDX) of the complex formed by**
7 **four armadillo domains of HSF2BP (first and second armadillo dimers in red and orange, respectively) and two**
8 **BRCA2-HBD peptides (in green and blue, respectively) into the cryo-EM map.** Two different zoom views are
9 shown, which highlight that the BRCA2-HBD peptides fit into the cryo-EM map after docking of the HSF2BP
10 armadillo domains.
11



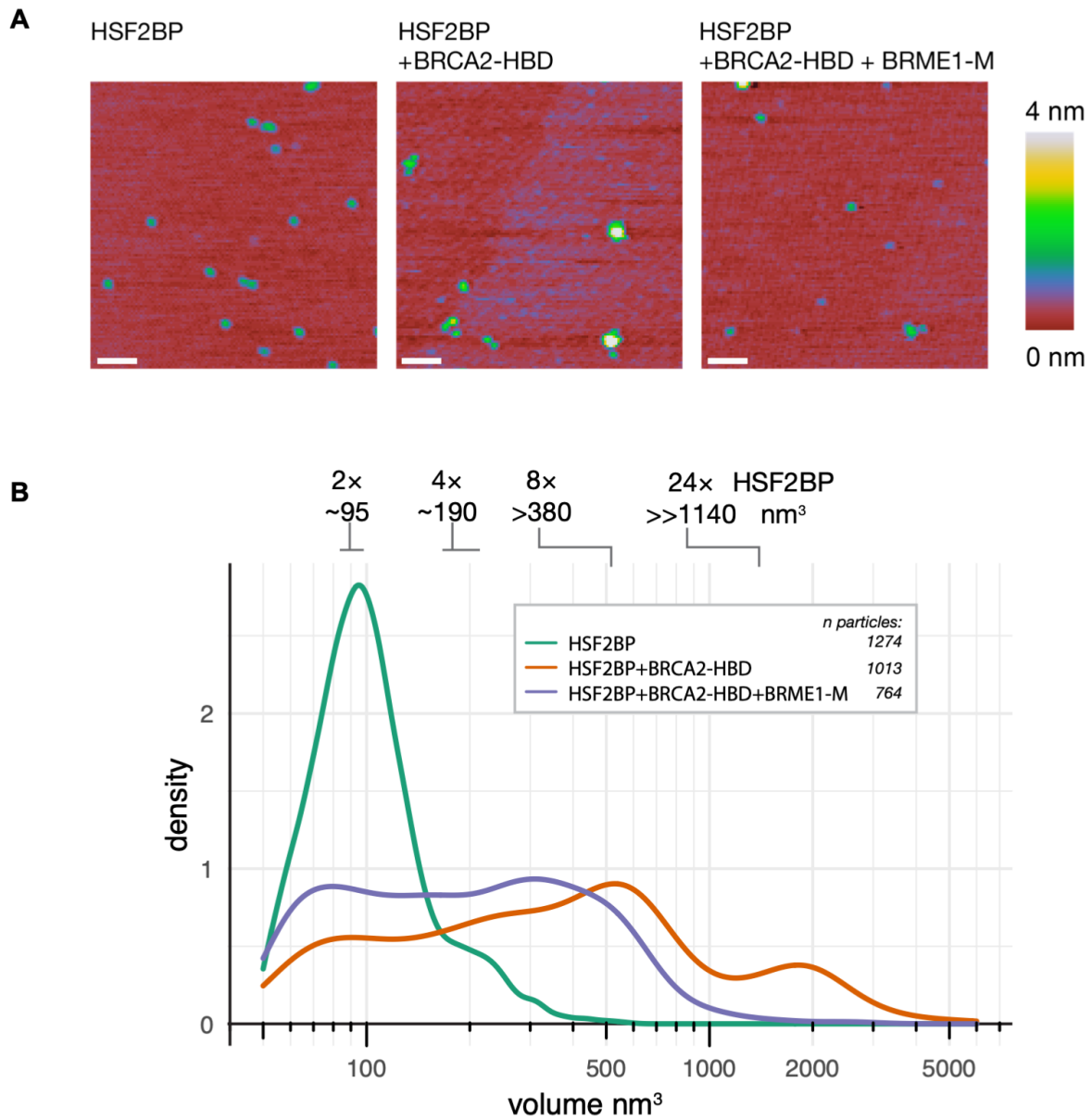
Suppl. Fig. 3. Extended data for the AlphaFold analysis of the HSF2BP dimer presented in Figure 2. (A) Accuracy of the 5 models of the HSF2BP dimer calculated by AlphaFold. Heat map showing the predicted relative position error (in Å) calculated by AlphaFold between all pairs of residues (HSF2BP residues from the first and second monomers are numbered as 1-334 and 335-668, respectively). The blue color observed in regions corresponding to intermolecular distances proves that the relative position of the two monomers is predicted with high confidence. **(B) Cartoon representation of the 5 models calculated by AlphaFold.** Superimposition of these models, each of them being displayed in a different color, shows that they all present the same secondary structure elements. Moreover, their 3D structures are identical, except for the position of the disordered N-terminal region (residues 1 to 19), the b-strand (residues 20 to 24), the first helix $\alpha 1$ (residues 25 to 45) and the loop between $\alpha 1$ and $\alpha 2$ (or hinge; residues 46 to 47), as shown in the main panel and in the zoom view rotated by 90° in the dashed boxed panel. Intermolecular disulfide bridges are displayed in black dots in the main panel. **(C) Superimposition of one of the AlphaFold models of the full-length HSF2BP dimer (in red) and the crystal structure of the complex between two HSF2BP armadillo dimers (white) and two BRCA-HBD peptides (blue) (PDB: 7BDX).**



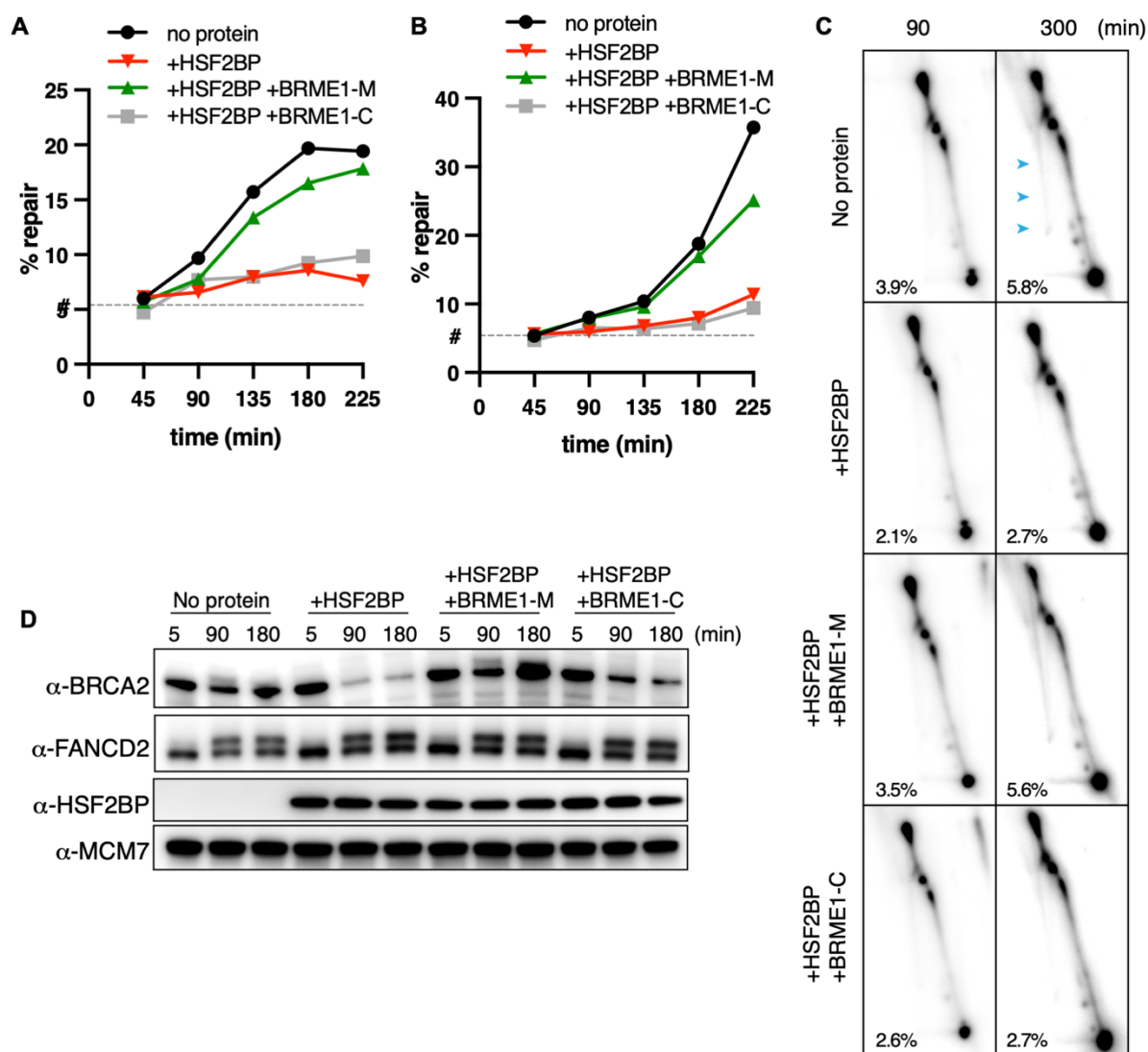
$K_d = 11 \text{ nM}$
 $\Delta H = -5750 \text{ cal/mol}$
 $-T\Delta S = -4843 \text{ cal/mol}$

$K_d = 21 \text{ nM}$
 $\Delta H = -1193 \text{ cal/mol}$
 $-T\Delta S = -9083 \text{ cal/mol}$

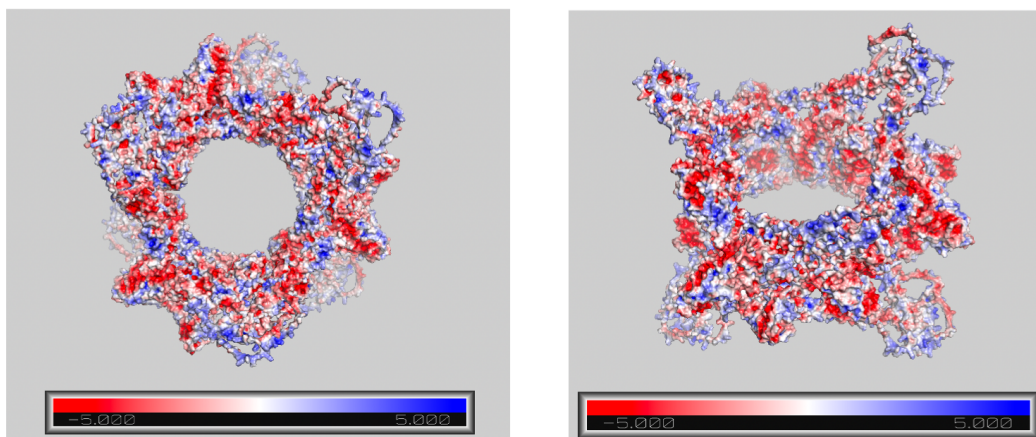
Suppl. Figure 4. Extended data for the Isothermal Titration Calorimetry (ITC) analysis presented in Figure 2D. (A) Binding of BRME1-M to full-length HSF2BP analyzed at 20°C. (B) Binding of BRME1-M to HSF2BP helix α1 analyzed at 20°C. A large decrease of the binding enthalpy is observed when measuring the affinity of BRME1-M against full length HSF2BP versus helix α1. Such a decrease is not observed at 30°C, as shown in Figure 2D. All these data are summarized in Table 2.



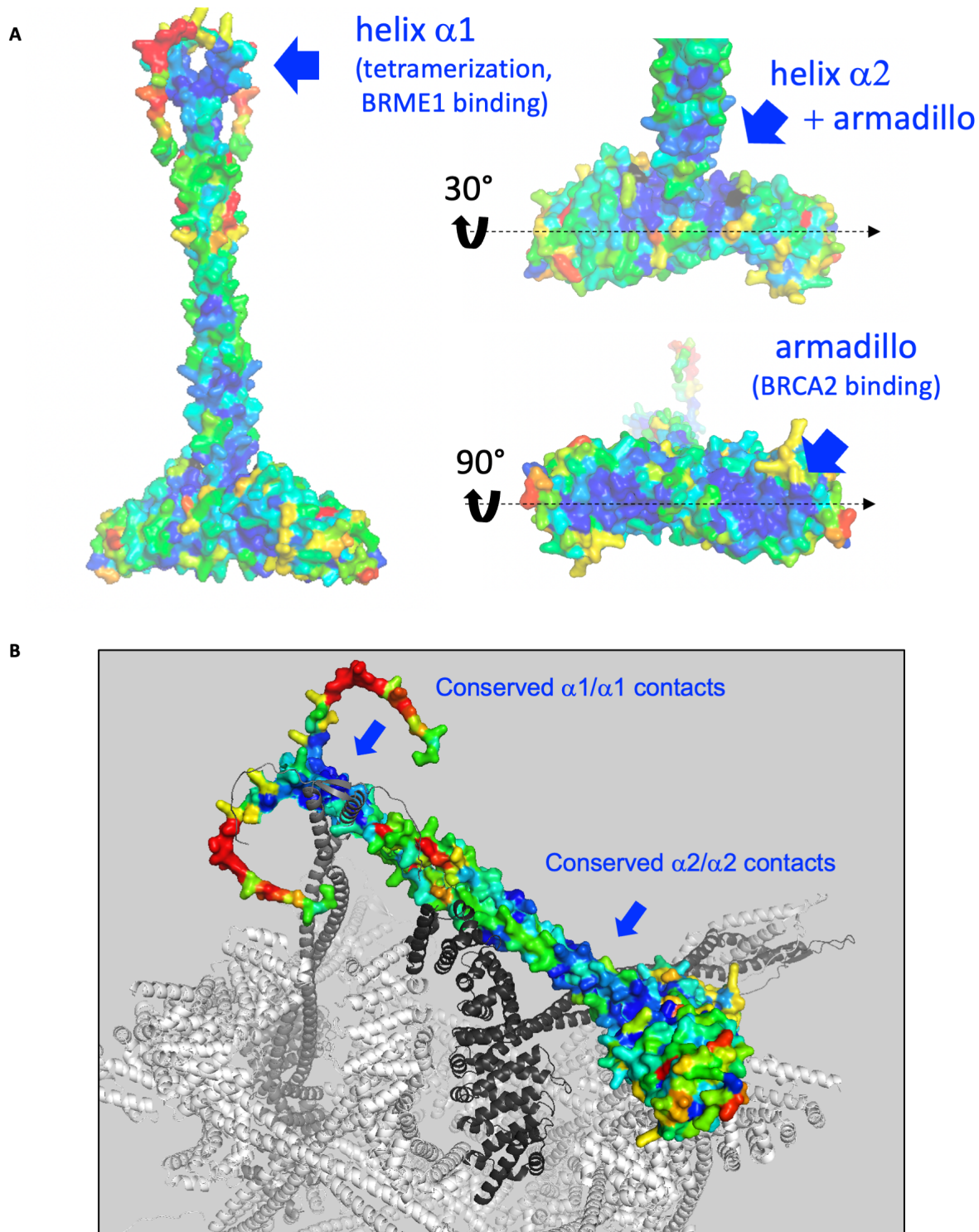
Suppl. Figure 5. Replicates and extended data for SFM experiments shown in Figure 3B,C. (A) Representative SFM scan images. Scale bar = 100 nm. **(B)** Density of volumes distributions of the HSF2BP-ARM dimers and HSF2BP+BRCA2-HBD complexes prepared following the protocol used for cryo-EM.



Suppl. Figure 6. Replicas of the *Xenopus* egg extract experiments shown in Figure 4. (A,B) Replicates of the cisplatin crosslink repair assay shown in Figure 4F. **(C)** Replicate of the 2D gel electrophoresis of HR intermediates shown in Figure 4G. **(D)** Replicate of the immunoblot experiment shown in Figure 4H.



Suppl. Figure 7. Analysis of the electrostatic potential at the surface of a 3D model of the complex formed by 24 HSF2BP molecules, as shown in Figure 2A. This surface is colored from red (negatively charged) to blue (positively charged). It is mainly negatively charged. The figure was obtained using Pymol 2.5.2.



Suppl. Figure 8. Analysis of the conservation of HSF2BP. (A) Different views of the surface of the HSF2BP dimer, as modeled by AlphaFold. This surface is colored as a function of the conservation of the residues in HSF2BP homologs, from red (non-conserved) to blue (strictly conserved) (conservation scores calculated using Consurf: <https://consurf.tau.ac.il>; Glaser et al., 2003). Three conserved patches are identified: one patch on helix $\alpha 1$; one patch on the armadillo domain and helix $\alpha 2$; one patch on the armadillo domain, at the interface with BRCA2. **(B) Interaction of one HSF2BP dimer, displayed as in (A), with the other HSF2BP dimers in the HSF2BP-BRCA2 model.** The other HSF2BP dimers are displayed in gray. Two of them, which contact the N-terminal coiled-coil region of the colored dimer, are colored in two different dark grays. The interdimeric contacts are conserved at the $\alpha 1/\alpha 1$ and $\alpha 2/\alpha 2$ interfaces. All these figures were obtained using Pymol 2.5.2.

Chapter 3. Characterization of the interaction between BRCA2-HSF2PB and BRME1

I. Preamble

In a second study of my PhD project, I aimed at describing how BRME1, another meiotic partner of HSF2BP, interacts with the HSF2BP-BRCA2 complex. To this end, together with Dr. S. Miron, I performed ITC, SEC-MALS, and electron microscopy to try to characterize the ternary complex. The main results of this study are described in a recent article submitted to *Nature Structural and Molecular Biology*.

As shown in the previous chapter, we obtained a cryo-EM model of the complex between full-length HSF2BP and BRCA2-HBD, which allows us to fit the densities of full-length HSF2BP bound to BRCA2-HBD that forms a 24:12 complex. Also, I knew from a recent publication ([Zhang et al., 2020](#)) that the N-terminal region of HSF2BP composed of helices $\alpha 1$ and $\alpha 2$ directly interacts with the C-terminal of BRME1. These authors proposed that BRME1 functions as a stabilizer of HSF2BP by binding to its N-terminal coiled-coil domain, which is aggregation prone but is stabilized as a 2:2 stoichiometric heterocomplex in the presence of BRME1 ([Zhang et al., 2022](#)).

Here, we focused on this interaction, and used different BRME1 peptides (synthesized peptides ordered from Genecust), in order to identify the smallest BRME1 fragment sufficient to bind to HSF2BP. We found that BRME1-M, corresponding to residues 602 to 641, bound to HSF2BP with an affinity of 18 nM. We then characterized the interaction between fragments of HSF2BP and BRME1 using X-ray crystallography ([Ghouil et al., submitted](#)), but many exploratory experiments were also performed to study full-length HSF2BP bound to BRME1.

First, using gel filtration chromatography, we could not co-elute the complex between full-length HSF2BP and BRME1-M in large quantities as it was highly unstable and precipitating. Still, co-elution of HSF2BP and BRME1-M indicated complex formation (**Figure 50**). In fact,

these proteins have very different isoelectric points (IP of HSF2BP: 5.43; IP of BRME1-M:10), therefore it is difficult to find a pH to form the complex without precipitation. With the help of the biophysics platform of the Institut Pasteur we could monitor complex aggregation and stability as a function of the temperature in different buffers using nanoDSF and DLS. The optimal condition provided by the platform (pH 9, NaCl 500 mM) did not impede complex aggregation. To characterize the complex, we also tried to crystallize full-length HSF2BP with BRME1-M but no crystals were observed, probably due to the flexibility of the N-terminal part of HSF2BP.

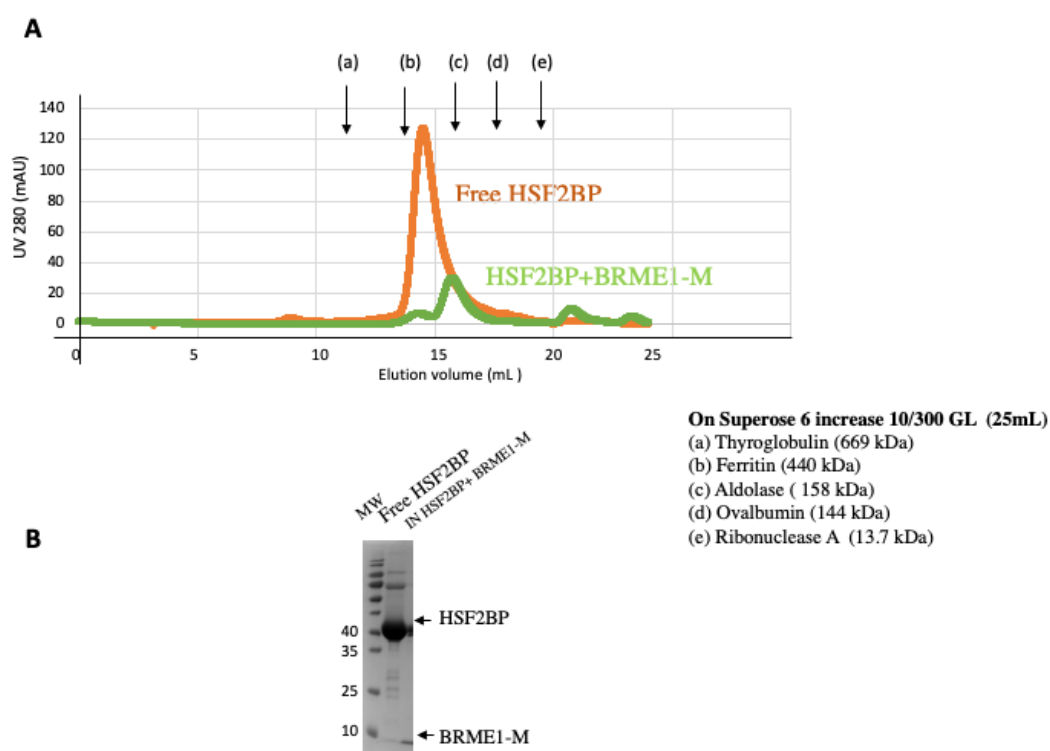


Figure 50. Purification of HSF2BP+BRME1-M.

(A) SEC profile of free HSF2BP and HSF2BP bound to BRME1-M, showing the absorption at 280 nm during elution through a Superose 6 increase in 25 mM Tris HCl pH 7.5, 250 mM NaCl, and 5 mM β me. **(B)** SDS- PAGE gel of fractions corresponding to the eluted free HSF2BP and the loaded fraction of the complex between HSF2BP and BRME1-M on the column (the eluted fractions of the complex were not visible on SDS-PAGE gel due to their weak concentration).

As we could not get crystals of the complex between full-length HSF2BP and BRME1-M, we performed SEC-SAXS on the complex using a fresh mixture of HSF2BP and BRME1 in a ratio of 1:1.5 (**Figure 51A**). The shape of the $P(r)$ suggests a very flexible multi-domain protein

complex (**Figure 51B**). In this case, the molecular weight of the molecule was deduced as comprised between 96 and 116 kDa, which suggests that HSF2BP bound to BRME1-M is a dimer. However, this experiment needed to be confirmed, as the low concentration of the complex in the SEC elution prevented an accurate estimation of its mass.

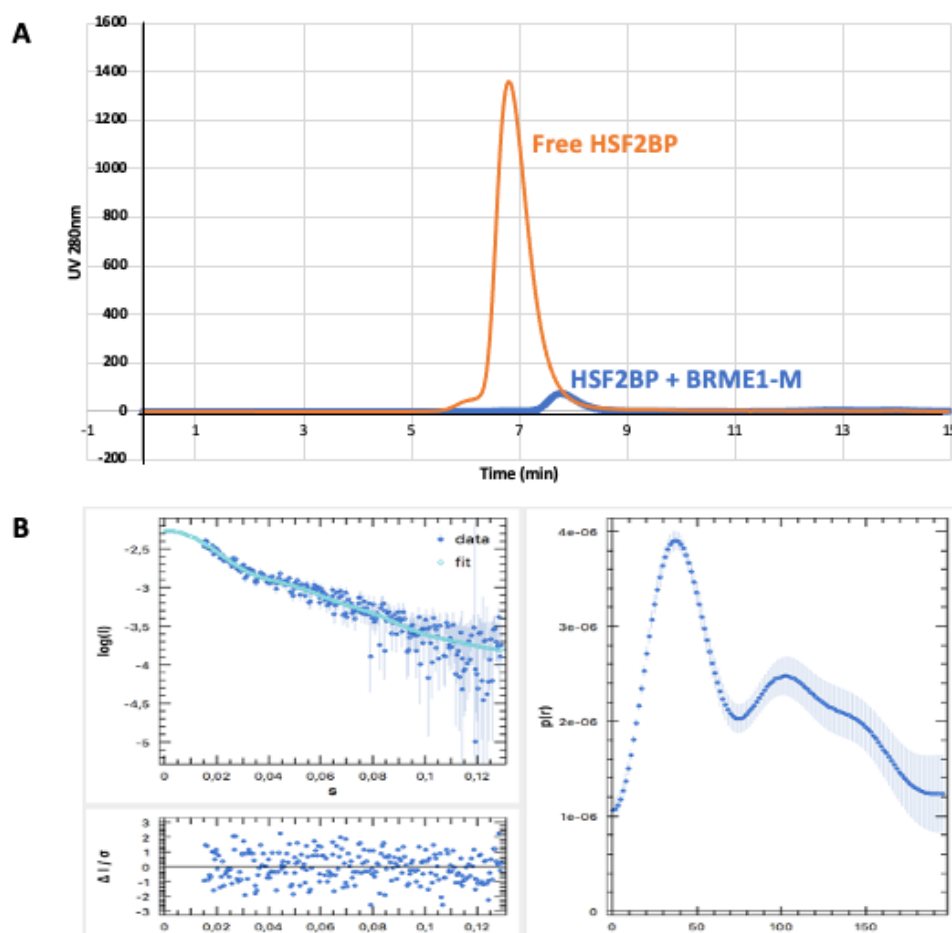


Figure 51. SEC-SAXS experiment performed on the HSF2BP-BRME1-M complex.

(A) SEC elution profiles of HSF2BP-BRME1-M compared to free HSF2BP, as recorded during the SEC-SAXS experiments on the SWING beamline (synchrotron SOLEIL). **(B)** Distance distribution $P(r)$, which displays a characteristic curve of a multidomain complex.

Dr. S. Miron, optimized the protocol used to obtain a concentrated sample of the complex and performed a SEC-MALS experiment at Synchrotron SOLEIL with the help of Dr G. David. She confirmed that tetrameric HSF2BP becomes a dimer after binding to BRME1-M (**Figure 52**). This recent data is consistent with the molecular mechanisms discussed in Ghouil et al., submitted.

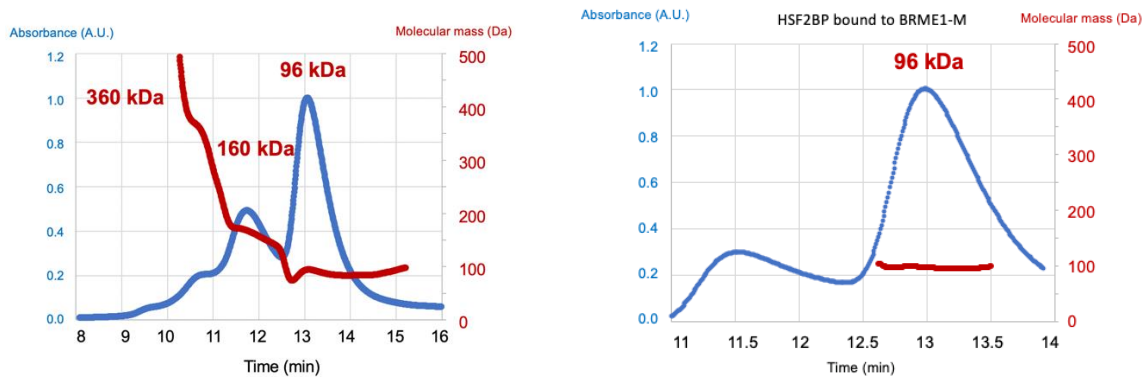


Figure 52. SEC-MALS of the HSF2BP-BRME1-M complex.

(Left) SEC-MALS profile of the elution. Three peaks were observed, which could correspond to 1- a mix of HSF2BP oligomers, 2- a tetramer of HSF2BP (160 kDa, close to 4×37 kDa), 3- a dimer of HSF2BP bound to two BRME1-M (96 kDa, close to $2 \times (37 + 4)$). **(Right)** Zoom on the peak of the complex.

Chapter 4. Characterization of the interaction between HSF2BP and SPATA22

Preamble

In this last part, I show the preliminary results of a third project that I initiated during my PhD, focused on the interaction between the HSF2BP-BRCA2-BRME1 complex and SPATA22. Indeed, HSF2BP interacts by coimmunoprecipitation with two other meiotic-specific partners, SPATA22 and MEIOB, in mice testis extracts ([Takemoto et al., 2020](#); [Zhang et al., 2020](#)). Moreover, it was shown in a large-scale yeast 2-hybrid study that HSF2BP interacts with SPATA22 ([Luck et al., 2020](#)). Our hypothesis is that the SPATA22/MEIOB complex acts as a recruiter of HSF2BP, which then promotes the unloading of the complex from single-stranded DNA. BRCA2 would then load the recombinases onto the DNA.

The aim was to explore the possibility of a direct interaction between the armadillo domain of HSF2BP and the SPATA22 protein and determine the three-dimensional structure of this complex (**Figure 53A**). The first structural description of SPATA22 was made by Ribeiro et al., 2021, who proposed a model of the complex between full-length MEIOB, the folded C-terminal OB domain of SPATA22 (SPATA22OB), and ssDNA (**Figure 53B, left panel**). However, SPATA22 has an N-terminal disordered region that was not modeled in this publication, and armadillo domains generally bind to disordered proteins (**Figure 53B, right panel**). We hypothesized that this N-terminal region binds to the armadillo domain of HSF2BP, and even found a weak homology between the conserved patch detected in the N-terminal region of SPATA22 and the BRCA2 motifs binding to HSF2BP (**Figure 53C**).

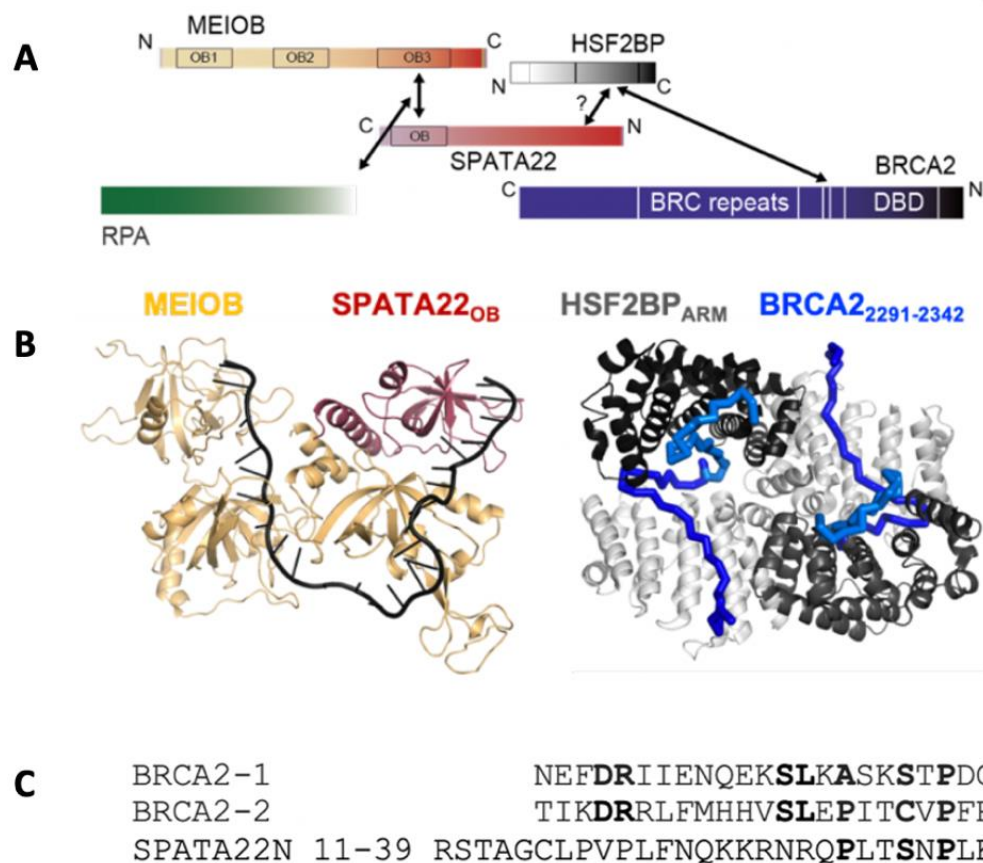


Figure 53. *In vitro* preliminary data on the interaction between HSF2BP and SPATA22.

(A) A network of protein-protein interactions regulating the formation of the synaptic filament in meiosis (adapted from Ribeiro et al., 2021). (B) 3D structures of complexes from this network. On the left, a model of the complex between MEIOB (in yellow), the folded C-terminal OB domain of SPATA22 (SPATA22_{OB}, in red) and ssDNA (in black) is displayed (Ribeiro et al., 2021). On the right, the solved crystal structure of the dimeric armadillo domain of HSF2BP (HSF2BP_{ARM} in grey) bound to a 51-aa BRCA2 fragment (motifs 1 and 2 in light and dark blue, respectively) is presented (Ghouil et al., 2021). (C) Sequence alignment of the BRCA2 fragment responsible for binding to HSF2BP (BRCA2-1 and -2, each able to bind to one armadillo domain) and the N-terminal region of SPATA22. Bolded residues correspond to the BRCA2 repeated motif binding to HSF2BP armadillo domain (Ghouil et al., 2021). These three sequences are all strongly evolutionary conserved.

1. Gel filtration chromatography

I first produced and purified two SPATA22 constructs of different lengths called SPATA22 long (1-238) and SPATA22 short (1-131), both containing the evolutionary conserved patch between R11 and D39 presented in **Figure 53C**. Then, I tested by SEC their binding to HSF2BP and/or its armadillo domain (**Figure 54A**). I noticed that the SPATA22 constructs were not stable and were rapidly degraded (**Figure 54B**). Also, SEC experiments performed on the complexes were not conclusive as free SPATA22 long and free H3 were eluting at the same volume (**Figure 54A,C**).

NMR was used to identify SPATA22 residues binding to HSF2BP. However, as the NMR experiments were recorded during several days, protein degradation was observed that hindered analysis of the spectra.

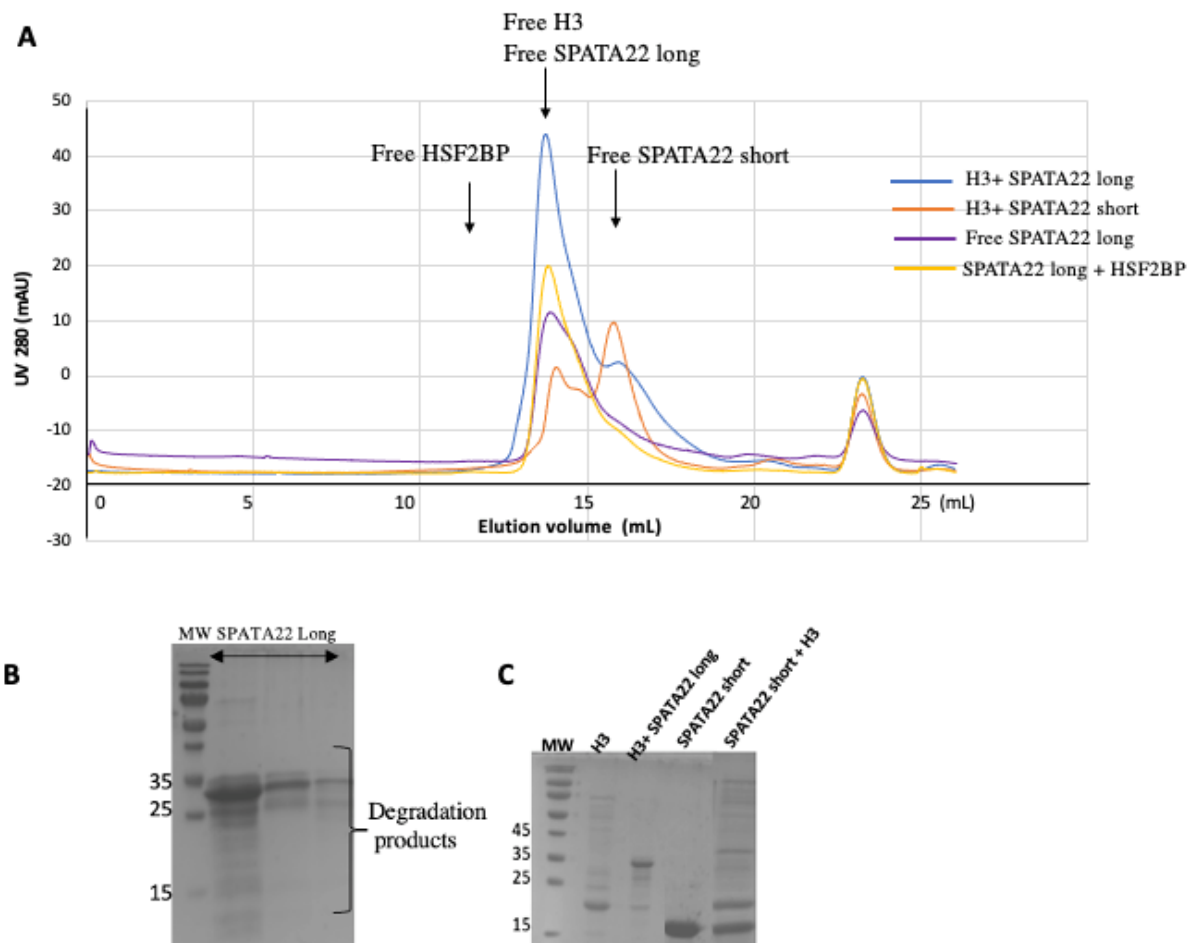


Figure 54. Analysis of the interaction between SPATA22 and HSF2BP/H3 by SEC.

(A) SEC profiles of H3/SPATA22short, H3/SPATA22long and HSF2BP/SPATA22long, showing the absorption at 280 nm after elution through a Superdex increase 200, in 25 mM Tris HCl pH 7.5, 250 mM NaCl, and 5 mM β me; the elution volume of the free proteins on the same column are indicated by black arrows. (B) SDS- PAGE gel of fractions corresponding to the purification of free SPATA22 long by SEC, showing the degradation products (lines correspond to MW in kDa and three fractions collected at the elution volume of the protein, around 14 mL). (C) SDS- PAGE gel of fractions corresponding to the different purifications performed in (A).

2. AlphaFold

Using AlphaFold Multimer (Evans et al., 2022), Dr. P. Legrand calculated models of the complexes between the armadillo domain of HSF2BP and several SPATA22 fragments. All the models converged towards one single 3D structure predicted with confidence (Figure 55). This structure showed that SPATA22N interacts with the armadillo domain of HSF2BP and competes with the C-terminal part of the BRCA2 HBD motifs for HSF2BP binding. In fact, the fragment from R27 to P36 of SPATA22 is located as the fragment from V2325 to P2334 in BRCA2 (Figure 55B), consistently with the sequence alignment shown in Figure 53C.

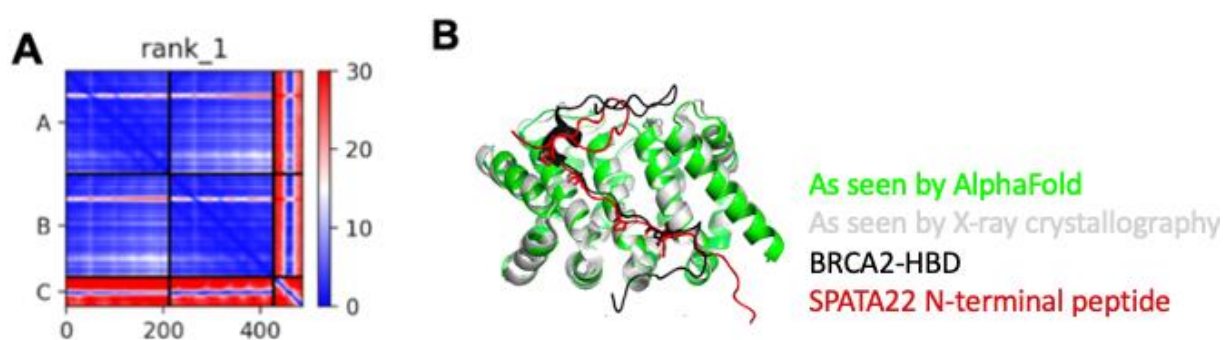


Figure 55. AlphaFold model of the complex between SPATA22 and H3.

(A) Representation of the error made by AlphaFold when positioning SPATA22 relatively to H3. On the x and y axes, HSF2BP armadillo residues are numbered as 1-213 (monomer A) and 214-426 (monomer B); SPATA22 residues are numbered as 427-486. The heat map showing the predicted relative position error (in Å) is blue at the position (x,y) when the distance between

residues x and y is predicted with an error of 0 Å, and red when this error is 30 Å (as shown on the scale bar). Here, this map indicates that the SPATA22 motif is positioned with high confidence at the surface of HSF2BP armadillo domain. **(B)** Superposition of the model calculated by AlphaFold Multimer for the armadillo domain (green) linked to SPATA22N (red) and the experimental structure obtained for the armadillo domain (grey) linked to one of the BRCA2 motifs (black).

3. Thermal stability of the armadillo domain in the presence of SPATA22

Guided by the AlphaFold Multimer predictions, we tested binding between HSF2BP as well as its H3 and H2 domains and different fragments of chemically synthesized peptides of SPATA22. Here I will show the results obtained with the peptide SPATA22N, from R11 to D39 (**Figure 53C**). The possibility of an interaction between the armadillo domain of HSF2BP and this peptide was first explored by measuring the thermal stability of the complex. The instrument named "Tycho" by Nanotemper allows fluorescence monitoring of protein unfolding by measuring the fluorescence signal of tryptophan and tyrosine residues during thermal denaturation of the protein. This signal depends on the environment of the aromatic residues; their progressive exposure to the solvent during protein unfolding is monitored, allowing the calculation of the inflection temperature of the process (or denaturation temperature). The SPATA22N peptide has no tryptophan or tyrosine residues. The measurement of the denaturation temperature of the H2 construct was compared to that of the H2/SPATA22 and H2/BRCA2-HBD complexes. The H2/BRCA2-HBD complex serves as a control because the interaction between the armadillo domain of HSF2BP and this BRCA2 fragment has been studied. Fluorescence measurements were performed in three buffers to test the effect of sodium chloride and Mg^{2+} ion concentration on the interactions (**Figure 56**).

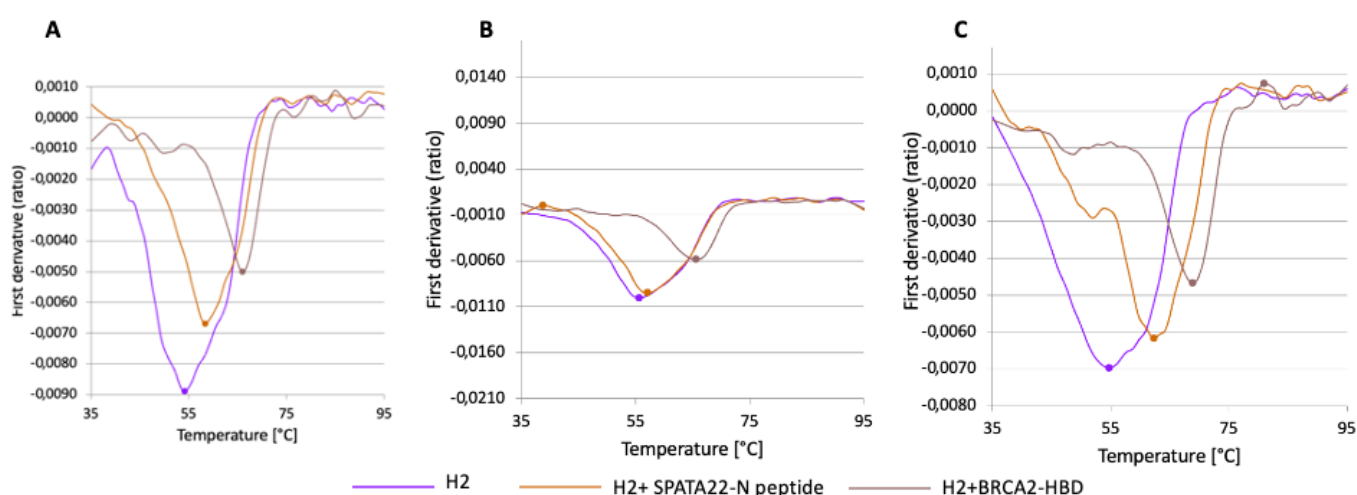


Figure 56. Thermal stability assays performed on the HSF2BP armadillo domain in the presence of SPATA22N.

First derivatives of fluorescence curves are displayed. These curves were measured with a Tycho (Nanotemper) on the armadillo domain alone (H2, purple), in the presence of BRCA2-HBD (brown), and in the presence of SPATA22N (orange) in 3 buffer conditions: (A) in 25 mM Tris-HCl pH 7.5, 5 mM β me **250 mM NaCl**. (B) in 25 mM Tris-HCl pH 7.5, 5 mM β me, 250 mM NaCl, **5 mM MgCl₂**. (C) in 25 mM Tris-HCl pH 7.5, 5 mM β me, **25 mM NaCl**.

In these experiments, we used the H2 construct instead of H3 because it was found to be easier to concentrate and freeze. It has a denaturation temperature of 54.2°C, versus 42.1°C for H3. It was chosen to carry out the manipulations for the characterization of the HSF2BP/SPATA22 interaction. Thermal denaturation measurements revealed a large change between the denaturation temperature measured for H2 alone and that of the H2/SPATA22N complex confirming that H2 forms a complex with SPATA22N in our conditions.

4. Isothermal Titration Calorimetry

Isothermal calorimetric titration experiments were carried out using the full-length HSF2BP or its armadillo domain together with SPATA22long, SPATA22short or the SPATA22 N-terminal peptide (SPATA22N).

a. First preliminary tests using H3 and SPATA22short

With the help of Dr. S. Miron, I carried out the first ITC tests with H3 at 30°C. I observed a small binding signal between H3 and SPATA22short or SPATA22 long respectively. (**Figure 57, Figure 58**). I could not reproduce this result because of protein degradation. Based on the AlphaFold results, we decided to use a synthetic SPATA22 peptide instead of larger recombinant peptides that are more difficult to work with.

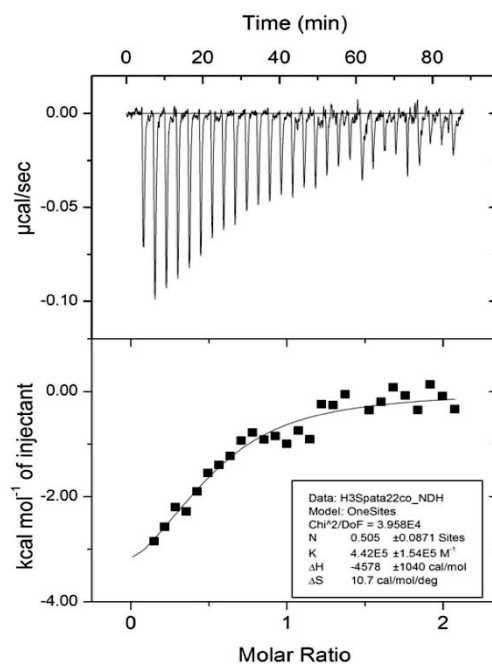


Figure 57. ITC measurement of the interaction between H3 and SPATA22short.

H3 and SPATA22short were both in 25 mM Tris-HCl pH 7.5, 5 mM β me, 250 mM NaCl.

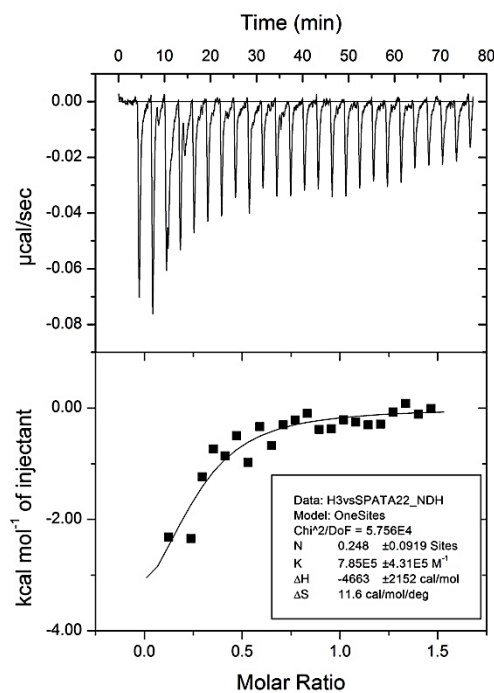


Figure 58. ITC measurement of the interaction between H3 and SPATA22long.

H3 and SPATA22long were both in 25 mM Tris-HCl pH 7.5, 5 mM β me, 250 mM NaCl.

b. Interaction between HSF2BP and SPATA22N at 3 different temperatures

With the help of Dr. Simona Miron, I carried out first ITC tests on HSF2BP binding to SPATA22N at 20°C, but I observed only a weak binding signal. Afterward, I decided to carry out further ITC tests at 10°C and 30°C. Using these experiments, I confirmed that HSF2BP binds to SPATA22N with an affinity of about 0.3 μ M (**Figure 59**).

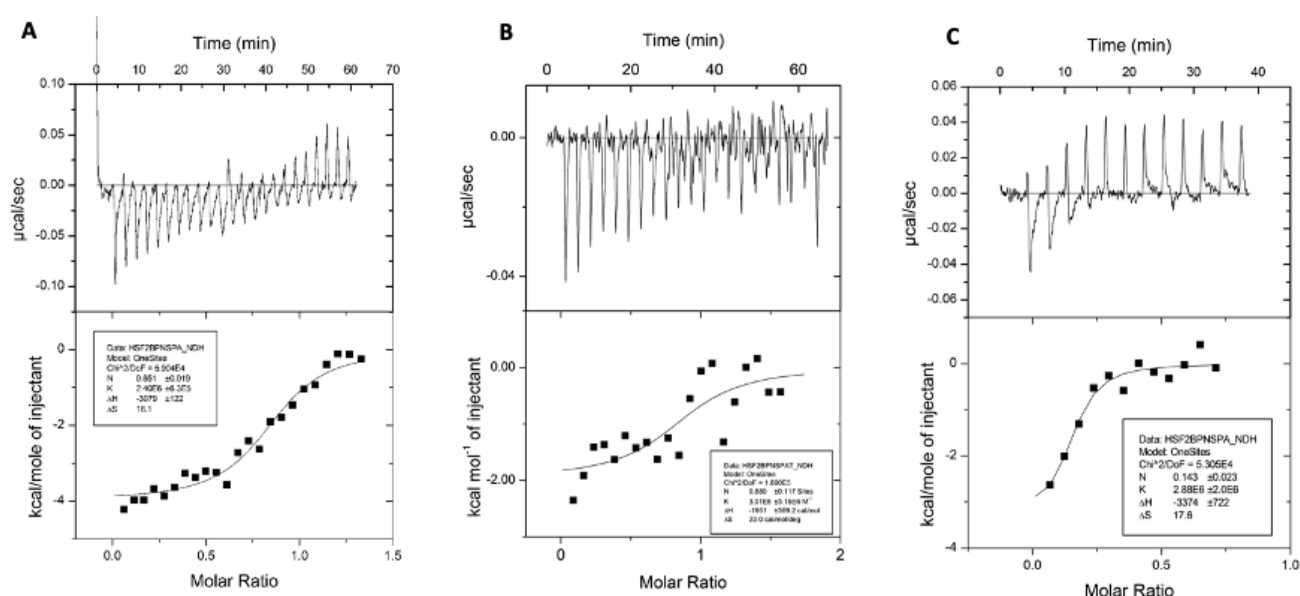


Figure 59. Calorimetry measurements of the interaction between HSF2BP and SPATA22N peptide.

(A) at 30 °C, (B) at 20 °C, and (C) at 10 °C, in 25 mM Tris-HCl pH 7.5, 5 mM βme, 250 mM NaCl.

c. Interaction between H2 and SPATA22N

Further ITC analysis was performed with H2 to characterize its affinity for SPATA22N. These experiments were carried out by Liza Boeffard-Dosierre during her Master 2 internship, with the help of Dr. Simona Miron. Analysis of the ITC curves showed that SPATA22N interacts with H2. The measured stoichiometry varied between 0.4 and 0.7 with an average of 0.6, which suggested that two H2 bind one SPATA22N, and the affinity was on the micromolar range (**Figure 60**).

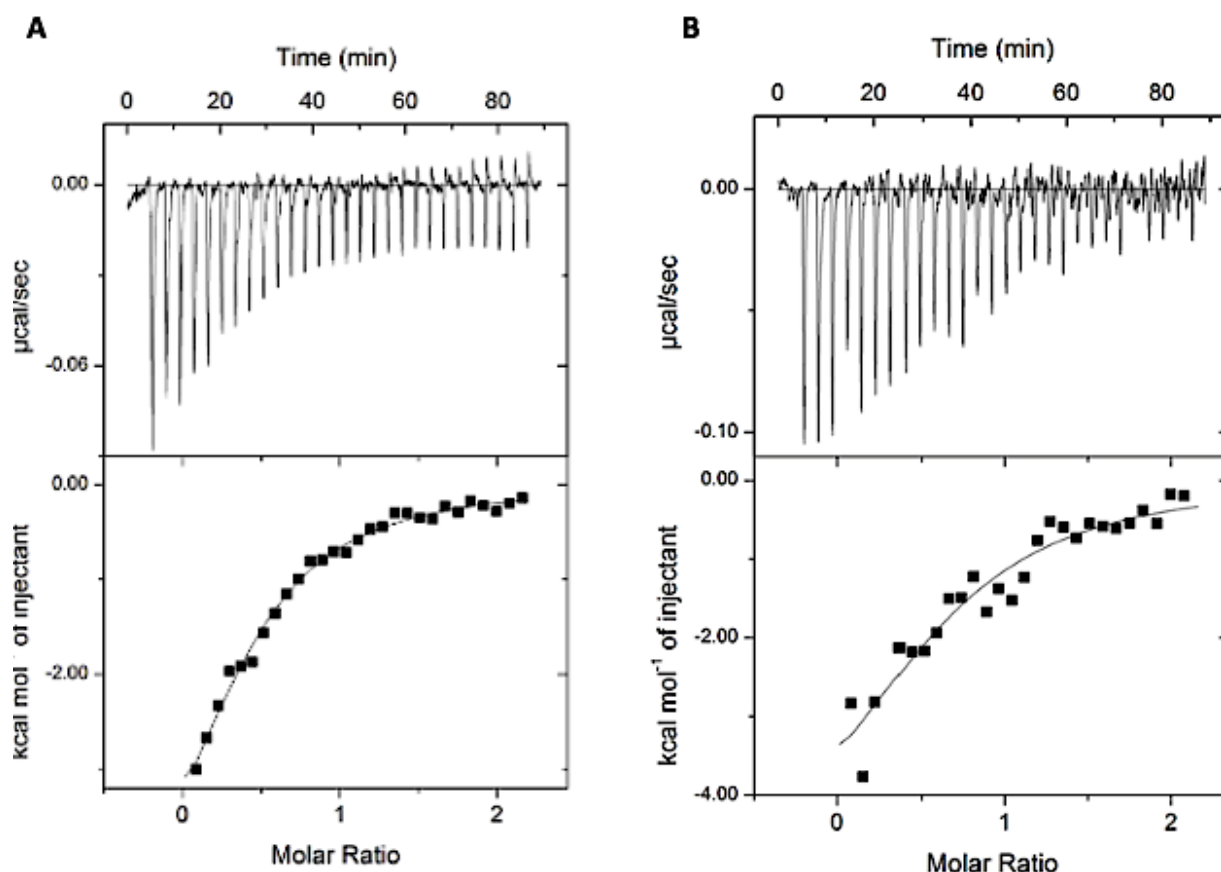


Figure 60. Calorimetry measurements of the interaction between (H2) and SPATA22N peptide.

(A). in 25 mM Tris-HCl pH 7.5, 5 mM β me, 100 mM NaCl. (B). duplicate. All experiments were performed at 20°C.

5. X-ray crystallography

Finally, crystallogenesis tests were conducted on the H3-SPATA22N and H2-SPATA22N complexes by testing a large number of conditions (precipitating agent, salt, concentration, temperature) at the HTX lab in Grenoble. Small crystals formed by H3-SPATA22N were identified and diffraction experiments were performed on these crystals at the ESRF MASSIF1 beamline. Two crystals diffracted anisotropically, diffraction patterns were collected over 360° and data were processed with the XDS software. XDS allows the

diffraction data integration, and XSCALE was used for data scaling and merging. Then, the datasets were processed with the STARANISO program.

The best resolution data were obtained from crystals grown in Sodium potassium phosphate 20 mM PEG3350 20% and Potassium sodium tartrate tetrahydrate 200 mM PEG3350 20%. With STARANISO, the two best datasets got their resolution improved from 9.4 Å to 3.44 Å, with a completeness of 91.9% and in the space group C2. Using COOT, a first electron density map showed the presence of H3 and the SPATA22N peptide. Work is in progress for the refinement of these 2 datasets.

Chapter 5. BRCA2 CTD insect cells

I was often asked whether a BRCA2 fragment larger than F0 could still form a complex with HSF2BP and whether a ring complex could still be observed with these constructs. In the lab, we initiated a side project aiming at producing and crystallizing the human BRCA2 DBD, BRCA2₂₄₄₁₋₃₁₉₇, in a complex with the small acidic protein DSS1. I produced a larger BRCA2 fragment, BRCA2₂₁₅₀₋₃₁₉₇ including the F0 IDR and the DBD, and tried to detect an interaction between this BRCA2 fragment (co-expressed with DSS1) and HSF2BP. Therefore, together with Dr. V. Ropars, I optimized the co-expression of BRCA2₂₁₅₀₋₃₁₉₇ and DSS1 in insect cells and purified the proteins (**Figure 61**).

After purifying BRCA2₂₁₅₀₋₃₁₉₇ and DSS1, electron microscopy experiments were performed in the presence and absence of HSF2BP looking for the formation of a ring-shaped complex. However, I obtained a very small amount of BRCA2₂₁₅₀₋₃₁₉₇ and this fragment was rapidly degraded into BRCA2 DBD. The Negative Staining EM images were noisy and heterogeneous so I could not conclude anything from this analysis.

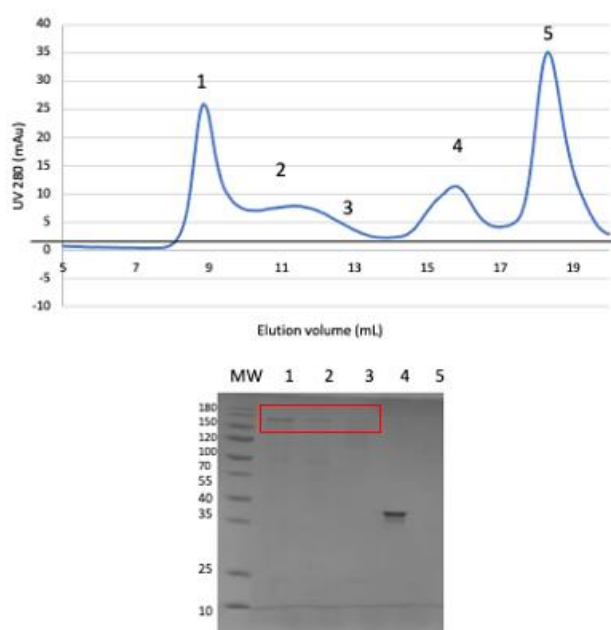


Figure 61. Last step purification of BRCA2₂₁₅₀₋₃₁₉₇.

SEC profile of BRCA2₂₁₅₀₋₃₁₉₇ (absorption at 280 nm) on a Superose 6 increase 10-300 GL in 20 mM Tris HCl pH 8, 150 mM NaCl, and 5 mM DTT. The SDS- PAGE gel of the fractions corresponding to the different eluted peaks is displayed, with line 0=MW (kDa), and lines 1-5=fractions annotated as 1-5 on the SEC profile.

DISCUSSION & PERSPECTIVES

I. About BRCA2 and HSF2BP

Brca2 is one of the most studied cancer predisposition genes. The protein encoded by this gene, BRCA2, is large (more than 3000 amino acids), and is mutated along its entire length in many patients with breast, ovarian, and prostate cancers. It is an essential actor in DNA damage repair by Homologous Recombination (HR), which explains why its inactivation is a source of genetic instability and therefore of cancer. However, it is still a challenge to identify BRCA2 mutations causing cancer in the population. This is critical, as it would significantly improve the follow-up of the women with these mutations in the population.

BRCA2 is also essential for fertility. Indeed, it is required for meiotic recombination. And similarly, variations in BRCA2 sequence might impact male and female fertility. However, BRCA2 residues contributing to meiotic recombination are poorly described, due to the embryonic lethality of *Brca2* KO in animals.

More generally, identifying functional motifs involved in homologous recombination, either in mitosis or in meiosis, is complicated because BRCA2 is mostly disordered: no well-characterized folded domain with known binding properties and/or functions can be detected, apart from its folded DNA binding domain. In the lab, we have focused on disordered and conserved regions of BRCA2, in order to discover their protein partners and reveal how binding to these partners is regulated, especially through phosphorylation. Among these conserved regions, I was interested in the central region encoded by exons 11, 12, 13 and 14, from S2213 to Q2342. This region is able to recruit the meiotic protein HSF2BP, a testis-specific protein, required for meiotic HR during spermatogenesis.

During my thesis, I mainly solved the very original and beautiful structures of BRCA2 fragment F15X bound to either the armadillo domain of HSF2BP or the full-length protein. Our collaborators Dr Alex Zelensky and Prof Roland Kanaar functionally characterized these interactions, both in cells and in mice. I further initiated structural studies in order to understand how the BRCA2-HSF2BP complex interacts with its meiotic partners BRME1 and SPATA22. Finally, I planned to analyze how phosphorylation of the disordered regions of these proteins regulates their binding properties in meiosis. All these points are discussed below.

II. The 3D structure of BRCA2 F15X bound to HSF2BP is original

1. The armadillo domain tetramerizes upon binding to BRCA2 F15X

- (i) Our structural analysis revealed that binding of the armadillo dimer to BRCA2 F15X triggers further oligomerization of this armadillo domain into a tetramer. The armadillo domain of HSF2BP contains four armadillo repeats, which form a charged groove delimited by helices $\alpha 1$, $\alpha 4$, $\alpha 7$, $\alpha 10$, and $\alpha 13$. This groove is able to recognize a 23 aa motif located in a conserved and disordered region of BRCA2. Two of these motifs are present in BRCA2, which wasn't previously recognized from its primary amino acid sequence. Each motif is encoded by its own exon (exons 12 and 13, respectively). Motifs 1 and 2 bind to identical residues in the armadillo domain of HSF2BP. Altogether, binding of these motifs to armadillo monomers triggers the assembly of a 2:4 complex, whose structural arrangement was never observed, at least to my knowledge.
- (ii) During my PhD thesis, several HSF2BP mutations associated to POI were published. Analysis of the crystal structure of the armadillo dimer bound to BRCA2 F15X suggested that two of these mutations, C128R and L186P, destabilize the armadillo dimer, whereas the third mutation S167L impairs interaction of HSF2BP with a yet unknown partner. The next steps of this project are to incorporate these mutations to carry out both structural and functional studies, in order to characterize their impact on complex formation and further on meiotic HR and fertility.

2. How does the armadillo domain specifically recognize the BRCA2 motif and which other proteins contain this motif?

To understand more about armadillo domains, let's summarize what is known about their structural organization. Many armadillo domains interact through their concave surface with

largely disordered partners. They differ much from one another by the number and 3D organization of their armadillo repeats. The intrinsic thermodynamic stability of the individual repeats and the resulting armadillo domain is mediated by interactions between the highly conserved hydrophobic residues within the repeat sequences (Madhurantakam et al., 2012). The resulting elongated scaffold binds its target in extended anti-parallel conformations with very regular binding topologies. A belt of conserved asparagine residues recognizes the main-chain atoms of the peptide, whereas specific pockets between adjacent repeats bind to the peptide side chains (Reichen et al., 2014). Therefore, the armadillo domain is an excellent scaffold for designing modular peptide-binding proteins. In our 3D structure as well, conserved asparagines from HSF2BP are positioned in the armadillo helices to mimic a polypeptide backbone. Their side-chain CO and NH₂ groups bind to the backbone atoms of the unfolded peptide backbone to form β -sheets, as described in Figure 4 from Ghouil et al. (2021). Specific pockets recognize the side chains of the BRCA2 motifs and might be able to recognize other proteins during meiosis.

In the lab, a list of 144 human proteins was created by searching, using the Webserver at <https://www.genome.jp/tools/motif/MOTIF2.html>, for a binding motif to the armadillo domain of HSF2BP inspired by motifs found in BRCA2 and SPATA22: [LR]-x-[AP]-x-[KT]-[SC]-x-P. This list contained a DNA repair protein (PMS1), several kinases (ALPK2, LMTK2, MOK, PINK1), ubiquitin ligases (MIB2, PZR3), a proteasome adaptor (ECM29) and a histone acetyltransferase (KAT6A). However, the binding motif was never detected twice in the same protein, as in BRCA2. By enlarging the definition of the binding motif, Liza Boeffard-Dossier found a meiotic transcription factor (HSF2), a chromatin remodeling protein involved in transcription regulation and DNA repair (INO80) and several ubiquitin ligases (BARD1, RNF169, RNF135), which were also identified by yeast two-hybrid (Luck et al., 2020). AlphaFold calculations performed by Dr Pierre Legrand predicted with high confidence a model for the complex between HSF2BP armadillo domain and the HSF2 motif, as well as HSF2BP armadillo domain and the INO80 motif (in subunit B). These interactions should now be tested experimentally.

The interaction between HSF2BP and HSF2 is particularly interesting to study in light of a very recent work, which revealed that, in plants, HSBP functions as a repressor of *HEI10* transcription and crossover numbers through its binding to heat shock factors (HSFs) (Kim et al., 2022). Indeed, HSBP inhibits HSF activity by direct binding: it forms hexamers

that bind a heptad repeat in HSFs, leading to their dissociation from active HSF trimers to inactive monomers (Morimoto et al., 1998). HSF binds to the *HEI10* promoter. Thus, HSBP represses the transcription of the gene coding for the E3 ligase HEI10, and this restricts the number of meiotic crossovers. This work suggests that the interaction between HSF2BP and HSF2 is essential in meiosis.

The interaction between HSF2BP and INO80 is also interesting to study, as it was reported that mouse INO80 is an essential meiotic factor for spermatogenesis (Serber et al., 2016). INO80 is expressed in developing spermatocytes during the early stages of meiotic prophase I. In *Ino80^{KO}* mice, most spermatocytes were unable to complete meiosis normally. While meiosis appeared to initiate properly, a wide range of synaptic defects quickly become evident, as impaired synapsis of homologous chromosomes, and defective processing of meiosis-associated DNA damage. Altogether, loss of INO80 caused an arrest during meiosis associated with a failure to repair DNA damage during meiotic recombination. Thus, INO80 is an excellent candidate when searching for functionally relevant new partners of HSF2BP in meiosis.

3. HSF2BP forms a ring-shaped complex upon binding to BRCA2

By extending our structural characterization to BRCA2 in complex with the full-length HSF2BP, we observed a ring-shaped 880 kDa hetero-oligomer by cryo-EM, which was supported by SFM and SEC-MALS data. This hetero-oligomer consisted of 24 HSF2BP and 12 BRCA2-HBD molecules organized into three interlocked diamond-shaped octameric ($8 \times \text{HSF2BP} + 4 \times \text{BRCA2-HBD}$) rings, confirming our previous proposal that HSF2BP can act as a polymerization factor for BRCA2. The 3D structure of this hetero-oligomer is remarkable, in that it has a high order of symmetry (D3) and a large inner diameter (about 100 Å), compared to what was observed for other ring-shaped oligomers involved in DNA repair. Moreover, the interfaces between its different components are all conserved, suggesting that it has a biological function in cells. As we did not detect a repeated motif similar to that of BRCA2 in other proteins, we concluded that only BRCA2 is able to trigger the assembly of such a ring-shaped complex. However, by increasing the number of known partners of the armadillo domain of HSF2BP, we should be able to better define the HSF2BP-binding motif, and we might discover new proteins triggering the assembly of HSF2BP oligomers.

III. What is the function of the interaction between BRCA2 and HSF2BP?

To understand the role of the high-affinity complex between BRCA2 and HSF2BP and its impact on meiotic HR and fertility, several *in cell* and *in vivo* experiments were performed:

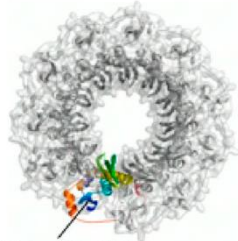
- (i) First, it was essential to validate or not the hypothesis of Shibuya and co-workers, who renamed HSF2BP as MEILB2 for MEIotic Localizer of Brca2, suggesting that MEILB2 localizes BRCA2 to the sites of meiotic DSBs in mice, thus favoring the loading of RAD51 and DMC1 recombinases in spermatocytes, which is essential for male fertility.

Shibuya and co-workers utilized the *in vivo* electroporation technique to inject a DNA coding for GFP-BRCA2 in testis. Thus, they expressed their green fluorescent protein (GFP)-fusion BRCA2 proteins in testis. They showed that BRCA2 localizes to recombination nodule-like foci only in the presence of HSF2BP, and that this localization depends on the HBD region of BRCA2. Moreover, such foci were specific to early prophase I cells, when DSBs are present, and co-localized with endogenous RPA2 signals. From this HSF2BP-dependent localization pattern of BRCA2 in prophase I spermatocytes, they concluded that HSF2BP recruits BRCA2 to meiotic DSBs.

Comparing these results to ours, we found by ITC that HSF2BP does not interact with the short linear ssDNA and dsDNA that we tested. However, we found that it interacts with SPATA22, a ssDNA binding protein that could localize HSF2BP to meiotic ssDNA. Our collaborators further tried to validate that HSF2BP recruits BRCA2 by deleting exon 12 (or exons 12-14) of BRCA2, and testing the impact of the resulting decrease (or lack) of HSF2BP-BRCA2 interaction in cells and in mice. They showed that, in mouse ES cells, deletion of exon 12 abolishes localization of a GFP-tagged HSF2BP protein to mitomycin C-induced foci. In mice expressing BRCA2 deleted from motif 1, no major difference in meiosis was detected: females and males were fertile, males had a normal sperm count and even increased testis sizes. So, we were not able to confirm that HSF2BP is essential to localize BRCA2 to meiotic DSBs. However, HSF2BP might be able to increase BRCA2 concentration at DSB. This regulated event might contribute to the meiotic process. It is not essential for the fertility of our mice, but might be functionally relevant in other contexts.

- (ii) Second, it was interesting to speculate about other functions of the ring-shaped complex.

N-ter Rad52 11-mer



N-ter Rad52 monomer



Therefore, we searched for similar structures in protein-protein interaction networks associated with DNA repair and meiosis. The HSF2BP-BRCA2 ring function can be discussed in light of what is known about the Rad52 ring in yeast. Rad52, a protein found in yeast as well as in mammals, is a mediator of Rad51 filament formation (Symington, 2002) and promotes strand exchange (Bi et al., PNAS 2004). In yeast, it plays 3 distinct roles during recombination: a presynaptic role necessary for Rad51 assembly, a synaptic role with Rad51 filaments, and a postsynaptic role after Rad51 dissociate (Miyazaki et al., 2004). Yeast and mammalian Rad52 form rings (Shinohara et al., 1998; Van Dyck et al. 1998; Stasiak et al., 2000). The assembled Rad52 interacts with ssDNA, which is recruited on the outer surface of the ring (see the figure on the left, adapted from Ma et al., 2021). In yeast, Rad52 stimulates Rad51 loading mostly through its disordered region (containing the RPA and Rad51 binding sites), which has to be coupled to the oligomerization domain, probably to increase the concentration of the disordered region next to the ssDNA (Ma et al., 2021). Thus, it might locally concentrate Rad51, allowing Rad51 filaments to grow efficiently. The Rad52 ring stabilizes Rad51 filaments, possibly through the interaction with Rad51 paralog complexes. Finally, it is sumoylated by the yeast segregase that is homologous to the mammalian p97 segregase (Bergink et al., 2013). Massive sumoylation leads to the dissociation of Rad52 and Rad51 from ssDNA and targets Rad52 for degradation. This might restrict Rad51 levels on ssDNA. Since Rad52 sumoylation is induced by DNA damage, p97 segregase targets SUMO only to Rad52-Rad51 complexes involved in recombination.

From a comparative point of view, we found that the ring structure of RAD52 is 2 times smaller than our complex. However, the BRCA2 fragment could play the role of the C-terminal part of RAD52, which is the unfolded part that interacts with RPA and RAD51. On the other hand, HSF2BP could play the role of the folded N-terminal region of RAD52 that oligomerizes into this ring form. Overall, the idea here is that the HSF2BP-BRCA2 ring may act as a platform that brings in other proteins, and is either sumoylated or

ubiquitinated after DNA damage to be recognized by p97 and get degraded, which would be one way to regulate RAD51 level on ssDNA.

IV. HSF2BP-BRCA2 ring assembly is regulated by BRME1 and SPATA22

In order to understand how the assembly and disassembly of the HSF2BP-BRCA2 complex is regulated, we explored several hypotheses.

- (i) We showed that HSF2BP binds to both BRCA2-HBD and BRME1-M, and that BRME1-M disrupts the ring-shaped complex by interfering with HSF2BP helix $\alpha 1$ tetramerization. Cell biology experiments performed by our collaborators confirmed that BRME1-M is able to interfere with the function of HSF2BP in cancer cells, in which overexpression of HSF2BP leads to BRCA2 degradation. In germinal cells, if BRME1 is present, then the ring-shaped complex should not be able to assemble, and this should impact protein ubiquitinylation in a DNA damage context. During meiosis, ubiquitin is localized on the chromosome axis and regulates the stabilization and degradation of recombination factors to enable the proper occurrence of synapsis, DSB repair, and crossover formation ([Rao et al., 2017](#)). It was reported that loss of BRME1 decreases the amount of HSF2BP foci, and reduced the ubiquitination of the autosomes and XY body in spermatocytes ([Li et al., 2020](#)). Our data suggest that BRME1 regulates the ubiquitination of key meiotic proteins by disrupting the HSF2BP-BRCA2 complex.
- (ii) We proposed that there is a competition between the BRCA2-HBD fragment and the N-terminal peptide of SPATA22 for HSF2BP binding. Indeed, the two peptides have some sequence similarities that suggest that they both bind to the HSF2BP armadillo domain. During meiotic HR, SPATA22 could recruit HSF2BP through its N-terminal region. Then, HSF2BP could interact with ubiquitin ligases, as proposed by yeast two-hybrid ([Luck et al., 2020](#)), and promote dissociation of the MEIOB-SPATA22 complex from ssDNA ([Rao et al., 2017](#)). Once SPATA22 is dissociated

from the DNA, HSF2BP could increase the local concentration of BRCA2 at the DSB to promote the loading of recombinases on ssDNA or further facilitate meiotic homologous recombination.

To support these hypotheses, it would be interesting to test *in vitro*, by ITC or Surface Plasmon Resonance (SPR), if SPATA22N is able to inhibit the assembly of the HSF2BP-BRCA2 ring, or if it is able to disassemble this ring. Given that the affinity of BRCA2-HBD for HSF2BP is on the nanomolar range, whereas the affinity of SPATA22 for HSF2BP is on the micromolar range, we could predict that only BRCA2-HBD can displace SPATA22 (and not the opposite). However, as BRCA2-HBD binding to HSF2BP is mediated by a large number of contact points, involving either motif 1 or motif 2, and characterized micromolar affinities, SPATA22 could displace individually the different interactions between BRCA2 motifs and armadillo domains.

It would also be interesting to test in cells and in a mouse model expressing a SPATA22 protein deleted from the SPATA22N motif, what is the impact of this motif on meiotic HR and fertility: whether SPATA22N triggers the recruitment of HSF2BP at the break, regulates the amount of SPATA22 on ssDNA, and the loading of RAD51 and DMC1 on ssDNA.

V. Can these interactions be regulated by phosphorylation of intrinsically disordered regions in BRCA2, BRME1, and SPATA22?

BRCA2, BRME1, and SPATA22 all exhibit large IDRs, which are the targets of kinases and phosphatases. By analyzing the regions of these proteins involved in protein-protein interactions, I observed that several serine, threonine, and tyrosine residues from the binding motifs are well-conserved, suggesting that a phosphorylation event could disrupt binding. Several kinases regulate the correct execution of meiosis. In particular, the Polo-like kinase (PLK) family phosphorylates a diverse group of substrates to control homolog pairing, synapsis, and meiotic recombination ([Brandt et al., 2021](#)). A few kinases even have testis-

specific splicing variants, as for example the catalytic subunit of PKA and the casein kinase II alpha. Null mice for these enzymes are sterile (Nolan et al., 2004; Xu et al., 1999).



In BRCA2-HBD, I identified S2303 and S2309 in BRCA2 motif 1, and S2326 in BRCA2 motif 2. These residues are potential targets of kinases. S2309 is highly conserved, and its mutation into asparagine abolished binding to HSF2BP (Ghouil et al., 2021). It would be interesting to identify the consequences of phosphorylation of S2309 on HR, meiosis and fertility. In BRME1-C, T605, S616 and T625 are also well-conserved. In SPATA22N, T33 and S34 are both conserved, and S34 is aligned with S2309 from BRCA2 in the HSF2BP binding motif. Here again, the consequences of their phosphorylation in meiosis have not been explored yet.

In summary, HSF2BP is a scaffold protein, which can, through its armadillo domain, recruit a large number of partners. I showed that it binds to the disordered regions of BRCA2 and SPATA22, however, much has to be done to accurately define a HSF2BP-binding motif and enlarge our knowledge of the ligands of the HSF2BP armadillo domain. My study provides new candidates that could be tested, as for example the transcription factor HSF2 and the chromatin remodeller INO80. Several ubiquitin ligases are also described as binding to HSF2BP by yeast two-hybrid experiments, which could contribute to HSF2BP-dependent BRCA2 degradation upon DNA damage. My work identifies potential phosphorylation sites that could regulate binding of HSF2BP to its partners. Even if the kinases phosphorylating these sites are unknown, mutating these sites in cells could give new information about meiotic regulation pathways.

APPENDIX

Review

Intrinsic Disorder and Phosphorylation in BRCA2 Facilitate Tight Regulation of Multiple Conserved Binding Events

Manon Julien ^{1,2}, Rania Ghouil ^{1,2,†}, Ambre Petitalot ^{3,4,†}, Sandrine M. Caputo ^{3,4} , Aura Carreira ^{2,4,5} and Sophie Zinn-Justin ^{1,2,*} 

- ¹ Institute for Integrative Biology of the Cell (I2BC), CEA, CNRS, Université Paris-Sud, 91190 Gif-sur-Yvette, France; Manon.julien@i2bc.paris-saclay.fr (M.J.); rania.ghouil@i2bc.paris-saclay.fr (R.G.)
² L'Institut de Biologie Intégrative de la Cellule (I2BC), UMR 9198, Paris-Saclay University, 91190 Gif-sur-Yvette, France; aura.carreira@curie.fr
³ Service de Génétique, Unité de Génétique Constitutionnelle, Institut Curie, 75005 Paris, France; ambre.petitalot@curie.fr (A.P.); sandrine.caputo@curie.fr (S.M.C.)
⁴ Institut Curie, Paris Sciences Lettres Research University, 75005 Paris, France
⁵ Unité Intégrité du Génome, ARN et Cancer, Institut Curie, CNRS UMR3348, 91405 Orsay, France
* Correspondence: sophie.zinn@cea.fr; Tel.: +33-169083026
† These authors have equally contributed to this review.

Abstract: The maintenance of genome integrity in the cell is an essential process for the accurate transmission of the genetic material. BRCA2 participates in this process at several levels, including DNA repair by homologous recombination, protection of stalled replication forks, and cell division. These activities are regulated and coordinated via cell-cycle dependent modifications. Pathogenic variants in *BRCA2* cause genome instability and are associated with breast and/or ovarian cancers. BRCA2 is a very large protein of 3418 amino acids. Most well-characterized variants causing a strong predisposition to cancer are mutated in the C-terminal 700 residues DNA binding domain of BRCA2. The rest of the BRCA2 protein is predicted to be disordered. Interactions involving intrinsically disordered regions (IDRs) remain difficult to identify both using bioinformatics tools and performing experimental assays. However, the lack of well-structured binding sites provides unique functional opportunities for BRCA2 to bind to a large set of partners in a tightly regulated manner. We here summarize the predictive and experimental arguments that support the presence of disorder in BRCA2. We describe how BRCA2 IDRs mediate self-assembly and binding to partners during DNA double-strand break repair, mitosis, and meiosis. We highlight how phosphorylation by DNA repair and cell-cycle kinases regulate these interactions. We finally discuss the impact of cancer-associated variants on the function of BRCA2 IDRs and more generally on genome stability and cancer risk.

Keywords: disorder; phosphorylation; cancer; DNA repair; mitosis; meiosis; variants; NMR; protein-protein interaction; 3D structure



Citation: Julien, M.; Ghouil, R.; Petitalot, A.; Caputo, S.M.; Carreira, A.; Zinn-Justin, S. Intrinsic Disorder and Phosphorylation in BRCA2 Facilitate Tight Regulation of Multiple Conserved Binding Events. *Biomolecules* **2021**, *11*, 1060. <https://doi.org/10.3390/biom11071060>

Academic Editor: Steffen Graether

Received: 8 June 2021

Accepted: 13 July 2021

Published: 20 July 2021

Publisher's Note: MDPI stays neutral with regard to jurisdictional claims in published maps and institutional affiliations.



Copyright: © 2021 by the authors. Licensee MDPI, Basel, Switzerland. This article is an open access article distributed under the terms and conditions of the Creative Commons Attribution (CC BY) license (<https://creativecommons.org/licenses/by/4.0/>).

1. Introduction

The BRCA2 protein is a ubiquitous protein essential for embryonic development: BRCA2 knockout mice show early embryonic lethality and hypersensitivity to irradiation [1]. Depletion of BRCA2 also causes a wide range of defects in DNA repair and recombination [2], protection of stalled replication forks [3], regulation of telomere length [4,5], mitosis [6,7], meiotic recombination, and fertility [8]. At the molecular level, BRCA2 interacts with the strand exchange (or recombinase) protein RAD51 (for RADiation sensitive protein 51) and facilitates its function in various Homologous Recombination (HR) contexts [1,9–11]. It is essential for RAD51-mediated HR in both mitotic and meiotic cells. A defect in BRCA2 HR function causes genetic instability and increases cancer risk. In addition, BRCA2 has a protective function during replicative fork stalling that is mechanistically distinct from repair by HR [3]. It prevents degradation of nascent strands at stalled forks

by stabilizing RAD51 filaments. BRCA2 variants with compromised fork protection exhibit increased chromosomal aberrations. Finally, during mitosis, BRCA2 inactivation impairs the completion of cell division, thus triggering alterations in chromosome number and abnormalities such as centrosome amplification [6,12]. Biallelic loss-of-function variants in *BRCA2* cause Fanconi's anemia type D1, which is a rare autosomal recessive cancer susceptibility disorder characterized by an increased number of chromosomal breaks after cells are exposed to DNA-damaging agents [13,14]. Pathogenic variants in one *BRCA2* allele confer higher risk of breast and/or ovarian cancers [15–17], as well as pancreatic and prostate cancers [18].

Despite the accumulated knowledge about BRCA2 essential functions, the molecular mechanisms associated with these functions are poorly described. This is in part due to the disordered character of BRCA2, which is examined in this review. Within the 3418 amino acids (aa) of BRCA2, one single domain of 700 residues is folded, as revealed by the analysis of the crystal structure of the mouse and rat homologous domains bound to a single-stranded DNA (ssDNA) and in interaction with the short acidic protein DSS1 (for Deleted in Split hand/Split foot protein 1) [19] (Figure 1A,B). Recently, several groups purified full-length BRCA2 and performed negative-staining electron microscopy, scanning force microscopy and fluorescence based single molecule analyses of this protein either free or bound to RAD51, DSS1, and ssDNA.

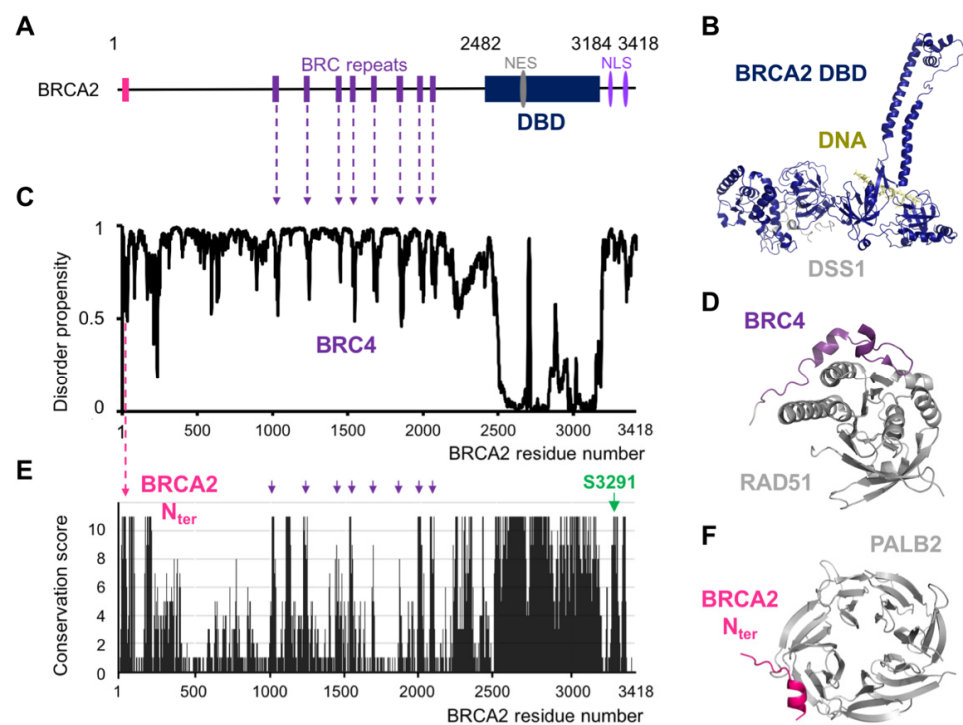


Figure 1. BRCA2 is predicted as mostly disordered, and small conserved motifs fold upon binding. (A) General view of BRCA2 structural organization. The folded DNA-binding domain (DBD) is displayed as a dark blue rectangle. The Nuclear Export Signal (NES) and Nuclear Localization Signal (NLS) are marked in grey and purple, respectively. The PALB2 and recombinase binding motifs are represented as pink and violet bars, respectively. (B) 3D model of the human DBD (dark blue) bound to an 8nt-ssDNA (limon green) and the small acidic protein DSS1 (grey). This model was built by homology based on the mouse DBD 3D structure, referenced as 1MJJE at the PDB; (C) disorder propensity as a function of BRCA2 residue number. This disorder score was calculated using the Webserver SPOT-Disorder2 [20]. Scores of 0 and 1 correspond to ordered and disordered residues, respectively. The position of the BRCA2 motif BRC4 is indicated in violet. (D) 3D structure of BRC4 (violet) bound to the ATPase domain of RAD51 (grey). This cartoon view corresponds to the 3D structure referenced as 1N0W. (E) Conservation of BRCA2 residues calculated from an alignment of

BRCA2 sequences from fishes to human. The conservation score was calculated using JALVIEW. Scores of 0 and 11 correspond to non-conserved and strictly conserved residues, respectively. The positions of the PALB2 binding domain (BRCA2_{Nter}) and of residue Ser3291 are indicated in pink and green, respectively. (F) 3D structure of BRCA2_{Nter} (pink) bound to PALB2 (grey). This cartoon view corresponds to the 3D structure referenced as 3EU7.

A large range of particle sizes was observed [21–23]. Selection of a subset of these particles led to the generation of 3D reconstructions for a dimeric form of full-length BRCA2 free and in complex with RAD51 [21]. Free BRCA2 was described as an elliptical dimeric molecule of 25 nm × 13 nm × 12 nm, with its folded domains localized at both vertexes of the ellipse [21]. In the presence of RAD51, the dimeric BRCA2 molecules formed a larger ellipse of 26 nm × 16 nm × 16 nm, with extra density present next to the region identified as corresponding to the BRC repeats. However, how the BRCA2 dimers assemble into these ellipses, the folded domains from each monomer being connected through structurally less characterized regions of BRCA2, is still unclear. Further electron microscopy, scanning force microscopy, and quantitative single-molecule fluorescence studies showed that purified full-length BRCA2 forms heterogeneous oligomeric structures, assembled at least in part through its N-terminal region BRCA2_{1–714} [24] or its central region around Phe1524 [23]; they revealed that these structures exhibit remarkable rearrangement by RAD51, DSS1, and ssDNA [22–24]. The BRCA2 apparent structural plasticity is a hallmark of proteins with intrinsically disordered regions (IDRs).

Several studies have reported that cancer-associated proteins are rich in IDRs [25,26]. These protein regions lack a stable secondary structure. They interact with their partners through interfaces that never reach the size of the largest interfaces of ordered complexes but are characterized by a specifically large surface per residue: IDRs use a larger portion of their surface for interaction with their partner, sometimes 50% of the whole, as opposed to only 5–15% for most ordered proteins [27,28]. In addition, because the free energy arising from the contacts between an IDR and its target is reduced by the free energy needed to fold the IDR, interactions with IDRs enable high specificity coupled with moderate affinities [28,29]. Finally, IDRs are highly accessible to enzymes, and thus rich in post-translational modifications (PTMs). Such PTMs represent transient events that regulate interactions mediated by IDRs. Functionally relevant binding sites as well as PTMs are generally conserved in IDRs, which facilitates their identification using bioinformatics tools [30,31]. Here, we review the predicted as well as experimentally demonstrated structural and functional properties of BRCA2 IDRs, with a special focus on phosphorylation sites regulating BRCA2 binding to partners. We also discuss the impact of BRCA2 variants identified in patients with breast and/or ovarian cancers, which are detected throughout the whole BRCA2 protein, including the IDRs. Most of these variants are of uncertain clinical significance (VUS), especially when they are detected in few patients and are located in poorly characterized IDRs.

2. BRCA2 Exhibits a Set of Conserved Motifs Predicted to Be Disordered

Analysis of BRCA2 protein sequence using disorder prediction tools provided a general view of the structural organization of this protein. We predicted BRCA2's propensity for disorder using SPOT-Disorder2 [20], the best program for discriminating between order and disorder as described in Nielsen et al. [32]. The resulting plot unambiguously showed that the ssDNA- and DSS1-binding domain is the unique folded domain of BRCA2, here named DBD for DNA Binding Domain (Figure 1C). Short regions with an intermediate disorder propensity were also identified. In the central region of BRCA2, these regions correspond to the eight BRC repeats (so called because it is repeated in BRCA2), which bind to the recombinase RAD51 and its meiotic-specific paralog DMC1 [11,33]. The fourth BRC repeat, BRC4, was crystallized when bound to the ATPase domain of RAD51: it remains in contact with RAD51 over a stretch of 28 aa (residues Leu1521 to Glu1548), and forms a β -hairpin and an α -helix in the complex, as shown in Figure 1D [11]. In order to further identify functional domains in the predicted disordered BRCA2 regions, we aligned

the sequences of 24 BRCA2 homologs, from human to fishes. We used Jalview 2.10.1 to calculate a conservation score per residue reflecting the conservation of the amino acid physico-chemical properties at each position in the BRCA2 sequence [34]. Figure 1E shows that the largest conserved region corresponds to the C-terminal DBD domain. However, small patches of conserved motifs are also revealed in the regions that are predicted to be disordered. In particular, BRC1, BRC2, BRC4, BRC7, and BRC8 are highly conserved, whereas the three other BRC repeats are only moderately conserved. Finally, such analysis demonstrated that several other motifs are predicted to be disordered and conserved. One of these motifs was already functionally characterized: the N-terminal region between Leu24 and Ser37 forms a short α -helix interacting with a hydrophobic pocket at the surface of the partner and localizer of BRCA2 (PALB2) (Figure 1F) [35]. This interaction is essential for BRCA2 localization at double-strand break (DSB) repair foci during HR. Other motifs have only been recently characterized. In the following sections, we will first focus on the functional role of the well-studied disordered motifs binding to RAD51 and PALB2, and then we will concentrate on a few of the new motifs identified more recently by different groups including us.

3. Structural Studies Illustrate the Role of BRCA2 Disordered Regions in DNA Repair by HR

BRCA2 contributes to genome integrity by being an essential factor of the HR pathway [36]. HR is required for the repair of DSBs, inter-strand crosslinks, and replicative DNA lesions using the genetic information from the sister chromatid as a template. Thus, HR takes place during S and G2 phases. Defects in this process generate unrepaired DNA DSBs, which are highly toxic for the cell, leading to genome instability, and increased risk of cancer.

The recruitment of BRCA2 to DNA damage sites is mediated by the PALB2 protein, which is itself recruited by BRCA1, presumably at the ssDNA/dsDNA junction produced after resection of the DNA break ends [37,38]. The BRCA2 region involved in PALB2 binding includes residues 24 to 37 [35]. As illustrated in the section above, the N-terminal region of BRCA2 is predicted to be disordered in solution. However, the crystal structure of the complex between the BRCA2 peptide from Leu24 to Ser37 and PALB2 showed that BRCA2 folds upon binding (Figure 1F; [35]). The localization of BRCA2 via PALB2 is essential for efficient HR. PALB2 mutants with impaired BRCA2 binding decrease the capacity for DSB-repair by HR and increase cellular sensitivity to ionizing radiation [39].

After its recruitment to the DNA damage locus, BRCA2 facilitates the displacement of the ssDNA binding protein Replication Protein A (RPA) and the loading of the recombinase RAD51 onto ssDNA. RPA binding is a pre-requisite for RAD51 filament formation, as it contributes to remove DNA secondary structures and protect DNA from nucleolytic degradation; however, RPA's high affinity for ssDNA is also an impediment for RAD51 nucleation [40,41]. The folded domain of BRCA2 binds to the acidic protein DSS1 (Figure 1B), which interacts with the DNA binding surface of RPA and favors RPA's release from ssDNA [19,42]. Moreover, BRCA2 central region, which is predicted to be disordered, contains eight conserved repeats, approximately 35 aa in size, the BRC repeats, which have the capacity to bind RAD51 (Figure 1A). As illustrated for BRC4 (from Leu1521 to Glu1548), the BRC motif folds upon interaction with the RAD51 ATPase domain (Figure 1D; [11]). BRC4 blocks ATP hydrolysis by RAD51; it favors nucleation of the ATP-bound form of RAD51 onto ssDNA, preventing its assembly on dsDNA [43]. The BRC repeats display different affinities for RAD51. Only the first four repeats have high affinity for monomeric RAD51 [44]. The other four repeats bind with low affinity to monomeric RAD51 and high affinity to the RAD51-ssDNA nucleoprotein filament [44]. Through these molecular interactions, BRCA2 favors the formation of a stable right-handed helical nucleoprotein filament of RAD51 on ssDNA, which is the active form for the search of sequence homology in the intact copy of the chromosome. Upon encountering a homologous sequence, the nucleoprotein filament pairs with the complementary strand, resulting in the displace-

ment of the non-complementary strand from the duplex to generate a D-loop structure (displacement loop) and promote DNA strand exchange.

In addition to its role in somatic cells, BRCA2 also contributes to HR during meiosis. The core HR machinery (BRCA2, PALB2, RAD51) is extended in meiosis with a set of meiosis-specific proteins, such as the ssDNA-binding proteins MEIOB and SPATA22 and the recombinase DMC1. BRCA2 interacts with both RAD51 and the meiosis-specific recombinase DMC1. It binds DMC1 via the RAD51-binding BRC repeats [33,45] and a DMC1-specific site located in a region predicted to be disordered between Ser2386 and Lys2411 [46]. However, no biophysical characterization of the interaction between BRCA2 and meiosis-specific proteins has been reported until recently.

4. During Interphase, the C-Terminal Disordered Region of BRCA2 Is Required for the Protection of Stalled Forks

BRCA2 is also essential for the protection of stalled replication forks (RF). Following replication stress, RF are slowed or stalled and, if not protected, newly replicated DNA can undergo unscheduled degradation by nucleases such as MRE11 [47]. BRCA2 has a protective function during replication fork stalling that is mechanistically distinct from repair by HR [3]. The C-terminal disordered and conserved region of BRCA2, from Ala3270 to Gly3305, binds to and stabilizes RAD51-ssDNA filaments, thus preventing nascent-strand degradation [3,48,49]. BRCA2 mutants with compromised fork protection exhibit increased spontaneous and HU-induced chromosomal aberrations that are alleviated by MRE11 inhibition.

Ser3291, in the BRCA2 C-terminal region binding to RAD51-ssDNA filaments, is strictly conserved (Figure 1E). It undergoes CDK (for Cyclin Dependent Kinase)-dependent phosphorylation at the G₂-M phase transition and dephosphorylation upon DNA damage [50]. Phosphorylation of Ser3291 blocks interaction between BRCA2 and oligomeric RAD51. This was demonstrated using two separation of function mutants, S3291A and S3291E, that abrogate RAD51 binding; cells bearing these mutations are defective in replication fork protection but are able to repair DSB by HR. Furthermore, BRCA2 and PALB2 facilitate the recruitment of Polη by directly interacting with the polymerase during the initiation of DNA synthesis [51]. The BRCA2 region from Leu1409 to Asn1596 (including BRC3 and BRC4) is responsible for binding to the polymerase. The trimeric complex stimulates the initiation of recombination-associated DNA synthesis by Polη. Altogether, at blocked replication forks, BRCA2 disordered regions, including its C-terminus, are essential for binding to RAD51 filaments and stimulating the initiation of DNA synthesis by Polη in vitro. Phosphorylation of Ser3291 promotes RAD51 filament disassembly, which in turn promotes entry into mitosis [52].

5. Nuclear Magnetic Resonance Analyses Support the Presence of Additional Disordered and Conserved Regions in BRCA2

Within the BRCA2 regions predicted to be disordered, four additional conserved fragments have been recently experimentally characterized: BRCA2_{48–284} [53], BRCA2_{250–500} (unpublished data), BRCA2_{1093–1158} (unpublished data) and BRCA2_{2213–2342} [54] (Figure 2A). These BRCA2 fragments were recombinantly produced in bacteria as ¹⁵N, ¹³C labeled proteins, purified by chromatography and further analyzed using solution-state Nuclear Magnetic Resonance (NMR), a biophysical technique uniquely suited for the structural characterization of soluble disordered proteins at the residue level [55].

Indeed, whereas X-ray crystallography and cryo-electron microscopy cannot describe the conformations of highly flexible proteins or protein regions retaining a large mobility, NMR provides information on their structural propensities in solution. The very common 2D NMR ¹H-¹⁵N Heteronuclear Single Quantum Coherence (HSQC) experiment is used to characterize the local chemical environment of each backbone amide bond atom and thus visualize the disorder propensity of a protein at the residue level. Here, the ¹H-¹⁵N HSQC spectra of the four BRCA2 fragments are presented. The narrow dispersion of their ¹H-¹⁵N correlation peaks in the ¹H dimension demonstrated that they are disordered protein

regions (Figure 2B). Further analysis of the ^1H , ^{15}N and ^{13}C chemical shifts of BRCA2_{48–284}, BRCA2_{1093–1158}, and BRCA2_{2213–2342} was performed to obtain the secondary structure propensity of these fragments at the residue level. Whereas BRCA2_{48–284}, BRCA2_{1093–1158} and BRCA2_{2213–2342} do not form any stable α -helix or β -strand, they contain small motifs adopting transient α -helical structures (Figure 2C).

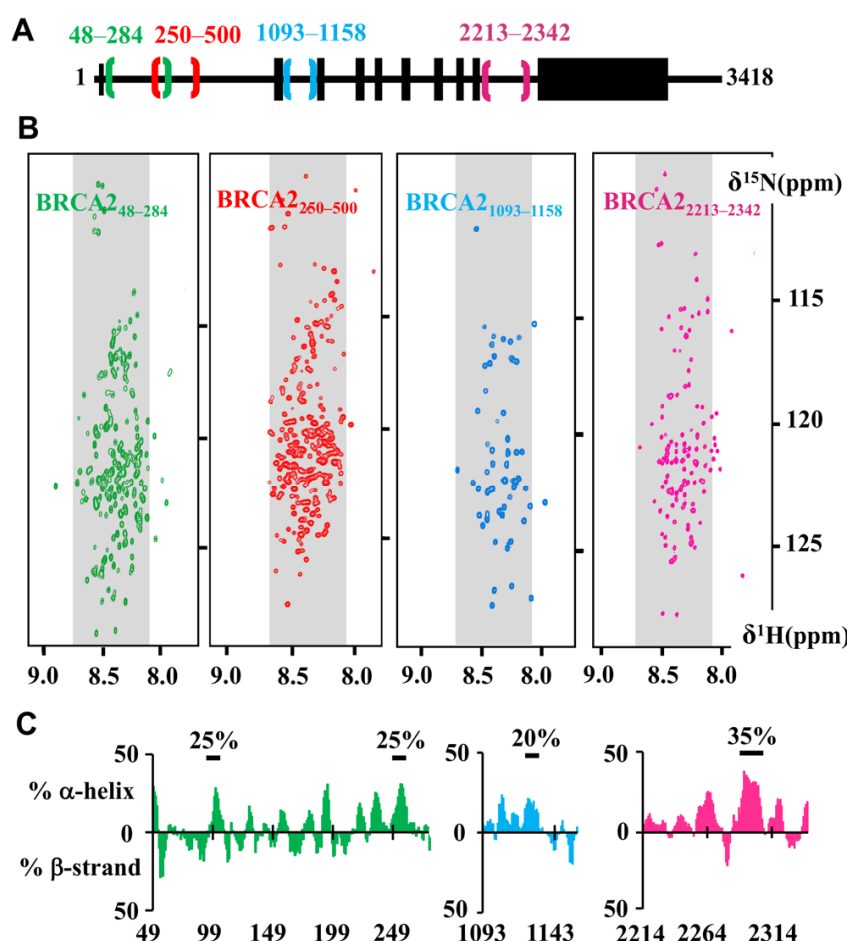


Figure 2. NMR analysis demonstrates that the conserved motifs BRCA2_{48–284}, BRCA2_{250–500}, BRCA2_{1093–1158}, BRCA2_{2213–2342} are disordered in solution. (A) Localization of the four fragments in the BRCA2 sequence. (B) 2D NMR ^1H - ^{15}N Heteronuclear Single Quantum Coherence (HSQC) spectra of the four fragments. These spectra were recorded on ^{15}N -labeled BRCA2_{48–284} at 200 μM in HEPES 50 mM, NaCl 75 mM, EDTA 1 mM, DTT 5 mM, pH 7.0 (green, [53]), ^{15}N -labeled BRCA2_{250–500} at 200 μM in phosphate 20 mM, NaCl 250 mM, pH 7.0 (red, 600 MHz CEA Saclay), ^{15}N -labeled BRCA2_{1093–1158} at 200 μM in 50 mM HEPES, 50 mM NaCl, 1 mM EDTA pH 7.0 (blue, 700 MHz CEA Saclay) and ^{15}N -labeled BRCA2_{2213–2342} 500 μM , in HEPES 50 mM, NaCl 50 mM, EDTA 1 mM, pH 7.0 (pink, [54]). Cysteines of BRCA2_{48–284} (C132A, C138A, C148A, C161A) and BRCA2_{250–500} (C279A, C311S, C315A, C341A, C393S, C419S, C480S) were mutated in order to favor their solubility. Grey backgrounds define the ^1H frequencies typical for disordered residues. Localization of most ^1H - ^{15}N peaks in the grey regions highlights the disorder propensity of these BRCA2 fragments; (C) Secondary structure propensity of three of these fragments. Propensities to form α -helices or β -strands were calculated for BRCA2_{48–284} (green), BRCA2_{1093–1158} (blue) and BRCA2_{2213–2342} (pink) from their ^1HN , ^{15}NH , ^{13}CO , $^{13}\text{C}\alpha$ and $^{13}\text{C}\beta$ NMR resonance frequencies using the ncSPC server [56]. Bold black lines underline the presence of transient secondary structure with the indicated percentage. BRCA2_{48–284} contains two short transient α -helices formed by residues 100 to 110 and 255 to 260, BRCA2_{1093–1158} exhibits one transient α -helix between residues 1122 and 1128 and BRCA2_{2213–2342} shows one transient α -helix between residues 2292 and 2303.

NMR can also be used to verify that a mutation does not affect the conformation of the fragment of interest, or identify structural defects in a protein mutant associated with a disease. Here, fragment BRCA2_{48–284} contains five cysteines. In IDRs, cysteines are solvent-exposed, and, under our working conditions, are quickly oxidized, thus favoring protein aggregation. We observed that, even in the presence of high concentrations (about 10 mM) of thiol reducer, intra and inter-cysteine bonds are already formed a few hours after the addition of the reducer. Mutation of cysteines into alanine is a common strategy to prevent IDR aggregation *in vitro*. We recorded 2D NMR ¹H-¹⁵N HSQC experiments on the BRCA2_{48–284} fragment either wild-type or with four cysteines mutated into alanine. The two ¹H-¹⁵N HSQC spectra are similar, demonstrating that the cysteine mutations do not modify the structural conformation of BRCA2_{48–284}; a construct with only one cysteine was further used for phosphorylation and binding studies [53]. Similarly, such strategy can be used to measure the impact of a cancer-associated mutation on the solution structure of a BRCA2 IDR [57].

6. BRCA2_{48–284} Phosphorylation by CDKs and PLK1 Ensures Correct DNA Repair before Mitosis and BRCA2 Midbody Localization during Cytokinesis

The characterization of the function of BRCA2_{48–284} started almost 20 years ago [58]. BRCA2_{48–284} contains two conserved patches between residues 63 to 93 and 164 to 230, phosphorylated by CDKs [7,59] and PLK1 (for Polo-Like Kinase 1) [57], respectively (Figure 3A). These phosphorylation events take place at the interphase to mitosis transition and were progressively associated with various mitotic functions of BRCA2.

In the conserved region BRCA2_{63–93}, phosphorylation by CDKs at Thr77 was identified by Western blot using an antibody raised against pThr77 [59]. This phosphorylation site belongs to a conserved motif that matches the optimal PLK1 binding motif Ser-[pSer/pThr]-[Pro/X] (Figure 3B). Consistently, a direct *in vitro* interaction was reported between BRCA2_{pThr77} and PLK1 [59]. This interaction brings together PLK1 and another BRCA2 partner: the RAD51 recombinase. It was proposed that, during the interphase to mitosis transition, BRCA2 acts as a molecular platform that facilitates PLK1-mediated RAD51 phosphorylation at position Ser14 [59]. This last phosphorylation event peaks in mitosis, and enhances the association of RAD51 with stressed replication forks for protecting the genomic integrity of proliferating human cells [59]. It stimulates the subsequent phosphorylation of RAD51 Thr13 by Casein Kinase 2 [59,60]. Di-phosphorylation of RAD51 at Ser14 and Thr13 is also detected in response to ionizing radiation [59]. Phosphorylation at Thr13 triggers direct binding to the FHA domain of NBS1, a component of the MRN complex involved in DSB DNA repair [60]. This interaction helps to increase the RAD51 concentration at the site of damage, and promotes efficient DNA repair by HR before mitosis onset [60]. Finally, other conserved CDK phosphosites characterized by the motif [pSer/pThr]-Pro are detected in BRCA2_{63–93} (Figure 2B). Consistently, we have observed *in vitro* that CDKs are able to phosphorylate not only Thr77 but also other conserved residues such as Thr64 and Ser93. A deeper characterization of the phosphorylation events taking place in this region may highlight complementary BRCA2-dependent mechanisms for entry into mitosis.

In 2003, Lin et al. identified another BRCA2 region between residues 193 and 207 that is highly phosphorylated in mitosis (Figure 3C; [58]). This region is a target for the kinase PLK1, and only Ser193 was clearly identified as a target of PLK1 in mitosis. However, mutation S193A did not completely abrogate the PLK1-dependent phosphorylation of BRCA2_{1–284}, whereas deletion of residues 193 to 207 did abolish phosphorylation, suggesting that other sites are phosphorylated next to Ser193. This highlights a very common situation in the IDP field; IDRs are enriched in phosphorylation sites, creating clusters with multiple sites. Identification of modification sites at very close positions in the protein sequence is challenging for mass spectrometry and Western-blot analyses. Recently, we monitored phosphorylation of BRCA2_{167–260} by PLK1 using 2D NMR ¹H-¹⁵N HSQC experiments (Figure 3D; [57]). Upon phosphorylation, the chemical environment of the backbone H, N amide bond atoms of the phosphoresidue is modified, which changes

the position of the corresponding ^1H - ^{15}N correlation peak in the spectrum (Figure 3D). Thus, four phosphosites were identified: pSer193, pThr207, pThr219, and pThr226 [57]. A function was proposed for the phosphorylation of both strictly conserved residues Ser193 and Thr207 (Figure 3C). The biological role of the phosphorylation of the less conserved Thr219 and Thr226 in human cells still remains to be clarified.

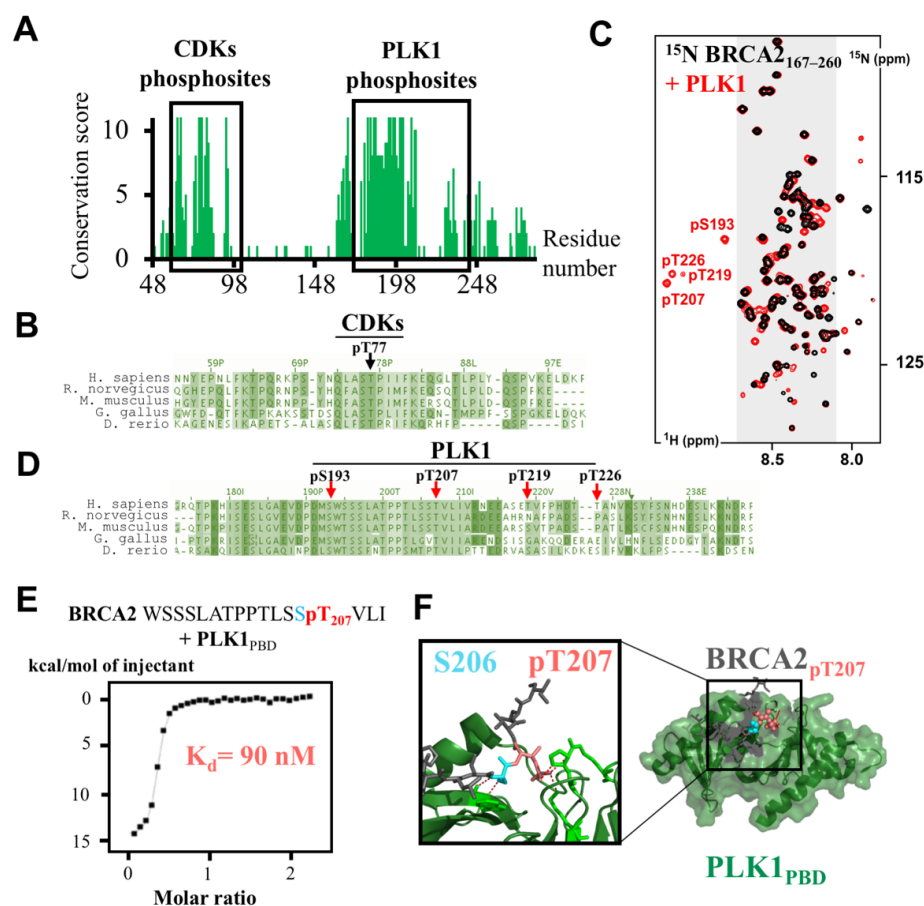


Figure 3. BRCA2₄₈₋₂₈₄ contains conserved CDKs and PLK1 phosphorylation sites and two PLK1 docking sites. (A) BRCA2₄₈₋₂₈₄ conservation profile, calculated as in Figure 1, shows two conserved patches: BRCA2₆₃₋₉₃ and BRCA2₁₆₄₋₂₃₀. These patches contain predicted as well as experimentally identified CDKs and PLK1 phosphorylation sites, marked by black boxes. (B,D) Alignments of the human, mouse, rat, chicken and zebra fish BRCA2 sequences corresponding to the regions boxed in (A) illustrate the conservation of the reported CDKs and PLK1 phosphorylation sites. Arrows point to the CDKs (black) and PLK1 (red) phosphorylation sites in these regions: pThr77 [7,59], pSer193 [7,59,60], pThr207, pThr219 and pThr226 [57]. (C) NMR analysis identified four PLK1-dependent phosphosites: pSer193, pThr207, pThr219 and pThr226 [57]. ^1H - ^{15}N SOFAST-HMQC spectra of BRCA2₁₆₇₋₂₆₀ (50 μM) were recorded before (black) and after (red) 12 hrs of in vitro phosphorylation by PLK1 (150 nM). (E) Isothermal Titration Calorimetry (ITC) thermogram revealed binding of a BRCA2 peptide containing pThr207 to the PBD domain of PLK1 (PLK1_{PBD}; [57]). (F) 3D structure of BRCA2₂₀₀₋₂₀₉(pThr207) bound to PLK1_{PBD} identified critical intermolecular interactions involving BRCA2 Ser206 and pThr207 [57]. In BRCA2₄₈₋₂₈₄, two PLK1 docking sites were identified, centered on either pThr77 [60] or pThr207 [57]. The X-ray structure of BRCA2₁₉₉₋₂₁₀(pThr207) bound to PLK1_{PBD} was recently solved (PDB code: 6GY2). Within BRCA2₁₉₉₋₂₁₀(pThr207) (grey, blue and salmon), side chains of BRCA2 Ser206 (blue) and pThr207 (salmon) directly bind to the two Polo-box motifs of the PBD (green), and drive the specificity of the interaction. PBD residues in interaction with pThr207 and Ser206 are displayed as green sticks, and red dotted lines mark the hydrogen bonds involved in these interactions.

BRCA2 pSer193 was the first phosphosite identified in this BRCA2 region. It was reported as essential for BRCA2 localization at the Flemming body during cytokinesis [7]. Indeed, BRCA2 S193A failed to localize at the midbody, while the phosphomimetic S193E was sufficient to restore BRCA2 localization. Moreover, phosphorylation of Thr77 that triggers PLK1 interaction with BRCA2 was proposed to increase phosphorylation of Ser193 by PLK1 and BRCA2 localization at the midbody. The protein able to recruit BRCA2 phosphorylated on Ser193 at the midbody is currently unknown. The actin-binding protein Filamin A could contribute to this recruitment; however, it interacts with BRCA2 DBD [61]. More work would be required to identify the BRCA2 partner binding to the highly conserved region centered on pSer193 and the strictly conserved hydrophobic residue Trp194 (Figure 3D).

7. BRCA2_{199–210} and BRCA2_{1093–1158} Mediate the Assembly of a Large Complex, Including PLK1, BUBR1, and PP2A, Regulating Chromosome Alignment during Mitosis

We recently confirmed that Thr207 was phosphorylated in mitosis, using an antibody raised against a BRCA2 peptide centered on pThr207 [57]. We also noticed that phosphorylation of BRCA2 Thr207 creates a docking site for the Polo-Box domain (PBD) of PLK1 (PLK1_{PBD}). This phospho-dependent interaction was confirmed by Isothermal Titration Calorimetry (ITC): the K_d measured between BRCA2_{194–210}(pThr207) and PLK1_{PBD} is close to 0.1 nM, (Figure 3E; [57]), as also reported for other interactions between phosphorylated peptides and PLK1_{PBD} [62], whereas the non-phosphorylated BRCA2 peptide BRCA2_{194–210} does not bind to PLK1_{PBD}. The complex between BRCA2_{194–210}(pThr207) and PLK1_{PBD} was crystallized, revealing that, as also described for other phosphorylated peptides, BRCA2_{199–210}(pThr207) binds in the cleft formed by the two Polo boxes of PLK1_{PBD} (Figure 3F). Surprisingly, mutating Thr207 into the phosphomimetic glutamate or aspartate did not generate any interaction with PLK1_{PBD}, showing that these mutations cannot be used as phosphomimetics to test the function of Thr207 phosphorylation in cells [57]. In mitosis, binding of BRCA2 pThr207 to PLK1 triggers the assembly of a larger complex containing BRCA2, PLK1, the mitotic checkpoint kinase BUBR1 (for Budding Uninhibited by Benzimidazole-Related 1), and the phosphatase PP2A (for Protein Phosphatase 2A) at the kinetochore (Figure 4A; [57]). Thus, BRCA2 serves as a platform that brings together BUBR1 and PLK1. This favors BUBR1 phosphorylation by PLK1 at tension-sensitive sites, involved in the regulation of the kinetochore-microtubule attachment [63]. In addition, breast cancer variants S206C and T207A impair PLK1 binding and result in unstable microtubule-to-kinetochore attachments, misaligned chromosomes, faulty chromosome segregation and aneuploidy [57]. This highlights the role of BRCA2 in preserving genome integrity during mitosis and shows how a simple phosphorylation event can be essential for genome integrity.

BRCA2 phosphorylation at Thr207 further triggers the assembly of a large complex including PLK1, BUBR1, and PP2A through poorly characterized interactions. Phosphorylation of BUBR1 by PLK1 promotes the interaction of its Leu-X-X-Ile-X-Glu motif with the B56 subunit of PP2A (Figure 4A; [64,65]). BRCA2_{1093–1158}, located in between the BRC1 and BRC2 motifs, also exhibits a conserved Leu-X-X-Ile-X-Glu motif that interacts with PP2A (Figure 4A,B; [66]). Thus, BUBR1 and BRCA2 might compete for binding to the same B56 subunit of PP2A. Through these interactions, PP2A protects the kinetochore-microtubule interaction from excessive destabilization by Aurora B [67].

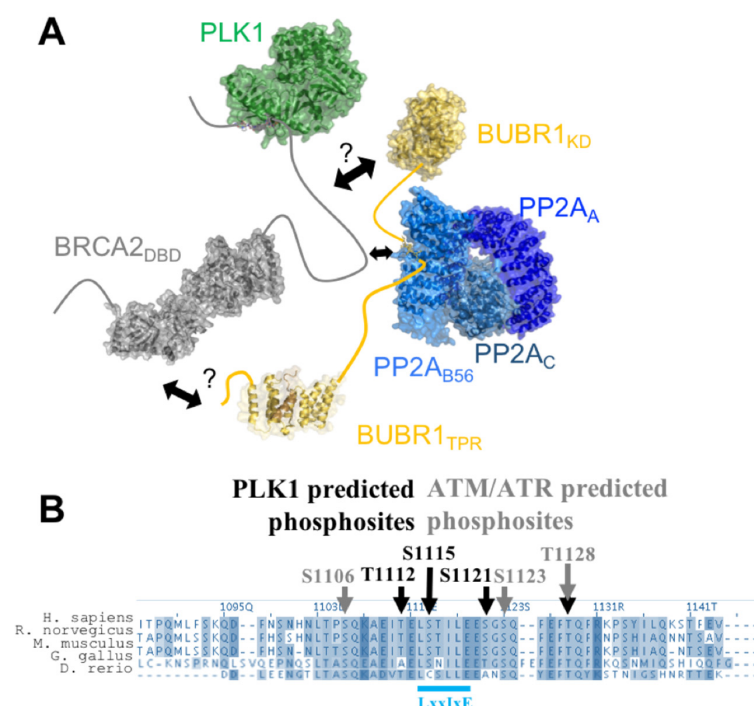


Figure 4. BRCA2_{1093–1158} contains predicted PLK1 and ATM/ATR phosphorylation sites and a PP2A-B56 binding site. **(A)** Scheme of the BRCA2/PLK1/BUBR1/PP2A complex, assembled upon phosphorylation of Thr207 by PLK1. Human BRCA2 (in grey) has a long N-terminal region, which interacts with PLK1_{PBD} (PDB code: 6GY2) upon phosphorylation of Thr207 by PLK1. No human full-length PLK1 structure has been elucidated yet: here the PLK1 model (green) is built using the *Danio rerio* PLK1 structure (PDB code: 4J7B). BRCA2 interacts with BUBR1 (yellow) through a controversial interface (arrows and question marks): Futamura et al. [68] reported an interaction between BRCA2_{2861–3176} and the kinase domain of BUBR1 (model built from the fly structure; PDB code: 6JJK), whereas Choi et al. [69] reported an interaction between BRCA2_{3189–3418} and the N-terminal region of BUBR1 including its TPR domain (residues 57 to 220; PDB code: 3SI5). BRCA2 and BUBR1 (PDB codes: 5JJA; 5K6S; 5SWF) interact with the B56 subunit of the phosphatase PP2A (3D structure of the whole protein formed by three subunits, in blue; PDB code: 2NPP) [64,66,70]. **(B)** Alignment of the human, mouse, rat, chicken and zebra fish sequences homologous to human BRCA2_{1093–1158}, highlighting the high conservation of the predicted PLK1 and ATM/ATR phosphorylation sites, as well as the PP2A binding site. Black and grey arrows point to the predicted phosphorylation sites for PLK1 and ATM/ATR, respectively. The docking site for the B56 subunit of the PP2A phosphatase identified in this region [66,71] is mediated by the L-X-X-I-X-E consensus motif (cyan), with X for any amino acid [66].

The conserved region BRCA2_{1093–1158} contains several highly conserved phosphorylation sites, predicted to be targets of either PLK1 or ATM (for Ataxia Telangiectasia Mutated) and ATR (for ATM and RAD3-related) (Figure 4B). A larger BRCA2 region, still located between BRC1 and BRC2, was reported to be phosphorylated by PLK1 during mitosis [72]. As phosphorylation of the Leu-X-X-Ile-X-Glu motif increases binding to the B56 subunit of PP2A [65], phosphorylation by PLK1 could regulate BRCA2 binding to this phosphatase at the kinetochore. Phosphorylation of BRCA2_{1093–1158} by ATM/ATR was also recently experimentally confirmed [71]. The authors showed that phosphorylation of the [Ser/Thr]-Gln motifs, specifically at Ser1123 and Thr1128, increases binding of BRCA2_{1113–1129} to the B56 subunit of PP2A. In addition, mutation of the three [Ser/Thr]-Gln motifs located in this BRCA2 region increases the sensitivity of cells to Poly(ADP-ribose) Polymerase inhibitors and leads to a loss of efficient RAD51 loading and HR-mediated DNA repair. These results revealed another role for the BRCA2/PP2A interaction in DNA repair, and suggested that PP2A-B56 might be a general regulator of BRCA2 function throughout the cell cycle.

8. Both Folded and Disordered Regions of BRCA2 Contribute to Its DNA Binding Properties

Purified full-length BRCA2 binds to DNA above a protein concentration of 2 to 20 nM [73–75]. It binds to both ssDNA and dsDNA; however, it displays a preference for ssDNA (as well as tailed) substrates over dsDNA [74]. The mouse BRCA2 DBD in complex with the acidic protein DSS1 interacts with ssDNA [19]. Native gel electrophoretic mobility-shift assays showed that it binds to oligo(dT), oligo(dC), and mixed ssDNA sequences but not to dsDNA. The crystal structures of the mouse DBD bound to DSS1 and an oligo(dT)₉ illustrates how the oligonucleotide/oligosaccharide-binding 2 and 3 motifs of this domain interact with small oligonucleotides (8 to 12 nt), as observed at concentrations above 3 μ M and independently of its tower fragment. The BRCA2 folded domain in complex with DSS1 further binds with a 10-fold higher affinity to larger oligonucleotides (32 to 36 nt) in the presence of its tower fragment [19]. The disordered BRCA2 region from residue 250 to 500 also contributes to DNA binding [75]. It is less conserved than the other disordered regions described in this review (Figures 1 and 5A).

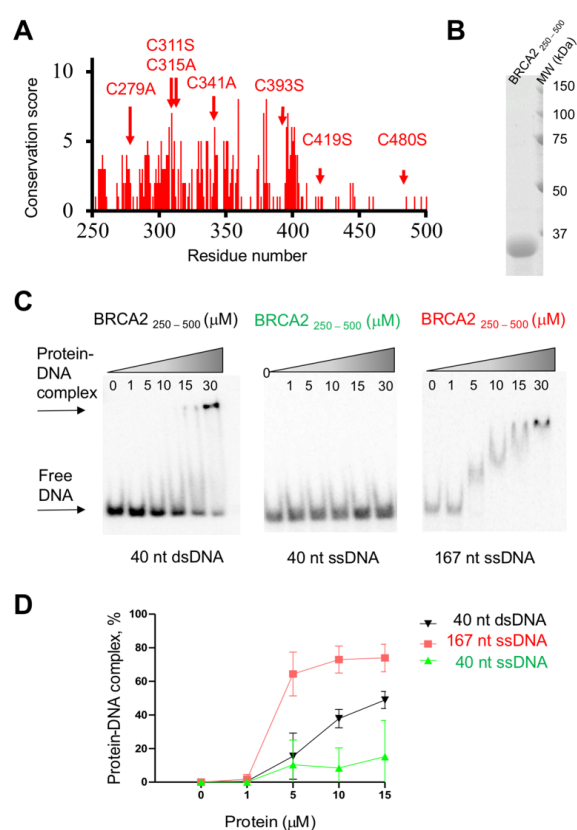


Figure 5. BRCA2_{250–500} contains a DNA binding site. (A) Conservation profile of BRCA2_{250–500} obtained as presented in Figure 1. Red arrows indicate the position of the seven cysteines that were mutated into alanine or serine depending on the amino acids found at these positions in the homologous BRCA2 sequences: C279A, C311S, C315A, C341A, C393S, C419S, C480S. (B) SDS-PAGE of purified recombinant BRCA2_{250–500}. (C) BRCA2_{250–500} binds to different DNA substrates, as observed by electrophoretic mobility shift assays. Increasing amounts of BRCA2_{250–500} were incubated at the indicated concentrations with 0.2 μ M (nucleotide) ³²P-labelled DNA substrates for 1 h at 37 °C. The protein–DNA complexes were resolved on 6% native polyacrylamide gels in 1X TAE buffer at 70 V for 75 min. The gels were dried and analyzed with a Typhoon PhosphorImager (Amersham Biosciences) using Image Quant software (GE Healthcare). (D) Quantification of the EMSA experiments, revealing that BRCA2_{250–500} binds to both ssDNA and dsDNA. In all gels, the ratio of protein–DNA complexes was calculated as the percentage of bound vs. free DNA. The experiments were repeated three times for each DNA substrate.

A Maltose-Binding Protein tagged BRCA2 WT fragment MBP-BRCA2_{250–500} produced in HEK293 human cells binds to both ssDNA and dsDNA at a concentration around 1 μ M, depending on the oligonucleotide sequence; it is the only BRCA2 fragment yet demonstrated to bind dsDNA [75]. When produced in bacteria as a variant in which all cysteines are mutated into alanine or serine (for solubility purposes, see above), BRCA2_{250–500} is disordered in solution (Figures 2B and 5B). Cysteines were shown as important for DNA binding to various DNA forms [75]. Consistently, the variant BRCA2_{250–500} produced in bacteria binds to ssDNA and dsDNA at higher (micromolar) concentrations (Figure 5C,D). It shows a preference for long ssDNA versus short ssDNA, and also binds to short dsDNA in our experiments (Figure 5C,D). This provides evidence that cysteines contribute to DNA binding but are not mandatory.

In cells, MBP-BRCA2_{250–500} significantly enhances RAD51 recombination activity: as the full-length BRCA2 protein, it stimulates RAD51-driven DNA strand exchange reaction in the presence (and only in the presence) of RPA. Full-length BRCA2 increases RAD51-mediated strand exchange at a 10-fold lower concentration, whereas the DBD shows only a weak stimulating effect, observable at a 30-fold higher concentration [19,75]. In the case of the DBD, this weak effect depends on its capacity to present DSS1 that exposes a negatively charged fragment competing with ssDNA for binding RPA [42]. In the case of BRCA2_{250–500}, which exhibits an isoelectric point of 5.3, both its reported capacity to bind DNA, potentially through its positively charged regions, and its still hypothetical capacity to mimic DNA, because of its negatively charged patches, could contribute to displace RPA from DNA.

9. A Conserved and Disordered BRCA2 Region Contains a Cryptic Repeat That Recruits HSF2BP, Thus Triggering BRCA2 Degradation

A recent search for new BRCA2 partners identified HSF2BP (also named MEILB2) as another BRCA2-binding protein, endogenously expressed in meiotic cells, and ectopically produced in cancer cells [76,77]. HSF2BP is required for meiotic HR during spermatogenesis; its disruption abolishes the localization of RAD51 and DMC1 recombinases in spermatocytes, leading to errors in DSB repair by meiotic HR and consequently male sterility [78]. HSF2BP exhibits an N-terminal α -helical oligomerization domain and a C-terminal Armadillo domain [76,79]. Within BRCA2_{2213–2342}, a highly conserved IDR binds to the Armadillo domain of HSF2BP (HSF2BP_{ARM}) (Figure 6A; [54,76]). NMR analysis confirmed that BRCA2_{2213–2342} is disordered in solution (Figure 2B) and that it directly interacts with HSF2BP_{ARM}: addition of unlabeled HSF2BP_{ARM} to an ¹⁵N-labeled BRCA2_{2213–2342} caused a global decrease of the intensities of the NMR 2D ¹H-¹⁵N HSQC peaks, with region from aa 2252 to aa 2342 showing the largest decrease (Figure 6B; [54]). Unexpectedly, ITC experiments revealed that this interaction is characterized by a high affinity, on the nanomolar range, which is the largest affinity ever measured for a BRCA2 interaction [54].

In addition, unexpectedly, our crystal structure of the complex showed that a dimeric HSF2BP_{ARM} (here chains A, D and B, C) further dimerizes through two BRCA2 peptides in order to form a tetramer (Figure 6C). The BRCA2 peptides (in magenta) run along the V shape groove formed by either chains A and C or chains B and D. Each peptide interacts through its N-terminal region with one HSF2BP_{ARM} monomer and through its C-terminal region with another HSF2BP_{ARM} monomer. These BRCA2 peptide regions are encoded by exons 12 and 13, respectively, but they contain the same sequence motif critical for binding to the conserved groove of an HSF2BP_{ARM} monomer (Figure 6C,D; [54]). Such repeated motif is responsible for HSF2BP_{ARM} tetramerization upon BRCA2 binding. Deletion of the motif encoded by exon 12 impaired tetramerization and caused a 1000-fold loss in affinity, leading to a micromolar affinity between HSF2BP and BRCA2. However, it did not impair meiotic HR and caused no fertility defect in mice [54]. Thus, the role of the high affinity interaction between HSF2BP and BRCA2 in meiosis is still unclear. In somatic cells, this interaction interferes with the role of BRCA2 in DNA inter-strand crosslink repair: it triggers proteasome-dependent degradation of BRCA2 [77]. More generally, the high

affinity interaction between HSF2BP and BRCA2 might contribute to control the levels of BRCA2 in cells.

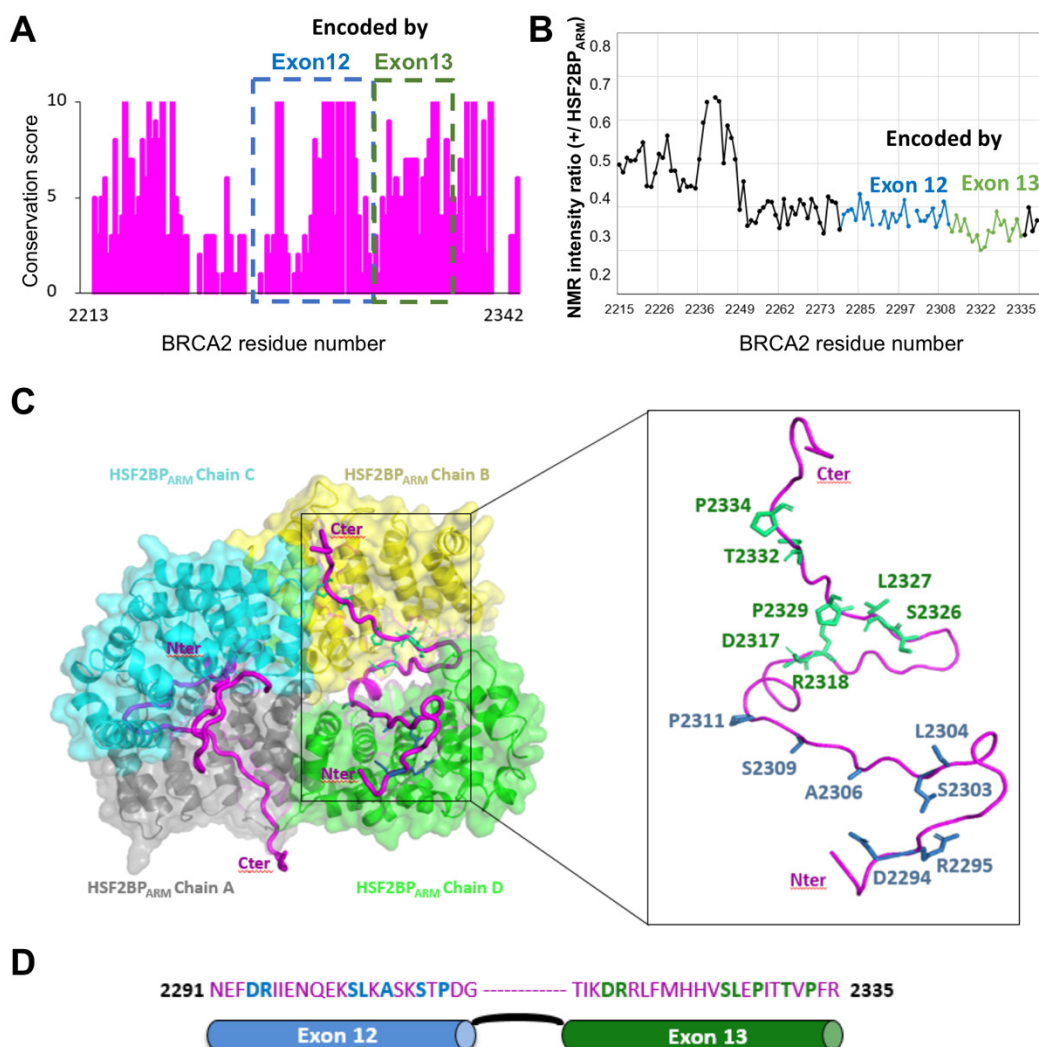


Figure 6. BRCA2_{2213–2342} interacts with HSF2BP, a protein essential for meiotic HR. **(A)** BRCA2_{2213–2342} conservation profile, as calculated in Figure 1. Regions encoded by exons 12 and 13 are boxed in blue and green, respectively. **(B)** NMR analysis of BRCA2_{2213–2342} interaction with the Armadillo domain of HSF2BP (HSF2BP_{ARM}) [54]. 2D ¹H-¹⁵N HSQC spectra were recorded on ¹⁵N-labeled BRCA2_{2213–2342}, either free or in the presence of HSF2BP_{ARM} (1:1 ratio, knowing that 1 BRCA2 peptide binds to 2 HSF2BP_{ARM}), at 950 MHz and 283 K. Ratios of peak intensities in the two conditions are plotted as a function of BRCA2 residue number. The points and curve fragments in blue and green correspond to residues encoded by exons 12 and 13 of BRCA2, respectively. **(C)** Crystal structure of the complex between BRCA2_{2291–2342} and HSF2BP_{ARM}, illustrating how the HSF2BP_{ARM} dimers, formed by chains A (grey) and D (green) and chains B (yellow) and C (cyan), are held together through their interactions with the two BRCA2 peptides (magenta) [54]. The HSF2BP_{ARM} domains are represented as both cartoon and surface, whereas the BRCA2 peptides are displayed as tubes. In the zoom view, only one BRCA2 peptide is shown. Its N-terminal region interacts with one HSF2BP_{ARM} domain through motif 1 (blue sticks), and its C-terminal region interacts with another HSF2BP_{ARM} domain through motif 2 (green sticks). Only the side chains of residues that are conserved in BRCA2 from fishes to mammals and are similar between motifs 1 and 2 are displayed. **(D)** Sequence of BRCA2 motifs 1 and 2, encoded by exons 12 and 13, respectively. Each motif binds to one HSF2BP_{ARM}. Residues conserved in BRCA2 from fishes to mammals and similar between motifs 1 and 2 are colored in blue and green, respectively.

10. BRCA2 Variants Detected in Patients with Cancers Are Mutated in Folded or Disordered Regions: Which of These Variants Are Pathogenic?

Germline pathogenic variants in the *BRCA2* cancer susceptibility gene result in an increased lifetime risk of breast, ovarian, and other cancers. Tumors forming in patients with a pathogenic variant in *BRCA2* exhibit significant structural and numerical chromosomal defects. Because *BRCA2* is directly involved in HR-mediated repair of DSB, inter-strand crosslinks, and replicative DNA lesions, the observed structural chromosomal alterations are thought to derive from the absence of RAD51-mediated *BRCA2* DNA repair activity. In contrast, whole-chromosomal defects detected in *BRCA2* mutant tumors and deficient cells are proposed to result from aberrations in both chromosome segregation and cell division. Assessing the pathogenicity of non-truncating missense variants of the *BRCA2* gene, by identifying defects caused by the encoded *BRCA2* mutant, is essential to improve the follow-up and treatment of patient families. In particular, tumors with *BRCA2* pathogenic variants associated with defective HR are sensitive to Poly(ADP ribose) polymerase inhibitors, the efficacy of which is mediated through synthetic lethality with *BRCA2* loss-of-function in cancer cells [80,81].

Interpretation of variants is currently based on a combination of population, computational, functional and segregation analyses. Each variant is assigned to one of the five following classes: benign, likely benign, uncertain significance, likely pathogenic and pathogenic [82]. First, nonsense or frameshift variants within the coding exons of *BRCA2*, as well as variants in the canonical splice site sequences of *BRCA2*, strongly alter the structure of the protein product and are presumed to confer loss-of-function [83–87]. They are generally classified as pathogenic. However, they may retain (partial) functionality through the expression of alternative protein isoforms, leading to possible incorrect risk estimations [87,88]. Second, missense variants can also be classified as benign or pathogenic when detected in a large set of families. However, the vast majority of these variants are individually rare in both the general population and cancer patients. Figure 7A represents the distribution and significance of missense variants in the French population, including those exhibiting splicing defects, along the *BRCA2* gene [89]. Variants are detected in the whole gene, with no preferred hot spot, and most of these variants are still of uncertain significance.

Focusing on missense variants in *BRCA2* IDRs, only W31S is nowadays being classified as pathogenic in the French variant database based on co-segregation analysis (S. Caputo, personal communication). This variant is localized in exon 3, and impairs *BRCA2* binding to PALB2, an essential event in HR ([37]; Figure 7B). In frame deletion of the whole, exon 3 was also classified as pathogenic based on clinical, functional, and co-segregation data [90,91], whereas variants causing only partial production of a *BRCA2* transcript deleted from exon 3 have variable impacts on tumorigenesis [92]. Similarly, in frame deletion of exon 11 impairs HR and was classified as likely pathogenic in ClinVar [87].

We recently showed that S206C and T207A lead to chromosomal instability including aneuploidy as observed in *BRCA2* mutated tumors, which we proposed could have an impact on cancer [57]. Ser206 and Thr207 are encoded by exon 7. This exon is not in frame, and S206C induces exon 7 skipping at 46%, thus impairing *BRCA2* function because of both the mutation and the low level of the variant expression [93]. However, the community is questioning the different types of variants of exon 7 because they often cause the expression of different transcripts including an in-frame delta 4-7 isoform (*BRCA2*_{delExons4-7}), which is transcribed into an HR competent protein [87,94,95]. However, no clinical data support the classification of the variants S206C, T207A or *BRCA2*_{delExons4-7} as benign or pathogenic [93,96]. In contrast, in frame deletion of exon 12 that causes a strong decrease in HSF2BP binding does not impact HR efficiency [97,98].

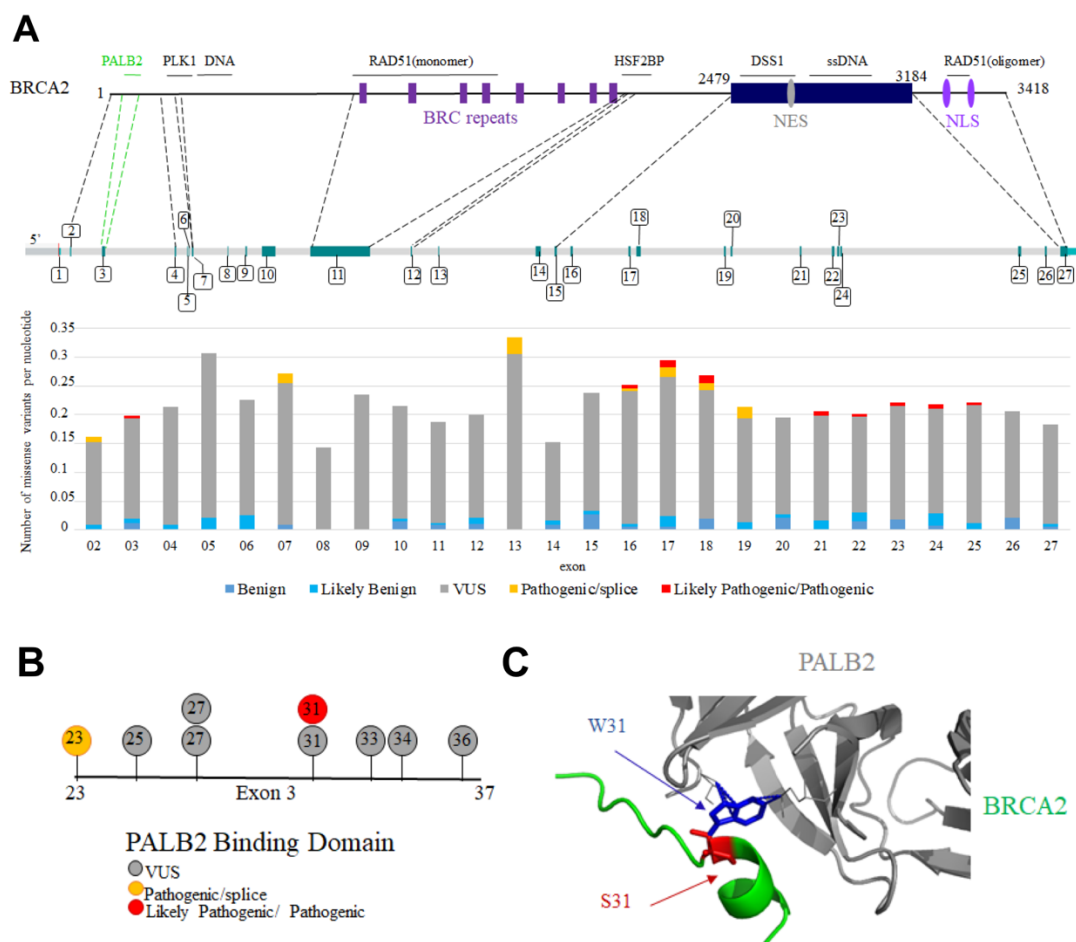


Figure 7. BRCA2 missense variants located in exons coding for disordered regions are generally of uncertain significance. (A) Distribution of the BRCA2 missense variants detected in patients with cancers in the French population. In the upper panel, BRCA2 protein and gene organization are schematized. Binding regions described in this review are indicated above the protein scheme. Protein regions encoded by exons of interest for this review are connected to their corresponding exons through dotted lines. Exon numbers are indicated. In the lower panel, the number of missense variants is represented per nucleotide and per exon of BRCA2, as deduced from the analysis of the French database. (B) BRCA2 variants mutated in the PALB2 binding site encoded by exon 3; (C) 3D structure of the interface between BRCA2 and PALB2, with a focus on the variant W31S. The wild-type Trp31 (blue) was mutated to a Ser (red) in the 3D structure referenced as PDB 3EU7 using the online server Missense3D [99].

As stated above, most high-throughput functional assays performed to improve the interpretation of variants are based on the evaluation of the HR function of BRCA2 [100–103]. Using this type of assays, pathogenic variants were identified in the *N*-terminal disordered region binding to PALB2 and in the *C*-terminal folded DBD binding to ssDNA and DSS1. This is consistent with the fact that these BRCA2 regions are essential for HR. However, other functions of BRCA2 were revealed, for example in the protection of stalled replication forks [3], during conflicts between DNA transcription and replication [104], at DNA-RNA hybrids [105,106] or in mitosis [57]. Disordered regions of BRCA2 contribute to these mechanisms, which can then be regulated by post-translational modifications. Defects in these emerging functions might also promote chromosome instability and tumorigenesis [107]. Thus, the concept of BRCAness should nowadays be redefined to include BRCA2 new functions, and the role of variants of IDRs should be reassessed to take into account new mechanisms potentially leading to tumorigenesis.

11. Conclusions

Here, we illustrated how BRCA2's large disordered regions serve to recruit kinases, phosphatases as well as other proteins involved in genome integrity. We described how the N-terminal and central regions of BRCA2 bind to PALB2, RAD51 and DNA, thus contributing, together with the C-terminal folded DNA binding domain, to the function of BRCA2 in DNA repair by HR. Testing the HR capacity of cancer-associated variants is still the most common approach used to experimentally validate the pathogenicity of these variants, i.e., their impact on tumorigenesis. In BRCA2 IDRs, a variant affecting Trp31 is nowadays being classified as pathogenic and impairs HR. A set of variants characterized by an intermediate HR efficiency (hypomorphic variants) were also identified, which are still not classified in the case of BRCA2, but could correspond to a new class associated with an intermediate cancer risk [108]. Other functional defects of BRCA2 might reveal additional variants with a pathogenic impact in IDRs. Indeed, the disordered regions of BRCA2 are involved in BRCA2 oligomerization, thus potentially indirectly regulating a number of other functions. In particular, mutating the BRC4 repeat was reported as significantly reducing BRCA2 ability to self-associate [23]. Further work is needed in order to identify the intramolecular interactions involved in BRCA2 oligomerization as well as their modes of regulation during DNA repair or throughout the cell cycle. BRCA2 central region is also able to recruit the meiotic protein HSF2BP, whose overexpression triggers BRCA2 degradation. Thus, BRCA2 IDRs might contribute to control BRCA2 level in cells.

Finally, BRCA2 IDRs are phosphorylated by kinases regulating DNA repair and mitosis. These phosphorylation events are still poorly described. However, they can be functionally critical and required for the coordination of the interphase and mitotic functions of BRCA2. Further studies combining biophysics and cell biology approaches are now needed to identify new phospho-dependent partners for the reported disordered and conserved motifs in BRCA2, as well as to elucidate the function of other less characterized conserved motifs. Such studies will enlarge our knowledge of the molecular events contributing to genome integrity. It will also enlarge the set of experimental assays available to assess the pathogenicity of variants. It will finally stimulate the design of new therapeutic strategies targeting cancers triggered by specific variants.

Author Contributions: Conceptualization, M.J., S.M.C., S.Z.-J.; Investigation, M.J., R.G., A.P.; Writing-Original Draft Preparation, M.J., R.G., A.P., S.M.C., S.Z.-J.; Writing-Review & Editing, S.M.C., A.C., S.Z.-J.; Visualization, M.J., R.G., A.P., S.Z.-J.; Supervision, S.Z.-J.; Funding Acquisition, M.J., S.M.C., A.C., S.Z.-J. All authors have read and agreed to the published version of the manuscript.

Funding: This research was funded by the French ANR grant FUNBRCA2 to A.C. and S.Z.J., the French Institut National du Cancer (INCA) to A.P. (PRT-K14-134) and S.C. and The Breast Cancer Research Foundation (BCRF) to A.P. It was also supported by the French Infrastructure for Integrated Structural Biology (<https://www.structuralbiology.eu/networks/frisbi>, ANR-10-INSB-05-01), by the CNRS IR-RMN-THC Fr3050 and by the CEA.

Institutional Review Board Statement: Not applicable.

Informed Consent Statement: Not applicable.

Data Availability Statement: Not applicable.

Acknowledgments: We are grateful to Philippe Cuniassé for the human BRCA2 DBD 3D model, as well as Simona Miron and Isaac Dumoulin for their help during the DNA binding assays and François-Xavier Theillet for advice and discussions.

Conflicts of Interest: The authors declare no conflict of interest.

References

1. Sharan, S.K.; Morimatsu, M.; Albrecht, U.; Lim, D.S.; Regel, E.; Dinh, C.; Sands, A.; Eichele, G.; Hasty, P.; Bradley, A. Embryonic lethality and radiation hypersensitivity mediated by Rad51 in mice lacking Brca2. *Nature* **1997**, *386*, 804–810. [[CrossRef](#)] [[PubMed](#)]
2. Lee, S.A.; Baker, M.D. Analysis of DNA repair and recombination responses in mouse cells depleted for Brca2 by SiRNA. *DNA Repair* **2007**, *6*, 809–817. [[CrossRef](#)] [[PubMed](#)]

3. Schlacher, K.; Christ, N.; Siaud, N.; Egashira, A.; Wu, H.; Jasin, M. Double-strand break repair-independent role for BRCA2 in blocking stalled replication fork degradation by MRE11. *Cell* **2011**, *145*, 529–542. [[CrossRef](#)] [[PubMed](#)]
4. Badie, S.; Escandell, J.M.; Bouwman, P.; Carlos, A.R.; Thanasoula, M.; Gallardo, M.M.; Suram, A.; Jaco, I.; Benitez, J.; Herbig, U.; et al. BRCA2 acts as a RAD51 loader to facilitate telomere replication and capping. *Nat. Struct. Mol. Biol.* **2010**, *17*, 1461–1469. [[CrossRef](#)]
5. Min, J.; Choi, E.S.; Hwang, K.; Kim, J.; Sampath, S.; Venkitaraman, A.R.; Lee, H. The breast cancer susceptibility gene BRCA2 is required for the maintenance of telomere homeostasis. *J. Biol. Chem.* **2012**, *287*, 5091–5101. [[CrossRef](#)]
6. Daniels, M.J.; Wang, Y.; Lee, M.; Venkitaraman, A.R. Abnormal cytokinesis in cells deficient in the breast cancer susceptibility protein BRCA2. *Science* **2004**, *306*, 876–879. [[CrossRef](#)]
7. Takaoka, M.; Saito, H.; Takenaka, K.; Miki, Y.; Nakanishi, A. BRCA2 phosphorylated by PLK1 moves to the midbody to regulate cytokinesis mediated by nonmuscle myosin IIC. *Cancer Res.* **2014**, *74*, 1518–1528. [[CrossRef](#)]
8. Sharan, S.K.; Pyle, A.; Coppola, V.; Babus, J.; Swaminathan, S.; Benedict, J.; Swing, D.; Martin, B.K.; Tessarollo, L.; Evans, J.P.; et al. BRCA2 deficiency in mice leads to meiotic impairment and infertility. *Development* **2004**, *131*, 131–142. [[CrossRef](#)] [[PubMed](#)]
9. Wong, A.K.; Pero, R.; Ormonde, P.A.; Tavtigian, S.V.; Bartel, P.L. RAD51 interacts with the evolutionarily conserved BRC motifs in the human breast cancer susceptibility gene brca2. *J. Biol. Chem.* **1997**, *272*, 31941–31944. [[CrossRef](#)] [[PubMed](#)]
10. Chen, P.L.; Chen, C.F.; Chen, Y.; Xiao, J.; Sharp, Z.D.; Lee, W.H. The BRC repeats in BRCA2 are critical for RAD51 binding and resistance to methyl methanesulfonate treatment. *Proc. Natl. Acad. Sci. USA* **1998**, *95*, 5287–5292. [[CrossRef](#)] [[PubMed](#)]
11. Pellegrini, L.; Yu, D.S.; Lo, T.; Anand, S.; Lee, M.; Blundell, T.L.; Venkitaraman, A.R. Insights into DNA recombination from the structure of a RAD51-BRCA2 complex. *Nature* **2002**, *420*, 287–293. [[CrossRef](#)] [[PubMed](#)]
12. Lee, H.; Trainer, A.H.; Friedman, L.S.; Thistlethwaite, F.C.; Evans, M.J.; Ponder, B.A.; Venkitaraman, A.R. Mitotic checkpoint inactivation fosters transformation in cells lacking the breast cancer susceptibility gene, Brca2. *Mol. Cell* **1999**, *4*, 1–10. [[CrossRef](#)]
13. Howlett, N.G.; Taniguchi, T.; Olson, S.; Cox, B.; Waisfisz, Q.; De Die-Smulders, C.; Persky, N.; Grompe, M.; Joenje, H.; Pals, G.; et al. Biallelic inactivation of BRCA2 in Fanconi anemia. *Science* **2002**, *297*, 606–609. [[CrossRef](#)]
14. Nalepa, G.; Clapp, D.W. Fanconi anaemia and cancer: An intricate relationship. *Nat. Rev. Cancer* **2018**, *18*, 168–185. [[CrossRef](#)]
15. Wooster, R.; Neuhausen, S.L.; Mangion, J.; Quirk, Y.; Ford, D.; Collins, N.; Nguyen, K.; Seal, S.; Tran, T.; Averill, D.; et al. Localization of a breast cancer susceptibility gene, BRCA2, to chromosome 13q12-13. *Science* **1994**, *265*, 2088–2090. [[CrossRef](#)]
16. Szabo, C.I.; King, M.C. Inherited breast and ovarian cancer. *Hum. Mol. Genet.* **1995**, *4*, 1811–1817. [[CrossRef](#)] [[PubMed](#)]
17. Kuchenbaecker, K.B.; Hopper, J.L.; Barnes, D.R.; Phillips, K.A.; Mooij, T.M.; Roos-Blom, M.J.; Jervis, S.; van Leeuwen, F.E.; Milne, R.L.; Andrieu, N.; et al. Risks of Breast, Ovarian, and Contralateral Breast Cancer for BRCA1 and BRCA2 Mutation Carriers. *JAMA* **2017**, *317*, 2402–2416. [[CrossRef](#)] [[PubMed](#)]
18. Mersch, J.; Jackson, M.A.; Park, M.; Nebgen, D.; Peterson, S.K.; Singletary, C.; Arun, B.K.; Litton, J.K. Cancers associated with BRCA1 and BRCA2 mutations other than breast and ovarian. *Cancer* **2015**, *121*, 269–275. [[CrossRef](#)]
19. Yang, H.; Jeffrey, P.D.; Miller, J.; Kinnucan, E.; Sun, Y.; Thoma, N.H.; Zheng, N.; Chen, P.L.; Lee, W.H.; Pavletich, N.P. BRCA2 function in DNA binding and recombination from a BRCA2-DSS1-ssDNA structure. *Science* **2002**, *297*, 1837–1848. [[CrossRef](#)]
20. Hanson, J.; Paliwal, K.K.; Litfin, T.; Zhou, Y. SPOT-Disorder2: Improved Protein Intrinsic Disorder Prediction by Ensembled Deep Learning. *Genom. Proteom. Bioinform.* **2019**, *17*, 645–656. [[CrossRef](#)]
21. Shahid, T.; Soroka, J.; Kong, E.; Malivert, L.; McIlwraith, M.J.; Pape, T.; West, S.C.; Zhang, X. Structure and mechanism of action of the BRCA2 breast cancer tumor suppressor. *Nat. Struct. Mol. Biol.* **2014**, *21*, 962–968. [[CrossRef](#)]
22. Sanchez, H.; Paul, M.W.; Grosbart, M.; van Rossum-Fikkert, S.E.; Lebbink, J.H.G.; Kanaar, R.; Houtsmuller, A.B.; Wyman, C. Architectural plasticity of human BRCA2-RAD51 complexes in DNA break repair. *Nucleic Acids Res.* **2017**, *45*, 4507–4518. [[CrossRef](#)] [[PubMed](#)]
23. Sidhu, A.; Grosbart, M.; Sanchez, H.; Verhagen, B.; van der Zon, N.L.L.; Ristic, D.; van Rossum-Fikkert, S.E.; Wyman, C. Conformational flexibility and oligomerization of BRCA2 regions induced by RAD51 interaction. *Nucleic Acids Res.* **2020**, *48*, 9649–9659. [[CrossRef](#)] [[PubMed](#)]
24. Le, H.P.; Ma, X.; Vaquero, J.; Brinkmeyer, M.; Guo, F.; Heyer, W.D.; Liu, J. DSS1 and ssDNA regulate oligomerization of BRCA2. *Nucleic Acids Res.* **2020**, *48*, 7818–7833. [[CrossRef](#)]
25. Iakoucheva, L.M.; Brown, C.J.; Lawson, J.D.; Obradovic, Z.; Dunker, A.K. Intrinsic disorder in cell-signaling and cancer-associated proteins. *J. Mol. Biol.* **2002**, *323*, 573–584. [[CrossRef](#)]
26. Babu, M.M.; van der Lee, R.; de Groot, N.S.; Gsponer, J. Intrinsically disordered proteins: Regulation and disease. *Curr. Opin. Struct. Biol.* **2011**, *21*, 432–440. [[CrossRef](#)] [[PubMed](#)]
27. Meszaros, B.; Tompa, P.; Simon, I.; Dosztanyi, Z. Molecular principles of the interactions of disordered proteins. *J. Mol. Biol.* **2007**, *372*, 549–561. [[CrossRef](#)]
28. Berlow, R.B.; Dyson, H.J.; Wright, P.E. Functional advantages of dynamic protein disorder. *FEBS Lett.* **2015**, *589*, 2433–2440. [[CrossRef](#)]
29. Dunker, A.K.; Brown, C.J.; Lawson, J.D.; Iakoucheva, L.M.; Obradovic, Z. Intrinsic disorder and protein function. *Biochemistry* **2002**, *41*, 6573–6582. [[CrossRef](#)]
30. Moesa, H.A.; Wakabayashi, S.; Nakai, K.; Patil, A. Chemical composition is maintained in poorly conserved intrinsically disordered regions and suggests a means for their classification. *Mol. Biosyst.* **2012**, *8*, 3262–3273. [[CrossRef](#)]

31. Habchi, J.; Tompa, P.; Longhi, S.; Uversky, V.N. Introducing protein intrinsic disorder. *Chem. Rev.* **2014**, *114*, 6561–6588. [[CrossRef](#)] [[PubMed](#)]
32. Nielsen, J.T.; Mulder, F.A.A. Quality and bias of protein disorder predictors. *Sci. Rep.* **2019**, *9*, 5137. [[CrossRef](#)]
33. Martinez, J.S.; von Nicolai, C.; Kim, T.; Ehlen, A.; Mazin, A.V.; Kowalczykowski, S.C.; Carreira, A. BRCA2 regulates DMC1-mediated recombination through the BRC repeats. *Proc. Natl. Acad. Sci. USA* **2016**, *113*, 3515–3520. [[CrossRef](#)]
34. Livingstone, C.D.; Barton, G.J. Protein sequence alignments: A strategy for the hierarchical analysis of residue conservation. *Comput. Appl. Biosci.* **1993**, *9*, 745–756. [[CrossRef](#)]
35. Oliver, A.W.; Swift, S.; Lord, C.J.; Ashworth, A.; Pearl, L.H. Structural basis for recruitment of BRCA2 by PALB2. *EMBO Rep.* **2009**, *10*, 990–996. [[CrossRef](#)] [[PubMed](#)]
36. Patel, K.J.; Yu, V.P.; Lee, H.; Corcoran, A.; Thistlethwaite, F.C.; Evans, M.J.; Colledge, W.H.; Friedman, L.S.; Ponder, B.A.; Venkitaraman, A.R. Involvement of Brca2 in DNA repair. *Mol. Cell* **1998**, *1*, 347–357. [[CrossRef](#)]
37. Xia, B.; Sheng, Q.; Nakanishi, K.; Ohashi, A.; Wu, J.; Christ, N.; Liu, X.; Jasin, M.; Couch, F.J.; Livingston, D.M. Control of BRCA2 cellular and clinical functions by a nuclear partner, PALB2. *Mol. Cell* **2006**, *22*, 719–729. [[CrossRef](#)]
38. Zhang, F.; Ma, J.; Wu, J.; Ye, L.; Cai, H.; Xia, B.; Yu, X. PALB2 links BRCA1 and BRCA2 in the DNA-damage response. *Curr. Biol.* **2009**, *19*, 524–529. [[CrossRef](#)]
39. Park, J.Y.; Singh, T.R.; Nassar, N.; Zhang, F.; Freund, M.; Hanenberg, H.; Meetei, A.R.; Andreassen, P.R. Breast cancer-associated missense mutants of the PALB2 WD40 domain, which directly binds RAD51C, RAD51 and BRCA2, disrupt DNA repair. *Oncogene* **2014**, *33*, 4803–4812. [[CrossRef](#)]
40. Chen, R.; Wold, M.S. Replication protein A: Single-stranded DNA's first responder: Dynamic DNA-interactions allow replication protein A to direct single-strand DNA intermediates into different pathways for synthesis or repair. *Bioessays* **2014**, *36*, 1156–1161. [[CrossRef](#)]
41. Ma, C.J.; Gibb, B.; Kwon, Y.; Sung, P.; Greene, E.C. Protein dynamics of human RPA and RAD51 on ssDNA during assembly and disassembly of the RAD51 filament. *Nucleic Acids Res.* **2017**, *45*, 749–761. [[CrossRef](#)]
42. Zhao, W.; Vaithiyalingam, S.; San Filippo, J.; Maranon, D.G.; Jimenez-Sainz, J.; Fontenay, G.V.; Kwon, Y.; Leung, S.G.; Lu, L.; Jensen, R.B.; et al. Promotion of BRCA2-Dependent Homologous Recombination by DSS1 via RPA Targeting and DNA Mimicry. *Mol. Cell* **2015**, *59*, 176–187. [[CrossRef](#)]
43. Carreira, A.; Hilario, J.; Amitani, I.; Baskin, R.J.; Shivji, M.K.; Venkitaraman, A.R.; Kowalczykowski, S.C. The BRC repeats of BRCA2 modulate the DNA-binding selectivity of RAD51. *Cell* **2009**, *136*, 1032–1043. [[CrossRef](#)] [[PubMed](#)]
44. Carreira, A.; Kowalczykowski, S.C. Two classes of BRC repeats in BRCA2 promote RAD51 nucleoprotein filament function by distinct mechanisms. *Proc. Natl. Acad. Sci. USA* **2011**, *108*, 10448–10453. [[CrossRef](#)]
45. Dray, E.; Siaud, N.; Dubois, E.; Doutriaux, M.P. Interaction between Arabidopsis Brca2 and its partners Rad51, Dmc1, and Dss1. *Plant Physiol.* **2006**, *140*, 1059–1069. [[CrossRef](#)] [[PubMed](#)]
46. Thorslund, T.; Esashi, F.; West, S.C. Interactions between human BRCA2 protein and the meiosis-specific recombinase DMC1. *EMBO J.* **2007**, *26*, 2915–2922. [[CrossRef](#)] [[PubMed](#)]
47. Hashimoto, Y.; Ray Chaudhuri, A.; Lopes, M.; Costanzo, V. Rad51 protects nascent DNA from Mre11-dependent degradation and promotes continuous DNA synthesis. *Nat. Struct. Mol. Biol.* **2010**, *17*, 1305–1311. [[CrossRef](#)] [[PubMed](#)]
48. Esashi, F.; Galkin, V.E.; Yu, X.; Egelman, E.H.; West, S.C. Stabilization of RAD51 nucleoprotein filaments by the C-terminal region of BRCA2. *Nat. Struct. Mol. Biol.* **2007**, *14*, 468–474. [[CrossRef](#)]
49. Davies, O.R.; Pellegrini, L. Interaction with the BRCA2 C terminus protects RAD51-DNA filaments from disassembly by BRC repeats. *Nat. Struct. Mol. Biol.* **2007**, *14*, 475–483. [[CrossRef](#)]
50. Esashi, F.; Christ, N.; Gannon, J.; Liu, Y.; Hunt, T.; Jasin, M.; West, S.C. CDK-dependent phosphorylation of BRCA2 as a regulatory mechanism for recombinational repair. *Nature* **2005**, *434*, 598–604. [[CrossRef](#)] [[PubMed](#)]
51. Buisson, R.; Niraj, J.; Pauty, J.; Maity, R.; Zhao, W.; Coulombe, Y.; Sung, P.; Masson, J.Y. Breast cancer proteins PALB2 and BRCA2 stimulate polymerase η in recombination-associated DNA synthesis at blocked replication forks. *Cell Rep.* **2014**, *6*, 553–564. [[CrossRef](#)]
52. Ayoub, N.; Rajendra, E.; Su, X.; Jeyasekharan, A.D.; Mahen, R.; Venkitaraman, A.R. The carboxyl terminus of Brca2 links the disassembly of Rad51 complexes to mitotic entry. *Curr. Biol.* **2009**, *19*, 1075–1085. [[CrossRef](#)]
53. Julien, M.; Miron, S.; Carreira, A.; Theillet, F.X.; Zinn-Justin, S. (1)H, (13)C and (15)N backbone resonance assignment of the human BRCA2 N-terminal region. *Biomol. NMR Assign.* **2020**, *14*, 79–85. [[CrossRef](#)] [[PubMed](#)]
54. Ghoul, R.; Miron, S.; Koornneef, L.; Veerman, J.; Paul, M.W.; Le Du, M.H.; Sleddens, E.; van Rossum-Fikkert, S.E.; van Loon, Y.; Felipe-Medina, N.; et al. BRCA2 binding through a cryptic repeated motif to HSF2BP oligomers does not impact meiotic recombination. *BioRxiv* **2020**. [[CrossRef](#)]
55. Dyson, H.J.; Wright, P.E. NMR illuminates intrinsic disorder. *Curr. Opin. Struct. Biol.* **2021**, *70*, 44–52. [[CrossRef](#)] [[PubMed](#)]
56. Tamiola, K.; Mulder, F.A. Using NMR chemical shifts to calculate the propensity for structural order and disorder in proteins. *Biochem. Soc. Trans.* **2012**, *40*, 1014–1020. [[CrossRef](#)] [[PubMed](#)]
57. Ehlen, A.; Martin, C.; Miron, S.; Julien, M.; Theillet, F.X.; Ropars, V.; Sessa, G.; Beaupere, R.; Boucherit, V.; Duchambon, P.; et al. Proper chromosome alignment depends on BRCA2 phosphorylation by PLK1. *Nat. Commun.* **2020**, *11*, 1819. [[CrossRef](#)] [[PubMed](#)]
58. Lin, H.R.; Ting, N.S.; Qin, J.; Lee, W.H. M phase-specific phosphorylation of BRCA2 by Polo-like kinase 1 correlates with the dissociation of the BRCA2-P/CAF complex. *J. Biol. Chem.* **2003**, *278*, 35979–35987. [[CrossRef](#)]

59. Yata, K.; Bleuyard, J.Y.; Nakato, R.; Ralf, C.; Katou, Y.; Schwab, R.A.; Niedzwiedz, W.; Shirahige, K.; Esashi, F. BRCA2 coordinates the activities of cell-cycle kinases to promote genome stability. *Cell Rep.* **2014**, *7*, 1547–1559. [\[CrossRef\]](#)
60. Yata, K.; Lloyd, J.; Maslen, S.; Bleuyard, J.Y.; Skehel, M.; Smerdon, S.J.; Esashi, F. Plk1 and CK2 act in concert to regulate Rad51 during DNA double strand break repair. *Mol. Cell* **2012**, *45*, 371–383. [\[CrossRef\]](#)
61. Mondal, G.; Rowley, M.; Guidugli, L.; Wu, J.; Pankratz, V.S.; Couch, F.J. BRCA2 localization to the midbody by filamin A regulates cep55 signaling and completion of cytokinesis. *Dev. Cell* **2012**, *23*, 137–152. [\[CrossRef\]](#) [\[PubMed\]](#)
62. Elia, A.E.; Rellos, P.; Haire, L.F.; Chao, J.W.; Ivins, F.J.; Hoepker, K.; Mohammad, D.; Cantley, L.C.; Smerdon, S.J.; Yaffe, M.B. The molecular basis for phosphodependent substrate targeting and regulation of Plks by the Polo-box domain. *Cell* **2003**, *115*, 83–95. [\[CrossRef\]](#)
63. Suijkerbuijk, S.J.; Vleugel, M.; Teixeira, A.; Kops, G.J. Integration of kinase and phosphatase activities by BUBR1 ensures formation of stable kinetochore-microtubule attachments. *Dev. Cell* **2012**, *23*, 745–755. [\[CrossRef\]](#) [\[PubMed\]](#)
64. Wang, X.; Bajaj, R.; Bollen, M.; Peti, W.; Page, R. Expanding the PP2A Interactome by Defining a B56-Specific SLiM. *Structure* **2016**, *24*, 2174–2181. [\[CrossRef\]](#) [\[PubMed\]](#)
65. Wu, C.G.; Chen, H.; Guo, F.; Yadav, V.K.; McIlwain, S.J.; Rowse, M.; Choudhary, A.; Lin, Z.; Li, Y.; Gu, T.; et al. PP2A-B' holoenzyme substrate recognition, regulation and role in cytokinesis. *Cell Discov.* **2017**, *3*, 17027. [\[CrossRef\]](#) [\[PubMed\]](#)
66. Hertz, E.P.T.; Kruse, T.; Davey, N.E.; Lopez-Mendez, B.; Sigurethsson, J.O.; Montoya, G.; Olsen, J.V.; Nilsson, J. A Conserved Motif Provides Binding Specificity to the PP2A-B56 Phosphatase. *Mol. Cell.* **2016**, *63*, 686–695. [\[CrossRef\]](#)
67. Foley, E.A.; Maldonado, M.; Kapoor, T.M. Formation of stable attachments between kinetochores and microtubules depends on the B56-PP2A phosphatase. *Nat. Cell Biol.* **2011**, *13*, 1265–1271. [\[CrossRef\]](#)
68. Futamura, M.; Arakawa, H.; Matsuda, K.; Katagiri, T.; Saji, S.; Miki, Y.; Nakamura, Y. Potential role of BRCA2 in a mitotic checkpoint after phosphorylation by hBUBR1. *Cancer Res.* **2000**, *60*, 1531–1535.
69. Choi, E.; Park, P.G.; Lee, H.O.; Lee, Y.K.; Kang, G.H.; Lee, J.W.; Han, W.; Lee, H.C.; Noh, D.Y.; Lekontsev, S.; et al. BRCA2 fine-tunes the spindle assembly checkpoint through reinforcement of BubR1 acetylation. *Dev. Cell* **2012**, *22*, 295–308. [\[CrossRef\]](#)
70. Wang, J.; Wang, Z.; Yu, T.; Yang, H.; Virshup, D.M.; Kops, G.J.; Lee, S.H.; Zhou, W.; Li, X.; Xu, W.; et al. Crystal structure of a PP2A B56-BubR1 complex and its implications for PP2A substrate recruitment and localization. *Protein Cell* **2016**, *7*, 516–526. [\[CrossRef\]](#)
71. Ambjoern, S.M.; Duxin, J.P.; Hertz, E.P.T.; Nasa, I.; Duro, J.; Kruse, T.; Mendez, B.L.; Rymarczyk, B.; Cressey, L.E.; van Overeem Hansen, T.; et al. A complex of BRCA2 and PP2A-B56 is required for DNA repair by homologous recombination. *BioRxiv* **2021**. [\[CrossRef\]](#)
72. Lee, M.; Daniels, M.J.; Venkitaraman, A.R. Phosphorylation of BRCA2 by the Polo-like kinase Plk1 is regulated by DNA damage and mitotic progression. *Oncogene* **2004**, *23*, 865–872. [\[CrossRef\]](#)
73. Thorslund, T.; McIlwraith, M.J.; Compton, S.A.; Lekontsev, S.; Petronczki, M.; Griffith, J.D.; West, S.C. The breast cancer tumor suppressor BRCA2 promotes the specific targeting of RAD51 to single-stranded DNA. *Nat. Struct. Mol. Biol.* **2010**, *17*, 1263–1265. [\[CrossRef\]](#)
74. Jensen, R.B.; Carreira, A.; Kowalczykowski, S.C. Purified human BRCA2 stimulates RAD51-mediated recombination. *Nature* **2010**, *467*, 678–683. [\[CrossRef\]](#)
75. Von Nicolai, C.; Ehlen, A.; Martin, C.; Zhang, X.; Carreira, A. A second DNA binding site in human BRCA2 promotes homologous recombination. *Nat. Commun.* **2016**, *7*, 12813. [\[CrossRef\]](#) [\[PubMed\]](#)
76. Brandsma, I.; Sato, K.; van Rossum-Fikkert, S.E.; van Vliet, N.; Sleddens, E.; Reuter, M.; Odijk, H.; van den Tempel, N.; Dekkers, D.H.W.; Bezstarosti, K.; et al. HSF2BP Interacts with a Conserved Domain of BRCA2 and Is Required for Mouse Spermatogenesis. *Cell Rep.* **2019**, *27*, 3790–3798.e7. [\[CrossRef\]](#)
77. Sato, K.; Brandsma, I.; van Rossum-Fikkert, S.E.; Verkaik, N.; Oostra, A.B.; Dorsman, J.C.; van Gent, D.C.; Knipscheer, P.; Kanaar, R.; Zelensky, A.N. HSF2BP negatively regulates homologous recombination in DNA interstrand crosslink repair. *Nucleic Acids Res.* **2020**, *48*, 2442–2456. [\[CrossRef\]](#)
78. Zhang, J.; Fujiwara, Y.; Yamamoto, S.; Shibuya, H. A meiosis-specific BRCA2 binding protein recruits recombinases to DNA double-strand breaks to ensure homologous recombination. *Nat. Commun.* **2019**, *10*, 722. [\[CrossRef\]](#) [\[PubMed\]](#)
79. Zhang, J.; Gurusaran, M.; Fujiwara, Y.; Zhang, K.; Echbarhi, M.; Vorontsov, E.; Guo, R.; Pendlebury, D.F.; Alam, I.; Livera, G.; et al. The BRCA2-MEILB2-BRME1 complex governs meiotic recombination and impairs the mitotic BRCA2-RAD51 function in cancer cells. *Nat. Commun.* **2020**, *11*, 2055. [\[CrossRef\]](#) [\[PubMed\]](#)
80. Farmer, H.; McCabe, N.; Lord, C.J.; Tutt, A.N.; Johnson, D.A.; Richardson, T.B.; Santarosa, M.; Dillon, K.J.; Hickson, I.; Knights, C.; et al. Targeting the DNA repair defect in BRCA mutant cells as a therapeutic strategy. *Nature* **2005**, *434*, 917–921. [\[CrossRef\]](#) [\[PubMed\]](#)
81. Bryant, H.E.; Schultz, N.; Thomas, H.D.; Parker, K.M.; Flower, D.; Lopez, E.; Kyle, S.; Meuth, M.; Curtin, N.J.; Helleday, T. Specific killing of BRCA2-deficient tumours with inhibitors of poly(ADP-ribose) polymerase. *Nature* **2005**, *434*, 913–917. [\[CrossRef\]](#) [\[PubMed\]](#)
82. Plon, S.E.; Eccles, D.M.; Easton, D.; Foulkes, W.D.; Genuardi, M.; Greenblatt, M.S.; Hogervorst, F.B.; Hoogerbrugge, N.; Spurdle, A.B.; Tavtigian, S.V.; et al. Sequence variant classification and reporting: Recommendations for improving the interpretation of cancer susceptibility genetic test results. *Hum. Mutat.* **2008**, *29*, 1282–1291. [\[CrossRef\]](#)

83. Caputo, S.; Benboudjema, L.; Sinilnikova, O.; Rouleau, E.; Beroud, C.; Lidereau, R.; French, B.G.G.C.C. Description and analysis of genetic variants in French hereditary breast and ovarian cancer families recorded in the UMD-BRCA1/BRCA2 databases. *Nucleic Acids Res.* **2012**, *40*, D992–D1002. [\[CrossRef\]](#) [\[PubMed\]](#)
84. Lesueur, F.; Mebirouk, N.; Jiao, Y.; Barjhoux, L.; Belotti, M.; Laurent, M.; Leone, M.; Houdayer, C.; Bressac-de Paillerets, B.; Vaur, D.; et al. GEMO, a National Resource to Study Genetic Modifiers of Breast and Ovarian Cancer Risk in BRCA1 and BRCA2 Pathogenic Variant Carriers. *Front. Oncol.* **2018**, *8*, 490. [\[CrossRef\]](#) [\[PubMed\]](#)
85. Rebbeck, T.R.; Friebel, T.M.; Friedman, E.; Hamann, U.; Huo, D.; Kwong, A.; Olah, E.; Olopade, O.I.; Solano, A.R.; Teo, S.H.; et al. Mutational spectrum in a worldwide study of 29,700 families with BRCA1 or BRCA2 mutations. *Hum. Mutat.* **2018**, *39*, 593–620. [\[CrossRef\]](#)
86. Parsons, M.T.; Tudini, E.; Li, H.; Hahnen, E.; Wappenschmidt, B.; Feliubadalo, L.; Aalfs, C.M.; Agata, S.; Aittomaki, K.; Alducci, E.; et al. Large scale multifactorial likelihood quantitative analysis of BRCA1 and BRCA2 variants: An ENIGMA resource to support clinical variant classification. *Hum. Mutat.* **2019**, *40*, 1557–1578. [\[CrossRef\]](#)
87. Mesman, R.L.S.; Calleja, F.; de la Hoya, M.; Devilee, P.; van Asperen, C.J.; Vrieling, H.; Vreeswijk, M.P.G. Alternative mRNA splicing can attenuate the pathogenicity of presumed loss-of-function variants in BRCA2. *Genet. Med.* **2020**, *22*, 1355–1365. [\[CrossRef\]](#)
88. Rosenthal, E.; Moyes, K.; Arnell, C.; Evans, B.; Wenstrup, R.J. Incidence of BRCA1 and BRCA2 non-founder mutations in patients of Ashkenazi Jewish ancestry. *Breast Cancer Res. Treat.* **2015**, *149*, 223–227. [\[CrossRef\]](#)
89. Houdayer, C.; Caux-Moncoutier, V.; Krieger, S.; Barrois, M.; Bonnet, F.; Bourdon, V.; Bronner, M.; Buisson, M.; Coulet, F.; Gaildrat, P.; et al. Guidelines for splicing analysis in molecular diagnosis derived from a set of 327 combined in silico/in vitro studies on BRCA1 and BRCA2 variants. *Hum. Mutat.* **2012**, *33*, 1228–1238. [\[CrossRef\]](#)
90. Muller, D.; Rouleau, E.; Schultz, I.; Caputo, S.; Lefol, C.; Bieche, I.; Caron, O.; Nogues, C.; Limacher, J.M.; Demange, L.; et al. An entire exon 3 germ-line rearrangement in the BRCA2 gene: Pathogenic relevance of exon 3 deletion in breast cancer predisposition. *BMC Med. Genet.* **2011**, *12*, 121. [\[CrossRef\]](#)
91. Caputo, S.M.; Leone, M.; Damiola, F.; Ehlen, A.; Carreira, A.; Gaidrat, P.; Martins, A.; Brandao, R.D.; Peixoto, A.; Vega, A.; et al. Full in-frame exon 3 skipping of BRCA2 confers high risk of breast and/or ovarian cancer. *Oncotarget* **2018**, *9*, 17334–17348. [\[CrossRef\]](#)
92. Tubeuf, H.; Caputo, S.M.; Sullivan, T.; Rondeaux, J.; Krieger, S.; Caux-Moncoutier, V.; Hauchard, J.; Castelain, G.; Fievet, A.; Meulemans, L.; et al. Calibration of Pathogenicity Due to Variant-Induced Leaky Splicing Defects by Using BRCA2 Exon 3 as a Model System. *Cancer Res.* **2020**, *80*, 3593–3605. [\[CrossRef\]](#)
93. Gaildrat, P.; Krieger, S.; Di Giacomo, D.; Abdat, J.; Revillion, F.; Caputo, S.; Vaur, D.; Jamard, E.; Bohers, E.; Ledemeney, D.; et al. Multiple sequence variants of BRCA2 exon 7 alter splicing regulation. *J. Med. Genet.* **2012**, *49*, 609–617. [\[CrossRef\]](#)
94. Thirthagiri, E.; Klarmann, K.D.; Shukla, A.K.; Southon, E.; Biswas, K.; Martin, B.K.; North, S.L.; Magidson, V.; Burkett, S.; Haines, D.C.; et al. BRCA2 minor transcript lacking exons 4–7 supports viability in mice and may account for survival of humans with a pathogenic biallelic mutation. *Hum. Mol. Genet.* **2016**, *25*, 1934–1945. [\[CrossRef\]](#)
95. Stauffer, S.; Biswas, K.; Sharan, S.K. Bypass of premature stop codons and generation of functional BRCA2 by exon skipping. *J. Hum. Genet.* **2020**, *65*, 805–809. [\[CrossRef\]](#)
96. Di Giacomo, D.; Gaildrat, P.; Abuli, A.; Abdat, J.; Frebourg, T.; Tosi, M.; Martins, A. Functional analysis of a large set of BRCA2 exon 7 variants highlights the predictive value of hexamer scores in detecting alterations of exonic splicing regulatory elements. *Hum. Mutat.* **2013**, *34*, 1547–1557. [\[CrossRef\]](#)
97. Li, L.; Biswas, K.; Habib, L.A.; Kuznetsov, S.G.; Hamel, N.; Kirchhoff, T.; Wong, N.; Armel, S.; Chong, G.; Narod, S.A.; et al. Functional redundancy of exon 12 of BRCA2 revealed by a comprehensive analysis of the c.6853A>G (p.I2285V) variant. *Hum. Mutat.* **2009**, *30*, 1543–1550. [\[CrossRef\]](#) [\[PubMed\]](#)
98. Meulemans, L.; Mesman, R.L.S.; Caputo, S.M.; Krieger, S.; Guillaud-Bataille, M.; Caux-Moncoutier, V.; Leone, M.; Boutry-Kryza, N.; Sokolowska, J.; Revillion, F.; et al. Skipping Nonsense to Maintain Function: The Paradigm of BRCA2 Exon 12. *Cancer Res.* **2020**, *80*, 1374–1386. [\[CrossRef\]](#) [\[PubMed\]](#)
99. Ittisoponpisan, S.; Islam, S.A.; Khanna, T.; Alhuzimi, E.; David, A.; Sternberg, M.J. Can Predicted Protein 3D Structures Provide Reliable Insights into whether Missense Variants Are Disease Associated? *J. Mol. Biol.* **2019**, *431*, 2197–2212. [\[CrossRef\]](#) [\[PubMed\]](#)
100. Guidugli, L.; Carreira, A.; Caputo, S.M.; Ehlen, A.; Galli, A.; Monteiro, A.N.; Neuhausen, S.L.; Hansen, T.V.; Couch, F.J.; Vreeswijk, M.P.; et al. Functional assays for analysis of variants of uncertain significance in BRCA2. *Hum. Mutat.* **2014**, *35*, 151–164. [\[CrossRef\]](#) [\[PubMed\]](#)
101. Toland, A.E.; Andreassen, P.R. DNA repair-related functional assays for the classification of BRCA1 and BRCA2 variants: A critical review and needs assessment. *J. Med. Genet.* **2017**, *54*, 721–731. [\[CrossRef\]](#)
102. Ikegami, M.; Kohsaka, S.; Ueno, T.; Momozawa, Y.; Inoue, S.; Tamura, K.; Shimomura, A.; Hosoya, N.; Kobayashi, H.; Tanaka, S.; et al. High-throughput functional evaluation of BRCA2 variants of unknown significance. *Nat. Commun.* **2020**, *11*, 2573. [\[CrossRef\]](#) [\[PubMed\]](#)
103. Richardson, M.E.; Hu, C.; Lee, K.Y.; LaDuca, H.; Fulk, K.; Durda, K.M.; Deckman, A.M.; Goldgar, D.E.; Monteiro, A.N.A.; Gnanaolivu, R.; et al. Strong functional data for pathogenicity or neutrality classify BRCA2 DNA-binding-domain variants of uncertain significance. *Am. J. Hum. Genet.* **2021**, *108*, 458–468. [\[CrossRef\]](#) [\[PubMed\]](#)

-
104. Shao, X.; Joergensen, A.M.; Howlett, N.G.; Lisby, M.; Oestergaard, V.H. A distinct role for recombination repair factors in an early cellular response to transcription-replication conflicts. *Nucleic Acids Res.* **2020**, *48*, 5467–5484. [[CrossRef](#)] [[PubMed](#)]
 105. Bhatia, V.; Barroso, S.I.; Garcia-Rubio, M.L.; Tumini, E.; Herrera-Moyano, E.; Aguilera, A. BRCA2 prevents R-loop accumulation and associates with TREX-2 mRNA export factor PCID2. *Nature* **2014**, *511*, 362–365. [[CrossRef](#)]
 106. Sessa, G.; Gomez-Gonzalez, B.; Silva, S.; Perez-Calero, C.; Beaupere, R.; Barroso, S.; Martineau, S.; Martin, C.; Ehlen, A.; Martinez, J.S.; et al. BRCA2 promotes DNA-RNA hybrid resolution by DDX5 helicase at DNA breaks to facilitate their repair double dagger. *EMBO J.* **2021**, *40*, e106018. [[CrossRef](#)]
 107. Byrum, A.K.; Vindigni, A.; Mosammaparast, N. Defining and Modulating ‘BRCAness’. *Trends Cell Biol.* **2019**, *29*, 740–751. [[CrossRef](#)] [[PubMed](#)]
 108. Shimelis, H.; Mesman, R.L.S.; Von Nicolai, C.; Ehlen, A.; Guidugli, L.; Martin, C.; Calleja, F.; Meeks, H.; Hallberg, E.; Hinton, J.; et al. BRCA2 Hypomorphic Missense Variants Confer Moderate Risks of Breast Cancer. *Cancer Res.* **2017**, *77*, 2789–2799. [[CrossRef](#)]

REFERENCES

- Aboussekhra, A., R. Chanet, A. Adjiri, and F. Fabre. "Semidominant Suppressors of Srs2 Helicase Mutations of *Saccharomyces Cerevisiae* Map in the RAD51 Gene, Whose Sequence Predicts a Protein with Similarities to Procaryotic RecA Proteins." *Molecular and Cellular Biology* 12, no. 7 (July 1992): 3224–34. <https://doi.org/10.1128/mcb.12.7.3224-3234.1992>.
- Aebi, U., and T. D. Pollard. "A Glow Discharge Unit to Render Electron Microscope Grids and Other Surfaces Hydrophilic." *Journal of Electron Microscopy Technique* 7, no. 1 (September 1987): 29–33. <https://doi.org/10.1002/jemt.1060070104>.
- Akers, Stacey N., Kunle Odunsi, and Adam R. Karpf. "Regulation of Cancer Germline Antigen Gene Expression: Implications for Cancer Immunotherapy." *Future Oncology (London, England)* 6, no. 5 (May 2010): 717–32. <https://doi.org/10.2217/fon.10.36>.
- Alik, Ania, Chafiaa Bouguechtouli, Manon Julien, Wolfgang Bermel, Rania Ghoul, Sophie Zinn-Justin, and Francois-Xavier Theillet. "Sensitivity-Enhanced ¹³ C-NMR Spectroscopy for Monitoring Multisite Phosphorylation at Physiological Temperature and PH." *Angewandte Chemie* 132, no. 26 (June 22, 2020): 10497–501. <https://doi.org/10.1002/ange.202002288>.
- Ambjørn, Sara M., Julien P. Duxin, Emil P. T. Hertz, Isha Nasa, Joana Duro, Thomas Kruse, Blanca Lopez-Mendez, et al. "A Complex of BRCA2 and PP2A-B56 Is Required for DNA Repair by Homologous Recombination." *Nature Communications* 12, no. 1 (September 30, 2021): 5748. <https://doi.org/10.1038/s41467-021-26079-0>.
- Andor, Noemi, Carlo C. Maley, and Hanlee P. Ji. "Genomic Instability in Cancer: Teetering on the Limit of Tolerance." *Cancer Research* 77, no. 9 (May 1, 2017): 2179–85. <https://doi.org/10.1158/0008-5472.CAN-16-1553>.
- Antoniou, Antonis C., Silvia Casadei, Tuomas Heikkinen, Daniel Barrowdale, Katri Pylkäs, Jonathan Roberts, Andrew Lee, et al. "Breast-Cancer Risk in Families with Mutations in PALB2." *The New England Journal of Medicine* 371, no. 6 (August 7, 2014): 497–506. <https://doi.org/10.1056/NEJMoal400382>.
- Baler, R., G. Dahl, and R. Voellmy. "Activation of Human Heat Shock Genes Is Accompanied by Oligomerization, Modification, and Rapid Translocation of Heat Shock Transcription Factor HSF1." *Molecular and Cellular Biology* 13, no. 4 (April 1993): 2486–96. <https://doi.org/10.1128/mcb.13.4.2486-2496.1993>.
- Barr, Francis A., Herman H. W. Silljé, and Erich A. Nigg. "Polo-like Kinases and the Orchestration of Cell Division." *Nature Reviews. Molecular Cell Biology* 5, no. 6 (June 2004): 429–40. <https://doi.org/10.1038/nrm1401>.
- Baudat, Frédéric, Yukiko Imai, and Bernard de Massy. "Meiotic Recombination in Mammals: Localization and Regulation." *Nature Reviews. Genetics* 14, no. 11 (November 2013): 794–806. <https://doi.org/10.1038/nrg3573>.
- Bergink, Steven, Tim Ammon, Maximilian Kern, Lothar Schermelleh, Heinrich Leonhardt, and Stefan Jentsch. "Role of Cdc48/P97 as a SUMO-Targeted Segregase Curbing Rad51-Rad52 Interaction." *Nature Cell Biology* 15, no. 5 (May 2013): 526–32. <https://doi.org/10.1038/ncb2729>.
- Bétermier, Mireille, Valérie Borde, and Jean-Pierre de Villartay. "Coupling DNA Damage and Repair: An Essential Safeguard during Programmed DNA Double-Strand Breaks?" *Trends in Cell Biology* 30, no. 2 (February 2020): 87–96. <https://doi.org/10.1016/j.tcb.2019.11.005>.
- Bi, Baoyuan, Nataliya Rybalchenko, Efim I. Golub, and Charles M. Radding. "Human and Yeast Rad52 Proteins Promote DNA Strand Exchange." *Proceedings of the National Academy of Sciences of the United States of America* 101, no. 26 (June 29, 2004): 9568–72. <https://doi.org/10.1073/pnas.0403205101>.
- Blanco, Miguel G., Joao Matos, and Stephen C. West. "Dual Control of Yen1 Nuclease Activity and Cellular Localization by Cdk and Cdc14 Prevents Genome Instability." *Molecular Cell* 54, no. 1 (April 10, 2014): 94–106. <https://doi.org/10.1016/j.molcel.2014.02.011>.

- Booth, David S., Agustin Avila-Sakar, and Yifan Cheng. “Visualizing Proteins and Macromolecular Complexes by Negative Stain EM: From Grid Preparation to Image Acquisition.” *Journal of Visualized Experiments: JoVE*, no. 58 (December 22, 2011): 3227. <https://doi.org/10.3791/3227>.
- Brandsma, Inger, and Dik C. Gent. “Pathway Choice in DNA Double Strand Break Repair: Observations of a Balancing Act.” *Genome Integrity* 3, no. 1 (November 27, 2012): 9. <https://doi.org/10.1186/2041-9414-3-9>.
- Brandsma, Inger, Koichi Sato, Sari E. van Rossum-Fikkert, Nicole van Vliet, Esther Sleddens, Marcel Reuter, Hanny Odijk, et al. “HSF2BP Interacts with a Conserved Domain of BRCA2 and Is Required for Mouse Spermatogenesis.” *Cell Reports* 27, no. 13 (June 25, 2019): 3790–3798.e7. <https://doi.org/10.1016/j.celrep.2019.05.096>.
- Brandt, James N., and Yumi Kim. “Targeting Polo-like Kinase in Space and Time during C. Elegans Meiosis.” *Cell Cycle (Georgetown, Tex.)* 20, no. 16 (August 2021): 1519–26. <https://doi.org/10.1080/15384101.2021.1953232>.
- Brillault, Lou, and Michael J. Landsberg. “Preparation of Proteins and Macromolecular Assemblies for Cryo-Electron Microscopy.” *Methods in Molecular Biology (Clifton, N.J.)* 2073 (2020): 221–46. https://doi.org/10.1007/978-1-4939-9869-2_13.
- Bruggen, P. van der, C. Traversari, P. Chomez, C. Lurquin, E. De Plaen, B. Van den Eynde, A. Knuth, and T. Boon. “A Gene Encoding an Antigen Recognized by Cytolytic T Lymphocytes on a Human Melanoma.” *Science (New York, N.Y.)* 254, no. 5038 (December 13, 1991): 1643–47. <https://doi.org/10.1126/science.1840703>.
- Burgoyne, Paul S., Shantha K. Mahadevaiah, and James M. A. Turner. “The Consequences of Asynapsis for Mammalian Meiosis.” *Nature Reviews. Genetics* 10, no. 3 (March 2009): 207–16. <https://doi.org/10.1038/nrg2505>.
- Caburet, Sandrine, Anne-Laure Todeschini, Cynthia Petrillo, Emmanuelle Martini, Nada D. Farran, Bérangère Legois, Gabriel Livera, Johnny S. Younis, Stavit Shalev, and Reiner A. Veitia. “A Truncating MEIOB Mutation Responsible for Familial Primary Ovarian Insufficiency Abolishes Its Interaction with Its Partner SPATA22 and Their Recruitment to DNA Double-Strand Breaks.” *EBioMedicine* 42 (April 2019): 524–31. <https://doi.org/10.1016/j.ebiom.2019.03.075>.
- Cadet, Jean, and J. Richard Wagner. “DNA Base Damage by Reactive Oxygen Species, Oxidizing Agents, and UV Radiation.” *Cold Spring Harbor Perspectives in Biology* 5, no. 2 (February 1, 2013): a012559. <https://doi.org/10.1101/cshperspect.a012559>.
- Carreira, Aura, and Stephen C. Kowalczykowski. “Two Classes of BRC Repeats in BRCA2 Promote RAD51 Nucleoprotein Filament Function by Distinct Mechanisms.” *Proceedings of the National Academy of Sciences of the United States of America* 108, no. 26 (June 28, 2011): 10448–53. <https://doi.org/10.1073/pnas.1106971108>.
- Carroni, Marta, and Helen R. Saibil. “Cryo Electron Microscopy to Determine the Structure of Macromolecular Complexes.” *Methods (San Diego, Calif.)* 95 (February 15, 2016): 78–85. <https://doi.org/10.1016/j.ymeth.2015.11.023>.
- Carusillo, Antonio, and Claudio Mussolino. “DNA Damage: From Threat to Treatment.” *Cells* 9, no. 7 (July 10, 2020): E1665. <https://doi.org/10.3390/cells9071665>.
- Chang, Hao-Yen, Chia-Yu Liao, Guan-Chin Su, Sheng-Wei Lin, Hong-Wei Wang, and Peter Chi. “Functional Relationship of ATP Hydrolysis, Presynaptic Filament Stability, and Homologous DNA Pairing Activity of the Human Meiotic Recombinase DMC1.” *The Journal of Biological Chemistry* 290, no. 32 (August 7, 2015): 19863–73. <https://doi.org/10.1074/jbc.M115.666289>.
- Chaplin, Amanda K., Steven W. Hardwick, Shikang Liang, Antonia Kefala Stavridi, Ales Hnizda, Lee R. Cooper, Taiana Maia De Oliveira, Dimitri Y. Chirgadze, and Tom L. Blundell. “Dimers of DNA-PK Create a Stage for DNA Double-Strand Break Repair.” *Nature*

- Structural & Molecular Biology* 28, no. 1 (January 2021): 13–19.
<https://doi.org/10.1038/s41594-020-00517-x>.
- Chapman, J. Ross, Martin R. G. Taylor, and Simon J. Boulton. “Playing the End Game: DNA Double-Strand Break Repair Pathway Choice.” *Molecular Cell* 47, no. 4 (August 24, 2012): 497–510. <https://doi.org/10.1016/j.molcel.2012.07.029>.
- Charlier, Cyril, Joseph M. Courtney, T. Reid Alderson, Philip Anfinrud, and Ad Bax. “Monitoring ¹⁵N Chemical Shifts During Protein Folding by Pressure-Jump NMR.” *Journal of the American Chemical Society* 140, no. 26 (July 5, 2018): 8096–99.
<https://doi.org/10.1021/jacs.8b04833>.
- Chatterjee, Nimrat, and Graham C. Walker. “Mechanisms of DNA Damage, Repair, and Mutagenesis.” *Environmental and Molecular Mutagenesis* 58, no. 5 (June 2017): 235–63.
<https://doi.org/10.1002/em.22087>.
- Chen, C. F., P. L. Chen, Q. Zhong, Z. D. Sharp, and W. H. Lee. “Expression of BRC Repeats in Breast Cancer Cells Disrupts the BRCA2-Rad51 Complex and Leads to Radiation Hypersensitivity and Loss of G(2)/M Checkpoint Control.” *The Journal of Biological Chemistry* 274, no. 46 (November 12, 1999): 32931–35.
<https://doi.org/10.1074/jbc.274.46.32931>.
- Chi, Peter, Stephen Van Komen, Michael G. Sehorn, Stefan Sigurdsson, and Patrick Sung. “Roles of ATP Binding and ATP Hydrolysis in Human Rad51 Recombinase Function.” *DNA Repair* 5, no. 3 (March 7, 2006): 381–91. <https://doi.org/10.1016/j.dnarep.2005.11.005>.
- Choi, Eunhee, Pil-Gu Park, Hae-Ock Lee, Yoo-Kyung Lee, Gyeong Hoon Kang, Jong Won Lee, Wonshik Han, et al. “BRCA2 Fine-Tunes the Spindle Assembly Checkpoint through Reinforcement of BubR1 Acetylation.” *Developmental Cell* 22, no. 2 (February 14, 2012): 295–308. <https://doi.org/10.1016/j.devcel.2012.01.009>.
- Ciccio, Alberto, and Stephen J. Elledge. “The DNA Damage Response: Making It Safe to Play with Knives.” *Molecular Cell* 40, no. 2 (October 22, 2010): 179–204.
<https://doi.org/10.1016/j.molcel.2010.09.019>.
- Cloud, Veronica, Yuen-Ling Chan, Jennifer Grubb, Brian Budke, and Douglas K. Bishop. “Rad51 Is an Accessory Factor for Dmc1-Mediated Joint Molecule Formation during Meiosis.” *Science (New York, N.Y.)* 337, no. 6099 (September 7, 2012): 1222–25.
<https://doi.org/10.1126/science.1219379>.
- Conway, Adam B., Thomas W. Lynch, Ying Zhang, Gary S. Fortin, Cindy W. Fung, Lorraine S. Symington, and Phoebe A. Rice. “Crystal Structure of a Rad51 Filament.” *Nature Structural & Molecular Biology* 11, no. 8 (August 2004): 791–96. <https://doi.org/10.1038/nsmb795>.
- Coral, Sandra, Luca Sigalotti, Maresa Altomonte, Arne Engelsberg, Francesca Colizzi, Ilaria Cattarossi, Eugene Maraskovsky, Elke Jager, Barbara Seliger, and Michele Maio. “5-Aza-2'-Deoxycytidine-Induced Expression of Functional Cancer Testis Antigens in Human Renal Cell Carcinoma: Immunotherapeutic Implications.” *Clinical Cancer Research: An Official Journal of the American Association for Cancer Research* 8, no. 8 (August 2002): 2690–95.
- Crickard, J. Brooks, and Eric C. Greene. “Biochemical Attributes of Mitotic and Meiotic Presynaptic Complexes.” *DNA Repair* 71 (November 2018): 148–57.
<https://doi.org/10.1016/j.dnarep.2018.08.018>.
- Cromie, G. A., J. C. Connelly, and D. R. Leach. “Recombination at Double-Strand Breaks and DNA Ends: Conserved Mechanisms from Phage to Humans.” *Molecular Cell* 8, no. 6 (December 2001): 1163–74. [https://doi.org/10.1016/s1097-2765\(01\)00419-1](https://doi.org/10.1016/s1097-2765(01)00419-1).
- Dai, Jieqiong, Oleg Voloshin, Svetlana Potapova, and R. Daniel Camerini-Otero. “Meiotic Knockdown and Complementation Reveals Essential Role of RAD51 in Mouse Spermatogenesis.” *Cell Reports* 18, no. 6 (February 7, 2017): 1383–94.
<https://doi.org/10.1016/j.celrep.2017.01.024>.

- De Smet, C., C. Lurquin, B. Lethé, V. Martelange, and T. Boon. "DNA Methylation Is the Primary Silencing Mechanism for a Set of Germ Line- and Tumor-Specific Genes with a CpG-Rich Promoter." *Molecular and Cellular Biology* 19, no. 11 (November 1999): 7327–35. <https://doi.org/10.1128/MCB.19.11.7327>.
- Delaforge, Elise, Jaka Kragelj, Laura Tengo, Andrés Palencia, Sigrid Milles, Guillaume Bouvignies, Nicola Salvi, Martin Blackledge, and Malene Ringkjøbing Jensen. "Deciphering the Dynamic Interaction Profile of an Intrinsically Disordered Protein by NMR Exchange Spectroscopy." *Journal of the American Chemical Society* 140, no. 3 (January 24, 2018): 1148–58. <https://doi.org/10.1021/jacs.7b12407>.
- Dray, Eloïse, Nicolas Siaud, Emeline Dubois, and Marie-Pascale Doutriaux. "Interaction between Arabidopsis Brca2 and Its Partners Rad51, Dmc1, and Dss1." *Plant Physiology* 140, no. 3 (March 2006): 1059–69. <https://doi.org/10.1104/pp.105.075838>.
- Dunker, A. Keith, Marc S. Cortese, Pedro Romero, Lilia M. Iakoucheva, and Vladimir N. Uversky. "Flexible Nets. The Roles of Intrinsic Disorder in Protein Interaction Networks." *The FEBS Journal* 272, no. 20 (October 2005): 5129–48. <https://doi.org/10.1111/j.1742-4658.2005.04948.x>.
- Dunker, A. Keith, and Richard W. Kriwacki. "The Orderly Chaos of Proteins." *Scientific American* 304, no. 4 (April 2011): 68–73. <https://doi.org/10.1038/scientificamerican0411-68>.
- Dyson, H. Jane, and Peter E. Wright. "Coupling of Folding and Binding for Unstructured Proteins." *Current Opinion in Structural Biology* 12, no. 1 (February 2002): 54–60. [https://doi.org/10.1016/s0959-440x\(02\)00289-0](https://doi.org/10.1016/s0959-440x(02)00289-0).
- Ehlén, Åsa, Charlotte Martin, Simona Miron, Manon Julien, François-Xavier Theillet, Virginie Ropars, Gaetana Sessa, et al. "Proper Chromosome Alignment Depends on BRCA2 Phosphorylation by PLK1." *Nature Communications* 11, no. 1 (April 14, 2020): 1819. <https://doi.org/10.1038/s41467-020-15689-9>.
- Elia, Andrew E. H., Lewis C. Cantley, and Michael B. Yaffe. "Proteomic Screen Finds P^{Ser}/P^{Thr}-Binding Domain Localizing Plk1 to Mitotic Substrates." *Science (New York, N.Y.)* 299, no. 5610 (February 21, 2003): 1228–31. <https://doi.org/10.1126/science.1079079>.
- Elia, Andrew E. H., Peter Rellos, Lesley F. Haire, Jerry W. Chao, Frank J. Ivins, Katja Hoepker, Duaa Mohammad, Lewis C. Cantley, Stephen J. Smerdon, and Michael B. Yaffe. "The Molecular Basis for Phosphodependent Substrate Targeting and Regulation of Plks by the Polo-Box Domain." *Cell* 115, no. 1 (October 3, 2003): 83–95. [https://doi.org/10.1016/s0092-8674\(03\)00725-6](https://doi.org/10.1016/s0092-8674(03)00725-6).
- Enguita-Marruedo, Andrea, Marta Martín-Ruiz, Eva García, Ana Gil-Fernández, María Teresa Parra, Alberto Viera, Julio S. Rufas, and Jesús Page. "Transition from a Meiotic to a Somatic-like DNA Damage Response during the Pachytene Stage in Mouse Meiosis." *PLoS Genetics* 15, no. 1 (January 2019): e1007439. <https://doi.org/10.1371/journal.pgen.1007439>.
- Esashi, Fumiko, Vitold E. Galkin, Xiong Yu, Edward H. Egelman, and Stephen C. West. "Stabilization of RAD51 Nucleoprotein Filaments by the C-Terminal Region of BRCA2." *Nature Structural & Molecular Biology* 14, no. 6 (June 2007): 468–74. <https://doi.org/10.1038/nsmb1245>.
- Evans, Richard, Michael O'Neill, Alexander Pritzel, Natasha Antropova, Andrew Senior, Tim Green, Augustin Žídek, et al. "Protein Complex Prediction with AlphaFold-Multimer." *BioRxiv*, January 1, 2022, 2021.10.04.463034. <https://doi.org/10.1101/2021.10.04.463034>.
- Felipe-Medina, Natalia, Sandrine Caburet, Fernando Sánchez-Sáez, Yazmine B. Condezo, Dirk G. de Rooij, Laura Gómez-H, Rodrigo Garcia-Valiente, et al. "A Missense in HSF2BP Causing Primary Ovarian Insufficiency Affects Meiotic Recombination by Its Novel Interactor C19ORF57/BRME1." *ELife* 9 (August 26, 2020): e56996. <https://doi.org/10.7554/eLife.56996>.

- Fisher, Charles K., and Collin M. Stultz. "Protein Structure along the Order-Disorder Continuum." *Journal of the American Chemical Society* 133, no. 26 (July 6, 2011): 10022–25. <https://doi.org/10.1021/ja203075p>.
- Fradet-Turcotte, Amélie, Justine Sitz, Damien Grapton, and Alexandre Orthwein. "BRCA2 Functions: From DNA Repair to Replication Fork Stabilization." *Endocrine-Related Cancer* 23, no. 10 (October 2016): T1–17. <https://doi.org/10.1530/ERC-16-0297>.
- Franca, Monica M., Yazmine B. Condezo, Maëva Elzaïat, Natalia Felipe-Medina, Fernando Sánchez-Sáez, Sergio Muñoz, Raquel Sainz-Urruela, et al. "A Truncating Variant of RAD51B Associated with Primary Ovarian Insufficiency Provides Insights into Its Meiotic and Somatic Functions." *Cell Death and Differentiation*, May 27, 2022. <https://doi.org/10.1038/s41418-022-01021-z>.
- Franz, André, Leena Ackermann, and Thorsten Hoppe. "Ring of Change: CDC48/P97 Drives Protein Dynamics at Chromatin." *Frontiers in Genetics* 7 (2016): 73. <https://doi.org/10.3389/fgene.2016.00073>.
- Fratta, Elisabetta, Sandra Coral, Alessia Covre, Giulia Parisi, Francesca Colizzi, Riccardo Danielli, Hugues Jean Marie Nicolay, Luca Sigalotti, and Michele Maio. "The Biology of Cancer Testis Antigens: Putative Function, Regulation and Therapeutic Potential." *Molecular Oncology* 5, no. 2 (April 2011): 164–82. <https://doi.org/10.1016/j.molonc.2011.02.001>.
- Fratta, Elisabetta, Luca Sigalotti, Francesca Colizzi, Alessia Covre, Hugues J. M. G. Nicolay, Riccardo Danielli, Ester Fonsatti, et al. "Epigenetically Regulated Clonal Heritability of CTA Expression Profiles in Human Melanoma." *Journal of Cellular Physiology* 223, no. 2 (May 2010): 352–58. <https://doi.org/10.1002/jcp.22040>.
- Furukawa, Ayako, Tsuyoshi Konuma, Saeko Yanaka, and Kenji Sugase. "Quantitative Analysis of Protein-Ligand Interactions by NMR." *Progress in Nuclear Magnetic Resonance Spectroscopy* 96 (August 2016): 47–57. <https://doi.org/10.1016/j.pnmrs.2016.02.002>.
- Gantchev, Jennifer, Amelia Martínez Villarreal, Scott Gunn, Monique Zetka, Neils Ødum, and Ivan V. Litvinov. "The Ectopic Expression of MeiCT Genes Promotes Meiomitosis and May Facilitate Carcinogenesis." *Cell Cycle* 19, no. 8 (April 17, 2020): 837–54. <https://doi.org/10.1080/15384101.2020.1743902>.
- Ghouil, Rania, Simona Miron, Lieke Koornneef, Jasper Veerman, Maarten W. Paul, Marie-Hélène Le Du, Esther Sleddens-Linkels, et al. "BRCA2 Binding through a Cryptic Repeated Motif to HSF2BP Oligomers Does Not Impact Meiotic Recombination." *Nature Communications* 12, no. 1 (July 29, 2021): 4605. <https://doi.org/10.1038/s41467-021-24871-6>.
- Glazer, Chad A., Ian M. Smith, Michael F. Ochs, Shahnaz Begum, William Westra, Steven S. Chang, Wenyue Sun, et al. "Integrative Discovery of Epigenetically Derepressed Cancer Testis Antigens in NSCLC." *PloS One* 4, no. 12 (December 4, 2009): e8189. <https://doi.org/10.1371/journal.pone.0008189>.
- Grey, Corinne, Frédéric Baudat, and Bernard de Massy. "PRDM9, a Driver of the Genetic Map." *PLoS Genetics* 14, no. 8 (August 2018): e1007479. <https://doi.org/10.1371/journal.pgen.1007479>.
- Grey, Corinne, and Bernard de Massy. "Chromosome Organization in Early Meiotic Prophase." *Frontiers in Cell and Developmental Biology* 9 (2021): 688878. <https://doi.org/10.3389/fcell.2021.688878>.
- Guillon, Hélène, Frédéric Baudat, Corinne Grey, R. Michael Liskay, and Bernard de Massy. "Crossover and Noncrossover Pathways in Mouse Meiosis." *Molecular Cell* 20, no. 4 (November 23, 2005): 563–73. <https://doi.org/10.1016/j.molcel.2005.09.021>.
- Gunasekaran, Kannan, Chung-Jung Tsai, Sandeep Kumar, David Zanuy, and Ruth Nussinov. "Extended Disordered Proteins: Targeting Function with Less Scaffold." *Trends in Biochemical Sciences* 28, no. 2 (February 2003): 81–85. [https://doi.org/10.1016/S0968-0004\(03\)00003-3](https://doi.org/10.1016/S0968-0004(03)00003-3).

- Håkansson, S., O. Johannsson, U. Johannsson, G. Sellberg, N. Loman, A. M. Gerdes, E. Holmberg, et al. "Moderate Frequency of BRCA1 and BRCA2 Germ-Line Mutations in Scandinavian Familial Breast Cancer." *American Journal of Human Genetics* 60, no. 5 (May 1997): 1068–78.
- Hammel, Michal, Yaping Yu, Brandi L. Mahaney, Brandon Cai, Ruiqiong Ye, Barry M. Phipps, Robert P. Rambo, et al. "Ku and DNA-Dependent Protein Kinase Dynamic Conformations and Assembly Regulate DNA Binding and the Initial Non-Homologous End Joining Complex." *The Journal of Biological Chemistry* 285, no. 2 (January 8, 2010): 1414–23. <https://doi.org/10.1074/jbc.M109.065615>.
- Hanahan, Douglas, and Robert A. Weinberg. "Hallmarks of Cancer: The next Generation." *Cell* 144, no. 5 (March 4, 2011): 646–74. <https://doi.org/10.1016/j.cell.2011.02.013>.
- Hays, E., N. Majchrzak, V. Daniel, Z. Ferguson, S. Brown, K. Hathorne, and S. La Salle. "Spermatogenesis Associated 22 Is Required for DNA Repair and Synapsis of Homologous Chromosomes in Mouse Germ Cells." *Andrology* 5, no. 2 (March 2017): 299–312. <https://doi.org/10.1111/andr.12315>.
- Her, Joonyoung, and Samuel F. Bunting. "How Cells Ensure Correct Repair of DNA Double-Strand Breaks." *The Journal of Biological Chemistry* 293, no. 27 (July 6, 2018): 10502–11. <https://doi.org/10.1074/jbc.TM118.000371>.
- Hernández, M. A., J. Avila, and J. M. Andreu. "Physicochemical Characterization of the Heat-Stable Microtubule-Associated Protein MAP2." *European Journal of Biochemistry* 154, no. 1 (January 2, 1986): 41–48. <https://doi.org/10.1111/j.1432-1033.1986.tb09356.x>.
- Hoeijmakers, Jan H. J. "DNA Damage, Aging, and Cancer." *The New England Journal of Medicine* 361, no. 15 (October 8, 2009): 1475–85. <https://doi.org/10.1056/NEJMr0804615>.
- Hunter, Neil. "Meiotic Recombination: The Essence of Heredity." *Cold Spring Harbor Perspectives in Biology* 7, no. 12 (October 28, 2015): a016618. <https://doi.org/10.1101/cshperspect.a016618>.
- Ishishita, Satoshi, Yoichi Matsuda, and Kazuhiro Kitada. "Genetic Evidence Suggests That Spata22 Is Required for the Maintenance of Rad51 Foci in Mammalian Meiosis." *Scientific Reports* 4 (August 21, 2014): 6148. <https://doi.org/10.1038/srep06148>.
- Jacques, David A., and Jill Trewheella. "Small-Angle Scattering for Structural Biology--Expanding the Frontier While Avoiding the Pitfalls." *Protein Science: A Publication of the Protein Society* 19, no. 4 (April 2010): 642–57. <https://doi.org/10.1002/pro.351>.
- Jasin, Maria, and Rodney Rothstein. "Repair of Strand Breaks by Homologous Recombination." *Cold Spring Harbor Perspectives in Biology* 5, no. 11 (November 1, 2013): a012740. <https://doi.org/10.1101/cshperspect.a012740>.
- Jay, Ash, Diedre Reitz, Satoshi H. Namekawa, and Wolf-Dietrich Heyer. "Cancer Testis Antigens and Genomic Instability: More than Immunology." *DNA Repair* 108 (December 2021): 103214. <https://doi.org/10.1016/j.dnarep.2021.103214>.
- Jensen, Ryan B., Aura Carreira, and Stephen C. Kowalczykowski. "Purified Human BRCA2 Stimulates RAD51-Mediated Recombination." *Nature* 467, no. 7316 (October 7, 2010): 678–83. <https://doi.org/10.1038/nature09399>.
- Julien, Manon, Chafiaa Bouguechtouli, Ania Alik, Rania Ghouil, Sophie Zinn-Justin, and François-Xavier Theillet. "Multiple Site-Specific Phosphorylation of IDPs Monitored by NMR." *Methods in Molecular Biology (Clifton, N.J.)* 2141 (2020): 793–817. https://doi.org/10.1007/978-1-0716-0524-0_41.
- Julien, Manon, Rania Ghouil, Ambre Petitalot, Sandrine M. Caputo, Aura Carreira, and Sophie Zinn-Justin. "Intrinsic Disorder and Phosphorylation in BRCA2 Facilitate Tight Regulation of Multiple Conserved Binding Events." *Biomolecules* 11, no. 7 (July 20, 2021): 1060. <https://doi.org/10.3390/biom11071060>.

- Julien, Manon, Simona Miron, Aura Carreira, François-Xavier Theillet, and Sophie Zinn-Justin. "1H, 13C and 15N Backbone Resonance Assignment of the Human BRCA2 N-Terminal Region." *Biomolecular NMR Assignments* 14, no. 1 (April 2020): 79–85. <https://doi.org/10.1007/s12104-019-09924-8>.
- Jumper, John, Richard Evans, Alexander Pritzel, Tim Green, Michael Figurnov, Olaf Ronneberger, Kathryn Tunyasuvunakool, et al. "Highly Accurate Protein Structure Prediction with AlphaFold." *Nature* 596, no. 7873 (August 2021): 583–89. <https://doi.org/10.1038/s41586-021-03819-2>.
- Kabsch, Wolfgang. "XDS." *Acta Crystallographica. Section D, Biological Crystallography* 66, no. Pt 2 (February 2010): 125–32. <https://doi.org/10.1107/S0907444909047337>.
- Kallio, Marko, Yunhua Chang, Martine Manuel, Tero-Pekka Alastalo, Murielle Rallu, Yorick Gitton, Lila Pirkkala, et al. "Brain Abnormalities, Defective Meiotic Chromosome Synapsis and Female Subfertility in HSF2 Null Mice." *The EMBO Journal* 21, no. 11 (June 3, 2002): 2591–2601. <https://doi.org/10.1093/emboj/21.11.2591>.
- Kang, Young H., Jung-Eun Park, Li-Rong Yu, Nak-Kyun Soung, Sang-Moon Yun, Jeong K. Bang, Yeon-Sun Seong, et al. "Self-Regulated Plk1 Recruitment to Kinetochores by the Plk1-PBIP1 Interaction Is Critical for Proper Chromosome Segregation." *Molecular Cell* 24, no. 3 (November 3, 2006): 409–22. <https://doi.org/10.1016/j.molcel.2006.10.016>.
- Keeney, S., and M. J. Neale. "Initiation of Meiotic Recombination by Formation of DNA Double-Strand Breaks: Mechanism and Regulation." *Biochemical Society Transactions* 34, no. Pt 4 (August 2006): 523–25. <https://doi.org/10.1042/BST0340523>.
- Kim, Juhyun, Jihye Park, Heejin Kim, Namil Son, Eun-Jung Kim, Jaeil Kim, Dohwan Byun, et al. "Arabidopsis HEAT SHOCK FACTOR BINDING PROTEIN Is Required to Limit Meiotic Crossovers and HEI10 Transcription." *The EMBO Journal* 41, no. 14 (July 18, 2022): e109958. <https://doi.org/10.15252/embj.2021109958>.
- Kim, Keun P., Beth M. Weiner, Liangran Zhang, Amy Jordan, Job Dekker, and Nancy Kleckner. "Sister Cohesion and Structural Axis Components Mediate Homolog Bias of Meiotic Recombination." *Cell* 143, no. 6 (December 10, 2010): 924–37. <https://doi.org/10.1016/j.cell.2010.11.015>.
- Kinebuchi, Takashi, Wataru Kagawa, Rima Enomoto, Kozo Tanaka, Kiyoshi Miyagawa, Takehiko Shibata, Hitoshi Kurumizaka, and Shigeyuki Yokoyama. "Structural Basis for Octameric Ring Formation and DNA Interaction of the Human Homologous-Pairing Protein Dmc1." *Molecular Cell* 14, no. 3 (May 7, 2004): 363–74. [https://doi.org/10.1016/s1097-2765\(04\)00218-7](https://doi.org/10.1016/s1097-2765(04)00218-7).
- Kohn, Jonathan E., Ian S. Millett, Jaby Jacob, Bojan Zagrovic, Thomas M. Dillon, Nikolina Cingel, Robin S. Dothager, et al. "Random-Coil Behavior and the Dimensions of Chemically Unfolded Proteins." *Proceedings of the National Academy of Sciences of the United States of America* 101, no. 34 (August 24, 2004): 12491–96. <https://doi.org/10.1073/pnas.0403643101>.
- Kragelund, Birthe B., Signe M. Schenstrøm, Caio A. Rebula, Vikram Govind Panse, and Rasmus Hartmann-Petersen. "DSS1/Sem1, a Multifunctional and Intrinsically Disordered Protein." *Trends in Biochemical Sciences* 41, no. 5 (May 2016): 446–59. <https://doi.org/10.1016/j.tibs.2016.02.004>.
- Krawczyk, Przemek M., Berina Eppink, Jeroen Essers, Jan Stap, Hans Rodermond, Hanny Odijk, Alex Zelensky, et al. "Mild Hyperthermia Inhibits Homologous Recombination, Induces BRCA2 Degradation, and Sensitizes Cancer Cells to Poly (ADP-Ribose) Polymerase-1 Inhibition." *Proceedings of the National Academy of Sciences* 108, no. 24 (June 14, 2011): 9851–56. <https://doi.org/10.1073/pnas.1101053108>.
- La Salle, Sophie, Kristina Palmer, Marilyn O'Brien, John C. Schimenti, John Eppig, and Mary Ann Handel. "Spata22, a Novel Vertebrate-Specific Gene, Is Required for Meiotic Progress in

- Mouse Germ Cells.” *Biology of Reproduction* 86, no. 2 (February 2012): 45.
<https://doi.org/10.1095/biolreprod.111.095752>.
- Lam, Isabel, and Scott Keeney. “Mechanism and Regulation of Meiotic Recombination Initiation.” *Cold Spring Harbor Perspectives in Biology* 7, no. 1 (October 16, 2014): a016634.
<https://doi.org/10.1101/cshperspect.a016634>.
- Lange, Julian, Shintaro Yamada, Sam E. Tischfield, Jing Pan, Seoyoung Kim, Xuan Zhu, Nicholas D. Socci, Maria Jasin, and Scott Keeney. “The Landscape of Mouse Meiotic Double-Strand Break Formation, Processing, and Repair.” *Cell* 167, no. 3 (October 20, 2016): 695-708.e16.
<https://doi.org/10.1016/j.cell.2016.09.035>.
- Le, Hang Phuong, Xiaoyan Ma, Jorge Vaquero, Megan Brinkmeyer, Fei Guo, Wolf-Dietrich Heyer, and Jie Liu. “DSS1 and SsDNA Regulate Oligomerization of BRCA2.” *Nucleic Acids Research* 48, no. 14 (August 20, 2020): 7818–33. <https://doi.org/10.1093/nar/gkaa555>.
- Lee, Ja Yil, Justin B. Steinfeld, Zhi Qi, YoungHo Kwon, Patrick Sung, and Eric C. Greene. “Sequence Imperfections and Base Triplet Recognition by the Rad51/RecA Family of Recombinases.” *The Journal of Biological Chemistry* 292, no. 26 (June 30, 2017): 11125–35.
<https://doi.org/10.1074/jbc.M117.787614>.
- Lee, Ja Yil, Tsuyoshi Terakawa, Zhi Qi, Justin B. Steinfeld, Sy Redding, YoungHo Kwon, William A. Gaines, Weixing Zhao, Patrick Sung, and Eric C. Greene. “DNA RECOMBINATION. Base Triplet Stepping by the Rad51/RecA Family of Recombinases.” *Science (New York, N.Y.)* 349, no. 6251 (August 28, 2015): 977–81.
<https://doi.org/10.1126/science.aab2666>.
- Lee, MiYoung, Matthew J Daniels, and Ashok R Venkitaraman. “Phosphorylation of BRCA2 by the Polo-like Kinase Plk1 Is Regulated by DNA Damage and Mitotic Progression.” *Oncogene* 23, no. 4 (January 29, 2004): 865–72. <https://doi.org/10.1038/sj.onc.1207223>.
- Lee, Robin van der, Marija Buljan, Benjamin Lang, Robert J. Weatheritt, Gary W. Daughdrill, A. Keith Dunker, Monika Fuxreiter, et al. “Classification of Intrinsically Disordered Regions and Proteins.” *Chemical Reviews* 114, no. 13 (July 9, 2014): 6589–6631.
<https://doi.org/10.1021/cr400525m>.
- Lee, Shauna A., and Mark D. Baker. “Analysis of DNA Repair and Recombination Responses in Mouse Cells Depleted for Brca2 by SiRNA.” *DNA Repair* 6, no. 6 (June 1, 2007): 809–17.
<https://doi.org/10.1016/j.dnarep.2007.01.007>.
- Lehman, Jason A., Derek J. Hoelz, and John J. Turchi. “DNA-Dependent Conformational Changes in the Ku Heterodimer.” *Biochemistry* 47, no. 15 (April 15, 2008): 4359–68.
<https://doi.org/10.1021/bi702284c>.
- Li, Miao, Haiwei Feng, Zexiong Lin, Jiahuan Zheng, Dongteng Liu, Rui Guo, Junshi Li, et al. “The Novel Male Meiosis Recombination Regulator Coordinates the Progression of Meiosis Prophase I.” *Journal of Genetics and Genomics = Yi Chuan Xue Bao* 47, no. 8 (August 2020): 451–65. <https://doi.org/10.1016/j.jgg.2020.08.001>.
- . “The Novel Male Meiosis Recombination Regulator Coordinates the Progression of Meiosis Prophase I.” *Journal of Genetics and Genomics = Yi Chuan Xue Bao* 47, no. 8 (August 2020): 451–65. <https://doi.org/10.1016/j.jgg.2020.08.001>.
- Li, Shan, Weiwei Xu, Bingying Xu, Shuchang Gao, Qian Zhang, Yingying Qin, and Ting Guo. “Pathogenic Variations of Homologous Recombination Gene HSF2BP Identified in Sporadic Patients With Premature Ovarian Insufficiency.” *Frontiers in Cell and Developmental Biology* 9 (2021): 768123. <https://doi.org/10.3389/fcell.2021.768123>.
- Lieber, Michael R. “The Mechanism of Double-Strand DNA Break Repair by the Nonhomologous DNA End-Joining Pathway.” *Annual Review of Biochemistry* 79 (2010): 181–211.
<https://doi.org/10.1146/annurev.biochem.052308.093131>.
- Lin, Horng-Ru, Nicholas S.Y. Ting, Jun Qin, and Wen-Hwa Lee. “M Phase-Specific Phosphorylation of BRCA2 by Polo-like Kinase 1 Correlates with the Dissociation of the

- BRCA2-P/CAF Complex.” *Journal of Biological Chemistry* 278, no. 38 (September 2003): 35979–87. <https://doi.org/10.1074/jbc.M210659200>.
- Lindahl, T. “Instability and Decay of the Primary Structure of DNA.” *Nature* 362, no. 6422 (April 22, 1993): 709–15. <https://doi.org/10.1038/362709a0>.
- . “Recovery of Antediluvian DNA.” *Nature* 365, no. 6448 (October 21, 1993): 700. <https://doi.org/10.1038/365700a0>.
- Lindahl, T., and D. E. Barnes. “Repair of Endogenous DNA Damage.” *Cold Spring Harbor Symposia on Quantitative Biology* 65 (2000): 127–33. <https://doi.org/10.1101/sqb.2000.65.127>.
- Lindahl, Tomas. “DNA Repair as a Biomarker. Foreword.” *Mutation Research/Fundamental and Molecular Mechanisms of Mutagenesis* 736, no. 1–2 (August 2012): 1. <https://doi.org/10.1016/j.mrfmmm.2012.03.001>.
- Liu, Jie, Tammy Doty, Bryan Gibson, and Wolf-Dietrich Heyer. “Human BRCA2 Protein Promotes RAD51 Filament Formation on RPA-Covered Single-Stranded DNA.” *Nature Structural & Molecular Biology* 17, no. 10 (October 2010): 1260–62. <https://doi.org/10.1038/nsmb.1904>.
- Lo, Thomas, Luca Pellegrini, Ashok R. Venkitaraman, and Tom L. Blundell. “Sequence Fingerprints in BRCA2 and RAD51: Implications for DNA Repair and Cancer.” *DNA Repair* 2, no. 9 (September 18, 2003): 1015–28. [https://doi.org/10.1016/s1568-7864\(03\)00097-1](https://doi.org/10.1016/s1568-7864(03)00097-1).
- Loeb, L. A., C. F. Springgate, and N. Battula. “Errors in DNA Replication as a Basis of Malignant Changes.” *Cancer Research* 34, no. 9 (September 1974): 2311–21.
- Luck, Katja, Dae-Kyum Kim, Luke Lambourne, Kerstin Spirohn, Bridget E. Begg, Wenting Bian, Ruth Brignall, et al. “A Reference Map of the Human Binary Protein Interactome.” *Nature* 580, no. 7803 (April 2020): 402–8. <https://doi.org/10.1038/s41586-020-2188-x>.
- Luo, Mengcheng, Fang Yang, N. Adrian Leu, Jessica Landaiche, Mary Ann Handel, Ricardo Benavente, Sophie La Salle, and P. Jeremy Wang. “MEIOB Exhibits Single-Stranded DNA-Binding and Exonuclease Activities and Is Essential for Meiotic Recombination.” *Nature Communications* 4 (2013): 2788. <https://doi.org/10.1038/ncomms3788>.
- Luo, Shih-Chi, Hsin-Yi Yeh, Wei-Hsuan Lan, Yi-Min Wu, Cheng-Han Yang, Hao-Yen Chang, Guan-Chin Su, et al. “Identification of Fidelity-Governing Factors in Human Recombinases DMC1 and RAD51 from Cryo-EM Structures.” *Nature Communications* 12, no. 1 (January 14, 2021): 115. <https://doi.org/10.1038/s41467-020-20258-1>.
- Ma, Emilie, Laurent Maloisel, Léa Le Falher, Raphaël Guérois, and Eric Coïc. “Correction: Ma et al. Rad52 Oligomeric N-Terminal Domain Stabilizes Rad51 Nucleoprotein Filaments and Contributes to Their Protection against Srs2. *Cells* 2021, 10, 1467.” *Cells* 10, no. 11 (November 17, 2021): 3207. <https://doi.org/10.3390/cells10113207>.
- Madhurantakam, Chaithanya, Gautham Varadamsetty, Markus G. Grütter, Andreas Plückthun, and Peer R. E. Mittl. “Structure-Based Optimization of Designed Armadillo-Repeat Proteins.” *Protein Science: A Publication of the Protein Society* 21, no. 7 (July 2012): 1015–28. <https://doi.org/10.1002/pro.2085>.
- Malik, Sadiya, Hiroko Saito, Miho Takaoka, Yoshio Miki, and Akira Nakanishi. “BRCA2 Mediates Centrosome Cohesion via an Interaction with Cytoplasmic Dynein.” *Cell Cycle (Georgetown, Tex.)* 15, no. 16 (August 17, 2016): 2145–56. <https://doi.org/10.1080/15384101.2016.1195531>.
- Manalastas-Cantos, Karen, Petr V. Konarev, Nelly R. Hajizadeh, Alexey G. Kikhney, Maxim V. Petoukhov, Dmitry S. Molodenskiy, Alejandro Panjkovich, et al. “ATSAS 3.0: Expanded Functionality and New Tools for Small-Angle Scattering Data Analysis.” *Journal of Applied Crystallography* 54, no. Pt 1 (February 1, 2021): 343–55. <https://doi.org/10.1107/S1600576720013412>.

- Mao, Zhiyong, Michael Bozzella, Andrei Seluanov, and Vera Gorbunova. "DNA Repair by Nonhomologous End Joining and Homologous Recombination during Cell Cycle in Human Cells." *Cell Cycle (Georgetown, Tex.)* 7, no. 18 (September 15, 2008): 2902–6. <https://doi.org/10.4161/cc.7.18.6679>.
- Martinez, Juan S., Catharina von Nicolai, Taeho Kim, Åsa Ehlén, Alexander V. Mazin, Stephen C. Kowalczykowski, and Aura Carreira. "BRCA2 Regulates DMC1-Mediated Recombination through the BRC Repeats." *Proceedings of the National Academy of Sciences of the United States of America* 113, no. 13 (March 29, 2016): 3515–20. <https://doi.org/10.1073/pnas.1601691113>.
- Masson, J. Y., and S. C. West. "The Rad51 and Dmc1 Recombinases: A Non-Identical Twin Relationship." *Trends in Biochemical Sciences* 26, no. 2 (February 2001): 131–36. [https://doi.org/10.1016/s0968-0004\(00\)01742-4](https://doi.org/10.1016/s0968-0004(00)01742-4).
- Massy, Bernard de. "Initiation of Meiotic Recombination: How and Where? Conservation and Specificities among Eukaryotes." *Annual Review of Genetics* 47 (2013): 563–99. <https://doi.org/10.1146/annurev-genet-110711-155423>.
- Matos, Joao, Miguel G. Blanco, Sarah Maslen, J. Mark Skehel, and Stephen C. West. "Regulatory Control of the Resolution of DNA Recombination Intermediates during Meiosis and Mitosis." *Cell* 147, no. 1 (September 30, 2011): 158–72. <https://doi.org/10.1016/j.cell.2011.08.032>.
- Mersch, Jacqueline, Michelle A. Jackson, Minjeong Park, Denise Nebgen, Susan K. Peterson, Claire Singletary, Banu K. Arun, and Jennifer K. Litton. "Cancers Associated with BRCA1 and BRCA2 Mutations Other than Breast and Ovarian." *Cancer* 121, no. 2 (January 15, 2015): 269–75. <https://doi.org/10.1002/cncr.29041>.
- Miao, Yilong, Pan Wang, Bingteng Xie, Mo Yang, Sen Li, Zhaokang Cui, Yong Fan, Mo Li, and Bo Xiong. "BRCA2 Deficiency Is a Potential Driver for Human Primary Ovarian Insufficiency." *Cell Death & Disease* 10, no. 7 (June 17, 2019): 474. <https://doi.org/10.1038/s41419-019-1720-0>.
- Migneault, Isabelle, Catherine Dartiguenave, Michel J. Bertrand, and Karen C. Waldron. "Glutaraldehyde: Behavior in Aqueous Solution, Reaction with Proteins, and Application to Enzyme Crosslinking." *BioTechniques* 37, no. 5 (November 2004): 790–96, 798–802. <https://doi.org/10.2144/04375RV01>.
- Mimitou, Eleni P., and Lorraine S. Symington. "Nucleases and Helicases Take Center Stage in Homologous Recombination." *Trends in Biochemical Sciences* 34, no. 5 (May 2009): 264–72. <https://doi.org/10.1016/j.tibs.2009.01.010>.
- Min, Jaewon, Eun Shik Choi, Kwangwoo Hwang, Jimi Kim, Srihari Sampath, Ashok R. Venkitaraman, and Hyunsook Lee. "The Breast Cancer Susceptibility Gene BRCA2 Is Required for the Maintenance of Telomere Homeostasis." *The Journal of Biological Chemistry* 287, no. 7 (February 10, 2012): 5091–5101. <https://doi.org/10.1074/jbc.M111.278994>.
- Mirdita, Milot, Konstantin Schütze, Yoshitaka Moriwaki, Lim Heo, Sergey Ovchinnikov, and Martin Steinegger. "ColabFold: Making Protein Folding Accessible to All." *Nature Methods* 19, no. 6 (June 2022): 679–82. <https://doi.org/10.1038/s41592-022-01488-1>.
- Modrich, Paul. "Mechanisms in Eukaryotic Mismatch Repair." *The Journal of Biological Chemistry* 281, no. 41 (October 13, 2006): 30305–9. <https://doi.org/10.1074/jbc.R600022200>.
- Moens, Peter B., Nadine K. Kolas, Madalena Tarsounas, Edyta Marcon, Paula E. Cohen, and Barbara Spyropoulos. "The Time Course and Chromosomal Localization of Recombination-Related Proteins at Meiosis in the Mouse Are Compatible with Models That Can Resolve the Early DNA-DNA Interactions without Reciprocal Recombination." *Journal of Cell Science* 115, no. Pt 8 (April 15, 2002): 1611–22. <https://doi.org/10.1242/jcs.115.8.1611>.
- Mondal, Gourish, Matthew Rowley, Lucia Guidugli, Jianmin Wu, Vernon S. Pankratz, and Fergus J. Couch. "BRCA2 Localization to the Midbody by Filamin A Regulates Cep55 Signaling and

- Completion of Cytokinesis.” *Developmental Cell* 23, no. 1 (July 17, 2012): 137–52.
<https://doi.org/10.1016/j.devcel.2012.05.008>.
- Morganella, Sandro, Ludmil B. Alexandrov, Dominik Glodzik, Xueqing Zou, Helen Davies, Johan Staaf, Anieta M. Sieuwerts, et al. “The Topography of Mutational Processes in Breast Cancer Genomes.” *Nature Communications* 7 (May 2, 2016): 11383.
<https://doi.org/10.1038/ncomms11383>.
- Morimoto, Akihiro, Hiroki Shibuya, Xiaoqiang Zhu, Jihye Kim, Kei-ichiro Ishiguro, Min Han, and Yoshinori Watanabe. “A Conserved KASH Domain Protein Associates with Telomeres, SUN1, and Dynactin during Mammalian Meiosis.” *The Journal of Cell Biology* 198, no. 2 (July 23, 2012): 165–72. <https://doi.org/10.1083/jcb.201204085>.
- Morimoto, R. I. “Regulation of the Heat Shock Transcriptional Response: Cross Talk between a Family of Heat Shock Factors, Molecular Chaperones, and Negative Regulators.” *Genes & Development* 12, no. 24 (December 15, 1998): 3788–96.
<https://doi.org/10.1101/gad.12.24.3788>.
- Motycka, Teresa A., Tadayoshi Bessho, Sean M. Post, Patrick Sung, and Alan E. Tomkinson. “Physical and Functional Interaction between the XPF/ERCC1 Endonuclease and HRad52.” *The Journal of Biological Chemistry* 279, no. 14 (April 2, 2004): 13634–39.
<https://doi.org/10.1074/jbc.M313779200>.
- Nakai, A, M Tanabe, Y Kawazoe, J Inazawa, R I Morimoto, and K Nagata. “HSF4, a New Member of the Human Heat Shock Factor Family Which Lacks Properties of a Transcriptional Activator.” *Molecular and Cellular Biology* 17, no. 1 (January 1997): 469–81.
<https://doi.org/10.1128/MCB.17.1.469>.
- Nik-Zainal, Serena, Helen Davies, Johan Staaf, Manasa Ramakrishna, Dominik Glodzik, Xueqing Zou, Inigo Martincorena, et al. “Landscape of Somatic Mutations in 560 Breast Cancer Whole-Genome Sequences.” *Nature* 534, no. 7605 (June 2, 2016): 47–54.
<https://doi.org/10.1038/nature17676>.
- Nolan, Michael A., Donner F. Babcock, Gunther Wennemuth, William Brown, Kimberly A. Burton, and G. Stanley McKnight. “Sperm-Specific Protein Kinase A Catalytic Subunit Calpha2 Orchestrates CAMP Signaling for Male Fertility.” *Proceedings of the National Academy of Sciences of the United States of America* 101, no. 37 (September 14, 2004): 13483–88. <https://doi.org/10.1073/pnas.0405580101>.
- Nowell, P. C. “The Clonal Evolution of Tumor Cell Populations.” *Science (New York, N.Y.)* 194, no. 4260 (October 1, 1976): 23–28. <https://doi.org/10.1126/science.959840>.
- Ochi, Takashi, Andrew N. Blackford, Julia Coates, Satpal Jhujh, Shahid Mehmood, Naoka Tamura, Jon Travers, et al. “DNA Repair. PAXX, a Paralog of XRCC4 and XLF, Interacts with Ku to Promote DNA Double-Strand Break Repair.” *Science (New York, N.Y.)* 347, no. 6218 (January 9, 2015): 185–88. <https://doi.org/10.1126/science.1261971>.
- Ogawa, T., X. Yu, A. Shinohara, and E. H. Egelman. “Similarity of the Yeast RAD51 Filament to the Bacterial RecA Filament.” *Science (New York, N.Y.)* 259, no. 5103 (March 26, 1993): 1896–99. <https://doi.org/10.1126/science.8456314>.
- Oliver, Antony W, Sally Swift, Christopher J Lord, Alan Ashworth, and Laurence H Pearl. “Structural Basis for Recruitment of BRCA2 by PALB2.” *EMBO Reports* 10, no. 9 (September 2009): 990–96. <https://doi.org/10.1038/embor.2009.126>.
- Orskov, E. R., and C. Fraser. “The Effects of Processing of Barley-Based Supplements on Rumen PH, Rate of Digestion of Voluntary Intake of Dried Grass in Sheep.” *The British Journal of Nutrition* 34, no. 3 (November 1975): 493–500. <https://doi.org/10.1017/s0007114575000530>.
- Paraskevopoulos, Konstantinos, Franziska Kriegenburg, Michael H. Tatham, Heike I. Rösner, Bethan Medina, Ida B. Larsen, Rikke Brandstrup, et al. “Dss1 Is a 26S Proteasome Ubiquitin Receptor.” *Molecular Cell* 56, no. 3 (November 6, 2014): 453–61.
<https://doi.org/10.1016/j.molcel.2014.09.008>.

- Passy, S. I., X. Yu, Z. Li, C. M. Radding, J. Y. Masson, S. C. West, and E. H. Egelman. "Human Dmc1 Protein Binds DNA as an Octameric Ring." *Proceedings of the National Academy of Sciences of the United States of America* 96, no. 19 (September 14, 1999): 10684–88. <https://doi.org/10.1073/pnas.96.19.10684>.
- Paul, Maarten W., Arshdeep Sidhu, Yongxin Liang, Sarah E. van Rossum-Fikkert, Hanny Odijk, Alex N. Zelensky, Roland Kanaar, and Claire Wyman. "Role of BRCA2 DNA-Binding and C-Terminal Domain in Its Mobility and Conformation in DNA Repair." *ELife* 10 (July 13, 2021): e67926. <https://doi.org/10.7554/eLife.67926>.
- Pellegrini, Luca, David S. Yu, Thomas Lo, Shubha Anand, MiYoung Lee, Tom L. Blundell, and Ashok R. Venkitaraman. "Insights into DNA Recombination from the Structure of a RAD51-BRCA2 Complex." *Nature* 420, no. 6913 (November 21, 2002): 287–93. <https://doi.org/10.1038/nature01230>.
- Petalcorin, Mark I. R., Vitold E. Galkin, Xiong Yu, Edward H. Egelman, and Simon J. Boulton. "Stabilization of RAD-51-DNA Filaments via an Interaction Domain in *Caenorhabditis Elegans* BRCA2." *Proceedings of the National Academy of Sciences of the United States of America* 104, no. 20 (May 15, 2007): 8299–8304. <https://doi.org/10.1073/pnas.0702805104>.
- Pittman, D. L., and J. C. Schimenti. "Recombination in the Mammalian Germ Line." *Current Topics in Developmental Biology* 37 (1998): 1–35. [https://doi.org/10.1016/s0070-2153\(08\)60170-2](https://doi.org/10.1016/s0070-2153(08)60170-2).
- Punjani, Ali, John L. Rubinstein, David J. Fleet, and Marcus A. Brubaker. "CryoSPARC: Algorithms for Rapid Unsupervised Cryo-EM Structure Determination." *Nature Methods* 14, no. 3 (March 2017): 290–96. <https://doi.org/10.1038/nmeth.4169>.
- Rao, H. B. D. Prasada, Huanyu Qiao, Shubhang K. Bhatt, Logan R. J. Bailey, Hung D. Tran, Sarah L. Bourne, Wendy Qiu, et al. "A SUMO-Ubiquitin Relay Recruits Proteasomes to Chromosome Axes to Regulate Meiotic Recombination." *Science (New York, N.Y.)* 355, no. 6323 (January 27, 2017): 403–7. <https://doi.org/10.1126/science.aaf6407>.
- Reichen, Christian, Chaithanya Madhurantakam, Andreas Plückthun, and Peer R. E. Mittl. "Crystal Structures of Designed Armadillo Repeat Proteins: Implications of Construct Design and Crystallization Conditions on Overall Structure." *Protein Science: A Publication of the Protein Society* 23, no. 11 (November 2014): 1572–83. <https://doi.org/10.1002/pro.2535>.
- Reuter, Marcel, Alex Zelensky, Ihor Smal, Erik Meijering, Wiggert A. van Cappellen, H. Martijn de Gruiter, Gijsbert J. van Belle, et al. "BRCA2 Diffuses as Oligomeric Clusters with RAD51 and Changes Mobility after DNA Damage in Live Cells." *The Journal of Cell Biology* 207, no. 5 (December 8, 2014): 599–613. <https://doi.org/10.1083/jcb.201405014>.
- Ribeiro, Felipe V., João A. Sá, Giovana O. Fistarol, Paulo S. Salomon, Renato C. Pereira, Maria Luiza A. M. Souza, Leonardo M. Neves, et al. "Long-Term Effects of Competition and Environmental Drivers on the Growth of the Endangered Coral *Mussismilia Braziliensis* (Verrill, 1867)." *PeerJ* 6 (2018): e5419. <https://doi.org/10.7717/peerj.5419>.
- Ribeiro, Jonathan, Emilie Abby, Gabriel Livera, and Emmanuelle Martini. "RPA Homologs and SsDNA Processing during Meiotic Recombination." *Chromosoma* 125, no. 2 (June 2016): 265–76. <https://doi.org/10.1007/s00412-015-0552-7>.
- Ribeiro, Jonathan, Pauline Dupaigne, Cynthia Petrillo, Cécile Ducrot, Clotilde Duquenne, Xavier Veaute, Carole Saintomé, et al. "The Meiosis-Specific MEIOB-SPATA22 Complex Cooperates with RPA to Form a Compacted Mixed MEIOB/SPATA22/RPA/SsDNA Complex." *DNA Repair* 102 (June 2021): 103097. <https://doi.org/10.1016/j.dnarep.2021.103097>.
- Robert, Thomas, Nathalie Vrielynck, Christine Mézard, Bernard de Massy, and Mathilde Grelon. "A New Light on the Meiotic DSB Catalytic Complex." *Seminars in Cell & Developmental Biology* 54 (June 2016): 165–76. <https://doi.org/10.1016/j.semcdb.2016.02.025>.

- Robertson, Ragan B., Dana N. Moses, YoungHo Kwon, Pamela Chan, Peter Chi, Hannah Klein, Patrick Sung, and Eric C. Greene. "Structural Transitions within Human Rad51 Nucleoprotein Filaments." *Proceedings of the National Academy of Sciences of the United States of America* 106, no. 31 (August 4, 2009): 12688–93. <https://doi.org/10.1073/pnas.0811465106>.
- Sakkiah, Sugunadevi, Silvia Senese, Qianfan Yang, Keun Woo Lee, and Jorge Z. Torres. "Dynamic and Multi-Pharmacophore Modeling for Designing Polo-Box Domain Inhibitors." Edited by Pratul K. Agarwal. *PLoS ONE* 9, no. 7 (July 18, 2014): e101405. <https://doi.org/10.1371/journal.pone.0101405>.
- Sánchez, Humberto, Maarten W. Paul, Malgorzata Grosbart, Sarah E. van Rossum-Fikkert, Joyce H. G. Lebbink, Roland Kanaar, Adriaan B. Houtsmuller, and Claire Wyman. "Architectural Plasticity of Human BRCA2-RAD51 Complexes in DNA Break Repair." *Nucleic Acids Research* 45, no. 8 (May 5, 2017): 4507–18. <https://doi.org/10.1093/nar/gkx084>.
- Sarge, K. D., S. P. Murphy, and R. I. Morimoto. "Activation of Heat Shock Gene Transcription by Heat Shock Factor 1 Involves Oligomerization, Acquisition of DNA-Binding Activity, and Nuclear Localization and Can Occur in the Absence of Stress." *Molecular and Cellular Biology* 13, no. 3 (March 1993): 1392–1407. <https://doi.org/10.1128/mcb.13.3.1392-1407.1993>.
- Sato, Koichi, Inger Brandsma, Sari E. van Rossum-Fikkert, Nicole Verkaik, Anneke B. Oostra, Josephine C. Dorsman, Dik C. van Gent, Puck Knipscheer, Roland Kanaar, and Alex N. Zelensky. "HSF2BP Negatively Regulates Homologous Recombination in DNA Interstrand Crosslink Repair." *Nucleic Acids Research* 48, no. 5 (March 18, 2020): 2442–56. <https://doi.org/10.1093/nar/gkz1219>.
- Schlacher, Katharina, Nicole Christ, Nicolas Siaud, Akinori Egashira, Hong Wu, and Maria Jasin. "Double-Strand Break Repair-Independent Role for BRCA2 in Blocking Stalled Replication Fork Degradation by MRE11." *Cell* 145, no. 4 (May 13, 2011): 529–42. <https://doi.org/10.1016/j.cell.2011.03.041>.
- Scully, Ralph, Arvind Panday, Rajula Elango, and Nicholas A. Willis. "DNA Double-Strand Break Repair-Pathway Choice in Somatic Mammalian Cells." *Nature Reviews. Molecular Cell Biology* 20, no. 11 (November 2019): 698–714. <https://doi.org/10.1038/s41580-019-0152-0>.
- Sehorn, Michael G., Stefan Sigurdsson, Wendy Bussen, Vinzenz M. Unger, and Patrick Sung. "Human Meiotic Recombinase Dmc1 Promotes ATP-Dependent Homologous DNA Strand Exchange." *Nature* 429, no. 6990 (May 27, 2004): 433–37. <https://doi.org/10.1038/nature02563>.
- Serber, Daniel W., John S. Runge, Debashish U. Menon, and Terry Magnuson. "The Mouse INO80 Chromatin-Remodeling Complex Is an Essential Meiotic Factor for Spermatogenesis." *Biology of Reproduction* 94, no. 1 (January 2016): 8. <https://doi.org/10.1095/biolreprod.115.135533>.
- Sfeir, Agnel, and Lorraine S. Symington. "Microhomology-Mediated End Joining: A Back-up Survival Mechanism or Dedicated Pathway?" *Trends in Biochemical Sciences* 40, no. 11 (November 2015): 701–14. <https://doi.org/10.1016/j.tibs.2015.08.006>.
- Sha, Jiahao, Zuomin Zhou, Jianmin Li, Lanlan Yin, Huanmin Yang, Gengxi Hu, Ming Luo, Hsiao Chang Chan, Kaiya Zhou, and Spermatogenesis study group. "Identification of Testis Development and Spermatogenesis-Related Genes in Human and Mouse Testes Using CDNA Arrays." *Molecular Human Reproduction* 8, no. 6 (June 2002): 511–17. <https://doi.org/10.1093/molehr/8.6.511>.
- Shahid, Taha, Joanna Soroka, Eric Kong, Laurent Malivert, Michael J. McIlwraith, Tillman Pape, Stephen C. West, and Xiaodong Zhang. "Structure and Mechanism of Action of the BRCA2 Breast Cancer Tumor Suppressor." *Nature Structural & Molecular Biology* 21, no. 11 (November 2014): 962–68. <https://doi.org/10.1038/nsmb.2899>.

- Shang, Yongliang, Tao Huang, Hongbin Liu, Yanlei Liu, Heng Liang, Xiaoxia Yu, Mengjing Li, et al. "MEIOK21: A New Component of Meiotic Recombination Bridges Required for Spermatogenesis." *Nucleic Acids Research* 48, no. 12 (July 9, 2020): 6624–39. <https://doi.org/10.1093/nar/gkaa406>.
- Sharan, S. K., M. Morimatsu, U. Albrecht, D. S. Lim, E. Regel, C. Dinh, A. Sands, G. Eichele, P. Hasty, and A. Bradley. "Embryonic Lethality and Radiation Hypersensitivity Mediated by Rad51 in Mice Lacking Brca2." *Nature* 386, no. 6627 (April 24, 1997): 804–10. <https://doi.org/10.1038/386804a0>.
- Sharan, Shyam K., April Pyle, Vincenzo Coppola, Janice Babus, Srividya Swaminathan, Jamie Benedict, Deborah Swing, et al. "BRCA2 Deficiency in Mice Leads to Meiotic Impairment and Infertility." *Development (Cambridge, England)* 131, no. 1 (January 2004): 131–42. <https://doi.org/10.1242/dev.00888>.
- Shibata, Atsushi. "Regulation of Repair Pathway Choice at Two-Ended DNA Double-Strand Breaks." *Mutation Research* 803–805 (October 2017): 51–55. <https://doi.org/10.1016/j.mrfmmm.2017.07.011>.
- Shibuya, Hiroki, Akihiro Morimoto, and Yoshinori Watanabe. "The Dissection of Meiotic Chromosome Movement in Mice Using an in Vivo Electroporation Technique." *PLoS Genetics* 10, no. 12 (December 2014): e1004821. <https://doi.org/10.1371/journal.pgen.1004821>.
- Shinohara, A., and M. Shinohara. "Roles of RecA Homologues Rad51 and Dmc1 during Meiotic Recombination." *Cytogenetic and Genome Research* 107, no. 3–4 (2004): 201–7. <https://doi.org/10.1159/000080598>.
- Shinohara, A., M. Shinohara, T. Ohta, S. Matsuda, and T. Ogawa. "Rad52 Forms Ring Structures and Co-Operates with RPA in Single-Strand DNA Annealing." *Genes to Cells: Devoted to Molecular & Cellular Mechanisms* 3, no. 3 (March 1998): 145–56. <https://doi.org/10.1046/j.1365-2443.1998.00176.x>.
- Siaud, Nicolas, Eloïse Dray, Isabelle Gy, Emmanuelle Gérard, Najat Takvorian, and Marie-Pascale Doutriaux. "Brca2 Is Involved in Meiosis in Arabidopsis Thaliana as Suggested by Its Interaction with Dmc1." *The EMBO Journal* 23, no. 6 (March 24, 2004): 1392–1401. <https://doi.org/10.1038/sj.emboj.7600146>.
- Sidhu, Arshdeep, Małgorzata Grosbart, Humberto Sánchez, Bram Verhagen, Nick L. L. van der Zon, Dejan Ristić, Sarah E. van Rossum-Fikkert, and Claire Wyman. "Conformational Flexibility and Oligomerization of BRCA2 Regions Induced by RAD51 Interaction." *Nucleic Acids Research* 48, no. 17 (September 25, 2020): 9649–59. <https://doi.org/10.1093/nar/gkaa648>.
- Simpson, Andrew J. G., Otavia L. Caballero, Achim Jungbluth, Yao-Tseng Chen, and Lloyd J. Old. "Cancer/Testis Antigens, Gametogenesis and Cancer." *Nature Reviews. Cancer* 5, no. 8 (August 2005): 615–25. <https://doi.org/10.1038/nrc1669>.
- Smith, Ian M., Chad A. Glazer, Suhail K. Mithani, Michael F. Ochs, Wenyue Sun, Sheetal Bhan, Alexander Vostrov, et al. "Coordinated Activation of Candidate Proto-Oncogenes and Cancer Testes Antigens via Promoter Demethylation in Head and Neck Cancer and Lung Cancer." *PloS One* 4, no. 3 (2009): e4961. <https://doi.org/10.1371/journal.pone.0004961>.
- Söding, Johannes, Andreas Biegert, and Andrei N. Lupas. "The HHpred Interactive Server for Protein Homology Detection and Structure Prediction." *Nucleic Acids Research* 33, no. Web Server issue (July 1, 2005): W244–248. <https://doi.org/10.1093/nar/gki408>.
- Song, Yifan, Frank DiMaio, Ray Yu-Ruei Wang, David Kim, Chris Miles, Tj Brunette, James Thompson, and David Baker. "High-Resolution Comparative Modeling with RosettaCM." *Structure (London, England: 1993)* 21, no. 10 (October 8, 2013): 1735–42. <https://doi.org/10.1016/j.str.2013.08.005>.

- Souquet, Benoit, Emilie Abby, Roxane Hervé, Friederike Finsterbusch, Sophie Tourpin, Ronan Le Bouffant, Clotilde Duquenne, et al. "Meiob Targets Single-Strand Dna and Is Necessary for Meiotic Recombination." *PLoS Genetics* 9, no. 9 (2013): e1003784. <https://doi.org/10.1371/journal.pgen.1003784>.
- Stasiak, A. Z., E. Larquet, A. Stasiak, S. Müller, A. Engel, E. Van Dyck, S. C. West, and E. H. Egelman. "The Human Rad52 Protein Exists as a Heptameric Ring." *Current Biology: CB* 10, no. 6 (March 23, 2000): 337–40. [https://doi.org/10.1016/s0960-9822\(00\)00385-7](https://doi.org/10.1016/s0960-9822(00)00385-7).
- Strebhardt, Klaus, and Axel Ullrich. "Targeting Polo-like Kinase 1 for Cancer Therapy." *Nature Reviews. Cancer* 6, no. 4 (April 2006): 321–30. <https://doi.org/10.1038/nrc1841>.
- Stumpe, Susanne, Stephan König, and Renate Ulbrich-Hofmann. "Insights into the Structure of Plant Alpha-Type Phospholipase D." *The FEBS Journal* 274, no. 10 (May 2007): 2630–40. <https://doi.org/10.1111/j.1742-4658.2007.05798.x>.
- Sunkel, C.E., and D.M. Glover. "Polo, a Mitotic Mutant of *Drosophila* Displaying Abnormal Spindle Poles." *Journal of Cell Science* 89, no. 1 (January 1, 1988): 25–38. <https://doi.org/10.1242/jcs.89.1.25>.
- Svergun, Dmitri I, and Michel H J Koch. "Small-Angle Scattering Studies of Biological Macromolecules in Solution." *Reports on Progress in Physics* 66, no. 10 (October 1, 2003): 1735–82. <https://doi.org/10.1088/0034-4885/66/10/R05>.
- Symington, Lorraine S. "Role of RAD52 Epistasis Group Genes in Homologous Recombination and Double-Strand Break Repair." *Microbiology and Molecular Biology Reviews: MMBR* 66, no. 4 (December 2002): 630–70, table of contents. <https://doi.org/10.1128/MMBR.66.4.630-670.2002>.
- Szabo, C., A. Masiello, J. F. Ryan, and L. C. Brody. "The Breast Cancer Information Core: Database Design, Structure, and Scope." *Human Mutation* 16, no. 2 (2000): 123–31. [https://doi.org/10.1002/1098-1004\(200008\)16:2<123::AID-HUMU4>3.0.CO;2-Y](https://doi.org/10.1002/1098-1004(200008)16:2<123::AID-HUMU4>3.0.CO;2-Y).
- Takaoka, Miho, Hiroko Saito, Katsuya Takenaka, Yoshio Miki, and Akira Nakanishi. "BRCA2 Phosphorylated by PLK1 Moves to the Midbody to Regulate Cytokinesis Mediated by Nonmuscle Myosin IIC." *Cancer Research* 74, no. 5 (March 1, 2014): 1518–28. <https://doi.org/10.1158/0008-5472.CAN-13-0504>.
- Takemoto, Kazumasa, Naoki Tani, Yuki Takada-Horisawa, Sayoko Fujimura, Nobuhiro Tanno, Mariko Yamane, Kaho Okamura, Michihiko Sugimoto, Kimi Araki, and Kei-Ichiro Ishiguro. "Meiosis-Specific C19orf57/4930432K21Rik/BRME1 Modulates Localization of RAD51 and DMC1 to DSBs in Mouse Meiotic Recombination." *Cell Reports* 31, no. 8 (May 26, 2020): 107686. <https://doi.org/10.1016/j.celrep.2020.107686>.
- Tang, Qin, Sowmya Iyer, Riadh Lobbardi, John C. Moore, Huidong Chen, Caleb Lareau, Christine Hebert, et al. "Dissecting Hematopoietic and Renal Cell Heterogeneity in Adult Zebrafish at Single-Cell Resolution Using RNA Sequencing." *Journal of Experimental Medicine* 214, no. 10 (October 2, 2017): 2875–87. <https://doi.org/10.1084/jem.20170976>.
- Thompson, Rebecca F., Matt Walker, C. Alistair Siebert, Stephen P. Muench, and Neil A. Ranson. "An Introduction to Sample Preparation and Imaging by Cryo-Electron Microscopy for Structural Biology." *Methods (San Diego, Calif.)* 100 (May 1, 2016): 3–15. <https://doi.org/10.1016/j.ymeth.2016.02.017>.
- Thorslund, Tina, Fumiko Esashi, and Stephen C. West. "Interactions between Human BRCA2 Protein and the Meiosis-Specific Recombinase DMC1." *The EMBO Journal* 26, no. 12 (June 20, 2007): 2915–22. <https://doi.org/10.1038/sj.emboj.7601739>.
- Tubbs, Anthony, and André Nussenzweig. "Endogenous DNA Damage as a Source of Genomic Instability in Cancer." *Cell* 168, no. 4 (February 9, 2017): 644–56. <https://doi.org/10.1016/j.cell.2017.01.002>.
- Tunyasuvunakool, Kathryn, Jonas Adler, Zachary Wu, Tim Green, Michal Zielinski, Augustin Židek, Alex Bridgland, et al. "Highly Accurate Protein Structure Prediction for the Human

- Proteome.” *Nature* 596, no. 7873 (August 2021): 590–96. <https://doi.org/10.1038/s41586-021-03828-1>.
- Van Houten, Bennett, Gloria A. Santa-Gonzalez, and Mauricio Camargo. “DNA Repair after Oxidative Stress: Current Challenges.” *Current Opinion in Toxicology* 7 (February 2018): 9–16. <https://doi.org/10.1016/j.cotox.2017.10.009>.
- Van Pel, A., P. van der Bruggen, P. G. Coulie, V. G. Brichard, B. Lethé, B. van den Eynde, C. Uyttenhove, J. C. Renauld, and T. Boon. “Genes Coding for Tumor Antigens Recognized by Cytolytic T Lymphocytes.” *Immunological Reviews* 145 (June 1995): 229–50. <https://doi.org/10.1111/j.1600-065x.1995.tb00084.x>.
- Walker, J. R., R. A. Corpina, and J. Goldberg. “Structure of the Ku Heterodimer Bound to DNA and Its Implications for Double-Strand Break Repair.” *Nature* 412, no. 6847 (August 9, 2001): 607–14. <https://doi.org/10.1038/35088000>.
- Wang, Hailong, and Xingzhi Xu. “Microhomology-Mediated End Joining: New Players Join the Team.” *Cell & Bioscience* 7 (2017): 6. <https://doi.org/10.1186/s13578-017-0136-8>.
- Wang, Yurong, Ling Liu, Chen Tan, Guiquan Meng, Lanlan Meng, Hongchuan Nie, Juan Du, et al. “Novel MEIOB Variants Cause Primary Ovarian Insufficiency and Non-Obstructive Azoospermia.” *Frontiers in Genetics* 13 (2022): 936264. <https://doi.org/10.3389/fgene.2022.936264>.
- Wartosch, Lena, Karen Schindler, Melina Schuh, Jennifer R. Gruhn, Eva R. Hoffmann, Rajiv C. McCoy, and Jinchuan Xing. “Origins and Mechanisms Leading to Aneuploidy in Human Eggs.” *Prenatal Diagnosis* 41, no. 5 (April 2021): 620–30. <https://doi.org/10.1002/pd.5927>.
- Whelan, Donna R., Wei Ting C. Lee, Yandong Yin, Dylan M. Ofri, Keria Bermudez-Hernandez, Sarah Keegan, David Fenyo, and Eli Rothenberg. “Spatiotemporal Dynamics of Homologous Recombination Repair at Single Collapsed Replication Forks.” *Nature Communications* 9, no. 1 (September 24, 2018): 3882. <https://doi.org/10.1038/s41467-018-06435-3>.
- Whitehurst, Angelique W. “Cause and Consequence of Cancer/Testis Antigen Activation in Cancer.” *Annual Review of Pharmacology and Toxicology* 54 (2014): 251–72. <https://doi.org/10.1146/annurev-pharmtox-011112-140326>.
- Wilkins, Deborah K., Shaun B. Grimshaw, Véronique Receveur, Christopher M. Dobson, Jonathan A. Jones, and Lorna J. Smith. “Hydrodynamic Radii of Native and Denatured Proteins Measured by Pulse Field Gradient NMR Techniques.” *Biochemistry* 38, no. 50 (December 1, 1999): 16424–31. <https://doi.org/10.1021/bi991765q>.
- Williamson, Mike P. “Using Chemical Shift Perturbation to Characterise Ligand Binding.” *Progress in Nuclear Magnetic Resonance Spectroscopy* 73 (August 2013): 1–16. <https://doi.org/10.1016/j.pnmrs.2013.02.001>.
- Wong, A. K., R. Pero, P. A. Ormonde, S. V. Tavtigian, and P. L. Bartel. “RAD51 Interacts with the Evolutionarily Conserved BRC Motifs in the Human Breast Cancer Susceptibility Gene Brca2.” *The Journal of Biological Chemistry* 272, no. 51 (December 19, 1997): 31941–44. <https://doi.org/10.1074/jbc.272.51.31941>.
- Wooster, R., G. Bignell, J. Lancaster, S. Swift, S. Seal, J. Mangion, N. Collins, S. Gregory, C. Gumbs, and G. Micklem. “Identification of the Breast Cancer Susceptibility Gene BRCA2.” *Nature* 378, no. 6559 (December 21, 1995): 789–92. <https://doi.org/10.1038/378789a0>.
- Wu, Yufan, Yang Li, Ghulam Murtaza, Jianteng Zhou, Yuying Jiao, Chenjia Gong, Congyuan Hu, et al. “Whole-Exome Sequencing of Consanguineous Families with Infertile Men and Women Identifies Homologous Mutations in SPATA22 and MEIOB.” *Human Reproduction (Oxford, England)* 36, no. 10 (September 18, 2021): 2793–2804. <https://doi.org/10.1093/humrep/deab185>.
- Xia, Bing, Qing Sheng, Koji Nakanishi, Akihiro Ohashi, Jianmin Wu, Nicole Christ, Xinggang Liu, Maria Jasin, Fergus J. Couch, and David M. Livingston. “Control of BRCA2 Cellular

- and Clinical Functions by a Nuclear Partner, PALB2.” *Molecular Cell* 22, no. 6 (June 23, 2006): 719–29. <https://doi.org/10.1016/j.molcel.2006.05.022>.
- Xu, Jingfei, Lingyun Zhao, Sijia Peng, Huiying Chu, Rui Liang, Meng Tian, Philip P. Connell, Guohui Li, Chunlai Chen, and Hong-Wei Wang. “Mechanisms of Distinctive Mismatch Tolerance between Rad51 and Dmc1 in Homologous Recombination.” *Nucleic Acids Research* 49, no. 22 (December 16, 2021): 13135–49. <https://doi.org/10.1093/nar/gkab1141>.
- Xu, X., P. A. Toselli, L. D. Russell, and D. C. Seldin. “Globozoospermia in Mice Lacking the Casein Kinase II Alpha’ Catalytic Subunit.” *Nature Genetics* 23, no. 1 (September 1999): 118–21. <https://doi.org/10.1038/12729>.
- Xu, Yang, Roger A. Greenberg, Ernst Schonbrunn, and P. Jeremy Wang. “Meiosis-Specific Proteins MEIOB and SPATA22 Cooperatively Associate with the Single-Stranded DNA-Binding Replication Protein A Complex and DNA Double-Strand Breaks.” *Biology of Reproduction* 96, no. 5 (May 1, 2017): 1096–1104. <https://doi.org/10.1093/biolre/iox040>.
- Xu, Yanhui, Yongna Xing, Yu Chen, Yang Chao, Zheng Lin, Eugene Fan, Jong W. Yu, Stefan Strack, Philip D. Jeffrey, and Yigong Shi. “Structure of the Protein Phosphatase 2A Holoenzyme.” *Cell* 127, no. 6 (December 2006): 1239–51. <https://doi.org/10.1016/j.cell.2006.11.033>.
- Yang, Haijuan, Philip D. Jeffrey, Julie Miller, Elspeth Kinnucan, Yutong Sun, Nicolas H. Thoma, Ning Zheng, Phang-Lang Chen, Wen-Hwa Lee, and Nikola P. Pavletich. “BRCA2 Function in DNA Binding and Recombination from a BRCA2-DSS1-SsDNA Structure.” *Science (New York, N.Y.)* 297, no. 5588 (September 13, 2002): 1837–48. <https://doi.org/10.1126/science.297.5588.1837>.
- Yang, Jianyi, Ivan Anishchenko, Hahnbeom Park, Zhenling Peng, Sergey Ovchinnikov, and David Baker. “Improved Protein Structure Prediction Using Predicted Interresidue Orientations.” *Proceedings of the National Academy of Sciences of the United States of America* 117, no. 3 (January 21, 2020): 1496–1503. <https://doi.org/10.1073/pnas.1914677117>.
- Yao, Chencheng, Dong Hou, Zhiyong Ji, Dongmei Pang, Peng Li, Ruhui Tian, Yuxiang Zhang, et al. “Bi-Allelic SPATA22 Variants Cause Premature Ovarian Insufficiency and Nonobstructive Azoospermia Due to Meiotic Arrest.” *Clinical Genetics* 101, no. 5–6 (May 2022): 507–16. <https://doi.org/10.1111/cge.14129>.
- Yoshima, T., T. Yura, and H. Yanagi. “Novel Testis-Specific Protein That Interacts with Heat Shock Factor 2.” *Gene* 214, no. 1–2 (July 3, 1998): 139–46. [https://doi.org/10.1016/s0378-1119\(98\)00208-x](https://doi.org/10.1016/s0378-1119(98)00208-x).
- Yu, X., S. A. Jacobs, S. C. West, T. Ogawa, and E. H. Egelman. “Domain Structure and Dynamics in the Helical Filaments Formed by RecA and Rad51 on DNA.” *Proceedings of the National Academy of Sciences of the United States of America* 98, no. 15 (July 17, 2001): 8419–24. <https://doi.org/10.1073/pnas.111005398>.
- Zakharyevich, Kseniya, Shangming Tang, Yunmei Ma, and Neil Hunter. “Delineation of Joint Molecule Resolution Pathways in Meiosis Identifies a Crossover-Specific Resolvase.” *Cell* 149, no. 2 (April 13, 2012): 334–47. <https://doi.org/10.1016/j.cell.2012.03.023>.
- Zhang, Jingjing, Yasuhiro Fujiwara, Shohei Yamamoto, and Hiroki Shibuya. “A Meiosis-Specific BRCA2 Binding Protein Recruits Recombinases to DNA Double-Strand Breaks to Ensure Homologous Recombination.” *Nature Communications* 10, no. 1 (February 13, 2019): 722. <https://doi.org/10.1038/s41467-019-08676-2>.
- Zhang, Jingjing, Manickam Gurusaran, Yasuhiro Fujiwara, Kexin Zhang, Meriem Echbarhi, Egor Vorontsov, Rui Guo, et al. “The BRCA2-MEILB2-BRME1 Complex Governs Meiotic Recombination and Impairs the Mitotic BRCA2-RAD51 Function in Cancer Cells.” *Nature Communications* 11, no. 1 (April 28, 2020): 2055. <https://doi.org/10.1038/s41467-020-15954-X>.

- Zhang, Jingjing, Jayakrishnan Nandakumar, and Hiroki Shibuya. "BRCA2 in Mammalian Meiosis." *Trends in Cell Biology* 32, no. 4 (April 2022): 281–84. <https://doi.org/10.1016/j.tcb.2021.09.003>.
- Zhao, Weixing, and Patrick Sung. "Significance of Ligand Interactions Involving Hop2-Mnd1 and the RAD51 and DMC1 Recombinases in Homologous DNA Repair and XX Ovarian Dysgenesis." *Nucleic Acids Research* 43, no. 8 (April 30, 2015): 4055–66. <https://doi.org/10.1093/nar/gkv259>.
- Zhao, Weixing, Sivaraja Vaithiyalingam, Joseph San Filippo, David G. Maranon, Judit Jimenez-Sainz, Gerald V. Fontenay, Youngho Kwon, et al. "Promotion of BRCA2-Dependent Homologous Recombination by DSS1 via RPA Targeting and DNA Mimicry." *Molecular Cell* 59, no. 2 (July 16, 2015): 176–87. <https://doi.org/10.1016/j.molcel.2015.05.032>.
- Zickler, Denise, and Nancy Kleckner. "A Few of Our Favorite Things: Pairing, the Bouquet, Crossover Interference and Evolution of Meiosis." *Seminars in Cell & Developmental Biology* 54 (June 2016): 135–48. <https://doi.org/10.1016/j.semcdb.2016.02.024>.
- . "Recombination, Pairing, and Synapsis of Homologs during Meiosis." *Cold Spring Harbor Perspectives in Biology* 7, no. 6 (May 18, 2015): a016626. <https://doi.org/10.1101/cshperspect.a016626>.
- Zimmerman, E. H. "Subungual Exostosis." *Cutis* 19, no. 2 (February 1977): 185–88.
- N.d.

